2006
Contents and Structures of the Universe

Sponsored by

. CNRS (Centre National de la Recherche Scientifique)
. CEA (Commissariat à l'Énergie Atomique)
. EU (European Union)
. IN2P3 (Institut National de Physique Nucléaire et de Physique des Particules)

XLIst Rencontres de Moriond
La Thuile, Val d'Aoste, Italie – March 18- 25, 2006

2006 Contents and Structures of the Universe

© Thế Giới Publishers
Printed in Vietnam
VN-TG-7176-1 (27-9-2006)

Proceedings of the XLIst RENCONTRES DE MORIOND
Contents and Strutures of the Universe
La Thuile, Val d'Aoste, Italie March 18 - 25, 2006

2006
Contents and Structures of the Universe

edited by

Christophe Magneville
Réza Ansari
Jacques Dumarchez
and
Jean Trân Thanh Vân

THẾ GIỚI
PUBLISHERS

The Cosmology Session of the XLIst Rencontres de Moriond

was organized by

J. Trân Thanh Vân (Orsay)

with the active collaboration of:

R. Ansari (Orsay),
M. Bucher (Orsay),
C. Canizares, (MIT)
J. Dumarchez (Paris),
K. Ganga (Paris),
Y. Giraud-Héraud (Paris),
D. Langlois (Paris),
C. Magneville (Saclay),
P. Petitjean (Paris),
J. Rich (Saclay).

2006 RENCONTRES DE MORIOND

The XLIst Rencontres de Moriond were held in La Thuile, Vallée d'Aoste, Italie.

The first meeting took place at Moriond in the French Alps in 1966. There, experimental as well as theoretical physicists not only shared their scientific preoccupations, but also the household chores. The participants in the first meeting were mainly French physicists interested in electromagnetic interactions. In subsequent years, a session on high energy strong interactions was also added.

The main purpose of these meeting is to discuss recent developments in contemporary physics and also to promote effective collaboration between experimentalists and theorists in the field of elementary particle physics. By bringing together a relatively small number of participants, the meeting helps to develop better human relations as well as a more thorough and detailed discussion of the contributions.

This concern of research and experimentation of new channels of communication and dialogue which from the start animated the Moriond meetings, inspired us to organize a simultaneous meeting of biologists on Cell Differenciation (1980) and to create the Moriond Astrophysics Meeting (1981). In the same spirit, we have started a new series on Condensed Matter Physics in January 1994. Common meetings between biologists, astrophysicists, condensed matter physicists and high energy physicists are organized to study the implications of the advances of one field into the others. I hope that these conferences and lively discussions may give birth to new analytical methods or new mathematical languages.

At the XLIst Rencontres de Moriond in 2006, three Physics sessions, and one Astrophysics session were held :

* March 11 - 18	"Electroweak Interactions and Unified Theories"
	"From Dark Halos to Light: Mass-to-Light Ratio versus Scale"
* March 18 – 25	"QCD and High Energy Hadronic Interactions"
	"Contents and Structures of the Universe"

I thank the organizers of the XLIST Rencontres de Moriond:

. A. Abada, A. Blondel, S. Davidson, P. Fayet, J.-M. Frère, H. Frisch, P. Hernandez, L. Iconnomidou-Fayard, M. Knecht, J. P. Lees, S. Loucatos, F. Montanet, L. Okun, A. Pich, S. Pokorski, G. Unal and D. Wood for the "Electroweak Interactions and Unified Theories" session,

. Laurence Tresse, Sophie Maurogordato, Nabila Aghanim, Alberto Cappi, Thierry Contini, David Elbaz, Eric Emsellem, Romain Teyssier, Marie Treyer, for the "From Dark Halos to Light : Mass-to-Light Ratio versus Scale" session

. E. Augé, E. Berger, S. Bethke, A. Capella, A. Czarnecki, D. Denegri, Y. Dokshitzer, N. Glover, B. Klima, L. Kluberg, M. Krawczyk, L. McLerran, B. Pietrzyk, Chung-I Tan and U. Wiedemann for the "QCD and High Energy Hadronic Interactions" session,

. R. Ansari, M. Bucher, C. Canizares, J. Dumarchez, K. Ganga, Y. Giraud-Héraud, D. Langlois, C. Magneville, P. Petitjean, J. Rich for the "Contents and Structures of the Universe" sesssion,

and the conference secretariat : C. Bareille, P. Chémali, I. Cossin, G. Dreneau, E. Hautefeuille, G. Hérent, M. Joguet, M. Jouhet, Pham Duy Tu, F. Warin and V. Zorica. I would like to thank particularly E. Hautefeuille who has taken care of the preparation of these proceedings. Special thanks to M.P. Bardey and N. Ribet for their gratefull contribution to these conferences since 1966, and for their precious memory of the spirit of Moriond.

I am also grateful to Enrico Belli, Fillippo Lucchini, Gian Luca Mazzeo, and Gian Franco Raino who contributed through their hospitality and cooperation to the well-being of the participants, enabling them to work in a relaxed atmosphere.

These Rencontres were sponsored by the European Union "Human Resources and Mobility" Activity, the Centre National de la Recherche Scientifique (INSU, SPM and FP), the "Centre National d'Études Spatiales", the European Space Agency, the Institut National de Physique Nucléaire et de Physique des Particules (IN2P3-CNRS), the Commissariat à l'Energie Atomique (DAPNIA) and the National Science Foundation. I would like to express my thanks for their encouraging support.

I sincerely wish that a fruitful exchange and an efficient collaboration between the physicists and the astrophysicists will arise from these Rencontres as from the previous ones.

J. Trân Thanh Vân

Contents and Structures of the Universe

XLIst Rencontres de Moriond
La Thuile, Italy (March 18 – March 25, 2006)

I – STANDARD MODEL AND COSMOLOGY PARAMETERS

CMB MAPS WITH CUBIC CORRELATIONS

RICHARD A. BATTYE AND ADAM MOSS
Jodrell Bank Observatory, University of Manchester, Macclesfield SK11 9DL, U.K.

In a recent paper we have suggested that the effects of a cubic symmetric network of domain walls, constituting the dark energy with $P/\rho = -2/3$, could create correlations in the cosmic microwave background qualitatively similar to those which have been observed. In this short note, we review the basic idea and go onto discuss a toy model for such correlations based on symmetry adapted harmonics (SASHs).

1 Anisotropic perturbations from dark energy

The assumption of global statistical isotropy (GSI) is one of the most fundamental and commonly accepted principles in cosmology. Therefore, it has been a surprise that the maps of the cosmic microwave background (CMB) published by the WMAP team [1] appear to be incompatible with this assumption on the very largest scales [2,3]. Given the very encouraging agreement of measurements on intermediate and small scales with the ΛCDM model, which is based on the GSI assumption, one might be tempted to ignore these anomalies, passing them off as an unknown instrumental systematic, a consequence of imperfect foreground subtraction, or a combination of both. However, no compelling explanation of this kind has yet been found and attempts to explain the observations as being due to known local structures cannot provide a sufficiently strong effect [4].

In a recent paper [5], we have put forward an idea which could, at least qualitatively, explain this phenomenon. It is based on the idea that the dark energy, thought to be responsible for the accelerated expansion of the universe, is a static lattice of domain walls, formed at a low-energy scale phase transition due to an unknown discrete symmetry. Such a lattice would behave as a relativistic analog of a soap film and its macroscopic behaviour could be described by an elastic continuum medium similar to a solid; the stability of the lattice is achieved due to the rigidity of the network. The medium would have $w = P/\rho \approx -2/3$ (P is the pressure and ρ is the density) and a relativistic sound speed which allow only perturbations on the largest scales to collapse. We note that $w = -2/3$, while not observationally favoured, is not incompatible with the present data [6].

The important thing to realise is that, due to causality, the lattice of walls cannot be compatible with GSI — there will be natural imperfections in the lattice as a consequence of the phase transition and the subsequent "solidification" process. Fortunately, the theory of relativistic elasticity used to model the perturbations in the energy-momentum tensor has the facility to incorporate anisotropy [7]. In fact, it was pointed out that anisotropic perturbations can be classified by the well-known Bravais lattices used in solid state physics. For definiteness, we will consider the case where the lattice has cubic symmetry in the subsequent discussion since it is the simplest case beyond GSI. Most of what we shall say can be adapted to more general

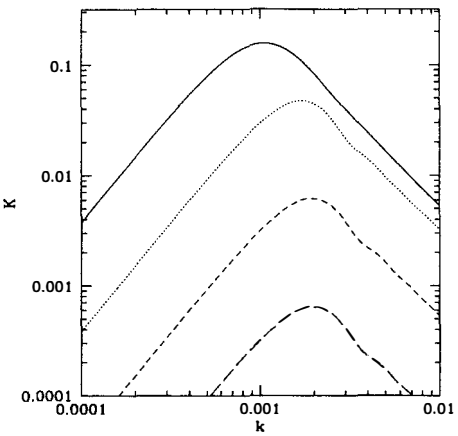

Figure 1: The normalized variance of the power spectrum, K, for a simple model with $w = -2/3$. The curves show varying levels of anisotropy $\Delta\mu/\rho$=0.1, 0.01, 10^{-3}, 10^{-4}, from top to bottom.

models.

In this simple (and probably unrealistic case) the anisotropy of the perturbations can be quantified in terms of the difference between the transverse rigidity, $\mu_{\rm T}$, and the longitudinal rigidity, $\mu_{\rm L}$, that is $\Delta\mu = \mu_{\rm T} - \mu_{\rm L}$. In fig. 1, we plot the kurtosis of the total density field (cold dark matter plus dark energy) on very large scales as a function of $\Delta\mu/\rho$. It can been seen that the largest violations of Gaussianity, which are actually due to the anisotropy (NB. one can be mistaken for the other [8]) are on scales probed by multipoles with $\ell < 10$ in the CMB anisotropy spectrum. This non-Gaussianity would lead to the power spectrum measured on different patches of the sky having unusual statistical properties and the fact that rotational invariance is broken will create correlations in the computed multipole coefficients. We shall show this explicitly in section 3.

2 Symmetry adapted harmonics

It is conventional to decompose the measured temperature anisotropies in terms of the natural orthogonal basis functions on a sphere, the spherical harmonics, $Y_{\ell m}(\hat{\mathbf{n}})$, and complex coefficients $a_{\ell m}$:

$$\frac{\Delta T}{T}(\hat{\mathbf{n}}) = \sum_{\ell,m} a_{\ell m} Y_{\ell m}(\hat{\mathbf{n}})\,. \tag{1}$$

Standard packages allow the calculation of the $a_{\ell m}$s from an observed map and most analyses of the maps are done in terms of them. Under the GSI assumption each of the real and imaginary parts of the coefficients are Gaussian random variables with zero mean and variance $C_\ell/\sqrt{2}$ where the C_ℓ can be computed for a given theory.

If a component of the CMB anisotropy has point symmetry (as suggested in the previous section) then the natural basis is not the spherical harmonics. This problem has been studied in the context of solid state physics and so-called symmetry adapted harmonics (SASHs) have been computed. These are combinations of the spherical harmonics which are compatible with the relevant symmetries.

In the case of cubic symmetry in a standard orientation relative to the Cartesian axes, it is clear that only ℓ even and m a multiple of 4 are allowed due to the four-fold symmetry. In the

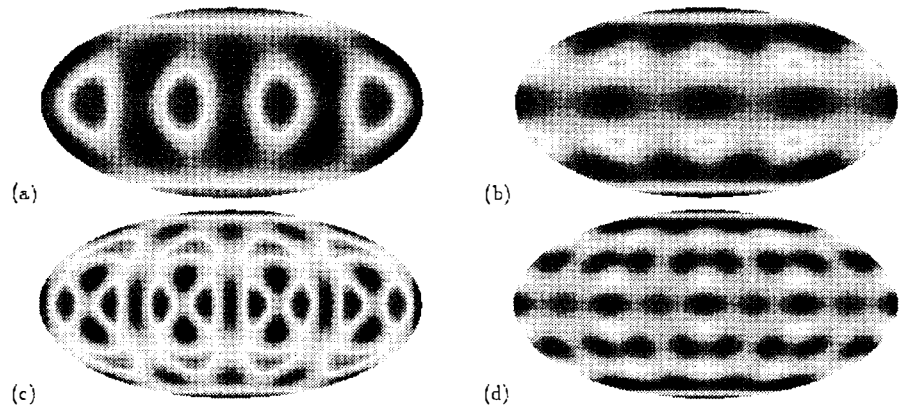

Figure 2: Hammer-Aitoff projections of the SASHs for (a) $\ell = 4$, (b) $\ell = 6$, (c) $\ell = 8$ and (d) $\ell = 10$. The cubic symmetry is visually apparent in these plots.

specific E_g representation of the O_h symmetry group (crystallographic group m3m) the SASHs for $\ell = 4, 6, 8, 10$ are[9]

$$\begin{aligned} X_4(\hat{\mathbf{n}}) &= 0.6455 Y_{4,0}(\hat{\mathbf{n}}) - 0.7638 Y^{\rm c}_{4,4}(\hat{\mathbf{n}}) , \\ X_6(\hat{\mathbf{n}}) &= 0.9354 Y_{6,0}(\hat{\mathbf{n}}) + 0.3536 Y^{\rm c}_{6,4}(\hat{\mathbf{n}}) , \\ X_8(\hat{\mathbf{n}}) &= 0.6960 Y_{8,0}(\hat{\mathbf{n}}) - 0.3940 Y^{\rm c}_{8,4}(\hat{\mathbf{n}}) - 0.6003 Y^{\rm c}_{8,8}(\hat{\mathbf{n}}) , \\ X_{10}(\hat{\mathbf{n}}) &= 0.9114 Y_{10,0}(\hat{\mathbf{n}}) + 0.2646 Y^{\rm c}_{10,4}(\hat{\mathbf{n}}) + 0.3150 Y^{\rm c}_{10,8}(\hat{\mathbf{n}}) , \end{aligned} \tag{2}$$

where $Y^{\rm c}_{\ell m}(\hat{\mathbf{n}}) = (Y_{\ell,m}(\hat{\mathbf{n}}) + Y_{\ell,-m}(\hat{\mathbf{n}}))/\sqrt{2}$. Maps in the Hammer-Aitoff projection of each of these modes are presented in fig. 2.

3 Toy model for cubic correlations

As a toy model let us consider an anisotropy field which comprises of two components, one which is a Gaussian random field specified by some C_ℓ and the other which has cubic correlations,

$$\frac{\Delta T}{T}(\hat{\mathbf{n}}) = \frac{\Delta T}{T}(\hat{\mathbf{n}})\Big|_{\rm Gaussian} + \frac{\Delta T}{T}(R\hat{\mathbf{n}})\Big|_{\rm cubic} , \tag{3}$$

where R is rotational matrix, specified by a direction and angle, with gives the orientation of the cubic symmetry relative to the Cartesian axes. The cubic component can be written in terms of the SASHs as

$$\frac{\Delta T}{T}(\hat{\mathbf{n}})\Big|_{\rm cubic} = \sum_l b_\ell X_\ell(\hat{\mathbf{n}}) , \tag{4}$$

where the b_ℓ are model dependent coefficients, which in principle can be computed for a specific model, and we have assumed that there is only one SASH for each value of ℓ, which is the case for low ℓ at least.

Each of the SASHs can be written in the form

$$X_\ell(\hat{\mathbf{n}}) = \sum_m c_{\ell m} Y_{\ell m}(\hat{\mathbf{n}}) , \tag{5}$$

where the $c_{\ell m}$s can be read off from eqn. 2. It is known that

$$Y_{\ell m}(R\hat{\mathbf{n}}) = \sum_{m'} D_{lmm'}(R) Y_{\ell m'}(\hat{\mathbf{n}}) \,, \tag{6}$$

where $D_{\ell mm'}(R)$ is the Wigner D-matrix associated with the rotation R, therefore if one decomposes the cubic component into spherical harmonics, one finds that the multipole coefficients are given by

$$a_{\ell m}^{\rm cubic} = b_\ell \sum_{m'} c_{\ell m'} D_{\ell m' m}(R) \,. \tag{7}$$

One can deduce from this that the cubic symmetry creates correlations amongst the multipole coefficients. It would be interesting to see if such an effect can be seen in the present data.

Acknowledgments

We have benefited from helpful conversations with Brandon Carter and Martin Bucher.

References

1. C.L. Bennett *et al*, ApJS **148**, 1 (2003).
2. H.K. Eriksen *et al*, ApJ **605**, 14 (2004).
3. K. Land and J. Magueijo, *Phys. Rev. Lett.* **95**, 071301 (2005)
4. C. Vale, astro-ph/0509039
5. R.A. Battye and A. Moss, astro-ph/0602377.
6. R.A. Battye and A. Moss, JCAP **0506**, 001 (2005)
7. L.D. Landau and E.M. Lifschitz, Thoery of Elasticity (Pergamon, London , 1959).
8. P. Ferreira and J. Mageuijo, *Phys. Rev.* D **56**, 4578 (1997)
9. C.J. Bradley and A.P. Cracknell, The Mathematical Theory of Symmetry in Solids (Clarendon Press, 1972).

Probing dark energy by a multi probe approach

A.Ealet
CPPM
CNRS/IN2P3-Luminy and Université de la Méditerranée,
Case 907, F-13288 Marseille Cedex 9, France

Evidence for the accelerated expansion of the Universe has accumulated in the last decade with the many cosmological observations from SNIa, CMB, cluster count, and most recently baryon oscillations. The theoretical origin of accelerated expansion remains one of the most challenging research activities today and a combination and comparison of different probes will help to discriminate different origins. In this contribution, we present a method, based on a frequentist approach, to combine different probes without any prior and constraints, As an application, a combination of current SNIa and CMB data with an evolving dark energy component is first compared to other analyses. The impact of future weak lensing surveys on the measurement of dark energy evolution is then studied in combination with future measurements of the cosmic microwave background and type Ia supernovae.

1 Introduction

Accelerated expansion on cosmological scales is one of the most challenging issue of the cosmology today. A homogeneous, isotropic, matter dominated universe, involving in the standard general relativity framework cannot accelerate. To generate acceleration, various theoretical schemes are currently invoked. The acceleration can be due to a cosmological constant or to a new component, named Dark Energy (DE), exhibiting or not an evolving energy density with negative pressure. In some models, this is the law of gravity on large scales which is modified.

Extracting dark energy properties thus requires a combined analysis of complementary data sets. Many combinations have already been performed in the literature with different types of data and procedures. We have choosen to use SNIa, CMB and weak lensing which seem powerful to constrain the parameters of an evolving equation of state when combined. Considering a flat Universe, we combine the data with a frequentist approach, avoiding the use of priors which means using the full correlations between the cosmological parameters and using identical assumptions for the dark energy properties of he 3 probes.

2 The framework

We have considered here 3 probes in two approachs:
-we first test our statistical method by an analysis of the first year of Wmap data [?] combined with the 'Gold sample' data of supernovae of type Ia compiled by Riess et al. [?]
-we then do simulations of mid term and a long term scenario with a fisher analysis. The mid term consist of adding the simulation of new data for the CMB expected from the Olimpo [?] balloon, a new supernovae SNIa sample from SNLS [?] and a weak lensing survey from the CFHTLS [?].

The long term scenario is a simulation of space projects as the Planck mission for CMB [?] and the SNAP/JDEM [?] project both for SNIa and weak lensing. For SNIa, we consider an intrinsic error of 0.15 for each supernova and we add an irreductible systematic error of 2 % on each redshift bin. A sample of 300 nearby SNIa as expected by SNfactory [?] is added in supernovae simulations. For the weak lensing simulation, we will only consider modes between $\ell = 10$ and 20000, avoiding small scales where instrumental systematics and theoretical uncertainties are more important.
The different assumptions used in these simulations for the mid term and long tèrm scenarii are summarised in Tab 1 of ref [?]. The framework and the tools used here can also be found in details in [?]. As it is not possible to constrain a completely unknown functional form $w(z)$ of the time evolution of the DE equation of state, we adopt a parametric representation: $w(z) = w_0 + w_a z/(1+z)$ which has an adequate asymptotic behaviour. We thus use two parameters, w_0 and w_a, to describe the time evolution of the equation of state.We have implemented the time evolving parametrization of the equation of state in simulations and analysis of the three probes we consider here.

We limit ourselves to the 9 cosmological parameters: $\theta = \Omega_b, \Omega_m, h, n_s, \tau, w_0, w_a, A$ and M_{s_0}, with the following standard definitions:
- (Ω_i , i=b,m) are densities for baryon and matter respectively (Ω_m includes both dark matter and baryons)
- h is the Hubble constant in units of 100 km/s/Mpc,
- n_s is the spectral index of the primordial power spectrum,
- τ is the reionisation optical depth,
- A is the normalisation parameter of the power spectrum for CMB and weak lensing (cf [?] for definitions). - M_{s_0} is the normalisation parameter from SNIa
- Dark energy is described by the previously defined w_0 and w_a parameters
The reference fiducial model of our simulation is a ΛCDM model with parameters $\Omega_m = 0.27$, $\Omega_b = 0.0463$, $n_s = 0.99$, $h = 0.72$, $\tau = 0.066$, $A = 0.86$, consistent with the first year data of the WMAP experiment. The universe is assumed flat. We also neglect the effect of neutrinos, using 3 degenerate families of neutrinos with masses fixed to 0.

We adopt a statistical approach based on a frequentist approach which consist on minimizing a $\chi^2(x, \sigma_x; \theta)$ with the MINUIT package [?]. We set a confidence level (CL) on any individual cosmological parameter θ_i by scanning the variable θ_i: for each fixed value of θ_i, we minimise again $\chi^2(x, \sigma_x; \theta)$ but with $n-1$ free parameters. The χ^2 difference, $\Delta\chi^2(\theta_i)$, between the new minimum and χ^2_0, allows us to compute the CL on the variable, assuming that the experimental errors are gaussian. This method can be easily extended to two variables. With this approach, the correlations between the variables are naturally taken into account and the minimisation fit can explore the whole phase space of the cosmological parameters. The full covariance matrix on all parameters is then used with no prior constraints on the parameters, avoiding biases from internal degeneracies. For the 9 parameters used here, each fit requires around 200 calculations of χ^2. The consumed CPU-time is dominated by the computation of the angular power spectrum (C_ℓ) of the CMB in CMBEASY [?]. This method is very powerful for studying the impacts of the parameters, since it is very simple to add or remove parameters, in contrast with the MCMC method, which requires the generation of a new chain.

3 Combination of current surveys

We first apply our statistical approach to the combination of SNIa and WMAP1 data, without any external constraints or priors. When the equation of state is considered constant, we obtain $w_0 = -0.92^{+0.10}_{-0.13}$ (1-σ) and the shape of the CL is relatively symmetrical around the value of w_0 obtained at the χ^2 minimum.

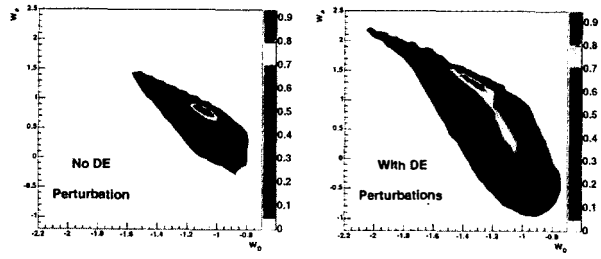

Figure 1: Contour plots with WMAP and SNIa data, for the 9 parameter fit with a z dependent EOS in the plane (w_0, w_a). Left hand plot has no dark energy perturbation.The right hand one have them when $w > -1$.

When a z dependence is added to the equation of state, the CL is still symmetrical with $w_0 = -1.09^{+0.13}_{-0.15}$ but w_a becomes asymmetrical with a long tail for smaller values of w_a. The 1-D CL for w_a gives the resulting CL at 68%(1σ) and 95%(2σ): $w_a = 0.82^{+0.21\ +0.42}_{-0.26\ -0.80}$. The solution found by the fit corresponds to a value of w slightly smaller than -1 for $z = 0$, and a value of w slightly larger than -1 for high z. The errors are such that the value of w is compatible with -1. However, this technically means that the Universe crosses the phantom line in its evolution. This region ($w < -1$) cannot be reached by the fit, if dark energy perturbations are computed in the CMBEASY version we use. We compare results when we removed the perturbations for the dark energy, and when we include them only when $w > -1$. The result is shown on the two plots of Fig. **??**. The first case is close to the result of Seljak et al. [?] who have likely removed dark energy perturbations but their central value is closer to $w = -1$ and gives errors for w_a larger than the ones we get.This can be explain by the different parametrisation and the bayesian approach they use.

Including dark energy perturbations only when $w > -1$, gives a minimum for $w_0 = -1.32^{+0.15}_{-0.19}$ and $w_a = 1.2^{+0.5}_{-0.8}$ at 1σ. This is some 2σ away from the no perturbation case. We remark that these values are very close to those obtained by Upadhye et al. [?], who use a procedure similar to ours, without any marginalisation on parameters, a weak constraint $w_0 + w_a \leq 0$ inside their fit. When dark energy perturbations are included, we observe also that the minimisation is more difficult and correlations between parameters increase.Then, we decided to to present simulated results without dark energy perturbations.

4 Simulation results

The combination of both mid term and long term data sets as described in section 1 is performed with, and without a redshift variation for the equation of state, Tab. **??** summarizes the different results. The SNLS survey combined with the nearby sample will improve the present precision on w by a factor 2. The expected contours from cosmic shear have the same behaviour as the CMB but provide a slightly better constraint on Ω_m and a different correlation with w: CMB and weak lensing data have a positive (w, Ω_m) correlation compared to SNIa data, which have a negative correlation. This explains the impressive gain when the three data sets are combined, yielding an expected precision for w of 10 %. Combining WMAP with Olimpo data helps to constrain w through the correlation matrix as Olimpo expects to have more information for the large ℓ of the power spectrum.

The simulated future space missions show an improved sensitivity to the time evolution of the equation of state. The combination of the probes with the full correlation matrix allows for the extraction of the whole information available. For instance, the large correlation between

Table 1: Expected sensitivity on cosmological parameters for three scenarii: Current supernova and CMB experiments, mid term and long term experiments as explain in the text. the 1σ errors are computed with the Fisher matrix techniques for 8 (9) free parameters in the first (second) column respectively.

Scenario	Today		Mid term		Long Term	
Ω_b	0.003	0.004	0.001	0.002	0.0008	0.0008
Ω_m	0.04	0.04	0.01	0.01	0.004	0.004
h	0.03	0.03	0.01	0.01	0.006	0.006
$\mathbf{n}_s$	0.03	0.03	0.006	0.009	0.003	0.003
τ	0.05	0.04	0.01	0.01	0.01	0.01
$\mathbf{w}_0$	0.11	0.22	0.02	0.10	0.02	0.04
$\mathbf{w}_a$	–	0.99	–	0.43	–	0.07
A	0.10	0.10	0.02	0.02	0.02	0.02
$\mathbf{M}_{s0}$	0.03	0.03	0.01	0.01	0.01	0.01

n_S and w_a observed for the weak lensing probe combined with the precised measurement of n_S given by the CMB, gives a better sensitivity on w_a than the simple combination of the two w_a values obtained separately for the CMB and weak lensing. Such an effect occurs for several other pairs of cosmological parameters considered in this study.

Finally, in the long term scenario, the weak lensing probe provides a sensitivity on the measurement of (w_0, w_a) comparable with those of the combined SN and CMB probes, whereas in the mid term scenario the information brought by weak lensing was marginal. Since we assign an irreducible systematic errors on SNIa and no systematic errors for WL estimation, conclusion should be taken with caution as it can have serious impacts on the final sensitivity and on the relative importance of each probe.

Acknowledgments

I want to thanks my collegues, C.Yèche, A. Réfrégier, D.Yvorf[a], C. Tao, A. Tilquin[b], J.-M. Virey[c] for the pleasure of performing this work together.

References

1. Bennett C. (WMAP Collaboration), 2003, Astrophys. J. Suppl. **148**, 1
2. Riess A.G. et al., 2004, Astrophys. J. **607**, 66
3. Masi S. et al., Olimpo Collaboration, 2003, Mem. S.A.It. Vol **74**, 96
4. http://cfht.hawaii.edu/Science
5. SNLS http://cfht.hawaii.edu_SNLS
6. Tauber J.A. et al., Planck Collaboration, 2004, Advances in Space Research, **34**, 491
7. Aldering G. et al., SNAP Collaboration, 2004, astro-ph/0405232
8. Wood-Vasey W.M. et al., Nearby Supernova Factory, 2004, New Astron.Rev. **48**, 637
9. Ch. Yeche, A. Ealet et al. A&A , 2006, 448,831
10. Hu, W., & Tegmark, M., 1999, Astrophys.J. **514**, L65
11. James F., 1978, CERN Program Library Long Writeup. D506.
12. Doran M., 2003, astro-ph/0302138
13. Seljak U. et al., astro-ph/0407372
14. Upadhye A. et al., astro-ph/0411803

[a]DSM/DAPNIA, CEA/Saclay, F-91191, Gif-sur-Yvette, France
[b]Centre de Physique des particules de Marseille,Case 907, F-13288 Marseille Cedex 9, France
[c]"Centre de Physique Théorique", Case 907, F-13288 Marseille Cedex 9, France.

FLUCTUATIONS IN THE CMB AND WEAK LENSING INDUCED BY COSMIC STRINGS

MARTIN LANDRIAU[1], PAUL SHELLARD[2] and EIICHIRO KOMATSU[1]
(1) Department of Astronomy, University of Texas at Austin,
1 University Station, C1400, Austin, TX 78712-0259, USA
(2) Department of Applied Mathematics and Theoretical Physics, University of Cambridge,
Centre for Mathematical Sciences, Wilberforce Road, Cambridge, CB3 0WA, UK

The formation of cosmic strings is a generic phenomenon in many theories of fundamental physics. In this paper, we present maps of CMB fluctuations and of weak lensing seeded by a network of cosmic strings. We extract power spectra from these maps and discuss their implication in the context of current and future observations.

1 Introduction

There has been a renewal of interest in cosmic strings [1] in recent years due to progress in theoretical physics. Indeed, it has been shown that all cosmologically viable SUSY GUTs predict the formation of topologically stable cosmic strings at the end of inflation [2]. It has also been realised that the same happens at the end of inflation in braneworlds cosmologies [3,4]. However, in the latter case, the "cosmic superstrings" are not a traditional topological defect, but it has been shown that networks will behave in a very similar fashion [5].

2 Methods

Our work uses cosmic string simulations based on the Nambu-Goto action, valid when a cosmic string's curvature radius is much larger than its thickness, so thatit can be treated as a 1D object.

$$\mathcal{S} = -\mu \int d^2\zeta \sqrt{-\gamma}, \tag{1}$$

from which we can derive the equations of motion

$$\ddot{\mathbf{x}} + 2\frac{\dot{a}}{a}(1-\dot{\mathbf{x}}^2)\dot{\mathbf{x}} = \epsilon^{-1}(\epsilon^{-1}\mathbf{x}')' \quad \text{and} \quad \dot{\epsilon} = -2\frac{\dot{a}}{a}\epsilon\dot{\mathbf{x}}^2 . \tag{2}$$

The equations of motion are solved using the Allen-Shellard code [6]. From the action, we also obtain the energy-momentum tensor of the strings

$$\Theta^{\mu\nu}\sqrt{-g} = \mu \int d\zeta(\epsilon\dot{x}_s^\mu\dot{x}_s^\nu - \epsilon^{-1}x_s'^\mu x_s'^\nu)\delta^{(3)}(\mathbf{x}-\mathbf{x}_s), \tag{3}$$

which we project onto a 3D grid. Transforming the problem from 3D QFT to a 1D effective action enables a longer dynamic range, roughly 3 times as long.

Figure 1: CMB temperature fluctuations seeded by a network of cosmic strings.

To solve the cosmological perturbations equations, we use the Landriau-Shellard code [7]. In Fourier space, the linearized Einstein-Boltzmann equations form 3 systems of $N_{eq} \simeq 40$ coupled ODE's. These can each be written as:

$$\frac{d\mathbf{y}}{d\eta} = \mathcal{A}(k,\eta)\mathbf{y} + q(\mathbf{k},\eta)\,. \tag{4}$$

Here, $\mathbf{y}$ and $\mathbf{q}$ are vectors of dimension N and $\mathcal{A}$ is a real $N \times N$ matrix. The components of $\mathbf{y}$ are the metric and matter perturbations and those of $\mathbf{q}$ are the components of $\Theta_{\mu\nu}$. The formal solution to the system is

$$\mathbf{y}(\eta) = Y(\eta)\left(\mathbf{c} + \int_0^\eta Y^{-1}(\eta')q(\eta')d\eta'\right)\,, \tag{5}$$

where Y are solutions to the homogeneous equations ($q = 0$) with initial conditions $Y = I$. So instead of solving $5 \times N_{eq}$ inhomgeneous equations (vector and tensor components need to be solved separately) on a N^3 grid, we are solving $3 \times N_{eq}^2$ homogeneous equations on a linear grid of dimension $\lesssim 2N$ For a typical grid size of 256^3, we have a reduction in CPU time of more than 1300, thus making the computation feasable.

3 CMB Fluctuations

Temperature fluctuations in the CMB are given, in the synchronous gauge, by

$$\frac{\delta T}{T} = \int_0^{\eta_0}\left(\dot{\tau}e^{-\tau}\left(\frac{\delta_\gamma}{4} - \mathbf{v_B}\cdot\hat{n} + \Pi^I_{ij}\hat{n}_i\hat{n}_j\right) - \frac{1}{2}e^{-\tau}\dot{h}_{ij}\hat{n}_i\hat{n}_j\right)d\eta\,, \tag{6}$$

where all the symbols have their usual meaning. In this work, as well as in our forthcoming work [9], only the last term (ISW) is relevant, as we start integrating after recombination.

In figure 1, we show two CMB maps, the first, an all-sky map with resolution $N_{side} = 64$ is obtained from a simulation which starts at $\eta_0/5$ and ends at η_0; the second is 25° a side, has a resolution $N_{side} = 1024$ and is obtained from a simulation that starts at $\eta_0/20$ ($\simeq 2.5\eta_{rec}$) and ends at $\eta_0/5$. In figure 2, we show the power spectra extracted from these maps. The normalisation, taken from our earlier work [8], is $G\mu/c^2 = 0.7 \times 10^{-6}$. One should note that, due to the limited dynamic range in both time and space, these spectra have an effective window function on the scales probed. We also show the temperature distribution of the small angle map, along with the $3-\sigma$ contours of a Gaussian distribution with the same power spectrum. The distribution is clearly non-Gaussian. In our forthcoming work [9], we will investigate this non-Gaussian signature further.

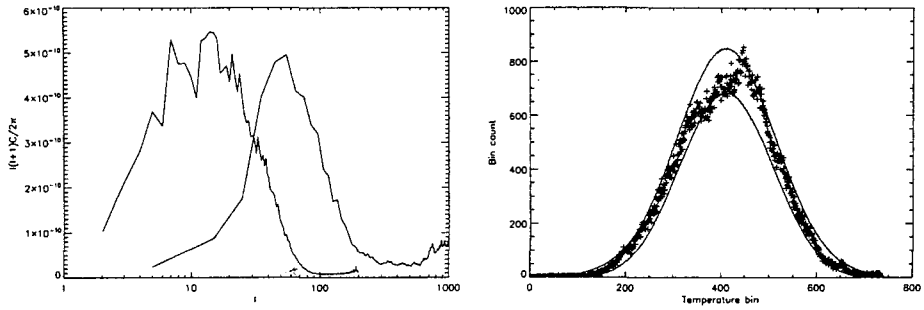

Figure 2: Power spectrum extracted from maps in figure 1 and temperature distribution in the small angle map.

4 Weak Lensing

The method initially developed to produce CMB maps can be very easily extended to study weak lensing. Our motivation in studying weak lensing is twofold. Firstly, weak lensing signal from strings may be important on scales where the CMB is dominated by foregrounds and the strings' signal is thus more difficult to observe. Also, a combination of several astrophysical signature increases chances of detection and ensures we are not confronted with a fluke.

Our goal is to compute maps and power spectrum of the convergence κ and shear, $\gamma = (\gamma_1, \gamma_2)$ fields, which are obtained from the amplification matrix:

$$\mathcal{A}_{ab} \equiv \frac{\mathcal{D}_{ab}(\lambda_S)}{\lambda_S} = \begin{pmatrix} 1-\kappa-\gamma_1 & -\gamma_2 \\ -\gamma_2 & 1-\kappa+\gamma_1 \end{pmatrix} = \mathcal{I} - (\kappa\mathcal{I} + \gamma_1\sigma_3 + \gamma_2\sigma_1)\,, \tag{7}$$

where the matrix $\mathcal{D}$ obeys the following evolution equation:

$$\mathcal{D}''_{ab} = R_{\mu\nu\alpha\beta}p^\nu p^\alpha n_a^\nu n_b^\beta \mathcal{D}_{cb}\,, \tag{8}$$

with the following initial conditions:

$$\mathcal{D}_{ab}(\lambda_O) = 0 \;\text{ and }\; \mathcal{D}'_{ab}(\lambda_O) = \mathcal{I}_{ab}\,, \tag{9}$$

In the above equation, p^μ is the tangent vector to the geodesic and the two vectors n_a^μ give the basis for the shear field and obey $n_a^\mu n_{b\,\mu} = \delta_{ab}$ and $n_a^\mu u_\mu = n_a^\mu p_\mu = 0$.

Choosing the conformal time for the affine parameter $\hat{\lambda} = \eta$ and the synchronous gauge $h_{0\mu} = 0$, the equation becomes, after integrating by parts and Fourier transforming:

$$\mathcal{D}^{(1)}_{ab} = \int_{\eta_S}^{\eta_0} \sum e^{-i\mathbf{k}.\mathbf{x}} \left[g_1 \left(k_l k_j \dot{h}_{ik} - k_l k_i \dot{h}_{jk} - k_j k_k \dot{h}_{il} + k_i k_k \dot{h}_{jl} \right) n^j n^k + (g_2 - g_3)\dot{h_{li}} \right] e_a^i e_b^l d\eta\,, \tag{10}$$

where the functions g_i are defined as:

$$g_1 = \int_{\eta_S}^{\eta} \lambda(\lambda_S - \lambda) a^{-2} d\eta \;\;,\;\; g_2 = \int_{\eta_S}^{\eta} \lambda(\lambda_S - \lambda) a^{-2} (\frac{\dot{a}}{a})^2 d\eta \;\text{ and }\; g_3 = -\frac{1}{2} a^{-2} \frac{\dot{a}}{a} \lambda(\lambda_S - \lambda) \tag{11}$$

and $\mathbf{n}$ and $\mathbf{e}_a$ are the spatial parts of p^μ and n_a^μ respectively.

In figure 3, we show a weak lensing map obtained from the same simulation as the all-sky CMB map of the previous section. The colour scheme shows the convergence, while the arrowless vectors show the shear. The right hand panel shows the shear power spectra extracted from it. The presence of B-modes is due scattering off several strings along the line-of-sight and could be a distinctive signature of cosmic strings.

Work containing results at smaller angles along with a more complete analysis will be published soon [10].

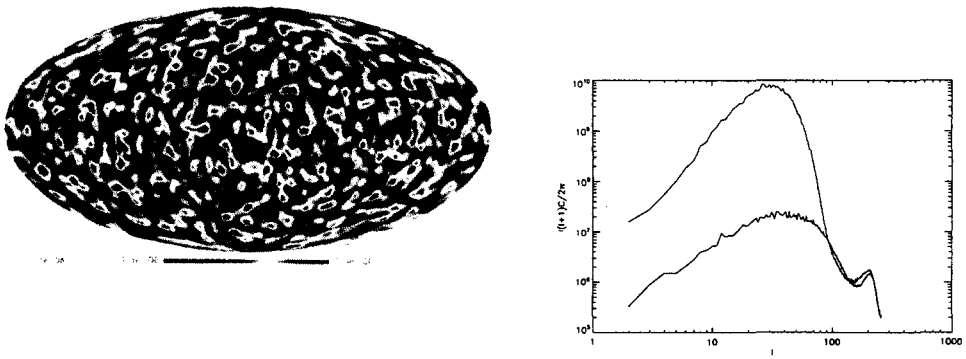

Figure 3: Weak lensing map and shear power spectrum extracted from it (E and B-modes are the upper and lower curves respectively).

5 Conclusion

We have presented results of on-going work on two major astrophysical signatures of cosmic strings: CMB fluctuations and weak lensing. Future work will include CMB contribution from recombination (both temperature and polarization)[11] as well as a more thorough non-Gaussian analysis. Other important work will focus on adapting the results of our simulations to specific experiments, taking into account noise, resolution, etc. in order to quantify as precisely as possible the probability of detection.

Acknowledgments

ML would like to thank the organizers for another great *Rencontres.* Simulations were performed using COSMOS, the Altix 3700 owned by the UK cosmology consortium, funded by PPARC, HEFCE, SGI and Intel. Some of the results obtained in this paper made use of the HEALPix package[12].

References

1. A. Vilenkin and E. P. S. Shellard. *Cosmic Strings and other Topological Defects* (Cambridge University Press, 2000).
2. R. Jeannerot, J. Rocher, and M. Sakellariadou, *Phys. Rev.* D **68**, 103514 (2003).
3. S. Sarangi and S.-H. H. Tye, *Phys. Lett.* B **536**, 185 (2002).
4. E. J. Copeland, R. C. Myers, and J. Polchinski, *JHEP*, **0406**, 013 (2004).
5. A. Avgoustidis and E. P. S. Shellard, *Phys. Rev.* D **73**, 041301 (2006).
6. B. Allen and E. P. S. Shellard, *Phys. Rev. Lett.*, **64**, 119 (1990).
7. M. Landriau and E. P. S. Shellard, *Phys. Rev.* D **67**, 103512 (2003).
8. M. Landriau and E. P. S. Shellard, *Phys. Rev.* D **69**, 023003 (2004).
9. M. Landriau and E. P. S. Shellard, in preparation.
10. M. Landriau, E. Komatsu, and E. P. S. Shellard, in preparation.
11. M. Landriau, E. P. S. Shellard, and E. Komatsu, in preparation.
12. K. Górski *et al.*, *ApJ*, **622**, 759 (2005)

WHAT HAVE WE LEARNED FROM CMB OBSERVATIONS?

ANTHONY LASENBY AND ANTHONY CHALLINOR
Astrophysics Group, Cavendish Laboratory, J. J. Thomson Avenue, Cambridge, CB3 0HE, UK

The cosmic microwave background (CMB) helps answer big questions such as what is the composition of the universe, what are its global properties such as geometry, topology and state of rotation, is there evidence for inflation, when did the universe reionize and what is the nature of dark energy. In this review we discuss how current observations of the CMB temperature anisotropies and polarization have provided (partial) answers to some of these questions.

1 Introduction

The cosmic microwave background (CMB) has played a major part in shaping our understanding of the large-scale properties of the universe. The last decade and a half has seen remarkable advances in observational cosmology and quantitative cosmological constraints now come from a number of complementary probes. The CMB occupies a special role in this programme due to its physics being particularly well understood (with the primary anisotropies requiring only linear theory), and in providing the most direct observational link to the physics of the early universe since the fluctuations were mostly imprinted around the time of recombination.

It is difficult to do justice to the question in the title within the available space. Moreover, the observational field moves quickly as A.L. will testify to, having faced the task of revising his talk on the eve of the conference following a major new data release from the WMAP satellite. However, we shall attempt to give a flavour of what we have learned from the primary CMB anisotropies in temperature and polarization, circa Spring 2006. In particular, we focus on the issues of the matter content of the universe as inferred from the morphology of the acoustic peaks, constraints on the geometry and dark energy sector from the peak locations and the integrated Sachs-Wolfe (ISW) effect, the new information coming from polarization measurements, CMB implications for inflation, and anomalous features in the large-angle temperature anisotropies. We concentrate on the primary anisotropies, which have been the main observational focus to date, although we make a few comments about secondary effects in Secs 7 and 10.

2 CMB Physics

We begin with a very brief review of the physics of the CMB temperature and polarization anisotropies.[1,2,3]

To a first approximation, the temperature anisotropies $\Theta(\hat{\boldsymbol{n}})$ have a contribution from density (scalar) perturbations given by

$$\Theta(\hat{\boldsymbol{n}}) = \Theta_0|_E + \psi|_E - \hat{\boldsymbol{n}}\cdot\boldsymbol{v}_b|_E + \int_E^R (\dot{\psi}+\dot{\phi})\,\mathrm{d}\eta\,, \tag{1}$$

and from tensor (gravity wave) perturbations

$$\Theta(\hat{\boldsymbol{n}}) = -\frac{1}{2}\int_E^R \dot{h}_{ij}\hat{n}^i\hat{n}^j\,\mathrm{d}\eta\,, \tag{2}$$

where the metric is taken as $\mathrm{d}s^2 = a^2(\eta)\{(1+2\psi)\mathrm{d}\eta^2 - [(1-2\phi)\delta_{ij}+h_{ij}]\mathrm{d}x^i\mathrm{d}x^j\}$, with the trace-free, transverse h_{ij} describing gravitational waves. The overdots denote derivatives with respect to conformal time η. The physical interpretation of Eqs (1) and (2) is straightforward. For scalar perturbations we see the intrinsic temperature fluctuation Θ_0 on the last scattering surface, at comoving distance $r_* \approx 14\,\mathrm{Gpc}$, modified by the gravitational redshift from the local potential ψ and a Doppler shift from the bulk velocity of the baryons $\boldsymbol{v}_b$. There is a further ISW contribution on large scales that arises from evolution of the gravitational potentials $\phi+\psi$: photons crossing a deepening potential well suffer more redshift climbing out than the the blueshift they gained falling in. For tensor perturbations, the anisotropies arise from the integrated effect of the anisotropic (local) expansion rate, i.e. the shear $\dot{h}_{ij}$. The variance of the spherical multipoles, a_{lm}, of $\Theta(\hat{\boldsymbol{n}})$ defines the temperature power spectrum C_l^T.

The fluctuations on the last-scattering surface are processed versions of the primordial curvature and gravity-wave perturbations, plausibly generated during inflation. For scalar perturbations, the processing mechanism is simply gravity on large scales, with acoustic physics and diffusion important on smaller scales. The acoustic oscillations of the plasma inside the sound horizon lead to a modulation of Θ_0 (and $\boldsymbol{v}_b$) with scale at last scattering. If only one mode of the primordial fluctuation is relevant (e.g. the adiabatic, growing mode as predicted in simple inflation models), the acoustic oscillations are "phased up" so that all Fourier components with a given wavelength reach an extremum at the same time and a series of acoustic peaks are imprinted in the C_l^T power spectrum. For adiabatic models these are at $l \sim n\pi d_A(r_*)/r_s$, where $d_A(r_*)$ is the angular diameter distance to last scattering and r_s is the sound horizon there; for isocurvature modes the peaks are shifted by $\pi d_A(r_*)/2r_s$. The same physics that gives rise to acoustic peaks in the CMB produces the recently-detected baryon acoustic oscillations in the clustering of galaxies.[4,5] For gravitational waves, the metric fluctuation h_{ij} is constant while the wavelength exceeds the Hubble radius, but oscillates with an amplitude decaying as a^{-1} once sub-Hubble. As a result, the tensor anisotropies are suppressed for $l > 60$.

2.1 CMB Polarization

For perturbations with wavelength $k^{-1} < 5\,\mathrm{Mpc}$. photon diffusion and the finite thickness ($\sim 80\,\mathrm{Mpc}$) of last scattering produce exponential damping of the anisotropies they subsequently produce.[6] The non-zero photon mean-free path allows the (local) production of a quadrupole anisotropy in the radiation field that generates linear polarization on further scattering.[7]

That part of the photon density matrix describing linear polarization (i.e. whose components are the Stokes parameters Q and U in some basis) can be decomposed into a gradient, or E-mode, part and a curl, or B-mode, part.[8,9] The E field is a scalar under parity while B is pseudoscalar, so, in the absence of parity-violating physics, B will be uncorrelated with E and

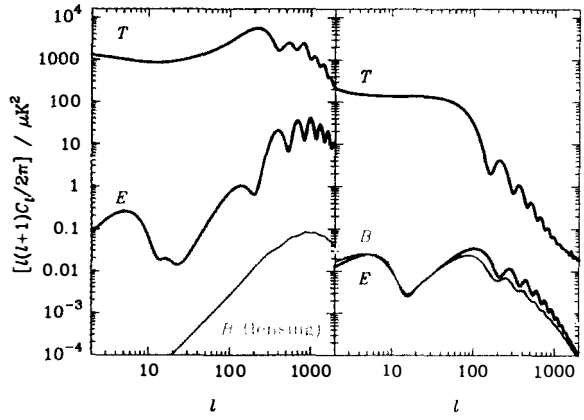

Figure 1: CMB temperature and polarization power spectra from scalar (left) and tensor perturbations (right) for a tensor-to-scalar ratio $r = 0.38$. The B-mode power generated by weak gravitational lensing is also shown.

the temperature anisotropies. This means we expect three additional non-zero power spectra: C_l^E, C_l^B and the cross-correlation $C_l^X \equiv C_l^{TE}$. In linear theory, scalar perturbations produce only E-mode polarization by symmetry, but gravity waves produce E and B in similar amounts.[8,9,10]

The power spectra from scalar and tensor perturbations are compared in Fig. 1. The gravitational wave amplitude is set to a value close to the current upper limit from the temperature anisotropies. Note that for scalar perturbations, C_l^E peaks at the troughs of C_l^T since the radiation quadrupole at last scattering is derived mostly from the plasma bulk velocity which oscillates $\pi/2$ out of phase with the intrinsic temperature. Re-scattering at reionization produces the 'bump' in the polarization spectra on large angles,[11] and damps the temperature and polarization spectra by $e^{-2\tau}$ on scales inside the horizon at that epoch. We also show the non-linear B-mode signal produced by weak gravitational lensing acting on the primary (E-mode) polarization.[12]

3 Current Power Spectra Measurements

The CMB temperature anisotropies have now been mapped over three decades of scale with a range of complementary techniques; we show a selection of recent measurements in Fig. 2. The agreement with the best-fit theoretical model is striking, and the measurements now clearly delimit the first three acoustic peaks. The WMAP3 temperature data[15] has retained the low quadrupole level found in WMAP1, though at slightly lower significance.

The first polarization detections were reported in 2002 by DASI.[13] Four other groups have since reported measurements of C_l^E; see Fig. 2. The data points are still very noisy but the qualitative agreement with the best-fit model to the temperature spectrum is impressive. The cross-correlation C_l^{TE} has also been measured by several groups and, with the arrival of the third-year WMAP data, the measurements are now quite precise for $l < 200$.[14] At present only upper limits exist for C_l^B but this should change with several experiments that are planned (and, possibly, with some that are already operational).

4 Matter Content

The relative heights of the acoustic peaks seen in the current T and E-mode data depend on the physical densities in matter $\Omega_m h^2$ and baryons $\Omega_b h^2$, and the primordial spectrum of cur-

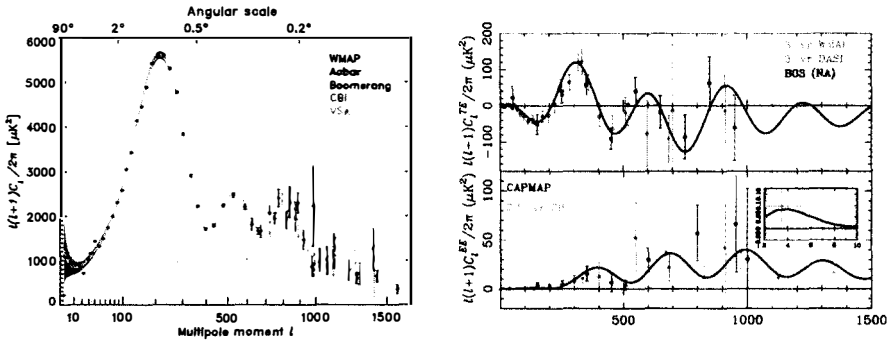

Figure 2: Recent CMB temperature (left; from Hinshaw et al.[15]) and polarization (right; C_l^{TE} top and C_l^E bottom) power spectra measurements. The solid lines in the polarization plots are the theoretical expectation on the basis of the temperature data and an optical depth $\tau = 0.08$.

vature perturbations (multiplied by $e^{-2\tau}$). For the matter dependencies, the relevant physics is the reduction in the bulk modulus of the plasma due to baryon inertia, the resonant gravitational driving of the acoustic oscillations for perturbations that enter the sound horizon before matter-radiation equality, and photon diffusion.[16] Increasing the matter density enhances the (compressional) 1st, 3rd etc. acoustic peaks for adiabatic perturbations, while, damping aside, increasing the matter density boosts the higher-order peaks relative to the lower ones.

In combination, these two effects have allowed accurate measurements of the baryon and CDM densities from the peak morphology. From the three-year WMAP data alone, $\Omega_b h^2 = 0.0223^{+0.0007}_{-0.0009}$ and $\Omega_m h^2 = 0.127^{+0.007}_{-0.01}$ in flat, ΛCDM models.[17] The implied baryon-to-photon ratio $(6.10 \pm 0.2) \times 10^{-10}$ predicts light-element abundances consistent with observations. There is some tension between the low matter density favoured by WMAP3 and the higher value favoured by tracers of large-scale structure, most notably weak gravitational lensing.[17] Better measurements of the third and higher peaks will be very helpful in sorting out this issue.

5 Geometry and Dark Energy

With the matter and baryon densities fixed by the morphology of the acoustic peaks, the acoustic oscillations become a standard ruler with which to measure $d_A(r_*)$, determined to be 13.7 ± 0.5 Gpc.[18] The dark energy model, curvature and sub-eV neutrino masses have no effect on the pre-recombination universe and they only affect the CMB through $d_A(r_*)$ and the late-time ISW effect (see below). The discriminatory power of the latter is limited by cosmic variance leading to the *geometric degeneracy* between curvature and dark energy.[19] For example, closed models with $\Omega_K = -0.3$ and $\Omega_\Lambda = 0$ are a good fit to the CMB data *alone* but imply a very low Hubble constant and $\Omega_m h$ in conflict with other datasets. Including data on the Hubble constant, large-scale structure or the supernovae Hubble diagram immediately forces the spatial sections to be close to flat. An interesting example of breaking this degeneracy with external data is provided by the measurement of baryon oscillations in the SDSS luminous red galaxy sample.[4] Baryon oscillations measure the same physical scale as the CMB acoustic peaks but at much lower redshift (here $z \sim 0.35$); combining with WMAP3 gives $\Omega_K = -0.01^{+0.014}_{-0.012}$ and $\Omega_\Lambda = 0.728^{+0.020}_{-0.027}$ for Λ models.[17]

The late-time ISW effect provides another way to constrain dark energy. This was first detected as a positive correlation between the large-angle first-year WMAP temperature data and the X-ray background and the projected number density of radio galaxies.[20] The physics

behind the correlation is that gravitational potential wells decay once dark energy dominates over the matter density so there is a positive correlation with tracers of the matter over-density on the line of sight. The effect has since been confirmed with several other tracers of large-scale structure. The correlation is sensitive to the relative densities in dark energy and matter as a function of redshift, and the expected decrease in the ISW correlation with redshift is now seen.[21] However, as yet there is no evidence for evolution in the dark energy density itself.

Interesting constraints on dynamical dark energy models are beginning to emerge when the CMB data is combined with other cosmological data. Very little of the constraining power comes from the ISW effect due to the combination of cosmic variance and the mitigating effect of dark energy clustering on the changes to the expansion rate.[22] Combining WMAP3 with galaxy clustering and supernovae datasets gives the constraint $w = -1.062^{+0.128}_{-0.079}$ and $\Omega_K = -0.024^{+0.016}_{-0.013}$ in scalar-field dark energy models.[17]

5.1 Slightly Closed Models

At this stage, one of the authors wishes to declare an interest. This is that with C. Doran, AL has developed a model[23] in which a slightly closed universe (closed at the few percent level) emerges naturally from inflation. This model has its basis in a conformal geometry approach to understanding Λ. It works with a simple $m^2\phi^2$ scalar field potential, but is novel in calculating the initial scalar field behaviour in terms of a power series expansion out of the big bang. The conformal geometry part gives a novel boundary condition at the *end* of the universe, and the combination of the two leads to a 'see-saw' type of behaviour in which the more generically curved the initial universe is, the closer to flatness it is today, and in which there is a natural linkage between Λ and the number of e-folds N of inflation. Specifically, one finds $\Lambda \sim \exp(-6N)$, which gives $\sim 10^{-122}$ in natural units if $N \sim 46$. Furthermore, 'closure' during inflation naturally gives a low k cutoff in the primordial spectrum, such as is apparently seen in the WMAP1 and WMAP3 results. Thus results such as those for w and Ω_K as reported at the end of the previous section, are very interesting in the context of this model, where one wants the universe to be just closed, and $w = -1$, so that dark energy can be purely geometrical.

6 E-Mode Polarization and TE Cross-Correlation

Apart from constraints on the reionization optical depth from large-angle polarization data (see Sec. 6.1), the power of the current polarization data for constraining parameters in adiabatic, ΛCDM models is rather limited. More important are the qualitative conclusions that we can draw from the data:

- The current measurements of $C_l^{\dot{E}}$ and C_l^{TE} are fully consistent with predictions based on the best-fit adiabatic model to C_l^T, providing an important independent test of the structure formation model.
- The well-defined oscillations in C_l^{TE} further support the phase coherence of the primordial fluctuations, i.e. all modes with a given wavelength oscillate in phase. This is a firm prediction of inflation models but is at odds with defect models.
- The (anti-)correlation between the polarization and temperature on degree scales (see Fig. 2) is *direct* evidence for fluctuations at last scattering that are outside the Hubble radius and are adiabatic.[24]
- The peak positions in polarization, as for the temperature, are in the correct locations for adiabatic initial conditions. Pre-WMAP3 analyses, combining CMB temperature and polarization with other cosmological probes/priors limit the contribution from isocurvature

initial conditions to the CMB power to be less than 30%, allowing for the most general correlated initial conditions.[25]

- That E-mode power peaks at the minima of the temperature power spectrum increases our confidence that the primordial power spectrum is a smooth function with no features 'hiding' on scales that reach a mid-point of their acoustic oscillation at last scattering (and so contribute very little to the temperature anisotropies).

6.1 Large-Angle Polarization from Reionization

The large-angle polarization generated at reionization was first seen in the TE correlation in the first-year WMAP data.[26] This provided a broad constraint on the optical depth with mean $\tau = 0.17$ – on the high side of what was expected based on plausible models for reionization. With the improved polarization analysis and further data in the third-year WMAP release,[14] excess power has now been measured in the large-angle C_l^E spectrum (see Fig. 2) corresponding to $\tau = 0.10 \pm 0.03$. This shifts slightly to $\tau = 0.09 \pm 0.03$ with the inclusion of all the WMAP data. To obtain the large-angle C_l^E spectrum required aggressive cleaning of Galactic foregrounds but a number of tests suggests that residual contamination is under control. The new mean value for the optical depth is more easily accommodated in astrophysical models for reionization than the earlier high value.

7 Damping Tail, SZ and the Amplitude of the Fluctuations

Photon diffusion on scales < 30 Mpc, and the comparable width of the last-scattering surface, washes out anisotropy from small-scale fluctuations. This exponential 'damping tail' in the temperature spectrum is seen in the ground and balloon-based data in the left plot in Fig. 2.

On scales $l > 2000$, the CBI, operating around 30 GHz, sees power in excess of that expected from the primary anisotropies at the 3σ level.[27] An excess is also seen at smaller angular scales (centred on $l \sim 5000$) with the BIMA array operating at 28.5 GHz.[28] Both analyses exclude point-source contamination as the source of the excess, suggesting instead that they are seeing a secondary contribution from the thermal Sunyaev-Zel'dovich (SZ) effect[29] in unresolved galaxy clusters. Optical follow-up of the BIMA fields shows no (anti-)correlation between galaxy over-densities and the anisotropy images, but the image statistics are consistent with SZ simulations. We note that data from the several high-resolution CMB experiments that will soon be operational should give a definitive answer as to the source of the excess small-scale power.

The SZ explanation favours a variance in the matter over-density $\sigma_8 \approx 1$ (with 1σ errors at the 20% level), higher than inferences from current CMB and large-scale structure data. In particular, the new WMAP3 data alone favour $\sigma_8 = 0.75 \pm 0.06$ compared to 0.92 ± 0.1 from the first-year data. This change is driven mainly by the new lower value for τ which favours a lower amplitude of primordial curvature fluctuations and a lower spectral index (see Sec. 8). Including non-CMB data tends to increase σ_8, with the WMAP3-alone value being most discrepant with weak lensing[17] and Ly-α forest data.[30,31]

8 CMB Constraints on Inflation

Inflation naturally predicts a universe that is very close to flat, consistent with the observed positions of the CMB acoustic peaks as discussed in Sec. 5. Significantly, it also naturally provides a causal mechanism for generating initial curvature fluctuations[32] and gravitational waves[33] with almost scale-invariant, power-law spectra. These spectra can be approximated as power laws over the range of scales relevant for cosmology:

$$\mathcal{P}_{\mathcal{R}} \approx A_s (k/k_0)^{n_s - 1} \quad , \quad \mathcal{P}_h \approx A_t (k/k_0)^{n_t} \, . \tag{3}$$

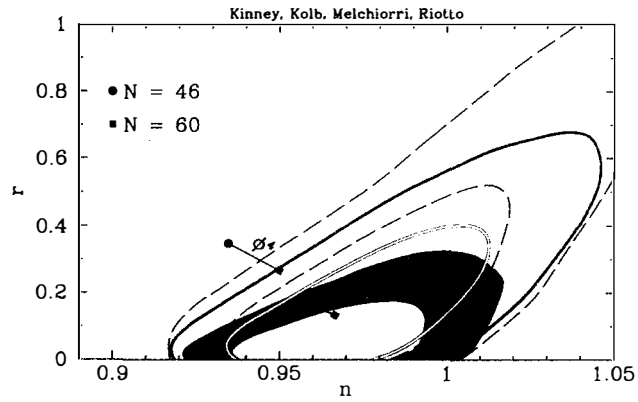

Figure 3: Constraints in the r-n_s plane for models with no running from Kinney et al.[35] Dark (blue) contours are 68% confidence regions and light (yellow) are 95%. The filled contours are from combining WMAP3 and the SDSS galaxy survey; open are with WMAP3 alone. These results assume the HST prior on H_0; dropping this prior gives the dashed contours. The predictions for $V \propto \Phi^2$ and Φ^4 are shown assuming that modes with $k = 0.002\,\mathrm{Mpc}^{-1}$ left the Hubble radius between 46 and 60 e-folds before the end of inflation.

The tensor amplitude depends only on the Hubble parameter at the time the mode k leaves the Hubble radius during inflation, i.e. when $k = aH$. The scalar amplitude and both spectral indices depend additionally on the evolution of H. In slow-roll inflation, where $V(\Phi)$ dominates the stress-energy of the inflaton field Φ and the evolution of Φ is slow, the observable parameters may be related to $V(\Phi)$ and its first two derivatives.[34] The tensor-to-scalar ratio $r \equiv A_t/A_s$ is given in this limit by

$$r = 8 \times 10^{-3} (E_{\rm inf}/10^{16}\,\mathrm{GeV})^4, \tag{4}$$

where the *energy scale of inflation* $E_{\rm inf} = V^{1/4}$ and we have taken $A_s = 2.36 \times 10^{-9}$.

Constraints in the r-n_s plane from WMAP3 and the SDSS galaxy survey are shown in Fig. 3, taken from Kinney et al.[35] The point $r = 0$ and $n_s = 1$ corresponds to inflation occurring at low energy with essentially no evolution in H (but note low-energy models can show significant deviations from $n_s = 1$); the gravitational waves are negligible and the curvature fluctuations have no preferred scale. This *Harrison-Zel'dovich* spectrum is clearly disfavoured by the data, but is not yet excluded at the 95% level. Attempts to pin down n_s with current CMB temperature data are still hampered by a degeneracy between n_s, A_s, the reionization optical depth τ and the baryon density.[36] The new WMAP3 measurement of τ helps considerably here leading to a marginalised constraint $n_s = 0.987^{+0.019}_{-0.037}$ in inflation-inspired models.[17] If one focuses instead on low-energy models ($r \approx 0$), which some model-builders favour since such models more naturally accommodate a field evolution $\Delta\Phi \ll m_{\rm Pl}$, the constraint becomes $n_s = 0.95 \pm 0.015$. *Within the context of low-energy models*, this is a significant detection of evolution during inflation and produces interesting constraints in model space.[37] The 95% upper limit on r from WMAP3 and SDDS is $r < 0.28$ for power-law spectra, thus limiting the inflationary energy scale $E_{\rm inf} < 2.4 \times 10^{16}$ GeV. We see from Fig. 3 that large-field models with monomial potentials $V(\Phi) \propto \Phi^p$ are now excluded at high significance for $p \geq 4$, but Φ^2 potentials are still a good fit. Limits on r at the 0.01 level are expected from ground-based B-mode polarization experiments within ~ 5 years. These will improve considerably over current limits on inflation models.

Slow-roll inflation predicts that any running of the spectral indices with scale should be

$O[(n_s - 1)^2]$. The lever arm for measuring running with the CMB alone is currently rather limited (with little sensitivity for $k > 0.05\,\mathrm{Mpc}^{-1}$ corresponding to $l > 700$), but there is persistent, though not yet compelling, evidence for non-zero running: WMAP3 alone gives $\mathrm{d}n_s/\mathrm{d}\ln k = -0.102^{+0.05}_{-0.043}$ allowing for gravitational waves.[17] Running near this mean value would be problematic for slow-roll inflation models, but the result is mostly driven by the large-angle ($l < 15$) C_l^T spectrum and a more definitive assessment from the CMB must await further small-scale observations from Planck and ongoing ground-based surveys. The current evidence for running weakens considerably when small-scale data from the Ly-α forest is included.[30,31] This is consistent with the Ly-α data favouring more small-scale power than the CMB extrapolation, and this tension is worsened by the inclusion of negative running.

8.1 Non-Gaussianity and Inflation

The fluctuations from single-field inflation should be adiabatic and any departures from Gaussian statistics should be unobservably small.[38] However, adiabaticity and Gaussianity can be violated in models with several scalar fields, for example the curvaton model.[39] As we have already noted, current data do allow a sizeable isocurvature fraction, but this is not favoured. Similarly, there is no evidence for non-Gaussianity from inflation. In many models, the non-Gaussian contribution to the gravitational potential at last scattering is a quadratic functional of the Gaussian part. The coupling kernel is denoted f_{NL} and the best constraints, assuming no scale-dependence, are $-54 < f_{\mathrm{NL}} < 114$ at 95% confidence from the three-point function of WMAP3.[17] Planck should be sensitive down to $f_{\mathrm{NL}} \sim 5$,[40] but this is still at a level where we should not expect to see anything in simple inflation models (which give $f_{\mathrm{NL}} \sim O(1)$ accounting for non-linear gravitational effects after inflation).

9 Large-Angle Anomalies

There are statistically-significant anomalies in the large-angle temperature anisotropies, as imaged by COBE[41] and WMAP,[42] that appear to signal departures from rotational invariance and/or Gaussianity; for a recent review and WMAP3 analysis, see Copi et al.[43] and references therein. The origin of these anomalies is still unknown; proposed explanations have included instrument systematics, residual Galactic foregrounds, gravitational effects of the local universe or theoretical exotica such as a compact topology or anisotropic dark energy. Here we focus on one particular proposal: that the universe has global rotation.

This was first investigated with regard to the WMAP data by Jaffe et al.[44] These authors found a statistically significant match between the large-angle WMAP data, and a Bianchi VII_h template. In Bianchi models, the universe is anisotropic but spatially homogeneous. The VII_h models allow both fluid shear and vorticity, and this gives rise to a distinctive spiral pattern in the CMB, with significant power extending out to $l \sim 25$ (see e.g. McEwen et al.[46] for a plot of the power in a Bianchi VII_h spiral versus l). An important feature of the VII_h models is that in the limit of small departures from isotropy, the background universe is *open*, and Jaffe et al. found that a significantly open universe, with $\Omega_0 = 0.5$, was picked out in the template fitting process. This is of course completely at odds with the results from the higher multipoles of the CMB, which point unambiguously to a nearly flat universe. Intriguingly, however, removing the best-fit Bianchi template resulted in a highly reduced significance for all of the previously found large-angle anomalies, including a non-Gaussian cold spot found by Vielva et al.,[45] which lies in position of the 'eye' of the best-fit Bianchi spiral. (Note that McEwen et al.,[46] however, using a directional wavelet approach, found that not all the significance of wavelet detections of non-Gaussianity were removed with the subtraction of a Bianchi template, in particular a detection of skewness in the wavelet coeffients remained.)

Since this point, the Bianchi template computations have been generalised by both Jaffe et al.[47] and Bridges et al.[48] to include a cosmological constant. This has allowed the investigation of whether one can retain the production of a spiral pattern of the right type to explain the large-angle anomalies, which requires a low Ω_{matter}, whilst having a universe close to flat, as required by the rest of the CMB and other data.

As found first by Jaffe et al.,[47] this is at first sight promising, since a degeneracy exists in the $(\Omega_{\dot{m}}, \Omega_\Lambda)$ plane (similar to the geometric degeneracy in the CMB) which allows a Bianchi template, morphologically identical to the original non-Λ one, to take on values which could correspond to a more acceptable cosmology. However, as confirmed in a detailed MCMC exploration by Bridges et al.,[48] the degenerate likelihood contours do not intersect areas of parameter space that 1- or 3 year WMAP data would prefer at any significance above 2σ. Thus this appears to confirm the conclusion that a physical Bianchi model is not responsible for the large-angle anomalies, and while the apparent match of such a model to the anomalies is intriguing, currently an alternative explanation needs to be sought.

10 Outlook

We end by briefly considering what we can expect from further CMB observations in the near future. For the temperature anisotropies, Planck, due for launch in 2008, should produce a cosmic-variance limited measurement of the power spectrum up to $l \sim 2000$. Many key parameters will be determined to percent-level precision and current tensions – for example between the running favoured by CMB data but not by Ly-α, and the relatively low matter density from WMAP3 – should be better understood. Further independent measurements of the lowest-l multipoles will shed light on the potential role of instrumental effects and residual foregrounds in the large-angle anomalies. On smaller scales, a number of arcminute-scale instruments are close to completion that aim to measure the high-l anisotropy power spectrum, and hence constrain the history and morphology of reionization through the kinetic SZ effect, and to survey for galaxy clusters via the thermal SZ effect. The small-scale experiments should also detect the effect of weak gravitational lensing in the CMB.[49]

In polarization we look forward to improvements in E-mode polarization data, from experiments currently collecting data in Antarctica, future years of WMAP, and from Planck. This data will particularly help in constraining non-standard models such as those with an admixture of adiabatic and isocurvature perturbations. Looking a little further ahead, a new generation of high-sensitivity instruments have the ambition of detecting the imprint of gravitational waves in B-mode polarization. They should be sensitive down to tensor-to-scalar ratios $r \sim 0.01$ – corresponding to an energy scale of inflation around 1×10^{16} GeV – and will place tight constraints on inflation models. There is also exciting secondary science that can be done with these instruments, such as better reconstruction of CMB lensing and hence improvements in neutrino masses and dark-energy properties from the CMB.

Acknowledgments

A.C. is supported by a Royal Society University Research Fellowship. Thanks to Will Kinney and Gary Hinshaw for permission to include their figures.

References

1. W. Hu and S. Dodelson, *Ann. Rev. Astron. Astrophys.* **40**, 171 (2002).
2. W. Hu, *Ann. Phys.* **303**, 203 (2003).

3. A. Challinor in *The Physics of the Early Universe*, ed. E. Papantonopoulos (Springer, Berlin, 2005).
4. D.J. Eisenstein *et al*, *Astrophys. J.* **633**, 560 (2005).
5. S. Cole *et al*, *Mon. Not. R. Astron. Soc.* **362**, 505 (2005).
6. J. Silk, *Astrophys. J.* **151**, 459 (1968).
7. M.J. Rees., *Astrophys. J. Lett.* **153**, 1 (1968).
8. M. Kamionkowski, A. Kosowsky and A. Stebbins, *Phys. Rev.* D **55**, 7368 (1997).
9. M. Zaldarriaga and U. Seljak, *Phys. Rev.* D **55**, 1830 (1997).
10. W. Hu and M. White, *Phys. Rev.* D **56**, 596 (1997).
11. M. Zaldarriaga, *Phys. Rev.* D **55**, 1822 (1997).
12. M. Zaldarriaga and U. Seljak, *Phys. Rev.* D **58**, 023003 (1998).
13. J.M. Kovac *et al*, *Nature* **420**, 772 (2002).
14. L. Page *et al*, *preprint* arXiv:astro-ph/0603450 (2006).
15. G. Hinshaw *et al*, *preprint* arXiv:astro-ph/0603451 (2006).
16. W. Hu and N. Sugiyama, *Phys. Rev.* D **51**, 2599 (1995).
17. D.N. Spergel *et al*, *preprint* arXiv:astro-ph/0603449 (2006).
18. D.N. Spergel *et al*, *Astrophys. J. Supp.* **148**, 175 (2003).
19. G. Efstathiou and J.R. Bond, *Mon. Not. R. Astron. Soc.* **304**, 75 (1999).
20. S. Boughn and R. Crittenden, *Nature* **427**, 45 (2004).
21. A. Cabre *et al*, *preprint* arXiv:astro-ph/0603690 (2006).
22. J. Weller and A.M. Lewis, *Mon. Not. R. Astron. Soc.* **346**, 987 (2003).
23. A. Lasenby and C. Doran, *Phys. Rev.* D **71**, 063502 (2005).
24. H.V. Peiris *et al*, *Astrophys. J. Supp.* **148**, 213 (2003).
25. J. Dunkley *et al*, *Phys. Rev. Lett.* **95**, 261303 (2005).
26. A. Kogut *et al*, *Astrophys. J. Supp.* **148**, 161 (2003).
27. J.R. Bond *et al*, *Astrophys. J.* **626**, 12 (2005).
28. K.S. Dawson *et al*, *preprint* arXiv:astro-ph/0602413 (2006).
29. R.A. Sunyaev and Y.B. Zeldovich, *Comm. Astrophys. Space Phys.* **4**, 173 (1972).
30. U. Seljak, A. Slosar and P. McDonald, *preprint* arXiv:astro-ph/0604335 (2006).
31. M. Viel, M.G. Haehnelt and A. Lewis, *preprint* arXiv:astro-ph/0604310 (2006).
32. J.M. Bardeen, P.J. Steinhardt and M.S. Turner, *Phys. Rev.* D **28**, 679 (1983).
33. A.A. Starobinskiĭ, *JETP Lett.* **30**, 682 (1979).
34. J.E. Lidsey *et al*, *Rev. Mod. Phys.* **69**, 373 (1997).
35. W.H. Kinney *et al*, *preprint* arXiv:astro-ph/0605338 (2006).
36. A. Lewis, *preprint* arXiv:astro-ph/0603753 (2006).
37. L. Alabidi and D.H. Lyth, *preprint* arXiv:astro-ph/0603539 (2006).
38. N. Bartolo *et al*, *Phys. Rep.* **402**, 103 (2004).
39. D.H. Lyth and D. Wands, *Phys. Lett.* B **524**, 5 (2002).
40. E. Komatsu and D.N. Spergel, *Phys. Rev.* D **63**, 063002 (2001).
41. G.F. Smoot *et al*, *Astrophys. J. Lett.* **396**, 1 (1992).
42. C.L. Bennett *et al.*, *Astrophys. J. Supp.* **148**, 1 (2003).
43. C. Copi *et al*, *preprint* arXiv:astro-ph/0605135 (2006).
44. T.R. Jaffe *et al*, *Astrophys. J. Lett.* **629**, 1 (2005).
45. P. Vielva *et al*, *Astrophys. J.* **609**, 22 (2004).
46. J.D. McEwen *et al*, *Mon. Not. R. Astron. Soc.* **369**, 1858 (2006).
47. T.R. Jaffe *et al*, *Astrophys. J.* **644**, 701 (2006).
48. M. Bridges *et al*, *preprint* arXiv:astro-ph/0605325 (2006).
49. A. Lewis and A. Challinor, *Phys. Rep.* **429**, 1 (2006).

Observational constraints and cosmological parameters

Antony Lewis[a]
Institute of Astronomy, Madingley Road, Cambridge, CB3 0HA, UK.

I discuss the extraction of cosmological parameter constraints from the recent WMAP 3-year data, both on its own and in combination with other data. The large degeneracies in the first year data can be largely broken with the third year data, giving much better parameter constraints from WMAP alone. The polarization constraint on the optical depth is crucial to obtain the main results, including $n_s < 1$ in basic six-parameter models. Almost identical constraints can also be obtained using only temperature data with a prior on the optical depth. I discuss the modelling of secondaries when extracting parameter constraints, and show that the effect of CMB lensing is about as important as SZ and slightly increases the inferred value of the spectral index. Constraints on correlated matter isocurvature modes are not radically better than before, and the data is consistent with a purely adiabatic spectrum. Combining WMAP 3-year data with data from the Lyman-α forest suggests somewhat higher values for σ_8 than from WMAP alone.

1 Introduction

The WMAP satellite has now provided three years worth of beautiful data giving a clear picture of the CMB temperature over most of the sky and allowing robust constraints on many cosmological parameters[7,23]. I shall briefly review parameter estimation methodology, then discuss in more detail topical issues relating to WMAP parameter constraints. I also discuss the utility of combining with other data, and show some example joint constraints obtained by combining with Lyman-α data. I shall assume familiarity with standard abbreviations and cosmological parameters.

2 Parameter estimation

The CMB sky is expected (and observed) to be closely Gaussian, and noise properties can also often be approximated as Gaussian. Given a set of parameters, linear-theory predictions for the CMB power spectrum can be computed quickly using numerical codes such as CAMB[14] and CMBFAST[22]. Since the statistics of observed sky or power spectrum estimators are quite well understood, we can therefore compute the likelihood of a given set of parameters given the observed data. We then wish to calculate the posterior distribution of various parameters of interest, P(parameters|data), given a set of priors. In potentially large dimensional parameter spaces, the information in the posterior distribution is most easily extracted by using a set of samples from the distribution. For example an estimate of the posterior mean of a given parameter is given simply by the average of the value of that parameter in the set of samples. More complicated quantities can also be computed from samples, for example the correlations of different parameters, marginalized two-dimensional distributions, etc.

The methods almost universally adopted for sampling are variations of the Metropolis-Hastings Markov Chain Monte Carlo[16,3,12]. These methods consists of constructing a way of exploring parameter space such that the value of the parameters at any given step are a sample from the posterior distribution. There is considerable choice in the details of how these methods are implemented[11,5]. A fairly complete implementation aimed at sampling and analysing non-pathological distributions (i.e. preferably unimodal and not too distorted) most common in cosmology is publicly available in the CosmoMC[b] package[12] used here; see also AnalyseThis[4].

[a] http://cosmologist.info
[b] http://cosmologist.info/cosmomc

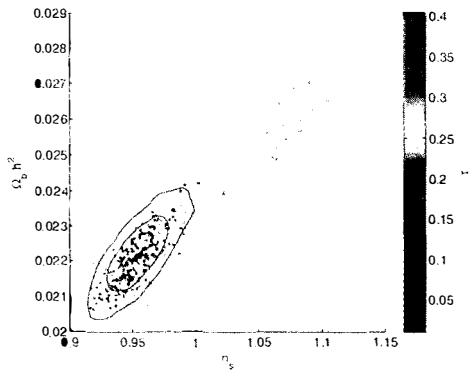

Figure 1: Constraints from WMAP 3-year temperature (points) and joint with polarization (68% and 95% contours) for a basic six parameter ΛCDM model (no tensors). The points represent samples from the posterior distribution, and are coloured by the value of the optical depth τ. Polarization constrains the optical depth, breaking the main flat-model degeneracy and suggesting $n_s < 1$.

Once a set of samples is available, almost every statistical question of interest can be answered using estimators constructed from the samples. The probability density at a point in parameter space is given simply by the number density of samples. Marginalized probabilities in reduced dimensions are given simply by the number density of samples for the parameters in those reduced dimensions. Furthermore often new priors or data can be added very quickly using importance sampling: a way of re-weighting samples based on the difference of the new and old likelihoods [12]. Chains for the WMAP 3-year analysis are available from the LAMBDA[c] website, and are compatible with CosmoMC's *GetDist* program.

3 WMAP 3-year constraints

It is well known from the WMAP first year data that with good measurements of only the first two acoustic peaks of the CMB temperature power spectrum there remains an important degeneracy between the spectral index n_s, the optical depth τ, the baryon density $\Omega_b h^2$ and the amplitude of fluctuations parameterized by A_s or σ_8. This degeneracy remains in the 3-year temperature data, as shown by the samples in Fig. 1.

3.1 Constraining the optical depth

A large scale polarization signal on the CMB can be generated at reionization due to scattering of the CMB quadrupole. By measuring the large scale E-mode power spectrum, one can therefore constrain the optical depth. The 3-year WMAP analysis makes a heroic attempt to clean out dominating foregrounds to extract this signal [17]. Various consistency checks (for example B-mode power spectrum consistent with zero) suggest that this has been achieved to sufficient accuracy to reliably constrain the optical depth. However the possibility of some unidentified foreground remains, and it is unclear how large the foreground-induced systematic error in the result is (unlike for the temperature analysis, there is no marginalization over the foreground templates or fitting uncertainties).

Using the WMAP 3-year result for the large scale polarization the optical depth τ can be constrained, breaking the main flat-model degeneracy, and suggesting that $n_s < 1$ in basic

[c] http://lambda.gsfc.nasa.gov/

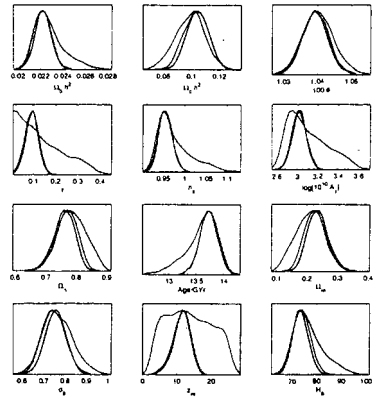

Figure 2: Constraints from WMAP 3-year temperature (red), temperature and polarization (black), and temperature with a Gaussian prior on the optical depth $\tau = 0.10 \pm 0.03$ (blue). The top six parameters have flat priors and are sampled using MCMC, the bottom six parameters are derived.

tensor-free models as shown in Fig. 1. In fact this is essentially the *only* information in the polarization that effects basic cosmological model parameters. For example if we take a prior on the optical depth $\tau = 0.10 \pm 0.03$ (consistent with the polarization result) essentially identical parameter constraints are obtained using only the temperature results as shown in Fig. 2. The polarization spectrum on smaller scales may however be useful for constraining extended models, for example with isocurvature modes. The improvement in parameter constraints from the better measurement of the temperature power spectrum with the 3-year data is relatively modest; using the same τ prior with the first year temperature power spectrum gives an almost identical constraint on n_s as using the 3-year data, though the matter densities are constrained rather better due to the better measurement of the second and third acoustic peaks.

Different priors on the optical depth or reionization redshift can be applied very quickly to existing chains using importance sampling. For example, my personal prior is approximately a Gaussian with $z_{\rm re} = 8 \pm 3$ truncated to zero at $z_{\rm re} < 6$, which is towards the lower end of the distribution obtained by WMAP (e.g. if there were an unidentified foreground remaining in the WMAP data, the value of the optical depth would be expected to come down further). In this case using WMAP temperature and polarization without tensors the $n_s < 1$ result is very significant ($n_s < 0.98$ at 2-sigma) and the value of σ_8 comes down a bit to 0.73 ± 0.05.

3.2 Effect of secondaries

The WMAP 3-year parameter analysis accounts for an SZ contribution by marginalizing over the amplitude of an analytic model calculated for a fixed fiducial set of parameters[23]. The effect of including SZ on the cosmological parameter constraints is not large, and comparable to that obtainable by changing priors in the base parameters. Since the SZ adds power on small scales, adding a contribution means that n_s has to decrease slightly, shifting the posterior distribution further down from $n_s = 1$. However when modelling secondaries, all relevant effects should be included. It is well known that CMB lensing also has a percent level effect on the relevant scales[13] — see Fig. 3. Lensing smooths out the acoustic peaks, and on WMAP scales the main effect is a reduction in the height of the third peak height, as well as smaller effects on the earlier peaks and troughs. The effect can be compensated by increasing n_s, so including lensing tends to *increase* n_s. The effect is shown in Fig 4 and is comparable magnitude to SZ, but has an opposite effect on n_s. The best fit sample has a slightly better χ^2 with lensing included,

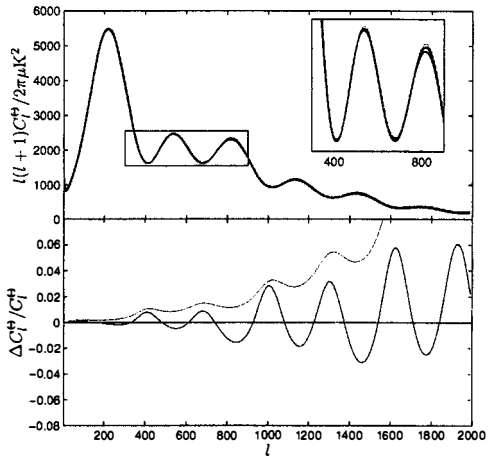

Figure 3: The theoretical unlensed (black) and smoother lensed (red) CMB temperature power spectra (top) and the difference (bottom blue) for a fiducial WMAP 3-year ΛCDM model with $n_s = 0.95$, $\tau = 0.09$. Green lines are unlensed but include the SZ spectrum [9] evaluated for fiducial parameters as used by the WMAP team (with marginalized amplitude) at 22.8GHz. At higher frequencies the SZ contribution is somewhat smaller.

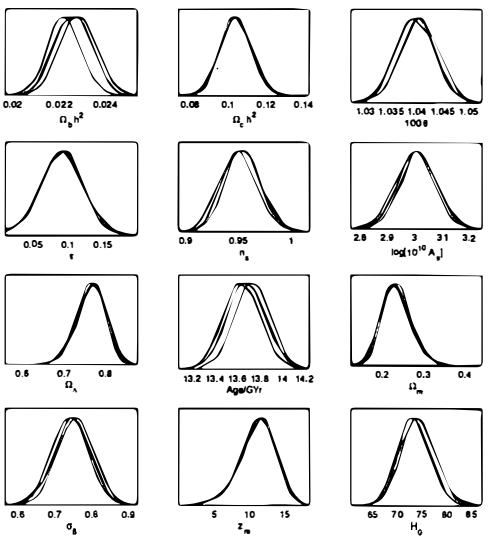

Figure 4: Six parameter WMAP 3-yr constraints with no secondary modelling (blue), marginalizing over SZ model amplitude (red) and marginalizing over SZ and including CMB lensing (black).

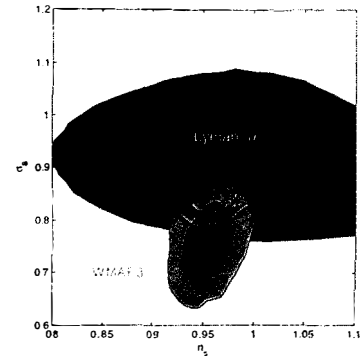

Figure 5: Constraints on the spectral index n_s and σ_8 from WMAP only (green), SDSS Lyman-α (blue [15]), and the joint constraint (red). Contours enclose 68% and 95% of the probability, and the model is ΛCDM with no tensors. Lyman alpha only contours are for fixed best-fit joint values of the other parameters and dependent upon this prior: they give a visual clue to the direction and amount by which the data pull the joint constraints, but the absolute position of the contours is fairly meaningless.

with $\Delta\chi^2 \sim 1$. Since the effect of secondaries is small, they do not have a large effect on the conclusions of the WMAP 3-year analysis. However if SZ is included it would seem sensible to also include CMB lensing. The CMB lensing effect can be computed very accurately and is trivial to include. The fact that SZ and lensing have nearly opposite effects suggests that in practice rather accurate WMAP constraints on n_s can be obtained by neglecting both. However the effect on $\Omega_b h^2$ is in the same direction, and including both shifts the mean up by nearly one sigma compared to including neither, giving $\Omega_b h^2 = 0.0228 \pm 0.0008$.

4 Combining data

WMAP alone provides good constraints on many parameters, especially those that are directly related to the power spectrum. For example the ratio of the sound horizon at last scattering to the angular diameter distance to last scattering is constrained to $\sim 1\%$. Other combinations of parameter are also measured very well, for example WMAP alone gives the linear theory constraints

$$\left(\frac{\Omega_m}{0.238}\right)\left(\frac{h}{0.73}\right)^{2.2}\left(\frac{e^{-\tau}\sigma_8}{0.689}\right)^{-0.9} = 1 \pm 0.01 \quad (1)$$

$$\left(\frac{e^{-\tau}\sigma_8}{0.689}\right)\left(\frac{h}{0.73}\right)^{1.15}\left(\frac{\Omega_m}{0.238}\right)^{-0.066} = 1 \pm 0.04. \quad (2)$$

However the third combination of these parameters is only constrained to 20%. Any data that can improve on these constraints in any direction can be used to improve parameter constraints. In addition external data provides an important consistency check, and any deviations from consistency may indicate departures from the assumed cosmological model.

The WMAP results are now so good that for simple models the small scale C_l can be predicted rather accurately from the WMAP data on larger scales. Data from other CMB experiments currently give relatively large errors on the smaller scale acoustic peaks, and the improvement to parameter constraints from including other CMB data on linear scales is now rather modest. To significantly improve parameter constraints from 3-year WMAP a tight constraint on the third acoustic peak would be very useful. As shown in Fig. 6 small scale

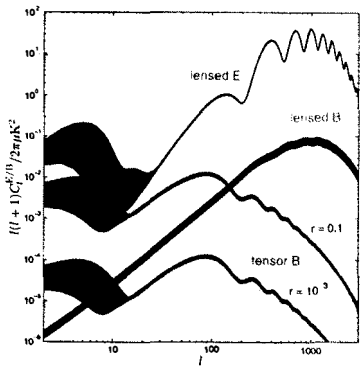

Figure 6: The 95%-confidence regions for the CMB polarization power spectra given WMAP 3-yr, Boomerang [8] and 2dF [19] data with an HST prior $h = 0.72 \pm 0.08$. The parameters varied are those for a constant spectral index ΛCDM model with insignificant neutrino mass and sharp reionization. The two tensor results are the B-mode power spectra expected from for a scale-invariant tensor-mode power spectrum with $A_T = 4r \times 10^{-9}$ and two possible values of r. The effect of tensors on the cosmological parameter constraints was neglected, and a prior $z_{re} > 6$ was assumed. This is an updated version of the figure in Lewis and Challinor [13].

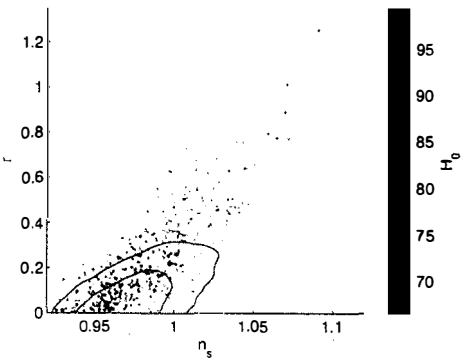

Figure 7: Allowing tensors, samples from WMAP 3-year temperature and polarization (points), compared to the joint constraint with SDSS Lyman-α data [15] (68% and 95% contours).

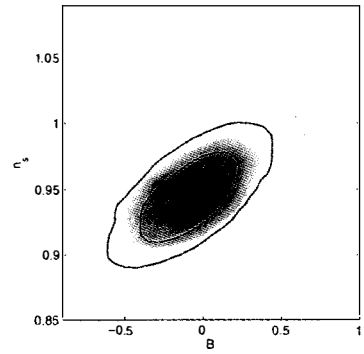

Figure 8: Constraints on the correlated matter isocurvature mode ratio B as defined in Gordon & Lewis [6] using WMAP 3-year data combined with small scale CMB [20,10] and 2dF data [19].

polarization observations have to be very sensitive to compete with the prediction that can be made from current data assuming a basic cosmological model, and it will be a while before small scale CMB E-polarization helps at all with constraining parameters in these models. However consistency with the predictions is an important consistency check.

The WMAP team give constraints with various combinations of data [23]. Of particular note is the significant increase in the expected value of σ_8 when including data from weak lensing. Here as an example I consider combination with Lyman-α data from SDSS [15]. This serves to measure the matter power spectrum scales much smaller than those directly probed by the CMB and hence has the potential to beak degeneracies involving n_s and σ_8. The data from Viel et al. [25] are less constraining that the SDSS results, so I concentrate on the latter here.

Figure 5 shows the joint constrain from WMAP and Lyman-α without tensors. As with weak lensing, adding Lyman alpha increases the values of σ_8 from the value preferred by WMAP alone, with the SDSS joint constraint giving $\sigma_8 = 0.86 \pm 0.03$. The joint constraint is actually otherwise fairly consistent with WMAP alone, for example the best fit sample has $\tau = 0.09, n_s = 0.97$, though it does favour higher values of $\Omega_m \sim 0.3$. It is consistent with $n_s < 1$ at two sigma with no running of the spectral index. A more detailed analysis is now given elsewhere. [24,21]

5 Extended models

One of the most interesting extensions of the basic 6-parameter ΛCDM model is one allowing for a contribution from tensors modes as predicted by some models of inflation. Figure 7 shows constraints on the tensor-scalar ratio r (defined in terms of the initial power spectra as in the WMAP papers) from WMAP alone, and when combined with Lyman-α. Clearly there is no evidence for a tensor contribution, however allowing for tensors does allow the possibility of $n_s \geq 1$: if tensors add power to the low-l multipoles, the spectral index can be bluer and still maintain the correct overall ratio of small and large scale power. Many future observations will be aimed at detecting the B-mode polarization signal from tensor modes, and Fig. 6 shows the expected spectrum for a couple of possible amplitudes in comparison to the predicted signal from lensed scalar modes. Further discussions of inflationary constraints from WMAP 3-year data are given elsewhere. [23,18,1]

Another interesting possibility is an isocurvature mode contribution. Probably the simplest possibility is a totally correlated contribution from matter isocurvature modes, for example from a curvaton model of inflation. Here the spectral index is fixed to that of the adiabatic modes,

and there is only one extra parameter, the ratio of isocurvature modes (which can be negative for anti-correlated modes). The updated [6] constraint is shown in Fig. 8, corresponding to a 95% confidence constraint $-0.42 < B < 0.25$. As with older data there is no evidence at all for isocurvature modes, which should not be surprising given that a simple adiabatic model fits the data well. The WMAP 3-year data does not radically improve the constraint because the main effect is on large scales where the first year data was already cosmic variance limited in the temperature. However degeneracy breaking does help, as does improved sensitivity on the polarization. I expect that more general isocurvature analyses (e.g. updating Bucher et al. [2]) should have a similar conclusion: no evidence for isocurvature modes, though a significant fraction still allowed.

6 Conclusions

The WMAP 3-year results appear to show a remarkable agreement with a simple six parameter ΛCDM model. Numerous extended models have been discussed by the WMAP team [23], though none fit the data significantly better. There is some tension by between the σ_8 values favoured by WMAP and weak lensing and Lyman-alpha data, and this deserves further investigation. The WMAP data alone suggest that either $n_s < 1$ or there is something else interesting, for example a significant tensor mode component.

Future CMB observations that can provide an accurate measurement of the optical depth or third acoustic peak are needed to constrain parameters significantly better with CMB alone. Precision measurements of the temperature spectrum to small scales should allow the spectral index to be determined independently of the polarization constraint on the optical depth. Current and future small scale polarization observations are unlikely to improve basic parameter constraints significantly, though they can be a good test of alternative models. Detecting large scale B-polarization from gravitational waves is of course the main goal of many future missions, and would be a powerful way to constrain models of inflation.

CMB observations are in principle clean way to constrain early universe perturbations and many cosmological parameters. However they are rather insensitive to other parameters, for example the late time evolution of the dark energy. To constrain these parameters complementary data are needed. Consistency with different data sets is a good check on the assumed cosmological model. If consistent other data sets can also be used to break partial degeneracies in the CMB constraints, giving better joint parameter estimates. Many additional data sets not considered here are analysed in combination with WMAP 3-year data in Spergel et al.[23].

Acknowledgements

I thank the organisers for inviting me to give this talk and an excellent conference. I thank Matteo Viel, George Efstathiou, Hiranya Peiris and fellow conferees for useful discussion. I thank K. Abazajian for making his Lyman-α CosmoMC modules public. I acknowledge the use of the Legacy Archive for Microwave Background Data Analysis[d] (LAMBDA). Support for LAMBDA is provided by the NASA Office of Space Science. I thank CITA for use of their Beowulf computer. I am supported by a PPARC Advanced Fellowship.

1. Alabidi L., Lyth D. H., 2006, astro-ph/0603539
2. Bucher M., Dunkley J., Ferreira P. G., Moodley K., Skordis C., 2004, Phys. Rev. Lett., 93, 081301, astro-ph/0401417
3. Christensen N., Meyer R., Knox L., Luey B., 2001, Class. Quant. Grav., 18, 2677, astro-ph/0103134

[d] http://lambda.gsfc.nasa.gov/

4. Doran M., Mueller C. M., 2004, JCAP, 0409, 003, astro-ph/0311311
5. Dunkley J., Bucher M., Ferreira P. G., Moodley K., Skordis C., 2005, MNRAS, 356, 925, astro-ph/0405462
6. Gordon C., Lewis A., 2003, Phys. Rev., D67, 123513, astro-ph/0212248
7. Hinshaw G., et al., 2006, astro-ph/0603451
8. Jones W. C., et al., 2005, astro-ph/0507494
9. Komatsu E., Seljak U., 2002, MNRAS, 336, 1256, astro-ph/0205468
10. Kuo C.-l., et al., 2004, ApJ, 600, 32, astro-ph/0212289
11. Lewis A., Bridle S., , CosmoMC Notes, http://cosmologist.info/notes/cosmomc.ps.gz
12. Lewis A., Bridle S., 2002, Phys. Rev., D66, 103511, astro-ph/0205436
13. Lewis A., Challinor A., 2006, Phys. Rept., 429, 1, astro-ph/0601594
14. Lewis A., Challinor A., Lasenby A., 2000, ApJ, 538, 473, astro-ph/9911177
15. McDonald P., et al., 2005, ApJ, 635, 761, astro-ph/0407377
16. Neal R. M., 1993, Probabilistic Inference Using Markov Chain Monte Carlo Methods, http://cosmologist.info/Neal93
17. Page L., et al., 2006, astro-ph/0603450
18. Peiris H., Easther R., 2006, astro-ph/0603587
19. Percival W. J., et al., 2001, MNRAS, 327, 1297, astro-ph/0105252
20. Readhead A. C. S., et al., 2004, ApJ, 609, 498, astro-ph/0402359
21. Seljak U., Slosar A., McDonald P., 2006, astro-ph/0604335
22. Seljak U., Zaldarriaga M., 1996, ApJ, 469, 437, astro-ph/9603033
23. Spergel D. N., et al., 2006, astro-ph/0603449
24. Viel M., Haehnelt M. G., Lewis A., 2006, astro-ph/0604310
25. Viel M., Haehnelt M. G., Springel V., 2004, MNRAS, 354, 684, astro-ph/0404600

FROM $\alpha(z)$ TO $w(z)$

C.J.A.P. MARTINS
CFP, Universidade do Porto, Rua do Campo Alegre 687, 4169-007 Porto, Portugal
and DAMTP, CMS, University of Cambridge, Wilberforce Road, Cambridge CB3 0WA, U.K.

I describe the theoretical motivation for and possible roles of cosmological scalar fields, focusing on the spacetime variation of fundamental couplings. I present our recent work on using varying couplings as a dark energy probe, and preliminary measurements of α using the Sunyaev-Zel'doich effect. Prospects for future improvements are also briefly described.

1 Theoretical Expectations

The deepest question of modern physics is whether or not there are fundamental scalar fields in nature. They are a key ingredient in the standard model of particle physics (cf. the Higgs particle, which is supposed to give mass to all other particles and makes the theory gauge-invariant), but there is so far no evidence that nature has any use for them. Yet in recent years we have come to realize that the early universe is an ideal place to search for scalar fields, if they exist at all, and there have been some possible hints for them in various contexts.

Observations suggest that the recent universe is dominated by an energy component whose gravitational behaviour is quite similar to that of a cosmological constant (as first introduced by Einstein). This could of course be the right answer, but the observationally required value is so much smaller than what would be expected from particle physics that a dynamical scalar field is arguably a more likely explanation. Theoretical motivation for such a field is not hard to find. In string theory, for example, dimensionful parameters are expressed in terms of the string mass scale and a scalar field vacuum expectation value.

Now, the slow-roll of this field (which is mandatory so as to yield negative pressure) and the fact that it is presently dominating the universe imply (if the minimum of the potential vanishes) that the field vacuum expectation value today must be of order m_{Pl}, and that its excitations are very light, with $m \sim H_0 \sim 10^{-33}$ eV. But a further consequence of this is seldom emphasized [1]: couplings of this field lead to observable long-range forces and time-dependence of the constant of nature (with corresponding violations of the Einstein Equivalence Principle).

A spacetime varying scalar field coupling to matter mediates a new interaction. If the recent evidence for varying couplings [2,3] is explained by a dynamical scalar field, this automatically implies the existence of a new force. A series of space missions (ACES, μSCOPE, STEP) will improve on current bounds on the Einstein Equivalence Principle by as many as 6 orders of magnitude. These must find violations if the current data is correct [4]. Note that since the scalar field is effectively massless on solar system scales, the new force will be similar to gravity in many respects. However, if the coupling is not precisely proportional to to mass, the new force will be composition-dependent, manifesting itself as a violation of the Weak Equivalence Principle (otherwise known as the Universality of Free Fall).

Moreover, in theories where a dynamical scalar field is responsible for varying α, the other gauge and Yukawa couplings are also expected to vary. Specifically, in GUTs there is a relation between the variation of α and that of the QCD scale, Λ_{QCD}, implying that the nucleon mass will vary when measured in units of an energy scale that is independent of QCD, such as the electron mass. We therefore expect variations of the proton-to-electron mass ratio, $\mu = m_p/m_e$. As a typical example[5], for the MSSM embedded on a GUT one has

$$\frac{\dot{\mu}}{\mu} \sim \frac{\dot{\Lambda}_{QCD}}{\Lambda_{QCD}} \sim R\frac{\dot{\alpha}}{\alpha}\,. \tag{1}$$

The parameter R is very model-dependent, not only in magnitude but even in sign. But the wide range of α-μ relations implies that simultaneous measurements of both are a powerful discriminating tool between competing models: we can in principle test GUT scenarios without ever needing to detect any GUT model particles, say at accelerators. Measurements of μ, although less explored than those of α, have been suggested a long time ago[6].

2 From α and μ to $w(z)$

A crucial observational goal is characterizing the properties of dark energy, and in particular to look for dynamical behaviour. A key property is its equation of state, $w = p/\rho$, and considerable effort has recently been put into trying to measure it. Current methods of choice are type Ia supernovae and (more recently) weak lensing. However, the question arises as to whether these are indeed the best tools for the task at hand. It has been known for some time[7] that supernova measurements are limited as a probe of the dark energy equation of state, especially if it is varying with redshift. Analysis of current and future constraints on the dark energy equation of state, from the various standard approaches and parametrized in the usual way[8], shows that a convincing detection of time variation of w is unlikely even with hypothetical future space-based experiments such as DUNE or JDEM (be it with SNAP or DESTINY). This is expected since any dynamical field providing the dark energy must be slow-rolling at the present time, and for slow variations there will always be a constant w model that produces nearly identical results over the redshift range where dark energy is dynamically important.

Luckily, better (and cheaper) alternatives are available. A potentially effective tool for probing dynamical dark energy has been suggested previously in [9,10], though not yet studied in detail: probing varying couplings is a key test to these models, and in particular the varying couplings can be used to infer the evolution of the scalar field, and thus to determine its equation of state. This is analogous to reconstructing the 1D potential for the classical motion of a particle once its trajectory has been specified. Previous efforts only considered the variation of α, but variations of μ may be easier to detect than those of α, although the number of such measurements is currently much smaller than the α dataset—the main reason for this is the difficulty in finding molecular Hydrogen clouds. One of the goals of the present work is to encourage further measurements of μ, which are expected to lead to tighter constraints on the evolution of the dark energy equation of state than those of α if R is indeed large.

Let us emphasize that having impreved measurements of both α and μ is extremely useful for various reasons. With both observables, the reconstruction will be a lot easier, not to mention less model-dependent. One has the advantage of a much larger lever arm in terms of redshift, since such measurements can be made up to redshifts of $z \sim 4$. This may not not seem a big advantage, since dark energy is only dynamically relevant at relatively low redshift, but in fact it is a key one, since the additional redshift coverage probes the otherwise unaccessible z range where scalar field dynamics is expected to be fastest, thus reducing (and possibly elliminating) the model-dependence that is unavoidable in the standard methods (where parametrisations like $w = w_0 + w_1 z$ are dangerously naive). Last but not least, it provides direct evidence

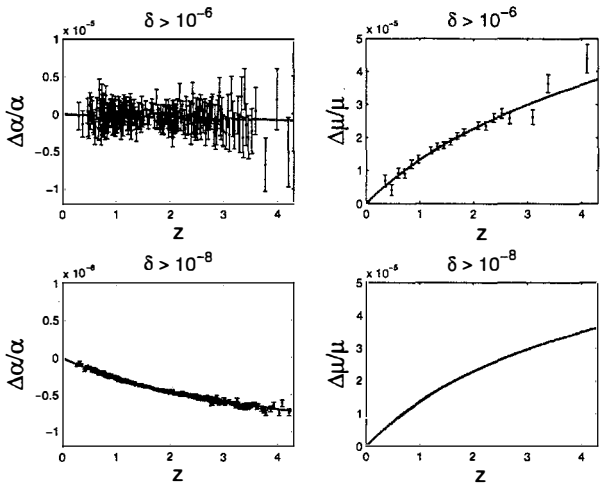

Figure 1: Simulated datasets expected for α and μ in the near future (top panels) and with CODEX (lower panels), assuming a particular dark energy model.

distinguishing dynamical dark energy from a cosmological constant, which given the current data may be very challenging for the standard cosmological tests. Figs. 1 and 2 show an example of our recent work [11] showing the benefits of a reconstruction using data on both couplings.

3 α from SZ

Becuase the reconstruction method requires calculating (first) derivatives of data, it is important to have a good redshift coverage. Therefore it is also important to have a method of measurement that can be applied to a large range of redshifts without changing systematics. Such a method does exist for measuring α: it is the Sunyaev-Zel'dovich effect. Its edshift-independence makes it ideal. The first two such measurements [12] yield

$$-0.023 < \left(\frac{\Delta\alpha}{\alpha}\right)_{Coma} < 0.029, \quad z = 0.02 \tag{2}$$

$$-0.001 < \left(\frac{\Delta\alpha}{\alpha}\right)_{A2163} < 0.061, \quad z = 0.203 \tag{3}$$

using data from MITO, SuZIE, OVRO and BIMA. These bounds are already significant, and an improvement of several orders of magnitude is expected in the coming years, when throusands of clusters will be at hand for this task.

4 Conclusions

The prospects for further, more accurate measurements of fundamental constants are definitely bright. The methods described above and other completely new ones that may be devised thus offer the real prospect of an accurate mapping of the cosmological evolution of the fine-structure constant, $\alpha = \alpha(z)$, and the proton to electron mass ratio, $\mu = \mu(z)$. This may well prove to be the most exciting area of research in the coming years. The worse that can happen to cosmology is the scenario where a number of cosmological parameters are fixed by WMAP, then nothing new happens until Planck comes along and merely adds one digit to the precision of each

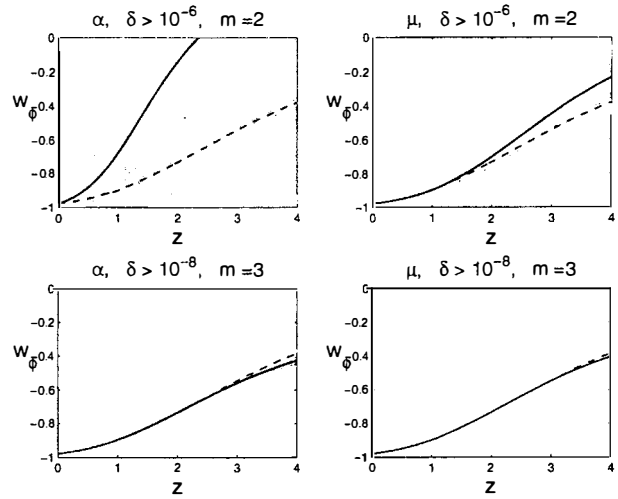

Figure 2: The reconstruction of the equation of state and its error band is shown for the datasets of Fig. 1. The dashed line represents the dark energy equation of state corresponding to the potential used to generate the simulated data and the solid line corresponds to the reconstruction's best fit. The dark and light region are the 1σ and 2σ confidence levels.

already-known parameter. After that cosmology may well be dead: there will be little incentive to pushing research further to figure out what the next digit is. However, if in the meantime violations of the Equivalence Principle and/or varying fundamental constants are unambiguously confirmed, then one will (finally) have evidence for the existence of new physics—most likely in the form of scalar fields—in nature (which one may legitimately hope that Planck is able to probe) and an entirely new era begins.

Acknowledgments

This work was funded by FCT (Portugal), through grant POCI/CTE-AST/60808/2004, in the framework of the POCI2010 program, supported by FEDER.

References

1. S. M. Carroll, *Phys. Rev. Lett.* **81**, 3067 (1998).
2. M. T. Murphy, J. K. Webb, and V. V. Flambaum, M.N.R.A.S. **345**, 609 (2003).
3. E. Reinhold *et al.*, *Phys. Rev. Lett.* **96**, 151101 (2006).
4. T. Damour, Astrophys. Sp. Sci. **283**, 445 (2003).
5. X. Calmet and H. Fritzsch, *Phys. Lett.* B **540**, 173 (2002).
6. R. I. Thompson, Astrophys. Lett. **16**, 3 (1975).
7. I. Maor, R. Brustein, and P. J. Steinhardt, *Phys. Rev. Lett.* **86**, 6 (2001).
8. A. Upadhye, M. Ishak, and P. J. Steinhardt, *Phys. Rev.* D **72**, 063501 (2005).
9. D. Parkinson, B. A. Bassett, and J. D. Barrow, *Phys. Lett.* B **578**, 235 (2004).
10. N. J. Nunes and J. E. Lidsey, *Phys. Rev.* D **69**, 123511 (2004).
11. P. P. Avelino, C. J. A. P. Martins, N. J. Nunes, and K. Olive, *Reconstructing the dark energy equation of state with varying couplings*, submitted to *Phys. Rev.* D (2006).
12. E. S. Battistelli *et al.*, *Measuring α with the SZ effect*, submitted to *Ap. J.* (2006).

BEST MEDIAN VALUES FOR COSMOLOGICAL PARAMETERS

M. ROOS
Department of Physical Sciences, Division of High Energy Physics, University of Helsinki, Helsinki

From the values quoted by five large, partially overlapping multiparameter fits for r, α_s, $w+1$, Ω_k, and Σm_ν one concludes that none of them differs significantly from zero, and that their correlations to other parameters are insignificant. In the determination of the other parameters they can therefore be ignored. However, since neutrinos are massive we select analyses including Σm_ν as a free parameter. We then combine the values obtained for ω_b, ω_m, h, τ, n_s, Σm_ν and A_s (or σ_8) to determine median values as well as 17-percentile and 83-percentile errors.

1 Introduction

Since July 2004 five large analyses [1,2,3,4,5] of cosmological parameters have appeared (we call them papers P1, P2, P3, P4 and P5) based on partly overlapping data. Since each analysis determines parameter values separately for different subsets of data and for several choices of parameter spaces, the results are *legio*. For instance, these five papers quote altogether 56 different values for the density of matter in the Universe, ω_m. The parameter values exhibit notable differences due to differing data selections, choices of priors, methods of analysis, simulation variance, and of course statistical fluctuations. The purpose of this review is to compare these five analyses, and to extract single representative values. A more complete version of this Moriond conference talk is publicly available [6]). Since the third year WMAP cosmological parameters [7] were presented at the Moriond Conference, I comment them briefly here.

2 Data sets and method of analysis

The papers P1–P5 all use the CMB $\langle TT \rangle$ [8] and $\langle TE \rangle$ [9] power spectra on large angular scales from the first year Wilkinson Microwave Anisotropy Probe (WMAP) observations. They analyze various combinations of the Sloan Digtal Sky Survey (SDSS) galaxy clustering data [10,11], the SDSS galaxy bias analysis at $z = 0.1$ [12], a recent sample of luminous red galaxies (LRG) [2], the 2dFGRS power spectrum of galaxy clustering [13], the supernova type Ia "gold" set data [14], Ly-α forest data [15], and the CMB temperature and polarization data measured by ACBAR [16], BOOMERanG [3], CBI [17,5], DASI [18], MAXIMA [19], and VSA [20]. All analyses quote results from fits to different subsets and combinations of data sets that are to a large extent overlapping and therefore not independent. Moreover, parts of the reported errors are systematic and not stochastic, so different data sets cannot be summarized using frequentist or Bayesian methods. Since the purpose of the present analysis is to obtain accurate information about parameter values rather than to test different sets for consistency or for correlations, we consider only fits to maximal data sets, not to subsets differing in selection or methods.

Many parameters are determined with quite low precision, the published 1σ errors are large, the correlations likewise insignificant, and the choices of data subsets demonstrate notable variations in the parameter values. The tendency in the cosmological literature is to draw optimistic conclusions from 1σ and 2σ confidence regions obtained by marginalization in many-parameter spaces. We think that parameter estimates from the five data sets, at their present state of accuracy, can well be combined without sophisticated methods.

We represent each measurement i of a parameter a by a Gaussian ideogram with central value a_i, symmetrized error δa_i, and unit area. (In least squares fitting one weights the area by $(\delta a_i)^{-2}$). We sum these ideograms and define our best values as medians, not means. In lieu of variances we define our errors as the 17-percentiles and the 83-percentiles of the sum ideogram. The most notable effect is then that these "errors" are always larger than the smallest individual error in the data set, whereas in statistical averaging errors always come out smaller than the smallest error entering. This reflects the systematic errors and selection errors which anyway cannot be treated statistically.

3 Parameter spaces and fits

The most general parameter space explored in the five papers is 13-dimensional, $\mathbf{p} = (\omega_b, \omega_m, \Omega_k, \Sigma m_\nu, \tau, h, \sigma_8, b, w, w_1, n_s, A_s, \alpha_s, r)$. However, all fits are done in a "standard" 6-parameter space of $\omega_b, \omega_m, \tau, h, \sigma_8, n_s$, or in a space enlarged to 7 parameters.

The matter density parameter ω_m is related to the normalized density parameter by $\Omega_m = \omega_m/h^2$ where h is the Hubble parameter in units of 100 km s^{-1} Mpc^{-1}. Similarly, $\Omega_b = \omega_b/h^2$ is the normalized baryon density parameter and $\Omega_{dm} = \omega_{dm}/h^2$ is the normalized density parameter of dark matter. The density parameter of dark energy is then $\Omega_\Lambda = 1 - \Omega_m - \Omega_k$, where Ω_k is the curvature or vacuum density. The ratio of pressure to energy density for dark energy is $w = w_0 + w_1(1-a)$, where a is the scale parameter of the Universe. The fraction of dark matter that amounts to neutrinos is $f_\nu = \Omega_\nu/\Omega_{dm}$. Assuming that the neutrinos are Majorana particles with standard freeze-out, the neutrino mass sum is $\Sigma m_\nu = 94.4\ \omega_{dm} f_\nu$ eV.

The parameters τ, n_s, α_s, A_s, r, b describe fluctuation properties: the scalar spectral index is n_s, the scalar amplitude is A_s, alternatively described by σ_8, the r.m.s linear mass perturbation in $8h^{-1}$ Mpc spheres. The ratio of tensor to scalar amplitudes is $r = A_t/A_s$, and the running of n_s with k is $\alpha_s = \mathrm{d}n_s/\mathrm{d}k$. The parameter τ measures the Thomson scattering optical depth to decoupling, and b is the bias factor describing the difference in amplitude between the galaxy power spectrum and that of the underlying dark matter.

3.1 Parameters r, α_s, w, w_0, w_1, Ω_k, $\Omega_0, \Sigma m_\nu$

P1, P3 and P4 quote upper limits (95% CL) for the parameter r, the smallest value being $r < 0.36$ in 7-parameter fits with $\alpha_s = 0$, $\Sigma m_\nu = 0$ and $w = -1$. The effect of including r as a seventh free parameter is that the information on the basic six parameters is degraded – their errors increase, but their central values change only within the quoted 1σ errors. Thus there is no significant evidence for $r \neq 0$, only for a commonly acceptable limit $r < 0.4$.

The parameter α_s as determined by P1 is consistent with zero. P3 quotes a value in rather marked disagreement with P1. The effect of including α_s in the P1 and P3 fits increases the errors of the basic parameters considerably. To proceed, we take $\alpha_s = 0$.

P1, P2, P3 and P4 have determined values of w in 7-parameter fits. In P1 and P3 this has very little effect on the errors and central values of the basic six parameters, more so in P4, but the correlations are still insignificant. Including w as a fifth parameter in P2 degrades the errors of their basic four parameters, but changes their central values by less than 1σ. One concludes

Table 1: Recommended values of parameters

Parameter	Definition	Median	83-/17-percentile, or 95% CL limit
$10^2\omega_b$	$10^2\times$ baryon density	2.28	$+0.12/-0.13$
$\Omega_b = \omega_b/h^2$	Normalized baryon density	0.048	$+0.005/-0.004$
ω_m	Total matter density	0.139	± 0.011
$\Omega_m = \omega_m/h^2$	Normalized matter density	0.286	$+0.030/-0.028$
$\Omega_{dm} = \Omega_m - \Omega_b$	Normalized dark matter density	0.238	$+0.030/-0.028$
$\Omega_\Lambda = 1 - \Omega_m - \Omega_k$	Normalized dark energy density	0.714	$+0.028/-0.030$
h	Hubble parameter [100 km/s Mpc]	0.687	$+0.034/-0.047$
Σm_ν	Neutrino mass sum		< 1.1 eV
τ	Thomson scattering optical depth to decoupl.	0.147	$+0.068/-0.064$
n_s	Scalar spectral index	0.962	$+0.030/-0.027$
$\ln(10^{10}A_s)$	Scalar fluctuation amplitude	3.12	$+0.14/-0.12$
σ_8	RMS linear mass perturb. in $8h^{-1}$ Mpc spheres	0.81	$+0.09/-0.14$
$r = A_t/A_s$	Tensor to scalar amplitude fluctuation ratio		< 0.4
$\alpha_s = \mathrm{dn_s/dk}$	Running scalar index	-0.011	± 0.012
w	Dark energy EOS	-0.92	$+0.17/-0.12$
Ω_k	Normalized vacuum density	-0.023	$+0.017/-0.050$

that there is no significant information indicating $w \neq -1$ or $w_1 \neq 0$. Although some correlayion to other parameters is claimed, it is not significant.

P2, P3 and P4 quote values for Ω_k for the case $w = -1$. The general tendency is confirmed that the inclusion of a free parameter Ω_k degrades the information on the basic parameters, yet the correlations are insignificant. In the sequel we shall only use parameter values determined under the assumptions of flat space and $r = \alpha_s = w_1 = w + 1 = 0$.

Since neutrino oscillations occur, that is a motivation to include Σm_ν in the fits. P1, P3 and P4 do search for neutrino information in 7-parameter fits, however only upper limits are given.

3.2 Parameters ω_b, Ω_b, ω_m, Ω_m, h

The ω_b values found in the five analyses are very consistent, uncorrelated with other parameters and robust against different choices of parameter sets and priors, and in good agreement with the BBN value[21].

The Hubble parameter h could be obtained from P1, P2, P3 and P4. Since P3 and P4 exhibit clearly the effect of a variable neutrino mass, we do not use P2 and P5 which do not vary Σm_ν. The parameter ω_m is determined better than $\Omega_m = \omega_m/h^2$, the preferred route to Ω_m is to use ω_m and h. The available input data are the P1 value for Ω_m, the P2 value for ω_m, and the ω_{dm} values from P3, P4, and P5. Combining these values in the most efficient way with h and ω_b one finds the median with smallest errors.

3.3 Parameters τ, n_s, A_s, σ_8

The parameters τ and Ω_k are significantly correlated[4], so if Ω_k is taken to be zero, also τ will be small. The median values of τ and n_s, based on data from P1, P3, P4, and P5 and the first year WMAP data[8,9] actually turn out to be rather close to what WMAP3 now reports[7].

Finally, P3, P4, and P5 quote values for the scalar fluctuation amplitude both as $\ln(10^{10}A_s)$ and as σ_8, P1 quotes σ_8. Since σ_8 is rather strongly correlated with τ and Ω_m, a more accurate determination of the latter could have been obtained if all experiments had agreed to fix σ_8 and τ at some common values.

4 Conclusions

By combining results from five large data analyses [1,2,3,4,5] we have obtained median values for the parameters ω_b, ω_m, h, τ, n_s, A_s and the derived parameters Ω_b, Ω_m, Ω_Λ, Ω_{dm}, σ_8, all summarized in Table 1. No significant values can be obtained for r, α_s, w, Ω_k and Σm_ν.

Note that although the new WMAP3 values are more accurate than the old ones, if combined with other data (WMAP3 offers 8 such alternatives [7]) the selection variance continues to be the dominating error.

Acknowledgments

My participation in Moriond XLI has been generously supported by the Magnus Ehrnrooth Foundation, Finland.

References

1. U. Seljak *et al*, *Phys. Rev.* D **71**, 103515 (2005).
2. D. J. Eisenstein *et al*, *Astrophys. J.* **633**, 560 (2005).
3. C. J. MacTavish *et al*, preprint arXiv astro-ph/0507503.
4. A. G. Sánchez *et al*, *Mon. Not. Roy. Astr. Soc.* **366**, 189 (2006)
5. J. L. Sievers *et al*, preprint arXiv astro-ph/0509203.
6. M. Roos, preprint arXiv astro-ph/0509089.
7. D. N. Spergel *et al*, preprint arXiv astro-ph/0603449.
8. G. Hinshaw et al., *Astrophys. J. Suppl.* **148**, 135 (2003).
9. A. Kogut et al., *Astrophys. J. Suppl.* **148**, 161 (2003).
10. M. Tegmark et al., *Astrophys. J.* **606**, 702 (2004).
11. M. A. Strauss et al., *Astron. J.* **124**, 1810 (2002).
12. U. Seljak et al., *Phys. Rev.* D **71**, 043511 (2005)).
13. S. Cole et al., *Mon. Not. Roy. Astr. Soc.* **362**, 505 (2005)
14. A. G. Riess et al., *Astrophys. J.* **607**, 665 (2004)).
15. P. McDonald et al., preprint arXiv astro-ph/0405013.
16. C. L. Kuo et al., *Astrophys. J.* **600**, 32 (2004).
17. A. C. S. Readhead et al., *Astrophys. J.* **609**, 498 (2004).
18. N. W. Halverson et al., *Astrophys. J.* **568**, 38 (2002).
19. S. Hanany et al., *Astrophys. J.* **545**, L5 (2000).
20. C. Dickinson et al., *Mon. Not. Roy. Astr. Soc.* **353**, 732 (2004)).
21. A. Cuoco et al., *Int. J. Mod. Phys.* **A19**, 4431 (2004).

LIMITS ON THE NEUTRINO MASS FROM COSMOLOGY AND THEIR IMPACT ON WORLD NEUTRINO DATA

P. SERRA
Dipartimento di Fisica, Università degli Studi di Roma "La Sapienza", P.le Aldo Moro 5, 00185, Rome, Italy

G. L. FOGLI, E. LISI, A. MARRONE
Dipartimento di Fisica and Sezione INFN di Bari, Via Amendola 173, 70126, Bari, Italy

A. MELCHIORRI
Dipartimento di Fisica and Sezione INFN, Università degli Studi di Roma "La Sapienza", P.le Aldo Moro 5, 00185, Rome, Italy

A. PALAZZO
Dipartimento di Fisica and Sezione INFN di Bari, Via Amendola 173, 70126, Bari, Italy

J. SILK
Astrophysics, Denys Wilkinson Building, Keble Road, OX13RH, Oxford, United Kingdom

We derive upper limits on the sum of neutrino masses from an updated combination of data from Cosmic Microwave Background experiments and Galaxy Redshifts Surveys. The results are discussed in the context of three-flavor neutrino mixing and compared with neutrino oscillation data, with upper limits on the effective neutrino mass in Tritium beta decay from the Mainz and Troitsk experiments and with the claimed lower bound on the effective Majorana neutrino mass in neutrinoless double beta decay from the Heidelberg-Moscow experiment.

1 Introduction

Cosmological observations have started to provide valuable upper limits on absolute neutrino masses (see, e.g., the reviews [1,2]), competitive with those from laboratory experiments. In particular, the combined analysis of high-precision data from Cosmic Microwave Background (CMB) anisotropies and Large Scale Structures (LSS) has already reached a sensitivity of $O(\mathrm{eV})$ (see, e.g., [3,4,5]) for the sum of the neutrino masses Σ,

$$\Sigma = m_1 + m_2 + m_3 \ . \tag{1}$$

We recall that the total neutrino energy density in our Universe, $\Omega_\nu h^2$ (where h is the Hubble constant normalized to $H_0 = 100$ km s^{-1} Mpc^{-1}) is related to Σ by the well-known relation $\Omega_\nu h^2 = \Sigma/(93.2\ \mathrm{eV})$ [6], and plays an essential role in theories of structure formation. It can thus leave key signatures in LSS data (see, eg.,[7]) and, to a lesser extent, in CMB data (see, e.g.,[8]). Recently, it has also been shown that accurate Lyman-α (Lyα) forest data [9], taken at face value, can improve the current CMB+LSS constraints on Σ by a factor of ~ 3, with important consequences on absolute neutrino mass scenarios[10].

On the other hand, atmospheric, solar, reactor and accelerator neutrino experiments have convincingly established that neutrinos are massive and mixed. World neutrino data are consistent with a three-flavor mixing framework (see [11] and references therein), parameterized in terms of three neutrino masses (m_1, m_2, m_3) and of three mixing angles $(\theta_{12}, \theta_{23}, \theta_{13})$, plus a possible CP violating phase δ.

Neutrino oscillation experiments are sensitive to two independent squared mass difference, δm^2 and Δm^2 (with $\delta m^2 \ll \Delta m^2$), hereafter defined as [12]

$$(m_1^2, m_2^2, m_3^2) = \mu^2 + \left(-\frac{\delta m^2}{2}, +\frac{\delta m^2}{2}, \pm \Delta m^2\right), \qquad (2)$$

where μ fixes the absolute neutrino mass scale, while the cases $+\Delta m^2$ and $-\Delta m^2$ identify the so-called normal and inverted neutrino mass hierarchies, respectively. Neutrino oscillation data indicate that $\delta m^2 \simeq 8 \times 10^{-5}$ eV^2 and $\Delta m^2 \simeq 2.4 \times 10^{-3}$ eV^2. They also indicate that $\sin^2\theta_{12} \simeq 0.3$, $\sin^2\theta_{23} \simeq 0.5$, and $\sin^2\theta_{13} \leq$ few%. However, they are currently unable to determine the mass hierarchy ($\pm\Delta m^2$) and the phase δ, and are insensitive to the absolute mass parameter μ in Eq. (2).

The absolute neutrino mass scale can also be probed by non-oscillatory neutrino experiments. The most sensitive laboratory experiments to date have been focussed on tritium beta decay and on neutrinoless double beta decay. Current experiments (Mainz [14] and Troitsk [15]) for the effective electron neutrino mass m_β [13] provide upper limits in the range $m_\beta \leq$ few eV.

Neutrinoless double beta decay ($0\nu2\beta$) experiments are instead sensitive to the so-called effective Majorana mass $m_{\beta\beta}$ (if neutrinos are Majorana fermions); all $0\nu2\beta$ experiments place only upper bounds on $m_{\beta\beta}$ (the most sensitive being in the eV range), with the exception of the Heidelberg-Moscow experiment [18], which claims a positive (but highly debated) $0\nu2\beta$ signal $m_{\beta\beta} > 0.17$ eV at 95% c.l. and corresponding to $m_{\beta\beta}$ in the sub-eV range at best fit [19,20].

In these proceedings, we will briefly illustrate the impact of the cosmological constraints on the sum of neutrino masses on the three-flavor mixing theoretical and observational scenario.

2 Bounds from cosmology, laboratory and astrophysics

The neutrino contribution to the overall energy density of the universe can play a relevant role in large scale structure formation and leave key signatures in several cosmological data sets. More specifically, neutrinos suppress the growth of fluctuations on scales below the horizon when they become non relativistic.

To constrain Σ from cosmological data, we perform a likelihood analysis comparing the recent observations with a set of models with cosmological parameters sampled as follows: cold dark matter (cdm) density $\Omega_{\rm cdm}h^2 \in [0.05, 0.20]$ in steps of 0.01; baryon density $\Omega_b h^2 \in [0.015, 0.030]$ (motivated by Big Bang Nucleosynthesis) in steps of 0.001; a cosmological constant $\Omega_\Lambda \in [0.50, 0.96]$ in steps of 0.02; and neutrino density $\Omega_\nu h^2 \in [0.001, 0.020]$ in steps of 0.002. We restrict our analysis to *flat* Λ-CDM models, $\Omega_{\rm tot} = 1$, and we add a conservative external prior on the age of the universe, $t_0 > 10$ Gyrs. The value of the Hubble constant in our database is not an independent parameter, since it is determined through the flatness condition. We adopt the conservative top-hat bound $0.50 < h < 0.90$ and we also consider the 1σ constraint on the Hubble parameter, $h = 0.71 \pm 0.07$, obtained from Hubble Space Telescope (HST) measurements [21]. We allow for a reionization of the intergalactic medium by varying the CMB photon optical depth τ_c in the range $\tau_c \in [0.05, 0.30]$ in steps of 0.02.

We restrict the analysis to adiabatic inflationary models with a negligible contribution of gravity waves. We let vary the spectral index n of scalar primordial fluctuations in the range $n \in [0.85, 1.3]$ and its running $dn/d\ln k \in [-0.40, 0.2]$ assuming pivot scales at $k_0 = 0.05$ Mpc^{-1}

and $k_0 = 0.002$ Mpc^{-1}. We rescale the fluctuation amplitude by a prefactor C_{110}, in units of the value $C_{110}^{\rm WMAP}$ measured by the Wilkinsin Microwave Anisotropy Probe (WMAP) satellite. Finally, concerning the neutrino parameters, we fix the number of neutrino species to $N_\nu = 3$, all with the same mass (the effect of mass differences compatible with neutrino oscillation being negligible in the current cosmological data [22]). An higher number of neutrino species can weakly affect both CMB and LSS data (see, e.g., [23]) but is highly constrained by standard big bang nucleosynthesis and is not considered in this work, where we focus on 3ν mixing.

The cosmological data we considered comes from observation of CMB anisotropies and polarization, galaxy redshift surveys and luminosity distances of type Ia supernovae. For the CMB data we use the temperature and cross polarization results from the WMAP satellite [3] using the method explained in [24] and the publicly available code.

Given a theoretical temperature anisotropy and polarization angular power spectrum in our database, we can therefore associate a $\chi^2_{\rm WMAP}$ to the corresponding theoretical model.

We further include the latest results from other CMB datasets. The CMB data analysis methods have been already described in [11] and will not be reported here.

In addition to the CMB data we also consider the real-space power spectrum of galaxies from either the 2 degrees Fields (2dF) Galaxy Redshifts Survey or the Sloan Digital Sky Survey (SDSS), using the data and window functions of the analysis of [25] and [4]. We restrict the analysis to a range of scales over which the fluctuations are assumed to be in the linear regime ($k < 0.2h^{-1}$ Mpc). When combining with the CMB data, we marginalize over a bias b for each data set considered as an additional free parameter.

We also include information from the Lyα Forest in the SDSS, using the results of the analysis of [10] and [9], which probe the amplitude of linear fluctuations at very small scales. For this data set, small-scale power spectra are computed at high redshifts and compared with the values presented in [9]. As in [10], we do not consider running.

We finally incorporate constraints obtained from the SN-Ia luminosity measurements of [26] using the so-called GOLD data set. Luminosity distances at SN-Ia redshifts are computed for each model in our database and compared with the observed apparent bolometric SN-Ia luminosities.

The results coming from from the joint analysis of CMB + SN-Ia + HST + 2dF + Lyα, assuming no running in the analysis, show a 2σ bound $\Sigma < 0.47$ eV, in very good agreement (despite the more approximate method we used) with the analysis already presented in [10]

Then we add bounds from laboratory and astrophysics. We consider confidence regions obtained from analysis of neutrino oscillation data, of m_β and $m_{\beta\beta}$ data and cosmological CMB+LSS data (see [11] for more details). Figure 1 shows such regions projected in the three coordinate planes. [a] Separate laboratory and cosmological upper bounds at the 2σ level are shown as dashed lines, while the regions allowed by the combination of laboratory, cosmological, and oscillation data are shown as thick solid curves for normal hierarchy and as thin solid curves for inverted hierarchy. It can be seen that the upper bounds on the $(m_\beta, m_{\beta\beta}, \Sigma)$ observables are dominated by the cosmological upper bound on Σ. This bound, via the (m_β, Σ) and $(m_{\beta\beta}, \Sigma)$ correlations induced by oscillation data, provides upper limits also on $m_{\beta\beta}$ and m_β, which happen to be stronger than the current laboratory limits by a factor ~ 4.

In Fig. 1, the tension (at 2σ) between the limits from cosmology and the lower limit on $m_{\beta\beta} > 0.17$ eV claimed by the Heidelberg-Moscow experiment is a clear symptom of possible problems, either in some data sets or in their theoretical interpretation, which definitely prevent any global combination of data. It would be premature to conclude that, e.g., the $0\nu2\beta$ claim is "ruled out" by cosmological data but it is anyway exciting that global neutrino data analyses have already reached a point where fundamental questions may start to arise.

[a] For the sake of brevity, the subdominant block of data (SN-Ia + HST) is not explicitly indicated in figure labels.

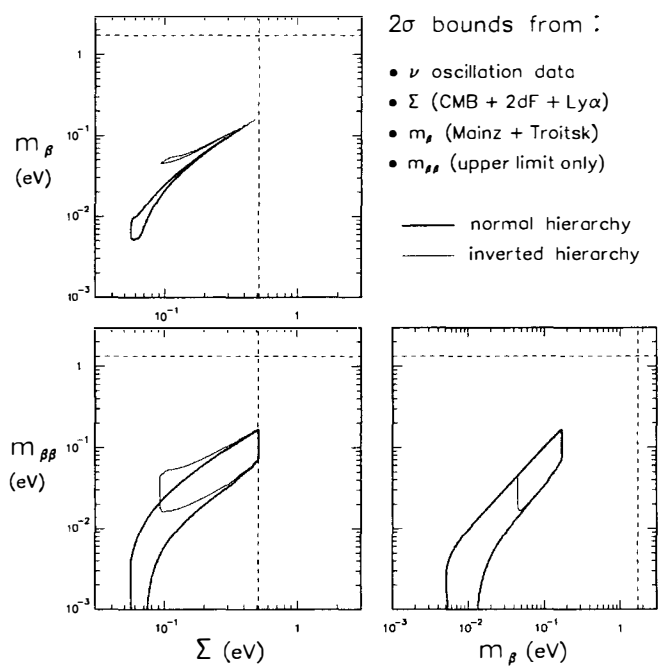

Figure 1: Global 3ν analysis in the $(m_\beta, m_{\beta\beta}, \Sigma)$ parameter space, using oscillation data plus laboratory data and cosmological data. This figure implements also upper limits (shown as dashed lines at 2σ level) on m_β from Mainz+Troitsk data, on $m_{\beta\beta}$ from $0\nu2\beta$ data, and on Σ from CMB+2dF+Lyα data. In combination with oscillation parameter bounds, the cosmological upper limit on Σ dominates over the laboratory upper limits on m_β and $m_{\beta\beta}$.

Acknowledgements

P.S. would like to thank the Organizers of the *XLIst Rencontres de Moriond 2006* workshop. The work of P.S. is supported by the COFIN 2004 027755 research project. The work of A.M. is supported by the Italian Ministero dell'Istruzione, Università e Ricerca (MIUR) through the "GEMINI" research project and Istituto Nazionale di Fisica Nucleare (INFN) through the "Astroparticle Physics" research project. The work of G.L.F., E.L., A.M.2, and A.P. is supported by the Italian Ministero dell'Istruzione, Università e Ricerca (MIUR) and Istituto Nazionale di Fisica Nucleare (INFN) through the "Astroparticle Physics" research project.

References

1. V. Barger, D. Marfatia and K. Whisnant, Int. J. Mod. Phys. E **12**, 569 (2003).
2. A.D. Dolgov, Phys. Rept. **370**, 333 (2002).
3. WMAP Collaboration, C.L. Bennett *et al.*, Astrophys. J. Suppl. **148**, 1 (2003).
4. SDSS Collaboration, M. Tegmark *et al.*, Phys. Rev. D **69**, 103501 (2004).
5. See also O. Lahav, "Massive Neutrinos and Cosmology," in *Neutrino 2004*.
6. Review of Particle Physics, S. Eidelman et al., Phys. Lett. B **592**, 1 (2004).
7. W. Hu, D.J. Eisenstein, and M. Tegmark, Phys. Rev. Lett. **80**, 5255 (1998).
8. C.P. Ma and E. Bertschinger, Astrophys. J. **455**, 7 (1995).
9. SDSS Collaboration, P. McDonald *et al.*, astro-ph/0405013.
10. U. Seljak *et al.*, astro-ph/0407372.
11. G. L. Fogli, E. Lisi, A. Marrone, A. Melchiorri, A. Palazzo, P. Serra and J. Silk, Phys. Rev. D **70** (2004) 113003 [arXiv:hep-ph/0408045].
12. G. L. Fogli, E. Lisi, D. Montanino, and A. Palazzo, Phys. Rev. D 65, 073008 (2002).
13. B.H.J. McKellar, Phys. Lett. B 97, 93 (1980); F. Vissani, Nucl. Phys. B (Proc. Suppl.) 100, 273 (2001); J. Studnik and M. Zralek, hep-ph/0110232. See also the discussion in Y. Farzan and A.Yu. Smirnov, Phys. Lett. B 557, 224 (2003).
14. C. Weinheimer, in the Proceedings of *Neutrino 2002*, p. 279.
15. V.M. Lobashev, in the Proceedings of *NPDC 17*, ed. by N. Auerbach, Zs. Fulop, Gy. Gyurky, and E. Somorjai, Nucl. Phys. A **719**, 153 (2003).
16. K. Eitel, "Direct Neutrino Mass Experiments," in *Neutrino 2004* [?].
17. S.M. Bilenky, J. Hosek, and S.T. Petcov, Phys. Lett. B 94, 495 (1980); J. Schechter and J.W.F. Valle, Phys. Rev. D 22, 2227 (1980).
18. H.V. Klapdor-Kleingrothaus, A. Dietz, H.L. Harney, and I.V. Krivosheina, Mod. Phys. Lett. A 16, 2409 (2001).
19. H.V. Klapdor-Kleingrothaus, A. Dietz, I.V. Krivosheina, and O. Chkvorets, Nucl. Instrum. Meth. A 522, 371 (2004).
20. H.V. Klapdor-Kleingrothaus, I.V. Krivosheina, A. Dietz, and O. Chkvorets, Phys. Lett. B 586, 198 (2004).
21. W. Freedman *et al.*, Astrophysical Journal, 553, 47 (2001).
22. J. Lesgourgues, S. Pastor, and L. Perotto, Phys. Rev. D 70, 045016 (2004).
23. R. Bowen *et al.*, Mon. Not. Roy. Astron. Soc. 334, 760 (2002).
24. L. Verde *et al.*, Astrophys. J. Suppl. 148, 195 (2003).
25. W.J. Percival *et al.*, Mon. Not. Roy. Astron. Soc. 327, 1297 (2001).
26. Supernova Search Team Collaboration, A.G. Riess *et al.*, Astrophys. J. 607, 665 (2004).
27. S. Hannestad, JCAP 0305, 004 (2003).
28. G.L. Fogli *et al.*, PRD 70, 113003 (2004).
29. V. Barger, D. Marfatia, and A. Tregre, Phys. Lett. B 595, 55 (2004).
30. P. Crotty, J. Lesgourgues, and S. Pastor, Phys. Rev. D 69, 123007 (2004).

PROSPECTS OF MEASURING NEUTRINO MASSES AND DARK ENERGY WITH WEAK LENSING TOMOGRAPHY

H. TU
Department of Physics and Astronomy, Ny Munkegade, 8000 Aarhus C, Denmark

We investigate how tomographic information can help to improve the sensitivity of future weak lensing surveys to neutrino masses and the equation of state parameter of dark energy. Systematics are carefully taken into account. We also outline other cosmological probes with similar abilities, which can be combined with weak lensing measurement.

1 Neutrinos and Dark Energy

Cosmology has reached a precision level that "nonstandard" parameters begin to be constrained. Those of great interest are for example the absolute neutrino mass scale and the dark energy equation of state w and/or its time evolution.

Neutrinos with masses in the sub-eV range constitute the hot dark matter. After decoupling, they stream out from overdense into underdense regions, smoothing out inhomogeneities at scales smaller than their free-streaming length $\lambda_{\rm fs}$. This leads to a suppresion of present matter power à la $\Delta P(k)/P(k) \simeq -8\,\Omega_\nu/\Omega_m$ at $k \gg 2\pi/\lambda_{\rm fs}$, where $\Omega_\nu h^2 \simeq \frac{\sum m_\nu}{93.5\ {\rm eV}}$ is their relic energy density. Direct laboratory experiments constrain the neutrino mass to $m_\nu \leq 2.2$ eV, and the KATRIN experiment is expected to pin down to 0.2 eV. In the mean time, cosmology imposes a bound of $\sum m_\nu \leq 0.4 - 1$ eV, depending on the survey(s) considered and data used (see e.g. Ref.[3,13]), but also on some not simultaneously well constrained parameter(s)[2]. We take the $(\sum m_\nu - w)$ degeneracy admitted in the CMB (+ LSS + SNIa) data as an example, and demonstrate how it can be broken by adding the weak lensing (tomography) data.

The dark energy density $\Omega_{\rm de}$ and the dark energy equation of state $w(z)$ determine the expansion rate of the universe

$$H^2(z) = H_0^2 \left[\Omega_m(1+z)^3 + \Omega_{\rm de}\, e^{3\times\int_0^z dz'\,[1+w(z')]}\right] . \qquad (1)$$

Dark energy also suppresses the growth rate of structure $D(a) \equiv P(k,a)/P(k,a=1)$. Best fit values $w \simeq -0.97$ or -1.023 (for a constant w) are found by e.g. combining WMAP with SNLS data, and the latter with baryon acoustic oscillation data from SDSS, respectively. Assuming a simple time evolution for $w(z)$, we obtain 1σ errors of order 0.05 from future weak lensing tomography data combined with CMB data (cf. Tabel 1).

2 Weak Lensing Tomography

Weak gravitational lensing/cosmic shear measurements trace directly matter distribution in a wide range of scales, without invoking a light-to-mass bias parameter. The Canada-France-

Hawaii Telescope Legacy Survey (CFHTLS) [4] already provides competitive constraints on σ_8 and Ω_m. The source galaxies can also be separated in two subsets based on their estimated photometric redshifts to infer satisfactory shear statistics. Future ambitious projects such as SNAP [5], LSST [7] will allow grouping the source galaxies into more redshift bins. We consider the weak lensing auto- and cross convergence spectrum in the case of a flat universe

$$C_\ell^{ij} = \frac{9}{16} H_0^4 \Omega_m^2 \int_0^{\chi_h} d\chi \, \frac{g_i(\chi) g_j(\chi)}{a^2 \chi^2} \, P(\ell/\chi, z) \,, \tag{2}$$

where $\chi = \int_0^z dz'/H(z')$ is the comoving radial distance, with χ_h denoting the horizon. The weighting function for the i-th tomography bin is given by

$$g_i(\chi) \equiv 2\chi \int_\chi^{\chi_h} d\chi' \, n(\chi') \, \frac{\chi' - \chi}{\chi'} \,, \quad \text{where} \quad n_i(z) \propto \bar{n}_i \left(\frac{z}{z_{0\,i}}\right)^{\alpha_i} \exp\left[-\left(\frac{z}{z_{0\,i}}\right)^{\beta_i}\right] \tag{3}$$

is the number of source galaxies per steradian at redshifts $[z, z+dz]$ in the i-th bin, normalised to $\int_0^\infty dz n_i(z) = 1$. The weak lensing statistics can roughly be understood as a projection of the 3-dimensional matter power spectrum $P(k,z)$ onto a 2-dimensional surface, with the most contribution coming from $k \sim \ell/(\chi(z_0)/2)$ (in the case of only one bin). While dark energy equation of state $w(z)$ determines majorly the projection, the neutrino mass alters dominantly the matter power spectrum. The efficiency of tomographic binning in gaining extra information can be quantified by the correlation coefficient $R^{ij} \equiv C_\ell^{ij}/\sqrt{C_\ell^{ii} C_\ell^{jj}}$.

3 Systematic Effects

i) Photometric redshift uncertainties:
current photometric techniques have uncertainties of $\lesssim 10\%$ per galaxy. The accuracy can be further improved for space-based surveys adopting IR-filters, as proposed for SNAP [5]. For a ground-based survey such as LSST, spectroscopic calibration of the photometric redshift system is required [7]. We follow the approach of Ref. [6], where the true number of galaxies per steradian in the i-th tomography bin is recovered by

$$n_i(z) = \int_{z_{\rm ph}^{(i)}}^{z_{\rm ph}^{(i+1)}} dz_{\rm ph} \, n_{\rm gal}(z) \, p(z_{\rm ph}|z) \,, \tag{4}$$

where $n_{\rm gal}(z)$ is the true overall galaxy number density at redshifts $[z, z+dz]$. The probability that a given z is measured as $z_{\rm ph}$ is assumed to be Gaussian, i.e. $p \propto \exp\left[-(z_{\rm ph} + z_{\rm bias} - z)^2/2\sigma_z^2\right]$, with $\sigma_z(z)$ and $z_{\rm bias}(z)$ the scatter and the bias parameters, respectively. In general, as long as the tomography bin width is sufficiently larger than σ_z, photometric undertainties should not present a problem to weak lensing tomography.
ii) Galaxy shape measurement errors:
this can be divided into multiplicative and additive errors. The former are due to errors in shear calibration and PSF size estimation. It is estimated to be 2% [8] currently, and is expected to be controlled to 1% by the time SNAP/LSST start. We follow the approach in Ref. [9] and define the convergence spectrum as $\hat{C}_\ell^{ij} = C_\ell^{ij} \times (1 + f_i + f_j)$, where f_i is the irreducible part of the shear calibration error in the i-th tomography bin, after averaging over all directions and redshifts within that bin. Additive errors arise when artificial shear signals are induced. Current simulations[8] suggest that they are controlled to under 10^{-3}. This kind of errors generally depends on ℓ and is more difficult to parametrise. We neglect them in our analysis.
iii) Theoretical uncertainties:
weak lensing surveys are sensitive to scales of several arcminutes, i.e. $\ell \sim 1000$. This means that

Table 1: Projected 1σ errors from various combinations of Planck and weak lensing. The labels "Wide" and "Deep" denote the two generic lensing surveys considered in this work, and the suffix number indicates the number of tomography bins used in the analysis.

	Planck	+Wide-1	+Wide-5	+Deep-1	+Deep-5
$\sigma(\sum m_\nu)$ (eV)	0.48	0.15	0.043	0.39	0.047
$\sigma(w_0)$	0.83	0.093	0.034	0.35	0.045
$\sigma(w_a)$	4.0	0.39	0.081	1.7	0.063
$\sigma(\Omega_{\rm de})$	0.08	0.020	0.0068	0.036	0.0099

dominant contribution to the signals comes from density perturbations of co-moving wavenumbers $k \simeq 1 \to 10\ h\ \mathrm{Mpc}^{-1}$ at $z \sim 0.5$. Weak lensing thus probes mostly the non-linear regime, and proper corrections to the linear matter power spectrum calculated with e.g. CMBFAST [10] must be applied. At present, all N-body simulations agree within $5-10\%$ for ΛCDM cosmologies, and there are various semi-analytical and fitting formulae, tested at best to roughly 10% against simulations for our use. In the future, this uncertainty need to be reduced to $1 \to 2\%$ [11]. In our present work we adopt the "halo model" approach (see e.g. Ref. [12]), and observe that the relative suppression ($\Delta P(k)/P(k)$) due to neutrino free-streaming seems to be smaller therein than when no non-linear corrections are applied.

4 Error Forecast

We consier generic wide (LSST-like) and deep (SNAP-like) surveys, combined with projected CMB measurements from PLANCK (1 year). We first apply a Fisher matrix analysis, where the lensing observable is the number-weighted convergence spectrum, $\mathbf{C}_\ell = n_i n_j \hat{C}_\ell^{ij}$. This has the advantage of reflecting changes in the photometric redshift parameters. For the dark energy equation of state, we adopt the parametrisation $w(z) = w_0 + w_a(1-a(z))$ for its time-dependence. Our fiducial model is a flat universe, described by 11 parameters: $\sum m_\nu = 0.07$ eV, $\Omega_{\rm de} = 0.7$, $\Omega_b h^2 = 0.0245$, $\Omega_c h^2 = 0.1225$, $\omega_0 = -1$, $\omega_a = 0$, $n_s = 1$, $\alpha_s = 0$, $\sigma_8 = 0.9$, $\tau = 0.05$ and $N_{\rm eff} = 3$. In addition, we marginalise over the nuisance parameters for the systematics, for which the fiducial values $z^i_{\rm bias} = 0$ and $\sigma^i_z = 0.05$, as well as $f_i = 0$ are chosen. Appropriate priors on them are also imposed.

We divide the redshift range $[0, 3]$ into $n_t = 1, 2, 3, 5, 8$ tomography bins. One sees that (cf. Table 1) weak lensing (wide) improves the w_0 and w_a error estimates from CMB alone by roughly a factor of ten. If tomographic information is used, both wide and deep surveys achieve comparable absolute errors. For the neutrino mass, we find a sensitivty of $\sigma(\sum m_\nu) < 0.05$ eV can be reached if 5 tomography bins are used. Table 2 demonstrates that weak lensing tomography indeed breaks the $\sum m_\nu - w$ degeneracy effectively: when five bins are used, fixing in the original model $\{N_{\rm eff}, \alpha_s, w_0, w_a\}$ at e.g. $\{3, 0, -1, 0\}$ (the 7 parameter model) only improves the 1σ error for $\sum m_\nu$ by 15%, whereas without tomography the difference is almost a factor of two.

5 Other Measurements for the Neutrino Mass

Baryon Acoustic Oscillations (BAO) measurements infer the Hubble parameter $H(z)$ and the angular diameter distance $D_A(z)$ separately. They therefore break the $\sum m_\nu - w$ degeneracy in a similar way as weak lensing does. They are orthogonal to SNIa measurement in the (Ω_m, w) parameter space. Using the recent SDSS LRG data combined with CMB (WMAP 3 year) + LSS + SNIa data, a robust bound of $\sum m_\nu \leq 0.62$ (11 parameters) or 0.48 eV (fixing $N_{\rm eff} = 3, w = -1$

Table 2: Projected 1σ constraints on the neutrino mass from various combinations of Planck and an LSST-like wide lensing survey (with one and five tomography bins) for two cosmological models.

Model	Cosmological probes	$\sigma(\sum m_\nu)$
11 parameters	Planck only	0.48 eV
11 parameters	Planck+Wide-1	0.15 eV
11 parameters	Planck+Wide-5	0.043 eV
7 parameters	Planck+Wide-1	0.082 eV
7 parameters	Planck+Wide-5	0.037 eV

and $\alpha_s = 0$) is derived [13].

CMB photons from the last scattering surface at $z \approx 1100$ are also deflected by the same large scale structure at $z \lesssim 3$. Extracting the weak lensing information encoded in the CMB signal from e.g. Planck will yield a $\sigma(\sum m_\nu)$ of 0.15 eV [14]. Prospects of determining the neutrino and dark energy properties shall be evaluated by combining all these measurements in a full Markov Chain Monte Carlo analysis [15].

Acknowledgments

We thank Steen Hannestad and Yvonne Wong for the nice collaboration, and Håkon Dahle, Alexandre Refregier and Richard Massey for the explanation on weak lensing systematics.

References

1. S. Hannestad, H. Tu and Y. Y. Y. Wong, arXiv:astro-ph/0603019.
2. S. Hannestad, Phys. Rev. Lett. **95** (2005) 221301 [arXiv:astro-ph/0505551].
3. J. Lesgourgues and S. Pastor, arXiv:astro-ph/0603494.
4. E. Semboloni *et al.*, arXiv:astro-ph/0511090.
5. R. Massey *et al.*, Astron. J. **127** (2004) 3089 [arXiv:astro-ph/0304418]; A. Refregier *et al.*, Astron. J. **127** (2004) 3102 [arXiv:astro-ph/0304419].
6. Z. M. Ma, W. Hu and D. Huterer, Astrophys. J. **636** (2005) 21 [arXiv:astro-ph/0506614].
7. http://www.lsst.org/
8. C. Heymans *et al.*, arXiv:astro-ph/0506112.
9. D. Huterer, M. Takada, G. Bernstein and B. Jain, Mon. Not. Roy. Astron. Soc. **366** (2006) 101 [arXiv:astro-ph/0506030].
10. U. Seljak and M. Zaldarriaga, Astrophys. J. **469** (1996) 437 [arXiv:astro-ph/9603033]; http://www.cmbfast.org/
11. D. Huterer and M. Takada, Astropart. Phys. **23** (2005) 369 [arXiv:astro-ph/0412142].
12. A. Cooray and R. Sheth, Phys. Rept. **372** (2002) 1 [arXiv:astro-ph/0206508].
13. A. Goobar, S. Hannestad, E. Mortsell and H. Tu, arXiv:astro-ph/0602155.
14. J. Lesgourgues, L. Perotto, S. Pastor and M. Piat, Phys. Rev. D **73** (2006) 045021 [arXiv:astro-ph/0511735].
15. L. Perotto, J. Lesgourgues, S. Hannestad, H. Tu and Y. Y. Y. Wong, arXiv:astro-ph/0606227; S. Hannestad, J. Lesgourgues, L. Perotto, H. Tu and Y.Y.Y. Wong, work in progress.

II – CURRENT OBSERVATIONS

SHAPELET ANALYSIS OF WEAK LENSING SURVEYS

JOEL BERGE[a], ALEXANDRE REFREGIER
Service d'Astrophysique, CEA Saclay, Orme des Merisiers, Bât. 709, 91191 Gif-sur-Yvette, France

RICHARD MASSEY
California Institute of Technology, MC 105-24, 1200 East California Boulevard, Pasadena, CA 91125, USA

Shapelets are basis functions well adapted to astronomical data and a convenient tool for weak lensing analysis. We present their formalism and the associated pipeline we use to analyse weak lensing surveys, with an emphasize on PSF modelling. We then show the preliminary mass map we infered from the weak lensing processing of a CFHTLS/Megacam image. We perform an E/B decomposition, which reveals significant E-mode detections. We finally find that this mass map matches well previous KSB cosmic shear measurement, and that the main halos that we detect have counterparts analyses of the same region of the sky in other wavelengths.

1 Introduction

Weak lensing is observable through the distorsion it produces in the image of distant galaxies, due to the gravitational potential of intervening large scale structures between those galaxies and the observer. After its first detections a few years ago, we now enter a new era in which we are aiming at measuring it with a high precision, so as to constrain cosmological parameters. To do so, we need to possess a precise and accurate tool, that allows us to deal with images inevitably noisy, pixellated, and convolved with a PSF. In this proceeding, after introducing the shapelet method, we show how to perform an actual shapelet decomposition and PSF modelling. We apply the presented method to real data, and show some preliminary results on a CFHTLS Deep field.

2 Shapelets

Shapelets are a complete, orthogonal, set of basis functions, with which one can efficiently decompose galaxy images [1,2,3,4]. Their Cartesian form consists of Hermite polynomials weighted with a gaussian. Their polar form, which we will use hereafter, consists of Laguerre polynomials weighted with a gaussian. An object with profile $f(r,\theta)$ can thus be decomposed into a weighted sum of polar shapelets basis functions $\chi_{n,m}$ as

$$f(r,\theta) = \sum_{n=0}^{\infty} \sum_{m=-n}^{n} f_{n,m}\chi_{n,m}(r,\theta;\beta) \quad (1)$$

[a]e-mail : joel.berge@cea.fr

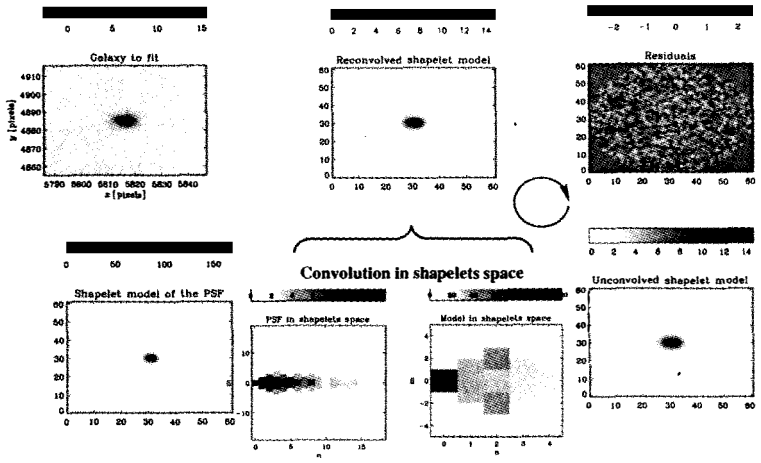

Figure 1: Illustration of a shapelet decomposition of a real galaxy image. The observed galaxy (top-left), a PSF model (bottom-left) and an analytical model of the galaxy (bottom-right) are the inputs to an iteration. This is used to convolve the analytical model with the PSF (bottom-center), and to compare a pixellised model (top-center) with the observed galaxy until residuals (top-right) are consistent with noise.

where $f_{n,m}$ is the shapelet coefficient of order (n, m), given by $f_{n,m} = \iint f(r,\theta)\chi_{n,m}(r,\theta;\beta)r\mathrm{d}r\mathrm{d}\theta$, where β is a typical scale. In practice, most of the shape information is contained within the first coefficients. This allows us to truncate the sum (1) to a certain maximum order of decomposition $n_{\max}$. Furthermore, the shapelets formalism provides an intuitive and analytical form for mathematical operations such as convolution, and provides a natural shear operator.. It is therefore well adapted to the challenge of cosmic shear measurement.

The way we use shapelets is summarized by Figure (1). We first isolate the galaxy that we want to decompose into shapelets (top-left). We then create an analytical shapelet model of this galaxy (bottom-right). Knowing *a priori* the PSF on that galaxy, and having a shapelets decomposition of it (bottom-left), we convolve it to the shapelet model of the galaxy in shapelets space (bottom-center). We pixellise our convolved model, so as to have a model of the observed galaxy (top-center), which we can directly compare to the original galaxy. We use a least-square fit to obtain a faithful convolved, pixellised, model of the galaxy, for which the residuals with the original galaxy are consistent with noise (top-right).

This way, we obtain an analytical model of galaxies, free from pixellization and noise, and deconvolved from the PSF, that we eventually use for measuring cosmic shear.

As mentioned above, the shapelets decomposition of a galaxy requires knowledge of the PSF at the position of each galaxy. Modelling the PSF is a crucial task, since the PSF ellipticity is typically 5-10%, while we are seeking for weak lensing distorsions of a few percents, and needs particular care. This is achieved by first selecting stars, and decomposing them into shapelets so as to have a shapelet model of the PSF at the position of the stars. Since shapelets use all the shape information for the PSF correction, we need to model all the shape information of the PSF, and not only its first moments as done by previous generation shear measurement techniques[5]. This includes the proper modelling of the wings of the PSF. The left two panels of Figure (2) show a typical PSF of the CFHTLS/Megacam Deep survey and its profile : although its FWHM is low ($\sim$ 0.7arcsec), its wings spread far from the center (5-6 arcsec). To obtain an acceptable model, we have to decompose it into shapelets to a high order of decomposition. The

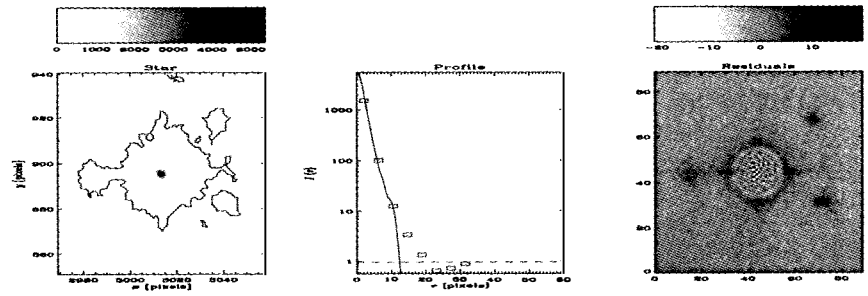

Figure 2: Left : typical CHFT/Megacam PSF, the solid line shows the SExtractor's size of the star. Center : profile of this PSF ; squares show the observed profile, the solid line is for the shapelet model profile. Right : residuals of the shapelets model relative to the observed PSF.

right panel of Figure (2) shows the residuals between the star on the left panel, and its shapelets model obtained with an order of decomposition $n_{\max} = 28$. Residuals due to its large wings are still visible but are two orders of magnitude smaller than the star brightness, and therefore negligeable. Finally, since the PSF must be known at the position of the galaxy that we want to correct, we interpolate its shapelets coefficients at the position of each galaxy, using polynomial basis functions.

Before using this pipeline on real data, we tested it on the STEP weak lensing simulations[6] and found good shear recovery. Our results are already competitive with older and best implementations of first generation shear measurement techniques.

3 Analysis of CFHTLS/Megacam images

We used the pipeline described above to analyse CFHTLS/Megacam images. We show here the preliminary results we obtained on the D1 field, which covers 1 deg^2 with an exposure time of 132 hours in the I band, which we selected for the weak lensing analysis. For convenience, in this preliminary analysis, we had to cut the original image into quarters, therefore introducing supplementary edge effects while modelling the PSF across the image. We thus put masks at the border of quarters, as shown by the black areas on Figure (3). This figure shows the mass map we infered from our weak lensing measurement, using a wavelet mass reconstruction method [7]. E modes, which are due to weak lensing, and trace the distribution of matter, are shown on the left panel. B modes, which are created by systematics and show spurious detections, are shown on the right panel. Clearly, there are significant E modes, without B mode counterparts. We detect approximately 4 such halos on one square-degree, which represent a number density roughly compatible with a ΛCDM cosmology and with Subaru results [8]. They match well detections made using an independent KSB shear measurement method [9]. They also have counterparts in a light map of the same region [10], and in X-ray detections [11]. Nonetheless, a few B modes remain, mostly on the edges of the image. They are however less numerous than, and are not correlated with, E modes. Thus, they do not plague the main halo detections on this image, and should disappear with future improvements of the PSF modelling.

4 Conclusion

The shapelets method is a new generation shear measurement method which aims at meeting the high precision shape measurement challenge. We developed an IDL pipeline which includes a PSF modelling, and tested it blindly on the STEP simulations, before using it on real images.

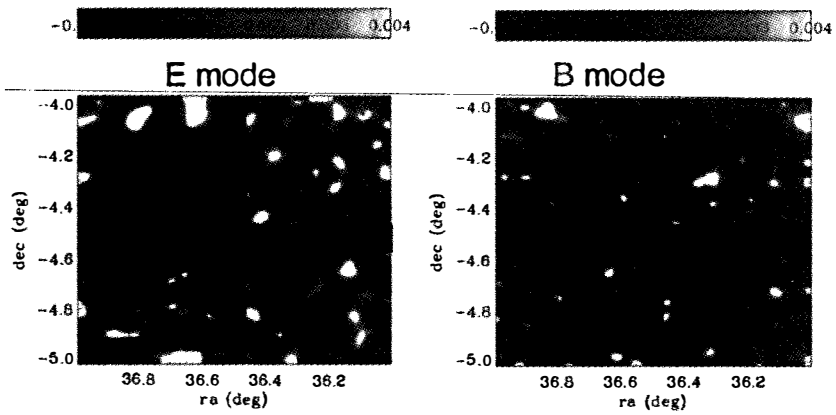

Figure 3: Mass map of the CFHT/Megacam D1 deep field. Light spots correspond to detections (left : E modes ; right : B modes). The black cross on fields corresponds to masks that we put after splitting the field into quarters.

So far, we have preliminary results on CFHTLS/Megacam Deep fields, which are comparable (and compatible) with other weak lensing analysis and with other wavelengths analysis of the same region of the sky. We are now applying the shapelets method to more images. These will be used to build a mass-selected halo catalogue which will be compared with the XMMLSS X-ray catalogue [12].

Acknowledgments

We thank Yannick Mellier, Raphael Gavazzi, Florian Pacaud, Sandrine Pires and Marguerite Pierre for useful discussions and for sharing their results. JB acknowledges financial support from a European Marie Curie grant for this Moriond conference.

This work is based in part on observations obtained with MegaPrime/MegaCam, a joint project of CFHT and CEA/DAPNIA, at the Canada-France-Hawaii Telescope (CFHT) which is operated by the National Research Council (NRC) of Canada, the Institut National des Science de l'Univers of the Centre National de la Recherche Scientifique (CNRS) of France, and the University of Hawaii. This work is based in part on data products produced at TERAPIX and the Canadian Astronomy Data Centre as part of the Canada-France-Hawaii Telescope Legacy Survey, a collaborative project of NRC and CNRS.

References

1. A. Refregier, *MNRAS* **338**, 35 (2003).
2. A. Refregier & D. Bacon, *MNRAS* **338**, 48 (2003).
3. R. Massey & A. Refregier, *MNRAS* **363**, 197 (2005).
4. R. Massey, A. Refregier & D. Bacon, astro-ph/0408568
5. N. Kaiser, G. Squires & T. Broadhurst, *ApJ* **449**, 460 (1995)
6. C. Heymans *et al*, *MNRAS* **368**, 1323 (2006) ; R. Massey *et al*, *in prep*
7. J.L. Starck, S. Pires & A. Refregier, A&A **451**, 1139 (2006)
8. S. Miyazaki *et al*, *ApJ* **580**, L97 (2002)
9. R. Gavazzi & G. Soucail, *A&A*, submitted, astro-ph/0605591
10. C. Marmo, private communication.
11. J. Bergé *et al*, *in prep.*
12. F. Pacaud *et al*, 2006, *MNRAS*, submitted ; M. Pierre *et al*, JCAP **9**, 11 (2004)

BOOMERanG-B03 observations of CMB anisotropy and polarization

P. de Bernardis[1,21], P.A.R. Ade[2], J.J. Bock[3], J.R. Bond[4], J. Borrill[5,6], A. Boscaleri[7], P. Cabella[8], C.R. Contaldi[4,9], B.P. Crill[10], G. De Gasperis[8], A. de Oliveira-Costa[11], G. De Troia[1], G. Di Stefano[12], P. Ehlers[13], E. Hivon[10], V. Hristov[14], A. Iacoangeli[1], A.H. Jaffe[9], W.C. Jones[14], T.S. Kisner[15,16], A.E. Lange[14], C.J. MacTavish[17], C. Marini Bettolo[1], S. Masi[1], P. Mason[14], P.D. Mauskopf[2], A. Melchiorri[1,21], T.E. Montroy[15], F. Nati[1], L. Nati[1], P. Natoli[8,18], C.B. Netterfield[13,17], E. Pascale[17], F. Piacentini[1], D. Pogosyan[4,19], G. Polenta[1], S. Prunet[20], S. Ricciardi[1], G. Romeo[12], J.E. Ruhl[15], P. Santini[1], M. Tegmark[11], E. Torbet[16], M. Veneziani[1], and N. Vittorio[8,18]

[1] *Dipartimento di Fisica, Universita' di Roma La Sapienza, Roma, Italy*
[2] *School of Physics and Astronomy, Cardiff University, Wales, UK*
[3] *Jet Propulsion Laboratory, Pasadena, CA, USA*
[4] *Canadian Institute for Theoretical Astrophysics (CITA), University of Toronto, ON, Canada*
[5] *Computational Research Division, Lawrence Berkeley National Laboratory, Berkeley, CA, USA*
[6] *Space Sciences Laboratory, University of California, Berkeley, CA, USA*
[7] *IFAC-CNR, Firenze, Italy*
[8] *Dipartimento di Fisica, Universita' di Roma Tor Vergata, Roma, Italy*
[9] *Department of Physics, Imperial College, London, UK*
[10] *Infrared Processing and Analysis Center, California Institute of Technology, Pasadena, CA, USA*
[11] *Department of Physics, Massachusetts Institute of Technology, Cambridge, MA, USA*
[12] *Istituto Nazionale di Geofisica e Vulcanologia, Roma, Italy*
[13] *Department of Astronomy and Astrophysics, University of Toronto, ON, Canada*
[14] *Department of Physics, California Institute of Technology, Pasadena, CA, USA*
[15] *Physics Department, Case Western Reserve University, Cleveland, OH, USA*
[16] *Department of Physics, University of California, Santa Barbara, CA, USA*
[17] *Department of Physics, University of Toronto, ON, Canada*
[18] *INFN, Sezione di Roma 2, Roma, Italy*
[19] *Department of Physics, University of Alberta, Edmonton, AB, Canada*
[20] *Institut d' Astrophysique de Paris, Paris, France*
[21] *INFN, Sezione di Roma 1, Roma, Italy*

The BOOMERANG -B03 experiment has performed three surveys (deep, shallow, galactic) of selected regions of the southern sky. Maps of the Stokes parameters I, Q, U at 145, 245, 345 GHz have been obtained, covering several hundreds of square degrees, with a resolution of $\sim 10'$. In the deep and shallow surveys, both at high Galactic latitudes, the 145 GHz I map is dominated by CMB anisotropy. The angular power spectrum c_ℓ^{TT} is consistent with previous measurements from BOOMERANG -B98 , with extended multipoles range and improved precision. A polarized CMB component is detected in the deep survey. The level and shape of c_ℓ^{TE} and c_ℓ^{EE} are consistent with the CMB polarization expected in the adiabatic inflationary model best fitting the c_ℓ^{TT}. Foregrounds are shown to be negligible in the deep survey at 145 GHz.

1 CMB polarization

CMB photons are last scattered by electrons at z $\sim$ 1100. Any local quadrupole anisotropy in the incoming photons creates a degree of linear polarization in the scattered photons. The expected polarization is quite weak ([1,2,3,4,5]). The polarization field can be expanded into a curl-free component (E-modes) and a curl component (B-modes). In standard cosmological models four non-zero power spectra can be obtained from these components: $\langle TT \rangle$, $\langle TE \rangle$, $\langle EE \rangle$, $\langle BB \rangle$. Density perturbations can only produce E-modes of polarization (see e.g. [6]). In the concordance model, $\langle EE \rangle \sim 0.01 \langle TT \rangle$: for this reason it is very difficult to measure CMB polarization. On large angular scales the polarization is sensitive to the details of the reionization history of the Universe. On smaller angular scales, peaks in the polarization spectra arise from the same acoustic oscillations at last scattering as those in the total intensity spectra. However, the peaks in the polarization spectra are predicted to be out of phase with the intensity peaks since the former are sourced by the velocity term of the photon-baryon fluid while the latter are generated by the density term. This effect provides the strongest constraint on the origin of the structure observed in the spectra. In the Inflation scenario a faint background of tensor perturbations (gravitational waves) is generated [7,8,9,10]. These produce quadrupole anisotropy at recombination, and, as a consequence, both E-modes and B-modes in the CMB polarization pattern. Their level depends on the energy scale of inflation, but is very weak, $\langle BB \rangle \sim 10^{-6} \langle TT \rangle$ (see e.g. [11,12]).

Detections of CMB polarization have been reported by the experiments DASI, CAPMAP, CBI, and WMAP, all using coherent techniques, and by BOOMERanG -B03 , on which we focus in this paper. DASI has detected $\langle TE \rangle$ at 2.9 σ and $\langle EE \rangle$ at 6.3 σ ([13]); CAPMAP ([14]) has detected $\langle EE \rangle$ at $\sim 2\sigma$; CBI ([15]) has detected $\langle EE \rangle$ at $\gtrsim 7\sigma$; WMAP has detected $\langle TE \rangle$ at many σ ([16]) and, very recently, $\langle EE \rangle$ at large angular scales ([17]). The polarization power spectra measured by these experiments are all consistent with the forecast from the "concordance" model best fitting the WMAP $\langle TT \rangle$ power spectrum. Their precision, however, is not yet good enough to improve significantly the constraints on the cosmological parameters, and we are still very far from the sensitivity required to constrain the mode of the perturbations , or to detect gravitational waves from inflation.

2 BOOMERanG -B03

At variance with all the other polarization experiments quoted above, BOOMERanG -B03 uses a completely different approach. It is a balloon-borne telescope, on a long-duration stratospheric platform, working at high frequencies with bolometric detectors. The instrument ([18]) derives directly from the BOOMERanG -98 experiment ([19,20,21,22,24,25,23,26,27,28]) but has been equipped with polarization sensitive bolometers (PSBs, see [29]). In these devices two separate bolometers observe the sky through the same feed structure but are sensitive to orthogonal polarization directions. Each bolometer signal is processed and amplified separately. The two signals are then differenced to obtain the Stokes parameter Q of linear polarization. The U parameter is measured by means of an identical PSB rotated by $\alpha = \pi/4$ in the focal plane with respect to the first one. We have introduced some redundancy by using four independent PSB pairs, covering with their principal axes the range $\alpha = [0, \pi]$ in $\pi/8$ steps. The four pixels are aligned on a constant azimuth line, and their projections on the sky are separated by 0.5^o. An additional row of four pixels is made with four two-color photometers operating at 245 and 345 GHz. The main purpose of these high frequency channels is to monitor the dust foreground and residual atmospheric noise. Table 1 summarizes the properties of the B03 receiver.

BOOMERanG -B03 uses repeated scans over the same sky pixel: at different times during the survey, the focal plane rotates by an angle γ with respect to the sky. Information on I, Q and

Table 1: Summary of the properties of the B03 receiver. The NET is the average noise of all the detectors in the band, at a frequency of 1 Hz.

Frequency	Bandwidth	#detectors	Beam FWHM	NET_{CMB}
145 GHz	45 GHz	8	$9.95'$	170 $\mu K\sqrt{s}$
245 GHz	80 GHz	4	$6.22'$	320 $\mu K\sqrt{s}$
345 GHz	100 GHz	4	$6.90'$	450 $\mu K\sqrt{s}$

Table 2: Surveys performed during the BOOMERANG -B03 flight.

Survey	center (RA,dec)	size (sq.deg.)	time per $7'$ pixel, per detector (s)
Deep	$5^h28', -45^o$	115	60
Shallow	$5^h28', -45^o$	1130	3.3
Galactic	$9^h12', -46^o$	390	4.7

U in each sky pixel thus comes from all the bolometers present in the focal plane, combined according to the relation

$$V^p_{i,k} = \frac{1}{2}\mathcal{S}_k \left[I_p + Q_p \cos[2(\alpha_k + \gamma_i)] + U_p \sin[2(\alpha_k + \gamma_i)]\right] + n_{i,k} \quad . \tag{1}$$

Here $V^p_{i,k}$ is the signal measured by bolometer k at time t_i; $\mathcal{S}_k$ is the responsivity of bolometer k; I_p, Q_p, U_p are the Stokes parameters of pixel p in the chosen celestial coordinates, and $n_{i,k}$ is the noise contribution to the i-th measurement on that pixel. This system of equations can be inverted and the Stokes parameters estimated if a sufficient number of measurements over a range of angles $\alpha_k + \gamma_i$ is taken.

This approach to measure polarization has the advantage of not requiring long integration time for each pixel (at variance with experiments using a polarization modulator, like a rotating polarizer or waveplate), but is prone to leakage of I into Q,U if the responsivity of the detectors is not stable, or not well calibrated. All the details of the instrument and of its calibration are described in ([18]), where we show that we have controlled the calibration and the data processing at a level sufficient to measure CMB polarization with $\sim 10\%$ precision.

3 Data

The instrument was launched by NASA-NSBF on Jan. 6, 2003, from Williams Field, near the McMurdo Station, in Antarctica (167° 5.760' E ; 77° 51.760' S). The flight lasted until Jan. 21, with a total of 311 hours. After day 11, the altitude dropped below 28 km, telescope pointing became difficult, and we had to stop observations. We devoted a total of 119 hours to scans on the deep survey region, a total of 79 hours to scans on the shallow survey region, and a total of 30 hours to scans over the Galactic plane. The characteristics of the surveys are summarized in table 2.

The polarization signal is very small. In the observations of the deep region at 145 GHz the contribution from CMB polarization is of the order of a thousandth of the noise for a single signal sample, and of the order of a tenth of the error for the final measurement of a single $3.5'$ pixel. In order to properly exclude instrumental artifacts and avoid the introduction of bias, we developed two completely independent analysis pipelines, one in Italy (IT) and one in North America (NA). Despite of the many different choices taken during the data analysis, the final maps and spectra are fully consistent. This is the best test of the robustness of the dataset

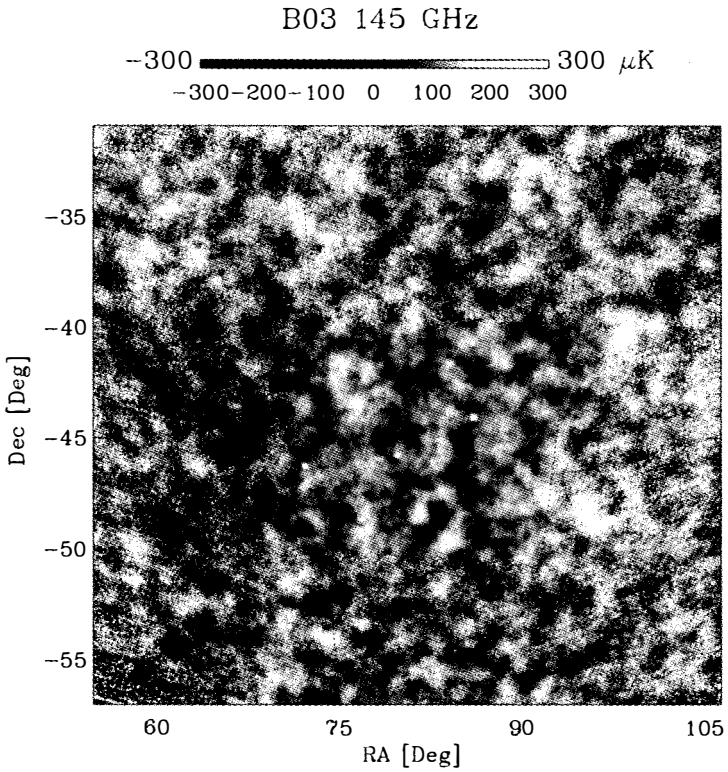

Figure 1: 145 GHz map obtained from the shallow and deep surveys combining the data from all 8 detectors. the pixelization is 7′

against alternative data selection and analysis procedures. We refer to [18] for the description of the pipelines converting the raw data into calibrated maps.

4 Maps of the Stokes Parameters

In fig. 1 we report the 145 GHz I map obtained from the shallow and deep surveys[18]. The lower noise deep survey is evident in the center of the figure. Here the typical noise per 7′ pixel is $\sim$ 6 μK: to date, this is the deepest map of the CMB. The morphology of the map is in excellent agreement with the map of the same region obtained from BOOMERANG -98 at 150 GHz and from WMAP at 94 GHz: we thus have detection of the same cosmological structures from three completely independent experiments. The CMB structures mapped at 145 GHz are evident also in the 245 and 345 GHz maps[18]. even if with lower S/N, due to the higher background on the bolometers, to the lower number of detectors in these bands, and to the presence of increasing contamination from interstellar dust emission. The expected ΔT_{rms} in the deep region for the range of multipoles between $50 \leq \ell \leq 900$ is $(93 \pm 4)\mu K$, where the uncertainty is dominated by cosmic variance. We measure $(90.2 \pm 2.3)\mu K$ at 145 GHz, $(90 \pm 20)\mu K$ at 245 GHz, $(130 \pm 30)\mu K$

at 345 GHz. These results are consistent with the extrapolation[30] of the anisotropy of cirrus dust emission, mapped by IRAS at 3000 GHz and by DIRBE at 1250 GHz [18]. Using the same model to extrapolate the dust contribution at 145 GHz, we find that its anisotropy has to be $< 4\mu K$. Since cirrus dust emission is polarized $\lesssim 10\%$ ([31]), we do not expect a polarized signal larger than 0.4 μK in this region. For comparison, the rms EE polarization signal is $\sim 4\mu K$ in our beam and with this pixelization. We can conclude that dust polarization is not expected to be a significant contaminant at 145 GHz in the deep survey region.

5 Power spectra

The intensity of the CMB signal can be expanded in spherical harmonics as $\Delta T(\hat{n}) = \sum_{\ell m} a^T_{\ell m} Y_{\ell m}(\hat{n})$. Similarly the linear polarization $Q+iU$ can be decomposed using the spin-2 weighted basis ${}_{\pm 2}Y_{\ell m}$

$$(Q \pm iU)(\hat{n}) = \sum_{\ell m} \left(a^E_{\ell m} \mp i a^B_{\ell m} \right) {}_{\pm 2}Y_{\ell m}(\hat{n}) \tag{2}$$

thus defining the scalar fields $T(\hat{n}) = \sum_{l,m} a^T_{lm} Y_{lm}(\hat{n})$, $E(\hat{n}) = \sum_{\ell m} a^E_{\ell m} Y_{\ell m}(\hat{n})$ and the pseudo-scalar $B(\hat{n}) = \sum_{\ell m} a^B_{\ell m} Y_{\ell m}(\hat{n})$. In the hypothesis that those quantities are Gaussian distributed and that the early Universe is isotropic, the cosmological information is encoded in the standard deviations and correlations of the coefficients:

$$\langle XY \rangle = \langle a^{X*}_{\ell m} a^{Y}_{\ell' m'} \rangle = c^{XY}_{\ell} \delta_{\ell \ell'} \delta_{m m'} \tag{3}$$

where the pairs $\langle XY \rangle$ can be $\langle TT \rangle$, $\langle EE \rangle$, $\langle BB \rangle$, $\langle TE \rangle$, $\langle TB \rangle$ and $\langle EB \rangle$. Those are the angular power spectra and, under the hypothesis of isotropy, can be estimated by averaging over m at each multipole number ℓ.

Both IT and NA power spectra estimation pipelines are based on the MASTER method [32] that computes the pseudo-$a_{\ell m}$ on a fraction of the sphere defined by the mask $W(\hat{n})$ which takes into account weighting and sky coverage. This yields the definition of mode-mode coupling kernels, that depend only on the weighting scheme. Using an appropriate ℓ-binning it is possible to solve for the underlying angular power spectra, taking into account the binning, the angular resolution of the instrument, the pixelization of the map, and any filter applied to the time stream.

MASTER is based on Monte Carlo simulations of signal-only time-streams (from simulations of the CMB sky), and on simulations of noise-only time-streams (from simulations of the instrument). Both data-streams are processed in the same way as the real data. The signal-only time-streams are used to define the transfer function, describing the effect of data filtering and partial sky coverage on the power spectra. The noise-only time-streams are used to estimate the noise in the power spectra. The signal simulations were obtained from random realization of the CMB sky, in temperature and polarization, for a given underlying cosmological model, and were projected in a time stream following the actual BOOMERANG scanning strategy. The noise simulations were obtained in the time domain, by means of random realizations of the noise power spectrum. This was iteratively estimated, taking into account noise correlations between channels as described in [18].

The measured power spectra are reported in [33,35,36] and summarized in Figure 2. The BOOMERANG -03 data improved the published measurements of the temperature angular power spectrum primarily over the third peak. The $< EE >$ polarization angular power spectrum and the polarization-temperature angular correlation provide detection of the CMB polarization at the level of 3.5 σ each.

As a check on the internal consistency of the data, we performed two complete jack-knife tests in which the time ordered data (TOD) are divided in two halves. I, Q, and U maps

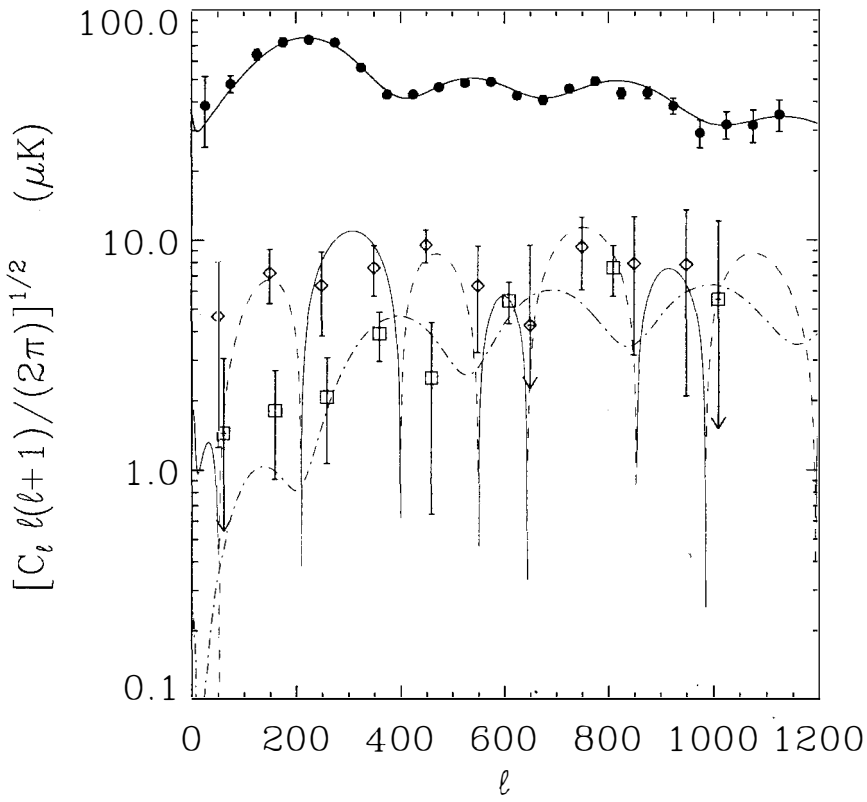

Figure 2: Angular power spectra measured by B03 . The top data (filled circles) are the B03 measurements of c_ℓ^{TT}. The continuous line is the adiabatic inflationary model best fitting the WMAP 3-years data ([34]). The middle data (empty diamonds) are the B03 measurements of $|c_\ell^{TE}|$. The line is from the same best fit model used for c_ℓ^{TT}: it is dashed for negative values of c_ℓ^{TE}. The bottom data (empty squares) are the B03 measurements of $|c_\ell^{EE}|$. The dot-dash line is from the same best fit model used for c_ℓ^{TT}

were generated from each half independently. The power spectra were then computed from the difference of the resultant maps and found to be consistent with zero. The temporal jackknife divides the data into a first half and a second half, in which the shallow and deep scans are each divided in order to ensure roughly equal coverage of the sky in each subset. As discussed in [18], the payload experienced a dramatic ($\simeq$ 9km) loss of altitude over the course of the flight. The first-half/second-half test was chosen to provide a check which is maximally sensitive to systematic effects related to the altitude drop, such as responsivity drifts, a degradation in the accuracy of the pointing reconstruction, or atmospheric contamination. The channel jackknife measures the difference between maps generated from the two halves of the focal plane. Each side of the focal plane accommodates two pairs of PSBs, allowing complete characterization of the three linear Stokes parameters. The sky coverage, filtering, and data flagging of this jackknife test are nearly identical to that of the full data set.

Additionally, we have modeled the potential systematic effects deriving from mis-estimation of various instrumental parameters. We used Monte Carlo simulations of signal-only time ordered data, processed varying those parameters randomly over their range of uncertainty with a Gaussian distribution. The parameters that have been changed are the relative calibration between channels ($\pm 0.4\%$), the polarization efficiency (± 0.03), the bolometer time constants ($\pm 10\%$), the beam ($\pm 0.3'$), and the angles of the polarizers axes respect to the telescope frame ($\pm 2^\circ$). The ranges of the various parameters correspond to their uncertainties obtained from the calibration measurement, as described in [18]. We obtain that the potential errors from mis-estimation of the instrumental parameters are all at least one order of magnitude lower than the statistical errors of the dataset.

6 Cosmological Parameters

The impact of the BOOMERANG -B03 data set on cosmology has been analyzed in detail in [37]. We find that the B03 data alone constrain the parameters of the ΛCDM model remarkably well and are consistent with constraints from a multi-experiment combined CMB data set. While the polarization data are not yet at the level of accuracy of the intensity data, cross checks of best fit parameters from the B03 polarization data and B03 TT data indicate consistent results. The peak and trough positions forecast by the TT and polarization spectra are in robust agreement. Isocurvature modes are starting to be constrained by the current CMB polarization data. Combining B03 data, other CMB data, and Large Scale Structure data, we set an upper limit for the sum of neutrino masses of $\lesssim 0.4eV$. With B03 we have demonstrated that high sensitivity bolometric polarization experiments are possible and effective and have started a path towards higher precision polarization data, which will play a larger role in constraining cosmology.

Acknowledgments

We gratefully acknowledge support from the CIAR, CSA, and NSERC in Canada; Agenzia Spaziale Italiana, University La Sapienza and Programma Nazionale Ricerche in Antartide in Italy; PPARC and the Leverhulme Trust in the UK; and NASA and NSF in the USA.

References

1. Rees, M., 1968, Ap.J.Lett., 53, L1
2. Kaiser, N., 1983, MNRAS, 202, 1169
3. Hu, W., White, M., 1997, New Astron., 2, 323
4. Kamionkowski, M. Kosowsky, A., & Stebbins, A. 1997, Phys. Rev. D, 55, 7368

5. Zaldarriaga, M., astro-ph/0305272.
6. Seljak, U., Pen, U., Turok, N., 1997, Phys. Rev. Lett., 79, 1615
7. Mukhanov V.F., Chibisov G.V., 1981, JETP Lett., 33, 532-535 (1981. Zh. Eksp. Teor. Fiz., 33, 549-553) see also astro-ph/0303077
8. Guth, A., & Pi, S. Y., 1982, Phys. Rev. Lett., 49, 1110
9. Linde, A., 1983, Phys. Lett., B129, 177.
10. Kolb, E.W., and Turner, M.S., The Early Universe, Addison-Welsey, 1990.
11. Copeland, E.J., Kolb, E.W., Liddle, A.R., and Lidsey, J.E. , 1993, Phys. Rev. Lett., 71, 219 ; 1993, Phys. Rev. D, 48, 2529.
12. Turner, M.S., 1993, Phys. Rev. Lett., 71, 3502; 1993, Phys. Rev. D., 48, 5539.
13. Leitch, E., Kovac, J., Halverson, N., Carlstrom, J., Pryke, C., & Smith, M. 2004, ApJ, submitted (astro-ph/0409357)
14. Barkats, D., Bischoff, C., Farese, P., et al., 2004, ApJ, submitted (astro-ph/0409380)
15. Readhead, A. C. S., Myers, S. T., Pearson, T. J., et al. 2004, Science, 306, 836 (astro-ph/0409569)
16. Kogut, A., Spergel, D. N., Barnes, C., et al. 2003, ApJS, 148, 161
17. L. Page, G. Hinshaw, E. Komatsu, et al. 2006, submitted to Ap.J., astro-ph/0603450
18. S. Masi, P. Ade, J. Bock, et al., 2006, submitted to Astronomy and Astrophysics, astro-ph/0507509.
19. P. de Bernardis, P. A. R. Ade, J. J. Bock, et al., 2000, Nature, 404, 955
20. Lange, A., Ade, P.A.R., Bock, J., et al., 2001, Phys.Rev., D 63, 042001
21. S. Masi, P.A.R.Ade, J.J.Bock, et al., Ap.J.Letters, 553, L93-L96, 2001
22. Netterfield, C., Ade, P., Bock, J.,et al., 2002, ApJ, 571, 604
23. de Bernardis, P., Ade, P., Bock, J., et al., 2002, ApJ, 564, 559
24. F. Piacentini, P. A. R. Ade, R. S. Bhatia, et al., 2002, Ap.J.Suppl.Ser., 138, 315
25. Polenta, G., Ade, P.A.R., Bock, J., et al., 2002, Ap.J., 572, L27
26. B. P. Crill, P. A. R. Ade, D. R. Artusa, et al., 2003, Ap.J.Supp.Ser., 148, 527
27. P. de Bernardis, P.A.R. Ade, A. Balbi, et al., in astro-ph/0311396, IAU Symposium 216: Maps of the Cosmos. Sydney 14-17 July 2003 - ASP Conference Series
28. Ruhl, J. E., Ade, P., Bock, J., et al., 2003, ApJ, 599, 786
29. Jones, B., Bhatia, R.S., Bock, J.J., Lange, A.E., A Polarization Sensitive Bolometric Detector for Observations of the Cosmic Microwave Background, 2003, SPIE, 4855, 227, astro-ph/0209132
30. Finkbeiner, D., Davis, M., & Schlegel, D., 1999, Ap.J., 524, 867
31. Pointhieu, N., et al., 2005, A&A submitted, astro-ph/0501427
32. E. Hivon, K.M. Gorski, C.B. Netterfield, B.P. Crill, S. Prunet, F. Hansen, 2002, ApJ, 567, 2
33. W. C. Jones, P. Ade, J. Bock, et al., 2005, Ap.J. accepted, astro-ph/0507494.
34. D. N. Spergel, R. Bean, O. Dore', et al., 2006, submitted to Ap.J., astro-ph/0603449.
35. F. Piacentini, P. Ade, J. Bock, et al., 2005, Ap.J. accepted, astro-ph/0507507.
36. T.E. Montroy, P. A. R. Ade, J. J. Bock, J. R. Bond, et al., 2005, Ap.J. accepted, astro-ph/0507514.
37. C.J. MacTavish, P. A. R. Ade, J. J. Bock, et al., 2005, Ap.J., accepted, astro-ph/0507503

A BAYESIAN ANALYSIS OF THE PRIMORDIAL POWER SPECTRUM

M. BRIDGES, A. N. LASENBY, M. P. HOBSON
Astrophysics Group, Cavendish Laboratory, Madingley Road, Cambridge CB3 0HE, UK

We present a Bayesian analysis of large scale structure (LSS) and cosmic microwave background (CMB) data to constrain the form of the primordial power spectrum following closely previous analyses [1]. We have extended the usual presumption of a scale invariant spectrum to include a running spectral index, a broken spectrum, a large scale cutoff in power, a binned reconstruction and a spectrum proposed by Lasenby & Doran. The result of our complete Bayesian analysis includes both the posterior probability distribution and also the weighting Bayesian evidence. We find compelling evidence in favour of the Lasenby & Doran spectrum.

1 Model Testing and Selection Framework

A Bayesian analysis provides a coherent approach to estimating model parameters $\mathbf{\Theta}$ and to determining which model M best describes the data, $\mathbf{D}$. These inferences can be summarised in Bayes' Theorem:

$$P(\mathbf{\Theta}|\mathbf{D}, M) = \frac{P(\mathbf{D}|\mathbf{\Theta}, M)P(\mathbf{\Theta}|M)}{P(\mathbf{D}|M)}, \tag{1}$$

where $P(\mathbf{\Theta}|\mathbf{D}, M)$ is the posterior, $P(\mathbf{D}|\mathbf{\Theta}, M)$ the likelihood, $P(\mathbf{\Theta}|M)$ the prior and $P(\mathbf{D}|M)$ the Bayesian evidence. We employ a Markov Chain Monte Carlo (MCMC) sampling procedure to explore the posterior distribution using an adapted version of the COSMOMC package with four CMB data sets; WMAP [2,3,4], ACBAR [5], VSA [6] and CBI [7]. We also include the 2dF Galaxy Redshift Survey [8],the Sloan Digital Sky Survey [9] and the Hubble Space Telescope key project [10]. At the stationary point of the Markov chain we sample from the posterior distribution and can extract marginalised constraints for each parameter.

The Bayesian evidence can be defined as the likelihood averaged over the prior:

$$\int P(\mathbf{D}|\mathbf{\Theta}, M)P(\mathbf{\Theta}|M)d^N\mathbf{\Theta}. \tag{2}$$

To evaluate this integral one could, naively randomly sample from the prior via MCMC and simply find the average. However, this method samples almost exclusively from areas of high likelihood thereby grossly over estimating the average likelihood and thus the evidence. Instead, we employ a reverse annealing schedule after an initial burn-in period, whereby we sample from $P(\mathbf{D}|\theta, M)^\lambda P(\theta|M)$ where λ is the inverse temperature and is lowered from 1 to ≈ 0. This ensures sufficient mobility over the entire parameter space to produce log-evidence estimates to within one unit from independent chains. One can then define the evidence as:

$$E(\lambda = 1) = \int P(\mathbf{D}|\mathbf{\Theta}, M)^\lambda P(\mathbf{\Theta}|M)d^N\mathbf{\Theta}. \tag{3}$$

2 Primordial Power Spectrum Parameterisation

We examine seven variants of the primordial spectrum that have aroused interest recently. The simplest, scale invariant Harrison-Zel'dovich spectrum is parameterised with just one free parameter, the amplitude A:

$$P(k) = A. \tag{4}$$

However, slow-roll inflationary scenarios are expected to imprint a slight slope in this spectrum, leading to the now ubiquitous power-law form characterised by an index n such that $P(k) = Ak^{n-1}$. Since we would expect generally the inflationary potential to be some function of scale we can characterise a running spectrum as also having a term $dn/d\ln k$:

$$P(k) = Ak^{n-1+(1/2)\ln k dn/d\ln k}. \tag{5}$$

WMAP observations show a reduction in power on large scales, we have attempted to model this as a single index spectrum with an abrupt cutoff on a scale k_c:

$$P(k) = \begin{cases} 0, & k < k_c \\ Ak^{n-1}, & k \geq k_c \end{cases} \tag{6}$$

A spontaneous symmetry-breaking phase transition in the early Universe could interrupt the inflationary potential leading to a break in the power spectrum. We have modelled this with two amplitudes A before the break starts at k_s and after it ends B, at k_e, where C and α are chosen for continuity:

$$P(k) = \begin{cases} A, & k \leq k_s \\ Ck^{\alpha-1}, & k_s < k \leq k_e \\ B, & k > k_e \end{cases} \tag{7}$$

Lasenby & Doran [11] (L & D) arrived at a novel spectrum by considering a boundary condition that restricts the total conformal time available in the universe and requires a closed geometry. The resultant predicted pertrubation spectrum encouragingly contains an exponential cutoff at low k and tends towards a single index model on small scales making it an intriguing possibility. The spectrum is described by:

$$P(k) = A(1 - 0.023y)^2(1 - \exp(-(y + 0.93)/0.47))^2 \tag{8}$$

with $y = \ln\left(\frac{k}{H_0/100} \times 3 \times 10^3\right) > -0.93$, where we fit the spectrum to the data by varying just the amplitude A.

A direct reconstruction of the form of the spectrum allows us to detect any interesting features directly from the data. We have concentrated on large scales using a linear interpolated reconstruction in eight bins in k (spaced $k_{i+1} = 1.275k_i$).

$$P(k) = \begin{cases} \frac{(k_{i+1}-k)a_i + (k-k_i)a_{i+1}}{k_{i+1}-k_i}, & k_i < k < k_{i+1} \\ a_n, & k \geq k_n \end{cases} \tag{9}$$

In addition to the primordial spectral parameters we vary the cosmology via: the physical baryon density $\Omega_b h^2$; the physical cold dark matter density $\Omega_c h^2$; the total energy density Ω_0 (parameterised as $\Omega_k = 1 - \Omega_0$); the Hubble parameter h ($H_0 = h \times 100\text{kms}^{-1}$) and the redshift of re-ionisation z_{re}.

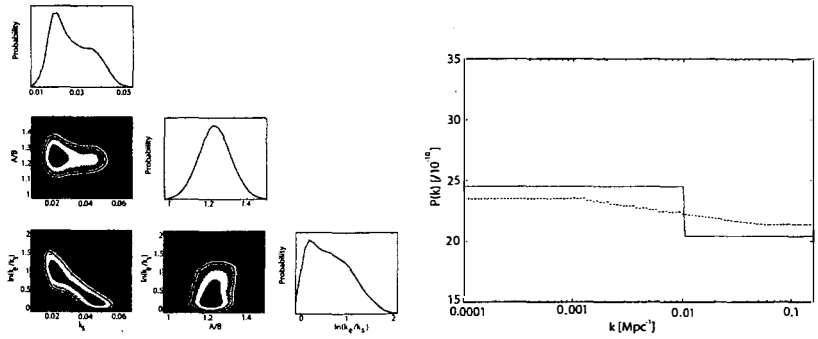

Figure 1: Marginalised 1D and 2D probability constraints on k_s, $\ln(k_e/k_s)$ and A/B (left) and examples of both the extended and sharply broken spectra preferred by the data (right).

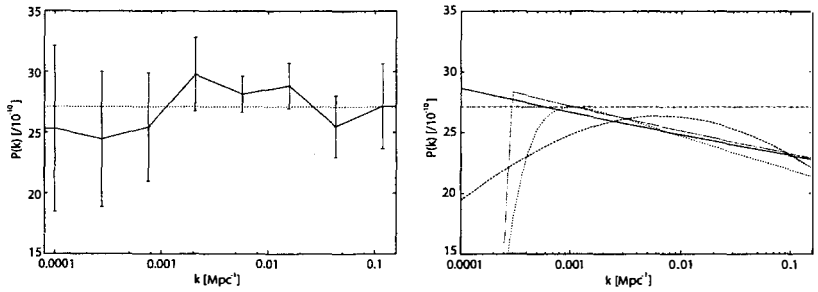

Figure 2: Binned reconstruction with 1σ errors in 8 bands of wavenumber k with the best fitting H-Z spectrum (dotted) for comparison (left) and best fitting spectra for a single index spectrum (full) with a cutoff (dotted), with a running index (long-dashed), the Lasenby & Doran (short-dashed) and the H-Z spectra (dot-dashed).

3 Parameter Constraints

The marginalised parameter constraints for the broken spectrum are bi-modal (see Fig. 1 left) with both sudden and extended breaks being allowed (illustrated by the peaks in likelihood at $\ln(k_e/k_s) \approx 0$ and 1 respectively). The spectra themselves are shown in Fig. 1 (right). We expect the extended break to be mimicing a power-law spectrum with a small index n. However, the sudden break could be evidence for a either a symmetry-breaking phase transition or possibly an artifiact of the combination of LSS datasets, the break scale being similar to that at which these datasets become important.

The reconstructed spectrum (Fig. 2 left) shows no deviation from a Harrison-Zel'dovich spectrum within 1σ, though we did detect a slight decrement in power on scales below about 0.001 Mpc^{-1}. Best fitting spectra for the remaining models are shown in Fig. 2 (right) where we see the preferred cutoff scale k_c to lie close to that produced naturally in the L & D spectrum.

4 Bayesian Model Selection -Results

Bayesian evidence values are just numbers, by convention we quote the Bayes' factor $\mathcal{B}$ representing the ratio of evidences (or difference in log-evidences) for each of the competing models with respect to a single reference model –in this case the single index model. To determine the significance of these factors we use the Jeffreys scale[12] where a log-evidence difference: $\Delta\ln E < 1$ is not significant, $1 < \Delta\ln E < 2.5$ significant, $2.5 < \Delta\ln E < 5$ strong and $\Delta\ln E > 5$ decisive.

Table 1: Differences of log evidences in the complete parameter space exploration.

Model	$\mathcal{B}$
Single Index	0.0 ± 0.7
H-Z	0.4 ± 0.8
Running	0.5 ± 0.7
Cutoff	0.8 ± 0.8
Broken	-0.3 ± 0.8
Binned	-1.8 ± 0.7

Table 2: Differences of log evidences (primordial parameters only) for all models within two fixed cosmologies.

Model	$\mathcal{B}$	$\mathcal{B}$
	Cosmo I	Cosmo II
Single Index	0.0 ± 0.6	0.0 ± 0.5
H-Z	-0.4 ± 0.5	-4.4 ± 0.5
Running	-2.1 ± 0.5	-0.8 ± 0.6
Cutoff	0.2 ± 0.6	0.4 ± 0.5
Broken	-0.5 ± 0.7	-2.7 ± 0.6
Binned	-5.2 ± 0.7	-6.1 ± 0.6
Lasenby & Doran	0.9 ± 0.6	4.1 ± 0.5

Three sets of evidence evaluations were performed, one complete parameter space exploration and two using fixed cosmologies oweing to computational limitiations computing the L & D spectrum efficiently in a varying cosmology. The results of the former show that there is a marginal preference for the cutoff spectrum -though with the estimated error this is not significant (see Table 1). We repeated the analysis varying just primordial parameters within a fixed cosmology $\Omega_0 = 1.04, \Omega_b h^2 = 0.0224, H_0 = 60, \Omega_{cdm} h^2 = 0.110$ (Cosmo I), within which the L & D spectrum was previously well fitted, and indeed in this cosmology it is preferred though not conclusively (see Table 2). We also performed the analysis within the best fit single index cosmology $\Omega_0 = 1.024, \Omega_b h^2 = 0.0229, H_0 = 61, \Omega_{cdm} h^2 = 0.118$ (Cosmo II) where one might reasonably expect the single index spectrum to outperform all others. However here we found a decisively strong selection of at least 3 units in log evidence in favour of L & D spectrum.

5 Conclusions

We performed a full Bayesian analysis of seven parameterisations of the primordial power spectrum including not only the estimation of cosmological and spectral parameters but also a value of the Bayesian evidence. A preference was seen for those models incorporating a large scale deficit in power. One such model was found to be the Lasenby & Doran spectrum.

References

1. Bridle S., Lewis A., Weller J., Efstathiou G., 2003, MNRAS, 342, L72
2. Verde L. et al., 2003, Astrophys. J. Suppl., 148, 195
3. Hinshaw G. et al., 2003, Astrophys. J. Suppl., 148, 135
4. Kogut A. et al., 2003, Astrophys. J. Suppl., 148, 161
5. Kuo C.L. et al., 2004, Ap. J., 600, 32
6. Dickinson C. et al., 2004, MNRAS, 353, 732
7. Readhead A.C.S. et al., 2004, ApJ, 609, 498–512

8. Percival W.J. et al., 2001, MNRAS, 327, 1297
9. Abazajian K., et al., 2003, ApJ, 126, 2081
10. Freedman W. L. et al., 2001, ApJ, 553, 47
11. Lasenby A.N., Doran, C., 2005, Phys.Rev. D 71, 063502
12. Jeffreys H., 1961, *Theory of Probability*, 3rd ed., Oxford University Press, Oxford
13. Beltran M., Garcia-Bellido J., Lesgourgues J., Liddle A., Slosar A., 2005, Phys. Rev. D, 71, 063532

WSLAP. A code for weak and strong lensing analysis and simulation.

J.M. Diego[1], M. Tegmark[2], P. Protopapas[3], H.B. Sandvik[4]
[1] *Instituto de Física de Cantabria. Avda. Los Castros s/n. 39005 Santander, Spain.*
[2] *MIT Kavli Institute for Astrophysics and Space Research, Cambridge, MA 02139, USA.*
[3] *Harvard-Smithsonian Center for Astrophysics, 60 Garden Street, Cambridge, MA 02138, USA.*
[4] *Max-Planck-Institut für Astrophysik, D-85748 Garching, Germany.*

We describe WSLAP: a method to estimate the mass distribution of a gravitational lens and the position of the sources from combined strong and weak lensing data. The algorithm combines weak and strong lensing data in a unified way producing a solution which is valid in both the weak and strong lensing regimes. The method is non-parametric allowing the mass to be located anywhere in the field of view. We find that combining weak and strong lensing information has two major advantages: it weakens the need for priors and/or regularization schemes for the intrinsic size of the background galaxies (this assumption was needed in previous strong lensing algorithms) and it corrects for biases in the recovered mass in the outer regions where the strong lensing data is less sensitive.The code is implemented into a software package called WSLAP (Weak & Strong Lensing Analysis Package) which is publicly available at http://darwin.cfa.harvard.edu/SLAP/.

1 Introduction

Lensing problems usually distinguish between two regimes, strong and weak. In the strong lensing regime, a background source galaxy appears as multiple images, while in the weak lensing regime, its image suffers a small distortion which typically elongates it in a direction orthogonal to the gradient of the potential. The two problems are normally studied separately and, at best, they are combined afterward. Only a few attempts have been made to combine both regimes in the same analysis (e.g. Bradac et al. 2005a, 2005b, Broadhurst, Takada, Umetsu et al. 2005b). In the early years of strong lensing data analysis, it was common to have only few constraints to work with. The small number of constraints made it impossible to extract useful information about the mass distribution of the lens without invoking a simple parametrization of the lens or the gravitational potential (Kneib et al. 1993, 1995, 1996, Broadhurst et al 1995, 2005a, Sand et al. 2002, Gavazzi et al. 2004). The common use of parametric models requires making educated

guesses about the cluster mass distribution, for instance that the dark matter halos trace the luminosity of the cluster or that galaxy profiles possess certain symmetries.
Nowadays, it is possible to obtain strong lensing images around the center of galaxy clusters with hundreds of arcs (Broadhurst et al. 2005a), where each arc contributes with several effective constraints in the process of solving for the projected mass distribution of the lens. In addition, weak lensing measurements provide shear constraints over a larger field of view. When added together, the number of constraints can be sufficiently high that non-parametric methods can be used in the reconstruction of the mass. Non-parametric approaches have been previously explored in several papers (Saha et al. 1997, Abdelsalam et al. 1988b, 1998c, Trotter et al. 2000, Williams & Saha 2001, Warren & Dye 2003, Saha & Williams 2004, Bradac et al. 2005a, 2005b, Treu & Koopmas 2004) and more recently in Diego et al. (2005a, 2005b,2006) (hereafter **papers I, II and III**). The reader can find a more detailed description of this presentation in paper III.

2 A linear formulation of a non-linear problem

The fundamental problem in lens modeling is the following: Given the N_θ positions of lensed images, θ, what are the corresponding positions β of the background galaxies and the mass distribution $m(\theta)$ of the lens? Mathematically this entails inverting the lens equation

$$\beta = \theta - \alpha(\theta, m(\theta - \theta')) \tag{1}$$

The lens equation (1) is implicitly non-linear in the variable $(\theta - \theta')$. However, by using non-parametric methods it is possible to express the above equation in a linear form. If we use a grid representation of the lens, the θ' positions of the masses are fixed by the grid and the non-linearity in the computation of α disappears. Since the strong lensing (SL hereafter) and weak lensing (WL hereafter) effects can be computed as a function of the deflection angle α, we can represent both the WL shear and the SL distortions as a linear function of the mass and the β positions of the sources (Diego et al. 2005a, 2005b, 2006).

$$\mathbf{\Phi} = \mathbf{\Gamma x}. \tag{2}$$

where the vector $\mathbf{\Phi}$ contains all the observed data (WL and SL), the vector $\mathbf{x}$ contains the unknown variables of our problem (masses in the grid and positions of the sources) and the matrix $\mathbf{\Gamma}$ is a known matrices relating the the masses in the grid with the measured deflection angle (SL) and shear distortions (WL). The solution of our problem can be found by just inverting the system of linear equations (2). The same system of equations can be used to simulate in a very fast way the data set ($\mathbf{\Phi}$) if we know the mass and source distribution ($\mathbf{x}$) and we use a multi-resolution grid with high enough resolution (large $\mathbf{\Gamma}$).

3 Performance of the method

The inversion of the system of linear equations (2) can be done in many different ways. We have focused on two different approaches, the fast bi-conjugate gradient and a slower, but more meaningful, quadratic programming algorithm (QADP) (Press et al. 1997). Using the bi-conjugate gradient it is possible to find a combined solution of the WL+SL data set in a few seconds. However, this approach can produce unphysical solutions with negative masses in some of the areas of the grid. A way to overcome this problem is by using a positively constrained quadratic programming algorithm. The solution will be constrained to have positive masses over the entire field of view but at the expense of reducing the speed. Typically a solution can be found with this second approach in about an hour. WSLAP allows to weight the WL and

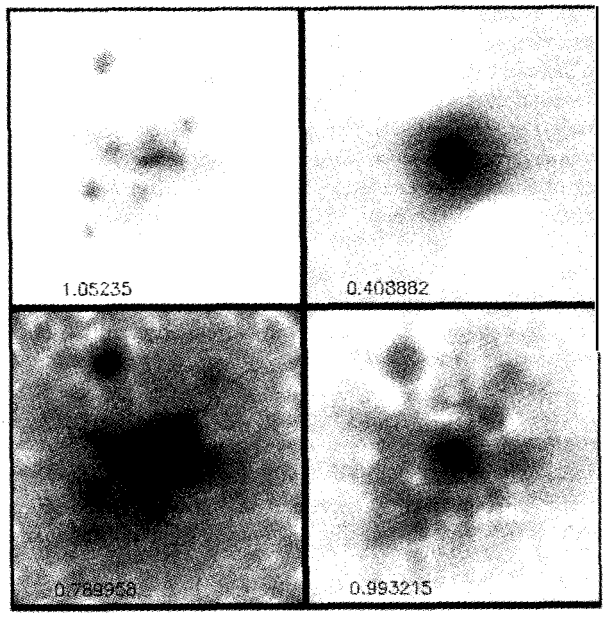

Figure 1: Recovered masses in the case of SL only (top right), WL only (bottom left) combined WL+SL (bottom right). The original mass distribution is shown in the top left panel. The field of view is 8.4 arcmin for each panel. The total mass is shown in the bottom of each panel.

SL data sets differently. We found that the optimal weights are the statistical noise of the shear measurements and an estimate of the size of the sources which originate the SL data set. This size is typically a few arcseconds (or a few pixels) for sources above redshift 0.3. By playing with the weights it is also possible to recover the solution assuming only WL (or SL) data is available. An example of this is shown in figure 1 where we show the original mass distribution (top left) and 3 different mass reconstructions. In the top right panel we show the case where only SL data is used. In this case, the data is sensitive only to the central region of the mass distribution. In the second case (bottom left) we use only WL data. Now the data is more sensitive to the outer regions but less sensitive to the central region. When both data sets are combined (bottom right), we achieve the best reconstruction. Typical errors in the reconstructed 1-dimensional profile are about 10-15 %. The combination of WL and SL data sets produces a better solution than using the two data sets separately. In papers I and II we discussed some of the problems when only SL data is used. In particular, we discussed the existence of the so called *point source solution.* This solution was capable of projecting the SL data set (arclets) back into the source plane and into sources smaller than the original size of the galaxies. The solution was unphysical and often with negative masses. In paper III we discussed how adding WL data prevents the algorithm of finding such solutions. Other problem found in papers I and II was that the solution was insensitive to the outer regions of the cluster. Again, adding WL introduces information beyond the Einstein radius and allows to reconstruct the mass distribution much further.
However, although the combination of WL+SL data improves the result we also observed some biases remaining in the result. As in papers I and II the algorithm still recovers a biased distribution in the very central region underpredicting (by about 50 %) the mass density inside the radial critical curve and overestimating the density between the radial and tangential critical curves (by about 20 %). The density between the Einstein ring and $\approx$ 500 kpc did not show

a significant bias in the simulated reconstruction but it was biased afterward. This bias is due to a memory effect. The final solution in the area beyond 500 kpc retains information about the initial condition. This area is normally less sensitive to the mass distribution than the more interior zones. WSLAP has been tested over a variety of simulations (and data) with satisfactory results. More work is needed to address some of the issues but we conclude that non-parametric methods are a good complement to the intrinsically more powerful parametric ones.

Acknowledgments

This work was supported by NSF CAREER grant AST-0134999, NASA grant NAG5-11099, the David and Lucile Packard Foundation and the Cottrell Foundation. The authors would like to thank David Hogg for useful discussions on quadratic programming and Masahiro Takada and Elizabeth E. Brait for useful comments.

References

1. Abdelsalam H.M., Saha P. & Williams, L.L.R., 1998a, New Astronomy Reviews, 42, 157.
2. Abdelsalam H.M., Saha P. & Williams, L.L.R., 1998b, MNRAS, 294, 734.
3. Abdelsalam H.M, Saha P. & Williams, L.L.R., 1998c, AJ, 116, 1541.
4. Bradac M., Schneider P., Lombardi M., Erben T., 2005a, A&A, 437, 49.
5. Bradac M., Erben T., Schneider P., Hildebrant H., Lombardi M., Schirmer M., Miralles J.-M., Clowe D., Schindler S., 2005b, A&A, 437, 39.
6. Broadhurst T.J., Taylor A.N., Peacock J.A., 1995, ApJ, 438, 49.
7. Broadhurst T., Benítez N., Coe D., Sharon K., Zekser K., White R., Ford H., Bouwens R., 2005a, ApJ, 621, 53.
8. Broadhurst T., Takada M., Umetsu K., Kong X., Arimoto N., Chiba M., Futamase T., 2005b, ApJ, 619, 143..
9. Diego J.M., Protopapas P., Sandvik H.B, Tegmark M. 2005a, MNRAS, 360, 477. (**Paper I**)
10. Diego J.M., Sandvik H.B., Protopapas P., Tegmark M., Benítez N., Broadhurst T., 2005b, MNRAS in press. eprint arXiv:astro-ph/0412191 (**Paper II**)
11. Diego J.M., Tegmark M., Protopapas P., Sandvik H.B., 2006, MNRAS submitted. eprint arXiv:astro-ph/0509103 (**Paper III**)
12. Gavazzi et al. 2004
13. Kneib J.-P., Mellier Y., Fort B., Mathez G., 1993,A&A, 273, 367.
14. Kneib J.-P., Mellier Y., Pello R., Miralda-Escudé J., Le Borgne J.-F.,Boehringer H., & Picat J.-P. 1995, A&A, 303, 27.
15. Kneib J.-P., Ellis R.S., Smail I.R., Couch W., & Sharples R. 1996, ApJ, 471, 643.
16. Press W.H., Teukolsky S.A., Vetterling W.T., Flannery B.P., 1997, *Numerical Recipes in Fortran 77*. Cambrdige University Press.
17. Saha, P., Williams, L.L.R., 1997, MNRAS, 292, 148.
18. Saha, P., Williams, L.L.R., 2004, ApJ, 127, 2604.
19. Sand D.J., Treu T. Ellis R.S. 2002, ApJ, 574, 129.
20. Treu T., Koopmans L.V.E., 2004, ApJ, 611, 739.
21. Trotter C.S., Winn J.N., Hewitt J. N., 2000, ApJ, 535, 671.
22. Warren S.J., Dye S., 2003, ApJ, 590, 673.
23. Williams L.L.R., & Saha P., 2001, AJ, 119, 439.

THE DIPOLE ANISOTROPY OF THE 2MASS REDSHIFT SURVEY

PİRİN ERDOĞDU AND THE 2MRS TEAM[a]
School of Physics & Astronomy, University of Nottingham, University Park, Nottingham, NG7 2RD, UK

We estimate the flux weighted acceleration on the Local Group (LG) from the near-infrared Two Micron All Sky Redshift Survey (2MRS). The near-infrared flux weighted dipoles are very robust because they closely approximate a mass weighted dipole, bypassing the effects of redshift distortions and require no preferred reference frame. We use this method with the redshift information to determine the change in dipole with distance. The LG dipole seemingly converges by 60 h^{-1}Mpc. Assuming convergence, the comparison of the 2MRS flux dipole and the CMB dipole provides a value for the combination of the mass density and luminosity bias parameters $\Omega_{\rm m}^{0.6}/b_{\rm L} = 0.40 \pm 0.09$

1 Introduction

The most popular mechanism for the formation of large-scale structure and motions in the Universe is the gravitational growth of primordial density perturbations. According to this paradigm, the peculiar acceleration vector $\mathbf{g}(\mathbf{r})$ is induced by the matter distribution around position $\mathbf{r}$ and if the density perturbations are small enough to be approximated by a linear theory, then the peculiar velocity field, $\mathbf{v}(\mathbf{r})$, is proportional to the peculiar acceleration:

$$\mathbf{v}(\mathbf{r}) = \frac{H_0 f(\Omega_{\rm m})}{4\pi G\bar{\rho}}\mathbf{g}(\mathbf{r}) = \frac{2f(\Omega_{\rm m})}{3H_0\Omega_{\rm m}}\mathbf{g}(\mathbf{r}), \qquad (1)$$

where $H_0 = 100\ h$ kms^{-1}Mpc^{-1} is the Hubble constant and $f(\Omega_{\rm m}) \simeq \Omega_{\rm m}^{0.6}$ is the logarithmic derivative of the amplitude of the growing mode of the perturbations in mass with respect to the scale factor (Peebles 1980).

It is now widely accepted that the dipole anisotropy of the cosmic microwave background (CMB) is a direct and accurate measurement of the LG peculiar velocity. The LG acceleration can also be estimated using surveys of the galaxies tracing the density inhomogeneities responsible for the acceleration. If the mass can be related to light by a bias parameter, b_L, then by comparing the CMB velocity vector with the acceleration vector obtained from the galaxy surveys, it is possible to investigate the cause of the LG motion and its cosmological implications.

[a] J.P. Huchra (CfA), O. Lahav (UCL), M. Colless (AAO), R.M. Cutri (IPAC), E. Falco (Harvard-Smithsonian), T. George (CFTC), T. Jarrett (IPAC), D. H. Jones (AAO), C.S. Kochanek (Ohio State), L. Macri (NOAO), J. Mader (Keck), N. Martimbeau (CfA), M. Pahre (CfA), Q. Parker (Maquarie), A. Rassat (UCL), W. Saunders (AAO, Maquarie)

Like peculiar acceleration, the flux of light received from a galaxy falls off inversely as the square of the distance. If the mass-to-light ratio is constant, we can relate the two by

$$\begin{aligned} \mathbf{g(r)} &= \mathrm{G}\sum_i M_i \frac{\hat{\mathbf{r}}_i}{r_i^2} \simeq \mathrm{G}\left\langle \frac{M}{L} \right\rangle \sum_i L_i \frac{\hat{\mathbf{r}}_i}{r_i^2} \\ &= 4\pi\mathrm{G}\left\langle \frac{M}{L} \right\rangle \sum_i \mathrm{S}_i \hat{\mathbf{r}}_i, \end{aligned} \tag{2}$$

where the sum is over all galaxies in the Universe, $\langle M/L \rangle$ is the average mass-to-light ratio and $\mathrm{S}_i = L_i/4\pi r^2$ is the flux of galaxy i. The peculiar velocity vector is derived by substituting Equation 2 into the second line of Equation 1. For a flux limited catalogue the observed LG velocity is

$$\mathbf{v(r)} = \frac{8\pi\mathrm{G}f(\Omega_\mathrm{m})}{3H_0\Omega_\mathrm{m}b_\mathrm{L}} \left\langle \frac{M}{L} \right\rangle \sum_i w_{L_i} \mathrm{S}_i \hat{\mathbf{r}}_i \tag{3}$$

where b_L is the luminosity bias factor introduced to account for the dark matter haloes not fully represented by 2MRS galaxies and $0 \leq w_{L_i} \leq 1$ is the weight assigned to galaxy i to account for the luminosity that was not observed due to the flux limit of the survey. With the inclusion of redshift information, we can calculate Equation 3 within concentric spheres with increasing radii and thus estimate the distance at which most of the LG velocity is generated generated (*the convergence depth*).

2 The Two Micron All-Sky Redshift Survey

The Two Micron All-Sky Redshift Survey (Huchra *et al.* 2005, Erdoğdu *et al.* 2006) is the densest all-sky redshift survey to date. The first phase of 2MRS is now complete. In this phase we obtained redshifts for approximately 23,150 2MASS galaxies from a total sample of 24,773 galaxies with extinction corrected magnitudes (Schlegel, Finkbeiner & Davis 1998) brighter than $K_\mathrm{s} = 11.25$. This magnitude limit corresponds to a median redshift of $z \simeq 0.02$ ($\simeq 6000$ km s^{-1}). Figure 1 shows all the objects in 2MRS in Galactic Aitoff Projection. Galaxies with $\mathbf{z} \leq 0.01$ are plotted in red, $0.01 < \mathbf{z} \leq 0.025$ are plotted in blue, $0.025 < \mathbf{z} < 0.05$ are plotted in green and $\mathbf{z} \geq 0.05$ are plotted in magenta. Galaxies without measured redshifts (around 1600) are plotted in black.

The 2MRS sample has very good photometric uniformity and an unprecedented integral sky coverage. The photometric uniformity is better than 4% over the sky including the celestial poles and the survey is essentially complete down to very low galactic latitudes (Huchra *et al.* 2005). In order to account for incompleteness at these galactic latitudes we fill the plane with galaxies sampled from adjacent longitude/distance bins.

3 Results

Figure 2 shows the three components and the magnitudes of the acceleration of the Local Group due to galaxies within a series of successively larger concentric spheres centred on the local group (top plot). The bottom plot shows convergence of the direction of the LG dipole where the misalignment angle is between the LG and the CMB dipoles ($v_{LG} = 627 \pm 22$ km s^{-1}, towards $l_{LG} = 273° \pm 3°$, $b_{LG} = 29° \pm 3°$, Bennett *et al.* 2003, Courteau & Van Den Bergh, 1999).

It is evident in the top plot that the LG velocity is dominated by structures within a distance of 6000 km s^{-1}. The 'tug of war' between the Great Attractor and the Perseus-Pisces is clearly evident. The dip in the velocity vector is an indication that the local flow towards the Great

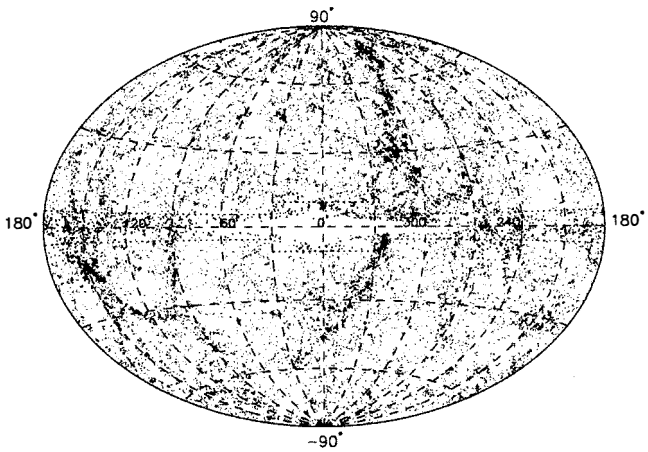

Figure 1: All Objects in the 2MASS Redshift Catalogue in Galactic Aitoff Projection. Galaxies with $z \leq 0.01$ are plotted in red, $0.01 < z \leq 0.025$ are plotted in blue, $0.025 < z < 0.05$ are plotted in green and $z \geq 0.05$ are plotted in magenta. Galaxies without measured redshifts are plotted in black. The masked region is outlined by dashed lines.

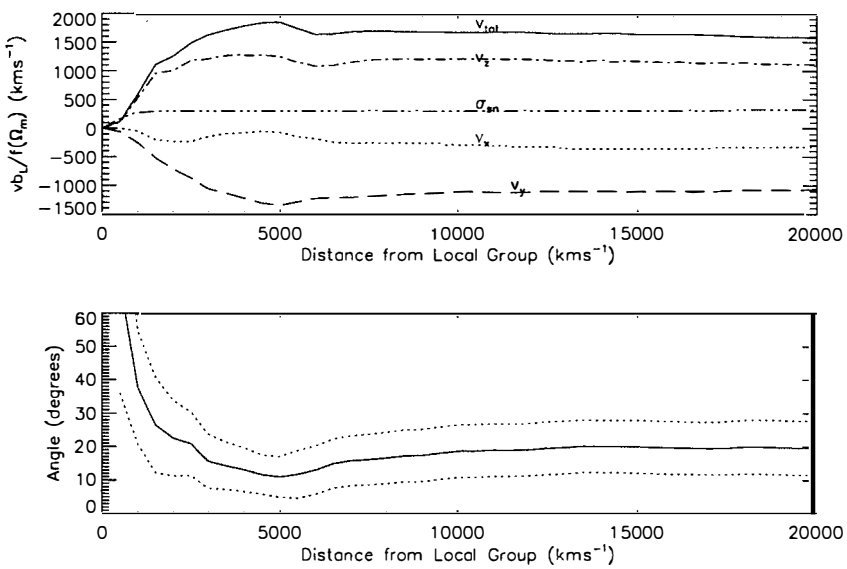

Figure 2: **Top**: Three components and the magnitudes of the acceleration of the Local Group due to galaxies within a series of successively larger concentric spheres centred on the local group. **Bottom**: Convergence of the direction of the LG dipole where the misalignment angle is between the LG and the CMB dipoles. The dotted lines denote 1σ errors from shot noise.

Attractor[b] is counteracted by the Perseus-Pisces complex in the opposite direction. The dipole seems to converge by 6000 $\mathrm{km\,s^{-1}}$.

The misalignment angle between the LG and the CMB dipole is smallest at 5000 $\mathrm{km\,s^{-1}}$where it drops to 12°±7° and increases slightly at larger distances presumably due to shot-noise. The direction of the flux dipole (l=251°±12°,b=37°± 10 °) is in good agreement with the 2MASS dipole derived by Maller *et al.* (2003). The difference in results is probably due to the fact that they use a higher latitude cutoff in the mask ($|b| < 7°$) and exclude all galaxies below this latitude. We confirm this by changing our treatment of the Zone of Avoidance to match theirs. We find that the flux dipole is very close to their dipole direction. Their limiting Kron magnitude is $K_s = 13.57$ which corresponds to an effective depth of 200 h^{-1} Mpc. As their sample is deep enough to pick out galaxies in the Shapley Supercluster, the comparison of their dipole value with our values suggests that the contribution to the LG dipole from structure further away than the maximum distance of our analysis is not significant.

Assuming convergence, we equate the velocity inferred from the CMB measurements with the value derived from a galaxy survey and obtain a value for the combination of the mass density and luminosity bias parameters: $\Omega_{\mathrm{m}}^{0.6}/b_{\mathrm{L}} = 0.40 \pm 0.09$. If we adopt $\Omega_{\mathrm{m}} = 0.23$ from the WMAP3 results (Spergel *et al.* 2006) we get $b_L \simeq 1$. This suggest that the 2MRS galaxies are unbiased.

A detailed description of the analysis and results outlined in this paper can be found in Erdoğdu *et al.* (2006).

Acknowledgments

OL acknowledges a PPARC Senior Research Fellowship. JPH, LM, CSK, NM, and TJ are supported by NSF grant AST-0406906, and EF's research is partially supported by the Smithsonian Institution. DHJ is supported as a Research Associate by Australian Research Council Discovery-Projects Grant (DP-0208876), administered by the Australian National University. This publication makes use of data products from the Two Micron All Sky Survey, which is a joint project of the University of Massachusetts and the Infrared Processing and Analysis Center/California Institute of Technology, funded by the National Aeronautics and Space Administration and the National Science Foundation. This research has also made use of the NASA/IPAC Extragalactic Database (NED) which is operated by the Jet Propulsion Laboratory, California Institute of Technology, under contract with the National Aeronautics and Space Administration and the SIMBAD database, operated at CDS, Strasbourg, France.

References

1. Bennett C.L., *et al.* , 2003, ApJS, 148, 1
2. Courteau S. & Van Den Bergh S., 1999, AJ, 118, 337
3. Erdoğdu P., *et al.* , 2006, MNRAS, in press (astro-ph/0507166)
4. Huchra J., Jarrett T.H., Skrutskie M., Cutri R., Schneider S., Macri L., Steining R., Mader J., Martimbeau N., George T., 2005, in Nearby Large-Scale Structures and the Zone of Avoidance ASP Conference Series, eds. K.P. Fairall, P.A. Woudt, 329, 135
5. Maller A.H., McIntosh D.H., Katz N. & Weinberg M.D., 2003, ApJ, 598, L1
6. Peebles P.J.E., 1980, *The Large-Scale Structure of the Universe*, Princeton University Press, Princeton
7. Schlegel D.J., Finkbeiner D.P., Davis M., 1998, ApJ, 500, 525
8. Spergel D.N., *et al.* , 2006, submitted to ApJ

[b]By 'Great Attractor', it is meant the entire steradian on the sky centred at ($l \sim 310°$,$b \sim 20°$) covering a distance of 20 h^{-1} Mpc to 60 h^{-1} Mpc.

THE SUPERNOVA LEGACY SURVEY : COSMOLOGICAL RESULTS FROM THE FIRST YEAR

D. FOUCHEZ, on behalf of the SNLS collaboration
Centre de Physique des Particules de Marseille, IN2P3-CNRS et Université de la Méditerranée , 13288 Marseille cedex 09, France

The first cosmological results from the SuperNova Legacy Survey are presented. The recipe to obtain the deep, homogenous and complete set of 71 identified type Ia supernovae is described. The construction of the Hubble diagram is supported by precise distance measurement. The steps to obtain this distance are good differential photometry, precise calibration and light-curve modelling. All steps are detailled to present the Hubble diagram. Finally the cosmological parameters are fitted from this diagram. A full error estimation (statistical and systematical) is presented.

1 Introduction

We present the first determination of cosmological parameters performed by the SuperNova Legacy Survey (SNLS) collaboration after analysing the observations of the first year. A large part of the information given in this proceeding has been exposed with more details in the Astier *et al* [1] collaboration paper. The general method used in the past [2 3 4] to derive cosmological parameters from type Ia supernovae (SNIa) using Hubble diagram is supposed known.

2 A deep homogenous and complete set if identified type Ia supernovae

2.1 The observatory facilities

The Supernovae Legacy Survey is based on an imaging survey for the photometric detection and light-curve follow-up in conjunction with a spectroscopic program for the supernova type identification and redshift determination.

The imaging take advantage of the Megacam camera mounted on the 3.6 meter CFHT telescope located in Hawaii which offer a wide field of view of 1^{o2} . The spectrocopy is done on two main telescopes : The 10-meter VLT and the 8-meter Gemini, plus additional time from the 10-meter KECK.

For the first three year of the SNLS program, about 250 hours per year have been dedicated to the imaging to follow four different fields (as part of the deep survey of the CFHTLS program) and 250 hours per year for the spectroscopy.

2.2 The detection and identification

The detection and follow up of supernovae is performed in the so-called rolling mode search : during each observational period of Megacam at CFHT (around 20 days every month), the same

field is observed every 4 days with 4 different filters . Reference images (without supernovae) are built from older nights, then detection and follow-up is automatically performed with those repeated observations.

Due to the rather fast rising of supernova light-curves, a fast detection procedure has to be set up in order to find quickly the supernova candidates we want to observe spectroscopically around their maximum luminosity. Two different pipeline have been designed to do this job, one which is triggered by human scanning, the other which automatically produce a list of candidate by analysing the detection shape and using appropriate selection on light-curve parameters. Both pipeline agree to more than 90% for magnitude above 24.0

When the candidate is choosen, it is observed spectroscopically with a delay that can be as short as 24 hours.

2.3 The current supernova sample

As in March 2006, 440 spectra of candidates have been observed. Among them 231 have been identified as type Ia supernovae.

This is the largest deep and homogenous set of type Ia light-curve sample ever observed. We will develop in the following sections the measurement of the cosmological parameters from the first year of this sample but it is important to mention here that many other scientific studies can be pursued. For example and non exhaustively : Supernova rates [6], supernova rise time, cosmic star formation history [5], progenitors, host galaxies etc

3 Precise measurement of the SNia sample

Only the first year of data has been released and will be presented here. The sample consist of 73 SNIa events. The initial set was 91 SNIa, but 10 where not analysed at the time of the publication due to missing reference images, 6 have only one band and 2 were classified as peculiar.

3.1 Differential photometry

The fluxes are measured using differential photometry [8]: For a given filter, the fluxes of the supernova is extracted from each image with a fit. As a first step, the PSF on each position of each image is described with a kernel [7]. The parameters of the model are the galaxy on a stamp, the position on the sky and the supernova flux on each image. Eq. 1 give the flux ($I(x,y)$), at the pixel level, that has to be adjusted on each image.

$$I(x,y) = Flux \times [Kernel \otimes PSF_{best}](x - x_{sn}, y - y_{sn}) + [Kernel \otimes Galaxy_{best}](x,y) + Sky \quad (1)$$

It result from this fitting procedure a flux measurement image per image with the covariance matrix associated. The errors are found to be about 12% higher that the photon statistics.

3.2 Photometric calibration

First of all, the same differential technique dicussed above is used to measure tertiary standard stars in each field. Then those tertiary stars are measured in same photometric night than some Landolt secondary stars. Using both information, a zero point that can be directly applied to the supernova flux measurement, is derived. The calibration residual found after this procedure are of the order of 1 to 3 %. The primary star is Vega.

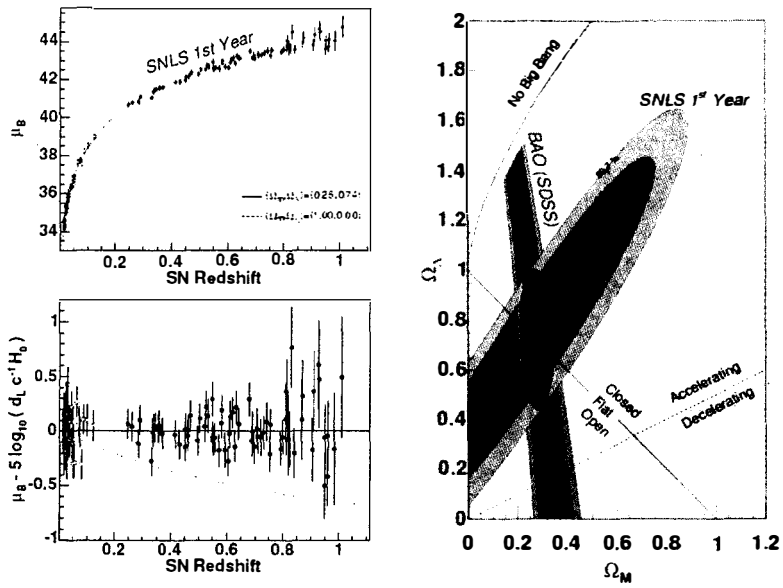

Figure 1: The Hubble diagram of 71 SNLS supernovae plus 44 nearby SNIa (Left) , Confidence level contour for the fit to Ω_M, Ω_Λ in *Lambda* cosmology from the SNIa Hubble diagram (light green) and from the SDSS baryonic oscillations (dark blue) with the combined contour at the intersection (Right).

4 Hubble Diagram and cosmology

4.1 Light-curve modelling and luminosity distance

The light-curves of the four bandpasses are fitted together using the SALT [9] procedure. Two parameters describe the variability of the SNIa light-curve, but the luminosity at maximum : s, the stretch parameter and c the color term. Those two parameters are used to correct for the 'brighter-slower' and 'brighter-bluer' behaviour. Using those two corrections, the SNIa can be standardized[9] and the distance is then derived from the magnitude at maximum in B rest frame , the stretch and the color (see Eq. 2)

$$\mu_B = m_B^* - M + \alpha(s-1) - \beta c \qquad (2)$$

4.2 Cosmological fit results

The Hubble diagram is presented in in Fig 1 (left). It uses the SNLS SNIa plus a sample of nearby SNIa that are reanalysed using the same procedure as the SNLS ones. The distance is the one describe in previous section and the redshift is the one determined from the spectroscopic observation of the supernova and/or its host galaxy. The distance is a function of the cosmological parameters which can then be fitted from the Hubble diagram data points. The comological parameters are fitted together with the α and β coefficients on all the light-curves. The cosmological parameter confidence level contours are presented in Fig 1 (right) for a *Lambda* cosmology.

Table 1: the systematic uncertainties

Source	$\delta\Omega_M$ (flat)	$\delta\Omega_tot$	δw (fixed $\delta\Omega_M$)	$\delta\Omega_M$ (with	δw BAO)
Zero points	0.024	0.51	0.05	0.004	0.040
Vega spectrum	0.012	0.02	0.03	0.003	0.024
Filter bandpasses	0.007	0.01	0.02	0.002	0.013
Malmquist bias	0.016	0.22	0.03	0.004	0.025
Sum (syst)	0.032	0.55	0.07	0.007	0.054
U-B color (stat)	0.02	0.12	0.05	0.004	0.024

4.3 Systematic uncertainties

For a more exhautive presentation of systematic uncertainties, check out Astier *et al* [1]. We present here the more representative ones.

From the result of the calibration procedure describe in previous section, a 1% to 3% uncertainty has been found and is accounted to a possible systematic effect in the zero point determination.

A comparison of the characteristics of the low and high z sample didn't show any hint of evolution hence no sytematical effects from evolution have been applied.

The Malquist bias resulting from the selection of the brightest objects at the high z limit of the survey, has been estimated, from Monte Carlo simultions, to change by 0.05 magnitude the highest point of the Hubble diagram

A summary of all the systematic uncertainties, expressed in term of errors on the cosmological parameters is presented on Table 1

Finally, the results on the comological parameters are:
$\Omega_M = 0.263 \pm 0.042(stat) \pm 0.032(syst)$ for a flat cosmology
and
$\Omega_M = 0.271 \pm 0.021(stat) \pm 0.007(syst)$
$w = -1.02 \pm 0.09(stat) \pm 0.054(syst)$ for a flat cosmology with constant equation of state and combined with the BAO SDSS results [10].

Statistical error is still dominant but we are reaching soon the systematic limit, that has to be reduced to take full advantage of the coming 700 SNIa expected at the end of the survey.

References

1. The Supernova Legacy Survey : Measurement of Ω_M, Ω_Λ and w from the first year dataset, Astier *et al A&A* **447**, 31 (2006).
2. Riess, A. G. *et al*, AJ 116 (1998), 1009
3. Perlmutter,S *et al*
4. Riess, A. G. *et al*, ApJ 607 (2004), 665
5. M. Sullivan *et al.*, arXiv:astro-ph/0605455.
6. J. D. Neill *et al.*, arXiv:astro-ph/0605148.
7. Alard, C. A& A 144 (2000), 363
8. Fabbro, S., Photométrie de supernovae de type Ia et implication cosmologiques (2001), PhD Thesis, Université Paris VI
9. J. Guy, P. Astier, S. Nobili, N. Regnault and R. Pain, arXiv:astro-ph/0506583.
10. D. J. Eisenstein *et al.*, Astrophys. J. **633**, 560 (2005)

THE ARCMINUTE MICROKELVIN IMAGER

K.J.B. GRAINGE
Cavendish Laboratory, JJ Thomson Avenue,
Cambridge CB3 0HE, England

The Arcminute Microkelvin Imager is a dual array interferometer designed specifically to survey for galaxy clusters through detecting their Sunyaev-Zel'dovich signatures on the microwave background. Construction of the Small Array is now complete and commissioning observations have mapped several clusters. The Large Array is required to remove the effects of confusing radio sources and will allow deep, blind surveys for clusters.

1 Motivation for a Galaxy Cluster Survey

Clusters of galaxies are the most massive collapsed objects in the Universe. They are sensitive probes of structure formation, both in the linear regime of growth and when merging, shocking and gradual virialisation occur. Determining the evolution of clusters, their mass function and structures is therefore of basic importance. A population of clusters at $z > 1$ is now known to exist [18]. However, more data and in particular an unbiased cluster survey are needed to understand cluster formation and early evolution at these redshifts. Optical and X-ray observations suffer from confusion and from a bias towards concentration of mass; another approach is to survey for clusters through detcting their Sunyaev–Zel'dovich (S–Z) effect.

2 The Sunyaev-Zel'dovich Effect

The S–Z effect [19] is a secondary anisotropy on the Cosmic Microwave Background (CMB) radiation due to inverse-Compton scattering of CMB photons from hot plasma in the gravitational potential of a cluster of galaxies. The S–Z effect has been detected by a number of different groups using a variety of observing techniques [4,15,17,12,16,8,7,14,21] (See e.g. Birkinshaw, 1999 [3] or Carlstrom, Holder and Reese, 2002 [6] for a full review).

CMB photons are up-scattered in energy with the result that, at frequencies below 220 GHz, one sees a decrease in the CMB temperature towards the cluster. In the Rayleigh-Jeans regime

this dip is given by

$$\Delta T = -2yT_{\rm cmb},$$

where y is the Comptonisation parameter

$$y = \int n_e \sigma_T \frac{kT_e}{m_e c^2} {\rm d}l.$$

Importantly the intensity of the S–Z effect is independent of redshift. The reason for this is that in such a Compton scattering process, the power lost by the electrons and given to the CMB photons is proportional to the energy density of the incident CMB radiation which is proportional to $(1+z)^4$; this exactly cancels out the cosmological drop in surface brightness proportional to $(1+z)^{-4}$.

S–Z surveys for clusters have long been advocated [11,5,2] and it is now widely recognised that such surveys are key measurements for cosmology. Such a method has several key advantages. Firstly, because the surface brightness of the S–Z effect does not decrease with redshift, one can detect clusters of galaxies all the way back to their epoch of formation. Further, the measured total flux density of the S–Z effect from a cluster is very closely related to its mass, which is precisely the quantity we wish to observe. This can be seen from the following. The brightness temperature of the S–Z effect is proportional to the integral of the gas pressure along the line of sight,

$$\Delta T_{\rm SZ} \propto \int nT \, {\rm d}l,$$

while the total flux density is proportional to the integral of the surface brightness over solid angle

$$\Delta S_{\rm SZ} \propto \int \Delta T_{\rm SZ} \, {\rm d}\Omega.$$

The flux density is therefore proportional to the total thermal energy in the cluster

$$\Delta S_{\rm SZ} \propto D_{\rm A}^{-2} \int nT \, {\rm d}V,$$

where $D_{\rm A}$ is the angular size distance. Because of the flatness of the angular size *vs* redshift relation, $D_{\rm A}$ is only weakly dependent on redshift. The total S–Z flux density from a cluster is thus a measure of its mass, since in gravitational collapse models the thermal energy is simply the gravitational potential energy of the cluster (assuming full virialisation). An S–Z survey that is complete down to a particular S–Z flux density limit would therefore be complete down to a cluster mass limit *with no limiting redshift* and largely *independent of the detailed cluster astrophysics*. A principal aim of the AMI project is to carry out this survey work [10].

3 AMI Hardware

AMI [9] comprises two synthesis arrays (shown in Figure 1), sited at Lord's Bridge, Cambridge. The Small Array consists of ten 3.7-m antennas situated inside a 30 × 40-m, 4.5-m high metal enclosure. The Large Array is an upgrade to the Ryle Telescope with all eight 13-m antennas now placed in a new 2-dimensional compact configuration. The dual array design gives AMI good temperature sensitivity over a very large range of angular scales, as well as the high flux sensitivity needed to identify and remove the effect of radio sources from the data (see Figure 2).

The telescope observes in the band 12–18 GHz with cryostatically cooled NRAO indium-phosphide front-end amplifiers and fully-cooled feeds. The overall system temperature is approximately 25 K. We detect a single linear polarisation, measuring Stokes' parameter $I+Q$. The radio frequency is mixed with a 24-GHz local oscillator, downconverting to an intermediate frequency (IF) band of 6–12 GHz. Amplification, equalisation, path compensation and

Figure 1: The AMI Small and Large arrays

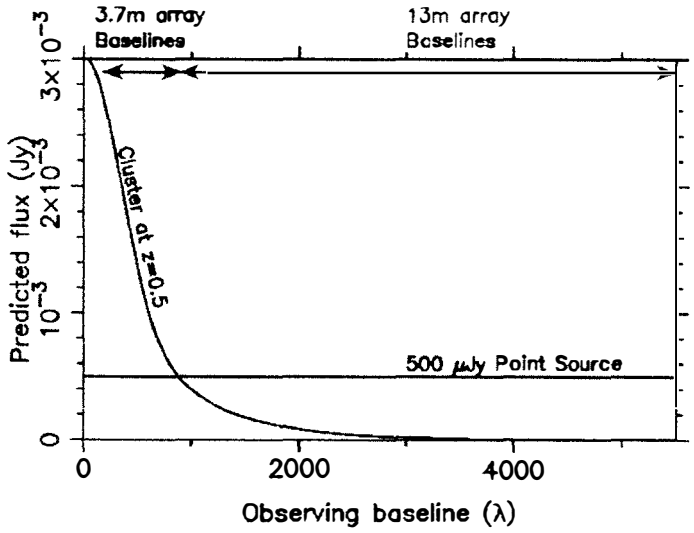

Figure 2: Simulated plot of interferometer detected flux against observing baseline for a galaxy cluster at $z = 0.5$ and a point source (for convenience the absolute value of the negative S–Z flux is plotted). Since the cluster has large angular extent, its flux is quickly resolved out as the baseline length is increased whilst the flux from the point source is constant. The Small Array of 3.7-m dishes is therefore required to give access to the short baselines which detect the S–Z effect and the Large Array will measure the flux of any point sources in the field and allow their effects to be subtracted.

automatic gain control are then applied to the IF signal. The correlator is an analogue Fourier transform spectrometer with 16 correlations formed for each baseline at path delays spaced by 25 mm. Both '+' and '−' correlations [20] are formed in this fashion by use of 0° and 180° hybrids respectively. From these, eight 0.75-GHz channels are synthesised.

4 Current Status

Construction of the Small Array is now complete. Results from the first commissioning observations [1] are discussed later in these proceedings [22]. The three outlying antennas of the RT have been successfully moved to form a compact Large Array with the East-West array of five previously used for S–Z work. The upgrade of the feed-assembly, IF chain and correlator is on schedule for completion by October 2006.

5 Acknowledgements

AMI is a project of the Cavendish Astrophysics Group and is supported by the Particle Physics and Astronomy Research Council.

References

1. AMI Collaboration, 2006, MNRAS, 369, L1
2. Bartlett J.G., Silk J., 1994, ApJ 423, 12
3. Birkinshaw M., 1999, Phys. Rep., 310, 97
4. Birkinshaw M., Hughes J. P., ApJ, 1994, 420, 33
5. Bond J.R., Meyers S.T., 1991, in: Trends in Astroparticle Physics, ed. Cline D., World Scientific, Singapore.
6. Carlstrom J. E., Holder G. P., & Reese E. D. 2002, ARA&A, 40, 643
7. Grainge K., Jones M. E., Pooley G. G., Saunders R., Edge A., MNRAS, 1993, 265, L57
8. Holzapfel W.L. et al., ApJ, 481, 35
9. Jones M. E., 2002, ASPC, 257 in 'AMiBA 2001: High-z Clusters, Missing Baryons, and CMB Polarization', edited by Lin-Wen Chen, Chung-Pei Ma, Kin-Wang Ng, and Ue-Li Pen., ASPC, San Fransisco, 257, 35
10. Kneissl R., Jones M., Saunders R., Eke V., Lasenby A., Grainge K., Cotter G., 2001, MNRAS, 328, 783
11. Korolev V.A., Sunyaev R.A., Yakubtsev L.A., 1986, Sov. Astron. Lett., 12, 141
12. Komatsu E. et al., 1999, ApJ, 516, L1
13. Kosowsky A., 2003, NewAR, 47, 939
14. Lancaster K. et al., 2005, MNRAS, 359, 16
15. Myers S. T., Baker J. E., Readhead A. C. S., Leitch E. M., & Herbig, T. 1997, ApJ, 485, 1
16. Pointecouteau E. et al., ApJ, 519, L115
17. Reese E. D., Mohr J. J., Carlstrom J. E., Joy M., Grego L., Holder G. P., Holzapfel W. L., Hughes J. P., Patel S. K., Donahue M., ApJ, 2000, 533, 38
18. Rosati P., Borgani S., Norman C., 2002, The Evolution of X-ray Clusters of Galaxies, ARAA, 40, 539
19. Sunyaev R. A., Zel'dovich Ya B., 1972, Comm. Astrophys. Sp. Phys., 4, 173
20. Thompson A. R., Moran J. M., Swenson G. W., 2001, "Interferometry and Synthesis in Radio Astronomy", pubs. John Wiley & Sons Inc.
21. Udomprasert P. S., Mason B. S., Readhead A. C. S., Pearson T. J., 2004, ApJ, 615, 63
22. Zwart J., 2006, these proceedings.

Half-Wave Plate Polarimetry with MAXIPOL

B. R. Johnson[5], M. E. Abroe[1], P. A. R. Ade[3], J. Bock[4], J. Borrill[7,9], J. Collins[2], S. Hanany[1], A. H. Jaffe[8], T. Jones[1], A. T. Lee[2,6], L. Levinson[10], T. Matsumura[1], B. Rabii[2], T. Renbarger[1], P. L. Richards[2], G. F. Smoot[2,6], R. Stompor[12], H. T. Tran[2,9], C. D. Winant[2], J. H. P. Wu[11], J. Zuntz[8]

[1] *School of Physics and Astronomy, University of Minnesota, Minneapolis, MN, 55455, USA*
[2] *Department of Physics, University of California, Berkeley, CA, 94720, USA*
[3] *School of Physics and Astronomy, Cardiff University, Cardiff, CF24 3YB, UK*
[4] *Jet Propulsion Laboratory, Pasadena, CA, 91109, USA*
[5] *Astrophysics, University of Oxford, Oxford, OX1 3RH, UK*
[6] *Physics Division, Lawrence Berkeley National Lab, Berkeley, CA, 94720, USA*
[7] *Computational Research Division, Lawrence Berkeley National Lab, Berkeley, CA, 94720, USA*
[8] *Astrophysics Group, Blackett Lab, Imperial College, London, SW7 2AZ, UK*
[9] *Space Sciences Laboratory, University of California, Berkeley, CA, 94720, USA*
[10] *Department of Particle Physics, Weizmann Institute of Science, Rehovot, Israel*
[11] *Department of Physics, National Taiwan University, Taipei, Taiwan*
[12] *Laboratoire Astroparticule et Cosmologie, Universite Paris 7, Paris, France*

We discuss the use of half-wave plate (HWP) polarimetry for bolometric measurements of the polarization anisotropy of the cosmic microwave background radiation (CMB). The information presented here comes from experience gained during a balloon-borne experiment called MAXIPOL, which is the instrument from the CMB temperature anisotropy experiment, MAXIMA, retrofitted with a rotating HWP and wire-grid analyzer. We describe the HWP polarimetry technique and associated systematic errors. For MAXIPOL, we found the method worked well and that after appropriate corrections, any residual HWP systematic errors were less than the statistical noise. Therefore, the method appears to be promising for E and B-mode characterization. The hardware and data analysis techniques developed for MAXIPOL may be useful for the development of future B-mode experiments.

1 Introduction

Interest in precise millimeter-wave polarimetry is growing because measurement of the anticipated B-mode gravitational wave signature of inflation in the CMB is becoming technologically possible. Newly developed detector arrays with multiplexed readouts promise to deliver sufficient sensitivity for detection of the faint B-mode signals;[1,2] heretofore, receiver sensitivity has limited measurements to the E-mode.[3,4,5,6,7] Once sufficient sensitivity is available, identifying methods for mitigating systematic errors becomes the paramount issue for next-generation experiments. Now is the time to characterize polarimetry techniques precisely, and identify those that will both be compatible with the new detector arrays, and produce acceptable levels of manageable systematic error. This paper is dedicated to the discussion of half-wave plate polarimetry, which is one candidate technology. This technique along with important sources of systematic error are described in Section 2. A measurement used to characterize this type of polarimeter is described in Section 3.

We used the MAXIMA instrument as a pathfinder to learn about CMB polarization measurements which use a rotating HWP as a polarization modulator. The optical arrangement of MAXIMA allowed HWP hardware to be installed and the high sensitivity of the receiver made detection of the E-mode polarization plausible in a ~24 hour flight. The retrofitted experiment is called MAXIPOL, and it is the first CMB experiment to observe the sky with a HWP polarimeter. In this paper we discuss some of the lessons learned from MAXIPOL about the systematic errors in HWP polarimetry, with the intention that this information will inform the design of future experiments. We find that any residual HWP systematic errors were less than the statistical noise in the time and map domain for MAXIPOL so the technique remains

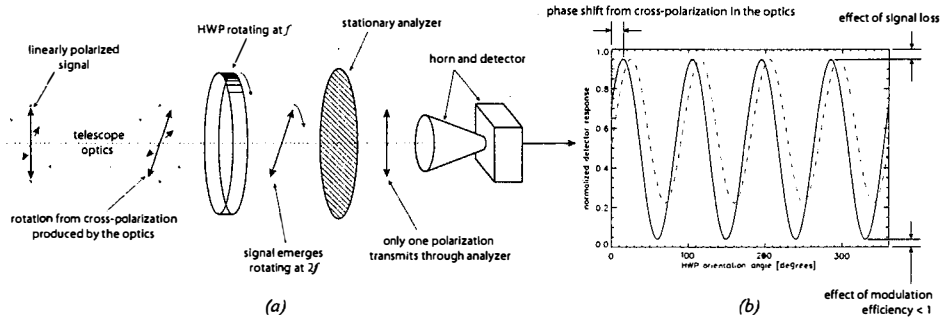

Figure 1: (*a*) Schematic drawing of HWP polarimeter hardware. (*b*) Two simulations of the detector output. The length of the signal vector in (*a*) corresponds to the degree of polarization. The effect of a few kinds of non-ideal performance is highlighted in (*b*). The modulated signal from a perfect polarimeter measuring a perfectly lineraly polarized source would extend from 0 to 1 in (*b*).

promising for E and B-mode characterization. The MAXIMA instrument and observations have been described in previous publications.[8,9,10,11,12,13,14,15,16,17,18,19] Detailed descriptions of the MAXIPOL results are being prepared.[20,21]

2 Half-Wave Plate Polarimetry

Linearly polarized light that propagates through a HWP rotating at a frequency f emerges linearly polarized with its orientation rotating at $2f$. If this light then passes through a fixed polarization analyzer and its intensity is subsequently detected, the output data stream will be modulated sinusoidally at $4f$. Perfectly polarized light will maximize the $4f$ amplitude and unpolarized light will yield no modulation. The phase of the output data is determined by the orientation of the incident polarization. Figure 1 shows a drawing of a HWP polarimeter and a simulated detector response. The fact that the detected signal is modulated at $4f$ is very important for several reasons. The modulation imposed by the HWP, combined with telescope scanning moves sky signals to a user-defined band in the frequency domain, which can be shifted away from any detector $1/f$ noise or other spurious instrumental signals. Unwanted signals at f, $2f$, and $3f$ from the HWP or its drive mechanism can easily be rejected. The HWP operates on polarized radiation only so polarized and unpolarized signals are cleanly separated. Further, a single detector rapidly measures the modulated Q and U Stokes parameters simultaneously, so systematic errors that complicate detector differencing techniques are avoided. The systematic errors that must be corrected in order to successfully use the technique are explained in detail below.

2.1 Cross-Polarization

Cross-polarization is an effect where power from one polarization state is moved to the orthogonal polarization. This phenomenon produces $Q \leftrightarrow U$ mixing if the phase of the two polarizations is preserved during the operation and $Q, U \leftrightarrow V$ mixing if it is not. For CMB measurements $Q \leftrightarrow U$ mixing is important because it leads to $E \leftrightarrow B$ mixing. HWP polarimeters like MAXIPOL are insensitive to V. Typical sources of cross-polarization are the reflective telescope optics and the horns, though the effect of the horns is not detectable if they follow the analyzer, which was the case for MAXIPOL. The MAXIPOL HWP should not produce spurious cross-polarization. However, achromatic HWPs under consideration for future experiments can produce spurious cross-polarization.[22]

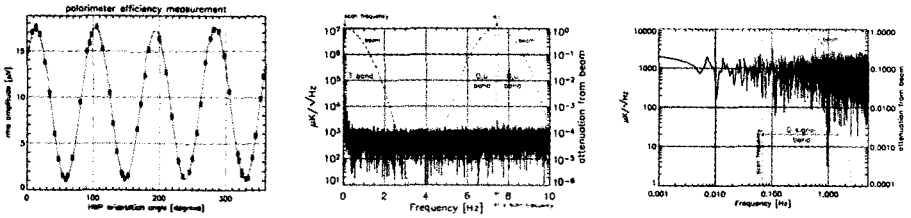

Figure 2: MAXIPOL polarimeter data from a typical photometer. (*a*.) Results from the pre-flight characterization of the polarimeter. (*b*) The power spectrum of 16 minutes of time-ordered flight data with the known systematic errors corrected. (*c*) The power spectrum of the demodulated time ordered polarization data for Q. Zero-frequency in (*c*) is $4f$ in (*b*). Sky signals appear in sidebands bounded by the dashed lines marking the telescope scan frequency and the frequency-domain representation of the telescope beam in panels (*b*) and (*c*). Nominal instrument noise is recovered in all cases.

Systematic errors arising from cross-polarization can be mitigated during data analysis by applying a calibration like the one ascertained by the measurement described in Section 3. Other instrumental effects that mimic cross-polarization are phase shifts from the bolometer time constant and offsets produced by misalignment between the crystal axes and the encoder. The combined effect of the MAXIPOL cross-polarization from the secondary and tertiary telescope mirrors and a HWP encoder offset appears as the phase shift in the modulation data in Figure 2(*a*).

2.2 Instrumental Polarization

Unpolarized incident light can become partially polarized inside the instrument through diffraction, oblique reflection, and by combining the incident signals with polarized emission. Sources of instrumental polarization that affect the transmitted signal are most serious because they operate on sky signals which have been modulated by the telescope scanning. For example, unpolarized CMB temperature anisotropies become spurious sky-stationary polarization anisotropies. Polarized signals radiated from telescope baffles located between the sky and the HWP are less serious, provided the baffle temperature changes are slow compared with the rate of modulation of sky-stationary signals. For MAXIPOL the instrumental polarization in transmission is $< 1\%$ so any $T_{sky} \rightarrow Q, U$ is not detectable.

2.3 Depolarization

The HWP for MAXIPOL is made from a single layer of anti-reflection coated sapphire. The behavior described in Section 2 applies only to frequencies $\nu = mc/2t\Delta n$ where Δn is the difference between the ordinary and extraordinary indices of refraction in the birefringent crystal, t is the propagation length through the crystal, m is an odd integer and c is the speed of light. Linearly polarized light at other frequencies emerges elliptically polarized from the HWP($Q, U \rightarrow V$ conversion). Typical analyzers like wire-grid polarizers do not mix V to I and total power detectors like bolometers are only sensitive to I emerging from the analyzer so the spurious V signal created by the HWP is rejected. However, the Q and U that are detected are smaller than the true Q and U of the actual signal, which means the polarimeter has partially depolarized the signal. The level of depolarization is described by a modulation efficiency. A typical photometer in the MAXIPOL polarimeter had a modulation efficiency of 92%, which means a perfectly polarized signal was measured to be 92% polarized by the instrument.

2.4 Other HWP Errors

Other known HWP systematic errors exist though they are less serious because they appear out of the Q, U signal sidebands on either side of $4f$ (see dashed curves in Figures 2(b) & 2(c)). For example, differential transmission resulting from use of a non-birefringent anti-reflection coating will produce a $2f$ signal. For MAXIPOL, thermal emission from the hardware used to rotate the HWP produced signals that appeared in the data stream at the harmonics of f. The most serious case was the $4f$ harmonic. Like the instrumental polarization signal from emission at $4f$, it could be separated from the sky stationary signals using the fact that the thermal emission signal drifts very slowly compared to the time scale of the sky signals. The power spectra in Figures 2(b) and 2(c) show that after correction of the known errors, the nominal detector noise is recovered.

Absorptive loss at 140 GHz in the HWP is low. The transmission is 98% for 3.18 mm of sapphire at 4 K. The absorption coefficient does not change significantly between 5.8 and 76 K so for MAXIPOL the exact HWP temperature was not important, provided it was stable on time scales that were long compared to the HWP rotation period.[23]

3 Polarimeter Characterization

The MAXPOL polarimeter was characterized with measurements in the laboratory before the flight. We made two measurements using a thermal source, which filled the beam and was chopped between 273 K and 300 K. First, the radiation was linearly polarized with a wire-grid mounted on the window of the cryostat. The orientation of the transmission axis of this polarizer and the analyzer were aligned to within a few degrees. The amplitude of the chopped signal was then measured at 54 orientations of the HWP angle, as shown in Figure 2(a). This test yielded the cross-polarization of the optical elements between the cryostat window and the HWP and the modulation efficiency of the polarimeter. Second, the same test was repeated with the window polarizer removed to give the transmission component of the instrumental polarization, which was constrained to be $< 1\%$.

References

1. Lanting, T. M., et al. 2005. *Appl. Phys. Lett.* 86, 112511.
2. Lee, A. T., et al. 1996. *Appl. Phys. Lett.* 69, 1801.
3. Page, L., et al. 2006. *ApJ submitted.*
4. Readhead, A. C. S., et al. 2004. *Science.* 306, 5697, pp. 836-844.
5. Barkats, D., et al. 2005. *ApJ.* 619, L127-L130.
6. Montroy, T. E., et al. *ApJ submitted.* astro-ph/0507514.
7. Kovac, J.M., et al. 2002. *Nature.* 420, 772.
8. Hanany, S., et al. 2000. *ApJ.* 545:L5-L9.
9. Balbi, A., et al. 2000. *ApJ.* 545:L1-L4.
10. Lee, A. T., et al. 2001. *ApJ.* 561:L1-L5.
11. Stompor, R., et al. 2001. *ApJ.* 561:L7-L10.
12. Abroe, M. E., et al. 2004. *ApJ.* 605, 607-613.
13. Lee, A. T., et al. 1998. *The Proc. of the "3 K Cosmology" Conf.* astro-ph/9903249.
14. Johnson, B. R., et al. 2003. *New Astronomy Reviews.* astro-ph/0308259.
15. Rabii, B. & Winant, C. D., et al. 2003. *Rev. Sci. Inst. submitted.* astro-ph/0309414.
16. Johnson. B. R., et al. 2004. *Ph.D. Thesis, University of Minnesota.*
17. Collins, J. S. 2006. Ph.D. Thesis. University of California, Berkeley. *in preparation.*
18. Winant. C. D. 2003. Ph.D. Thesis. University of California. Berkeley.
19. Rabii. B. 2002. Ph.D. Thesis. University of California, Berkeley.
20. Johnson, B. R., Collins, J., et al. 2006. *ApJ. in preparation.*
21. Wu. J. H. P., et al. 2006. *ApJ. in preparation.*
22. Hanany, S., et al. 2005. *Appl. Opt.* 44, 4666-4670.
23. Afsar, M. N. & Chi, H. 1991. *16th Int. Conf. on Infrared and Millimeter Waves.* SPIE Pub, Vol. 1576.

THE NEAR-IR GALAXY LUMINOSITY FUNCTION FROM SDSS AND UKIDSS

J. LOVEDAY
Astronomy Centre, University of Sussex, Falmer, Brighton BN1 9QH, England

We combine spectroscopic galaxy redshifts from the Sloan Digital Sky Survey (SDSS) with K-band photometry from the UKIRT Infrared Deep Sky Survey (UKIDSS) Large Area Survey (LAS) Early Data Release. K-band number counts show that UKIDSS LAS is complete in galaxies to a Petrosian magnitude $K \approx 16$, about two magnitudes deeper than the 2MASS Extended Source Catalogue. We present preliminary estimates of the K-band luminosity function of galaxies detected by both the UKIRT Infrared Deep Sky Survey and the Sloan Digital Sky Survey. Although the matched sample size is much smaller than that used in previous work utilising 2MASS photometry, our results are consistent with these earlier results, and suggest that UKIDSS LAS is more complete in low surface brightness galaxies than 2MASS.

1 Introduction

The study of galaxies in near-infrared (near-IR) light offers several advantages over optical wavelengths.

1. Light of $\sim 2\mu$m in wavelength provides an accurate tracer of the mass in evolved stars and is relatively insensitive to recent episodes of star formation. Near-IR light thus traces stellar mass rather than star-formation activity.

2. The K-correction in near-IR wavelengths is approximately independent of a galaxy's spectral energy distribution (SED).

3. The effects of reddening and extinction by dust are less in the near-IR than in the optical.

The recent advent of large-area infrared detectors has made possible large surveys in the near-IR. Pre-eminent amongst these is the 2 Micron All Sky Survey (2MASS) [9], which covers the entire sky in the J, H and K_s bands to a K_s-band depth of 14.3 (10σ point source). This is, however, a relatively shallow survey, with a typical galaxy redshift $\bar{z} < 0.1$. It is thus impossible to use 2MASS to investigate evolutionary properties of galaxies. Here we utilise data from a new near-infrared galaxy survey, in combination with optical and spectroscopic data, in order to estimate the K-band galaxy luminosity function.

2 Data

We use Data Release 5 (DR5) of the Sloan Digital Sky Survey (SDSS) and the Early Data Release (EDR) of the UKIRT Infrared Deep Sky Survey (UKIDSS).

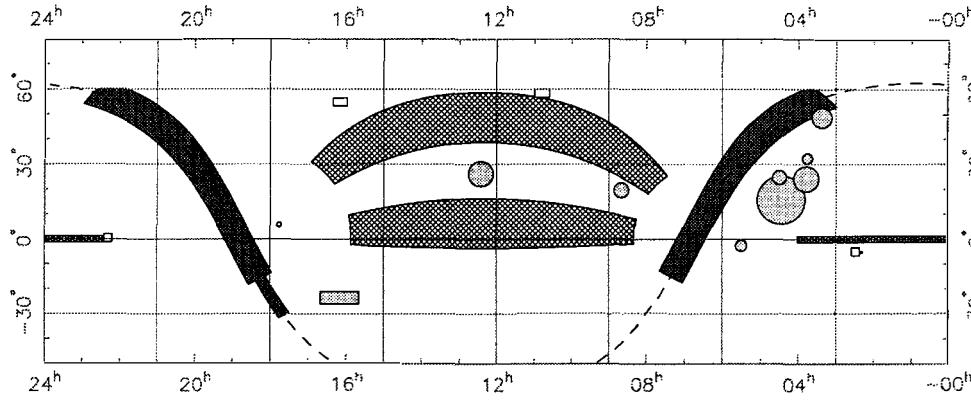

Figure 1: Equatorial all-sky plot showing locations of UKIDSS sub-surveys. Cross-hatch: LAS, dark grey: GPS; light grey: GCS; open rectangles: DXS. The single UDS field lies adjacent to DXS field at 2^h18^m RA, $-5°$ dec. Figure taken from reference [7].

Table 1: Sub-survey areas (square degrees) and K-band depths in Vega magnitudes for a point source at 5σ. Final (7-year), 2-year and EDR statistics are quoted.

Survey	7-year		2-year		EDR	
	Area	K limit	Area	K limit	Area	K limit
LAS	4028	18.2	2120	18.2	27.3	18.1
GPS	1868	19.0	1868	18.2	14.9	18.1
GCS	1067	18.6	604	18.2	7.0	18.1
DXS	35	20.8	12.6	20.8	2.4	20.6
UDS	0.77	22.8	0.77	22.8	0.77	21.1

2.1 UKIDSS

UKIDSS [7] utilises the new Wide Field Camera (WFCAM) on the 3.8 metre UK Infra-Red Telescope (UKIRT) to survey the sky in the $ZYJHK$ bands from 0.8 to 2.5 μm. It actually comprises five sub-surveys: the Large Area Survey (LAS), the Galactic Plane Survey (GPS), the Galactic Clusters Survey (GCS), the Deep eXtragalactic Survey (DXS) and the Ultra-Deep Survey (UDS). Areas and depths for these sub-surveys are given in Table 1 and the sky distribution of survey fields is shown in Figure 1. The survey began in May 2005 and is scheduled to take seven years to complete, with well-defined goals after two years of survey operation (see Table 1). An Early Data Release (EDR) [4], comprising about 1% of the final survey data, was released to the ESO community in February 2006. The first large data release (DR1) is scheduled for July 2006, and will include about 10% of the final survey data. Data will become public to the world 18 months after they are released within ESO.

The UKIDSS LAS is well matched to SDSS, and here we use galaxies detected in UKIDSS LAS "EDR+" (which includes areas of sky with incomplete filter coverage) and SDSS DR5 to measure the K-band luminosity function.

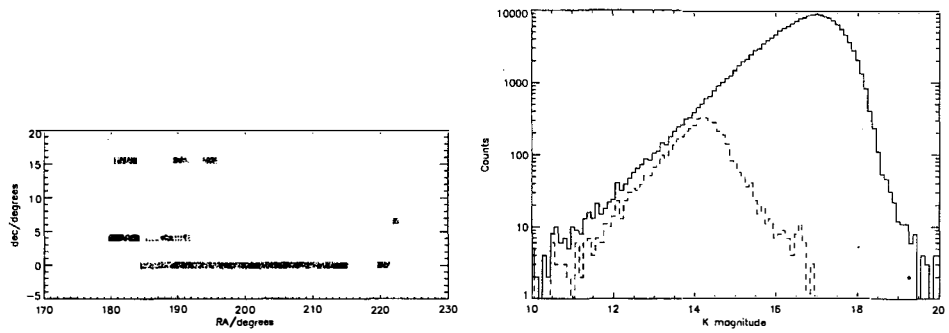

Figure 2: Left: Equatorial distribution of the 3,249 UKIDSS-SDSS matched galaxies with redshifts. Right: unnormalised Petrosian K-band number counts for all LAS galaxies (continuous line) and matched galaxies with redshifts (dashed line).

2.2 SDSS

We use Data Release 5 (DR5) [12] of the SDSS main galaxy sample. This release, made public in July 2006, has an imaging area of 8000 deg^2 and a spectroscopic area of 5740 deg^2. The main spectroscopic sample of galaxies [10] is flux-limited to an extinction-corrected Petrosian r band magnitude limit of $r < 17.77$. The DR5 version of this sample contains 783,263 galaxy targets, of which 455,995 have a measured redshift.

2.3 Data Matching

UKIDSS EDR data is pre-matched in the WFCAM Science Archive[11] to SDSS DR2. However, in order to maximise the number of galaxies with SDSS redshifts, we have matched to SDSS DR5. We utilise the Starlink TOPCAT programme and match on equatorial coordinates with a tolerance of 2 arcsec (more than 99% of objects match within 1 arcsec). Of 1,373,166 unique detections in the LAS, 11,835 match up with an SDSS DR5 main sample galaxy. Of these galaxies, 4,584 include a K-band detection. We estimate the effective sky coverage of the matched galaxies with K-band photometry as follows. SDSS DR5 imaging data covers 8000 deg^2 and the main galaxy sample includes 783,263 targets (of which 455,995 have a measured redshift). The estimated sky coverage is then given by $8,000 \times 4,584/783,263 \approx 46.8$ deg^2. Of the 4,584 matched galaxies with K-band photometry, 3,249 have an SDSS redshift. The spectroscopic incompleteness is automatically allowed for by our luminosity function estimators.

The sky-distribution of these matched galaxies is shown in the left panel of Figure 2. The right panel shows Petrosian K-band number counts for all LAS galaxies and for matched galaxies with redshifts. We see that LAS galaxy counts are complete to roughly $K = 16$, with a turnover in the counts near $K = 17$. As expected, the magnitude limit for a complete sample of LAS galaxies, being extended sources, is significantly brighter than the point-source limit given in Table 1. The matched counts are complete only to $K = 14$. This limit is due to the relatively shallow depth of SDSS spectroscopy ($r < 17.77$) combined with the reddest typical galaxy colour, $(r - K) \approx 3.8$ (Fig. 3), and is only half a magnitude or so deeper than galaxy samples selected from 2MASS. In order to estimate a K-band luminosity function which is unbiased with respect to galaxy colour, a magnitude limit of $K < 14$ must be applied to the matched sample, giving a complete sample of 1,287 galaxies.

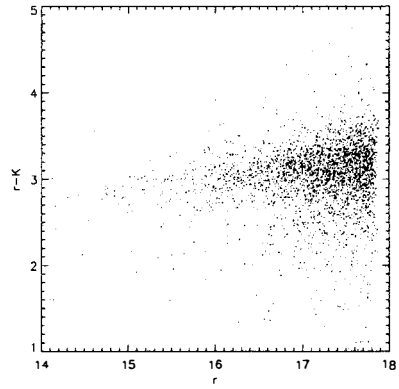

Figure 3: $(r-K)$–r colour-magnitude diagram for matched UKIDSS-SDSS galaxies. The r-band magnitude limit of $r = 17.77$ is that of SDSS spectroscopy.

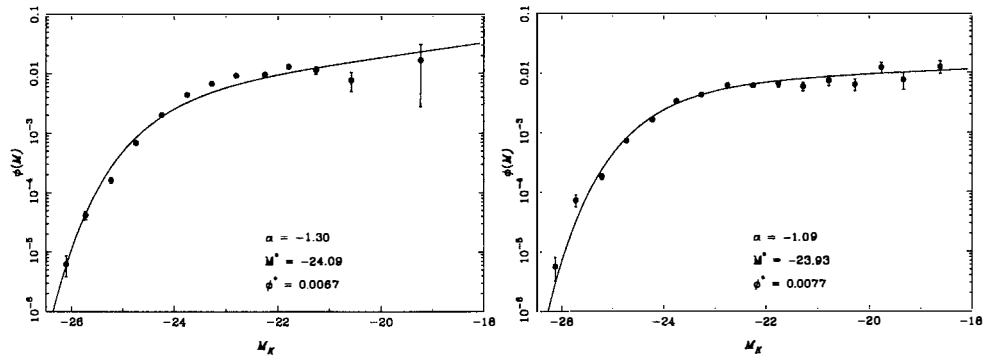

Figure 4: K-band luminosity functions estimated from (left) a complete sample of 1,287 galaxies and (right) via the bivariate $\phi(M_r, M_K)$ distribution of 3,249 galaxies, incomplete in faint, red galaxies.

3 K-Band Luminosity Function

We first K-correct apparent K-band magnitudes to a bandpass that is blue-shifted by a factor of 1.1 to $z = 0.1$. This means that galaxies at the median redshift of the SDSS main sample, $\bar{z} = 0.1$, have a K-correction that is independent of galaxy type. The amplitudes, and hence uncertainties, of the K-corrections are also minimised in this way. K-corrections are performed using `kcorrect v4_1_4`[2].

The luminosity function (LF) is then determined using both parametric (Schechter function) and non-parametric (stepwise maximum likelihood) estimators that are independent of density-inhomogeneities [8,5]. The resulting LF is shown in the left panel of Figure 4. Due to the small sample size, the faint end of this LF is poorly determined, and despite the estimated faint-end slope parameter $\alpha = -1.3$ in the Schechter function fit, the stepwise estimate is clearly consistent with a "flat" faint-end slope of $\alpha = -1.0$.

One can utilise all 3,249 UKIDSS-SDSS matched galaxies by estimating the bivariate luminosity function $\phi(M_r, M_K)$, allowing for the known r-band selection, and then integrating over M_r to obtain an estimate of $\phi(M_K)$. The resulting LF is shown in the right panel of Figure 4. Using this larger dataset, one indeed finds a faint-end slope parameter closer to $\alpha = -1.0$. One should bear in mind that the least-luminous galaxies in this sample will be bluer in $(r-K)$ colour than average: they are constrained to have $r < 17.77$ by the spectroscopic flux limit but

have no explicit cut in K-band magnitude.

Both of these estimates hint at a slightly steeper faint-end slope α than has been measured for K-band LFs determined using 2MASS photometry [3,6,1]. This is to be expected since UKIDSS LAS probes to lower surface-brightness limits than the comparatively shallow 2MASS observations, and there is a correlation between luminosity and surface-brightness.

The UKIDSS EDR sample is too small to subdivide by galaxy type, surface-brightness or redshift. This situation will change with the First Data Release (DR1) of UKIDSS in July 2006, which will contain about ten times as much data as EDR. While still not providing quite as many matches with SDSS as 2MASS, UKIDSS DR1 will enable one to probe evolution in the K-band LF over the redshift range $0 \lesssim z \lesssim 0.5$ for the first time.

Acknowledgements

My attendance at this meeting was made possible by financial support from PPARC.

References

1. Bell, E.F., McIntosh, D.H., Katz, N., Weinberg, M.D., 2003, ApJ, 585, 117
2. Blanton M.R., Roweis S., 2006, submitted to AJ, (astro-ph/0606170)
3. Cole S., et al., 2001, MNRAS, 326, 255
4. Dye S., et al., 2006, submitted to MNRAS (astro-ph/0603608)
5. Efstathiou, G., Ellis, R.S. & Peterson, B.A., 1988, MNRAS, 232, 431
6. Kochanek C.S. et al., 2001, ApJ, 560, 566
7. Lawrence A. et al., 2006, submitted to MNRAS (astro-ph/0604426)
8. Sandage, A., Tammann, G.A. & Yahil, A., 1979, ApJ, 232, 352
9. Skrutskie M.F., et al., 2006, AJ, 131, 1163
10. Strauss M.A. et al., 2002, AJ, 124, 1810
11. http://surveys.roe.ac.uk/wsa
12. http://www.sdss.org/dr5

DETECTION OF THE ISW EFFECT AND CORRESPONDING DARK ENERGY CONSTRAINTS

J. D. MCEWEN[1], P. VIELVA[2], M. P. HOBSON[1], E. MARTÍNEZ-GONZÁLEZ[2], A. N. LASENBY[1]
[1] *Astrophysics Group, Cavendish Laboratory, Cambridge, UK*
[2] *Instituto de Física de Cantabria, CSIC-Universidad de Cantabria, Santander, Spain*

Abstract

Using a directional spherical wavelet analysis we detect the integrated Sachs-Wolfe (ISW) effect, indicated by a positive correlation between the Wilkinson Microwave Anisotropy Probe (WMAP) and NRAO VLA Sky Survey (NVSS) data, at the 3.9σ level. In a flat universe the detection of the ISW effect provides direct and independent evidence for dark energy. Moreover, we use our detection to constrain the dark energy density Ω_Λ. We obtain estimates for Ω_Λ consistent with other analysis techniques and data sets and rule out a zero cosmological constant at greater than 99% significance.

1 Introduction

Strong observational evidence now exists in support of the Λ cold dark matter (ΛCDM) fiducial model of the universe. Much of this evidence comes from recent measurements of the cosmic microwave background (CMB) anisotropies, in particular the Wilkinson Microwave Anisotropy Probe (WMAP) data[2]. At this point, the confirmation of the fiducial ΛCDM model and the existence of dark energy by independent physical methods is of particular interest. One such approach is through the detection of the integrated Sachs-Wolfe (ISW) effect[9].

It is not feasible to separate directly the contribution of the ISW effect from the CMB anisotropies. Instead, as first proposed by Crittenden & Turok[7], the ISW effect may be detected by cross-correlating the CMB anisotropies with tracers of the local matter distribution (for redshift in the range $0 \leq z \leq 2$). A cross-correlation indicative of the ISW effect was detected first by Boughn & Crittenden[3] and since by many other authors. In these proceedings we give a very brief overview of our recent work[6] using directional spherical wavelets to detect the ISW effect and contrain dark energy parameters.

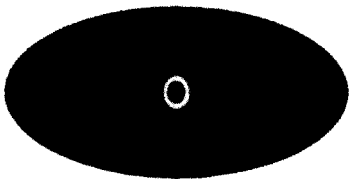

(a) SMHW

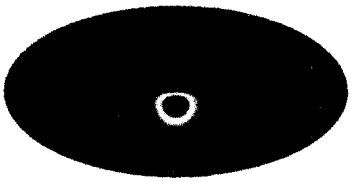

(b) SBW

Figure 1: Spherical wavelets at scale $a = b = 0.2$.

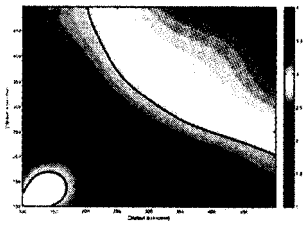

(a) SMHW

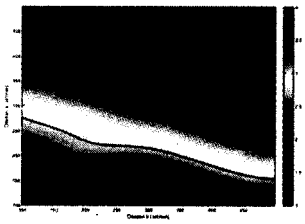

(b) SBW

Figure 2: Wavelet covariance N_σ surfaces with two and three N_σ contours shown.

2 Analysis procedure

2.1 Continuous spherical wavelet transform

Wavelets are an ideal tool to search for the ISW effect[11,6] due to the scale and spatial localisation provided by a wavelet analysis. To perform an analysis of full-sky CMB maps, Euclidean wavelets must be extended to spherical geometry. We apply our fast CSWT algorithm[7,8], which is based on the spherical wavelet transform developed by Antoine, Vandergheynst and colleagues [1,13] and the fast spherical convolution developed by Wandelt & Górski[12]. We consider two spherical wavelets in our subsequent analysis: the spherical Mexican hat wavelet (SMHW) and the spherical butterfly wavelet (SBW). These spherical wavelets are illustrated in Fig. 1.

2.2 Wavelet covariance estimator

The covariance of the wavelet coefficients is used as an estimator to detect any cross-correlation between the CMB and the local matter distribution. The wavelet coefficient covariance estimator is denoted $\hat{X}_\psi^{\rm NT}(a,b)$, where (a,b) define the size of the anisotropic dilation (note that perfect reconstruction is not possible in the case of anisotropic dilations[7]). For a given cosmological model, the theoretical wavelet covariance is given by[6]

$$X_\psi^{\rm NT}(a,b,\gamma) = \sum_{\ell=0}^{\infty} {p_\ell}^2 \, b_\ell^{\rm N} \, b_\ell^{\rm T} \, C_\ell^{\rm NT} \sum_{m=-\ell}^{\ell} |(\psi_{a,b})_{\ell m}|^2 \ , \qquad (1)$$

where $\psi_{\ell m}$ are the spherical harmonic coefficients of the wavelet, $C_\ell^{\rm NT}$ is the cross-power spectrum for the model considered and b_ℓ and p_ℓ are beam and pixel window functions respectively.

2.3 Data and simulations

The detection of the ISW effect is cosmic variance limited, hence we require (near) full sky maps in our analysis. We consider the WMAP co-added map and the NVSS radio source catalogue[4]. The near full-sky coverage and source distribution of the NVSS data make it a suitable probe of the local matter distribution to use. To quantify the significance of any correlations between the data we simulate 1000 Gaussian co-added maps, constructed by mimicking the WMAP observing strategy and co-added map construction technique.

2.4 Procedure

The analysis consists of computing the wavelet covariance estimator described in section 2.2 for a range of scales and orientations. We consider only those scales where the ISW signal is expected to be significant, ranging over dilation scales from $100'$–$500'$, in steps of $50'$, and consider five evenly spaced orientations in the domain $[0, \pi)$. Any deviation from zero in the wavelet covariance estimator for any particular scale or orientation is an indication of a correlation between the WMAP and NVSS data and hence a possible detection of the ISW effect. An identical analysis is performed using the simulated co-added CMB maps in order to construct significance measures for any detections made. Finally, we use any detections of the ISW effect to constrain dark energy parameters.

3 Results and discussion

3.1 Detection of the ISW effect

A positive wavelet covariance outside of the 99% significance level is detected on a number of scales and orientations. On examining the distribution of the wavelet covariance statistics from the simulations, the covariance statistics appear to be approximately Gaussian distributed. This implies that the approximate significance of any detections of a non-zero covariance can be inferred directly from the N_σ level. In Fig. 2 we plot the N_σ surfaces for each wavelet in (a, b) space. The maximum detection made for each wavelet occurs at $N_\sigma = 3.9$ on wavelet scales about $(a, b) = (100', 300')$. The wavelet analysis allows us to localise on the sky those regions that contribute most strongly to the covariance detected. These localised regions are evenly distributed over the entire sky and do not appear to be the sole source of the correlation between the data.[6] In addition, we test whether foregrounds or WMAP systematics are responsible for the correlation but find no evidence to support this.[6] The correlation we detect therefore appears to be consistent with a signal due to the ISW effect.

3.2 Constraints on dark energy

We use our detection of the ISW effect to constrain dark energy parameters by comparing the theoretically predicted wavelet covariance signal for different cosmological models with that measured from the data. In particular, we constrain Ω_Λ over the range $0 < \Omega_\Lambda < 0.95$, assuming a pure cosmological constant (we allow the equation-of-state parameter w to vary in our previous work[6]). For other cosmological parameters we assume concordance model values[11]. The likelihood distributions computed using each wavelet are shown in Fig. 3. Within error bounds the parameter estimates obtained from the mean of the distributions are consistent with each other and with estimates made using other techniques and data sets. We also show in Fig. 3

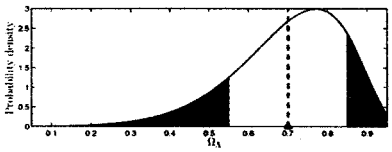

(a) SMHW likelihood distribution for Ω_Λ

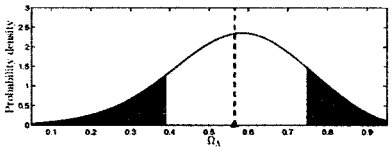

(b) SBW likelihood distribution for Ω_Λ

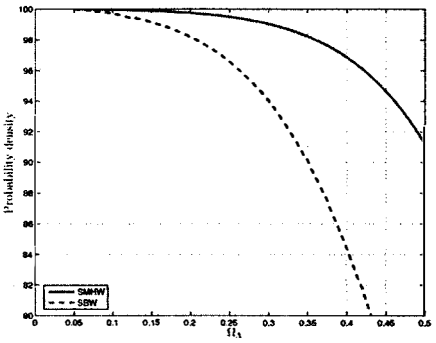

(c) Cumulative probability functions $P(\Omega_\Lambda > x)$

Figure 3: Likelihood distributions and cumulative probability functions for Ω_Λ when $w = -1$. Confidence regions at 68% (yellow), 95% (light-blue) and 99% (dark-blue) are also shown on the likelihood distributions, with the parameter estimates made from the mean of the distribution shown by the triangle and dashed line. The cummulative probability functions show the probability $P(\Omega_\Lambda > x)$ for the SMHW (solid) and SBW (dashed).

the cumulative probability $P(\Omega_\Lambda > x)$. For both wavelets, we have very strong evidence for the existence of dark energy.

4 Conclusions

Using directional spherical wavelets we have made a detection of the ISW effect at the 3.9σ level. In a flat universe the ISW effect exists only in the presence of dark energy, hence our detection may be interpreted as independent evidence for dark energy. We rule out a model with no dark energy ($\Omega_\Lambda = 0$) at $> 99\%$ significance.

Acknowledgements

We thank Jacques Delabrouille and Daniel Mortlock for insightful discussions and comments. See McEwen et al. 2006[6] for additional acknowledgements.

References

1. Antoine J. -P. and Vandergheynst P., 1998, J. of Math. Phys., 39, 8, 3987
2. Bennett C. L. et al. (WMAP team), 2003a, ApJS, 148, 1
3. Boughn S. P., Crittenden R. G., 2002, Phys. Rev. Lett., 88, 21302
4. Condon J. J., 1998, ApJ, 115, 1693
5. Crittenden R. G., Turok N., 1996, Phys. Rev. Lett., 76, 575
6. McEwen J. D., Vielva P., Hobson M. P., Martínez-González E., Lasenby A. N., 2006, submitted to Mon. Not. Roy. Astron. Soc. (astro-ph/0602398)
7. McEwen J. D., Hobson M. P., Mortlock D. J., Lasenby A. N., 2005, submitted to IEEE Trans. Sig. Proc. (astro-ph/0506308)
8. McEwen J. D., Hobson M. P., Lasenby A. N., Mortlock D. J., 2004, XXXIXth Recontres de Moriond

9. Sachs R. K., Wolfe A. M., 1967, ApJ, 147, 73
10. Spergel D. N. et al. (WMAP team), 2003, ApJS, 148, 175
11. Vielva P., Martínez-González E., Tucci M., 2006, Mon. Not. Roy. Astron. Soc., 365, 891
12. Wandelt B. D., Górski K. M., 2001, Phys. Rev. D., 63, 123002, 1
13. Wiaux Y., Jacques L., Vandergheynst P., 2005, ApJ, 632, 15

JOINT MULTI-COMPONENT ANALYSIS OF ARCHEOPS AND WMAP OBSERVATIONS OF THE CMB ANISOTROPIES

G. Patanchon

Physics & Astronomy, Hennings Building, 6224 Agricultural Road
Vancouver B.C. V6T 1Z1, Canada

We present a joint multi-component analysis of Archeops and WMAP first year observations of Cosmic Microwave Background (CMB) anisotropies. The comparison of the two data sets allows us to verify, on Archeops sky coverage (20% of the total sky), the compatibility between the two experiments observing the sky in a large range of wavelengths between 22 and 90 GHz for WMAP and at 143 and 217 GHz (also 353 and 545 GHz) for Archeops. We find that CMB anisotropies detected by both experiments are fully compatible except for an amplitude parameter attributed to absolute calibration discrepancies. The multi-component analysis allows us to detect weak residual systematics in Archeops maps attributed to residual galactic and atmospheric emissions.

1 Introduction

The CMB is one of the most powerful probe in Cosmology. The shape of the spatial power spectrum depends on cosmological parameters describing in the frame of the standard model, the matter content, the geometry, and the evolution of the Universe. Since the first detection of CMB anisotropies by COBE satellite in 1992, numerous ground–based and balloon–borne experiments aimed at measuring the CMB power spectrum and improved constraints on cosmological parameters. The Archeops[a] balloon–borne experiment allowed to measure for the first time with a good accuracy, by observing a large fraction of the sky (30%), the CMB anistropies at intermediate angular scales (1-5o). Recently WMAP satellite, after three years of data acquisition, provided measurement of CMB power spectrum with unprecedented accuracy in a wide range of multipole scales [6].

Archeops and WMAP probe similar angular scales at different wavelengths, with different foregrounds and different systematic effects. Although the noise level in WMAP observations is lower, Archeops is sensitive enough to constrain very significantly the 143 and 217 GHz CMB anisotropy emission. In the following, we performed a quantitative comparison and a joint analysis of Archeops and WMAP observations on the Archeops coverage. The main objectives of this analysis are to check the compatibility of the two experiments, to confirm the cosmological nature of WMAP and Archeops detections and to investigate the residual foreground contamination and systematics in both experiments.

[a] http://www.archeops.org

2 Data

The Archeops experiment was launched on February 7, 2002 from the balloon base in Esrange, near Kiruna (Sweden). 11.7 hours of useful data were taken during the arctic night, in four different frequency bands: 143, 217, 353 and 545 GHz, covering about 30 percent of the total sky with 12 arc-min angular resolution for the best channels [1]. Time ordered data of detectors at 143 GHz and 217 GHz used for the present analysis have been cleaned from atmospheric and galactic dust emissions using data at higher frequencies (353 and 545 GHz). A high-pass filter at 0.1 Hz is also applied to the data before the map-making, in order to remove large scale noise drifts. See [5] for details on the processing.

The WMAP space probe, launched by NASA in 2001, is a large telescope for imaging the total emission of the sky at 5 different frequency channels: 23, 33, 41, 61, and 94 GHz (Ka, K, Q, V, W bands), with a resolution ranging from about 0.2 to 0.9 degrees (limited by diffraction), and with full sky coverage [6]. Foreground cleaned versions of the Q, V and W-band maps using external galaxy templates have been used in the generation of the WMAP three-year CMB power spectrum by the WMAP team, and are available to the community (http://lambda.gsfc.nasa.gov/).

We have performed some processing of WMAP foreground cleaned maps in order to match Archeops map transfer function. We extract mono-dimensional data from maps reproducing Archeops scanning strategy, then we low-pass filter the data as done for Archeops and reproject them. We also partially correct spherical harmonic coefficients to match Archeops 143 GHz resolution (assuming a spherical beam). We mask the pixels which are not common to all the observed maps, as well as regions in the galactic plane and strong point sources. The procedure applied to the maps and the processing pipeline have been validated by numerous Monte Carlo simulations.

3 Model & method

CMB anisotropies are the dominant emission from the sky in both Archeops and WMAP "cleaned" observations. Nevertheless, some residual foreground emissions and systematics could be present at a low level. We model the observed maps by a noisy linear mixture of unknown components including CMB. This simple model writes for the observed map from detector d:

$$x_i(\theta,\phi) = \sum_{c=1}^{N_c} A_{ic} s_c(\theta,\phi) + n_i(\theta,\phi), \tag{1}$$

s_c the spatial distribution of component c, n_i is the noise map for that observation i, and A_{ic} is the element of the "mixing matrix" A which represents the amplitude of component c in map i. Note that this amplitude depends on the component's emission law, as well as on the calibration coefficient assumed for observation i.

The covariance matrix of the maps is defined for multipole ℓ as: $R(\ell) = \langle\, x(\ell,m)\, x(\ell,m)^\dagger \,\rangle$, where $x(\ell,m)$ are the coefficients of the field on the basis of real spherical harmonics. From 1, and assuming independence between each component and noise, we obtain:

$$R(\ell) = AC(\ell)A^t + N(\ell). \tag{2}$$

where $C(\ell)$ and $N(\ell)$ are the component and noise power spectra respectively.

Our analysis of Archeops and WMAP observations is based on the adjustment of the model of the cross- and auto- power spectra of the observed maps to their measured counterparts $\widehat{R}(q)$ averaged over multipole bins q. In practice, we minimize a measure of the mismatch between $R(q)$ (just replace ℓ by q in 2) and $\widehat{R}(q)$ with respect to the parameters of our model which are:

the mixing matrix A, the bin-averaged component power spectra $C(q)$ and noise power spectra $N(q)$ (note that part of the parameters only can be estimated). The criterion we minimize is derived from the maximum likelihood of the data under a Gaussian stationary model of components and noise, and writes:

$$\Phi(\theta) = \sum_{q=1}^{Q} n_q D\left(\widehat{R}(q), R(q,\theta)\right), \tag{3}$$

where $D(R_1, R_2) = \frac{1}{2}\left[\mathrm{tr}\left(R_1 R_2^{-1}\right) - \mathrm{logdet}(R_1 R_2^{-1}) - N_d\right]$ is the Kullback divergence between matrices R_1 and R_2. Description of the method can be found in [2].

The estimated component power spectra are corrected from partial sky coverage effects, beam transfer function, and filtering of the time ordered data (estimated by Monte Carlo simulations, see [7] for details on the procedure), following the MASTER approach described in [4]. Errors on parameter estimation are computed analytically using Fisher formalism. For validation, analytical errors are compared to the dispersion obtained from Monte Carlo simulations. The number of significant components in data, which is *a priori* unknown is inferred by measuring the goodness of fit of parameters for various number of components in the model.

4 Results from joint analysis

In the following, we present the results from the blind analysis of Archeops and WMAP observed maps. Series of likelihood tests varying in each step the number of estimated components show that three components are significant in data. The likelihood is very satisfactory when three components or more are estimated. Figure 1 shows the estimated amplitude of each component in each Archeops and WMAP channel (estimated elements of the mixing matrix A) for a three components model. The main component, which is very dominant in all channels, is interpreted as CMB anisotropies. It shows constant (CMB) temperature in WMAP channels as expected in the frame of standard model, but is significantly under the predicted CMB emission spectrum in all Archeops maps (by 6-8%). This is interpreted as due to errors of the Archeops absolute calibration on the dipole. The two other detected components are significant in Archeops maps only, since their amplitude is compatible with 0 in WMAP channels. They are residual systematics in Archeops.

Despite the presence of residual components in Archeops maps, this analysis demonstrates that CMB anisotropies are the only source of correlation between Archeops and WMAP and that they are described by a single component template across frequencies. Therefore, Archeops and WMAP provide compatible measurements of CMB anisotropies, except for an amplitude coefficient. The estimated power spectrum of CMB anisotropies from the joint analysis is shown in Figure 1 (right). We verify that the measured spectrum is fully compatible with the best fit cosmological model computed by WMAP team. In addition to this test, we have verified that the cross power spectrum between Archeops and WMAP is compatible with the best fit power spectrum model.

The first residual component is detected in all Archeops channels with a relatively constant amplitude across channels, independently of the observation frequency. This residual component is a mixture of residual galactic dust emission (seen in the estimated map as bright emission close to the galactic plane) and of slow systematic drifts in the Archeops time ordered data (as indicated in the map by elongated structures forming stripes in the Archeops scanning direction), probably due essentially to atmospheric emission. The component is a "common mode" residual, seen by all detectors. The second residual component, already reported in [7], is detected only in the 217 GHz channels, and is probably due to residual atmospheric emission.

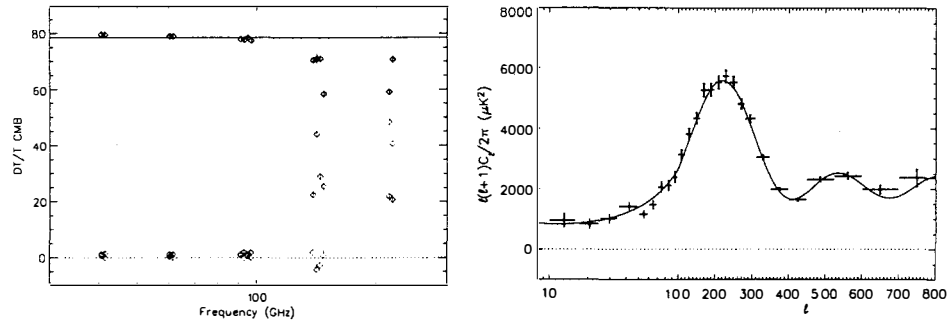

Figure 1: Left: elements of the estimated mixing matrix A_{tc}, giving the amplitude in CMB temperature units of each component (normalized in rms) in each observed map, from the blind analysis assuming three components. Error bars are statistical and do not include calibration uncertainty. The first component (in black) is CMB anisotropies. The straight line corresponds to an average of CMB amplitude in WMAP maps. The two other components (in blue and red) are residual systematics in Archeops. Right: estimated CMB power spectrum from the joint multi-component of Archeops and WMAP (after correction from unresolved point source emissions) compared to the prediction of the best fit model of WMAP data.

5 Conclusion

We have performed a joint analysis between Archeops and WMAP observations of the CMB anisotropies in order to check the compatibility between the two data sets and detect residual systematics. We used a multi-component method allowing to estimate blindly the power spectra of independent components in the maps as well as their amplitude across frequency channels. We showed that CMB anisotropies detected in both experiments are compatible since they are the only source of correlation between Archeops and WMAP and they can be described by a single component template across Archeops and WMAP frequency channels. The power spectrum of this "common" component is compatible with the best fit WMAP cosmological model. However, we identified a discrepancy in the amplitude of the CMB anisotropies between both experiments (lower by 6-8% in Archeops with respect to WMAP) attributed to an error in Archeops absolute calibration on dipole. We also identified two weak additional component in Archeops maps resulting from residual atmospheric and galactic emission.

Acknowledgments

The author thanks the Archeops collaboration. This work was supported by the Canadian Space Agency. The author acknowledge the use of the Legacy Archive for Microwave Background Data Analysis (LAMBDA), and the use of the software package CMBFAST (http://www.cmbfast.org). Some results of this paper have been derived using the HEALPix[3] package.

References

1. Benoît, A., Ade, P., Amblard, A. et al., *A&A*, 399, L19, 2003.
2. J. Delabrouille, J.F. Cardoso, J. Delabrouille, *MNRAS*, 346, 1089, 2003.
3. Gorski K. M., Hivon E. & Wandelt B. D., 1998, `astro-ph/9812350`.
4. Hivon E., Gorski K. M., Netterfield C. B. et al., *ApJ*, 567, 2, 2002
5. J.F. Macías-Pérez et al., accepted for publication in *A&A*, 2006, `astro-ph/0603665`.
6. D.N. Spergel et.al., submitted to *ApJ*, 2006.
7. M. Tristram et al., *A&A*, 436, 785, 2005

Weak Lensing Mass Reconstruction of the Galaxy Cluster Abell 209

S. Paulin-Henriksson, V. Antonuccio-Delogu
INAF / Osservatorio Astrofisico di Catania, Via Santa Sofia 78, I-95123 Catania, Italy

We describe step by step the typical weak gravitational lensing analysis of the galaxy cluster Abell 209 ($z \sim 0.2$), using a heavily modified version of the KSB algorithm applied to an archival R-band image of this cluster taken with the CFHT-12k. A parametric modelling with NFW profile gives a total mass within R_{200} of about $2 \times 10^{15}\ M_{\odot}$, slightly larger than the value derived by Mercurio et al.[10] using radial velocities.

1 Introduction

The galaxy cluster Abell 209 ($z = 0.209$) is a particularly interesting target for a weak lensing mass reconstruction, because it is probably not completely virialised[4,10,3], is well covered by observations and the evolutionary properties of its galaxy populations have already been meticulously analysed[4,10].

This contribution describes the analysis perfomed on a deep R-band image, based on the KSB+ weak lensing analysing method[7,8,6], throught a pipeline implemented at the Catania Astrophysical Observatory (Italy) and tested on STEP simulated images [5,9]. This work is a preliminary step towards a more complete forthcoming analysis in R and B bands.

2 Data description

We use archival CFHT-12k images in R band, reduced and stacked by Haines, Mercurio et al.[4,10] in the framework of their photo-spectrometric analysis. These data were kindly provided by the Capodimonte observatory (Italy). Data are complete for $R \lesssim 25$.

As this analysis is perfomed directly on stacked images, the overlaps between CCD may contain some PSF (Point Spread Function) instabilities. For this reason we mask these overlapped regions. Unfortunately, the cluster center lies exactly within such a CCD overlap. We extend the data with a HST/WFPC2 field of about 1 arcmin in the broad red filter F702W, centered on the cluster center.

3 The weak lensing analysis

3.1 Step 1 - building star and background galaxy catalogues

The weak lensing signal is carried by background galaxies, lensed by the foreground cluster. On the other hand, stars carry the information about the PSF. The first step of the analysis is to build star and background galaxy catalogues.

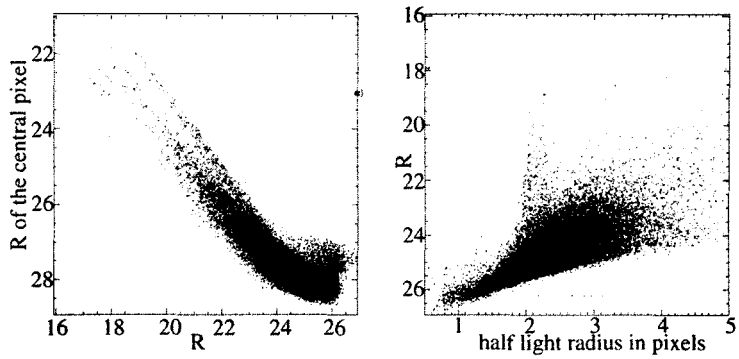

Figure 1: Left panel: magnitude - central magnitude diagram for all objects detected in the R-band image. Right panel: radius - magnitude diagram for the same objects. In both panels, stars are in red. Cluster (background respectively) galaxies are in light (dark resp.) blue. Other objects (black and dark purple) are excluded from the analysis.

The star identification is made in the 3 parameter space r_h, R, $R_{\max}$. r_h is the half-light-radius (eg. the radius inside which one have 50% of the total flux of the object), R is the magnitude in the R band, and $R_{\max}$ is the magnitude of the central pixel (eg. the pixel containing the centroid estimated by SExtractor[2]). Figure 1 shows the star sequence in red. It is important to note that all these 3 parameters are necerssary for the star selection. Typically 10% of the objects that would be selected as stars by 2 of the 3 parameters, are finally rejected by the third parameter. Finally we get an average star density of $\sim 0.22.\mathrm{arcmin}^{-2}$ (eg. ~ 22 stars per CCD).

The foreground / background galaxy selection is a straightforward cut on R. The values for this cut are choosen to give an almost uniform background galaxy density (while the foreground galaxy density is highly peaked around the cluster center), and will be optimised in future. After the mask, the averaged background galaxy density all over the field is $\sim 15.\mathrm{arcmin}^{-2}$. This number will be optimised when we will include the B image in the analysis.

3.2 Step 2 - PSF interpolation

The PSF is interpolated from stars, independently for each CCD, using a 2-degree-2-dimentional polynomial for each of 6 components of the PSF properties, as required by the KSB method. This is illustrated with the ellipticity on figure 2. The fact that, after the smearing and anisotropy corrections, the PSF shows such small and smooth variations all around the field, even from a CCD to another, is not at all assumed at any step of the analysis. It is a sign of the very good data quality.

3.3 Step 3 - Tests of the PSF subtraction

To test the PSF subtraction, we perform three statistical tests:

1. We study the correlations between corrected galaxy ellipticities and uncorrected star ellipticities, as shown on figure 3 (a, b, c, d): As expected, the significant correlation due to the PSF before any correction is not significant anymore after the PSF subtraction.

2. We study the correlations between the intensity of the shear $|\gamma|$ and object size for different magnitude bins, as shown on figure 3 (e). As expected for most of the rg bins, the error bars do not overlap and one clearly see that the weak lensing signal increases with the

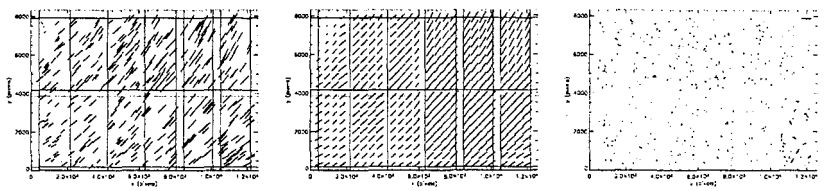

Figure 2: Star ellipticities over the field (for a window radius of 2 pixels, see the KSB analysing method details). Left panel: before corrections (i.e. observed ellipticities). Middle panel: PSF interpolated from the left panel. Right panel: residuals of the fit. In all panels, vectors lie along the major axis, while their length is proportional to the ellipticity: $|\epsilon| = \frac{\sqrt{(Q_{11}-Q_{22})^2+4Q_{12}^2}}{Q_{11}+Q_{22}}$. The scale shown in the upper right corners is $|\epsilon| = 0.05$. The straight lines show the CCD overlaps, which are not taken into account in the interpolation process.

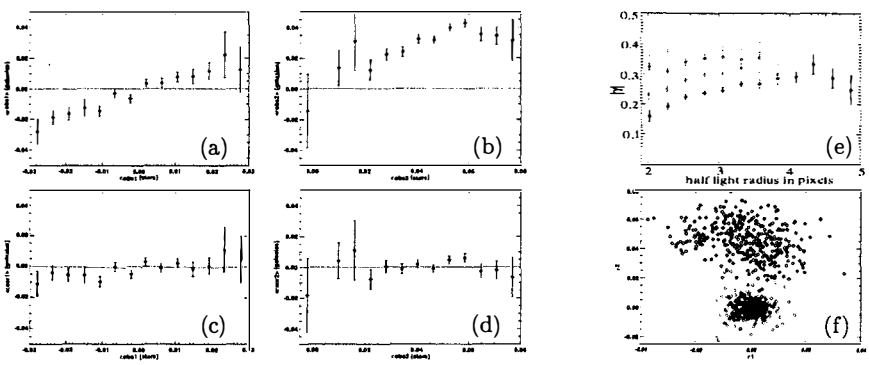

Figure 3: Panels a and c (b and d respectively): $< \epsilon_1 >_{\rm bin}$ ($< \epsilon_2 >_{\rm bin}$ resp.) of galaxies with respect to ϵ_1 (ϵ_2 resp.) of the nearest star. Panels a and b (c and d respectively) show the significant (unsignificant resp.) correlation before (after resp.) the anisotropic correction. Panel e: Average value $< |\gamma| >_{\rm bin} = < \sqrt{\gamma_1^2+\gamma_2^2} >_{\rm bin}$ of galaxies as a function of $r_{1/2\,\Phi}$, for 4 different magnitude bins. In black: $17.5 \lesssim R \lesssim 20.0$ (i.e. the 25% brightest galaxies), in red: $20.0 \lesssim R \lesssim 20.8$, in dark blue: $20.8 \lesssim R \lesssim 21.4$, and in light blue: $21.4 \lesssim R \lesssim 25.8$ (i.e. the 25% faintest galaxies). Panel f: ϵ_1 against ϵ_2 of stars before (black) and after (red) the anisotropic correction.

magnitude, ultimately with the optical depth. Note that the error bars do include the errors on the measured ellipticity.

3. We compare star corrected and uncorrected ellipticities, as shown on figure 3 (f). As expected after the subtraction, the distribution is centered around 0, with a very lower standard deviation.

3.4 Step 4 - Mass reconstruction

Fitting a NFW profile

We have used parametric mass reconstruction to get a preliminary estimate of the mass within a given aperture. We fit a NFW (Navarro-Frenk-White)[11] to the tangential shear data[14]. The maximum likelihood values for the two NFW free parameters are: $r_{200} = 2.0\,h^{-1}\,$Mpc and $M_{200} = 1.9 \times 10^{15}\,M_\odot$. r_{200} is the radius inside which the average density is equal to 200 times the cosmological critical density, and M_{200} is the mass inside r_{200}.

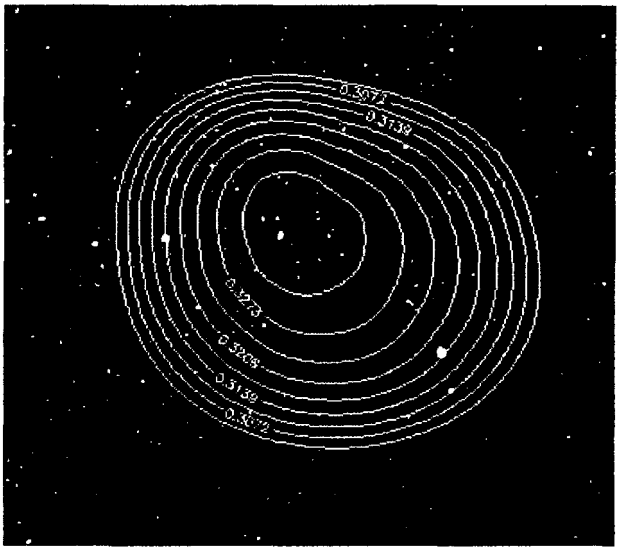

Figure 4: Mass reconstructed profile. The box is about $10' \times 10'$ wide (1 pixel = $0.206''$), which, at the redshift of A209 ($z = 0.209$) corresponds to about 2.5 h^{-1} Mpc. Contours are logarithmically spaced and the central contour corresponds to a surface mass density of $0.25 \times 10^5\ M_{\odot}.\mathrm{arcmin}^{-2}$

Direct mass reconstruction

We have used the method described in Seitz & Schneider[13], based on the solution of a Poisson equation for the quantity $K = \ln(1-\kappa)$, where: $\kappa = \sigma/\Sigma_{crit}$ is the projected surface density in units of the critical density[1]. The resulting profile is shown in figure 4. The elongation of the isodensity contour hints at the presence of two clumps of galaxies which have recently merged, as suggested by previous analysis[10].

Acknowledgments

This work is supported by the European Commission, VI Framework Program for Reserach and Development, *Marie Curie* Project MTKD-CT-2004-002995 "COSMOCT" .

References

1. Bartelmann M., King, L.J. and Schneider P., 2001, A&A, 378, 361
2. Bertin E. and Arnouts S., 1995, A&A, 117, 393
3. Giovannini G. Feretti L., Govoni F. et al., astro-ph/0601285
4. Haines C.P., Mercurio A., Merluzzi P. et al., 2004, A&A, 425, 783
5. Heymans C., Van Waerbeke L., Bacon D. et al., 2006, MNRAS, 368, 1323
6. Hoekstra H., Franx M., Kuijken K. et al., 1998, ApJ, 504, 636
7. Kaiser N., Squires G. and Broadhurst T., 1995, ApJ, 449, 460
8. Luppino G.A. and Kaiser N., 1997, ApJ, 475, 20
9. Massey R., Heymans C., Bergé J. et al., 2006, under development
10. Mercurio A., Busarello, G., Merluzzi, P. et al., 2004, A&A, 424, 79
11. Navarro J.F., Frenk C.S, and White S.D.M., 1997, ApJ, 490, 493
12. Paulin-Henriksson S. , Antonuccio-Delogu V. et al., under development
13. Seitz S. and Schneider, P., 2001, A&A, 374, 740
14. Wright C.O. and Brainerd T.G., 2000, ApJ, 534, 34

DETECTING SHOCK WAVES IN COSMOLOGICAL SMOOTHED PARTICLE HYDRODYNAMICS SIMULATIONS

C. PFROMMER[1,2], V. SPRINGEL[2], T.A. ENSSLIN[2], M. JUBELGAS[2]
1) Canadian Institute for Theoretical Astrophysics
2) Max-Planck Institut für Astrophysik

Shock waves during cosmological structure formation not only play a decisive role for the thermalization of gas in virializing structures but also for the acceleration of relativistic cosmic rays through diffusive shock acceleration. We present a novel formalism of identifying and measuring the shock strength on the fly in smoothed particle hydrodynamics simulations. Our formalism is applicable both to non-relativistic thermal gas, and to plasmas composed of cosmic rays and thermal gas. We apply our methods to study the properties of structure formation shocks in high-resolution hydrodynamic simulations of the Lambda cold dark matter model. We find that most of the energy is dissipated in weak shocks internal to galaxy clusters with low Mach numbers. Collapsed cosmological structures are surrounded by external shocks with higher Mach numbers up to 1000, but they play only a minor role in the energy balance of thermalization. This finding has important consequences for our understanding of the spatial distribution of relativistic particles in the cosmic large-scale structure, since it suggests that the ratio of the energy density of the cosmic ray proton population to the thermal gas within galaxy clusters increases with the cluster radius. Such an increase is required to explain the huge extended radio synchrotron halos of galaxy clusters by the injection of relativistic electrons through hadronic interactions of the cosmic ray protons with the ambient gas.

1 Motivation

Cosmological shock waves form abundantly in the course of structure formation, both due to infalling cosmic plasma which accretes onto filaments, sheets and halos, as well as due to supersonic flows associated with merging substructures. Additionally, shock waves in the interstellar and intracluster media can be powered by non-gravitational energy sources, e.g. as a result of supernova explosions.

Cosmologically, shocks are important in several respects and connected to the following interesting questions. (1) Shock waves dissipate gravitational energy associated with hierarchical clustering into thermal energy of the gas contained in dark matter halos, thus supplying the intra-halo medium with entropy and thermal pressure support: where and when is the gas heated to its present temperatures, and which shocks are mainly responsible for it? (2) Shocks also occur around moderately overdense filaments, heating the intragalactic medium. Sheets and filaments are predicted to host a warm-hot intergalactic medium with temperatures in the range $10^5\,\mathrm{K} < T < 10^7\,\mathrm{K}$ whose evolution is primarily driven by shock heating from gravitational perturbations developing into mildly nonlinear, non-equilibrium structures. Thus, the shock-dissipated energy traces the large scale structure and contains information about its dynamical history. (3) Besides thermalization, collisionless shocks are also able to accelerate ions through diffusive shock acceleration. These energetic ions are reflected at magnetic irregularities through

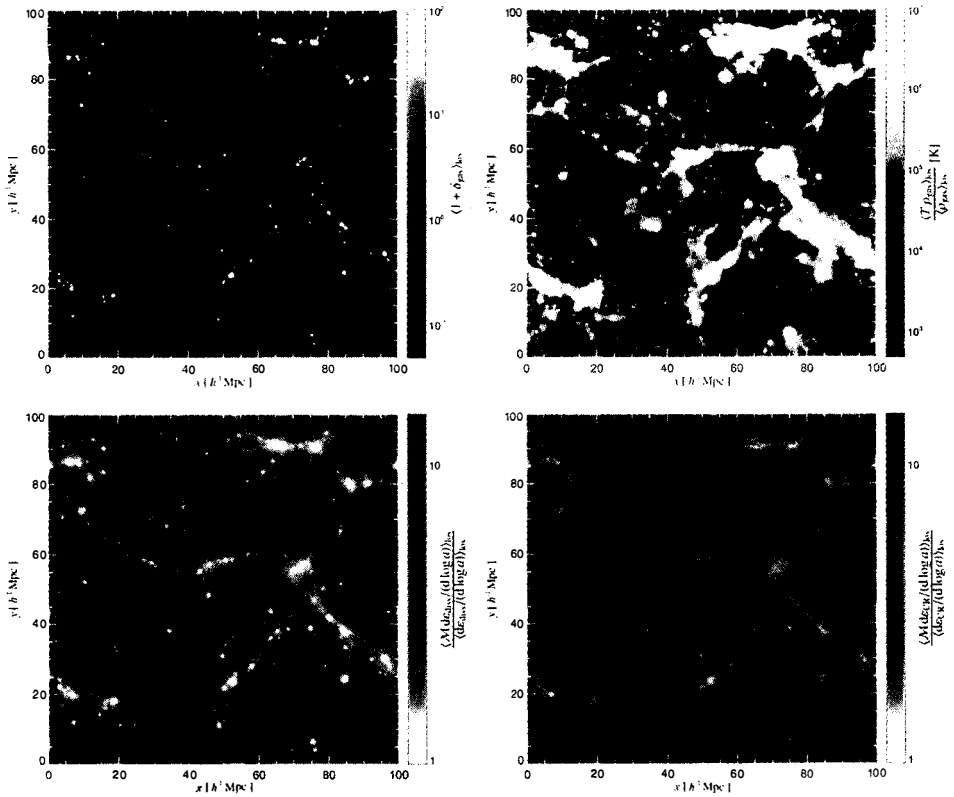

Figure 1: Visualization of a non-radiative cosmological simulation at redshift $z = 0$ where the cosmic ray (CR) energy injection was only computed while the effect of the CR pressure on the dynamical evolution was not taken into account. The **top panels** show the overdensity of the gas and the mass weighted temperature of the simulation. The **bottom panels** show a visualization of the strength of structure formation shocks. The color hue of the map on the left-hand side encodes the spatial Mach number distribution weighted by the rate of energy dissipation at the shocks. The map on the right-hand side shows the Mach number distribution weighted by the rate of CR energy injection above the momentum threshold of hadronic CRp-p interactions. The brightness of each pixel is determined by the respective weights, i.e. by the energy production density. Most of the energy is dissipated in weak shocks which are situated in the internal regions of groups or clusters, while collapsed cosmological structures are surrounded by strong external shocks (shown in blue). Since strong shocks are more efficient in accelerating CRs, the CR injection rate is more extended than the dissipation rate of thermal energy.

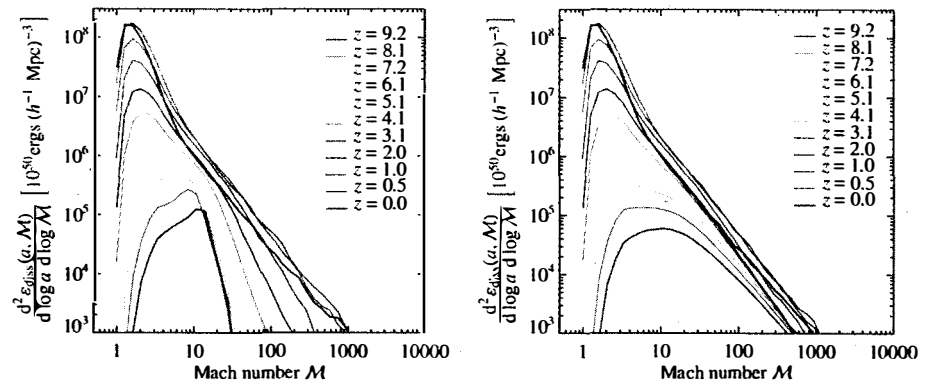

Figure 2: Influence of reionisation (at redshift $z = 10$) on the Mach number statistics of non-radiative cosmological simulations. The figure on the **left-hand side** shows the differential Mach number distribution $d^2\epsilon_{diss}(a,\mathcal{M})/(d\log a\, d\log\mathcal{M})$ for our simulation with reionisation while the figure on the **right-hand side** shows this distribution for the simulation without reionisation. Strong shocks are effectively suppressed due to an increase of the sound velocity after reionisation.

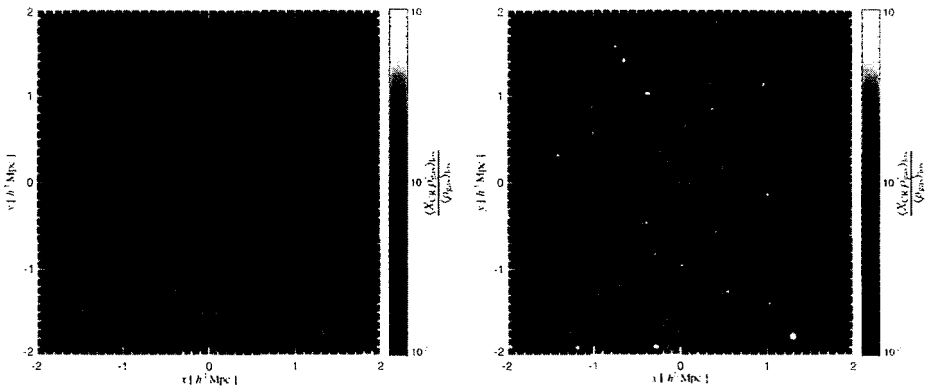

Figure 3: Visualization of the pressure contained in CRs relative to the total pressure $X_{CR} = P_{CR}/(P_{CR} + P_{th})$ in a zoomed simulation of an individual galaxy cluster with mass $M = 10^{14}h^{-1}M_{\odot}$. The map on the **left-hand side** shows a non-radiative simulation with CRs accelerated at structure formation shock waves while the map on the **right-hand side** is from a simulation with dissipative gas physics including cooling, star formation, supernova feedback, and structure formation CRs. The relative CR pressure X_{CR} declines towards a low central value of $X_{CR} \simeq 10^{-4}$ in the non-radiative simulation due to a combination of the following effects: CR acceleration is more efficient at the peripheral strong accretion shocks compared to weak central flow shocks, adiabatic compression of a composite of CRs and thermal gas disfavors the CR pressure relative to the thermal pressure due to the softer equation of state of CRs, and CR loss processes are more important at the dense centers. Interestingly, X_{CR} reaches high values at the center of the parent halo and each galactic substructure in our radiative simulation due to the fast cooling gas which transforms into stars in the densest regions while diminishing thermal pressure support relative to that in CRs. This additional CR pressure support has important consequences for the thermal gas distribution at cluster centers and alters the resulting Sunyaev-Zel'dovich effect significantly.

magnetic resonances between the gyro-motion and waves in the magnetized plasma and are able to gain energy in moving back and forth through the shock front: what are the cosmological implications of such a CR component, and does this influence the cosmic thermal history? (4) Simulating realistic CR distributions within galaxy clusters will provide detailed predictions for the expected radio synchrotron and γ-ray emission. What are the observational signatures of this radiation that is predicted to be observed with the upcoming new generation of γ-ray instruments and radio telescopes?

2 Structure formation shock waves and cosmic rays

We develop a formalism that is able to measure the shock strength instantaneously during an SPH simulation (Pfrommer et al. 2006). The method is applicable both to non-relativistic gas, and to plasmas composed of CRs and thermal gas. We apply our methods to study the properties of structure formation shocks in high-resolution hydrodynamic simulations of the Lambda cold dark matter (ΛCDM) model using an extended version of the distributed-memory parallel TreeSPH code GADGET-2 (Springel, 2005) which includes self-consistent CR physics (Enßlin et al. (2006), Jubelgas et al. (2006)). Fig. 1 shows the spatial distribution of structure formation shocks in comparison to the density and temperature distribution while Fig. 2 shows the cosmological Mach number distribution at different redshifts.

The main results are as follows. (1) Most of the energy is dissipated in weak shocks internal to collapsed structures while collapsed cosmological structures are surrounded by external shocks with much higher Mach numbers, up to $\mathcal{M} \sim 1000$. Although these external shocks play a major role locally, they contribute only a small fraction to the global energy balance of thermalization. (2) More energy per logarithmic scale factor and volume is dissipated at later times while the mean Mach number decreases with time. This is because of the higher pre-shock gas densities within non-linear structures, and the significant increase of the mean shock speed as the characteristic halo mass grows with cosmic time. (3) A reionisation epoch at $z_{\rm reion} = 10$ suppresses efficiently strong shocks at $z < z_{\rm reion}$ due to the associated increase of the sound speed after reionisation. (4) Strong accretion shocks efficiently inject CRs at the cluster boundary. This implies that the dynamical importance of shock-injected CRs is comparatively large in the low-density, peripheral halo regions, but is less important for the weaker flow shocks occurring in central high-density regions of halos. Zoomed simulations of individual galaxy clusters support this picture (cf. Fig. 3).

3 Conclusions

We studied the properties of cosmological shock waves using a technique that allows us to identify and measure the shock strength on-the-fly during a smoothed particle hydrodynamics simulation. Invoking a model for CR acceleration in shock waves, we have carried out the first self-consistent hydrodynamical simulations that follows the CR physics self-consistently. The resulting pressure distribution of CRs within galaxy clusters matches the required distribution of CRs to explain the huge extended radio synchrotron halos of galaxy clusters by the injection of relativistic electrons through hadronic interactions of the CR protons with the ambient gas.

References

1. T.A. Enßlin, C. Pfrommer, V. Springel and M. Jubelgas, *astro-ph/***0603484**, (2006).
2. M. Jubelgas, V. Springel, T.A. Enßlin and C. Pfrommer, *astro-ph/***0603485**, (2006).
3. C. Pfrommer, V. Springel, T.A. Enßlin and M. Jubelgas, *MNRAS* **367**, 113 (2006).
4. V. Springel, *MNRAS* **364**, 1105 (2005).

HOT AND COLD SPOTS IN THE WMAP SKY

GRAZIANO ROSSI and RAVI K. SHETH
Department of Physics and Astronomy, University of Pennsylvania, PA 19104, USA

The *Cosmic Microwave Background* is a primary tool for determining the global properties, content, and history of the universe and for placing important constraints on cosmological models. In particular, the Gaussianity of the primordial fluctuations is a basic assumption of modern cosmology. In a Gaussian sky, the shape of the correlation function of peaks, $\xi_{pk-pk}(\theta)$, depends only on the underlying power spectrum [1]. It is predicted to have a wealth of structure, much more than does the correlation function of all pixels, and to depend in a precisely quantified way on peak height. We present accurate measurements of both $\xi_{pk-pk}(\theta)$ and $\xi_{pix-pix}(\theta)$ in the WMAP sky with high signal-to-noise ratio, which provide a stringent test of the assumption that the primordial fluctuations were Gaussian. We also investigate the corresponding marked correlation functions, and the number density of hotspots.

1 Data Pipeline

We use the foreground-cleaned sky maps from the *WMAP* third-year CMB data for the W1 assembly (Legacy Archive for Microwave Background Data Analysis) [2]. Our analysis procedure ignores data inside the Kp0 galactic mask (23.5 % of pixel cut). We lower the resolution of the *HEALPix* map to $N_{side} = 256$, remove monopole and dipole moments outside the applied mask (degraded to the same resolution), and then search for local extrema using HOTSPOT [3]. Finally we assign to each extrema its correct *HEALPix* coordinates and pixel noise according to $\sigma(p) = \sigma_0/\sqrt{N_{obs}(p)}$, where σ_0 is the noise dispersion per map.

2 Number density of peaks

In a 2D Gaussian random field, the total number of peaks of arbitrary height is: [4]

$$n_{pk}(-\infty) = (4\pi\sqrt{3})^{-1}\theta_*^{-2} \,, \qquad (1)$$

where $\theta_* = \sqrt{2}\sigma_1/\sigma_2$. This number can be readily computed, since:

$$\sigma_n^2 = \sum_l \frac{(2l+1)}{4\pi}\Big[C_l + \sigma_N^2 \Delta\Omega\Big] l^{2n} \cdot W_{WMAP} \cdot W_{HEALPix} \ . \tag{2}$$

A theoretical power spectrum is adopted and the pixel area, noise (see Figure 1) and smoothing are consistent with the CMB map at the given resolution. The calculation is in good agreement with the data. For example (W1 channel), at $N_{side} = 256$ the observed hotspot numerical density is $n_{pk,calc}(-\infty) = 6601$ sterad^{-1}, and the predicted one is $n_{pk,th}(-\infty) = 6642$ sterad^{-1}.

Figure 1: Noise per pixel distribution at $N_{side} = 256$ for the 3^{th} year WMAP data (W1 channel, Kp0 mask). The temperature scale is logarithmic, in mK units.

3 Two-point correlation functions: results

The two-point standard or "unweighted" correlation function ξ of a discrete distribution is a measurement of clustering and can be seen as an excess of probability of finding a pair at a distance θ, compared to a random catalogue. It is defined as

$$dP = n[1 + \xi(\theta)]d\Omega \ , \tag{3}$$

where dP is the probability of finding a data point within a solid angle $d\Omega$ at distance θ from another randomly chosen data point. The usual estimator is

$$\xi(\theta) = \frac{DD(\theta)}{RR(\theta)} - 1 \ , \tag{4}$$

where $RR(\theta)$ and $DD(\theta)$ are the number of random and data pairs, respectively. The marked correlation function differs from the previous one because one weights by some "mark" when measuring clustering statistics. So, if the usual estimator for the unweighted correlation function is (4), then the weighted correlation function is $WW(\theta)/RR(\theta)$, where $WW(\theta)$ is the number of weighted pairs, and the marked statistics is simply $WW(\theta)/DD(\theta)$.

We computed the two-point correlation functions and the marked statistics both for peaks (Figure 2) and pixels (Figure 3) in the WMAP sky. Theoretical small-angle predictions for the hotspots correlations have been quantified by Heavens and Sheth (1999), where they looked

at the point-point correlation function of the locations of maxima above a certain threshold. Theoretical formalism for the pixel-pixel correlations is provided in Jensen and Szalay (1986) and Hernández-Monteagudo et al. (2004). We extended their technique to account for a more rigorous pixel-noise treatment (see Figure 1). In particular, for the simplified case when the pixel-pixel noise σ is assumed to be the same, the pixel correlation function is given by:

$$1+\xi_\nu(\theta)=\int_0^\infty d\sigma p(\sigma)\Big[1+H_{-1}^{-2}(\nu/\sqrt{2})\sum_{k=1}^{\infty}\frac{[C(\theta)/(C(0)+\sigma^2)]^{2k}H_{2k-1}^2(\nu/\sqrt{2})}{2^{2k}(2k)!}\Big]\,, \qquad (5)$$

where $C(\theta)=\sum(2l+1)C_lP_l(\cos\theta)\cdot W_{WMAP}\cdot W_{HEALPix}/4\pi$, and W_{WMAP} and $W_{HEALPix}$ are the *WMAP* and *HEALPix* window functions, respectively. For the marked correlation we have instead:

$$M_\nu(\theta)=\frac{\int_{\nu\sigma}^\infty d\delta_1\int_{\nu\sigma}^\infty p(\delta_1,\delta_2)\delta_1\delta_2 d\delta_2}{<\delta>^2\int_{\nu\sigma}^\infty d\delta_1\int_{\nu\sigma}^\infty p(\delta_1,\delta_2)d\delta_2}\,, \qquad (6)$$

where $<\delta>=\int_{\nu\sigma}^\infty d\delta p(\delta)\delta/\int_{\nu\sigma}^\infty d\delta p(\delta)$ and $\delta=T-<T>$.

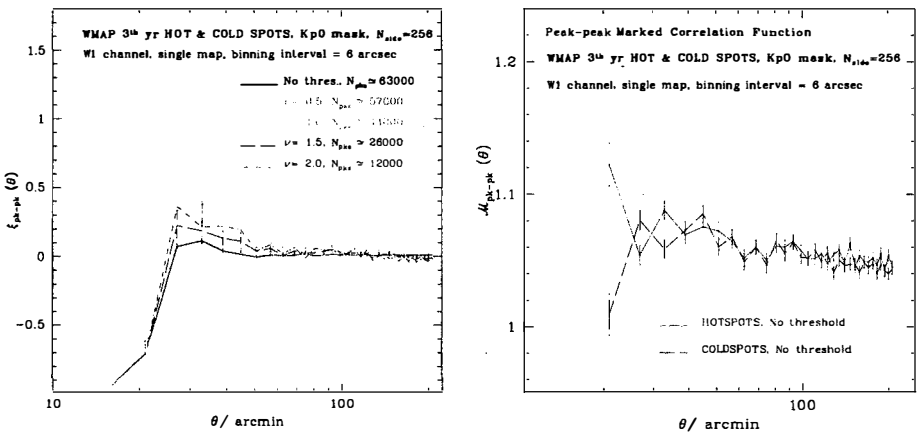

Figure 2: (Left panel) Peak-peak correlation functions of the 3^{th} year WMAP hot and cold spots. Different lines indicate cold spots, errorbars represent hot spots. Various thresholds are also plotted – as indicated in the figure – and the approximate number of hotspots is provided. The Kp0 mask is applied at a resolution of $N_{side}=256$. The results are in agreement with the theoretical small-angle predictions presented in Heavens & Sheth (1999). (Right panel) Marked correlation functions of the 3^{th} year WMAP hot and cold spots.

4 Summary and future work: gravitational lensing of the CMB

We calculated the number density of hotspots from the third year *WMAP* data and show consistency with the theory of 2D Gaussian random fields [4]. We analyzed both the peak-peak and pixel-pixel correlation functions and their marked correlations. which appear to be in agreement with theoretical predictions [1,5,6].

A future goal is to attempt a detection of the effects of gravitational lensing. While effects on lensing on the entire set of WMAP pixels are expected to be negligible, lensing effects on peak-peak correlations are expected to be considerably larger. Gravitational lensing changes the positions of peaks and modifies their shapes slightly. Correlation between peak height and

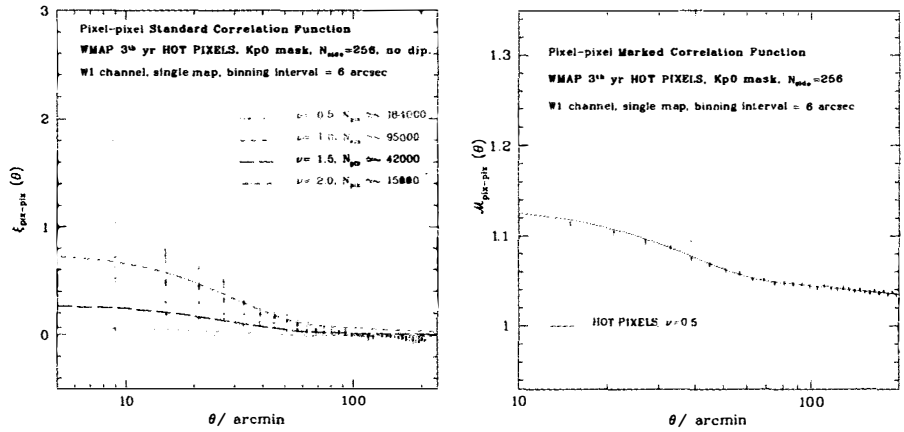

Figure 3: (Left panel) Pixel-pixel correlation functions of the 3^{th} year WMAP hot pixels. Different thresholds are plotted – as indicated in the figure – and the approximate number of hot pixels is provided. Different lines represent the theoretical calculation (5). The Kp0 mask is applied at a resolution of $N_{side} = 256$. (Right panel) Marked correlation function of the WMAP data hot pixels. The solid line is equation (6).

curvature, expected in purely Gaussian random fields, is modified by lensing. Combination of the shape and clustering measurements should allow for a more significant detection of the lensing signal.

Acknowledgments

We acknowledge the use of the *L*egacy *A*rchive for *M*icrowave *B*ackground *D*ata *A*nalysis. Support for *LAMBDA* is provided by the National Aeronautics and Space Administration (NASA) Office of Space Science. Some of the results in this paper have been derived using the *HEALPix* package [3]. We acknowledge support from NASA grant NNG05GK81G.

References

1. Heavens, A. F. and Sheth, R. K., 1999, MNRAS, 310, 1062-1070
2. Hinshaw, G. et al., 2006, astro-ph/060345
3. Górski, K. M. et al., 1999, in Proc. MPA/ESO Conf. "Evolution of Large-Scale Structure: From Recombination to Garching"
4. Bond, J. R. and Efstathiou, G., 1987, MNRAS, 226, 655-68
5. Jensen, L. G. and Szalay, A. S., 1986, ApJ, 305, L5-L9
6. Hernández-Monteagudo et al., 2004, A&A, 413, 833-842

FIRST RESULTS FROM THE SUPER-EXTENDED VERY SMALL ARRAY.

A. Scaife and the VSA Collaboration
Cavendish Astrophysics, Cavendish Laboratory, Madingley Road, Cambridge, CB3 0HE, England.

We present preliminary observations made with the newly upgraded VSA. We explain the details of the upgrade and discuss the current observing program of the telescope. New observations made with the super-extended array at high ℓ will allow precise measurement of the fourth and subsequent peaks and also enable us to investigate the excess power seen at $\ell > 2000$ by the CBI experiment. We present initial S–Z images and predictions for the current observing program.

1 Introduction

The Very Small Array (VSA) is a fourteen element interferometer. It is located at the Teide Observatory in Tenerife. In its current configuration it operates at a frequency of 33 GHz with a bandwidth of 1.5 GHz. Previous configurations of the telescope have been used to measure the CMB power spectrum out to $\ell \sim 1600$. In conjunction with its previous results the new super-extended configuration the VSA will be able to investigate the form of the power spectrum for $\ell \sim 150 - 2500$. At high ℓ the fourth and subsequent peaks can be used to break degeneracies that exist between cosmological parameters. In addition the VSA will be able to examine the excess power seen at $\ell > 2000$ by CBI (Readhead et al., 2004). This power may be due to integrated SZ effect from clusters lying along the line of sight. The differences between the CBI and VSA instruments and their respective data reduction pipelines will provide an excellent basis on which to investigate this effect.

2 Description of the Super-Extended VSA

The VSA comprises fourteen antennas mounted on a tilting table to provide elevation tracking. Each antenna tracks individually in azimuth allowing fringe rate filtering of noise sources such as the Sun and Moon as well as rejection of both groundspill and cross-talk signals. This ability enables the telescope to observe during both day and night periods and increases the integration time available. Each antenna uses a low noise HEMT front end amplifier fed by a corrugated horn feed and parabolic mirror assembly. The new super-extended mirrors have a diameter of 60cm and are made of carbon-fibre in order to be light enough for the telescope to support without major re-engineering. The rigid mirrors are attached to the feed horns using flexible aluminium supports. These mirrors are significantly larger than those used in the compact and extended configurations in order to improve the flux sensitivity of the array. The maximum baseline of the array has also been increased to ~ 4m to achieve the angular resolution necessary for high ℓ measurements. In addition to these changes the front end amplifier on each antenna is also being upgraded to further improve the sensitivity of the array.

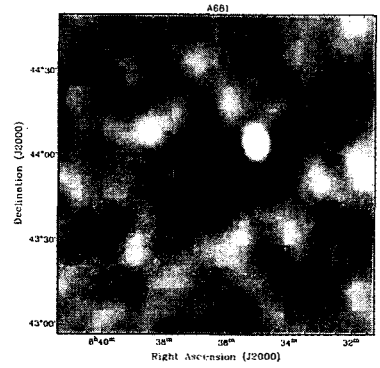

Figure 1: Abell 681 seen by the Super-extended VSA (without radio source subtraction).

With the improvements to the sensitivity of the main array it has also been necessary to improve the sensitivity of the dedicated source subtraction baseline adjacent to the main array. This system, comprising two 3.7m antennas, has been broadbanded to 6GHz by fitting a correlator of the type used for the AMI telescope (Kneissl et al, 2001) in order to more effectively remove contamination from radio sources within the fields under observation.

3 Preliminary results and current observing scheme

The first objective of the new array is the observation of medium redshift galaxy clusters using the Sunyaev–Zel'dovich effect. Initial results have been promising and include the first SZ observations of some lesser studied Abell clusters, eg Figure 1. A sample of clusters selected from the NORAS catalogue with redshifts of $0.1 < z < 0.15$ will be used in conjunction with X-ray data, where available, to provide an estimate of H_0 and f_{gas}.

The longer term objectives of the array are the observation of primary anisotropies in the CMB. These objectives are two fold: the first is an observing scheme targeting individual pointings for long integration times in order to constrain the amount of power found at $\ell > 2000$; the second to use mosiaced observations for increased $\Delta\ell$ resolution and to measure the fourth and subsequent acoustic peaks with high temperature sensitivity. A simulation of the predicted performance is shown in Figure 2 (Taylor, 2004). One particular objective of these observations is to investigate the primordial fluctuation index, offering the possibility of rejecting the $n_S = 1$, Harrison–Zel'dovich spectrum and allow us to determine whether there is any "running" in the index.

As with previous observations at 33 GHz the removal of radio point sources from the field is very important. The VSA employs a joint source subtraction strategy with the Ryle telescope in Cambridge (Waldram et al. 2003). The improved sensitivity of the array has necessitated a deeper survey with the Ryle of those fields under observation. This survey is then used to make pointed observations of contaminant sources using the VSA's own source subtraction baseline at 33 GHz.

The current status of the telescope sees the first of these long term objectives already underway.

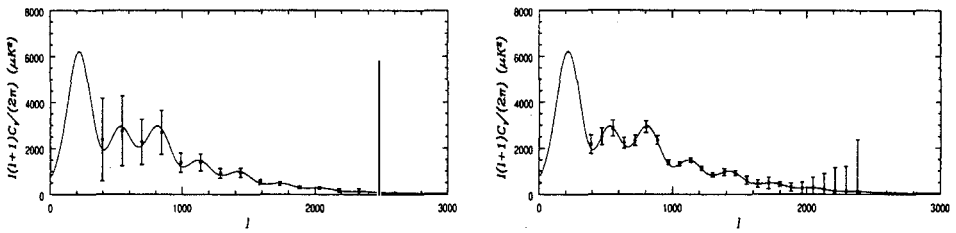

Figure 2: Prediction of super-extended VSA results after 18 months of observations. Right: 3 deep field observations. Left: three 19-field mosaics for fine $\Delta\ell$ resolution. Points are uncorrelated with each other and error bars are $1-\sigma$; at low ℓ errors are dominated by sample variance and at high ℓ by receiver noise.

4 Summary

The VSA in its previous configurations has measured the CMB power spectrum from $\ell = 150$ - 1600. Its previous results have been in good agreement with those of other CMB experiments. The current observing program will measure the fourth and subsequent acoustic peaks with good signal-to-noise and will be useful in breaking existing degeneracies between cosmological parameters. Its measurements of the power at $\ell > 2000$ will also investigate the contribution from the integrated SZ effect of clusters along the line of sight. The upgraded VSA will provide good sensitivity and angular resolution whilst at the same time maintaining its excellent rejection of systematics.

Acknowledgments

The VSA is a collaboration between Cavendish Astrophysics, IAC and Jodrell Bank and is supported by PPARC. I would like to acknowledge the support of a PPARC studentship. I would also like to thank all those who work on the VSA for their contributions.

References

1. Lee A.T. et al., 2001, *ApJ*, 561, L1.
2. Netterfield C.B. et al., 2002, *ApJ*, 571, 604.
3. Halverson N.W. et al., 2002, *ApJ*, 568, 38.
4. Scott P.F. et al., 2003, *MNRAS*, 341, 1076.
5. Silk, J., 1968, *ApJ*, 151, 459.
6. Pearson T.J. et al., 2003, *ApJ*, 591, 556.
7. Mason B.S. et al., 2003, *ApJ*, 591, 540.
8. Kuo C.L. et al., 2003, *ApJ*, submitted (astro-ph/0212289).
9. Grainge K.J.B. et al., 2003, *MNRAS*, 341, L23.
10. Bennett C.L. et al., 2003, *ApJS*, 148, 1.
11. Hinshaw, G. et al., 2003, *ApJS*, 148, 63.
12. Spergel D.N. et al., 2003, *ApJ*, 148, 175.
13. Watson R.A. et al., 2003, *MNRAS*, 341, 1057.
14. Taylor A.C. et al., 2003, *MNRAS*, 341, 1066.
15. Rubiño-Martin J.A. et al., 2003, *MNRAS*, 341, 1084.
16. Slosar, A. et al., 2003, *MNRAS*, 341, L29.
17. Dickinson, C. et al., 2004, submitted to *MNRAS*, astro-ph/0402498.
18. Rebolo, R. et al., 2004, submitted to *MNRAS*, astro-ph/0402466.

19. Savage, R. et al., 2003, *MNRAS*, in press, astro-ph/0308266.
20. Smith, S. et al., 2004, submitted to *MNRAS*, astro-ph/0401618.
21. Taylor A.C., Grainge K., Jones M.E., Pooley G.G., Saunders R.D.E., Waldram E.M., 2001, *MNRAS*, 327, L1
22. Waldram E.M., Pooley G.G., Grainge K.J.B., Jones M.E., Saunders R.D.E., Scott P.F., Taylor A.C., 2003, *MNRAS*, 342, 915
23. Hobson M.P., Maisinger K., 2002, *MNRAS*, 334, 569.
24. Kneissl, R. et al, 2001, *MNRAS*, 328, 783.
25. Readhead et al., 2004, *ApJ*, 609, 498,

THE LYMAN-α FOREST, WMAP YEAR THREE AND WARM DARK MATTER

Matteo Viel[1,2]
[1] *Institute of Astronomy, Madingley Road, CB3 0HA Cambridge, UK*
[2] *INAF-Osservatorio Astronomico di Trieste, via G.B. Tiepolo 11, I-34131 Trieste, Italy*

I present constraints on cosmological parameters and on the mass of a warm dark matter particle combining Cosmic Microwave Background data, the galaxy power spectrum and Lyman-α forest quasar samples.

1 Introduction

The Lyman-α forest, the absorption of neutral hydrogen along the line-of-sight to distant quasars, is a powerful cosmological tool. Measurements of the matter power spectrum from Lyman-α forest data extend to smaller scales ($\sim 3-80$ comoving Mpc) and probe a redshift range ($z = 2-4$) complementary to estimates of the matter power spectrum from Cosmic Microwave Background (CMB), galaxy surveys or weak gravitational lensing observations. Here, I will review some of the (recent) most important results that have been achieved when combining the Lyman-α forest data sets available with larger scale measurements in order to constraint cosmological parameters and the mass of a warm dark matter particle. In particular, I will focus on the inferred amplitude of the matter power spectrum, σ_8, and I will exploit the capabilities of the SDSS quasar (QSO) data set in constraining the mass of the sterile neutrino.

2 Cosmological Parameters

We rely on two different QSO data sets: the SDSS Lyman-α forest data of McDonald et al. (2006), which consist of 3035 quasar spectra with low resolution ($R \sim 2000$) and low signal-to-noise (~ 10 per pixel) spanning a wide range of redshifts ($z = 2.2-4.2$) ; the LUQAS and C02 samples used in Viel, Haehnelt & Springel (2004), which contain mainly high resolution, high signal-to-noise spectra at $z \sim 2.5$ (VHS).

We use the CosmoMC code[6] to perform the parameter estimation (we assume the Universe to be flat and that there is no tensor or neutrino contribution). In the left panel of Figure 1, we show the 1 and 2-σ constraints in the $\sigma_8 - n_s$ plane that have been obtained from: the VHS sample (cyan light contours); the SDSS sample[7] (dark blue contours); the WMAP3 results recently obtained by Spergel et al. (2006) (light green contours); the joint WMAP3+VHS analysis (white empty contours) and the joint WMAP3+SDSS analysis (dark blue empty contours).

The main points can be summarized as follow: *i*) the Lyman-α forest can constrain the amplitude and slope of the power spectrum but these constraints are more useful if combined with other observables; *ii*) the high resolution VHS data set at $z \sim 2.5$ is in agreement with the new WMAP3 data, even though it has lost its constraining power and its only effect is to shift

Table 1: Summary of the constraints on σ_8 and n_s for the VHS and SDSS samples. SDSS-d refers to the analysis of SDSS data by Viel& Haehnelt (2006). The quoted errors are the 68% confidence limits.

	WMAP3	WMAP3+VHS	WMAP3+SDSS	WMAP3+SDSS-d	WMAP3+EXT+SDSS-d	WMAP3+EXT+SDSS
σ_8	0.76 ± 0.05	0.78 ± 0.05	0.86 ± 0.03	0.80 ± 0.04	0.78 ± 0.03	0.80 ± 0.04
n_s	0.96 ± 0.02	0.96 ± 0.02	0.96 ± 0.02	0.96 ± 0.01	0.96 ± 0.01	0.96 ± 0.02
n_{run}	-	-	-	-	-	-0.002 ± 0.01

up the best fit WMAP3 only power spectrum amplitude; *iii*) the inferred SDSS+WMAP3 power spectrum amplitude is 2σ off the WMAP3 only estimate, thus the two data sets are marginally consistent [14,21].

We carried on our independent analysis of the SDSS data set by performing Taylor expansion of the flux power with respect to astrophysical and cosmological parameters using a coarse grid of high-resolution large box size hydrodynamical simulations [16,19] (we label this method as SDSS-d). In the right panel of Figure 1 (note the different axis range), we show the combined analysis of SDSS-d and WMAP3 and SDSS-d+WMAP3+other experiments: VSA[3], CBI [11], ACBAR[5] and the 2dF galaxy power spectrum [10]. We note that SDSS-d (thick dash-dotted black line) is in better agreement with WMAP3 than SDSS and if we include the other experiments (thin dashed line) the constraints become tighter. The useful numbers are summarized in Table 1. The value of the spectral index of the joint analysis is in perfect agreement with the value of WMAP3 only. Note that the inferred value of the running, $n_{run} = -0.002 \pm 0.015$ at $k = 0.002$ Mpc^{-1}, with the SDSS-d analysis is larger than that of Seljak et al. (2006b), $n_{run} = -0.02 \pm 0.012$, and perfectly consistent with zero.

The Lyman-α forest data appears to be in reasonable agreement with the CMB and other data sets which probe the matter power spectrum at larger scales. A discrepancy still remains with the SDSS data set and the inferred power spectrum of McDonald et al. (2005) that seems to suggest more power at the forest scales, when compared to larger scales experiments. For the near future further progress is likely to be driven by a better understanding of the systematic theoretical uncertainties, rather than the compilation of larger data sets [7,20].

3 Warm Dark Matter

Warm dark matter (WDM) has been advocated in order to solve some apparent problems of standard cold dark matter (CDM) scenarios at small scales, namely: the excess of galactic satellites, the cuspy and high density of galactic cores, the large number of galaxies filling voids. All these problems would be alleviated if the dark matter (DM) is made of warm particles, whose effect would be to suppress structures below the Mpc scale. Thus, the Lyman-α forest is an ideal tool to constraint WDM models. We perform high-resolution hydrodynamical simulations in a WDM scenario and compute the flux power as a function of particle mass, we implement this in the framework of the SDSS-d analysis described in the previous section.

Viel et al. (2005) used the LUQAS sample of high resolution quasar absorption spectra to set a lower limit of 2 keV for the sterile neutrino mass. More recently, exploiting the small statistical errors and the large redshift range of the SDSS Lyman-α forest data, Seljak et al. (2006a) found a lower limit of 14 keV. If the latter result is correct, a large fraction of the sterile neutrino parameter space can be ruled out (assuming that all the DM is made of sterile neutrinos); together with constraints from X-ray fluxes, this rules out the possibility that DM consists of sterile neutrinos, unless they are produced by resonant oscillations caused by a large leptonic asymmetry in the early Universe (see Abazajian & Koushiappas 2006 and all the references therein).

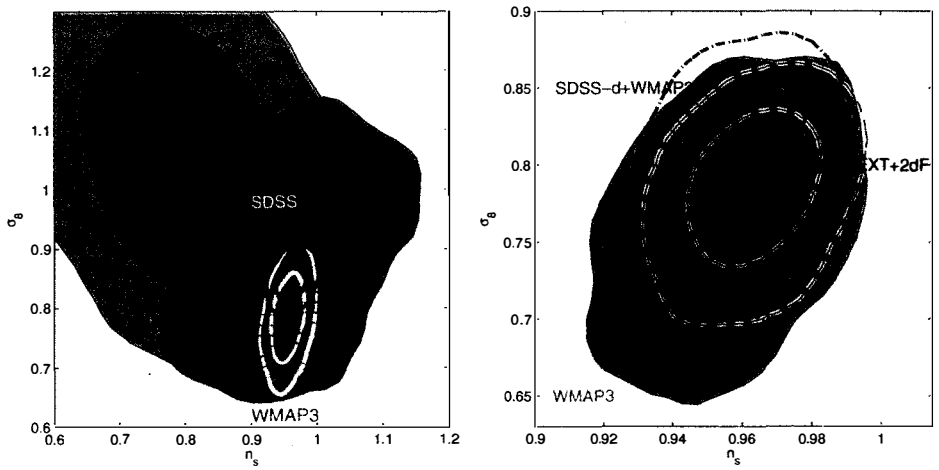

Figure 1: 1 and 2σ likelihoods for σ_8 and n_s marginalized over all other parameters. *Left panel:* Constraints are for WMAP3 only (green), the LUQAS+Croft data sets as analysed by VHS (cyan) and the SDSS Lyman-α forest data of M05 (blue). The thick dashed white empty contours refer to WMAP3 + VHS, while the solid blue contours are for WMAP3 + SDSS. *Right panel:* Combined analysis with the SDSS-d method adding smaller scale CMB data sets and the 2dF galaxy power spectrum (Note the different range plotted).

We combine WMAP3, 2dF, CBI, ACBAR and VSA with the SDSS flux power measurements, even though it is basically this last one that constrains the parameter m_s. In the left panel of Figure 2 we show the 1-dimensional marginalized likelihoods for (1 keV)$/m_s$, with m_s the sterile neutrino mass, for several redshift ranges. The 2σ lower limits for the sterile neutrino mass are: 3.9, 8.1, 10.3 keV for $z \leq 3.2, 3.6, 4.2$, respectively (i.e. we use only the SDSS flux power in this redshift range). The corresponding limits for an early decoupled thermal relic are: 0.9, 1.6, 1.9 keV. Also shown (continuous black line) is the constraint obtained by Viel et al. (2005) using the LUQAS and C02 samples [2,4,17,22]. The SDSS data improve the constraint from the high resolution data at $z \sim 2.5$ by a factor 5. This is mainly due to the extension of the SDSS data to higher redshift where the flux power spectrum is most sensitive to the effect of WDM. The smaller statistical errors of the flux power spectrum and the coverage of a substantial range in redshift help to break some of the degeneracies between astrophysical and cosmological parameters and also contribute to the improvement. In the right panel of Figure 2, we show the constraints for the spectral index n_s and the mass of the sterile neutrino. The error bars get smaller by a factor almost 2 (3) if we include all the data compared to including $z \leq 3.6$ ($z \leq 3.2$).

If we combine this bound with the constraint derived from X-ray flux observations in the Coma cluster periphery, we find that the only allowed sterile neutrino mass is $\sim$ 10 keV (in the standard production scenario with non-resonant neutrino oscillations). Adding constraints based on X-ray fluxes from the Andromeda galaxy or the Milky Way, we find that dark matter particles cannot be sterile neutrinos, unless the latter are produced by resonant oscillations.

Acknowledgments

Numerical computations were done on the COSMOS supercomputer at the Department of Applied Mathematics and Theoretical Physics in Cambridge. COSMOS is a UK-CCC facility which is supported by HEFCE and PPARC. We acknowledge the use of the Legacy Archive for

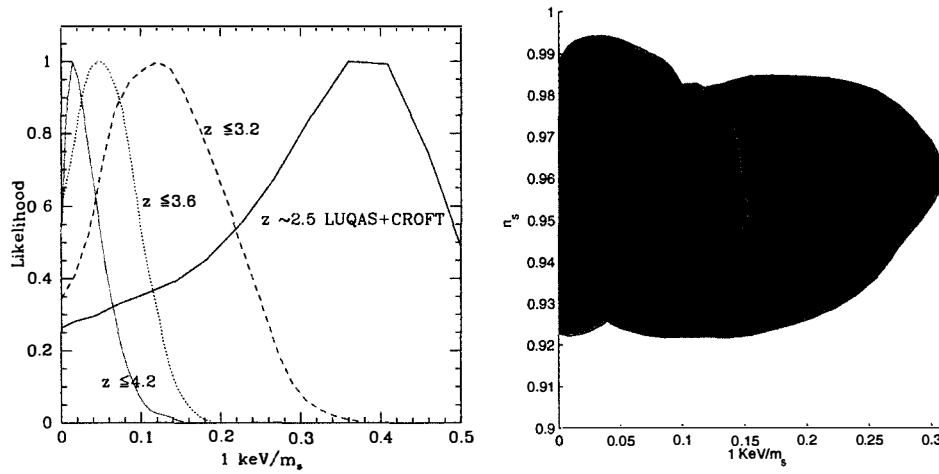

Figure 2: *Left panel:* 1-dimensional constraints for the parameter 1 keV/m_s, with m_s the mass of a sterile neutrino, combining SDSS, WMAP3, smaller scales CMB experiments and the 2dF. Different flux power redshift ranges are considered to show the constraining power of high redshift data. *Right panel:* 2-dimensional constraints in the (n_s,keV/m_s) plane.

Microwave Background Data Analysis (LAMBDA). I acknowledge support from a EU grant for young scientists.

References

1. Abazajian, K., Koushiappas, S. M., 2006, astro-ph/0605271
2. Croft R. A. C., et al., 2002, ApJ, 581, 20
3. Dickinson C., et al., 2004, MNRAS, 353, 732
4. Kim T. S., Viel M., Haehnelt M. G., Carswell R. F., Cristiani S., 2004, MNRAS, 347, 355
5. Kuo C.-l., et al., 2004, ApJ, 600, 32
6. Lewis A., Bridle S., 2002, PRD, 66, 103511
7. McDonald P., et al., 2005, ApJ, 635, 761
8. McDonald P. et al., 2005, Mon. Not. Roy. Astron. Soc., 360, 1471
9. McDonald P. et al., 2006, ApJS, 163, 80
10. Percival W. J., et al., 2001, MNRAS, 327, 1297,
11. Readhead A. C. S., et al., 2004, ApJ, 609, 498,
12. Seljak U., et al., 2005, PRD, 71, 103515
13. Seljak U., Makarov A., McDonald P., Trac H., 2006a, astro-ph/0602430
14. Seljak U., Slosar A., McDonald P., 2006b, astro-ph/0604335
15. Spergel D. N., et al., 2006
16. Springel V., 2005, MNRAS, 364, 1105,
17. Viel M., Haehnelt M. G., Springel V., 2004, MNRAS, 354, 684
18. Viel M., Lesgourgues J., Haehnelt M. G., Matarrese S., Riotto A., 2005, PRD, 71, 063534
19. Viel M., Haehnelt M. G., 2006, MNRAS, 365, 231,
20. Viel M., Haehnelt M. G., Springel V., 2006, MNRAS, 367, 1655
21. Viel M., Haehnelt M. G., Lewis A., 2006, astro-ph/0604310
22. Zaroubi S., Viel M., Nusser A., Haehnelt M., Kim T. S., 2006, MNRAS, in press

EARLY SCIENCE WITH AMI

JONATHAN T. L. ZWART
Astrophysics Group, Cavendish Laboratory, J. J. Thomson Avenue, Cambridge, CB3 0HE, England

AMI, an instrument for detecting clusters of galaxies via the Sunyaev-Zel'dovich effect, has recently begun observing. I outline AMI's observing strategy and present some of AMI's first observations of clusters.

1 Searches for Galaxy Clusters

The fundamental importance of detecting the population, and characterizing the properties, of clusters of galaxies, in particular out to high redshift, is widely appreciated. However, the classical methods of finding clusters, via their emission (in the optical, infra-red and in X-rays), suffer from intensity diminution as $(1+z)^4$ and from confusion and biases to concentration.

It has long been advocated[1,2,3] that the way round these problems is to survey for clusters in the Sunyaev-Zel'dovich[4,5,6] (SZ) effect, that is, the change of the temperature of the CMB in the direction of the cluster by inverse-Compton scattering of the CMB by the cluster plasma. SZ observations have been made routinely with the OVRO/BIMA array[7] and the Ryle Telescope[8] (RT) since the early 1990s. Yet even these particular radio interferometers are not optimal for SZ work—their shortest baselines are too long and so resolve out most of a cluster's SZ signal (Figure 1(a)). It is important to have a telescope whose synthesized beam is matched to the size of a typical cluster. There is a need for dedicated cluster survey instruments, such as ACT[9], AMI[10], AMiBA[11], SPT[12] or SZA[13]. All except ACT and SPT are interferometers, with the advantage over the (higher bandwidth) bolometers that they in practice reject contaminating primordial CMB anisotropies below a particular ℓ.

2 Detecting Galaxy Clusters with AMI

The design and commissioning of AMI, which comprises a Small Array (SA) and a source-subtracting Large Array (LA), are described elsewhere in these proceedings[14]. One of AMI's

main science goals is to measure the comoving number density of clusters as a function of cosmic epoch, $N(m, z)$, with different and fewer biasing effects than other methods. AMI's selection function has only a weak dependence on redshift. Targeted observations of clusters will enable us to improve our understanding of cluster physics. One will also be able to constrain cosmological parameters—for example, SZ observations, when combined with X-ray information, potentially allow direct measurement of q_0—as well as examining the CMB power spectrum at angular scales $\ell \gtrsim 3000$. Once clusters have been detected via the SZ effect, follow-up with optical and infra-red observations[15] will allow us to measure their redshifts and hence $N(m, z)$.

3 Observing Strategy

This is as follows:

- Early Targets—pointed observations of known clusters before the LA is operational. These targets must have favourable radio environments. One requires that the confusion noise—a function of the limiting flux of the source subtractor, the LA—is much less than the thermal noise on the SZ decrement. The limiting flux depends on the integration time. There is an uncertainty in the confusion noise given the unknown faint source population[16]. The early target observations will permit calibration of the cluster scaling relations in time for the first AMI surveys.

- First Blind Surveys—observations of $10 \approx 1$ deg^2 AMI fields, free of known clusters, bright radio sources and bright stars, are due to begin[15].

- More Blind Surveys—two surveys exploring different regions of the cluster density function: one wide and shallow (six months over 100 deg^2), yielding massive lower redshift clusters; and one narrow and deep (one year over 10 deg^2), yielding lower mass, higher redshift clusters.

- Surveys of Equatorial Fields—with North-South baselines, it will be possible to survey the XMM Large Scale Structure Survey regions and other multi-wavelength deep fields. We hope to understand the selection function of different cluster-finding methods and also cluster scaling relations; a joint analysis will further provide information on cluster physics.

4 Selection of Early Cluster Targets

It is essential for AMI to observe known X-ray- and optically-selected clusters, with their widely available data in these other wavebands, in order to calibrate the scaling relations ($L-T$, $L-M$ and so on) before a blind SZ survey. There are three main sub-samples of first targets:

- NORAS: we made cuts to the NORAS[17] catalogue ($L_X > 7 \times 10^{44}$ergs^{-1}, $z > 0.1$, $\delta > 30°$) leaving 17 clusters. Combining with archive X-ray data will yield f_g and H_0 at low redshift.

- MACS: we selected the 15 brightest ($L_X > 10^{45}$ergs^{-1}) and highest redshift ($z > 0.3$) clusters from the Massive Cluster Survey (MACS[18]). Comparison of the MACS and NORAS sub-samples will measure the evolution of the scaling relations with redshift. We will jointly analyse SZ and X-ray data to measure $f_g(z)$ and q_0.

- High-redshift: we included in our sample the increasing number of high-redshift clusters as they were reported in the literature.

In 2004, we began to survey these clusters for point sources using the RT. By June 2006, when the RT was switched off, we had reduced the original list of around 80 clusters to a sample of 31 that was free from the brightest 15-GHz sources and therefore more favourable for SZ work. Those sources cut from the sample at this stage will become candidates again once the LA is observing.

5 Observations of Early Cluster Targets

AMI began observing[19] known clusters in August 2005. Using only seven out of the 10 SA antennas, and six out of eight frequency sub-channels, we detected Abell 1914 at 17σ in just 34 hours (Figure 1). The integrated flux density of -8.6 ± 0.5 mJy was consistent with a simple X-ray-derived model for the intracluster gas. Eighteen point sources, detected by the RT and the longer baselines of the SA, were subtracted. This indicates a clear need for our LA source subtraction strategy. We further found that the spectrum of the decrement in A1914 measured by AMI was consistent with an SZ spectrum (Figure 1(d)). Figures 2(a) and 2(b) respectively show AMI detections of NORAS and MACS clusters.

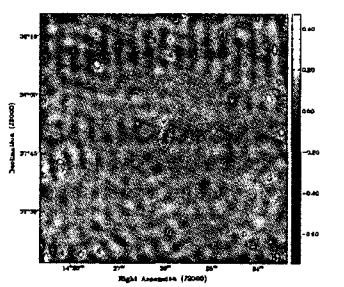

(a) A 228-hour observation with the RT (after source subtraction)

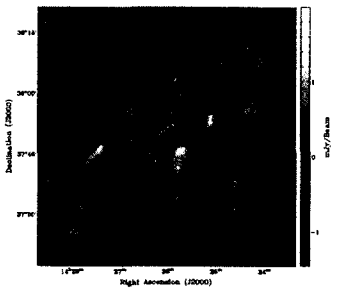

(b) AMI-SA long baseline map (before source subtraction)

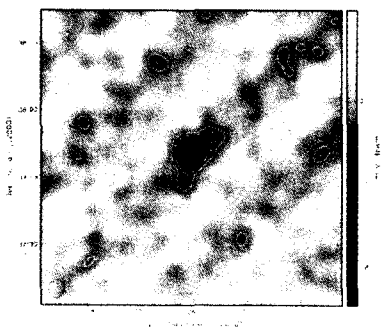

(c) 34 hours with AMI-SA (short baselines, after source subtraction)

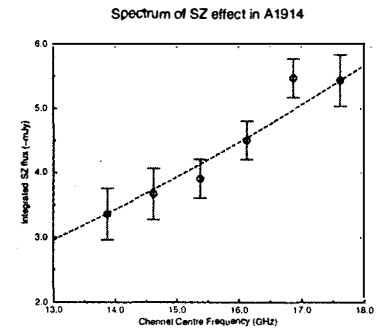

(d) Spectrum of SZ effect in A1914, constrained to pass through the 13.875-GHz point

Figure 1: Abell 1914 measured with the RT and AMI-SA

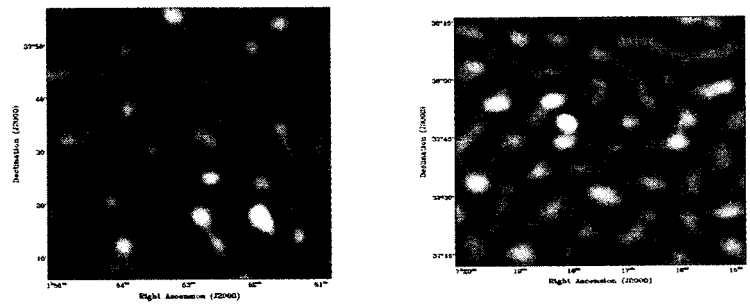

(a) A 10-hour observation of Abell 263 at $z = 0.3$ (Natasha Hurley-Walker)

(b) 8 hours at the $z = 0.545$ cluster MACS 0717+37

Figure 2: AMI detections of optical- and X-ray-selected clusters

Acknowledgments

AMI is a project of the Cavendish Astrophysics Group and is supported by the Particle Physics and Astronomy Research Council. I acknowledge the support of a PPARC Studentship. I am grateful to AMI collaborators for their kind assistance, in particular, Richard Saunders and Keith Grainge.

References

1. See e.g. V. A. Korolev, R. A. Sunyaev & L. A. Yakubtsev, *Soviet Astr. Lett.* **12**, 141 (1986).
2. See e.g. J. R. Bond, S. T. Meyers, in: Trends in Astroparticle Physics, ed. D. Cline, World Scientific, Singapore (1991).
3. See e.g. J. G. Bartlett & J. Silk, *ApJ* **423**, 12 (1994).
4. R. A. Sunyaev & Y. B. Zel'dovich, *CoASP* **4**, 173 (1972).
5. See e.g. M. Birkinshaw, *Phys. Rept.* **310**, 97 (1999).
6. See e.g. J. E. Carlstrom, *ARA&A* **40**, 643 (2002).
7. See e.g. M. Joy *et al.*, *ApJ* **551**, L1 (2001).
8. See e.g. K. J. B. Grainge *et al.*, *MNRAS* **329**, 890 (2002).
9. A. Kosowsky, astro-ph/0402234 (2004).
10. R. Kneissl *et al.*, *MNRAS* **328**, 783 (2001).
11. See e.g. P. T. P. Ho *et al.*, *Mod. Phys. Lett. A* **19**, 993 (2004).
12. SPT Collaboration, astro-ph/0411122 (2004).
13. See e.g. J. E. Carlstrom, Cosmology with the Sunyaev-Zel'dovich Effect, APS Meeting Abstracts (2002).
14. K. J. B. Grainge, in these proceedings.
15. J. T. L. Zwart, in: Proceedings of XXXIXth Rencontres de Moriond (2004).
16. T. L. Culverhouse, in: Proceedings of XXXIXth Rencontres de Moriond (2004).
17. H. Böhringer *et al.* ApJS **129**, 35 (2000).
18. H. Ebeling *et al.* *ApJ* **553**, 668 (2001).
19. AMI Collaboration, *MNRAS* **369(1)**, L1 (2006).

III – THEORETICAL INSIGHTS

D-BRANE AS A MODEL FOR COSMOLOGICAL DARK ENERGY

I.Ya. AREF'EVA
Department of Theoretical Physics, Steklov Mathematical Institute of Russian Academy of Sciences, Gubkin st., 8, 119991, Moscow, Russia

Results of study of the dark energy model derived from the Cubic Superstring Field Theory (CSSFT) describing the non-BPS brane decay are presented. In this model the acceleration of the Universe is driven by a nonlocal stringy Higgs mechanism. Near the origin of time the model has phantom behaviour and then appears a periodic crossing of the $w = -1$ barrier.

1 Introduction

Recent results of WMAP [1] together with Ia supernovae data give a strong support that the present time DE state parameter is close to -1: $w = -0.97^{+0.07}_{-0.09}$, or without an a priori assumption that the Universe is flat and together with large-scale structure and supernovae data $w = -1.06^{+0.13}_{-0.08}$. From a theoretical point of view the domain of w covers three essentially different cases. The first case, $w > -1$, is achieved in quintessence models containing an extra light scalar field which is not in the Standard Model set of fields. The second case, $w = -1$, is the cosmological constant. The third case, $w < -1$, is called a "phantom" one[2] and can be realized by a scalar field with a ghost (phantom) kinetic term. In this case all natural energy conditions are violated and there are problems of an instability at classical and quantum levels. Since experimental data do not contradict with a possibility $w < -1$ a study of such models attracts a lot of attention and some of these attempts are presented at this conference (more references can be found in [3,6]).

A possible way to evade the instability problem for models with $w < -1$ is to yield a phantom model as an effective one, arising from a more fundamental theory without a negative kinetic term. In this talk we present results of study of a cosmological SFT tachyon model [3,4,5,6]. The model is based on SFT formulation of a fermionic NSR string with the GSO$-$ sector [7]. In this model a scalar field is the open string tachyon, which describes according to the Sen conjecture [8] a dynamical transition of a non-BPS D-brane to a stable vacuum (see [9] for review). This stable string theory is supposed to be described by a VSFT (a Vacuum String Field Theory). The model that we are going to present is an approximation to VSFT. VSFT is stable and one has to discuss only an application of the used approximation to a full string theory to particular physical problems.

2 Model

Our model is given by the following action

$$S = \int d^4x\sqrt{-g}\left(\frac{R}{2\kappa^2} + \frac{1}{\lambda_4^2}\left(-\frac{\xi^2\alpha'}{2}g^{\mu\nu}\partial_\mu\phi(x)\partial_\nu\phi(x) + \frac{1}{2}\phi^2(x) - \frac{1}{4}\Phi^4(x) - T\right)\right) \qquad (1)$$

g is the metric, κ is a gravitational coupling constant, ϕ is a tachyon field. The model (1) is supposed to describe a D3 non-BPS brane embedded in the 10-dimensional space time and it is obtained via dimensional reduction of the 10-dimensional CSST (more precisely the fermionic NSR string with the GSO− sector) tachyon action,

$$\frac{1}{\lambda_4^2} = \frac{v_6 M_s^4}{g_o}(\frac{M_s}{M_c})^6 \quad \text{and} \quad \Phi = e^{\frac{\alpha'}{8}\Box_g}\phi, \quad \text{where} \quad \Box_g = \frac{1}{\sqrt{-g}}\partial_\mu\sqrt{-g}g^{\mu\nu}\partial_\nu,$$

T is a tension of the D3-brane, α' is the string tension related with a characteristic string scale $M_s = 1/\sqrt{\alpha'}$, g_o is the open string dimensionless coupling constant, M_c is a characteristic scale of the compactification, v_6 is a volume of the 6-dimensional compact space and $\xi^2 \approx 0.9556$ is a constant dictated by CSSFT.

In the spatially flat FRW metric with a scale factor $a(t)$ and space homogenous tachyon field Friedmann equations in terms of a dimensionless time $t \to t\sqrt{\alpha'}$ have the form [3]

$$3H^2 = \frac{\kappa^2}{\lambda_4^2}\left(\frac{\xi^2}{2}\dot{\phi}^2 - \frac{1}{2}\phi^2 + \frac{1}{4}\Phi^4 + \mathcal{E}_1 + \mathcal{E}_2 + \Lambda\right), \qquad \dot{H} = \frac{\kappa^2}{\lambda_4^2}\left(-\frac{\xi^2}{2}\dot{\phi}^2 - \mathcal{E}_2\right) \tag{2}$$

where

$$\mathcal{E}_1 = -\frac{1}{8}\int_0^1 ds(e^{\frac{1}{8}s\mathcal{D}}\Phi^3)\mathcal{D}e^{-\frac{1}{8}s\mathcal{D}}\Phi, \quad \mathcal{E}_2 = -\frac{1}{8}\int_0^1 ds(\partial_t e^{\frac{1}{8}s\mathcal{D}}\Phi^3)\partial_t e^{-\frac{1}{8}s\mathcal{D}}\Phi \tag{3}$$

and $\Phi = e^{\frac{1}{8}\mathcal{D}}\phi$, $\mathcal{D} = -\partial_t^2 - 3H(t)\partial_t$. $H \equiv \dot{a}/a$ is the Hubble parameter and the dot denotes the time derivative. The equation of motion for the tachyon is

$$\left(\xi^2\mathcal{D} + 1\right)e^{-\frac{1}{4}\mathcal{D}}\Phi = \Phi^3. \tag{4}$$

Equations (2)-(4) are complicated because of the presence of an infinite number of derivatives and a non-flat metric. See [15] for a model originated from the bosonic string.

3 Rolling Tachyon in the flat background

Equation of motion (4) in the flat background is

$$\left(-\xi^2\partial_t^2 + 1\right)e^{\frac{1}{4}\partial_t^2}\Phi(t) = \Phi(t)^3. \tag{5}$$

where $\Phi = e^{-\frac{1}{8}\partial_t^2}\phi$. This equation and analogous equations for a cubic bosonic string action have been already studied in [10,11,12,13]. If one ignores the factor $e^{-\frac{1}{8}\partial_t^2}$ in the R.H.S. of (5) one equation tachyon in the usual Higgs potential. It has two minima located at $\Phi_0 = \pm 1$. The operator $e^{s\partial_t^2}$ on smooth functions for positive s can be rewritten in an integral form and this allows to rewrite this equation in the form

$$\int dt' C(t-t')\Phi(t') = \Phi(t)^3, \qquad C(t) = \frac{\xi^2(1-4t^2)+1}{\sqrt{\pi}}e^{-t^2} \tag{6}$$

Using an iteration procedure a numeric solution of the boundary problem $\Phi(\pm\infty) = \pm 1$ has been found [11]. On Fig. 1 A. we present this solution[11] (it is valid for $\xi^2 < \xi_{\rm cr} \approx 1.38$).

The tachyon field ϕ (a dull line interpolating between ± 1 on Fig.1.A) starts from $t = 0$ with a non-zero velocity (a line with maximum near at zero presents $\dot{\phi}$), rolls down to the minimum of the tachyon potential and eventually stops in the minimum. Φ has a similar behaviour (a bright line on Fig.1.A). For $\xi^2 \neq 0$ and $\xi^2 < \xi_{\rm cr}^2$ there are damping fluctuations near the minimum (for $\xi = 0$ there are no fluctuations).

To make our consideration more transparent let us remind behavior of the energy and the pressure in the flat case[13]. We see from (2) that the non-local energy $\mathcal{E}_2$ plays the role of an extra kinetic term. It is very instructive to write $\mathcal{E}_2$ in the form $\mathcal{E}_2 = -\mathcal{K}[\Phi]\frac{\dot{\phi}^2}{2}$. When $\mathcal{K}[\Phi] > \xi^2$ the model has a ghost like total kinetic term. Numerical calculations show that for $q^2 = 0$ the values of $\mathcal{K}[\Phi]$ are always positive, see Fig.1.B. Therefore the model has phantom behaviour during all time of evolution. For the case $\xi^2 = 0.96$ (string case) the effective kinetic energy $\frac{q^2}{2}\dot{\phi}^2 + \mathcal{E}_2$ for

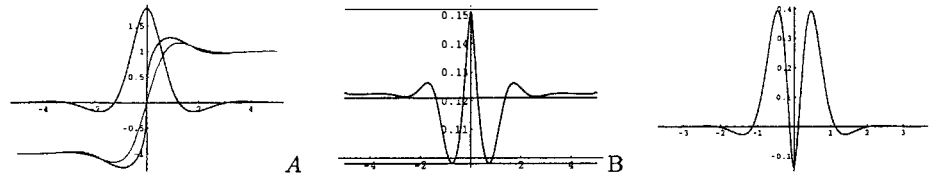

Figure 1: A. Solution to eq.(5); B.$\mathcal{K}[\Phi](t)$ for $q^2 = 0$; C. The effective kinetic energy $\mathcal{E}_2 + \frac{q^2}{2}\dot{\phi}^2$ for $q^2 = 0.96$

the solution Fig.1.A is presented on Fig.1.C. We see that the model for small time has phantom behavior but it has not the phantom behaviour always. This change occurs when Φ is closed to ± 1 and here one can use the linear approximation[6].

The main conclusion from these examples is that non-local operator $e^{\partial_t^2}$ changes drastically the evolution of the system. Without the usual kinetic term in the L.H.S. of equation (5) the late time behavior of the tachyon is just stopping with monotonically decreasing velocity in the minimum of the potential. This is a property of a phantom and the above analysis justifies the phantom approximation used in [3,4]. The usual kinetic term in the L.H.S. of equation (5) accelerates the field but for actual ξ^2 the phantom character reveals and the tachyon eventually stops in the minimum.

4 Rolling Tachyon in the FRW Universe

The above consideration indicates that in the non-flat case one can use two approximations: a phantom approximation and a linearization. It is natural to expect that the first one works for a small time and the second for a later time. For the rolling in the flat case the value of T is note essential, but from the Sen conjecture it is equal to $1/4$ (this corresponds to zero cosmological constant in the non-perturbative vacuum $\phi = \pm 1$). In the non-flat case the D3-brane tension should be shifted[3] to be $T = 1/4 + \Lambda$ and Λ is found from an requirement of existence of a rolling solution. To make this proposal more transparent it is worth to consider a model with dynamical Λ such that it does not disturb the form of the Higgs potential. Such model has been proposed in [4], see also [5] and [16].

4.1 Phantom Approximation

In the phantom approximation we have

$$\dot{H} = \frac{1}{2m_p^2}\dot{\phi}^2, \qquad 3H^2 = \frac{1}{m_p^2}\left(-\frac{1}{2}\dot{\phi}^2 + V(\phi)\right). \tag{7}$$

where $m_p^2 = \lambda_4^2 M_s^2/\kappa^2$ and we make a rescaling of time $t \to t\sqrt{[< K(\phi) > -\xi^2]}$, $< K(\phi) >$ is an average of $K(\phi)$ at a first stage of evolution. For a special potential [4]

$$V(\phi) = \frac{1}{2}(1-\phi^2)^2 + \frac{1}{12m_p^2}\phi^2(3-\phi^2)^2$$

the solution to (7) is $\phi(t) = \tanh(t)$, $H = \frac{1}{2m_p^2}(\phi - \frac{1}{3}\phi^3)$. For this model $H_0 \approx H(\infty) = 1/3m_p^2$. Assuming that M_c and M_s are two different parameters and ignoring all factors of order 1, as well as the coupling constant and v_6 we get for the Hubble parameter in the real time $H_0 \sim M_s/m_p^2 \sim M_s\frac{M_s^2}{M_p^2}(\frac{M_s}{M_c})^6$. Assuming that $M_c \sim M_p$ we get $H_0 \sim M_p(\frac{M_s}{M_p})^9$. An assumption $M_s \sim 10^{-6.6}M_p$ gives $H \sim 10^{-60}M_p$.

4.2 A Late time Linearization

The linearization $\phi = 1 + \psi$ of (4) has the form

$$3H^2 = \frac{\kappa^2}{\lambda_4^2}\left(\frac{\xi^2}{2}\dot\psi^2 - \frac{1}{2}\psi^2 + \frac{3}{2}\Psi^2 + \mathcal{E}_1 + \mathcal{E}_2 + T\right), \quad \dot H = \frac{\kappa^2}{\lambda_4^2}\left(-\frac{\xi^2}{2}\dot\psi^2 - \mathcal{E}_2\right) \qquad (8a)$$

where

$$\mathcal{E}_1 = -\frac{3}{8}\int_0^1 ds e^{\frac{1}{8}s\mathcal{D}}\Psi\mathcal{D}e^{-\frac{1}{8}s\mathcal{D}}\Psi, \quad \mathcal{E}_2 = -\frac{3}{8}\int_0^1 ds\partial_t e^{\frac{1}{8}s\mathcal{D}}\Psi\partial_t e^{-\frac{1}{8}s\mathcal{D}}\Psi$$

and $T = -\frac{1}{4} + \Lambda_0$. The equation of motion for ψ (4) is

$$(\xi^2\mathcal{D} + 1)e^{-\frac{1}{4}\mathcal{D}}\Psi = 3\Psi. \qquad (9)$$

Assuming that $H \approx H_0 = \frac{\kappa}{\lambda_4}\sqrt{\frac{\Lambda_0}{3}}$ and keeping only the the decreasing solution we get

$$\Psi = Ae^{-\bar r t}\sin(\bar\nu t + \bar\varphi) \quad \text{where} \quad \bar r + i\bar\nu = \frac{3}{2}H_0 + \sqrt{\frac{9H_0^2}{4} + m^2}, \quad m = r + i\nu, \quad r \approx 1.1365,\ \nu \approx 1.7051$$

and corrections to the Hubble parameter is $H = \frac{\kappa}{\lambda_4}\sqrt{\frac{\Lambda_0}{3}} - \frac{\kappa^2}{g_c^2}C_H e^{-2\bar r t}\sin(2\bar\nu t + \varphi_H)$, see [6] for more details.

I am grateful to L.V. Joukovskaya, A.S. Koshelev, S.Yu. Vernov and I.V. Volovich for collaboration and useful discussions. The work is supported in part by RFBR grant 05-01-00758, INTAS grant 03-51-6346 and Russian President's grant NSh-2052.2003.1.

1. D.N. Spergel et al., astro-ph/0603449
2. R.R. Caldwell, Phys.Lett. **B545** (2002) 23.
3. I.Ya. Aref'eva, astro-ph/0410443.
4. I.Ya. Aref'eva, A.S. Koshelev, S.Yu. Vernov, astro-ph/0412619; Phys. Lett. **B628** (2005) 1; Phys. Rev. **D72** (2005) 064017.
5. I.Ya. Aref'eva and L.V. Joukovskaya, JHEP 0510:087,2005.
6. I.Ya. Aref'eva and A.S. Koshelev, hep-th/0605085.
7. I.Ya. Arefeva, D.M. Belov, A.S. Koshelev, P.B. Medvedev, Nucl. Phys **B638**(2002) 3.
8. A. Sen, hep-th/0410103.
9. K. Ohmori, hep-th/0102085; I.Ya. Aref'eva, D.M. Belov, A.A. Giryavets, A.S. Koshelev, P.B. Medvedev, hep-th/0111208; W. Taylor, hep-th/0301094.
10. N. Moeller, B. Zwiebach, JHEP **0210** (2002) 034; H.Yang, hep-th/0209197.
11. Ya.I. Volovich, J. Phys. **A36** (2003) 8685.
12. V.S. Vladimirov, Ya.I. Volovich, math-ph/0306018.
13. I.Ya. Aref'eva, L.V. Joukovskaya, A.S. Koshelev, JHEP **0309** (2003) 012.
14. C.R. Preitschopf, C.B. Thorn, S.A. Yost, Nucl. Phys. **B337** (1990) 363; I.Ya. Aref'eva, P.B. Medvedev, A.P. Zubarev, Nucl. Phys. **B341** (1990) 464.
15. G. Calcagni, JHEP 05 (2006) 012.
16. V. Forini, G. Grignani, G. Nardelli, hep-th/0502151.

ASTROPHYSICAL SIGNATURES OF LIGHT DARK MATTER

Y. ASCASIBAR
Astrophysikalisches Institut Potsdam
An der Sternwarte 16, Potsdam 14482, Germany

According to the current paradigm, most of the matter in the Universe is thought to be in the form of so-called dark matter, such a misleading name meaning that it does not emit nor absorb light. There is at present no idea of what dark matter particles may be, or, more precisely, there are plenty of ideas out there. This short contribution focuses on Light Dark Matter (LDM) particles, but many of the issues discussed here would also apply to other dark matter candidates. The bottom line is that dark matter particles may not directly interact with light or baryons, but they may decay or annihilate into "daily stuff" such as photons, electrons or positrons, and these do certainly yield an indirect signature which, in principle, could be detected with present-day technology. In particular, the LDM scenario makes several predictions on both particle and cosmological scales that, intriguingly, seem to be at least marginally consistent with current experimental and observational data.

1 Not so dark matter

Beyond its existence (and even that is sometimes called into question), very little is known about the nature of dark matter particles and their physical properties. Perhaps the first and most basic parameter is their mass, $m_{\rm dm}$, which determines to a great extent how they could interact amongst themselves, as well as with visible matter.

Weakly Interacting Massive Particles (WIMPs) are nowadays one of the most popular dark matter candidates. They are considerably heavier than ordinary particles ($m_{\rm dm} > 1$ GeV), and therefore provide an excellent candidate for Cold (i.e. non-relativistic) Dark Matter (CDM).

On the other extreme of the spectrum, the mass of Warm Dark Matter (WDM) particles is just of the order of a few keV. These candidates are mildly relativistic (their kinetic energy is comparable to their rest mass), and therefore they tend to erase small-scale perturbations of the primordial density field. For $m_{\rm dm} = 1$ keV and $\Omega_{\rm dm} = 0.25$, the free-streaming length would be about 300 kpc, quite comparable to galactic scales. Actually, it is indeed controversial whether the WDM scenario would be compatible with both the recent WMAP results and with

measurements of the matter power spectrum on small scales. Lighter, fully relativistic particles such as Hot Dark Matter (HDM) have even larger free-streaming lengths, and are thus well known not to constitute a significant fraction of the total matter density.

Light Dark Matter, with a mass $m_{\rm dm} \sim$ MeV, would also be non-relativistic, and therefore it would not have any noticeable influence on the power spectrum. What makes it interesting is that it may decay [1] or annihilate [2], producing electron-positron pairs and gamma-ray photons.

In very general terms, these processes can be written as

$$\mathrm{dm} \rightarrow \mathrm{something} \tag{1}$$

and

$$\mathrm{dm_A} + \mathrm{dm_B} \rightarrow \mathrm{something} \tag{2}$$

In the first case, a dark matter particle (whatever its mass) decays into something that can hit a detector, while in the second, a dark matter particle of type A interacts with another of type B (which may be equal to A or not). The number of somethings produced per unit time per unit volume would be given by

$$\dot{n} \propto n_{\rm dm} \Gamma_{\rm decay} \propto \rho_{\rm dm} \tag{3}$$

and

$$\dot{n} \propto n_{\rm A} n_{\rm B} \langle \sigma v \rangle \propto \rho_{\rm dm}^2 \tag{4}$$

respectively. The constants $\Gamma_{\rm decay}$ and $\langle \sigma v \rangle$ represent the decay rate and the thermal average of the interaction cross-section. As far as we are concerned, these quantities may be regarded as free parameters (actually, normalization constants) that relate the dark matter density to the emissivity. Therefore, we can obtain theoretical predictions of the expected flux at the Earth by specifying the density of the Milky Way dark matter halo and the physical properties of the dark matter particle. Or, on the other hand, one may use the (non) observed emission to constrain both components.

2 Reality

Compatibility with current (non) detections is indeed an obvious requirement for any dark matter candidate. The LDM scenario was actually built to be "invisible", in the sense that special care was taken to explain why such low-mass particles (or the mediators of their interactions) had not been detected in particle accelerators [2]. On the other hand, their decay or annihilation should not produce more gamma rays than observed from the galactic centre (see Section 4 below).

These requirements impose some constraints, more precisely upper or lower limits, on the model parameters. However, much more interesting results are obtained for the *positive* predictions, i.e. effects that should be detected if the model was true.

First, if these particles are to account for the cosmic dark matter, they must *exactly* satisfy the relic density criterion, i.e. $\Omega_{\rm dm} \sim 0.25$. This is not an upper or lower limit, but a very precise constraint that effectively reduces the number of free parameters by one.

Second, LDM particles have also been proposed to explain the positron excess detected at the centre of the Milky Way [3]. As will be shown below, reproducing both the observed intensity and morphology of the electron-positron annihilation line places strong constraints on the nature of LDM particles and their possible interactions [4].

Finally, the LDM scenario has also made several predictions on particle physics scales. In particular, the existence of new mediating bosons would affect the neutrino-quark cross-section, while mediating fermions would change the ratio between the anomalous magnetic moments of the electron and the muon. These effects might contribute to the so-called NuTeV anomaly and the discrepancy between different estimates of the fine structure constant, respectively [5]. It is

interesting to note that the model was not intentionally built to explain either phenomenon, and therefore both cases should be regarded as genuine predictions, made *before* the outcome of the experiment was known.

3 The 511 keV line

Perhaps the best-known success story of the LDM scenario is nevertheless the explanation of the 511 keV line from the galactic centre. This line was detected three decades ago, and it was soon identified with the annihilation of electron-positron pairs at rest. However, its recent observation by the SPI spectrometer onboard the INTEGRAL satellite revealed an extended morphology, which could be fairly well described by a Gaussian with ~ 10 degrees full-width half-maximum over the sky. Astrophysical sources could actually provide the number of positrons required to explain the observed intensity of the line, but they certainly have a hard time when it comes to the morphology [6].

LDM is an admitedly exotic alternative, but it provides a simple and elegant explanation. Furthermore, if the observed emission is indeed due to dark matter-generated positrons, it would put extremely srtringent constraints on both the density profile of the Milky Way and the physical properties of LDM particles.

A thorough comaprison with INTEGRAL/SPI data [4] shows that LDM particles should be self-annihilating rather than decaying. The required cross-section implies that, in order to satisfy the relic density criterion, both bosonic and fermionic mediators must exist. The LDM particle itself should be bosonic.

On the other hand, assuming that LDM is entirely responsible for the emission would imply that that the intensity of the 511 keV line would accurately map the density of the galactic dark matter halo. In particular, it would provide a very sensitive probe of the inner logarithmic slope of the density profile. For the best-fitting model, $\gamma = 1.03 \pm 0.04$, which is in excellent agreement with the result expected from cosmological numerical simulations. It must be said, though, that such a tiny error budget does not include the (obviously much larger) systematic error arising from several simplifying assumptions underlying the estimate, such as spherical symmetry or local annihilation.

4 Gamma rays

The particle mass $m_{\rm dm}$ is not tightly constrained but the 511 keV data alone. However, an upper limit can be obtained by demanding that the emission of gamma ray photons is below current observational limits.

Initially, two dark matter particles annihilate into an electron-positron pair. These particles will rapidly loose their energy and the positrons would eventually annihilate almost at rest with ambient electrons, yielding the 511 keV line. Gamma rays are emitted by the initially relativistic particles ($E \sim m_{\rm dm}c^2$) by means of several physical mechanisms.

The actual amount of radiation thus emitted is at present a rather controversial issue. While some authors [7] find $m_{\rm dm} < 20$ MeV (or even $m_{\rm dm} < 3$ MeV when in-flight annihilation is taken into account [8]) in order not to overproduce gamma rays, some others [4] find the more conservative limit $m_{\rm dm} < [30 - 100]$ MeV. The final result turns out to be fairly sensitive to the details of the emission mechanisms [9], and most importantly to the precise way in which the theoretical prediction is compared to the observational data.

5 Heat from cold dark matter

However, not all the energy of the electron-positron pair is radiated away in gamma-ray photons. Some fraction of it (which depends on the local conditions) is transferred to the surrounding baryonic gas.

On cosmic scales, the redshifted 511 keV line has been suggested to contribute to the diffuse soft gamma-ray background [10,11]. Several authors have also considered the effect of gas heating on the cosmic microwave background, as well as on the thermal history of the Universe [12,13].

On the scale of individual objects, annihilating LDM would effectively act as a "cosmic heater" at the centre of *every* dark matter halo, providing an energy source that is completely independent from (and perhaps larger than) feedback from star formation. This might have only a moderate effect in our Galaxy, but it can be dramatic in very small systems at high redshift (where it can inhibit gas cooling by ionizing it) or in galaxy clusters, where the dynamical time is shorter than the cooling time and therefore the gas must flow towards the centre (where the heating is dominant) as it cools. Simple energy arguments [14] show that the heat injected by annihilating dark matter particles into the baryonic gas phase would play a significant role on galaxy formation and evolution for 1 MeV $< m_{\rm dm} <$ 4 GeV.

6 Conclusions

The moral of this short story is twofold. First, an annihilating dark matter particle with $m_{\rm dm} \sim$ 10 MeV is so far perfectly compatible with all experimental evidence available, be it accelerator constraints, the relic dark matter density of the Universe, or the maximum gamma-ray radiation from the galactic centre. Most intriguingly, it is also compatible with several observations that are not so easily accomodated within the standard picture (at least, not without a considerable degree of fine-tuning), such as the morphology of the galactic 511 keV line, the NuTeV anomaly or the value of the anomalous magnetic moment of the muon. None of these results would actually *require* the existence of LDM particles, but it is somewhat surprising that none of them (not even in combination) are able to rule it out either.

Second, and more generally, it is now widely accepted that dark matter plays a crucial role in the formation of galaxies and cosmic structures. Here it is suggested that its influence might go well beyond gravitation. In particular, it can decay and annihilate into electrons, positrons, photons, or even more visible stuff if $m_{\rm dm}$ is large enough (although, as a rule of thumb, heavier candidates tend to be more "invisible"). Some of the signatures may be difficult to detect, but some others may be as obvious as determining whether a galaxy can form stars or not.

Acknowledgments

First and foremost, I would like to thank Céline Bœhm for convinving me to spend some time thinking about exotic light dark matter particles. Then I would also like to thank the organizers of the conference for such a nice and stimulating environment to talk about them, and last (but by no means least) to the European Union and the Astrophysikalisches Institut Potsdam for providing the necessary funding.

References

1. D. Hooper, and L.-T. Wang, *Phys. Rev.* D **70**, 063506 (2004).
2. C. Boehm and P. Fayet, *Nucl. Phys.* B **683**, 219 (2004)
3. C. Boehm, D. Hooper, J. Silk, M. Casse and J. Paul, *Phys. Rev. Lett.* **92**, 101301 (2004)
4. Y. Ascasibar, P. Jean, C. Boehm and J. Knödlseder, *MNRAS* **368**, 1695 (2006).

5. C. Boehm and Y, Ascasibar, *Phys. Rev.* D **70**, 115013 (2004).
6. J. Knödlseder *et al.*, *Astron. and Astrophys.* **441**, 513 (2005).
7. J. F. Beacom, N. F. Bell and G. Bertone, *Phys. Rev. Lett.* **94**, 171301 (2005)
8. J. F. Beacom and H. Yuksel, astro-ph/0512411 (2006)
9. C. Boehm and P. Uwer, hep-ph/0606058 (2006)
10. K. Ahn, and E. Komatsu, *Phys. Rev.* D **72**, 061301 (2005)
11. Y. Rasera *et al.*, *Phys. Rev.* D **73**, 103518 (2006)
12. M. Mapelli, A. Ferrara and E. Pierpaoli, *MNRAS* **in press**, astro-ph/0603237 (2006)
13. L. Zhang *et al.*, *Phys. Rev.* D **submitted**, astro-ph/0603425 (2006)
14. Y. Ascasibar and C. Boehm, *Phys. Rev. Lett.* **submitted**, (2006).

CAN WE FURTHER CONSTRAIN THE AXION?

M. BELTRÁN, J. GARCíA-BELLIDO
Departamento de Física Teórica C-XI, Universidad Autónoma de Madrid, Cantoblanco, 28049 Madrid, Spain

In this work we update the constraints on the QCD axion mass if the dominant production mechanism was via the coherent oscillations of the axion field around the minimum of its potential or via *misalignment angle*. We study the diffusion of the phase of the massles axion field during the de Sitter phase of the Universe and find that for some inflationary models, the distribution of the initial misalignement angle can populate all the available range $[-\pi, \pi]$. This fact has strong implications for the axionic relic density and isocurvature perturbations. Together with CMB, LSS and SNae observations we find tight constraints for the possible values of the mass of the QCD axion.

1 Introduction

For decades particle physicists have wondered why the QCD sector of the Standard Model does not violate the CP symmetry. This issue has been called the *Strong CP problem*. One of the most elegant solutions to this enigma was proposed in 1977 by R. Peccei and H. Quinn[3] and consists of making Θ a dynamical variable that would naturally go to zero in order to minimize its potential energy. In order to achieve this, a global chiral $U(1)_{\rm PQ}$ symmetry, namely the Peccei-Quinn symmetry, needs to be spontaneously broken at an unknown energy scale f_a. Soon after it was realised[4] that a (initially massless) pseudoscalar boson, called the *axion* should be present as a consequence of the symmetry breaking. The axion and the phase of the symmetry breaking field are related as:

$$a(\vec{x}) = \frac{f_a}{N}\Theta(\vec{x}) \tag{1}$$

Where N is the number of degenerate QCD vacua associated with the color anomaly of the PQ symmetry and will be taken to be 1 throught this work. Some time later, when the temperature of the universe lowers to $T \sim T_{\rm QCD} \simeq 200$MeV, instanton effects explicitly break the symmetry and generate a mass term for the axion. Its zero temperature value is:[5]

$$m_a = \frac{\sqrt{z}}{1+z}\frac{f_\pi m_\pi}{f_a} = 6.2\,\mu\text{eV}\left(\frac{10^{12}\text{ GeV}}{f_a}\right) \tag{2}$$

where $z = m_u/m_d \simeq 0.56$ is the mass ratio of up to down quarks. m_π and f_π are the pion mass and decay constant.

In the original axion model a physical meaning was given to the symmetry breaking scale by fixing it to the electroweak scale, at around 100 GeV, which was soon ruled out by direct searches[5]. In the currently accepted *invisible axion* model, the scale f_a is in principle arbitrary, and well above the electroweak scale. The axion coupling to matter is weak enough to pass

undetected. Such a field, however, acts like a weakly interacting massive particle and could constitute today's dark matter.

2 Axion production mechanisms

2.1 Thermal production

If the coupling of axions to other species is strong enough then it is possible that an axionic thermal population existed at higher energies. If this is the case a relic density of thermally generated axions would be present nowadays. Their contribution to the matter density of the universe today is:[7]

$$\Omega_{\rm a}^{\rm TH}h^2 = \frac{m_a}{130\,{\rm eV}}\left(\frac{10}{g_F}\right) \tag{3}$$

In order to have a stable population of thermal axions m_a should be at least of order 10^{-3} eV.[7] However, this bound is forbidden by astrophysical data which exclude a mass range of $0.01{\rm eV} < {\rm m_a} < 200$ keV for the QCD axion. [5,8]

2.2 Axionic string decay

If the scale f_a is below the reheating temperature of the universe after inflation, axionic cosmic strings would have formed after the second symmetry breaking. These strings typically decay into axions. Different groups have studied their relic energy density finding an agreement within an order of magnitude:[9]

$$\Omega_{\rm a}^{\rm str}h^2 \simeq 4\Delta_{\rm QCD}\left(\frac{1\mu{\rm eV}}{m_a}\right)^{1.18} \tag{4}$$

where $\Delta_{\rm QCD} = 3^{\pm 1}$ takes into account all the uncertainties in the QCD phase transition.

2.3 Misalignment angle

When the PQ symmetry is explicitly broken, the phase of the field Θ may or may not be at the minimum of its potential. We call Θ_1, the initial value of the massless phase, the misalignment angle.

If Θ_1 is not exactly equal to zero, the sudden appearance of a mass term generates an extra potential energy term. As soon as the expansion of the universe lowers to $3H \simeq m_a(T)$ the field starts rolling down towards the minimum, starting from a height in the potential determined by Θ_1. This is made explicit in the misalignment angle relic density contribution expression:[10]

$$\Omega_{\rm a}h^2 \simeq 7.24 g_{*,1}^{-5/12}\langle\Theta_1^2\rangle\left(\frac{200{\rm MeV}}{\Lambda_{\rm QCD}}\right)^{\frac{3}{4}}\left(\frac{1\mu{\rm eV}}{m_a}\right)^{\frac{7}{6}} \tag{5}$$

with $\Omega_{\rm a} = \rho_a/\rho_c = \rho_a\frac{8\pi G}{3H_0^2}$ and $g_{*,1}$ is the number of relativistic degrees of freedom when the axion aquires its mass.

The value of $\langle\Theta_1^2\rangle$

The rms of the initial misalignment angle is not given by any field theory, however its value should be inferred from some inflationary and statistical remarks.

Assuming that the Peccei-Quinn symmetry was broken at an energy above the scale of inflation, the de Sitter quantum fluctuations need to be considered and they induce a stochastic diffusion of the axion away from the symmetric value $\theta = 0$.

The probability $\mathcal{P}(\theta, N_e)$ of finding a certain value θ at a time given by the number of e-folds N_e satisfies a Fokker-Planck equation with diffusion coefficient $D \equiv H/(2\pi f_a)$:

$$\frac{\partial \mathcal{P}}{\partial N_e} = \frac{1}{2} D^2 \frac{\partial^2 \mathcal{P}}{\partial \theta^2} \implies \mathcal{P}(\theta, N_e) = \frac{1}{\sqrt{2\pi D^2 N_e}} \exp\left[-\frac{(\theta - \theta_1)^2}{2D^2 N_e} \right] . \tag{6}$$

A given inflationary domain will have a particular initial value Θ_1. After a few e-folds of inflation, the root mean square distance from Θ_1 will be

$$\langle \Theta_1^2 \rangle^{1/2} = \langle (\Theta - \Theta_1)^2 \rangle^{1/2} = \frac{H}{2\pi f_a} \times \sqrt{N_e} . \tag{7}$$

The observed homogeneity and flatness of the present cosmological horizon require around 70 e-folds. However, inflation may have started many more e-folds before and the Brownian diffusion of the axion could be completed by the time inflation ended in our patch. The values of the misalignment angle *within our present horizon* could be evenly distributed in the range $[-\pi, \pi]$. Thus, when QCD instanton effects generate a mass for the axion, its initial value is washed out and the mean energy density of the axion is proportional to $\frac{\pi^2}{3}$.

3 Isocurvature modes

Since the axion is very weakly coupled it may not have participated of the reheating of the universe at the end of inflation and thus its fluctuations on large scales are necessarily isocurvature in nature. This imposes strong constrains since we have no evidence of such a contribution in the CMB anisotropies. An upper bound can be imposed on the amount of isocurvature present in the CMB and it is parametrized as $f_{\rm iso}$. It is related to f_a as:

$$f_{\rm iso} = \frac{(\delta T/T)_{\rm iso}}{(\delta T/T)_{\rm ad}} = \sqrt{\frac{\alpha}{1-\alpha}} \simeq 4.6 \times 10^4 \langle \Theta_1^2 \rangle^{1/2} \left(\frac{f_a}{10^{10}\,\mathrm{GeV}} \right)^{7/3} \langle \mathcal{S}_a^2 \rangle^{1/2} \tag{8}$$

4 Analysis and results

We want to constrain the mass of the axion generated *before inflation* and via the misalignment angle production. In order to do this, we sampled the likelihood distribution from a six dimensional parameter space with the following sets of data: CMB data, coming from WMAP (TT and TE spectra), VSA, CBI and ACBAR; large scale structure data, from the 2dFGRS and the SDSS catalogue; and the gold-supernovae data.[11,12,13] For this, we used our modified version of CosmoMC.[14] We find the following values for the parameters relevant for this analysis:

$$\alpha < 0.06 \text{ at } 95\% \text{ c.l; and } \Omega_{\rm CDM} h^2 = 0.12 \pm 0.03 \text{ at } 95\% \text{ c.l} \tag{9}$$

and used them to constrain the axionic window in the $M_{\rm inf}$ vs f_a parameter space.

4.1 Results: Chaotic Inflation $m^2\phi^2$

We studied the diffusion of the phase inside a chaotic inflationary model, and found that it reaches total diffusion for inflationary scales $H_{\rm inf} > 27.4 \times 10^{12}$GeV. The predicted inflationary scale for this model is $H_{\rm inf} \simeq 10^{14}$. Since we assume $f_a > H_{\rm inf}$ we can write eq. (5) as:

$$\Omega_{\rm a} h^2 \simeq 1.6 \left(\frac{f_a}{10^{12}\mathrm{GeV}} \right)^{\frac{7}{6}} \tag{10}$$

for the whole range in f_a.

We find then that the bounds on $\Omega_{\rm CDM} h^2$ cannot be reconciled with the existence of a population of misalignment angle axions. Results are sketched on Figure 1.

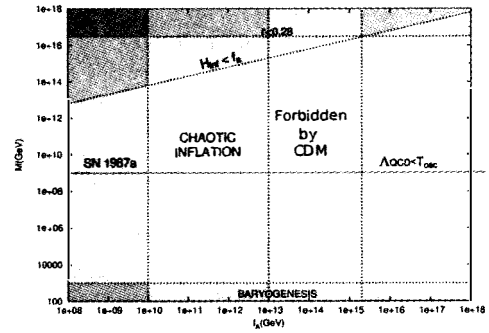

Figure 1: Bounds on the $M_{\rm inf} - f_a$ plane for chaotic inflation with quadratic potential. Prior bounds on $M_{\rm inf}$ the inflationary scale come from r and baryogenesis. Those on f_a come from astrophysical bounds and from avoiding damping of the axion oscillations at the QCD scale ($3H(T_{\rm QCD}) < m_a$). We also require $T_{\rm reh} < f_a$ but reheating is so unefficient for chaotic models that this bound is not constraining at all.

4.2 Results: Hybrid Inflation

We find that for hybrid models there exists an allowed region of values in the plane $M_{\rm inf} - f_a$. However it is tightly constrained by both the cold dark matter energy density and the isocurvature contribution.

5 Conclusions

We have shown that, if the Peccei-Quinn symmetry breaking occurred before inflation, further considerations on the diffusion of the phase of the massless symmetry breaking field lead to tight constrains for the mass of the axion. In particular, we see that data is not compatible with an axion produced via misalignment angle if inflation was chaotic, as suggested by the latest WMAP data release. This conclusion does not exclude the existence of the QCD axion but narrows the possibility of detecting it as a considerable portion of the cold dark matter.

Acknowledgments

We would like to thank Julien Lesgourgues for useful comments and discussion and generous help with the code. The work of MB was supported by the "Consejería de Educación de la Comunidad de Madrid- FPI program". See full paper for further acknowledgements and references.

References

1. V. Baluni, *Phys. Rev.* D19 (1979)2227; R. J. Crewther, P. Di Vecchia, G. Veneziano and E. Witten, Phys. Lett. B **88** (1979) 123 [Erratum-ibid. B **91** (1980) 487].
2. N. F. Ramsey. Phys. Rept. **43** (1978) 409: I. S. Altarev *et al.*, Phys. Lett. B **276** (1992) 242.
3. R. D. Peccei and H. Quinn. Phys. Rev. Lett. **38** (1977) 1440
4. S. Weinberg, Phys. Rev. Lett. **40** (1978) 223; F. Wilczek, Phys. Rev. Lett. **40** (1978) 279.
5. Axion reviews include: J.E. Kim, Phys. Rep. **150** (1987) 1; H.-Y. Cheng, Phys. Rep. **158** (1988) 1; R.D. Peccei, in 'CP Violation', ed. by C. Jarlskog, World Scientific Publ., 1989, pp 503-551; G.G. Raffelt, Phys. Rep. **198** (1990) 1.

6. W.A. Bardeen and S.-H.H. Tye, Phys. Lett. **B74** (1978) 229; J. Ellis and M.K. Gaillard, Nucl. Phys. **B150** (1979) 141; T.W. Donnelly et al., Phys. Rev. **D18** (1978) 1607; D.B. Kaplan, Nucl. Phys. **B260** (1985) 215; M. Srednicki, Nucl. Phys. **B260** (1985) 689; P. Sikivie, in 'Cosmology and Particle Physics', ed. E. Alvarez et al., World Scientific, 1987, pp 143-169.
7. E. W. Kolb and M. S. Turner, "The Early Universe", Addison-Weseley (1990).
8. S. Hannestad, A. Mirizzi and G. Raffelt, JCAP **0507** (2005) 002.
9. D. Harari and P. Sikivie, Phys. Lett. **B195** (1987) 361; R.A. Battye and E.P.S. Shellard, Nucl. Phys. **B423** (1994) 260, Phys. Rev. Lett. **73** (1994) 2954 and erratum-ibid. **76** (1996) 2203.
10. M. Beltrán and J. García-Bellido, in preparation.
11. L. Bennett *et al.* [WMAP Collaboration],Astrophys. J. Suppl. **148**, 1 (2003); D. N. Spergel *et al.*,Astrophys. J. Suppl. **148**, 175 (2003); H. V. Peiris *et al.*,Astrophys. J. Suppl. **148**, 213 (2003);C. Dickinson *et al.*,Mon. Not. Roy. Astron. Soc. **353**, 732 (2004); T. J. Pearson *et al.* [CBI Collaboration],Astrophys. J. **591**, 556 (2003); C. l. Kuo *et al.* [ACBAR Collaboration],Astrophys. J. **600**, 32 (2004).
12. J. A. Peacock *et al.* [2dFGRS Collaboration],Nature **410**, 169 (2001); M. Tegmark *et al.* [SDSS Collaboration],Astrophys. J. **606**, 702 (2004).
13. A. G. Riess *et al.* [Supernova Search Team Collaboration],Astrophys. J. **607**, 665 (2004).
14. A. Lewis and S. Bridle,Phys. Rev. D **66**, 103511 (2002);

Mimicking phantom behaviour on the brane

Mariam Bouhmadi-López
Institute of Cosmology and Gravitation, University of Portsmouth, Mercantile House, Hampshire Terrace, Portsmouth PO1 2EG, UK

A de Sitter space-time can be seen as a boundary between quintessence-like behaviour and phantom-like behaviour. We show that in a 5D dilatonic bulk, where the dilaton has an exponential potential, with an induced gravity term on the brane, whose matter content corresponds only to vacuum energy, the brane undergoes a phantom-like stage where it faces a curvature singularity in its infinite future. The singularity can be interpreted as the "big rip" singularity pushed towards an infinite future cosmic time. The phantom-like behaviour on the brane occurs without violating the null energy condition. There is another solution where the brane can undergo an early-epoch (transient) inflationary phase induced by the dilaton field.

1 Introduction

A plethora of different theoretical models has been proposed in order to explain the late-time acceleration of the universe as suggested by observations of Supernovae type Ia (SNIa), the cosmic microwave background anisotropies and the large scale structure (see for example [1]). A possible explanation for this evolution is the usual vacuum energy represented by a cosmological constant providing a negative pressure [1]. However, the observational value of Λ is about 120 orders of magnitude smaller than that established from field theory methods.

So far, alternative phenomenological models have been proposed to describe the late-time acceleration of the universe. One approach is to consider an effective dark energy component in the energy momentum tensor [1] like in phantom energy models [2,3,4]. In these models the null energy condition is not satisfied. Hence, the energy density is an increasing function of the scale factor in an expanding Friedmann-Lemaître-Robertson-Walker (FLRW) universe. This may lead to the occurrence of a big rip singularity in the future evolution of a phantom energy dominated universe [2,3,4].

An alternative approach to account for the late-time acceleration of the universe is to consider a generalised Einstein theory of gravity like brane-world models (for reviews see [5]) where the observable four-dimensional (4D) universe is a brane (hyper-surface) embedded in a higher-dimensional space (bulk). For example, the Dvali, Gabadadze and Porrati (DGP) model [6] has a self-accelerating solution at late-time which is asymptotically de Sitter [7]. This model corresponds to a 5D induced gravity brane-world model [7,8]. An induced gravity brane-world model has two solutions (depending on the embedding of the brane in the bulk [7]). One of these solutions (the positive branch) can account for the late-time evolution of the universe [7]. The other solution (the negative branch) can describe the early-time evolution of the universe [8].

We will show that in a 5D dilatonic bulk with an induced gravity term on the brane, whose matter content corresponds only to vacuum energy, the positive branch solution undergoes a

phantom-like stage without violating the null energy condition. On the other hand, the negative branch solution can undergo an early-epoch (transient) inflationary phase induced by the dilaton field.

2 The model

We consider a 5D dilatonic solution obtained by Feinstein et al [10,11] *without an induced gravity term on the brane.* The 5D dilatonic solution reads [11]

$$ds_5^2 = \frac{1}{\xi^2} r^{2/3(k^2-3)} dr^2 + r^2(-dt^2 + \gamma_{ij} dx^i dx^j), \tag{1}$$

where γ_{ij} is a 3D spatially flat metric. The bulk potential corresponds to

$$V(\phi) = \Lambda \exp[-(2/3)k\phi]. \tag{2}$$

The parameters k and ξ in Eq. (1) measure the magnitude of the 5D cosmological constant Λ

$$\Lambda = \frac{1}{2}(k^2 - 12)\xi^2. \tag{3}$$

The 5D scalar field scales logarithmically with the radial coordinate r [11]

$$\phi = k \log(r). \tag{4}$$

¿From now on, We will consider only the case $k > 0$ (the main conclusions of the paper does not depend on the sign of k); i.e. the scalar field is a growing function of the coordinate r.

We consider an empty homogeneous and isotropic brane (filled only with the brane tension $\lambda(\phi)$) embedded in the previous 5D dilatonic solution Eq. (1) and whose trajectory on the bulk is described by the following parametrisation

$$t = t(\tau), \quad r = a(\tau), \quad x_i = constant, \quad i = 1 \ldots 3, \tag{5}$$

where τ corresponds to the proper time of the brane. Then the brane metric reads

$$ds_4^2 = g_{\mu\nu}\, dx^\mu dx^\nu = -d\tau^2 + a^2(\tau)\gamma_{ij} dx^i dx^j. \tag{6}$$

For an induced gravity brane-world model [7,8], there are two physical ways of embedding the brane on the bulk when a $\mathbb{Z}_2$-symmetry across the brane is assumed. We will refer to a brane as the positive branch when the location of the brane $r = a(\tau)$ is such that

$$ds_5^2 = \frac{1}{\xi^2} r^{2/3(k^2-3)} dr^2 + r^2(-dt^2 + \gamma_{ij} dx^i dx^j), \quad r > a(\tau). \tag{7}$$

On the other hand, we will refer to a brane as the negative branch when the location of the brane $r = a(\tau)$ is such that

$$ds_5^2 = \frac{1}{\xi^2} r^{2/3(k^2-3)} dr^2 + r^2(-dt^2 + \gamma_{ij} dx^i dx^j), \quad r < a(\tau). \tag{8}$$

The Israel junction condition at the brane [9] describes the cosmological evolution of the brane through the modified Friedmann equation

$$H^2 = \frac{1}{6\alpha}\left\{\lambda + \rho + \frac{3}{\kappa_5^4 \alpha}\left[1 + \epsilon\sqrt{1 + 4\kappa_5^4 \alpha^2 \xi^2 a^{-2k^2/3} + \frac{2}{3}\kappa_5^4 \alpha \lambda}\right]\right\}, \tag{9}$$

where $\epsilon = \pm 1$ and α is a positive parameter which measures the strength of the induced gravity term and has dimensions of mass squared. From now on, $\epsilon = 1, -1$ corresponds to the positive and negative branches, respectively. On the other hand, the junction condition of the scalar field at the brane [9] constrains the brane tension $\lambda(\phi)$

$$k\sqrt{\xi^2 a^{-\frac{2}{3}k^2} + H^2} = \epsilon \frac{\kappa_5^2}{2}\frac{d\lambda}{d\phi}. \tag{10}$$

3 Positive branch and phantom-like behaviour

In the positive branch ($\epsilon = 1$) and for a vacuum brane, the brane tension is a growing function of the scalar field or equivalently of the scale factor of the brane. This can be easily seen from Eqs. (4) and (10) [a]. We would like to stress that in a standard 4D FLRW expanding universe filled with a phantom energy component, the energy density behaves in this way too: the energy density is a growing function of the scale factor [2,3].

The Hubble parameter H is an increasing function of the scale factor. Consequently, the brane is super-inflating (the time derivative of H is positive on the brane) as the brane expands and moves in the bulk. At high energy (small values of the scale factor), H reaches a constant positive value. Consequently, there is no big bang singularity on the brane. Indeed, the brane geometry is asymptotically de Sitter in the past. On the other hand, at very large values of the scale factor H diverges and there is a singularity in the future evolution of the brane. The divergence of the Hubble parameter for very large values of the scale factor might point out the existence of a big rip singularity in the future evolution of the brane; i.e. the scale factor and Hubble parameter blow up in a finite cosmic time in the future evolution of the brane. However, there is no big rip singularity on the future evolution of the brane because at large value of the scale factor

$$H \sim \frac{k^2}{\kappa_5^2 \alpha} \ln(a), \tag{11}$$

and, consequently, the Hubble rate does not grow as fast as in phantom energy models with a constant equation of state where a big rip singularity takes place on the future evolution of a homogeneous and isotropic universe [2,3]. Indeed, the singularity on the brane occurs in an infinite future cosmic time where the scale factor and the Hubble parameter diverge. This kind of singularity can be interpreted as a "big rip" pushed towards an infinite cosmic time of the brane. We would like to stress that this singularity appears only on the brane and not in the bulk. Indeed, large values of the scale factor correspond to large values of the extra coordinate r (where the bulk is asymptotically flat) and the only bulk singularity is located at $r = 0$.

4 Negative branch and early inflation

In the negative branch ($\epsilon = -1$) and for a vacuum brane, the brane tension is a decreasing function of the scalar field or equivalently of the scale factor of the brane. This can be easily seen from Eqs. (4) and (10) [b]. At high energy (small values of the scale factor), the brane tension reaches infinite positive values. On the other hand, for very large value of the scale factor the brane tension vanishes.

The Hubble parameter is a decreasing function of the scale factor. At high energy, H reaches a constant positive value. Consequently, there is no big bang singularity on the brane. On the other hand, at very large values of the scale factor, the Hubble parameter vanishes (the brane is asymptotically Minkowski in the future). Consequently, unlike the positive branch, the negative branch is never super-inflating, although the negative branch always undergoes an inflationary period.

The brane behaves in two different ways depending on the values acquired by k^2. For $k^2 \leq 3$, the brane is eternally inflating. A similar behaviour was found in [11] in a dilatonic brane-world model without an induced gravity term. On the other hand, the brane undergoes an initial stage of inflation when $k^2 > 3$. Later on the brane starts decelerating. This second behaviour was not

[a] The same property can be shown by solving analytically the constraint equation (10). We refer the reader to [12] for more details.

[b] The constraint equation (10) can also be solve analytically in this case [12] and it can be explicitly shown that the brane tension decreases as the brane expands.

found in [11] for a vacuum brane. Then, the inclusion of an induced gravity term on a dilatonic brane-world model with an exponential potential on the bulk allows inflation to take place in the negative branch, even if it does not for a vanishing induced gravity parameter (for $k^2 > 3$). This behaviour has some similarity with steep inflation [13], where high energy corrections to the Friedmann equation in RS scenario [5] permit an inflationary evolution of the brane with potentials too steep to sustain it in the standard 4D case, although the inflationary scenario introduced by Copeland et al in [13] is supported by an inflaton confined in the brane while in our model inflation on the brane is induced by a dilaton field on the bulk.

5 Conclusions

We study the behaviour of a vacuum dilatonic brane-world model; i.e. the matter content of the brane is specified by the brane tension, with an induced gravity term on the brane with a constant induced gravity parameter α. We assume a $\mathbb{Z}_2$-symmetry across the brane. The dilatonic potential is an exponential function of the bulk scalar field.

In the vacuum positive branch, the brane tension is a growing function of the scale factor and, consequently, mimics the behaviour of a phantom energy component on the brane. However, the brane tension does not violate the null energy condition. The expansion of the brane is super-inflationary; i.e. the Hubble parameter is a growing function of the cosmic time. The brane faces a curvature singularity in its future evolution, where the Hubble parameter, brane tension and scale factor diverge. The singularity happens in an infinite cosmic time. Therefore, the singularity can be interpreted as a "big rip" singularity pushed towards an infinite future cosmic time.

In the vacuum negative branch, the brane tension is a decreasing function of the scale factor. Unlike the positive branch, the branch is not super-inflating. However, it always undergoes an early inflationary expansion. The inflationary expansion can be eternal ($k^2 \leq 3$) or transient ($k^2 > 3$).

Acknowledgments

MBL is supported by the Spanish Ministry of Education, Culture and Sport (MECD).

References

1. E. J. Copeland, M. Sami and S. Tsujikawa, arXiv:hep-th/0603057.
2. R. R. Caldwell, *Phys. Lett.* B **545**, 23 (2002); R. R. Caldwell, M. Kamionkowski and N. N. Weinberg, *Phys. Rev. Lett.* **91**, 071301 (2003).
3. M. Bouhmadi-López and J. A. Jiménez Madrid, *JCAP*, **0505**, 005 (2005).
4. S. Nojiri, S. D. Odintsov and S. Tsujikawa, *Phys. Rev.* D **71**, 063004 (2005).
5. R. Maartens, *Liv. Rev. Rel.* **7**, 7 (2004); A. Lue, *Phys. Rept.* **423**, 1 (2006).
6. G. R. Dvali, G. Gabadadze and M. Porrati, *Phys. Lett.* B **485**, 208 (2000).
7. C. Deffayet, *Phys. Lett.* B **502**, 199 (2001).
8. M. Bouhmadi-López and D. Wands, *Phys. Rev.* D **71**, 024010 (2005); M. Bouhmadi-López, R. Maartens and D. Wands, *Phys. Rev.* D **70**, 123519 (2004).
9. K. i. Maeda and D. Wands, *Phys. Rev.* D **62**, 124009 (2000).
10. A. Feinstein, K. E. Kunze and M. A. Vazquez-Mozo, *Phys. Rev.* D **64**, 084015 (2001).
11. K. E. Kunze and M. A. Vazquez-Mozo, *Phys. Rev.* D **65**, 044002 (2002).
12. M. Bouhmadi-López, arXiv:astro-ph/0512124.
13. E. J. Copeland, A. R. Liddle and J. E. Lidsey, *Phys. Rev.* D **64**, 023509 (2001).

STRINGS, BRANES AND COSMOLOGY: WHAT CAN WE HOPE TO LEARN?

C.P. BURGESS
Department of Physics & Astronomy, McMaster University
1280 Main Street West, Hamilton, Ontario, Canada L8S 4M1
and
Perimeter Institute for Theoretical Physics
31 Caroline Street North, Waterloo, Ontario, Canada N2L 2Y5.

This article briefly summarizes the motivations for — and recent progress in — searching for cosmological configurations within string theory, with a focus on how much we might reasonably hope to learn about fundamental physics from precision cosmological measurements.

1 Why String Cosmology?

The last few years have seen a number of scientific gatherings which have brought together string theorists and cosmologists in a way which would have been unheard-of only a few years ago, stimulated by a relatively recent convergence of interest between these two fields. This convergence is interesting in its own right, promising as it does to relate the laws of nature at the smallest of distances to the behaviour of the universe as a whole, as seen writ large across the sky by contemporary cosmologists. But the possibility that there should be such a connection also contains within itself a puzzle, to do with why it is possible for these two fields usefully to inform one another at all.

1.1 Why doesn't string theory decouple from cosmology?

What is so puzzling about a connection between string theory and cosmology? The puzzle inherent in this field is intimately tied up with its promise: the potential it holds out for a connection between the workings of nature on the smallest of distance scales and the properties of the universe at large. Such a connection is intrinsically puzzling because of a fundamental property of nature, which might be called the *Principle of Decoupling*.

> *The Principle of Decoupling:* Although the world comes to us in many scales, these scales can each be understood on their own terms since their properties do not depend strongly on all of the details of the physics of other scales.

For example, we know that atoms are built from constituents (electrons and nuclei) which are much smaller than the atoms themselves, and some of these constituents (nuclei) themselves consist of still smaller things like quarks and gluons. But a detailed understanding of atomic properties (*i.e.* the spectra and chemistry of atoms) depends only on gross properties of their constituents (like the nuclear mass and charge). In particular, it does *not* depend on any of the

complicated details of how they are constructed from their own constituents. Historically, this is why it was possible to understand atomic physics before having a complete understanding of nuclear physics. Indeed, this property of nature could be argued to be an important part of the reason why Science is possible at all, since it shows why we can hope to understand part of what is going on in nature without having to understand everything at once.

This gives rise to the puzzle: given the decoupling of scales in nature, how can cosmology — the understanding of the properties and behaviour of the largest objects known — possibly depend on the details of string theory — our best candidate for a theory of nature at the very smallest of scales? After all, we don't have meetings at which condensed-matter physicists or atomic physicists expect to learn much that is useful from string theorists. These meetings don't take place because string theory is likely to get right all of the details of atomic and condensed matter physics provided only that it predicts the existence of electrons and nuclei, and it gets right the laws of electromagnetism (as expressed by QED). For this reason there is little to be gained by comparing string predictions with detailed measurements of condensed matter phenomena.

There seem to be three reasons why string theory can usefully inform cosmology, and vice versa.

1. *Access by cosmology to very high energies:* This is the traditional reason for the decades-old development of a fruitful interface between astrophysics and particle physics. Some astronomical systems (like active galactic nuclei or ultra-high-energy cosmic rays) can involve physical processes involving astronomically large energies, whose understanding requires knowing how high-energy elementary particles behave.

   The same can be true for cosmology because we know that the observable early universe is well described by the Hot Big Bang model, but only if special initial conditions (homogeneity, isotropy, flatness, and a spectrum of primordial density fluctuations) are chosen before the earliest epoch (nucleosynthesis) for which we have direct observational evidence. Although nuclear physics seems to suffice for understanding nucleosynthesis, particle physics is required in order to understand the origin of the special initial conditions. In particular, the extremely high energies associated with string theory are very likely to be important if these initial conditions are explained by a very early epoch of inflationary universal expansion.[1]

2. *Dependence on UV-sensitive properties:* Cosmology is unusual because the vast majority of cosmological models rely for their phenomenological success on properties which are notoriously sensitive to microscopic details. For example specific models of Dark Energy [2] or inflation [3,4] often depend on the existence of very shallow scalar potentials which give rise to extremely light scalar masses, $M_\phi \leq H$, where H is the Hubble scale at the epoch of interest. But scalar masses are famously difficult to keep from getting large contributions when the short-distance (UV) sector of the theory is integrated out. To take an extreme case, most Dark Energy models require $M_\phi < 10^{-33}$ eV, while it is difficult to make the contribution to M_ϕ due integrating out a particle of mass m smaller than $\delta M_\phi \sim m^2/M_p$, where $M_p = (8\pi G)^{-1/2} \sim 10^{18}$ GeV. This correction is already larger than M_ϕ for $m > 10^{-3}$ eV, and so is many orders of magnitude too large even for the electron, for which $m_e \sim 5 \times 10^5$ eV.

3. *Difficulty of modifying gravity on long distance scales:* Much of the evidence for the existence of exotic matter (like the scalar particles just mentioned) in cosmology is based on inferences which assume General Relativity is the correct theory of gravity. But General Relativity has never been experimentally tested over distances as large as required for cosmological applications, and this observation has led many people to try to avoid the

need for exotic matter by instead appropriately modifying gravity at long distances. Some phenomenological success can be achieved along these lines, provided one is judicious in the modifications which are made.

However, what this line of argument misses is that it is *extremely* difficult to embed any modification of gravity at long distances into any kind of a sensible theory of short-distance physics. This is because we now know that General Relativity is the most general kind of interaction which a massless spin-two particle can have which is consistent with very general principles (like special relativity, stability and unitarity), and as a result we have a very general understanding as to *why* General Relativity provides a good description of gravity.[5,6] So far as is known, it seems very likely that *any* sensible theory of gravity must look in the far infrared (IR) like a combination of scalar fields and gauge fields interacting with General Relativity, and there is no compelling theory which is both consistent with measurements in the solar system and in astrophysics and yet also observably different from gravity at very long distances in a phenomenologically successful way.[7] This indicates that consistency issues at short distances provide an important clue as to what is possible to entertain as a description of nature over long distances.[a]

For the above reasons there is at present an unusual opportunity at the interface between cosmology and microphysics, which provides a real chance for learning something important about nature. The opportunity arises because the very success of cosmological models relies in detail on properties (like shallow scalar potentials) which we know to be extremely sensitive to the details of short-distance physics. Furthermore, it is not generic that these microscopic details provide phenomenologically successful models for cosmology. The condition that a model *both* provide successful phenomenology *and* be sensibly embedded into microscopic physics is very strong, making the finding of examples which do both a worthwhile exercise. Furthermore, as we now argue, there is an opportunity for information to flow in *both* directions, with potential theoretical insights for both string theory and cosmology.

1.2 What is useful for cosmologists

We first ask how short-distance physics can be useful for practical cosmologists interested in understanding observational data. The utility here comes from the observation that cosmological observations (marvellously precise though they are) are likely to remain inadequate into the foreseeable future for unambiguously differentiating amongst the many competing phenomenological cosmological models.[9]

However cosmological observations provide only part of the clues as to what is going one. We must also weed out those models which do not make sense when embedded into more microscopic theories, and it is the interplay between these two kinds of constraints which makes the exercise theoretically constrained. In practice this means ruthlessly rejecting those models of cosmology which predict low-energy ghosts, instabilities or violations of the experimental tests of gravity within the solar system or for binary pulsars. Such a restriction dramatically reduces the number of models which require more detailed scrutiny.

1.3 What is useful for string theorists

The information exchange between string theory and cosmology is likely also to be of use to string theorists, for the following reason. String theory involves an enormous number of degrees of freedom and so may be expected to enjoy an equally enormous number of solutions. A precise

[a] It must be emphasized that because these issues deal with *long-distance* problems, they may be unambiguously addressed using current knowledge — using standard Effective Field Theory techniques [8] — and in particular need not await an eventual 'final' theory of Quantum Gravity, as is sometimes argued.

counting of how many solutions there might be requires an understanding the form of the potential which stabilizes the many fields of the theory, but recent progress [10,11,12] in computing this potential for some types of string vacua indicates there to be more than 10^{100} such vacua. A central question for string theorists is to find which solutions can describe the universe around us, and to understand why the universe should end up being described by these solutions rather than by the many other possible solutions.

Cosmology may help this process in two ways. First, cosmology can help to *find* string vacua with acceptable phenomenology. It can do so because the direct examination of various vacua is impractical, given the likely enormous number of solutions which exist. What can be useful when looking for potentially realistic vacua, however, is the identification of low-energy *modules* which capture one or another of the phenomenologically desirable features required to describe our low-energy world. For instance, these could include modules for ensuring an acceptable particle spectrum; a mechanism for understanding the electroweak hierarchy, and so on. Some of these modules can involve cosmology, such as by demanding the existence of an early inflationary phase; a candidate for dark matter; or an understanding of the observed features of the dark energy density.

The second useful role cosmology might play for string theory is by providing potentially measurable signals for comparison with experiments. Recall that the existence of an enormous number of vacua makes the extraction of a theory's predictions much more complicated, since the properties of each vacuum provide in principle a separate set of predictions for what might be found around us. The most likely way in which such a theory will be tested in practice is through its statements about the *correlations* of the properties to be found about any particular vacuum, along the lines of: "Any vacuum which has property X must also have property Y". For instance, X might be the statement "contains the standard model gauge group, and Y might be "has 3 generations of chiral fermions".

Cosmology can usefully contribute to the kinds of statements, X and Y, since it is plausible that our understanding of why the universe is the way it is now will depend on our understanding of where it has been in its past. For instance X or Y might include "has at least 60 e-foldings of inflation", or "has such-and-such a relic abundance of cosmic strings". In particular, one can hope that the class of string solutions which give a reasonable description of cosmology might also lead to a restricted class of particle physics properties to be compared with laboratory experiments.

2 Branes and naturalness

An important way in which string theory has influenced thinking about more phenomenological issues can be traced to the discovery of branes.[13] This discovery has radically changed the kinds of low-energy implications which the vacua of the theory can have, and this has in turn led to a number of important new insights into the nature of the various 'naturalness' problems which arise within the effective theories relevant for phenomenology.

2.1 Why are branes important?

The main reason why branes have provided new insights into low-energy naturalness problems is because the study of the low-energy properties of vacua containing branes has identified a number of important (and overly restrictive) hidden assumptions which had been hitherto made regarding what is possible for the low-energy limit of a sensible high-energy theory.

The identification of such assumptions is crucial for naturalness problems, because these problems in essence amount to statements like: "a broad class of low-energy theories (obtained by integrating out heavy modes in some fundamental theory) have a generic property X, which

is not observed to be true in nature." Property X here might be: "has a Higgs mass similar in size to the Planck mass", or "has a large cosmological constant." It is crucial to know when these unwanted but generic properties depend on hidden assumptions, since these may prove to be unwarranted and so may be the loopholes through which nature evades the problem.

For instance, a very important hidden assumption which the study of branes has identified is the assumption that all interactions 'see' the same number of spacetime dimensions. This assumption is violated, for instance, if particles like photons arise from open strings, which at low energies are localized on the branes on which such strings must end. In this case photons must propagate only within the dimensions spanned by the branes, while gravitons can move throughout the full extra-dimensional environment. Among the suggestive new insights which have emerged in this way are:

1. *A Lower String Scale:* The string scale need not be close to the Planck scale,[14] opening up interesting new possibilities for understanding the electroweak hierarchy with the string scale being associated with the intermediate scale [15] or the TeV scale.[16]

2. *Large Extra Dimensions:* A possibility which is related to (but not identical with) having the string scale at the TeV scale is that extra dimensions can be much larger than had been thought, being potentially as large as micron size.[16]

3. *Decoupling 4D Vacuum Energy from 4D Curvature:* In four dimensions a large vacuum energy is identical with a large cosmological constant, and so also with a large 4D curvature. (This connection underlies the cosmological constant problem since the curvature is observed to be small while the vacuum energy is expected to be large.) Higher-dimensional brane solutions show that this connection need not survive to higher dimensions, where large 4D energies can co-exist with flat 4D geometries.[17,18]

4. *Non-locality:* Locality is normally automatically ensured for effective theories because these theories are defined by integrating out only very heavy states. However since brane constructions can allow extra dimensions to be large compared with particle-physics length scales, the effective theories which result can admit a restricted form of nonlocality. They can do so because the observable particles might now be identified as those living on a collection of branes, rather than simply in terms of a low-energy limit. For instance, interactions which are obtained by integrating out modes which are *not* heavy compared with TeV scales — such as bulk Kaluza Klein (KK) states — can mediate nominally nonlocal correlations into the remaining fields.

These possibilities show why string theory may have the potential to teach us a considerable amount about how to think about any new physics which might be encountered in future observations, even if the string scale should turn out to be much higher than the energies being directly probed in these experiments. The fact that string theory makes it plausible that the particles we observe might be trapped on branes within extra dimensions, and that this possibility changes how we think about general naturalness issues, makes it worthwhile to take the possibility of brane localization very seriously.

3 String Inflation

Inflation is the simplest application of string theory to cosmology to motivate, because it could easily involve energy scales which are so high that they could plausibly directly probe string-related physics. Furthermore, recent precision measurements [19] of the properties of the cosmic microwave background radiation (CMBR) have accumulated impressive evidence supporting

the existence of an early inflationary epoch. One of the pleasures of this particular meeting at Moriond was the very recent announcement of the most precise such measurements [20] to date.

Observations of the CMBR are only sensitive to essentially three numbers in any slow-roll inflationary model:[3] the inflationary Hubble scale, $H_{\rm inf}$, and its first and second logarithmic derivatives with respect to the scale factor, evaluated at 'horizon exit' (*i.e.* the moment when observable scales cross the Hubble scale). (It is conventional to describe these latter two derivatives in terms of two small dimensionless slow-roll parameters, ϵ and η.)

In principle these three parameters provide one relationship amongst the four observables defined by the amplitude and spectral tilts of the primordial spectrum of scalar and tensor perturbations to the metric, although the full power of this prediction is difficult to fully exploit until tensor fluctuations are detected. In the meantime, one may instead constrain ϵ and η from measurements of the scalar spectral tilt, n_s, as measured from the fluctuations in the CMBR, and from upper limits on r, defined as the ratio of the amplitude of tensor fluctuations to the amplitude of scalar fluctuations.

At present, current measurements are only now starting to be able to distinguish between the predictions of broad classes of models. Three classes of models which may be distinguished in this way are:[19,20]

1. *Large-Field Models,* for which ϵ and η vary inversely with the value of the inflaton field: $\propto (M_p/\varphi)^p$, for some $p > 0$;

2. *Small-Field Models,* for which ϵ and η are proportional to a positive power of the value of the inflaton field: $\propto (\varphi/M_p)^p$, for some $p > 0$;

3. *Hybrid Models,* for which field evolution at the end of inflation involves at least a two-dimensional field space, and for which the slow-roll parameters depend on parameters in the potential which govern the couplings between these fields.

Varying the various parameters in these models leads to predictions which fill regions of the observable $r - n_s$ plane. In the limit where $H_{\rm inf}$ is essentially constant during horizon exit (*i.e.* $\epsilon, \eta \approx 0$), all slow-roll models approach the scale-invariant point, corresponding to an unobservably small amplitude for tensor modes and a precisely Harrison-Zeldovich (HZ) spectrum: $(r, n_s) = (0, 1)$. But each of the above classes tends to sweep out a different region of predictions within the $r - n_s$ plane, all of which overlap near the scale-invariant HZ point. In particular, the bulk of small-field models (although not all) tend to prefer $n_s < 1$, while the bulk of hybrid models (although not all) prefer $n_s > 1$. What is exciting about the latest CMBR observations [20] is that they are now beginning to exclude the HZ point which is common to all classes of models, and as a result are beginning to provide observationally-justifiable preferences amongst these models.

3.1 Why embed inflation within string theory?

Given the few quantities to which observations are sensitive, the skeptical reader might reasonably wonder whether it is premature to invest considerable effort in finding inflationary evolution within string theory. There are nevertheless several good reasons for doing so. In particular, inflationary models must be embedded into a fundamental theory like string theory in order to understand the following issues:

1. *Naturalness:* Are the choices made in order to obtain acceptable values for $H_{\rm inf}$, ϵ and η inordinately sensitive to short-distance (UV) effects, or must they be finely-tuned in order to achieve sufficient inflation? (And if anthropic arguments are used to explain these tunings,[21] what assigns the probabilities [22] which must be used in order to have an adequate explanation?)

2. *Reheating:* At the end of inflation how does the energy associated with inflation get converted into observable heat (as is required in order to launch the present-day Hot Big Bang epoch)? As anyone who lives in a cold climate knows: a warm house requires *both* an efficient furnace and good insulation. Likewise, for inflation it is not sufficient for there to be a channel for coupling energy between the inflationary and observed sectors, one must also show that too much energy is not lost into any unobserved degrees of freedom. But this question cannot be addressed without a proper theory (like string theory) of what are *all* of the relevant degrees of freedom at inflationary energies.[23]

3. *Initial Conditions:* What justifies the choices which are made for initial conditions *before* inflation? This question can arise because part of the motivation for inflation is to explain the unusual initial conditions of Hot Big Bang cosmology. And inflation can itself require special initial conditions for some kinds of inflationary models (such as for hybrid models, for example). For such models the full microscopic theory is required in order to understand the origin of these initial conditions. Whether initial conditions really are a problem depends on the type of model of interest, since for some cases (like some large-field models) inflation can be an *attractor* solution, inasmuch as it is the endpoint for a broad class of initial conditions. Alternatively, for some cases (like for small field models) one can instead appeal to eternal inflation to explain why the inflating initial conditions might come to dominate the later universe.[24,25,26]

3.2 Why is string inflation so hard to find?

Twenty years of experience has shown that it is quite difficult to embed inflation into string theory in a controllable way. This is somewhat paradoxical given that supersymmetric string vacua provide so many massless scalar fields for which the corresponding scalar potential is completely flat (and so for which $\epsilon = \eta = 0$). The problem arises because a convincing case for a slow roll requires a complete understanding of the potential for these fields even after supersymmetry breaks. In particular one must check that this stabilizing potential does not introduce new, steep, directions into the potential along which the fields will prefer to roll. Although a number of mechanisms were proposed over the years taking advantage of supersymmetric flat potentials,[3] the difficulty in reliably computing supersymmetry-breaking effects, together with cosmological problems with the resulting potentials in the few calculable cases,[27] proved to be an obstacle to further progress.

The introduction of branes proved to be the way forward for string inflation, although the initial brane-brane proposal [28] also relied on supersymmetry for the flatness of its potential (and so suffered from the same calculational difficulties to do with supersymmetry breaking as did earlier ideas). The decisive advantage of branes became apparent only much later, for two reasons. First, it was realized that supersymmetry breaking can become calculable, based on the mutual attraction of a brane-antibrane pair [29,30] or branes at angles, [31] leading to the brane-antibrane mechanism of inflation. With calculability came an explosion of scenarios, including models using $D3$ branes attracted towards $D7$ branes,[32] branes undergoing relativistic motion,[33] intrinsically stringy modes [34] and assisted inflation using string axions [35] and more — see ref. 3 for more extensive references than are possible here.

The second reason branes proved to be crucial for progess was the insight they provided [10,11] into the stabilization of the many scalar fields of string vacua. Once the simplest vacuum with all moduli stabilized was obtained,[12] its combination with the brane-antibrane inflationary mechanism led to the first inflationary scenario with a plausibly detailed string pedigree.[36,37] Shortly thereafter, variations on this theme also led to the discovery of inflationary scenarios for which it is the modulus describing the size of the extra dimensions (and its axionic superpartner) which is the inflaton.[38] Improved understanding of the potentials which stabilize the moduli of

string vacua, has allowed better and better control over the approximations which are required in order to establish inflation, enabling more detailed connections to be made to the properties of explicit string vacua.[39,40]

3.3 How natural is inflation in string theory?

Now that some plausibly stringy inflationary models exist, how fine-tuned do they appear to be? Although it is still a bit early to draw definitive conclusions, since comparatively few corners of field space have been explored to this point, some tentative conclusions can be drawn. For instance, so far all of the proposals but one (including in particular all of the brane-antibrane scenarios) seem to require the same amount of fine-tuning as do their field theoretical counterparts: *i.e.* slow roll inflation requires parameters must be adjusted to within a part in 100 or 1000. In the one example for which inflation seems natural[39] it is a modulus, $X/M_p \sim \ln(L/\ell_s)$, of the extra dimensions which is the inflaton. (Here L is the length of a cycle in the extra dimensions, M_p is the 4D Planck mass and ℓ_s is the string length scale.) It is natural because it takes advantage of a mechanism earlier identified [41] in the field-theoretic limit, wherein the inflaton potential takes the schematic form

$$V(X) = V_0 - A\,X^c \exp[-a\,(X/M_p)^c] + \cdots\,, \tag{1}$$

where V_0, A, a and c are constants, and the ellipses represent terms which become important only as inflation ends. Such a potential has a slow roll provided that $X \gg M_p$, but the point is that this is *generic* to the domain of validity of the effective theory in which this potential appears. It is generic because $X \gg M_p$ corresponds to the condition $L \gg \ell_s$, which is a prerequisite for describing the dynamics of L in an effective field theory. It is clearly of considerable interest to see whether this example is representative, and if so to identify reliably the regions of solution space where inflation occurs so naturally.

3.4 What kind of stringy effects can we hope to measure?

Given that inflation appears to be possible in string theory, and given the wealth and precision of current observations, can we expect there to be any stringy 'smoking guns' awaiting us in the sky? Of course, a complete answer to this question must await a proper exploration of the reheating problem in models containing both inflation and a realistic standard model sector, since it is only then that we can see how many stringy remnants might survive into the late-time universe which we can observe. But three kinds of broad conclusions about observable signals can already be drawn.

1. *Remnant Cosmic Strings:* Within the brane-antibrane inflationary mechanism inflation ends when the brane and antibrane annihilate, and although not completely understood, it was recognized from the beginning [29] that this process is likely to generate an extremely rich spectrum of post-inflationary remnants.[b] The key point for observational purposes is that cosmic strings are special amongst these remnants inasmuch as they can plausibly be produced with observable string tensions and residual abundances,[43] although whether they can live long enough to survive to the present epoch is a somewhat model-dependent issue.[44]

2. *Observational Constraints Among Slow-Roll Parameters:* In all of the calculations to date the conclusion that the observed 4 dimensions inflate in a particular string (or string-motivated) model is drawn using a low-energy 4D effective field theory. As such, their

[b] For high-dimension branes the cascade of annihilations of these remnants might in some circumstances provide a dynamical explanation for why 3-branes might be more abundant at late times,[29] an idea which when investigated in a fully cosmological context also predicts the same for 7-branes.[42]

direct predictions for the CMBR fall within the category of predictions for 4D slow-roll inflationary models. In particular, brane-antibrane models tend to fall into the category of hybrid inflation models, with the earliest models predicting [37] a 'blue' spectral index $n_s > 1$. (Subsequent more detailed studies have shown this conclusion not to be robust against adjustment of the details of the model, with $n_s < 1$ being possible for some choices of parameters.[45]) By contrast, moduli-driven models, like those of the 'racetrack' type,[38,40] are of the small-field type for which $n_s < 1$ is more robustly preferred. (Indeed the most recent of these [40] obtained $n_s = 0.95$ in what was probably the last theoretical calculation not to be biased by the most recent observations [20] which favour this value.) It is remarkable that the preference of the current data [20] for $n_s < 1$ already differentiates amongst some of these models at a statistically significant level, by differentiating amongst the classes of low-energy inflationary field theories to which they give rise.[46]

One might hope that string theory might be more predictive than are the low-energy field theories which describe their effects at low energies. For instance, this would occur if it happened that not all of the three-dimensional inflationary parameter space — *i.e.* $H_{\rm inf}$, ϵ and η — of the 4D field theories were generated by varying the underlying parameters of the string models through all of their allowed values. This would be an attractive possibility if it were true, since it might permit a definitive test of string-based inflation by observations. Unfortunately there is as yet no evidence that string models do not explore the entire parameter space of 4D inflationary slow rolls, although admittedly the parameter space of the string-based models has not yet been extensively explored.

3. *Non-Decoupling Effects:* Everything known about string theory is consistent with the dynamics around string vacua being described at low energies by an appropriate effective field theory — although the occasional worry does get raised.[47] This allows a fairly robust analysis of the influence of high-energy states on inflationary predictions for the CMB since it is possible to analyze its effects in the effective field theory limit. And this theory can be taken to be four dimensional provided that the physics of interest around horizon exit is itself four-dimensional. Since the cosmological backgrounds of interest are time-dependent, care must be taken when performing this analysis to keep track the additional conditions which arise in this case for the validity of the effective-field theory description.[8]

   The results of such an analysis are interesting. First, one finds that by far the majority of effective interactions do not perturb the standard slow-roll inflationary predictions for the CMBR, with a vast number of effects first arising at order $(H_{\rm inf}/M)^2$, where M is the relevant string (or KK) scale describing the relevant high-energy physics.[48] This is good news, since it ensures the robustness of the standard predictions to high-energy string details. But there can be exceptions to this statement, of two types.[49] One type involves non-adiabatic time-dependent effects during the e-foldings just before horizon exit. These effects can cause deviations from the predictions of slow-roll inflation because they violate the assumptions on which the slow-roll calculations rely. Their existence is interesting since it motivates a careful search within the observations for deviations from standard slow-roll predictions.[c]

   Alternatively, there can also be static effects [49] which are larger than $O[(H_{\rm inf}/M)^2]$ because they arise with coefficients of order $(v/M)^2$, where $v \gg H_{\rm inf}$ is the scale in the scalar potential which gives rise to inflation: $H_{\rm inf} \sim v^2/M_p$. However, most of these $(v/M)^2$ effects arise as modifications of the inflaton potential and so represent a change in the connection between the slow-roll parameters and the underlying string parameters, rather

[c] It should be remarked parenthetically that the expected deviations [49] can be physically distinguished from those predicted by the more speculative 'transplanckian' effects [50] which have been much discussed recently.

than an observable deviation from the physical predictions of slow-roll inflation themselves.

It is clear that it is still early days for the exploration of the implications of string theory for cosmology in the very early and more recent universe. But the preliminary results are encouraging, and the prospects remain bright for learning something interesting about the physics of very high energies.

Acknowledgements

I wish to thank the organizers of Moriond 2006 for arranging such a pleasant and stimulating environment for discussions — and such excellent snow conditions — as well as for their kind invitation to speak. My understanding of the issues involved at the interface of string theory and cosmology has benefited immensely from interactions with many collaborators. My research has been funded in part by McMaster University, the Killam Foundation, and by the Natural Sciences and Engineering Research Council of Canada.

References

1. A. H. Guth, Phys. Rev. **D23** (1981) 347; A. D. Linde, Phys. Lett. **B108** (1982) 389; A. Albrecht and P. J. Steinhardt, Phys. Rev. Lett. **48** (1982) 1220.
2. E. J. Copeland, M. Sami and S. Tsujikawa, [hep-th/0603057].
3. A. Linde, eConf **C040802** (2004) L024 [J. Phys. Conf. Ser. **24** (2005) 151] [hep-th/0503195]; C. P. Burgess, Pramana **63** (2004) 1269 [hep-th/0408037]; F. Quevedo, Class. Quant. Grav. **19** (2002) 5721, [hep-th/0210292].
4. For reviews, see, A. Linde, *Particle Physics and Inflationary Cosmology*, Harwood Academic Publishers (1990) [hep-th/0503203]; E. W. Kolb and M. S. Turner, *The Early Universe*, Addison-Wesley (1990); A. R. Liddle and D. H. Lyth, *Cosmological Inflation and Large-Scale Structure*, Cambridge University Press (2000).
5. S. Weinberg and E. Witten, Phys. Lett. B **96** (1980) 59.
6. See, for instance, S. Weinberg, *The Quantum Theory of Fields*, Cambridge University Press (1995), p. 253.
7. For a recent heroic effort, and its problems, see G. R. Dvali, G. Gabadadze and M. Porrati, Phys. Lett. B **485** (2000) 208 [hep-th/0005016]; M. A. Luty, M. Porrati and R. Rattazzi, JHEP **0309** (2003) 029 [hep-th/0303116]; D. Gorbunov, K. Koyama and S. Sibiryakov, Phys. Rev. D **73** (2006) 044016 [hep-th/0512097]; A. Adams, N. Arkani-Hamed, S. Dubovsky, A. Nicolis and R. Rattazzi, [hep-th/0602178]; G. Gabadadze and A. Iglesias, [hep-th/0603199]; C. Charmousis, R. Gregory, N. Kaloper and A. Padilla, [hep-th/0604086].
8. For a recent review see C. P. Burgess, Living Rev. Rel. **7** (2004) 5 [gr-qc/0311082].
9. A. Albrecht, J. A. Frieman and M. Trodden, in *Proc. of the APS/DPF/DPB Summer Study on the Future of Particle Physics (Snowmass 2001)* ed. N. Graf, eConf **C010630** (2001) P409 [hep-ph/0111080]; I. Maor, R. Brustein, J. McMahon and P. J. Steinhardt, Phys. Rev. D **65** (2002) 123003 [astro-ph/0112526]; I. Maor and R. Brustein, Phys. Rev. D **67** (2003) 103508 [hep-ph/0209203]; S. L. Bridle, O. Lahav, J. P. Ostriker and P. J. Steinhardt, Science **299** (2003) 1532 [astro-ph/0303180]; M. Beltran, J. Garcia-Bellido, J. Lesgourgues, A. R. Liddle and A. Slosar, Phys. Rev. D **71** (2005) 063532 [astro-ph/0501477]; E. V. Linder and D. Huterer, Phys. Rev. D **72** (2005) 043509 [astro-ph/0505330]; P. Mukherjee, D. Parkinson and A. R. Liddle, Astrophys. J. **638** (2006) L51 [astro-ph/0508461]; P. Mukherjee, D. Parkinson, P. S. Corasaniti, A. R. Liddle and M. Kunz, [astro-ph/0512484].

10. S. B. Giddings, S. Kachru and J. Polchinski, Phys. Rev. D **66** (2002) 106006 [hep-th/0105097];
11. S. Sethi, C. Vafa and E. Witten, Nucl. Phys. B **480** (1996) 213 [hep-th/9606122]; K. Dasgupta, G. Rajesh and S. Sethi, JHEP **9908** (1999) 023 [hep-th/9908088].
12. S. Kachru, R. Kallosh, A. Linde and S. P. Trivedi, Phys. Rev. D **68** (2003) 046005 [hep-th/0301240]; B. S. Acharya, [hep-th/0212294]; R. Brustein and S. P. de Alwis, Phys. Rev. D **69** (2004) 126006 [hep-th/0402088]; F. Denef, M. R. Douglas and B. Florea, JHEP **0406** (2004) 034 [hep-th/0404257]; F. Denef, M. R. Douglas, B. Florea, A. Grassi and S. Kachru, [hep-th/0503124].
13. For a review with references see J. Polchinski, *TASI Lectures on D-Branes* [hep-th/9611050].
14. P. Horava and E. Witten, *Nucl. Phys.* **B475** (1996) 94 [hep-th/9603142]; *Nucl. Phys.* **B460** (1996) 506 [hep-th/9510209]; E. Witten, *Nucl. Phys.* **B471** (1996) 135 [hep-th/9602070]; J. Lykken, *Phys. Rev.* **D54** (1996) 3693 [hep-th/9603133]; I. Antoniadis, N. Arkani-Hamed, S. Dimopoulos and G. Dvali, *Phys. Lett.* **B436** (1998) 257 [hep-ph/9804398].
15. K. Benakli, *Phys. Rev.* **D60**, 104002 (1999) [hep-ph/9809582]; C. P. Burgess, L. E. Ibáñez and F. Quevedo, *Phys. Lett.* **B447**, 257 (1999) [hep-ph/9810535];
16. N. Arkani-Hamed, S. Dimopoulos and G. Dvali, *Phys. Lett.* **B429** (1998) 263 [hep-ph/9803315]; *Phys. Rev.* **D59** (1999) 086004 [hep-ph/9807344].
17. N. Arkani-Hamed, S. Dimopoulos, N. Kaloper and R. Sundrum, Phys. Lett. B **480** (2000) 193, [hep-th/0001197];
    S. Kachru, M. B. Schulz and E. Silverstein, Phys. Rev. D **62** (2000) 045021, [hep-th/0001206].
18. S. M. Carroll and M. M. Guica, [hep-th/0302067]; Y. Aghababaie, C. P. Burgess, S. L. Parameswaran and F. Quevedo, Nucl. Phys. B **680** (2004) 389 [hep-th/0304256]; Y. Aghababaie *et al.*, JHEP **0309** (2003) 037 [hep-th/0308064].
19. H. V. Peiris *et al.*, Astrophys. J. Suppl. **148** (2003) 213 [astro-ph/0302225]; V. Barger, H. S. Lee and D. Marfatia, Phys. Lett. B **565** (2003) 33 [hep-ph/0302150]; S. M. Leach and A. R. Liddle, Phys. Rev. D **68** (2003) 123508 [astro-ph/0306305].
20. D.N. Spergel, et.al., (http://lambda.gsfc.nasa.gov/product/map/dr2/map_bibliography.cfm); L. Alabidi and D. H. Lyth, [astro-ph/0603539].
21. R. Bousso and J. Polchinski, "Quantization of four-form fluxes and dynamical neutralization of the cosmological constant," JHEP **0006** (2000) 006; L. Susskind, "The anthropic landscape of string theory," (hep-th/0302219); T. Banks, M. Dine and E. Gorbatov, "Is there a string theory landscape?," (hep-th/0309170).
22. M. R. Douglas, [hep-th/0405279]; B. S. Acharya, F. Denef and R. Valandro, JHEP **0506** (2005) 056 [hep-th/0502060]; J. Kumar, [hep-th/0601053].
23. For some recent discussions of reheating within an explicity stringy context see: N. Barnaby, C. P. Burgess and J. M. Cline, JCAP **0504** (2005) 007 [hep-th/0412040]; A. R. Frey, A. Mazumdar and R. Myers, Phys. Rev. D **73** (2006) 026003 [hep-th/0508139]; L. Kofman and P. Yi, Phys. Rev. D **72** (2005) 106001 [hep-th/0507257]; D. Chialva, G. Shiu and B. Underwood, JHEP **0601** (2006) 014 [hep-th/0508229]; X. Chen and S. H. Tye, [hep-th/0602136]; P. Langfelder, [hep-th/0602296].
24. A. D. Linde, Phys. Lett. B **162** (1985) 281; A. D. Linde, D. A. Linde and A. Mezhlumian, Phys. Rev. D **49**, 1783 (1994) [gr-qc/9306035].
25. P. J. Steinhardt, In: *The Very Early Universe*, ed. G.W. Gibbons, S.W. Hawking and S.Siklos, Cambridge University Press, (1983); A. D. Linde, Cambridge University preprint Print-82-0554 (1982); A. Vilenkin, Phys. Rev. D **27**, 2848 (1983).
26. A. D. Linde, Phys. Lett. B **327**, 208 (1994) [astro-ph/9402031]; A. Vilenkin, Phys. Rev.

Lett. **72**, 3137 (1994) [hep-th/9402085].
27. R. Brustein and P. J. Steinhardt, Phys. Lett. B **302** (1993) 196 [hep-th/9212049].
28. G. R. Dvali and S. H. H. Tye, Phys. Lett. B **450** (1999) 72 [hep-ph/9812483].
29. C. P. Burgess, M. Majumdar, D. Nolte, F. Quevedo, G. Rajesh and R. J. Zhang, JHEP **0107** (2001) 047 [hep-th/0105204].
30. G. R. Dvali, Q. Shafi and S. Solganik, [hep-th/0105203].
31. J. Garcia-Bellido, R. Rabadan and F. Zamora, JHEP **0201**, 036 (2002); N. Jones, H. Stoica and S. H. H. Tye, JHEP **0207**, 051 (2002); M. Gomez-Reino and I. Zavala, JHEP **0209**, 020 (2002).
32. J. P. Hsu, R. Kallosh and S. Prokushkin, JCAP **0312** (2003) 009 [hep-th/0311077]; F. Koyama, Y. Tachikawa and T. Watari, [hep-th/0311191]; H. Firouzjahi and S. H. H. Tye, Phys. Lett. B **584** (2004) 147 [hep-th/0312020]. J. P. Hsu and R. Kallosh, JHEP **0404** (2004) 042 [hep-th/0402047];
33. E. Silverstein and D. Tong, Phys. Rev. D **70** (2004) 103505 [hep-th/0310221]; M. Alishahiha, E. Silverstein and D. Tong, Phys. Rev. D **70** (2004) 123505 [hep-th/0404084]; X. G. Chen, JHEP **0508** (2005) 045 [hep-th/0501184]; [astro-ph/0507053]; D. Cremades, F. Quevedo and A. Sinha, JHEP **0510** (2005) 106 [hep-th/0505252].
34. O. DeWolfe, S. Kachru and H. Verlinde, JHEP **0405** (2004) 017 [hep-th/0403123]; N. Iizuka and S. P. Trivedi, [hep-th/0403203]; B. Freivogel, V. E. Hubeny, A. Maloney, R. Myers, M. Rangamani and S. Shenker, JHEP **0603** (2006) 007 [hep-th/0510046].
35. S. Dimopoulos, S. Kachru, J. McGreevy and J. G. Wacker, [hep-th/0507205].
36. S. Kachru, R. Kallosh, A. Linde, J. Maldacena, L. McAllister and S. P. Trivedi, JCAP **0310** (2003) 013 [hep-th/0308055];
37. C. P. Burgess, J. M. Cline, H. Stoica and F. Quevedo, JHEP **0409** (2004) 033 [hep-th/0403119].
38. J. J. Blanco-Pillado *et al.*, JHEP **0411** (2004) 063 [hep-th/0406230]. Z. Lalak, G. G. Ross and S. Sarkar, [hep-th/0503178].
39. J. P. Conlon and F. Quevedo, JHEP **0601** (2006) 146 [hep-th/0509012].
40. J. J. Blanco-Pillado *et al.*, [hep-th/0603129].
41. C. P. Burgess, P. Martineau, F. Quevedo, G. Rajesh and R. J. Zhang, JHEP **0203** (2002) 052 [hep-th/0111025].
42. A. Karch and L. Randall, Phys. Rev. Lett. **95** (2005) 161601 [hep-th/0506053].
43. S. Sarangi and S. H. H. Tye, Phys. Lett. B **536** (2002) 185 [hep-th/0204074];
44. E. J. Copeland, R. C. Myers and J. Polchinski, JHEP **0406** (2004) 013 [hep-th/0312067]; G. Dvali, R. Kallosh and A. Van Proeyen, JHEP **0401** (2004) 035 [hep-th/0312005]; G. Dvali and A. Vilenkin, JCAP **0403** (2004) 010 [hep-th/0312007]; L. Leblond and S. H. H. Tye, JHEP **0403** (2004) 055 [hep-th/0402072]; K. Dasgupta, J. P. Hsu, R. Kallosh, A. Linde and M. Zagermann, [hep-th/0405247].
45. J. M. Cline and H. Stoica, Phys. Rev. D **72**, 126004 (2005) [hep-th/0508029].
46. This point is also made in Q. G. Huang, M. Li and J. H. She, hep-th/0604186.
47. T. Banks, [hep-th/0412129].
48. N. Kaloper, M. Kleban, A. Lawrence, S. Shenker, [hep-th/0201158]; N. Kaloper, M. Kleban, A. Lawrence, S. Shenker, and L. Susskind, [hep-th/0209231].
49. C. P. Burgess, J. M. Cline, F. Lemieux and R. Holman, JHEP **0302** (2003) 048 [hep-th/0210233]; C. P. Burgess, J. M. Cline and R. Holman, JCAP **0310** (2003) 004 [hep-th/0306079].
50. J. Martin and R. H. Brandenberger, Phys. Rev. D **63**, 123501 (2001) [hep-th/0005209]; R. H. Brandenberger and J. Martin, Mod. Phys. Lett. A **16**, 999 (2001) [astro-ph/0005432]; R. Easther, B. R. Greene, W. H. Kinney and G. Shiu, Phys. Rev. D **64**, 103502 (2001) [hep-th/0104102]; R. Easther, B. R. Greene, W. H. Kinney and G. Shiu, [hep-th/0110226];

R. Easther, B. R. Greene, W. H. Kinney and G. Shiu, Phys. Rev. D **66**, 023518 (2002) [hep-th/0204129].

SIGNATURES OF EXTRA DIMENSIONS

CARLA CARVALHO
Departamento de Física, Instituto Superior Técnico,
Av. Rovisco Pais, Lisboa 1049-001, Portugal

This contribution reports on the formulation of a model for the brane-bulk interaction contemplating a universe with an arbitrary expansion history defined on a moving boundary of the bulk spacetime. The coupling between the brane and the bulk degrees of freedom is established by imposing that the modes emitted from the brane satisfy the gauge defined in the bulk. A method is currently being developed for the calculation of the bulk graviton propagator with a view toward the calculation of the linearized cosmological perturbations in a one brane Randall-Sundrum scenario.

In a braneworld scenario, where the observable universe consists of a (3+1)-dimensional timelike hypersurface embedded in a higher-dimensional bulk spacetime, the interaction between the brane and the embedding space will be intrinsically higher-dimensional. From the point of view of the brane, this would appear to generate dissipation and non-locality. Such effects, unaccounted for by an effective (3+1)-dimensional description, could explain in a novel way features not fully explained by standard cosmology, thus allowing for potential observational signatures for the presence of extra dimensions.

In particular, an understanding of the nature of the brane-bulk interaction is required to investigate any possible differences in the predictions for the cosmological perturbations between the standard (3+1)-dimensional cosmology and a braneworld cosmology. In (3+1)-dimensional cosmology, for each $\mathbf{k}$ sector into which linearized cosmological perturbations can be diagonalized, the number of degrees of freedom is finite, described by a finite number of coupled ordinary differential equations. In the presence of an extra dimensional bulk, however, this number is infinitely enlarged. When the extra dimension is of finite size, the spacing between the discretely infinite bulk degrees of freedom is proportional to the inverse of the size of the extra dimension. A very small extra dimension generates a large mass gap between the zero mode and the infinite tower of bulk excitations. When the extra dimension is infinite, the bulk degrees form a continuum. A suppression of the coupling of the lowest energy bulk degrees of freedom to those on the brane is achieved by the warping of the bulk spacetime. In both cases, a (3+1)-dimensional gravity is recovered on large scales on the brane.[1] Higher dimensional effects would only be expected on very small scales, or in the very early universe.

A Model for the Brane-bulk Interaction: In Binétruy, Bucher and Carvalho,[2] a model was devised for the brane-bulk interaction in the case of a single (3+1)-dimensional brane endowed with a singular Z_2-symmetric stress-energy distribution and embedded in a five-dimensional anti-de Sitter bulk spacetime. Initial conditions must be specified for the infinite number of bulk degrees of freedom. From the bottom vertex of the Penrose diagram for maximally extended

AdS, formed by the null surface H_- and the timelike surface for the origin of the extra dimension, emerge all possible timelike trajectories for the brane. Hence, depending on the quantum state for the incoming bulk degrees of freedom at the past Cauchy horizon H_- and on the quantum state for the brane degrees of freedom at the intersection with H_-, different trajectories for the brane and consequently different induced expansion histories are contemplated. The model was built in analogy with the mechanical interaction of an harmonic oscillator coupled to a string, with the oscillator representing the degrees of freedom localized on the brane and the string those of the bulk. Different examples of increased complexity were considered.

For a constant coupling, a description of dissipation is obtained, with excitations of the oscillator decaying and emitting waves which propagate in the string. From the equation of motion for the oscillator of mass m

$$\ddot{q}(t) + \bar{\omega}^2 q(t) = F(t)/m \equiv \gamma \partial u/\partial x|_{x=0} \tag{1}$$

and with the ansatz for the field on the string $u_\omega(t,x) = \sin[\omega x - \phi(\omega)]e^{-i\omega t}$, it is found that the quantum operator for the oscillator degree of freedom is given by $q(t) = u(t, x = 0)$, where

$$u(t,x) = \int_0^{+\infty} (d\omega/\sqrt{2\pi\mu\omega}) \sin[\omega x - \phi(\omega)][\hat{a}(\omega)e^{-i\omega t} + \hat{a}(\omega)^\dagger e^{+i\omega t}] \tag{2}$$

and μ is the linear density of the string. This reflects the fact that the annihilation and creation operators on the oscillator $\hat{a}_{osc}(t)$ and $\hat{a}^\dagger_{osc}(t)$ are superpositions of string modes of different frequency ω. From the point of view of an observer localized on the brane, all the relevant physics may be encapsulated into the spectral density function $\rho(\omega)$, where

$$\hat{a}_{osc}(t) = \int_0^{+\infty} d\omega \rho^{1/2}(\omega) \exp[-i\omega t]\hat{a}(\omega). \tag{3}$$

Any operator localized on the oscillator at time t will be a linear combination of $\hat{a}_{osc}(t)$ and $\hat{a}^\dagger_{osc}(t)$. The commutation relation for $\hat{a}_{osc}(t)$ and $\hat{a}^\dagger_{osc}(t)$ yields the following two results: for small times, the oscillator behaves as if uncoupled from the string and a quantum on the oscillator does not evolve with time; for sufficiently large times, the operators almost commute, which means that quanta created in the oscillator escape the oscillator and propagate away along the string, becoming inaccessible to an operator localized on the oscillator.

A variation in the string density, which translates in a variation of the propagation speed, leads to a portion of the outgoing wave being transmitted to the right and another being reflected to the left back towards the oscillator. The spectral density has a picket fence profile, consisting of an ordinary resonance masked by a function with periodically spaced spikes. On the other side of the junction, only near a resonance will there be significant penetration of the string incoming waves towards the oscillator. This reproduces the effect of the curvature in the bulk with the consequent generation of non-locality.

The case of a time-varying coupling constant with one or more oscillators was also worked out. Assuming that the coupling constant is temporarily switched on, quanta are produced by parametric resonance, with the *in* and *out* vacua related by a Bogoliubov transformation. The Bogoliubov coefficients describe the fundamental bulk-brane interaction processes. Of particular interest are the coefficients describing oscillator *out* states, for those are the only states accessible to an observer localized on the oscillator. An initial state expressible as a tensor product of oscillator and bulk modes becomes highly entangled. The attenuation of the coefficients relating the oscillator to itself results from the decay of the oscillator excitations into modes on the string. The measurement of the state of the oscillator at late times in terms of the initial state will be dominated by the correlations of the bulk modes. It follows that the *out* annihilation and creation operators on the brane $a_{brane,out}$ and $a^\dagger_{brane,out}$ can be expressed as a linear combination

of $a_{brane,in}$ and $a^\dagger_{brane,in}$ on the one hand, and of $a_{bulk,in}(\omega)$ and $a^\dagger_{bulk,in}(\omega)$ on the other. Defining $A_{brane,in}$ and $A_{bulk,in}$ entirely on the brane and in the bulk respectively, both normalized such that $[A_{brane,in}, A^\dagger_{brane,in}] = [A_{bulk,in}, A^\dagger_{bulk,in}] = 1$, then there are three possibilities for $a_{brane,out}$:

$$a_{brane,out} = \cos[\theta]A_{brane,in} + \sin[\theta]A_{bulk,in}, \quad 0 \leq \theta \leq 2\pi; \tag{4}$$

$$a_{brane,out} = \cosh[\xi]A_{brane,in} + \sinh[\xi]A^\dagger_{bulk,in}, \quad 0 \leq \xi < +\infty; \tag{5}$$

$$a_{brane,out} = \sinh[\xi]A^\dagger_{brane,in} + \cosh[\xi]A_{bulk,in}, \quad 0 \leq \xi < +\infty. \tag{6}$$

The measurement of the perturbations today measures in part the initial state on the brane and in part the initial state in the bulk, the relative importance being described by the Bogoliubov coefficients.

Boundary Conditions and Gauge Fixing: The inevitable mixing in the present brane state of the brane and bulk states at early times raises the question of how the gauge condition in the bulk is preserved. In the presence of a timelike surface moving in the semi-infinite bulk, modes may be produced or scattered off by the surface into the bulk which violate the gauge in the bulk. The Israel matching conditions provide ten of the required fifteen boundary conditions for the degrees of freedom of a five-dimensional spacetime. Although the Israel matching conditions must be satisfied in every gauge, they are not sufficient to determine in a specific gauge the reflection of the bulk gravitons off the brane. Five supplementary gauge conditions are needed. These must be chosen so that no forbidden gauge modes are emitted or reflected by the brane into the bulk, thus rendering reflection off the boundary unique and consistent, and prescribing the continuation of the gauge into the bulk.

In Bucher and Carvalho,[3] the appropriate boundary conditions were established both for electromagnetic and for linearized gravitational waves. For the case of a planar flat boundary, a perfect conductor or a perfect gravitational mirror accordingly, this was solved by considering a decomposition into plane waves in the bulk and working out the reflection conditions on the brane. For illustration, consider the vector potential $\mathbf{A}$ whose time evolution is described by $A_{\mu;\nu\nu} = 0$. The residual gauge freedom is characterized by scalars such that $\Lambda_{;\nu\nu} = 0$ which generate transformations that preserve the Lorentz gauge condition $A_{\mu;\mu} = 0$. In an infinite region, once $\mathbf{A}$ and its normal derivative have been specified on a Cauchy surface, its propagation forward in time is unambiguous because the initial data for Λ can be propagated from the same Cauchy surface. For a semi-infinite region, however, pure gauge modes may propagate in from the timelike boundary. Gauge conditions on the boundary are required to specify which pure gauge modes are emitted and how they are reflected off the boundary, thus fixing the time evolution completely. Consistent with the Lorentz gauge, two physical modes

$$\hat{\mathbf{e}}^\mu_{(1)}(\hat{\mathbf{k}}) = \frac{\hat{\mathbf{e}}^\mu_{(x)} - \hat{\mathbf{k}}^\mu(\hat{\mathbf{k}}\cdot\hat{\mathbf{e}}_x)}{\sqrt{1-(\hat{\mathbf{k}}\cdot\hat{\mathbf{e}}_x)^2}}, \quad \hat{\mathbf{e}}^\mu_{(2)}(\hat{\mathbf{k}}) = \frac{\hat{\mathbf{e}}^\mu_{(y)} - \hat{\mathbf{k}}^\mu(\hat{\mathbf{k}}\cdot\hat{\mathbf{e}}_y)}{\sqrt{1-(\hat{\mathbf{k}}\cdot\hat{\mathbf{e}}_y)^2}} \tag{7}$$

and a pure gauge (longitudinal) mode

$$\hat{\mathbf{e}}^\mu_{(L)}(\hat{\mathbf{k}}) = \frac{1}{\sqrt{2}}(\hat{\mathbf{e}}^\mu_t + \hat{\mathbf{k}}^\mu) \tag{8}$$

are found. A fourth polarization is excluded and denoted forbidden

$$\hat{\mathbf{e}}^\mu_{(F)}(\hat{\mathbf{k}}) = \frac{1}{\sqrt{2}}(\hat{\mathbf{e}}^\mu_t - \hat{\mathbf{k}}^\mu). \tag{9}$$

Inside the conductor, $\mathbf{E} = \mathbf{B} = 0$, from which it follows that $\mathbf{E}_\parallel$ and $\mathbf{B}_\perp$ vanish on the boundary. If the gauge inside the conductor is fixed by setting the component of the 4-vector potential

parallel to the boundary $\underline{\mathbf{A}} = 0$, or

$$\hat{\mathbf{t}} \cdot \mathbf{A} = 0, \tag{10}$$

then by continuity these components must satisfy Dirichlet conditions at the boundary. Upon a reflection off the brane, $\hat{\mathbf{e}}_x$, $\hat{\mathbf{e}}_y$ and $\hat{\mathbf{e}}_t$ switch sign but $\hat{\mathbf{k}}$ and $\hat{\mathbf{n}}$ remain unaltered. In order for incoming longitudinal modes to scatter off the conductor into outgoing longitudinal modes without the creation of forbidden ones, then the normal component must satisfy a Neumann boundary condition

$$\nabla_{\hat{\mathbf{n}}}(\hat{\mathbf{n}} \cdot \mathbf{A}) = 0. \tag{11}$$

Although here physical and pure gauge modes transform separately into physical and pure gauge modes respectively, in general they mix. Similarly the case of linearized metric perturbations $\bar{\mathbf{h}}$ can be considered. Imposing the Lorentz gauge $\bar{h}_{ab;b} = \nabla_b[h_{ab} - (1/2)g^{(0)}_{ab}h] = 0$, it is found that the boundary conditions derived from the Israel matching conditions

$$\frac{\partial}{\partial n}(\hat{\mathbf{t}}_1 \cdot \bar{\mathbf{h}} \cdot \hat{\mathbf{t}}_2) = 0 \tag{12}$$

are complemented by those for reflection of pure gauge modes

$$\hat{\mathbf{n}} \cdot \bar{\mathbf{h}} \cdot \hat{\mathbf{t}}_1 = 0, \quad \frac{\partial}{\partial n}(\hat{\mathbf{n}} \cdot \bar{\mathbf{h}} \cdot \hat{\mathbf{n}}) = 0 \tag{13}$$

to enforce the respect for the gauge condition in the bulk.

For a curved boundary in a curved bulk, where a decomposition in plane waves is no longer possible, the supplementary boundary conditions were extrapolated from the previous case and modified to account for the curvature. Their consistency with conservation of stress-energy on the boundary and the Israel matching conditions was demonstrated.

The Tensor Propagator: Finally, to describe propagation between two points on the brane, the explicit form of the retarded graviton propagator in AdS must be computed. Propagation can be described as an expansion of brane localized propagators with insertions of bulk mediated propagation.[2] The technique developed for scalar degrees of freedom is now being extended to tensors using the method described in ref. 4. Relating points $\underline{\mathbf{x}}$ and $\underline{\mathbf{x}}'$ at different tangent spaces, tensor propagators are expanded as a combination of a basis of bitensors, invariant at each tangent space and upon $(\underline{\mathbf{x}} \leftrightarrow \underline{\mathbf{x}}')$, where the coefficients are functions of the invariant separation between the points.

Work in progress[5] applies the formal results developed so far to the actual problem of computing the evolution of the cosmological perturbations of the coupled brane-bulk system for various expansion histories and various choices for the physical degrees of freedom on the brane.

Acknowledgments: The author thanks the Organizing Committee of the Rencontres de Moriond for a wonderful meeting and Martin Bucher for valuable comments. The author also thanks Fundação para a Ciência e a Tecnologia and the European Union for support.

References

1. L. Randall and R. Sundrum, *Phys. Rev. Lett.* **83**, 3370 (1999), *Phys. Rev. Lett.* **88**, 4690 (1999).
2. P. Binétruy, M. Bucher and C. Carvalho, *Phys. Rev.* D **70**, 043509 (2004).
3. M. Bucher and C. Carvalho, *Phys. Rev.* D **71**, 083511 (2005).
4. E. D'Hoker, D. Z. Freedman and S. Mathur, *Nucl. Phys.* B **562**, 330 (1999).
5. M. Bucher, C. Carvalho and M. Remazeilles, in preparation.

DARK ENERGY ACCRETION ONTO BLACK HOLES

E.O. BABICHEV, V.I. DOKUCHAEV AND Yu.N. EROSHENKO
Institute for Nuclear Research of the Russian Academy of Sciences,
60th October Anniversary Prospect 7a, 117312 Moscow, Russia

Solution for a stationary spherically symmetric accretion of the relativistic perfect fluid with an arbitrary equation-of-state $p(\rho)$ onto the Schwarzschild black hole is presented. It is shown that accretion of phantom energy is accompanied with a gradual decrease of the black hole mass. Masses of all black holes tend to zero in the phantom energy universe approaching to the Big Rip.

1 Introduction

Our Universe apparently undergoes a period of accelerated expansion. In the framework of General Relativity this means that a considerable part of the cosmological density consists of dark energy component with a negative pressure [1]. There are several theoretical candidates for a dark energy in the universe: cosmological constant (vacuum energy), dynamically evolving fields such as quintessence [2] or a more general k-essence [3] and geometrical dark energy (deviation from General Relativity including extra-dimensional generalizations). The dynamical dark energy models seem to be more realistic in resolving the problem of fine-tuning as they admit to construct "tracker" [4] or "attractor" [3] solutions without addressing to the antropic principle.

One of the peculiar feature of the cosmological dark energy is a possibility of the Big Rip scenario [5]: the infinite expansion of the universe during a finite time. The Big Rip scenario is realized if a dark energy is in the form of the phantom energy with $\rho + p < 0$. In this case the Big Rip scenario provides the unrestrained growing of the cosmological phantom energy density grows and as a result the disruption of all bound objects up to subnuclear scale. Note, however that the condition $\rho + p < 0$ is not enough for the realization of the Big Rip [6]. A model independent analysis of the supernova data [7] showed that a presence of the phantom energy with an equation-of-state $-1.2 < w < -1$ is preferable in the present moment of time. Some analogy between phantom and QFT in curved space-time may be traced [8]. The entropy of the universe with phantom energy is discussed in [9]. On quantum level the phantom dark energy can be described as an unstable scalar ghost field. Possible ultraviolet stabilization of phantom field may be achieved e. g. by combining the scalar and vector fields [10]. Nevertheless the physical origin of dark energy is still controversial.

Usually the evolution of quintessence or k-essence are considered in view of cosmological problems. However in the presence of compact objects such as black holes, the behavior of dark energy should be sufficiently different from that in the cosmological consideration. Indeed, what would be the fate of black holes in the universe filled with the phantom energy and approaching to the Big Rip? In contrast to the ordinary bound objects, the black holes cannot be disrupted in any classical processes. Recently we showed that all black holes gradually decrease their

masses and finally disappear very near the Big Rip [11].

Here we study in details the stationary accretion of dynamical dark energy into the black hole. As a model of dark energy we consider the relativistic perfect fluid with a negative pressure. The regular investigation of an accretion of perfect fluid on the compact objects is started since a formulation of the Bondi problem in the newtonian approximation [12]. The corresponding relativistic formulation of the perfect fluid accretion problem onto the Schwarzschild black hole were made by Michel [13] for the case of a polytropic equation-of-state. Below we describe the solution for a stationary accretion of the relativistic perfect fluid with an arbitrary equation-of-state $p(\rho)$ onto the Schwarzschild black hole. Using this solution we show that the black hole mass diminishes by accretion of the phantom energy. Masses of all black holes gradually tend to zero in the phantom energy universe approaching to the Big Rip. The diminishing of a black hole mass is caused by the violation of the energy domination condition $\rho + p \geq 0$ which is a principal assumption of the classical black hole 'non-diminishing' theorems [14]. The another consequence of the existence of a phantom energy is a possibility of traversable wormholes [15]. In [16,17,18,19] authors studied the accretion of scalar quintessence field onto black hole, using the specific quintessence potentials $V(\phi)$ for obtaining the analytical solutions for black hole mass evolution. We use here an essentially different approach for the description of dark energy accretion onto a black hole. Namely, we model the dark energy by perfect fluid with a negative pressure.

2 General equations

Let us consider the spherical accretion of dark energy onto a black hole. We assume that the dark energy density is sufficiently low, so that the space-time geometry can be described by the Schwarzschild metric (i. e. the test field approximation). We model the dark energy by a perfect fluid with energy-momentum tensor: $T_{\mu\nu} = (\rho + p)u_\mu u_\nu - p g_{\mu\nu}$, where ρ is the density and p is the pressure of the dark energy and u_μ is the four-velocity $u^\mu = dx^\mu/ds$ of the fluid. The integration of the time component of the energy-momentum conservation law $T^{\mu\nu}{}_{;\nu} = 0$ gives the first integral of motion

$$(\rho + p)\left(1 - \frac{2}{x} + u^2\right)^{1/2} x^2 u = C_1, \tag{1}$$

where $x = r/M$, $u = dr/ds$ and C_1 is a constant determined below. Given the equation-of-state $p = p(\rho)$, one can introduce the function n by the relation:

$$\frac{d\rho}{\rho + p} = \frac{dn}{n}. \tag{2}$$

The function n plays a role of an effective particle number density ('concentration') in the fluid. At the same time, one can use n for the formal description of the fluid without correlation with any physical particles. In this case n is an auxiliary function. For a general equation-of-state, $p = p(\rho)$, we obtain from (2) the following solution for n:

$$\frac{n(\rho)}{n_\infty} = \exp\left(\int_{\rho_\infty}^{\rho} \frac{d\rho'}{\rho' + p(\rho')}\right), \tag{3}$$

From the conservation of energy-momentum along the velocity $u_\mu T^{\mu\nu}{}_{;\nu} = 0$, using (3) we obtain the another first integral:

$$\frac{n(\rho)}{n_\infty} u x^2 = -A, \tag{4}$$

where n_∞ (an effective 'concentration' of the dark energy at the infinity) was introduced formally for convenience. In the case of inflow $u = (dr/ds) < 0$, and the constant $A > 0$. From (1) and (4) one can easily obtain

$$\frac{\rho + p}{n}\left(1 - \frac{2}{x} + u^2\right)^{1/2} = C_2, \tag{5}$$

where

$$C_2 = \frac{\rho_\infty + p(\rho_\infty)}{n(\rho_\infty)}. \tag{6}$$

Let us now calculate the radial 4-velocity component and the fluid density on the event horizon of the black hole, $r = 2M$. Setting $x = 2$, we obtain from Eqs. (4), (5) and (6)

$$\frac{A}{4}\,\frac{\rho_{\rm H} + p(\rho_{\rm H})}{\rho_\infty + p(\rho_\infty)} = \frac{n^2(\rho_{\rm H})}{n^2(\rho_\infty)}, \tag{7}$$

where $\rho_{\rm H}$ is the density on the $x = 2$ horizon. Thus, having specified the density at infinity ρ_∞, the equation of state $p = p(\rho)$, and the flux A and using definition (2) of the concentration, we can calculate the fluid density $\rho_{\rm H}$ on the event horizon of the black hole from (7). Given the density on the horizon $\rho_{\rm H}$, we can easily determine the radial fluid 4-velocity component on the horizon from (4):

$$u_{\rm H} = -\frac{A}{4}\,\frac{n(\rho_\infty)}{n(\rho_{\rm H})}. \tag{8}$$

We will see below that the constant A which determines the flux is fixed for fluids with $\partial p/\partial\rho > 0$. This can be done through finding of the critical point. Following Michel [13] we obtain the parameters of critical point:

$$u_*^2 = \frac{1}{2x_*}, \quad V_*^2 = \frac{u_*^2}{1 - 3u_*^2}, \tag{9}$$

where

$$V^2 = \frac{n}{\rho + p}\,\frac{d(\rho + p)}{dn} - 1. \tag{10}$$

From this by using (2) it follows that $V^2 = c_s^2(\rho)$, where $c_s^2 = \partial p/\partial\rho$ is the squared effective speed of sound in the media. Combining (5), (6), (9) and (10) we find the following relation:

$$\frac{\rho_* + p(\rho_*)}{n(\rho_*)} = \left[1 + 3c_s^2(\rho_*)\right]^{1/2}\frac{\rho_\infty + p(\rho_\infty)}{n(\rho_\infty)}, \tag{11}$$

which gives the ρ_* for an arbitrary equation-of-state $p = p(\rho)$. Given ρ_* one can find $n(\rho_*)$ using (3) and values x_*, u_*, using (9) and (10). Then substituting the calculated values in (4) one can find the constant A. Note that there is no critical point outside the black hole horizon ($x_* > 1$) for $c_s^2 < 0$ or $c_s^2 > 1$. This means that for unstable perfect fluid with $c_s^2 < 0$ or $c_s^2 > 1$ a dark energy flux onto the black hole depends on the initial conditions. This result has a simple physical interpretation: the accreting fluid has the critical point if its velocity increases from subsonic to trans-sonic values. In a fluid with a negative c_s^2 or with $c_s^2 > 1$ the fluid velocity never crosses such a point. It should be stressed, however, that fluids with $c_s^2 < 0$ are hydrodynamically unstable (see discussion in [21,22]). The Eq. (5) together with (3) and (4) describe the requested accretion flow onto the black hole. These equations are valid for perfect fluid with an arbitrary equation-of-state $p = p(\rho)$, in particular, for a gas with zero-rest-mass particles (thermal radiation) and for a gas with nonzero-rest-mass particles. For a nonzero-rest-mass gas the couple of equations (4) and (5) is reduced to similar ones found by Michel [13]. One would note that the set of equations (3), (4) and (5) are also correct in the case of dark energy and phantom energy $\rho + p < 0$. In this case concentration $n(\rho)$ is positive for any ρ and constant C_2 in (5) is negative.

The black hole mass changes at a rate $\dot{M} = -4\pi r^2 T_0^r$ due to the fluid accretion. With the help of (4) and (5) this can be expressed as

$$\dot{M} = 4\pi A M^2 [\rho_\infty + p(\rho_\infty)]. \tag{12}$$

It follows from (12) that a black hole mass increases as it accretes e. g. a gas of particles when $p > 0$, but decreases as it accretes the phantom energy when $p + \rho < 0$. In particular, this implies that the black hole masses in the universe filled with phantom energy must decrease. This result is general. It does not depend on the specific form of the equation-of-state $p = p(\rho)$; only the satisfaction of the condition $p + \rho < 0$ is important. The physical cause of the decrease in the black hole mass is as follows: the phantom energy falls to the black hole, but the energy flux associated with this fall is directed away from the black hole. If we ignore the cosmological evolution of the density ρ_∞, then we find the law of change in the black hole mass from (12) to be

$$M = M_i \left(1 - \frac{t}{\tau}\right)^{-1}, \tag{13}$$

where M_i is the initial mass of the black hole, and τ is the evolution time scale

$$\tau = 1/\left\{4\pi A M_i [\rho_\infty + p(\rho_\infty)]\right\}. \tag{14}$$

3 Model with a Linear Equation-of-State

Let us consider the model of dark energy with a general linear equation-of-state

$$p = \alpha(\rho - \rho_0), \tag{15}$$

where α and ρ_0 are constants. Among the other cases, this model describes an ultrarelativistic gas ($p = \rho/3$), a gas with an ultra-hard equation-of-state ($p = \rho$), and the simplest model of dark energy ($\rho_0 = 0$ and $\alpha < 0$). The quantity α is related to the parameter $w = p/\rho$ of the equation-of-state by $w = \alpha(\rho - \rho_0)/\rho$. An equation-of-state with $w = const < 0$ throughout the cosmological evolution is commonly used to analyze cosmological models. The matter with such an equation-of-state is hydrodynamically unstable and can exist only for a short period. Our equation-of-state (15) for $\alpha > 0$ does not have this shortcoming. For $\alpha > 0$, it also allows the case of hydrodynamically stable phantom energy to be described, which is not possible when using an equation-of-state with $w = const < -1$. In the real Universe, the equation-of-state changes with time (i. e., w depends on t). Therefore, Eq. ((15) has a physical meaning of an approximation to the true equation-of-state only in a limited ρ range. From the physical point of view, the condition $\rho > 0$ must be satisfied for any equation-of-state in a comoving frame of reference. In particular, the state of matter with $\rho = 0$, but $p \neq 0$, is physically unacceptable. The corresponding constraints for the equation-of-state (15) are specified by conditions (23) and (24) given below. For $\alpha < 0$, there is no critical point for the accreted fluid flow. For $\alpha > 0$, using (9) we obtain the parameters at the critical point

$$x_* = \frac{1 + 3\alpha}{2\alpha}, \quad u_*^2 = \frac{\alpha}{1 + 3\alpha}. \tag{16}$$

Note that the parameters of the critical point (16) in the linear model (15) are determined only by $\partial p/\partial \rho = \alpha$ and do not depend on ρ_0, which fixes the physical nature of the fluid under consideration: a relativistic gas, dark energy, or phantom energy. Note also that no critical point exists beyond the event horizon of the black hole for $\alpha > 1$ (this corresponds to a nonphysical

situation with a superluminal speed of sound). Let us calculate the constant A, which defines the energy flux onto the black hole. We find from (3) that

$$\frac{n}{n_\infty} = \left| \frac{\rho_{\rm eff}}{\rho_{\rm eff,\infty}} \right|^{1/(1+\alpha)}, \tag{17}$$

where we introduce an effective density $\rho_{\rm eff} \equiv \rho + p = -\rho_0\alpha + (1+\alpha)\rho$. Using (11) we obtain

$$\left(\frac{\rho_{\rm eff_*}}{\rho_{\rm eff,\infty}} \right)^{\alpha/(1+\alpha)} = (1+3\alpha)^{1/2}, \tag{18}$$

where $\rho_{\rm eff_*}$ and $\rho_{\rm eff,\infty}$, are the effective densities at the critical point and at infinity, respectively. Substituting (18) into (17) and using (4), we obtain for the linear model

$$A = \frac{(1+3\alpha)^{(1+3\alpha)/2\alpha}}{4\alpha^{3/2}}. \tag{19}$$

It is easy to see that $A \geq 4$ for $0 < \alpha < 1$. $A = 4$ for $\alpha = 1$ (this corresponds to $c_s = 1$); i.e., the constant A is on the order of 1 for relativistic speeds of sound. Using (19), we obtain from (14)

$$\tau = \left[\pi M_i (\rho_\infty + p_\infty) \frac{(1+3\alpha)^{(1+3\alpha)/2\alpha}}{\alpha^{3/2}} \right]^{-1}. \tag{20}$$

To determine the fluid density on the event horizon of the black hole, we substitute (17) into (7) to yield

$$\rho_{\rm H} = \frac{\alpha\rho_0}{1+\alpha} + \left(\rho_\infty - \frac{\alpha\rho_0}{1+\alpha} \right) \left(\frac{A}{4} \right)^{(1+\alpha)/(1-\alpha)}, \tag{21}$$

where A is given by (19). For $0 < \alpha < 1$, the effective density on the horizon $\rho_{\rm eff,H}$ cannot be lower than $\rho_{\rm eff,\infty}$. A radial 4-velocity component on the horizon can be found from (8) and (21):

$$u_{\rm H} = -\left(\frac{A}{4} \right)^{-\alpha/(1-\alpha)}, \tag{22}$$

The value of $u_{\rm H}$ changes from 1 to 1/2 for $0 < \alpha < 1$.

A linear model (15) describes the phantom energy when $\rho_\infty/\rho_0 < \alpha/(1+\alpha)$. In this case, $\rho + p < 0$. However, the requirement that the density ρ be nonnegative should be taken into account. This parameter can formally be negative in the range $0 < \alpha \leq 1$. Such a nonphysical situation imposes a constraint on the linear model ((15) under consideration. For a physically proper description of the accretion process, we must require that the density ρ be nonnegative. We obtain the following constraint on the validity range of the linear model from (21) for hydrodynamically stable phantom energy:

$$\frac{\alpha}{1+\alpha} \left[1 - \left(\frac{A}{4} \right)^{-(1+\alpha)/(1-\alpha)} \right] < \frac{\rho_\infty}{\rho_0} < \frac{\alpha}{1+\alpha}. \tag{23}$$

As follows from (23), at a given α, we can always choose the parameters ρ_0 and ρ_∞ in such a way that $\rho > 0$ for any $r > 2M$. On the other hand, the model (15) describes the quintessence (not the phantom energy) for the entire r range only if $p < 0$. Consequently, a physically proper description of the quintessence can be obtained from (21) if

$$\frac{\alpha}{1+\alpha} < \frac{\rho_\infty}{\rho_0} < \frac{\alpha}{1+\alpha} \left[\frac{1}{\alpha} + \left(\frac{A}{4} \right)^{-(1+\alpha)/(1-\alpha)} \right]. \tag{24}$$

For some specific choices of α in linear model (more specifically, for $\alpha = 1/3$, 1/2, 2/3, and 1) and also in the case of Chaplygin Gas with $p = -\alpha/\rho$, the corresponding radial functions $\rho(x)$ and $u(x)$ can be calculated analytically [11].

4 Dark Energy Accretion onto a Moving and Rotating Black Hole

Let us consider the accretion onto a moving and rotating black hole in the special case of a linear equation-of-state with $\alpha = 1$. The condition $\alpha = 1$ allows an exact analytical expression to be derived for the accretion rate of dark energy onto a black hole. For $\alpha = 1$, we easily find from (17) that

$$\frac{n}{n_\infty} = \left| \frac{\rho_{\text{eff}}}{\rho_{\text{eff},\infty}} \right|^{1/2}. \tag{25}$$

We have the continuity equation for the particle number density $(nu^\mu)_{;\mu} = 0$. Let us introduce the scalar field ϕ in terms of which the fluid velocity can be expressed as follows (there is no torsion in the fluid):

$$\frac{\rho + p}{n} u_\mu = \phi_{,\mu}. \tag{26}$$

Using (25) and (26) we derive an equation for the auxiliary function ϕ:

$$\phi^{\mu}_{;\mu} = 0. \tag{27}$$

Exactly the same equation arises in the problem of the accretion of a fluid with the equation-of-state $p = \rho$. Thus, we reduce the problem of a black hole moving in dark energy with an equation-of-state $p = \rho - \rho_0$ to the problem of a fluid with an extremely hard equation-of-state, $p = \rho$. Using the method suggested in [23], we obtain the mass evolution law for a moving and rotating black hole immersed in dark energy with the equation-of-state $p = \rho - \rho_0$:

$$\dot{M} = 4\pi(r_+^2 + a^2)[\rho_\infty + p(\rho_\infty)]u^0_{\text{BH}}, \tag{28}$$

where $r_+ = M + (M^2 - a^2)^{1/2}$ is an event horizon radius of a rotating black hole, $a = J/M$ is a specific angular momentum of the black hole (rotation parameter), and u^0_∞ is the zeroth 4-velocity component of the black hole relative to the fluid. Expression (28) for $u^0_{\text{BH}} = 0$ reduces to (12) for a Schwarzschild ($a = 0$) black hole at rest.

5 Black Holes in the Big Rip Universe

Now we turn to the problem of the black hole evolution in the universe with the Big Rip when a scale factor $a(t)$ diverges at finite time [5]. For simplicity we will take into account only dark energy and will disregard all others forms of energy. The Big Rip solution is realized for in the linear model (15) for $\rho + p < 0$ and $\alpha < -1$. From the Friedman equations for the linear equation-of-state model one can obtain: $|\rho + p| \propto a^{-3(1+\alpha)}$. Taking for simplicity $\rho_0 = 0$ we find the evolution of the density of a phantom energy in the universe:

$$\rho_\infty = \rho_{\infty,i} \left(1 - \frac{t}{\tau}\right)^{-2}, \tag{29}$$

where

$$\tau^{-1} = -\frac{3(1+\alpha)}{2} \left(\frac{8\pi}{3}\rho_{\infty,i}\right)^{1/2} \tag{30}$$

and $\rho_{\infty,i}$ is an initial density of the cosmological phantom energy and the initial moment of time is chosen so that the 'doomsday' comes at time τ. From (29) and (30) it is easy to see that the Big Rip solutionis realized for $\alpha \equiv \partial p/\partial\rho < -1$. In general, the satisfying the condition $\rho + p < 0$ is not enough for the possibility for Universe to come to Big Rip. From (12) using (29) we find the black hole mass evolution in the universe coming to the Big Rip:

$$M = M_i \left(1 + \frac{M_i}{\dot{M}_0 \tau} \frac{t}{\tau - t}\right)^{-1}, \tag{31}$$

where

$$\dot{M}_0 = (3/2)\, A^{-1} |1 + \alpha|, \tag{32}$$

and M_i is the initial mass of the black hole. For $\alpha = -2$ and typical value of $A = 4$ (corresponding to $u_H = -1$) we have $\dot{M}_0 = 3/8$. In the limit $t \to \tau$ (i.e. near the Big Rip) the dependence of black hole mass on t becomes linear, $M \simeq \dot{M}_0(\tau - t)$. While t approaches to τ the rate of black hole mass decrease does not depend on both an initial black hole mass and the density of the phantom energy: $\dot{M} \simeq -\dot{M}_0$. In other words masses of all black holes in the universe tend to be equal near the Big Rip. This means that the phantom energy accretion prevails over the Hawking radiation until the mass of black hole is the Planck mass. However, formally all black holes in the universe evaporate completely at Planck time before the Big Rip due to Hawking radiation.

6 Scalar field accretion

In remaining let us confront our results with the calculations of (not phantom) scalar field accretion onto the black hole [16,17,18,19]. The dark energy is usually modelled by a scalar field ϕ with potential $V(\phi)$. The perfect fluid approach is more rough because for given 'perfect fluid variables' ρ and p one can not restore the 'scalar field variables' ϕ and $\nabla\phi$. In spite of the pointed difference between a scalar field and a perfect fluid we show below that our results are in a very good agreement with the corresponding calculations of a scalar field accretion onto the black hole. The standard-form Lagrangian of a scalar field is $L = K - V$, where K is a kinetic term of a scalar field ϕ and V is a potential. For the standard choice of a kinetic term $K = \phi_{;\mu}\phi^{;\mu}/2$ the energy flux is $T_{0r} = \phi_{,t}\phi_{,r}$. Jacobson [16] found the scalar field solution in Schwarzschild metric for the case of zero potential $V = 0$: $\phi = \dot{\phi}_\infty[t + 2M\ln(1 - 2M/r)]$, where ϕ_∞ is the value of the scalar field at the infinity. In [18] it was shown that this solution remains valid also for a rather general form of runaway potential $V(\phi)$. For this solution we have $T_0^r = -(2M)^2\dot{\phi}_\infty^2/r^2$ and correspondingly $\dot{M} = 4\pi(2M)^2\dot{\phi}_\infty^2$.

The energy-momentum tensor constructed from Jacobson solution completely coincides with one for perfect fluid in the case of ultra-hard equation-of-state $p = \rho$ under the replacement $p_\infty \to \dot{\phi}_\infty^2/2$, $\rho_\infty \to \dot{\phi}_\infty^2/2$. It is not surprising because the theory of a scalar field with a zero potential $V(\phi)$ is identical to perfect fluid consideration [24]. In a view of this coincidence it is easily to see the agreement of our result (12) for $\dot{M}$ in the case of $p = \rho$ and the corresponding result of [16,18]. To describe the phantom energy the Lagrangian of a scalar field must have a negative kinetic term [5], e. g., $K = -\phi_{;\mu}\phi^{;\mu}/2$ (for a more general case of negative kinetic term see [20]). In this case the phantom energy flux onto black hole has the opposite sign, $T_{0r} = -\phi_{,t}\phi_{,r}$, where ϕ is the solution of the same Klein-Gordon equation as in the case of standard scalar field, however with a replacement $V \to -V$. For zero potential this solution coincides with that obtained by Jacobson [16] for a scalar field with the positive kinetic term. Lagrangian with a negative kinetic term and $V(\phi) = 0$ does not describe, however, the phantom energy. At the same time, the solution for scalar field with potential $V(\phi) = 0$ is the same as with a positive constant potential $V_0 = const$, which can be chosen so that $\rho = -\dot{\phi}^2/2 + V_0 > 0$. A corresponding scalar field represents the required accreting phantom energy $\rho > 0$ and $p < -\rho$ and provides a black hole decreasing with the rate $\dot{M} = -4\pi(2M)^2\dot{\phi}_\infty^2$. A simple example of phantom cosmology without a Big Rip [25] is realized for a scalar field with the potential $V = m^2\phi^2/2$, where $m \sim 10^{-33}$ eV. After short transition phase this cosmological model tends to the asymptotic state with $H \simeq m\phi/3^{1/2}$ and $\dot{\phi} \simeq 2m/3^{1/2}$. In the Klein-Gordon equation the m^2 term (with a mentioned replacement $V \to -V$) is comparable to other terms only at the cosmological horizon distance. This means that the Jacobson solution is valid for this case also. Calculating the corresponding energy flux one can easily obtain $\dot{M} = -4\pi(2M)^2\dot{\phi}_\infty^2 = -64M^2m^2/3$. For $M_0 = M_\odot$ and $m = 10^{-33}$ eV the effective time of black hole mass decrease is $\tau = (3/64)M^{-1}m^{-2} \sim 10^{32}$ yr.

Acknowledgments

This work was supported in part by the Russian Foundation for Basic Research grants 04-02-16757 and 06-02-16342, and the Russian Ministry of Science grant 1782.2003.2.

References

N. Bahcall, J.P. Ostriker, S. Perlmutter and P.J. Steinhardt, *Science* **284**, 1481 (1999); C.L. Bennett *et al.*, *Astrophys. J. Suppl. Ser.* **148**, 1 (2003).
2. C. Wetterich, *Nucl. Phys.* B **302**, 668 (1988); P.J.E. Peebles and B. Ratra, *Astrophys. J.* **325**, L17 (1988); A. Albrecht and C. Skordis, *Phys. Rev. Lett.* **84**, 2076 (2000).
3. C. Armendariz-Picon, T. Damour and V. Mukhanov, *Phys. Lett.* B **458**, 209 (1999); Takeshi Chiba, Takahiro Okabe and Masahide Yamaguchi, *Phys. Rev.* D **62**, 023511 (2000).
4. I. Zlatev, L. Wang, P. Steinhardt, *Phys. Rev. Lett.* **82**, 895 (1998); P. Steinhardt, L. Wang, I. Zlatev, *Phys. Rev.* D **59**, 123504 (1999).
5. R.R. Caldwell, *Phys. Lett.* B **545**, 23 (2002); R.R. Caldwell, M. Kamionkowski and N.N. Weinberg, *Phys. Rev. Lett.* **91**, 071301 (2003).
6. B. McInnes, *JHEP* **0208**, 029 (2002); M. Bouhmadi-Lopez, J.A.J. Madrid, *JCAP* **0505**, 005 (2005).
7. U. Alam, V. Sahni, T.D. Saini, A.A. Starobinsky, *Mon. Not. Roy. Astron. Soc.* **354**, 275 (2004).
8. S. Nojiri, S.D. Odintsov, *Phys. Lett.* B **562**, 147 (2003).
9. I. Brevik, S. Nojiri, S.D. Odintsov, L. Vanzo, *Phys. Rev.* D **70**, 043520 (2004).
10. V.A. Rubakov, arXiv:hep-th/0604153.
11. E.O. Babichev, V.I. Dokuchaev and Yu.N. Eroshenko, *Phys. Rev. Lett.* **93**, 021102 (2004); E.O. Babichev, V.I. Dokuchaev, and Yu.N. Eroshenko, *JETP* **100**, 528 (2005).
12. H. Bondi, *Mon. Not. Roy. Astron. Soc.* **112**, 195 (1952)).
13. F.C. Michel, Ap. Sp. Sc. **15**, 153, (1972).
14. S.W. Hawking and G.F.R. Ellis, *The large scale structure of space-time*, (Cambridge University Press, England, 1973), Chapter 4.3.
15. M. Visser, S. Kar and N. Dadhich, *Phys. Lett.* B **90**, 201102 (2003); P.F. Gonzalez-Diaz, *Phys. Rev.* D **68**, 084016 (2003).
16. T. Jacobson, *Phys. Lett.* B **83**, 2699 (1999).
17. R. Bean and J. Magueijo, *Phys. Rev.* D **66**, 063505 (2002).
18. A. Frolov and L. Kofman, *J. Cosmology Astrop. Phys.* **5**, 9 (2003).
19. W.G. Unruh, *Phys. Rev.* D **14**, 3251 (1976); L.A. Urena-Lopez and A.R. Liddle, *Phys. Rev.* D **66**, 083005 (2002); M.Yu. Kuchiev and V.V. Flambaum, *Phys. Rev.* D **70**, 044022 (2004).
20. P.F. Gonzalez-Diaz, *Phys. Lett.* B **586**, 1 (2004).
21. J.C. Fabris and J. Martin, *Phys. Rev.* D **55**, 5205 (1997).
22. S.M. Carroll, M. Hoffman and M. Trodden, *Phys. Rev.* D **68**, 023509 (2003).
23. L.I. Petrich, S.L. Shapiro and S.A. Teukolsky, *Phys. Rev. Lett.* **60**, 1781 (1988).
24. V.N. Lukash, *JETP* **52**, 5 (1980).
25. M. Sami and A. Toporensky, *Mod. Phys. Lett. A* **19**, 1509 (2004).

SUPERSYMMETRIC F_D-HYBRID INFLATION

Björn Garbrecht
School of Physics & Astronomy, The University of Manchester
Oxford Road, Manchester M13 9PL, UK

We present F_D-inflation, a variant of supersymmetric F-term hybrid inflation with a subdominant D-term, which controls the decay of heavy gauge-sector fields produced during preheating after inflation. Late decays of these particles give rise to an entropy release and therefore to dilution of gravitinos which would otherwise be in conflict with big-bang-nucleosynthesis. After inflation, the inflaton acquires a vacuum expectation value of TeV-scale, which gives rise to the μ-term of the MSSM as well as to TeV-scale Majorana masses for right-handed neutrinos. Baryogenesis takes place through thermal resonant leptogenesis.

Supersymmetric models for hybrid inflation [1,2] are of great interest, as they tie together particle physics beyond the Standard Model with the inflationary paradigm. As a consequence, they may not only be tested through their predictions for the spectrum of primordial density fluctuations. They also should implement a successful scenario for hot Big Bang cosmology with a viable mechanism for baryogenesis and have to avoid on the other hand the overproduction of unwanted relics, such as topological defects and gravitinos. Finally, their predictions might also be directly accessible to future laboratory experiments, such as the LHC.

An intriguing observation is that due to soft supersymmetry breaking, the singlet inflaton naturally acquires an electroweak-scale vacuum expectation value. When coupling the inflaton to the MSSM Higgs fields, one therefore obtains a μ-term of supersymmetry breaking scale, providing a relation between electroweak and SUSY scales[3]. One may however see a disadvantage in this model, since it requires small superpotential couplings for the inflaton of less than 10^{-5} in order not to lead to a high reheat temperature inducing the overproduction of gravitinos.

Here we present a recently suggested model[4] which assumes that the gauge symmetry of the inflaton-waterfall sector is a $\mathrm{U}(1)_X$, which is hidden to the MSSM sector. Let us consider the superpotential

$$W = \kappa \hat{S}\left(\hat{X}_1\hat{X}_2 - M^2\right) + \lambda \hat{S}\hat{H}_u\hat{H}_d + \frac{\rho}{2}\hat{S}\hat{N}_i\hat{N}_i + h^{\nu}_{ij}\hat{L}_i\hat{H}_u\hat{N}_j + W^{(\mu=0)}_{\mathrm{MSSM}}, \quad (1)$$

where $W^{(\mu=0)}_{\mathrm{MSSM}}$ is the MSSM superpotential without the μ-term. The inflaton singlet is denoted by $\hat{S}$, and $\hat{X}_{1,2}$ are chiral superfields of $\mathrm{U}(1)_X$-charge one and minus one, respectively. The MSSM-Higgs fields are denoted by $\hat{H}_{u,d}$, and there are three right handed neutrinos $\hat{N}_i$, $i = 1, \ldots, 3$. We assume that the coupling of the inflaton to the N_i is at tree level O(3)-symmetric, which opens up the possibility of baryogenesis by low-scale resonant leptogenesis [5,6].

The superpotential (1) is of the form suitable for standard F-term inflation. In the D-term potential V_D, we allow for a subdominant Fayet-Iliopoulos term m_{FI}

$$V_D = \frac{g^2}{8}\left(|X_1|^2 - |X_2|^2 - m^2_{\mathrm{FI}}\right)^2, \quad (2)$$

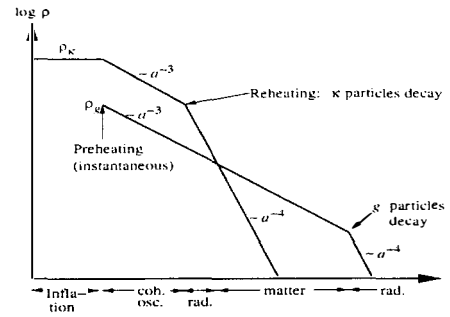

Figure 1: *The thermal history of the Universe in the F_D-model.*

where g is the $U(1)_X$ gauge-coupling constant. The Fayet-Iliopoulos term may be radiatively generated after the breakdown of $U(1)_X$ and is then naturally subdominant when compared to M. At the end of inflation, the usual waterfall transition occurs after which the waterfall fields attain the vacuum expectation values $X_{1,2} = M$, $S = 0$. The mass eigenstates are then given by

$$X_\pm = \frac{1}{\sqrt{2}}(X_1 \pm X_2)\,, \tag{3}$$

where X_+ is of mass $\sqrt{2}\kappa M$ and X_- of mass gM. These types of particles are both produced through preheating during the waterfall transition. The key observation is that for $m_{\rm FI} = 0$, the superpotential (1) and the D-term potential are invariant under a discrete D-parity, $X_1 \to X_2$ or equivalently $X_\pm \to \pm X_\pm$. As a consequence, the superheavy g-sector particles X_- are stable unless $m_{\rm FI} \neq 0$, which then allows for their decay into κ-sector X_+-particles.

Therefore, the X_- particles may dominate the energy density of the Universe after inflation until they decay at late times, *cf.* Figure 1. This late time decay leads to a dilution of gravitinos, such that a gravitino abundance in accordance with big bang nucleosynthesis can be achieved without the requirement of tiny tree-level couplings.

An extensive analytical and numerical study of the thermal history of the Universe as well as a discussion of other issues such as topological defects is subject of work in progress [7], demonstrating explicitly the viability of the the F_D-model. We also present a detailed discussion of the consequences for collider phenomenology. In conclusion, the F_D-model represents a formulation of a minimal model for cosmology and particle physics. Its motivation is beyond a purely empirical level, since it avoids fine tunings, most importantly the gauge hierarchy problem by the incorporation of the MSSM; and it will be testable by collider experiments in the near future.

The author acknowledges fruitful collaboration with Constantinos Pallis and Apostolos Pilaftsis on this topic.

References

1. E. J. Copeland, A. R. Liddle, D. H. Lyth, E. D. Stewart and D. Wands, *Phys. Rev.* D **49**, 6410 (1994).
2. G. R. Dvali, Q. Shafi and R. K. Schaefer, *Phys. Rev. Lett.* **73**, 1886 (1994).
3. G. R. Dvali, G. Lazarides and Q. Shafi, *Phys. Lett.* B **424**, 259 (1998).
4. B. Garbrecht and A. Pilaftsis, *Phys. Lett.* B **636**, 154 (2006).
5. A. Pilaftsis *Phys. Rev.* D **56**, 5431 (1997).
6. A. Pilaftsis and T. Underwood *Nucl. Phys.* B **692**, 303 (2004).
7. B. Garbrecht, C. Pallis and A. Pilaftsis, to appear.

WMAP Constraints on Dissipative Models of Inflation

Lisa M. H. Hall

Department of Applied Mathematics, University of Sheffield, Sheffield, S3 7RH, England

We explore the parameter space of dissipative inflation. In this class of models, non-equilibrium effects lead to a damping term in the equation of motion. In turn, the inflationary field (called the inflation) dissipates energy in the form of radiation, thereby preventing the universe from supercooling. Distinguishable power spectra characteristics have been identified from dissipative models, including oscillatory features. A crude parameter analysis showed that reasonable values of the model's parameters give a good fit to the WMAP data. An MCMC analysis of the parameter space of several dissipative models has been undertaken using WMAP data. Characteristics unique to these models will be discussed and constraints are placed on the level of dissipation in inflation.

1 Introduction

In the original model of inflation, the early universe undergoes exponential expansion and supercools as a result of a radiation redshift[1]. A subsequent, independent phase of reheating is required to return the universe to a radiation dominated state [2–6].

This original picture ignores any interaction of the inflationary scalar field. It was, however, shown that interaction with a thermal bath leads to an additional friction term in the equation of motion[7]. Hence, if the universe begins in a thermally excited state, the inflaton equation of motion should pick up a sizable friction term from such interactions[8]. The interaction results in radiation production, which prevents the universe from supercooling. This effect lead to the name *warm inflation*[9]. Since the characteristic friction terms are not limited to finite temperature effects, the more general name *dissipative inflation* shall be adopted here. Over the past years, dissipative models have been shown to be a valid description of the early universe. [10–18].

A study of the cosmological perturbations noted interesting characteristics in the power spectra from dissipative inflation[20]; running of the spectral index is predicted, while temperature dependent coupling between the field perturbations can lead to oscillatory spectra. A crude best-fit parameter estimation was completed with the first year WMAP data (WMAPI) [19] for one model[21]. In this case, parameters exist which map one model of warm inflation to observational CMB data.

I discuss an initial Markov Chain Monte Carlo (MCMC) parameter walk for the dissipative parameters using CosmoMC[27]. Only the results from the first-year WMAP data will be discussed; results from the WMAP second release data will be published elsewhere. Several models of dissipation are considered and a general form for the friction term is investigated.

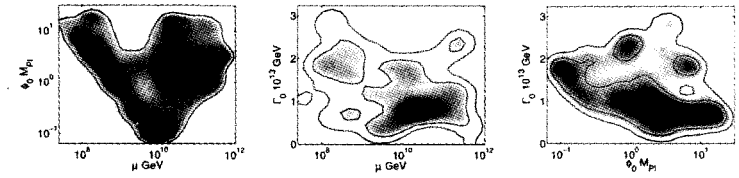

Figure 1: Case I: Preliminary WMAPI marginalised constraints on the dissipative parameters, μ,ϕ_0,Γ_0

2 Dissipative Dynamics

In an expanding, homogeneous universe, the dissipative inflaton equation of motion is given by

$$\ddot{\phi} + (3H + \Gamma)\dot{\phi} + V_{,\phi} = 0, \tag{1}$$

where $V(\phi, T)$ is the thermodynamic potential and $\Gamma(\phi, T)$ is the damping term due to interactions between the inflaton ϕ and surrounding fields.

Accounting for dissipation, the zero curvature Friedmann and continuity equations become

$$3H^2 = \frac{8\pi}{m_{pl}^2}\left(\frac{1}{2}\dot{\phi}^2 + V(\phi) + \rho_r\right), \qquad \dot{\rho}_r + 4H\rho_r = \Gamma\dot{\phi}^2. \tag{2}$$

When $\Gamma \equiv \Gamma(\phi, T)$, the perturbed equation of motion leads to a non-trivial coupling of the perturbed radiation and inflaton fields, which leads to oscillations in the spectrum. For the extent of this work, the fluctuations are taken to be thermally generated. The dissipative inflationary dynamics are described in Hall et al[21], where a full discussion of the background and perturbation solutions can be found.

It is convenient to adopt a general form for the friction term

$$\Gamma(\phi, T) = \Gamma_0 \left(\frac{\phi}{\phi_0}\right)^{\alpha} \left(\frac{T_0}{T}\right)^{\beta}. \tag{3}$$

Choices of α and β relate to specific dissipative models. When $\alpha = \beta = 0$, the friction term is a constant, which is not physical. We will consider three cases:

- **Case I** $\alpha = 1$, $\beta = 0$
- **Case II** $\alpha = 2$, $\beta = 0$
- **Case III** $\alpha = 2$, $\beta = 1$

which are aimed to cover a wide range of possible friction terms. The expected curvature perturbation power spectra, $\mathcal{P}_{\mathcal{R}}$, for these models have already been explored[20,21]. Case I leads to a flat spectrum of curvature perturbations, with an inherent amount of blue to red running. Case III exhibits oscillations in the power spectrum, with diminishing amplitude for increasing wavenumber.

Case I represents the two-tier, zero-temperature model proposed by Berera and Ramos[18,26]. The friction term is calculated using a close-to-equilibrium approach and can be approximated by

$$\Gamma(\phi) \approx \frac{g^3 h^2 \phi}{512\pi^2} = \gamma\phi. \tag{4}$$

Case III simulates the original Hosoya and Sakagami model[7], in which the inflaton interacts with a heat bath of temperature, T, with coupling, g:

$$\Gamma(\phi, T) \propto \frac{g^4\phi^2}{T}. \tag{5}$$

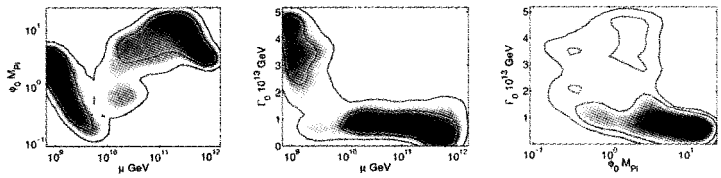

Figure 2: Case II: Preliminary WMAPI marginalised constraints on the dissipative parameters, μ,ϕ_0,Γ_0

	Case I	Case II
μ [GeV]	1.9×10^{10}	8.5×10^{11}
ϕ_0 [M_{Pl}]	6.2	2.3
Γ_0 [GeV]	7.5×10^{12}	2.3×10^{13}
$ln\mathcal{L}$	727.1	726.6

Table 1: Best fit values for the dissipative parameters for Cases I and II

The chosen inflaton potential originates from soft supersymmetry breaking:

$$V(\phi) = \mu^2 \left(\phi^2 \log \frac{\phi^2}{\phi_0^2} + \phi_0^2 - \phi^2 \right). \tag{6}$$

3 Numerical Simulation

A numerical code has been developed for calculating the power spectrum from dissipative models[20]. The code integrates both the background and perturbative equations in order to calculate the curvature power spectrum.

In combination with CosmoMC, the code allows a full exploration of the parameter space of dissipative models. While the cosmological parameters were included in the Monte Carlo walk, this talk concentrates on the dissipative parameters; we have marginalised over the cosmological parameters. Two priors have been assumed on the friction coefficient. Firstly, strong dissipation is assumed, $\Gamma > 3H$ (due to the calculation of thermal fluctuations) and the code cannot simulate the supercooled limit ($\Gamma \to 0$). Note, however, that slow-roll *supercooled* inflation cannot occur with this potential, since the standard slow-roll equations are difficult to satisfy. Secondly, for large values of the friction term, the inflaton rolls extremely slowly and large numbers of e-folds, N, can be obtained. Since the friction term is proportional to perturbative coupling constants, large friction terms are seemingly unphysical and a large N cut-off has been implemented, ($N < 300$). In these limits, the code defaults to an abnormally large power amplitude and exploration of those regions is suppressed.

4 Results

For cases I and II, the allowed regions of parameter space are shown in Fig.1 and Fig.2 respectively. The 1σ and 2σ contours are shown. Note that, at the time of writing, the MCMC chains are non-convergent, explaining the irregular parameter regions. It is noticeable that several distinct regions of likelihood appear in the parameter space; in particular, case II appears bimodal. It is not clear at present, whether this effect is due to the non-convergence or if the likelihood surface is multimodal.

The best fit parameters are given in Table 1. Notice that the energy scale of the potential, μ, is extremely high. In case II, this scale is higher, but the scale of the inflaton, ϕ_0, is decreased. The χ^2 values are also given in terms of the likelihood, $\mathcal{L}$, where $\chi^2_{eff} = -2 \ln \mathcal{L}$.

Case I can be physically related to the two-tier model of Berera and Ramos, as in Eqn.(4). If $g \approx h$, the approximate 1σ bound, $0.3 < \Gamma_0 < 2.0$, corresponds to $0.19 < g < 0.30$, which is within the perturbative regime.

For case III, oscillatory spectra are observed, with decreasing amplitude, as expected. It is widely accepted that the primordial power spectrum needs to be closely scale invariant to explain the acoustic structure in the CMB. However, each oscillation has its minimum at $\mathcal{P}_k = 0$, which ultimately implies zeroes in the acoustic spectrum. A variation in μ or Γ_0 results in a change in overall amplitude, while a difference in ϕ_0 leads to a phase change. None of the parameters helps to recover a scale invariant spectrum. Since WMAP does not see such a strong deviation from scale invariance, oscillations on this scale can be instantly ruled out.

5 Conclusion

A full MCMC analysis has been completed for dissipative models of inflation, in which an additional friction term Γ dominates over the expansion, H. Three models of dissipation, described by the parameters, μ, ϕ_0 and Γ_0, were compared to the first year WMAP data. In each case, the power spectrum was altered due to the dissipative terms. For two cases, in which $\Gamma = \Gamma(\phi)$, the 1 and 2σ parameter regions were found and best fit values are found to be within physically acceptable bounds. The results have been compared to particle physics models of dissipation, with good agreement. The third case, in which $\Gamma = \Gamma(\phi, T)$, oscillatory spectra differ too greatly from scale invariance. This results in a poor fit to the CMB. At the time of writing, the MCMC chains had not converged and only the preliminary results have been given. Fully converged chains compared to the WMAPII data will be published elsewhere. The work in this talk was completed in full collaboration with Hiranya Peiris, at KICP, Chicago.

References

1. A. H. Guth, "The Inflationary Universe: A Possible Solution To The Horizon And Flatness Problems," Phys. Rev. D **23**, 347 (1981).
2. A. Albrecht, P. J. Steinhardt, M. S. Turner and F. Wilczek, Phys. Rev. Lett. **48** (1982) 1437.
3. A. D. Dolgov and A. D. Linde, Phys. Lett. B **116**, 329 (1982).
4. L. F. Abbott, E. Farhi and M. B. Wise, Phys. Lett. B **117**, 29 (1982).
5. L. Kofman, A. D. Linde and A. A. Starobinsky, Phys. Rev. Lett. **73**, 3195 (1994)
6. L. Kofman, A. D. Linde and A. A. Starobinsky, Phys. Rev. D **56**, 3258 (1997)
7. A. Hosoya and M. a. Sakagami, Phys. Rev. D **29**, 2228 (1984).
8. I. G. Moss, Phys. Lett. B **154**, 120 (1985).
9. A. Berera, Phys. Rev. Lett. **75**, 3218 (1995)
10. A. Berera, Phys. Rev. D **54**, 2519 (1996)
11. A. Berera, Phys. Rev. D **55**, 3346 (1997)
12. A. Berera, M. Gleiser and R. O. Ramos, Phys. Rev. D **58**, 123508 (1998)
13. A. Berera, M. Gleiser and R. O. Ramos, Phys. Rev. Lett. **83**, 264 (1999)
14. J. Yokoyama and A. D. Linde, Phys. Rev. D **60**, 083509 (1999)
15. I. G. Moss, Nucl. Phys. B **631**, 500 (2002)
16. A. Berera and R. O. Ramos, Phys. Rev. D **63**, 103509 (2001)
17. I. D. Lawrie, Phys. Rev. D **66**, 041702 (2002)
18. A. Berera and R. O. Ramos, Phys. Lett. B **567**, 294 (2003)
19. H. V. Peiris *et al.*, Astrophys. J. Suppl. **148** (2003) 213
20. L. M. H. Hall, I. G. Moss and A. Berera, Phys. Rev. D **69**, 083525 (2004)
21. L. M. H. Hall, I. G. Moss and A. Berera, Phys. Lett. B **589**, 1 (2004)
22. L. M. H. Hall and I. G. Moss, Phys. Rev. D **71**, 023514 (2005)
23. V. N. Lukash, Sov. Phys. JETP **52**, 807 (1980) [Zh. Eksp. Teor. Fiz. **79**, (1980)].
24. J. M. Bardeen, Phys. Rev. D **22**, 1882 (1980).
25. D. H. Lyth, Phys. Rev. D **31**, 1792 (1985).
26. A. Berera and R. O. Ramos, Phys. Lett. B **607**, 1 (2005)
27. A. Lewis and S. Bridle, Phys. Rev. D **66** (2002) 103511 [arXiv:astro-ph/0205436].
28. L. Verde *et al.*, Astrophys. J. Suppl. **148** (2003) 195

Looking for TransPlanckia in the CMB

Hael Collins
Department of Physics, University of Massachusetts, Amherst MA 01003

R. Holman
Department of Physics, Carnegie Mellon University, Pittsburgh PA 15213

The exponential stretching of length scales during inflation leads to the possibility that effects occurring at the smallest distance scales might be imprinted on large scale observables such as the CMB power spectrum. To be able to make credible predictions, we need to be able to construct an effective theory that absorbs the effects of new physics that could modify the initial state of inflaton quantum fluctuations. We provide such a formalism in terms of an *effective* initial state. We describe the formalism, the divergence structure of the effective theory and describe how it will be applied to computing TransPlanckian effects in inflation

1 Introduction

Observational data lend credence to the idea that the primordial metric perturbations observed in the CMB[1] were produced during an inflationary epoch in the early universe. In fact, the data are strong enough to be able to constrain various models of inflation; as an example, WMAP3 data[1] together with large scale structure information places severe pressure on inflationary models based on certain power law potentials for the inflaton[2].

While only 60–70 e-folds of inflation are necessary to solve the various fine tuning problems inflation was devised to deal with, most models tend to inflate for many more e-folds than this. As a consequence, length scales corresponding to the largest cosmological structures today had their origin in quantum fluctuations whose length scales corresponded to sub-Planckian sizes during inflation. A natural question to ask is the following: if the length scales can be stretched from sub-Planckian sizes to cosmological, can *physical* effects from scales smaller than the Planck length be imprinted on cosmological observables such as the CMB? This is the "trans-Planckian" problem[3] of inflation; we will take "trans-Planckian" here to mean energy scales larger than the Hubble scale during inflation.

While it has been dubbed a problem, this peculiar effect of inflation could just as easily be called an opportunity. The downside of this effect is that if it did happen, it would be an egregious violation of the notion of decoupling of scales which underlies most of physics. If such an infiltration of short-distance physics could propagate to the longest distance measured, we would have a difficult time in understanding why we have been able to neglect this effect in high energy collisions, for example. On the other hand, there is an incredible upside if the physics scales up. In this case, measurements of the CMB would be able to access physics well beyond any currently envisaged accelerator.

It is this possibility that motivates us to find ways to accurately estimate the size of *generic* trans-Planckian signals. Our approach is to develop an effective theory description of this effect.

This is based on a perturbative expansion that uses the smallness of the ratio of the two natural scales—H, the Hubble scale during inflation and M, the scale associated with new physics. If the signal were only suppressed by H/M, it could conceivably be observed in the not too distant future.

From the perspective of the effective theory principle, new physics can appear in either the time evolution of the inflaton and its fluctuations or in their "initial" states. The first of these—how the system evolves—is more familiar since the evolution of the quantum fluctuations of the inflaton is determined by its interaction Hamiltonian. The form of the general set of possible corrections that we can add to this Hamiltonian, encoding the effects of the unknown physics, is rather constrained by the space-time symmetries. Given these constraints, the size of the corrections from the unknown physics relative to the leading prediction for an inflationary model is usually suppressed by a factor[4] of $(H/M)^2$. The other ingredient—the state of the inflaton—is more directly related to the trans-Planckian problem because it is the details of the initial state we have chosen which are being stretched to vast scales. The leading correction from these effects is typically much less suppressed, scaling instead[5] as H/M.

In this article, we will concentrate on the effect of trans-Planckian physics on the initial state[6]. We give a general parametrization of this initial state that contains corrections to the standard initial state in both the IR as well as the UV. We then discuss how the renormalization program is modified in the presence of this state and discuss the effects of this state on the problem of back-reaction onto the stress energy tensor.

2 An Effective Theory of Initial Conditions

Let's recall how the power spectrum is usually computed in inflation. We consider the gauge invariant variable Φ which is a linear combination of inflaton and metric perturbations; it behaves as a free field during inflation. We quantize it in the usual way: first decompose Φ in terms of the appropriate modes (solutions of the massless, minimally coupled, free scalar field equations of motion) and then convert the coefficients to operators acting on the relevant Fock space. If we write

$$\Phi(\eta, \vec{x}) = \int \frac{d^3k}{(2\pi)^3} \left[\mathcal{U}_k(\eta)\ e^{i\vec{k}\cdot\vec{x}} a_{\vec{k}} + \mathcal{U}_k^*(\eta) e^{-i\vec{k}\cdot\vec{x}} a_{\vec{k}}^\dagger \right], \tag{1}$$

where η is conformal time, then

$$\left[\frac{d^2}{d\eta^2} + 2aH\frac{d}{d\eta} + k^2 \right] \mathcal{U}_k = 0. \tag{2}$$

How do we pick the appropriate solution of Eq. 2? The standard answer is to pick the linear combination that matches to the flat space vacuum as $\eta \to -\infty$. This is the so-called Bunch-Davies (BD) vacuum $|BD\rangle$. The reasoning here is that at short-distances, the field should not be able to tell that the spacetime is curved so that the vacuum should just be the Minkowski one.

We have to take into account the possibility that as we try to match to the flat space ground state at short distance, it may be that the dynamics itself changes. For example, suppose the inflaton is a fermionic composite particle, with a scale of compositeness M. Then at distances shorter than M^{-1}, the scalar field description is completely inappropriate in terms of looking for the vacuum state. If $M \sim M_{\rm pl}$, then we expect that at distances shorter than M^{-1}, we would expect both the field dynamics and gravity to be described by more complicated operators. What we can glean from this discussion is that assuming that we can make use of the scalar mode equations to arbitrarily short distances, and hence to argue that the BD vacuum is the "natural" choice of ground state, is a *radical* statement. A *much* more conservative statement

is that we should choose a ground state that is general enough to encode possible corrections to the Klein-Gordon equation of motion coming from physics at energy scales larger than M.

We implement this by the imposition of boundary conditions at the initial time hypersurface $\eta = \eta_0$. If we start with the BD modes, $\mathcal{U}_k^{\rm BD}$, we write our modes as

$$\begin{aligned} \mathcal{U}_k(\eta) &= N_k \left[\mathcal{U}_k^{\rm BD}(\eta) + e^{\alpha_k}\mathcal{U}_k^{\rm BD*}\right], \\ e^{\alpha_k} &= \frac{\omega_k - \varpi_k}{\omega_k^* + \varpi_k} \\ N_k &= \frac{1}{\sqrt{1 - e^{\alpha_k + \alpha_k^*}}}. \end{aligned} \tag{3}$$

Here ω_k is the frequency appearing in the scalar field equation, while

$$\partial_\eta \mathcal{U}_k(\eta_0) = -i\varpi_k \mathcal{U}_k(\eta_0). \tag{4}$$

The structure function e^{α_k} describes how the state differs from the assumed vacuum at different scales. At very large distances, if we are considering an excited state the structure function need not vanish; but the signals of new physics should not be very apparent since the approximation that the theory is that of a nearly free scalar field is good far below M. In this regime, it is natural for the effects of new physics to be suppressed by powers of k/M.

Our goal here is to implement an effective theory description of the initial state. From this perspective, the state in Eq. 3 is only meant to be appropriate for observables measured at scales well below M, and not that for a complete theory which is applicable to measurements made at any scale. As a consequence, the effective states can contain structures which are the analogues of the nonrenormalizable operators used in an effective field theory Lagrangian. In both cases, the theory remains predictive at long distances since there is a natural small parameter given by the ratio of the energy or momentum of the process being studied to the scale of new physics M. In both cases too, renormalization of the theory can introduce further higher order corrections so that an infinite number of constants is often needed to make a prediction to arbitrary accuracy; but to any finite accuracy, only a small number are needed since the rest are suppressed by high powers of the small ratio of scales. At scales near M, the effective Lagrangian description breaks down but at these energies we should be able to observe the dynamics which produced the nonrenormalizable operators in the low energy effective theory. Similarly, once we probe short distances directly, we should see corrections to the Klein-Gordon equation and the modes $U_k(\eta)$ given in Eq. 3 should be replaced with the correct short-distance eigenmodes.

The effective theory description of the initial state relies upon the smallness of the measured scale, $k_{\rm exp}$, compared with the scale of new physics, M, but this ratio is also influenced by the expansion,

$$\frac{a(\eta_{\rm now})}{a(\eta_0)}\frac{k_{\rm exp}}{M} \ll 1, \tag{5}$$

and the earliest time for which perturbative calculation works is one which does quite saturate this bound,

$$\frac{a(\eta_0^{\rm earliest})}{a(\eta_{\rm now})} \sim \frac{k_{\rm exp}}{M}. \tag{6}$$

Although this time dependence of scales limits the applicability of the effective theory, it should not be seen as anything mysterious or that η_0 must be chosen either at this bound or at a time when some nontrivial dynamics is occurring. To study the inflationary prediction for the cosmic microwave background power spectrum, for example, it is sufficient to choose an "initial time" when all of the features of the currently observed power spectrum are just within the horizon during inflation and which still satisfies the condition in Eq. 5 for a well behaved perturbation

theory. What the effective theory approach accomplishes is not a complete description of the theory to an arbitrarily early time, but rather it provides a completely generic parameterization of the effects of these earlier epochs or of higher scale physics once the state has entered a regime where they can be treated perturbatively.

3 Renormalization

If the initial state deviates from the standard vacuum state the renormalizability of the theory has to be checked. A major difference from the flat space case is that the information of interest concerns time evolution of the field modes as opposed to what happens in the S-matrix approach. The correct approach to this problem involves the Schwinger-Keldysh or closed-time path formalism[7].

The divergences that arise when using the general initial state described above are of two types. The first, which we call bulk divergences, are the usual ones that would be encountered even with the standard vacuum. They can be absorbed by the standard local counterterms and the coupling constants in the theory acquire their usual scale dependence.

The more interesting divergences are those arising from the change of initial state. What we have shown is that they only appear on the initial time hypersurface and can be absorbed by counterterms associated with this hypersurface. The fields inherit their mass dimension from the full $3+1$ theory but the operators contained in the boundary counterterm Lagrangian are classified according to whether their mass dimension is greater than, less than or equal to the dimension of the boundary surface. The structure function can be expanded as

$$e^{\alpha_k^*} = \sum_{n=0}^{\infty} d_n \frac{H^n(\eta_0)}{\Omega_k^n(\eta_0)} + \sum_{n=1}^{\infty} c_n \frac{\Omega_k^n(\eta_0)}{a^n(\eta_0) M^n}. \tag{7}$$

where $\Omega_k(\eta_0)$ is a generalized frequency, defined through the BD modes by

$$\mathcal{U}_k^{\mathrm{BD}}(\eta) = \frac{e^{-i\int_{\eta_0}^{\eta} d\eta' \, \Omega_k(\eta')}}{a(\eta)\sqrt{2\Omega_k(\eta)}}. \tag{8}$$

The two series are associated with IR and UV aspects of the initial state; the IR part can be viewed as a non-vacuum excitation of the BD state since at large distances we expect the Klein-Gordon description to be a good one. The divergences associated with this part of the initial state can be absorbed by renormalizable (on the initial time hypersurface) counterterms. Trans-Planckian effects are encoded in the second series and these divergences require irrelevant operators on the boundary to absorb them.

This formalism can also be used to renormalize the expectation value of the stress energy tensor and thus to understand the issue of the backreaction of the initial state on inflationary dynamics. If the expansion rate during inflation is denoted by H, and M_{pl} and M correspond respectively to the Planck mass and to the scale of new physics responsible for that structure, we find that the size of this back-reaction, relative to the vacuum energy sustaining the inflation, is suppressed at least by

$$\frac{H^2}{M_{\mathrm{pl}}^2} \frac{H}{M}. \tag{9}$$

4 Conclusion

The basic idea of the effective theory of an initial state is that a discrepancy can exist between what is the true state of the system and the state we have chosen to use in a quantum field theory, which thereby defines the propagator and the matrix elements of operators. Over distances

where have a good empirical understanding of nature and a reasonable knowledge about the relevant dynamics, we can usually make an appropriate choice for this state. Yet there always exist shorter distances where the behavior of nature is unknown and the correct state might not match with that we obtained by extrapolating our understanding at long distances down to these much shorter scales. This discrepancy is particularly important for inflation, where the relevant fields and their dynamics have not been observed directly and where the natural energy scale, the Hubble scale H, can be an appreciable fraction of the Planck scale, $M_{\rm pl}$. At this scale, gravity becomes strongly interacting and so we do not even have a predictive understanding of the behavior of space-time. Since inflation naturally produces a set of primordial perturbations through the inherent quantum fluctuations of a field, it is important to determine, from a very general perspective, the observability of the features at short distances compared with $1/H$ through their imprint on this primordial spectrum. While this imprint is not expected to be observed in the most recent experiments[1], future observations of the microwave background and of the large scale structure over large volumes of the observed universe should be able to extract the spectrum of primordial perturbations to a far better precision.

The ultimate goal of this program is to compute the power spectrum of inflationary perturbations as a function of the structure function of the initial state. Once this is done, we will be able to fit the coefficients c_n, d_n in Eq. 7 and determine, in a controlled fashion, whether or not trans-Planckian physics changes in the initial state can affect the CMB.

5 Acknowledgments

R. H. would like to thank the organizers for a great conference and the weather for dumping so much snow! This work was supported in part by DOE grant No. DE-FG03-91-ER40682 and the National Science Foundation grant No. PHY02-44801.

References

1. Spergel *et al.*, *Wilkinson Microwave Anisotropy Probe (WMAP) Three Year Results: Implications for Cosmology*, http://lambda.gsfc.nasa.gov/product/map (2006).
2. William H. Kinney, Edward W. Kolb, Alessandro Melchiori, Antonio Riotto, astro-ph/0605338, Jerome Martin, Christophe Ringeval, astro-ph/0605367.
3. J. Martin and R. H. Brandenberger, Phys. Rev. D **63**, 123501 (2001) [hep-th/0005209]; R. H. Brandenberger and J. Martin, Mod. Phys. Lett. A **16**, 999 (2001) [astro-ph/0005432].
4. N. Kaloper, M. Kleban, A. E. Lawrence and S. Shenker, Phys. Rev. D **66**, 123510 (2002); N. Kaloper, M. Kleban, A. Lawrence, S. Shenker and L. Susskind, JHEP **0211**, 037 (2002).
5. R. Easther, B. R. Greene, W. H. Kinney and G. Shiu, Phys. Rev. D **67**, 063508 (2003); C. P. Burgess, J. M. Cline, F. Lemieux and R. Holman, JHEP **0302**, 048 (2003) [hep-th/0210233]; C. P. Burgess, J. M. Cline and R. Holman, JCAP **0310**, 004 (2003) [hep-th/0306079];
6. H. Collins and R. Holman, Phys. Rev. D **71**, 085009 (2005) [hep-th/0501158]; hep-th/0507081; hep-th/0605107 and references therein.
7. J. S. Schwinger, J. Math. Phys. **2**, 407 (1961); L. V. Keldysh, Zh. Eksp. Teor. Fiz. **47**, 1515 (1964) [Sov. Phys. JETP **20**, 1018 (1965)]; K. T. Mahanthappa, Phys. Rev. **126**, 329 (1962); P. M. Bakshi and K. T. Mahanthappa, J. Math. Phys. **41**, 12 (1963).

INFLATION, STRINGS, CMB ANISOTROPIES AND BARYOGENESIS

R. JEANNEROT
Instituut-Lorentz for Theoretical Physics,
Niels Bohrweg 2, 2333 CA Leiden, The Netherlands

In this talk, I shall focus on theories beyond the Standard Model which predict massive neutrinos. Hybrid inflation emerges naturally in these theories: the slow-rolling inflaton field is a gauge singlet which couples with a GUT Higgs field which triggers the end of inflation. In the standard scenario, spontaneous symmetry breaking takes place at the end of inflation at a scale M; $M_{GUT} > M > M_Z$ for inflation to solve the GUT monopole problem and cosmic strings always form at this intermediate scale. WMAP data constrain $M \in [10^{14.5} - 10^{15.5}]$ GeV and the singlet-Higgs coupling $\kappa \in [10^{-7} - 10^{-2}]$. The spectral index $n_s \gtrsim 0.98$ in slight conflict with WMAP3. When the symmetry which is broken at the end of inflation is gauged $B - L$, both the inflaton and the strings decay into right-handed neutrinos. There are then two competing non-thermal scenarios for baryogenesis via leptogenesis which take place at the end of inflation, during reheating and from cosmic strings decay. Which of the two scenarios dominates depends on the inflaton-neutrino sector parameters.

1 Introduction

Up to the discovery of the 'acoustic' peaks in the CMB power spectrum [1], there were two compelling mechanisms for explaining cosmological perturbations: inflation and cosmic strings [2]. Since cosmic strings predict a single peak, they are now excluded as main source of the cosmological perturbations. However, a mixed scenario with both inflation and cosmic strings with a string contribution less than about 10% is still allowed by the data[3,4]. In many models with both inflation and strings, the scalar perturbations are dominated by the scalar perturbations from inflation, and the string contribution may be too low for detection via the CMB temperature anisotropies. However they could be detected via the B-type polarization of the CMB [5].

From a theoretical point of view, inflation is often associated with the formation of cosmic strings. Perhaps the best particle physics motivated model of inflation is hybrid inflation [6]. It arises naturally in Supersymmetric (SUSY) Grand unified Theories (GUTs) [7,8], in effective strings theories and in brane worlds. Naturally meaning that the fields and the potential leading to hybrid inflation are needed to build the theory itself (I now focus on the case of SUSY GUTs) and the coupling constant which enters is the order unity. In either cases, spontaneous symmetry breaking takes place at the end of inflation [a] and cosmic strings form [8,12,13,14]. In this talk I will consider Standard hybrid inflation in the context of SUSY GUTs. And I shall be mainly concerned about models which contain $B-L$ as a gauge symmetry and predict massive neutrinos via the See-saw mechanism [15].

[a] In non minimal models of hybrid inflation such as shifted inflation [10] or smooth inflation [11], spontaneous symmetry breaking takes place before or during inflation, and no defect form at the of inflation.

In section 2, I show that cosmic strings always form at the end of standard [b] hybrid inflation when inflation solves the GUT monopole problem. In section 3, I study the CMB anisotropies which are predicted by these models. Matching theoretical predictions with the data gives constraints on two of the GUT parameters, the Spontaneous Symmetry Breaking (SSB) scale at the end of inflation and the relevant coupling constant [16,17]. In section 4, I show that when the symmetry which is broken at the end of inflation is gauged $B-L$, there are two competing non-thermal baryogenesis scenarios which take place after inflation: from reheating, and from cosmic strings decay [18].

2 Inflation and cosmic strings

2.1 Inflation from particle physics

Inflation must come from the particle physics model describing fundamental interactions at high energies. As a particle physicist, the first question i will ask is 'Can we get inflation from the Standard Model?' On general grounds, the answer is 'No', because the inflationary energy scale would be the order of 100 GeV which is far too low to produced the required amount of primordial perturbations [c]. The next question i will ask is 'Can we get inflation from the simplest extensions of the Standard Model?' As an aparté, we know since the discovery of neutrinos oscillations that neutrinos are massive and hence that the Standard Model must be extended. In order to explain the smallness of the observed neutrinos masses, one could just add a gauge singlet and a tiny coupling constant. However, by adding a $U(1)_{B-L}$ gauge symmetry to the Standard Model gauge group $G_{SM} = SU(3)_c \times SU(2)_L \times U(1)_Y$, massive neutrinos become a prediction [15]. Adding the idea of unification of the gauge coupling constants, one is lead to grand unified theories. So I shall rephrase the question as 'Can we get inflation from a grand unified theory?' At first sight, 'the unification scale $M_{GUT} \sim 10^{16}$ GeV is just the energy scale needed for inflation to explain the cosmological perturbations'.

It turns out that when building a model of slow-roll inflation in a theory beyond the Standard Model three ingredients are usually needed: SUSY, which provides the required flatness of the potential, a Standard Model singlet, the slow-rolling field, and GUT Higgs fields transforming under a gauge group G whose rank is larger than the rank of the Standard Model gauge group, i.e. rank$(G) > 4$ [8,13].

2.2 Standard hybrid inflation

Hybrid inflation [6] uses two fields instead of one, a gauge singlet S and a Higgs field Φ. Hybrid inflation is arguably the best particle physics motivated model of inflation. In the context of SUSY GUTs, there are two Higgs superfields Φ and $\bar{\Phi}$ in complex conjugate representations of the GUT gauge group G_{GUT} which lower the rank of the group by one unit when acquiring vacuum expectation values (VEV) at the end of inflation. The superpotential is given by

$$W_{\rm inf} = \kappa S(\bar{\Phi}\Phi - M^2), \tag{1}$$

where a suitable U(1) R-symmetry under which W and S transform in the same way ensures the uniqueness of this superpotential at the renormalizable level. The scalar potential has an inflationary valley, which is a valley of local minima, at $S > M$ and $|\Phi| = |\bar{\Phi}| = 0$. At tree level, the potential along this valley is $V_{infl} = \kappa^2 M^2$. S is the slowing rolling field and slow-roll conditions thus apply to S. Since $|\Phi| = |\bar{\Phi}| = 0$ during inflation, there is no symmetry

[b] *Standard* refers to the standard model of SUSY hybrid inflation [7] where SSB takes place at the end of inflation

[c] However it has been recently suggested that an MSSM flat direction might be suitable for inflation [19]. Even though this proposal requires strong fine-tuning, it is interesting in two ways: first of all it uses standard model physics, and second there is no need of standard model singlet.

breaking induced by these Higgs fields VEV during inflation. Inflation terminates as S falls below its critical value $S_c = M$ and inflation ends in a phase transition during which the Higgs fields acquire non-zero VEV equal to M: Spontaneous Symmetry Breaking (SSB) takes place at the end of inflation. The SSB scale M and is proportional to the inflationary scale $V_{infl}^{1/4}$, the proportionality coefficient being the squared root of the singlet-Higgs coupling κ.

The Higgs fields representations Φ and $\bar{\Phi}$ are conjugate N-dimensional representations of the GUT gauge group. We are now focusing on GUT which contain gauged $U(1)_{B-L}$ and predict massive neutrinos via See-saw. The component of of Φ (and $\bar{\Phi}$) which gets a VEV at the end of inflation transforms as an Standard Model singlet, and it also transforms either as an $SU(2)_R$ doublet or as an $SU(2)_R$ triplet. In a realistic model where there are no unwanted light fields between the scale M and the GUT scale, it is the only component which remains light below M_{GUT} [17] ($M < M_{GUT}$, see section 2.3). The scalar potential along the inflationary valley is flat at tree level. It is lifted by loop corrections, which are non-zero during inflation because SUSY is spontaneously broken, and by SUGRA corrections. Assuming minimum Khäler potential it is given by [16,17]

$$\begin{aligned}\frac{V}{\kappa^2 M^4} &= 1 + \frac{\kappa^2 \mathcal{N}}{32\pi^2}\left[2\ln\left(\frac{\kappa^2 M^2 x^2}{\Lambda^2}\right) + (x^2+1)^2\ln(1+x^{-2}) + (x^2-1)^2\ln(1-x^{-2})\right] \\ &+ 2x^4\left(\frac{M}{m_{\rm p}}\right)^4 + |a|^2 x^2\left(\frac{M}{m_{\rm p}}\right)^2 + A\frac{m_{3/2}}{M}x, \end{aligned} \tag{2}$$

where $m_{\rm p}$ is the reduced Planck mass and Λ a cutoff scale; $x = |S|/M$ so that $x \to 1$ at the critical point; $A = 4\cos(\arg m_{3/2} - \arg S)$, we assume that $\arg S$ is constant during inflation; $\mathcal{N} = 1 - 3$ depending on wether the components of Φ and $\bar{\Phi}$ which get a VEV at the end of inflation transform as an $SU(2)_R$ doublet or triplet and wether the symmetry group which breaks at the end of inflation contains an $SU(2)_R$ or an $U(1)_R$ symmetry. Hidden sector VEV which lead to low energy SUSY breaking are $\langle z\rangle = a m_{\rm p}$ and $\langle W_{\rm hid}(z)\rangle = m_{3/2}\exp^{-|a|^2/2} m_{\rm p}^2$, with $m_{3/2}$ the gravitino mass; the cosmological constant in the global minimum is set to zero by hand. All subdominant terms are dropped.

2.3 Cosmic strings form at the end of standard hybrid inflation

Since SSB takes place at the end of inflation, cosmic strings always form if the later solves the GUT monopole problem [13]. The underlying reason being that the rank of the gauge group is lowered by one unit at the end of inflation [8,13]. This is illustrated in reference [12] where an exhaustive study of all SSB breaking patterns for all GUT gauge groups with rank less than height and phenomenologically acceptable has been performed. The aim of this section is to understand why indeed cosmic strings form. Further details can fe found in reference [13].

Suppose that the Standard Model gauge group G_{SM} is embedded in a GUT gauge group G_{GUT}. This must be broken down to G_{SM} at around $M_{GUT} \sim 10^{16}$ GeV, which is the scale at which the gauge couplings unify

$$G_{GUT} \overset{M_{GUT}}{\to} ... \to G_{SM} \overset{10^2\ \rm GeV}{\to} SU(3)_c \times U(1)_Q. \tag{3}$$

In SUSY. the breaking of G_{GUT} down to G_{SM} can be direct of via intermediate symmetry groups, whereas in the non SUSY case there must be at least one intermediate step. If (some of) the Higgs fields used to break G_{GUT} have a superpotential given by Eq.(1) [d]. inflation takes place and the spontaneous symmetry breaking of G_{GUT} takes place at the end of inflation. But in this scenario, cosmologically catastrophic monopoles which ought to form in all GUTs, form after inflation. In order to cure the monopole problem, one must introduce an intermediate

[d] The rank of G_{GUT} has to be strictly greater than the rank of G_{SM} [13]

symmetry group H, a subgroup of G_{GUT}, and use Φ, $\bar{\Phi}$ not to break the GUT itself but this intermediate symmetry group H; the symmetry breaking scale M of H is $< M_{GUT}$. H must be chosen in such a way that the monopoles form between G_{GUT} and H and no unwanted defect form when H breaks down to G_{SM}

$$G_{GUT} \overset{\text{Monopoles}}{\rightarrow} ...H \overset{\Phi,\bar{\Phi},\text{ No unwanted defect}}{\rightarrow} ... \rightarrow G_{SM} \overset{10^2\text{ GeV}}{\rightarrow} SU(3)_c \times U(1)_Q. \quad (4)$$

It can be shown that the rank of H must be greater than five, that it must contain a U(1) factor [8,13], and that cosmic strings always form when H breaks down to G_{SM} [8,12,13].

$$G_{GUT} \overset{\text{Monopoles}}{\rightarrow} ...H \overset{\text{Inflation, Cosmic Strings}}{\rightarrow} ... \rightarrow G_{SM} \overset{10^2\text{ GeV}}{\rightarrow} SU(3)_c \times U(1)_Q. \quad (5)$$

3 CMB constraints and predictions

If the strings which form at the end of inflation are stable down to low energy, they will contribute to the CMB temperature anisotropies. The perturbations from inflation and cosmic strings are uncorrelated and they add up independently [8]

$$\left(\frac{\delta T}{T}\right)_{\text{tot}} = \sqrt{\left(\frac{\delta T}{T}\right)^2_{\text{inf}} + \left(\frac{\delta T}{T}\right)^2_{\text{cs}}}. \quad (6)$$

The inflation contribution to the quadrapole is

$$\left(\frac{\delta T}{T}\right)_{\text{inf}} = \frac{1}{12\sqrt{5}\pi m_{\text{p}}^3} \frac{V^{3/2}}{V'}\bigg|_{\sigma=\sigma_Q}, \quad (7)$$

with a prime denoting derivative w.r.t. the real normalized inflaton field $\sigma = \sqrt{2}|S|$, and the subscript Q denoting the time observable scales leave the horizon. V is the scalar potential along the inflationary trajectory given by Eq.(2). The tensor perturbations from inflation $(\delta T/T)_{\text{tens}} \sim 10^{-2} H/m_{\text{p}}$ are very small.

The string induced perturbations are proportional to the string tension $(\delta T/T)_{\text{cs}} = yG\mu$, with μ the tension and y parameterizing the density of the string network. Recent simulations predicts $y = 9 \pm 2.5$ [20], but values in the range $y = 3 - 12$ can be found in the literature [2]. The strings are formed by the Higgs fields Φ and $\bar{\Phi}$ which wind around the string in opposite directions. They are not BPS and do not satisfy the Bogomolnyi bound and hence they are lighter than BPS strings forming at the same energy scale [16]. The string tension is

$$\mu = 2\pi M^2 \theta(\beta), \quad \text{with} \quad \theta(\beta) =\sim 2.4 \ln(2/\beta)^{-1} \quad (8)$$

where the function θ encodes the correction away from the BPS limit and $\beta = (m_\phi/m_A)^2 \simeq (\kappa/g_{\text{GUT}})^2$ with $g^2_{\text{GUT}} \approx 4\pi/25$. Requiring the non-adiabatic string contribution to the quadrupole to be less than 10% gives the bound [16]

$$G\mu < 2.3 \times 10^{-7}\left(\frac{9}{y}\right) \quad \Rightarrow \quad M < 2.3 \times 10^{15}\sqrt{\frac{(9/y)}{\theta(\beta)}}. \quad (9)$$

The bound which comes from pulsar timing (the stochastic gravitational wave background produced by cosmic strings can disrupt pulsar timing and this has not been observed) is $G\mu < 1.0 \times 10^{-7}$ [21]; it is more stringent, but it has also more uncertainties. It corresponds to the 10% bound with $y = 20.7$.

Temperature anisotropies from both inflation and cosmic strings depend on two parameters, the SSB scale M of the intermediate symmetry group H, see Sec 2., and the singlet-Higgs

coupling constant κ, see Eq.(1). Matching the theoretical predictions with the observed value $(\delta T/T) = 6.6 \times 10^{-6}$ [4] gives a constrain on M versus κ, see figure 1 [16,17]. The intermediate symmetry breaking scale must be very close to the GUT scale, $M \in [10^{14.5} - 10^{15.5}]$ GeV and the coupling constant $\kappa \in [10^{-7} - 10^{-2}]$. If the strings are unstable [17], larger values of κ are allowed.

The spectral index n_s is calculated using the slow-roll parameters and also depends on the singlet-Higgs coupling constant κ; it is also shown on figure 1 [16,17]. n_s is undistinguishable from unity for small values of κ, smaller than unity for intermediate values of κ and bigger than unity for large values of κ. It is extremely difficult to get a spectral index smaller than 0.98 with hybrid inflation except maybe with non-minimal models [27]. This is in slight conflict with WMAP 3-years data, and if these were to be confirmed, it would be excluded.

The string contribution $B = \left(\frac{\delta T}{T}\right)_{\rm tot} / \left(\frac{\delta T}{T}\right)_{\rm cs}$ is also a function of the coupling κ. It is negligibly small for most of the parameter space and saturates the 10% bound for large values of κ, which is the best interesting region for both n_s and baryogenesis (see Sec. 4). It is shown in figure 2 [16].

Further details can be found in references [16,17].

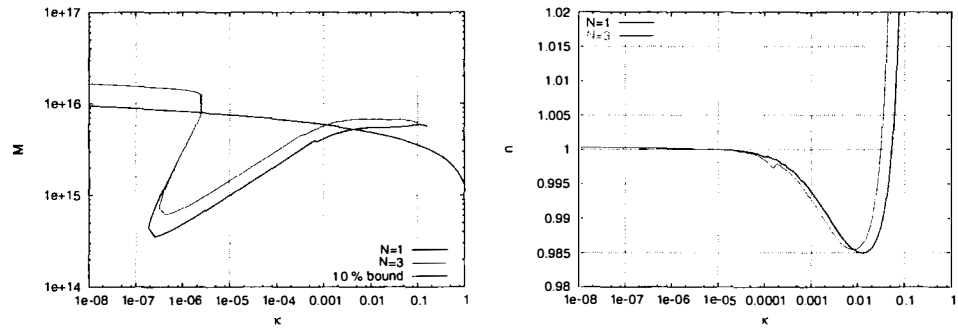

Figure 1: Left: CMB constraints on M as a function κ for $\mathcal{N} = 1, 3$ (blue curves) and the 10% bound (pink curve). Right: predictions for the spectral index n_s as function of κ for $\mathcal{N} = 1, 3$.

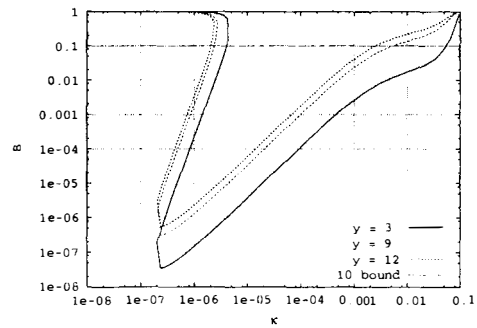

Figure 2: The string contribution $\left(\frac{\delta T}{T}\right)_{tot} / \left(\frac{\delta T}{T}\right)_{\rm cs}$ as a function of κ for $y = 3, 6, 9$.

4 Baryogenesis via leptogenesis at the end of inflation

Baryogenesis aims to explain the observed matter-antimatter asymmetry of the Universe. It must take place after inflation, since any previously produced baryon asymmetry is washed-out. Standard GUT baryogenesis is ruled out because any GUT scale produced baryon asymmetry is erased by sphalerons transitions unless the universe possesses a $B-L$ asymmetry [e] [22]. A primordial $B-L$ asymmetry is naturally obtained in theories beyond the standard model which contain gauged $B-L$ via the out-of-equilibrium decay of heavy Majorana right-handed neutrinos [23]. This scenario known has leptogenesis is perhaps the best particle physics motivated model of baryogenesis. Thermal leptogenesis requires a symmetry breaking scale $\sim 10^{15}$ GeV and a reheating temperature $T_R \sim 10^{10}$ GeV [24]. Such high reheating temperature leads to an overproduction of gravitinos which decay lately and disrupt the predictions of nucleosynthesis.

When $G_{GUT}, H \supset U(1)_{B-L}$ and the Φ and $\bar{\Phi}$ fields entering the inflation superpotential given by equation (1) are the $B-L$ breaking Higgs fields, gauged $B-L$ is broken at the end of inflation and the strings which form at the end of inflation are the so-called $B-L$ cosmic strings [25]. There are then two competing non-thermal scenarios for leptogenesis which take place after inflation: from reheating during inflation [26] and from cosmic strings decay [18,25].

- Non-thermal leptogenesis during reheating

  The $B-L$ breaking Higgs field Φ which enters the inflationary superpotential Eq.(1) gives a superheavy Majorana mass to the right-handed neutrinos ($W \supset \Phi NN$ or $W \supset \Phi^2 NN/m_{\rm p}$) and reheating proceeds via production of heavy right-handed neutrinos and sneutrinos. Right-handed (s)neutrinos decay into electroweak Higgs(ino) and (s)leptons ($W \supset H_u LN$), CP is violated through the one-loop radiative correction involving a Higgs particle and by the self-energy correction, and lepton asymmetry is non-thermally produced when the right-handed neutrinos are out-of-equilibrium, i.e. when $T_R < M_{N_i}$. If $T_R > M_{N_1}$, the lepton asymmetry produced is wash-out by L-violating processes involving right-handed neutrinos until $T < M_{N_1}$, where M_{N_1} is the mass of the lightest right-handed neutrino. If $M_{N_1} > m_\Phi/2$, where m_Φ is the mass of the Higgs field in the true vacuum, the inflaton cannot decay into right-handed neutrinos and reheating must be gravitational. The resulting baryon asymmetry depends on the reheating temperature at the end of inflation, which depends on the mass M_{N_i} of the heaviest right-handed neutrinos the inflaton can decay into, on the symmetry breaking scale M which is constrained by CMB data as a function of the coupling κ (see Sec. 3) and on the CP violating parameter [18].

- Non-thermal leptogenesis from cosmic strings decay

  The strings which form at the end of inflation are the so-called $B-L$ cosmic strings [25]. The main decay channel of $B-L$ strings is into right-handed neutrinos and they also lead to non-thermal leptogenesis [25,18]. The resulting baryon asymmetry depends upon the amount of energy loss by the network into right-handed neutrinos and on the density of strings at the end of inflation; it also depends on the symmetry breaking scale M at the end of inflation which is constrain by CMB as a function of κ [18].

Which of these two scenarios dominates depends on wether the inflaton decay into right-handed neutrino is kinematically allowed and wether the lightest right-handed neutrino N_1 is in thermal equilibrium at reheating. Results, which take into account the CMB constraints derived in the previous section, are shown in figures 3 and 4. Further details can be found in reference [18].

[e] Sphalerons transition violate $B+L$ and conserve $B-L$, where B and L are respectively number and lepton number.

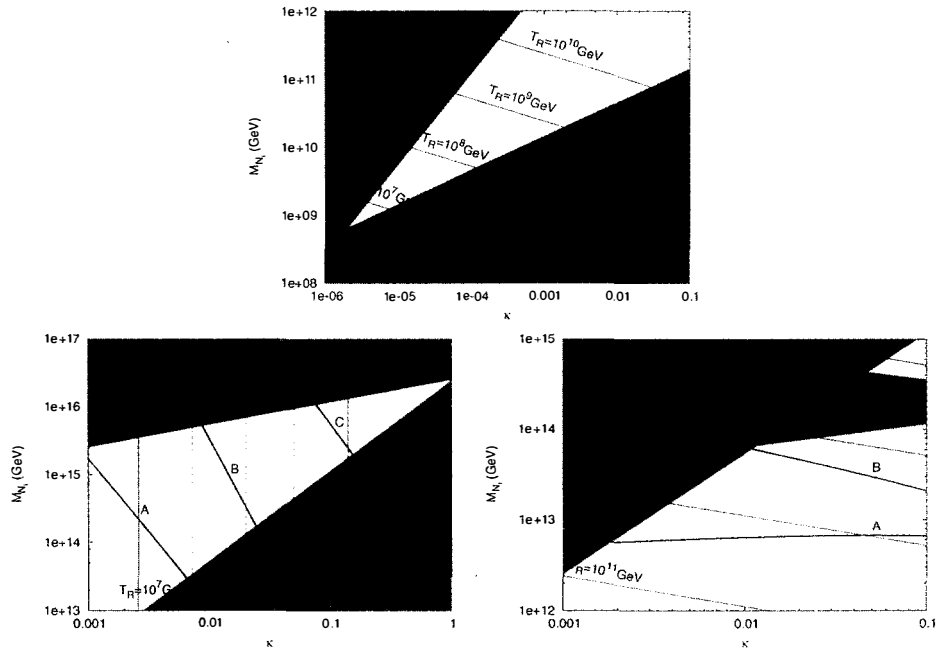

Figure 3: The mass M_{N_i} of the heaviest right-handed neutrino the inflaton can decay into as a function of the coupling κ. The white regions give the measured value of n_B/s. The colored regions are excluded. Top: $M_{N_1} < m_\phi/2$ and $M_{N_i} > T_R$, both strings and inflation contribute non-thermally to ΔB. Bottom: $M_{N_1} > m_\phi/2$, reheating is gravitational and only strings contribute non-thermally to ΔB. Bottom Left: $M_{N_1} > T_R$, there is no wash out. Bottom Right: $M_{N_1} < T_R$, there is also a thermal contribution.

5 Conclusions

GUT which predict massive neutrinos are good candidates for hybrid inflation. Cosmic strings form at the end of inflation and, if they stable down to low energy, they contribute to CMB anisotropies together with inflation. The symmetry breaking scale is constrained by CMB data to the range $M \in [10^{14.5} - 10^{15.5}]$ GeV and the relevant coupling $\kappa \in [10^{-7} - 10^{-2}]$. Scalar perturbations from inflation dominate for a large part of the parameter space and it might be impossible to detect the strings using the temperature anisotropies of the CMB. They could however be detected via the B-type polarization of the CMB [5].

Hybrid inflation predicts a spectral index $n_s \gtrsim 0.98$. It is very difficult to get smaller values except maybe by going to non minimal models [27]; hence if the three year WMAP central value $n_s = 0.951^{+0.015}_{-0.019}$ were to be confirmed, hybrid inflation with minimal SUGRA could be excluded. But even if scalar perturbations are dominated by scalar perturbations from inflation, tensor perturbations (which are negligible for hybrid inflation) can nonetheless be dominated by tensor perturbations from cosmic strings; this can allow a larger value of n_s [4].

Finally, when $B - L$ is broken at the end of inflation, baryogenesis via leptogenesis takes place after inflation during reheating and/or via cosmic strings decay; which of the two scenarios dominates depends upon the various parameters in the inflaton-neutrino sector.

Acknowledgments

I wish to acknowledge Marieke Postma for enjoyable collaboration. I also wish to thank The Dutch Organization for Scientific Research [NWO] for financial support.

References

1. C. B. Netterfield *et al.* [Boomerang Collaboration], Astrophys. J. **571**, 604 (2002) [arXiv:astro-ph/0104460].
2. A. Vilenkin and E. P. S. Shellard, *"Cosmic strings and other topological defects"*, Cambridge monographs on mathematical physics, Cambridge University Press, England, 1994; M. B. Hindmarsh and T. W. B. Kibble, Rept. Prog. Phys. **58** (1995) 477 [arXiv:hep-ph/9411342].
3. L. Pogosian, I. Wasserman and M. Wyman, arXiv:astro-ph/0604141.
4. D. N. Spergel *et al.*, arXiv:astro-ph/0603449.
5. U. Seljak and A. Slosar, arXiv:astro-ph/0604143.
6. A. Linde, Phys. Rev. D **49**, 748 (1994) [arXiv:astro-ph/9307002].
7. G. R. Dvali, Q. Shafi and R. K. Schaefer, Phys. Rev. Lett. **73**, 1886 (1994) [arXiv:hep-ph/9406319].
8. R. Jeannerot, Phys. Rev. D **56** (1997) 6205 [arXiv:hep-ph/9706391].
9. R. Kallosh, arXiv:hep-th/0109168, R. Kallosh and A. Linde, JCAP **0310**, 008 (2003) [arXiv:hep-th/0306058].
10. R. Jeannerot, S. Khalil, G. Lazarides and Q. Shafi, JHEP **0010**, 012 (2000) [arXiv:hep-ph/0002151].
11. G. Lazarides and C. Panagiotakopoulos, Phys. Rev. D **52**, 559 (1995) [arXiv:hep-ph/9506325].
12. R. Jeannerot, J. Rocher and M. Sakellariadou, Phys. Rev. D **68**, 103514 (2003) [arXiv:hep-ph/0308134].
13. R. Jeannerot, arXiv:hep-th/0604214.
14. N. T. Jones, H. Stoica and S. H. H. Tye, JHEP **0207**, 051 (2002) [arXiv:hep-th/0203163].
15. M. Gell-Mann, P. Ramond and R. Slansky, in *Supergravity*, P. van Nieuwenhuizen and D. Freeman eds., North Holland, Amsterdam 1979, p. 315; T. Yanagida, Prog. Theor. Phys. **64** (1980) 1103; R. N. Mohapatra and G. Senjanovic, Phys. Rev. Lett. **44** (1980) 912; J. Schechter and J. W. F. Valle, Phys. Rev. D **22** (1980) 2227.
16. R. Jeannerot and M. Postma, JHEP **0505** (2005) 071 [arXiv:hep-ph/0503146].
17. R. Jeannerot and M. Postma, arXiv:hep-th/0604216.
18. R. Jeannerot and M. Postma, JCAP **0512** (2005) 006 [arXiv:hep-ph/0507162].
19. R. Allahverdi, K. Enqvist, J. Garcia-Bellido and A. Mazumdar, arXiv:hep-ph/0605035, D. H. Lyth, arXiv:hep-ph/0605283.
20. M. Landriau and E. P. S. Shellard, Phys. Rev. D **69** (2004) 023003 [arXiv:astro-ph/0302166].
21. A. N. Lommen, arXiv:astro-ph/0208572.
22. V. A. Kuzmin, V. A. Rubakov and M. E. Shaposhnikov, Phys. Lett. B **191**, 171 (1987).
23. M. Fukugita and T. Yanagida, Phys. Lett. B **174**, 45 (1986).
24. W. Buchmuller, R. D. Peccei and T. Yanagida, Ann. Rev. Nucl. Part. Sci. **55**, 311 (2005) [arXiv:hep-ph/0502169].
25. R. Jeannerot, Phys. Rev. Lett. **77**, 3292 (1996) [arXiv:hep-ph/9609442].
26. G. Lazarides and Q. Shafi, Phys. Lett. B **258**, 305 (1991). G. Lazarides, Springer Tracts Mod. Phys. **163**, 227 (2000) [arXiv:hep-ph/9904428].
27. M. Bastero-Gil, S. F. King and Q. Shafi, arXiv:hep-ph/0604198.

DOMAIN WALL DYNAMICS IN MODELS WITH MULTIPLE VACUA

ADAM MOSS AND RICHARD A. BATTYE
Jodrell Bank Observatory, University of Manchester, Macclesfield, Cheshire SK11 9DL, UK

In this article we discuss the evolution of domain wall networks, focusing on the dynamics of walls in the cubic anisotropy model. In this model a global $O(N)$ symmetry is broken to a set of discrete vacua either on the faces, or vertices of a (hyper)cube. Since the model allows for wall junctions, lattice structures are locally stable and modifications to the standard scaling law are possible. However, we find that since there is no scale which sets the distance between walls, the walls appear to evolve toward a self-similar regime with $L \sim t$. We also discuss the possibility of walls having a conserved topological winding which could lead to frustration of the network.

1 Introduction

Topological defects are ubiquitous in field theory and commonly appear in condensed matter systems. In cosmology, topological defects can arise from the breaking of spontaneous symmetries in the early universe. Most of the work on defect networks has focused on cosmic strings - the study of domain walls has generally been discouraged due to the commonly accepted view that such a network will either over-close the universe or destroy the isotropy of the Cosmic Microwave Background (CMB). However, this assumption relies on the fact that the network immediately enters a self-similar scaling regime and the walls are formed at a high energy transition. In this scenario, wall decay processes are efficient and, on average, there is a single domain wall per horizon volume from initial formation through to the present day with domains growing as fast as causality allows (the characteristic lengthscale $L \sim t$). An alternative kind of behaviour has been envisaged for models with more complicated vacuum structure. It could be that the network frustrates and $L \sim a(t)$ allowing the network to act as a dark energy candidate with pressure to density ratio $w = P/\rho = -2/3$, if the scale of symmetry breaking is sufficiently low [1].

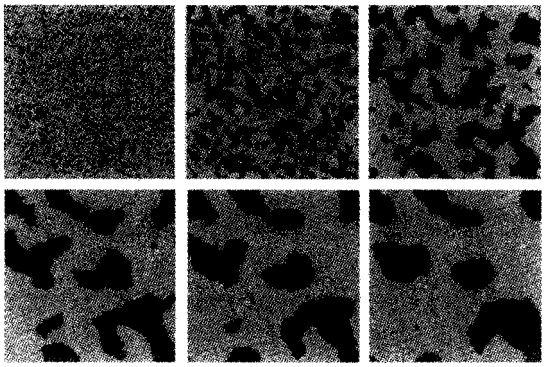

Figure 1: Dynamics of walls in the Z_2 model. The time slices are taken in steps of 500 starting from the initial state (top-left to bottom-right). Dark-grey regions represent the minima {-} and light-grey the minima {+}.

2 Simple Domain Wall Networks

Domain walls occur in systems whose vacuum manifold has two or more discrete, degenerate minima. Consider, for example, a model with a single scalar field ϕ, standard relativistic kinetic terms and a self-interaction potential with Z_2 symmetry given by

$$V(\phi) = \frac{\lambda}{4}(\phi^2 - \eta^2)^2. \tag{1}$$

At finite temperatures the potential receives thermal corrections and the effective mass is a function of temperature T. As the universe cools there exists a critical temperature T_c at which the field undergoes a second-order phase transition from $\langle\phi\rangle = 0$ to $\langle\phi\rangle = \pm\eta$. As this transition occurs at a finite rate there exists a correlation length ξ between domains, which is bounded by causality. In this scenario, the initial wall distribution consists of a series of $+$ and $-$ clusters, primarily in the form of a single infinite wall separating domains.

Numerical simulations of defect networks of this type were first performed by Press, Ryden and Spergel [2]. In order to calibrate our results in other models we have performed a suite of simulations in the case of Z_2 symmetry breaking. The Euler-Lagrange equation of motion for ϕ was discretized on a regular, two dimensional cubic grid with P points in each direction and a spatial separation size Δx. We evolve this equation using a second order time, fourth order space leapfrog algorithm to accurately represent any large spatial gradients associated with the domain walls. The boundary conditions we employ are periodic, and so in obtaining any quantitative information regarding the evolution of the wall network we limit the total time of the simulation to the light crossing time. This is the time taken for two signals emitted from the same point travelling in opposite directions to interfere with each other, and is given in terms of the number of simulation timesteps by $P\Delta x/(2\Delta t)$. Initial conditions were created by randomly distributing $+$ and $-$ vacua at each grid point. Since our main objective is to observe the late time dynamics the only requirement of the initial conditions is to distribute the value of ϕ randomly. The total number of the walls in the network is then fitted to the power law $n \propto t^{-\alpha}$, where the exponent α is predicted to be unity for the case of dynamical scaling.

The dynamical evolution for a sample simulation is shown in Fig. 1. The formation of an infinite domain is clearly apparent containing what are effectively closed walls, with a single vacuum state eventually occupying the entire grid. Results for the scaling exponent α are consistent with that of unity.

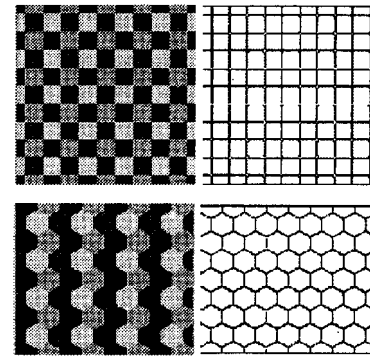

Figure 2: Regular tilings of the plane constructed in the cubic anisotropy model. The square tilings on the top are constructed from a broken O(2) model with $\epsilon > 0$ and the hexagonal tilings on the bottom from a broken O(4) model with $\epsilon < 0$. The figures on the left show distinct vacuum states in different shades of grey and the figures on the right are the corresponding energy density associated with each wall.

3 Cubic Anisotropy Model

We now extend this treatment to investigate the stability properties and dynamical evolution of a network of domain walls where a global $O(N)$ symmetry is broken to a set of discrete vacua with (hyper)cubic symmetry[3]. In these models walls can be joined at string-like junctions in 3D (vortex-like in 2D) allowing for stable lattice structures. This contrasts with the Z_2 model where the dynamics are typically dominated by the evolution of an single large domain with closed walls inside it. We consider models for a global vector field $\phi = (\phi_1, .., \phi_N)$ with a self-interaction potential given by

$$V(\phi) = \frac{\lambda}{4}\left(|\phi|^2 - \eta^2\right)^2 + \epsilon \sum_{i=1}^{N} \phi_i^4 . \tag{2}$$

If $\epsilon = 0$ then the model has $O(N)$ symmetry, but this is broken to a discrete (hyper)cubic symmetry when $\epsilon \neq 0$. In the case of $N = 2$, the potentials for $\epsilon > 0$ and $\epsilon < 0$ are, from the point of view of the structure of the vacuum manifold, essentially the same modulo a rotation. When $N \geq 3$ the structure of the vacuum manifold is different in the two cases. In the $\epsilon > 0$ case the minima reside at the vertices of a (hyper)cube and in the $\epsilon < 0$ case the minima reside at the faces (or the vertices of an (hyper)octahedron - the dual of the cube). The structure of the vacuum manifold means that there is an important distinction in the types of walls produced in the $\epsilon > 0$ and $\epsilon < 0$ models. In the former, X type junctions will form (such as four walls meeting at a string/vortex) whilst in the latter, Y type junctions will form (such as three walls meeting at a string/vortex). The ability of the vacuum manifold to support junctions means that regular tilings of the plane can be constructed. In the case of $\epsilon > 0$, X type junctions can be used to construct a square type lattice, while the Y type junctions in the $\epsilon < 0$ model can be used to construct a hexagonal lattice. These are illustrated in Fig. 2, which shows the output of numerically solving the field equations.

In simulations where initial conditions are random, we find that these networks again converge toward a self-similar scaling regime. There are hints that the scaling exponent is slightly less than unity, but we attribute these as being due to the finite box size and grid resolution which we are forced to use. These results are, in some sense, no surprise since the model has no scale in it which fixes the size of the domains. The only length scale is the horizon size and hence the wall network loses energy as fast as the causality allows, that is, $L \sim t$.

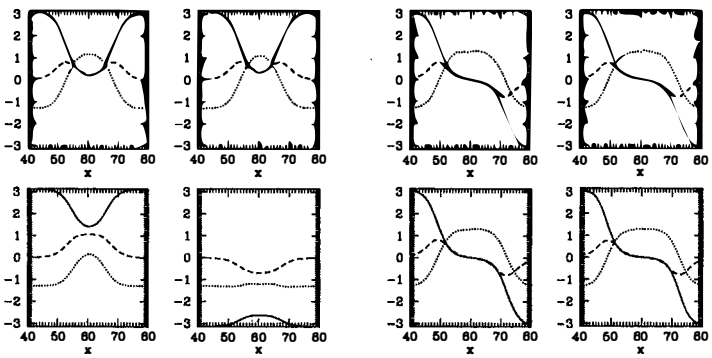

Figure 3: Evolution of a wall system with a multiply connected potential given by Eqn. 3 as a function of the Cartesian coordinate x. The figure on the left shows two adjacent walls with zero net winding. The dashed line shows the value of ϕ_1, the dotted line the value of ϕ_2 and the solid line the phase θ between ϕ_1 and ϕ_2. There is an attraction between walls and they annihilate each other. The figure on the right shows two adjacent walls with a 2π net winding which leads to repulsion.

4 Further Models

The models considered so far do not preclude the possibility of more complicated models leading to frustration of the network. There may be topological reasons why walls cannot become arbitrarily close to each other. Let us consider, for example, the vector field $\phi = (\phi_1, \phi_2)$ with potential

$$V(\phi) = \frac{\lambda}{4}\left(|\phi|^2 - \eta^2\right)^2 + \epsilon\phi_1^4 . \tag{3}$$

If the symmetry breaking parameter $\epsilon < 0$ the minima are given by $\phi_1 = \pm\sqrt{\lambda\eta^2/(\lambda + 4\epsilon)}$, $\phi_2 = 0$. In this model, walls still exist between + and − regions but there is further topological information on the wall associated with the winding of the field. Consider two initial static parallel walls at some small separation distance, as shown in Fig. 3. When the two walls have a zero net winding around the vacuum manifold they attract and annihilate each other, whereas when the adjacent walls complete a 2π winding around the vacuum manifold they repel. Hence, in this case the parallel wall number can be interpreted as a conserved topological winding number. Models in which parallel walls are protected from becoming too close due to the existence of windings have been proposed by Carter [4] and appear to offer some mechanism for the wall network to frustrate.

Acknowledgments

We have benefited from useful discussions with Nuno Antunes, Steven Appleby, Alan Bray, Brandon Carter, Elie Chachoua, Alan Duffy and Mark Hindmarsh.

References

1. M. Bucher and D. N. Spergel, Phys. Rev. D60, 043505 (1999) [astro-ph/9812022].
2. W. H. Press, B. S. Ryden and D. N. Spergel, Astrophys. J. 347, 590 (1990).
3. R. A. Battye and A. Moss, (2006) [astro-ph/0605057].
4. B. Carter, (2006) [hep-ph/0605029].

TOWARDS INFLATION AND DARK ENERGY COSMOLOGIES IN STRING-GENERATED GRAVITY MODELS

ISHWAREE P. NEUPANE
Department of Physics and Astronomy, University of Canterbury,
Private Bag 4800, Christchurch 8004, New Zealand
and
Central Department of Physics, Tribhuvan University
Kirtipur, Kathmandu, Nepal

We discuss how the string α'-correction to the usual Einstein action, which comprises a Gauss-Bonnet integrand multiplied by non-trivial functions of the (common) modulus field χ and/or the dilaton field ϕ, can explain several novel phenomena, such as a four-dimensional flat Friedmann-Robertson-Walker universe undergoing a cosmic inflation at the early epoch, as well as a cosmic acceleration at late times.

String/M theory has the prospect of unification of all interactions (electromagnetic, weak, strong and gravitational), providing inter-relationships between quantum mechanics and general relativity. However, it has not been developed to the stage where the full theory may be employed to construct a detailed cosmology. The assumptions which make string cosmology a challenging subject are the existence of extra dimensions and supersymmetry. Modern (super)string theory or M theory has additional features: now it goes beyond the perturbative approach popularised in the 80's and 90's and takes into account the effects due to branes, fluxes and non-trivial cycles in the extra dimensions, providing new avenues for studying the theory of inflation or cosmic acceleration, via flux or time-dependent comapcifications.

The four-dimensional effective gravitational action of our interest here is given by

$$S = \int d^4x\sqrt{-g}\left[\frac{1}{2\kappa^2}R - \gamma\,(\Delta\chi)^2 - V(\chi) - \zeta\,(\Delta\phi)^2 + \frac{1}{8}[\lambda(\phi) - \xi(\chi)]\mathcal{R}^2_{GB}\right], \qquad (1)$$

where κ is the inverse Planck mass $m_{\rm Pl}^{-1} = (8\pi G_N)^{1/2}$ and $\mathcal{R}^2_{GB} \equiv R^2 - 4R_{\mu\nu}R^{\mu\nu} + R_{\mu\nu\rho\chi}R^{\mu\nu\rho\chi}$ is the Gauss-Bonnet (GB) integrand. Here ϕ may be viewed as a dilaton, which has no potential. χ is an ordinary scalar (or inflaton field) which, in particular cases, could be a modulus field associated with the overall size of extra dimensions. In a known example of heterotic string compactification [1,2], $\lambda(\phi) = \lambda_1\, e^{\phi} + \cdots$ and $\xi(\chi) \propto (\ln(2) - \frac{2\pi}{3}\cosh(\chi)) + \cdots$. Recently, Nojiri et al. [3] examined a special (asymptotic) class of solutions for the system (1) with the choice $V(\chi) = V_0\, e^{-\chi/\chi_0}$ and $\xi(\chi) = \xi_0 e^{\chi/\chi_0}$, deleting the ϕ-dependent terms. The analysis was extended in [4] by introducing higher (than second order) curvature corrections, but in the χ=const background. We present here a more general class of solutions for the model (1). For simplicity, we shall start our discussion by neglecting all the dilaton related terms. We find it convenient to define the following variables [5] (in the units $\kappa = 1$):

$$X \equiv \gamma\,(\dot\chi/H)^2 = \gamma\chi'^2, \quad Y \equiv V(\chi)/H^2, \quad U \equiv \xi(\chi)H^2 \quad \varepsilon \equiv \dot H/H^2 = H'/H, \qquad (2)$$

where the dot (prime) denotes a derivative w.r.t. the proper time t (the number of e-folds, $N = \int H\,dt = \ln(a/a_0)$), with $a(t)$ being the scale factor of the universe. For $U = 0$ (or $\xi(\chi) = 0$), the equations of motion are $Y = 3 + \varepsilon$ and $X = -\varepsilon$, which are remarkably simple. However, different choice of ε implies different Y and hence different $V(\chi)$, and so is the equation of state (EOS) parameter w, which is defined by $w = -2\varepsilon/3 - 1$. Is it then all worthy?

Though it may be desirable to construct a cosmological model that gives rise to $w \approx -1$, for the model to work, the field χ must relax its potential energy after inflation down to a sufficiently low value, possibly very close to the present value of the cosmological constant. An exponential potential, $V(\chi) = V_0\, e^{-\lambda_0 \chi}$, is perhaps the best choice, as it gives rise to cosmological attractors[6] in presence of a barotropic (matter/radiation) field, but it is more plausible that the coupling λ_0 is a function of χ itself, or the number of e-folds, $N \equiv |\ln(a_f/a_i)|$. We shall look for a more general potential that supports a relaxation of gravitational vacuum energy or dark energy[5].

In an accelerating spacetime, the Gauss-Bonnet term is positive, i.e., $\mathcal{R}^2_{GB} = 24\frac{\dot{a}^2\ddot{a}}{a^5} > 0$. The effective potential, which may be defined by $\Lambda(\chi) \equiv V(\chi) - \frac{1}{8}\,\xi(\chi) R^2_{GB}$, can be (exponentially) small for $V(\chi) \approx \frac{1}{8}\,\xi(\chi) R^2_{GB}$. We find it convenient to impose the condition[5,7]

$$\Lambda(\chi) \equiv H^2(3 + \varepsilon), \tag{3}$$

so that $\Lambda(\chi) \geq 0$ for $\varepsilon \geq -3$ or equivalently when the EOS parameter $w \leq 1$. There is now only one free parameter in the model, which may be fixed either by allowing one of the variables in (2) to take a fixed (but arbitrary) value or by making an appropriate ansatz. Here we consider both these cases. First consider the case of power-law inflation, for which

$$a(t) \equiv e^{\omega(t)} \equiv (c_0 t + t_1)^{-1/\varepsilon_0}\,, \tag{4}$$

where c_0 and t_1 are arbitrary constants. This actually implies that $\varepsilon \equiv \dot{H}/H^2 = \varepsilon_0$. For $\varepsilon_0 < 0$, $c_0 > 0$ and t_1 may be set zero, but, for $\varepsilon_0 > 0$, one may take $c_0 < 0$ and set $t_1 = t_\infty$, which ensures that the scale factor grows with t in either case. With (4), we find $H \propto e^{\varepsilon_0 N}$ and $\xi(\chi)H^2 = c_2\, e^{\alpha_+ N} + c_3\, e^{\alpha_- N}$, where $\alpha_\pm = \frac{1}{2}\left(\varepsilon_0 - 5 \pm \sqrt{9(\varepsilon_0+3)^2 - 32}\right)$. For the reality of $\alpha_\pm$, it is required that $\varepsilon_0 > -1.11$ or $\varepsilon_0 < -4.88$; we rule out the latter as it implies $w > 1$.

Spurred on by this example, we make no assumption about the form of scale factor, and instead consider the ansatz that during a given epoch we may make the approximation

$$U \equiv \xi(\chi) H^2 \equiv e^{\alpha_0 + \alpha N}, \tag{5}$$

where α_0 and α are arbitrary at this stage. The allow us to write ε in a closed form:

$$\varepsilon = \beta \tanh \beta(N + N_1) - \hat{\beta} \quad \Rightarrow H \propto \cosh \beta(N + N_1)\, e^{-\hat{\beta} N}, \tag{6}$$

where N_1 is a free parameter, $\hat{\beta} \equiv (16 + \alpha)/4$ and $\beta \equiv \frac{1}{4}\sqrt{9\alpha(\alpha+8) + 208}$. Initially, N may take a large negative value, $N \equiv \ln(a/a_0) \ll 0$, since $a \ll a_0$. As we wish to obtain an inflationary solution with sufficiently large number of e-folds, say 65 e-folds, it is reasonable to take $N_1 \sim \mathcal{O}(65)$. For $\Delta N \equiv N + N_1 \lesssim 0$, the universe is not accelerating, but it starts to accelerate ($\varepsilon > -1$) for $\Delta N \gtrsim 0.2$. The solution where $-6 < \alpha < -4$ (or $-2 < \alpha < 1$) is accelerating with an EOS parameter $w \geq -1$; of course, the solution where $\alpha < -6$ (or $\alpha > 1$) solution is also accelerating but in this case, since $\varepsilon > 0$ or $X < 0$. χ acts as a phantom (see Fig. 1(a)). The potential $V(\chi)$ is a somewhat complicated function of N (or χ), namely

$$V(\chi) = H^2\,(3 + \varepsilon + 3(\varepsilon + 1)U)\,. \tag{7}$$

Note that at the onset of inflation, $\varepsilon \approx -1$ (or $w \approx -1/3$), the Gauss-Bonnet term is not contributing; inflation can be mainly due to the potential. After a certain number of e-folds

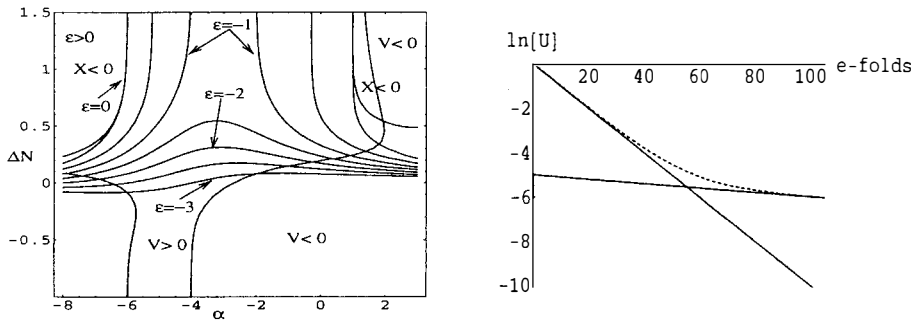

Figure 1: (a) The ΔN - α phase space, with $U \equiv 0.5e^{\alpha N}$. The almost horizontal line with $\varepsilon = -3$ separates the regions between $\Lambda(\chi) > 0$ and $\Lambda(\chi) < 0$. With a small value of $\alpha_0 \lesssim \ln(0.3)$, the region between $\alpha = -4$ and $\alpha = -6$ separats and moves to a more negative value of ΔN. (b) The qualitative behaviour of the term $U = \xi(\chi)H^2 \equiv e^{\alpha_0+\alpha N} + e^{\alpha_1+\hat{\alpha}N}$ as a function of ΔN, with $\alpha_0 = 0$, $\alpha_1 = -5$, $\alpha = -0.1$ and $\hat{\alpha} = -0.01$.

of expansion, $\beta(N + N_1) \gtrsim 2$, the variable X takes an almost constant value, $x_0(\alpha)$, and for $U \ll 1$, $V(\chi)$ is well approximated by $V(\chi) \propto H^2 \propto e^{2(\beta-\hat{\beta})} = V_0 e^{-p\chi}$ with $p \equiv 2(\hat{\beta} - \beta)\lambda_0$ and $\lambda_0 = \sqrt{\frac{\gamma}{x_0(\alpha)}} = |\chi'|_{\beta\Delta N>2}$. In fact, for $\beta\Delta > 2$, we get $\Lambda(\chi) = \Lambda_0 e^{-p\chi}$.

The scale factor of the universe after inflation would naturally become much larger than its initial value, but it is smaller than a_0 (the present value), so $-\mathcal{O}(1) \lesssim N < 0$. Our approximation (5) that U be given by a single exponential term may break down at some intermediate epoch (cf Fig 1(b)). At late times, U is approximated by the term $\propto e^{\hat{\alpha}N}$; the solution is given by (6), with α and N_1 replaced by $\hat{\alpha}$ and N_0. For $N + N_0 \lesssim 0$, the universe is in a deceleration phase which implies that inflation must have stopped during the intermediate epoch. As N crosses N_0, or when $N + N_0 > 0$, the universe may begin to accelerate for the second time.

It is generally believed that during inflation, the inflaton and graviton field undergo quantum-mechanical fluctuations, leading to scalar (density) and tensor (gravity waves) fluctuations, which in turn would give rise to significant effects on the large-scale structures of the universe at the present epoch. In turn, it may be hoped that the spectra of perturbations provide a potentially powerful test of the inflationary hypothesis. In this respect, one may ask whether the solution of the type (6) can generate scalar perturbations of the desired magnitudes, like $\delta_H \sim 2 \times 10^{-5}$ and $n \simeq 0.95$. The spectral index is given by

$$n \simeq 1 - 4\epsilon + 2\eta, \tag{8}$$

where $\epsilon \equiv 2(\ln H)'/\chi'^2$ and $\eta \equiv 2\left[H''/H - (\ln H)'(\ln \chi')'\right]/\chi'^2$. Inflationary predictions with $\xi(\chi) \neq 0$ can be different from those with $\xi(\chi) = 0$ (see, e.g. [7,8]). In our model, a spectral index of magnitude $n \approx 0.95$ may be obtained with $\alpha \simeq -5.964$ or with $\alpha \sim \mathcal{O}(0)$ (cf Fig. 2). Furthermore, for $\alpha \approx -6$ and $\alpha \gtrsim 0$, the tensor-to-scalar ratio is small, $r \equiv A_T/A_S \ll 0.4$.

So far we discussed the case with no ϕ-dependent terms in the starting action. However, it is possible that the dilaton plays a special role in the present accelerated phase of the universe. In the presence of ϕ-dependent terms, one may introduce two more dimensionless variables:

$$\Phi \equiv \lambda(\phi)H^2, \quad W \equiv \zeta\,(\dot{\phi}/H)^2. \tag{9}$$

First consider the case $\zeta = 0$, so that there is no the kinetic term for ϕ. Φ is assumed to be non-zero; of course, its time variation must be small at late times, so as not to conflict with ground based solar system tests of GR. Here we do not impose any condition like (3). Especially, for $U = \Phi$, for which ϕ is behaving similarly as χ and hence $f \equiv \lambda(\phi) - \xi(\chi) = 0$, we find

$$X = -(\ln U)', \quad Y = 3 + (\ln U)'/2, \quad \varepsilon = (\ln U)'/2. \tag{10}$$

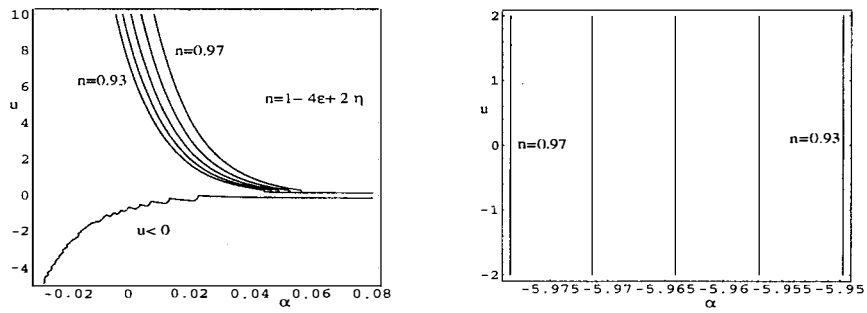

Figure 2: The contour plot of α and u ($\equiv \exp(\alpha_0)$), showing the value of the spectral index $n = 1 - 4\epsilon + 2\eta$ in the range [0.93, 0.97]; n is independent of the value of u for a large value of α (< -4).

The solution $U \propto e^{\alpha N}$ leads to an accelerated expansion for $\alpha > -2$; in particular, for $\alpha = 0.18$, we get $\varepsilon = 0.09$ and hence $w = -1.06$. For the above solution, a dark energy EOS parameter in the range $w_{DE} = -1.06^{+0.13}_{-0.08}$ may be obtained with $\alpha = 0.18^{-0.39}_{+0.24}$. In particular, for $\alpha = 0$, the effect is similar to that of a pure cosmological constant term, for which $\varepsilon = 0$ or $w = -1$.

In the case $\zeta \neq 0$, the field equations are solved explicitly, for example, with $U = \Phi = \text{const} \equiv \Phi_0$. In this case, there exist three branches of solution: the first branch is explained by $\varepsilon = \sqrt{6}\tanh(\sqrt{6}(N + N_0)) - 3$ and $W = -3\Phi_0(1 + 2\varepsilon)$. For this solution the universe enters into an accelerating phase for $N + N_0 \gtrsim 0.22$. Especially, for $N + N_0 \gg 0$, one has $\varepsilon \simeq 0 - 0.55$ and $W \simeq 0.3\Phi_0$, i.e., $\Phi_0 > 0$, ϕ behaves as a canonical scalar. Either both of the other two branches support an inflationary phase with $w > -1$, or only one of the branches supports inflation with $w < -1$. In the latter case, the second branch is not accelerating since $w > -1/3$.

In summary, we have shown that the string α'-correction of the Gauss-Bonnet form plays an important and interesting role in explaining the early and late time accelerating phases of the universe, with singularity-free solutions. For constant dilaton phase of the standard scenario, the model predicts during inflation spectra of both density perturbations and gravitational waves that may fall well within the experimental bounds. It is hoped that the analysis in this paper helps for explaining both the inflation and the cosmic acceleration at late times. For completeness, in particular, in order to study the transition between deceleration and acceleration, one may have to include matter fields which is also the constituent that we know dominates the universe during deceleration. The effective EOS parameter, w_{eff}, may more positive than w_{DE}.

This work was supported in part by the Marsden fund of the Royal Society of New Zealand.

References

1. I. Antoniadis, E. Gava and K.S. Narain, *Phys. Lett.* B **283**, 209 (1992).
2. I. Antoniadis, J. Rizos and K. Tamvakis, *Nucl. Phys.* B **415**, 497 (1994).
3. S. Nojiri, S.D. Odintsov and M. Sasaki, *Phys. Rev.* D **71**, 123509 (2005).
4. M. Sami, A. Toporensky, P.V. Tretjakov and S. Tsujikawa, *Phys. Lett.* B **619**, 193 (2005).
5. I.P. Neupane and B.M.N. Carter, hep-th/0510109, *Phys. Lett. B*, in press.
6. E.J. Copeland, A.R. Liddle and D. Wands. *Phys. Rev.* D **57**. 4686 (1998).
7. I.P. Neupane and B.M.N. Carter. hep-th/0512262. *JCAP*. in press.
8. J.c. Hwang and H. Noh, *Phys. Rev.* D **61**, 043511 (2000);
   C. Cartier, J.c. Hwang and E.J. Copeland, *Phys. Rev.* D **64**, 103504 (2001).
9. I.P. Neupane, *hep-th/0602097* (to be published).

FLOWING FROM SIX TO FOUR DIMENSIONS

C. PAPINEAU
Laboratoire de Physique Théorique, Université Orsay-Paris Sud
91405 Orsay Cedex, France

We consider a codimension two scalar theory with brane-localised Higgs type potential. The six-dimensional field has Dirichlet boundary condition on the bounds of the transverse compact space. The regularisation of the brane singularity yields renormalisation group evolution for the localised couplings at the classical level. In particular, a tachyonic mass term grows at large distances and hits a Landau pole. We exhibit a peculiar value of the bare coupling such that the running mass parameter becomes large precisely at the compactification scale, and the effective four-dimensional zero mode is massless. Above the critical coupling, spontaneous symmetry breaking occurs and there is a very light state.

1 Introduction

Dynamical generation of small mass scales via logarithmic renormalisation group running often occurs in theories which, in the limit of vanishing couplings, possess massless degrees of freedom. Once small couplings are turned on in UV, a theory may become strongly coupled in IR, with the corresponding IR scale serving as the mass scale of the low energy effective theory. A notable example of such a case is of course QCD.

In these proceedings, we present a class of models in which massless or very light degrees of freedom emerge upon turning on small couplings in a theory which originally had heavy states only. Unless the existence of massless states is dictated by a symmetry (Goldstone modes), this requires some sort of IR–UV mixing. In general terms, our models have two widely separated high energy scales, the UV cutoff scale Λ and the intermediate compactification scale R^{-1}. Once the small coupling $\mu = \mu(\Lambda)$ is turned on at the UV cutoff scale, it experiences renormalisation group running and increases towards low energies. Remarkably enough, the coupling becomes stronger in the infrared provided that its bare value is negative or, equivalently, the 4d localised mass is tachyonic. There exists a small critical value $\mu(\Lambda) = \mu_c$ such that the running coupling blows up precisely at the scale R^{-1}, i.e., $\mu(R^{-1}) = \infty$. At this point a massless mode appears in the spectrum.

For μ slightly smaller than μ_c, the light mode has positive mass squared proportional to $(\mu_c^2 - \mu^2)$, whereas at μ slightly above μ_c the low energy theory is in a symmetry breaking phase. Thus, $\mu(\Lambda) = \mu_c$ is the point of the second order phase transition. Let us stress that these features occur at the level of classical field theory.

In our models as they stand, the bare couplings are free parameters, so the choice $\mu \approx \mu_c$ (and hence the theory near the phase transition point) requires fine tuning. It would be interesting to see if there exists a dynamical mechanism driving the theory to the critical coupling (more generally, driving the parameters to the point where $\mu(R^{-1}) = \infty$).

2 The model

We consider a scalar field in a six-dimensional flat space. There is no scalar potential in the bulk, and Higgs-type scalar potential on a brane located at the origin of the compact dimensions. The action is [a]

$$\begin{aligned} S &= \int d^4x d^2y \left[\frac{1}{2}(\partial_M \phi)^2 - V_\delta(\phi)\right] , \\ V_\delta(\phi) &= \left(-\frac{\mu^2}{2}\phi^2 + \frac{\lambda}{4}\phi^4\right) \cdot \delta^2(y) . \end{aligned} \tag{1}$$

The singularity at $y = 0$ is resolved by introducing a disk $r \leq \epsilon$ and regularising the potential into

$$\begin{aligned} V(\phi) &= \frac{1}{\pi\epsilon^2}\left(-\frac{\mu^2}{2}\phi^2 + \frac{\lambda}{4}\phi^4\right) \quad \text{for } 0 \leq r \leq \epsilon , \\ V(\phi) &= 0 \qquad\qquad\qquad\qquad\quad \text{for } \epsilon \leq r \leq R . \end{aligned} \tag{2}$$

We consider a theory on a disk whose radius R is very large, $R^{-1} \ll \epsilon^{-1}$. The parameter μ^2 is dimensionless and may be considered a very small coupling constant i.e. $\mu^2 \ll 1$. Goldberger and Wise [1] argued that the coupling runs [b] with the energy scale Q as

$$\mu^2(Q) = \frac{\mu^2}{1 + \frac{\mu^2}{2\pi}\ln\frac{Q}{\Lambda}} \quad , \tag{3}$$

where Λ is the UV cutoff and $\mu^2 \equiv \mu^2(\Lambda)$ is the coupling constant entering the potential (2). This regularisation has a natural interpretation as finite transverse size $\epsilon = \Lambda^{-1}$ of the brane. Equation (3) implies that the coupling $\mu^2(Q)$ grows in the infrared.

Let us impose the Dirichlet boundary condition

$$\phi(r = R) = 0 .$$

If the coupling vanishes, or, more generally, if the running coupling at the compactification scale is small, $\mu^2(R^{-1}) \ll 1$, the theory is fully six-dimensional: there are no zero or light modes, whereas the Kaluza-Klein states have masses of order R^{-1}.

The question is what happens when $\mu^2(R^{-1})$ hits the infrared pole. In other words, what does this theory describe when the bare coupling μ^2 is equal or close to its critical value

$$\mu_c^2 = \frac{2\pi}{\ln\frac{R}{\epsilon}} . \tag{4}$$

As follows from this expression, μ_c^2 can (and actually, for perturbative treatment, has to) be small, which requires that $\ln(R/\epsilon)$ is large. Thus, it is legitimate to make use of the leading-log approximation and this is what we are going to do. Incidentally, in the theory on a disk, the formula for the running (3) is also valid in the leading-log approximation only.

Splitting the four-dimensional usual coordinates and the transverse ones, the 6d equations of motion can be read from the regularised action (2)

$$\begin{cases} -p^2\phi - \triangle_2\phi + \left[-\frac{\mu^2}{\pi\epsilon^2}\phi + \frac{\lambda}{\pi\epsilon^2}\phi^3\right] = 0 & \text{for } 0 \leq r \leq \epsilon , \\ -p^2\phi - \triangle_2\phi = 0 & \text{for } \epsilon \leq r \leq R , \end{cases} \tag{5}$$

where $p^2\phi$ is to be understood as the 4d momentum. These equations are indeed Schrödinger equations in two dimensions.

In the following section, we present some results when fine-tuning $\mu^2(\Lambda)$ around μ_c^2.

[a] We use the convention $(+,-,-,-,-,-)$ for the metric.

[b] The classical running was recently discussed in connection with neutrino masses [2]. The phenomenon is well-known in two-dimensional quantum mechanics [4].

3 Six-dimensional description

Let us first work above the background $\phi = 0$ so that we can consider the linearised equations of motion. We decompose the scalar field into $\phi(x^\mu, r, \theta) = e^{il\theta}\phi_l(r)\sigma_l(x^\mu)$ with l an integer. With this set, $\sigma_0(x^\mu)$ is the usual zero mode that one would have derived from a Kaluza-Klein scheme when working with the torus. In the following, we shall only consider this mode.

Plugging the previous decomposition into the equations of motion (5) and asking that the 4d momentum p^2 is very small compared to the relevant scales (R^{-1}, Λ), one gets the following solution

$$\begin{aligned} \phi(r) &= A \cdot J_0(\frac{\mu}{\sqrt{\pi}}\frac{r}{\epsilon}) && \text{for} \quad r \leq \epsilon \,, \\ \phi(r) &= B\left[J_0(|p|r) - \frac{J_0(|p|R)}{N_0(|p|R)} \cdot N_0(|p|r)\right] && \text{for} \quad r \geq \epsilon \,, \end{aligned} \tag{6}$$

where J_0 and N_0 are Bessel functions of the first and second kind. The Dirichlet condition was imposed for the outside solution, and we assumed that p^2 could be negative.

Matching conditions for both the solution and its derivative $d\phi/dr$ at $r = \epsilon$ lead to the four-dimensional mass squared

$$p^2 \equiv m^2_{(4)} = \frac{8\pi}{R^2}\frac{\mu_c^2 - \mu^2}{\mu_c^4} = \frac{8\pi}{R^2}\frac{1}{\mu^2(R^{-1})} \quad . \tag{7}$$

This result can be understood qualitatively by noticing that the Dirichlet boundary condition forces all modes to acquire a mass, in the spirit of the Scherk–Schwarz mechanism [3]. Then from a naive 4d viewpoint, the mass of a would-be zero mode has both the contribution due to the boundary condition, and an additional contribution, of opposite sign, coming from the localised tachyonic term,

$$m^2_{(4),\text{naive}} = \frac{z_0^2}{R^2} - \frac{\mu^2}{\pi R^2} \quad , \tag{8}$$

where z_0 is the first zero of the Bessel function J_0 and the factor $1/(\pi R^2)$ in the second term comes from the KK expansion of the zero mode. Equation (8) indeed predicts phase transition, but for $\mu_c^2 = (\pi z_0^2)$. The correct value, eq. (4), however, contains an inverse logarithmic factor coming from the running and the correct expression for the mass is actually slightly more involved than the simple guess (8).

From equation (7), we conclude that exactly at the critical coupling, there indeed exists a massless mode. For μ^2 slightly above μ_c^2, the mode becomes tachyonic. In this region, as in the 4d Standard Model electroweak symmetry breaking, the $\lambda\phi^4$ term has to be taken into account, and the field develops expectation value. The classical six-dimensional solution in this case is

$$\phi_c^2 = \frac{\mu^2 - \mu_c^2}{\lambda} \quad . \tag{9}$$

The effective Higgs vev is therefore $\sigma^2 = \int d^2y \phi_c^2$. Developping the field $\phi(r,p) = \phi_c(r) + \xi(r,p)$, one finds that the fluctuation's mass is

$$m_\xi^2 = \frac{16\pi}{R^2}\frac{\mu^2 - \mu_c^2}{\mu_c^4} = 2\,|m^2_{\text{tachyon}}| \quad . \tag{10}$$

This expression is valid for small $(\mu^2 - \mu_c^2)$.

4 Low energy effective theory

In this section, we compare the results of section 3 to the 4d effective theory. Specifically, we want to show that the 6d phase transition properties remain valid at low energy.

The interesting field configuration away from the brane is

$$\phi(x^\mu, r) \;=\; \sigma(x^\mu) \cdot \zeta(r) \;, \tag{11}$$

where $\zeta(r)$ is the general outside solution (6). It is normalised to unity $\int \zeta^2 d^2y = 1$, and therefore σ has a canonical kinetic term. Resolving the brane is equivalent to defining $\zeta(0) = \zeta(\epsilon)$.

The effective 4d potential for $\sigma(x^\mu)$ is obtained by integrating the potential (1) and the transverse kinetic term over the extra dimensions. One finds

$$V_{eff}(\sigma) \;=\; \frac{m_{(4)}^2}{2}\sigma^2 + \frac{\lambda_{(4)}}{4}\sigma^4 \;,$$

where

$$\lambda_{(4)} = \frac{64\pi^2}{\mu_c^8}\,\frac{\lambda}{R^4}.$$

The value of $m_{(4)}^2$ is precisely the same as in (7), which establishes the correspondence between the 6d and the 4d approaches in the unbroken phase. For $m_{(4)}^2 < 0$, the 4d expressions for the vev and the Higgs mass are $\sigma^2 = -m_{(4)}^2/\lambda_{(4)}$ and $m_\xi^2 = -2m_{(4)}^2$. These coincide with the results of section 3, so that the correspondence exists in the broken phase as well.

5 Conclusions

The toy model we presented in this small report possess rich physics: running couplings, phase transitions, spontaneous symmetry breaking and infrared strong dynamics which all occur at the level of classical field theory. Interestingly enough, very light modes and standard four-dimensional physics are generated out of a higher dimensional theory with large scales only. This mechanism could be of relevance for the problem of electroweak symmetry breaking and mass generation. Of course, an important step to make before addressing this phenomenological issue is the inclusion of other fields like chiral 4d fermions and gravitational interaction. In these proceedings, we focused on the main basic features of the models under consideration. More detailed information can be found in Ref.[5].

Acknowledgments

I would like to express my gratitude to organising committee for very warm hospitality. This work was supported in part by the RTN grants MRTN-CT-2004-503369.

References

1. W.D. Goldberger and M.B. Wise, *Phys. Rev.* D **65**, 025011 (2002) [arXiv:hep-th/0104170].
2. E. Dudas, C. Grojean and S. K. Vempati, "Classical running of neutrino masses from six dimensions" [arXiv:hep-ph/0511001].
3. J. Scherk and J. H. Schwarz, *Nucl. Phys.* B **153**, 61 (1979);
   E. Cremmer, J. Scherk and J. H. Schwarz, *Phys. Lett.* B **84**, 83 (1979)
4. R. J. Henderson and S. G. Rajeev, *J. Math. Phys.* **39**, 749 (1998) [arXiv:hep-th/9710061 and arXiv:hep=th/9609109];
   S. N. Solodukhin, *Nucl. Phys.* B **541**, 461 (1999) [arXiv:hep-th/9801054].
5. E. Dudas, C. Papineau, V. A. Rubakov, *JHEP* **0603**, 085 (2006) [arXiv:hep-th/0512276]

Do vortons form?

Marieke Postma
NIKHEF,Kruislaan 409, 1098 SJ Amsterdam,The Netherlands

In this talk I will discuss the formation and cosmology of vortons. Vortons are cosmic string loops stabilized by a current. Their formation depends on two key ingredients. Firstly, on the number of fermionic zero mode solutions (which requires a proper treatment of the gravitino field). And secondly, on the strength of the zero mode interactions with the thermal background. I will argue that vorton formation is unlikely if the reheat temperature is high.

1 Introduction

In this talk I will discuss the formation and cosmology of vortons. Vortons are cosmic string loops stabilized by a current, that act as cold dark matter particles. The requirement that they do not overclose the universe can severely constrain the underlying particle theory. Whether vortons are produced in the early universe depends on the number of zero mode solutions, as well as on the zero mode interactions with the thermal background. But before discussing this in more detail, I will start with a short introduction to cosmic strings and fermionic currents.

2 Cosmic strings & fermionic currents

Cosmic strings, like all topological defects, form during phase transitions. Phase transition are a common ingredient of particle physics: they arise in the standard model (the electroweak and QCD phase transition), as well as in many theories beyond the standard model (e.g. grand unified theories and hybrid inflation). The simplest model in which strings form is the Abelian-Higgs model. In this theory the Higgs field has the famous "Mexican hat"-potential. Symmetry breaking takes place as the Higgs field rolls down from the false vacuum — on the top of the hat — to the true vacuum — the rim of the hat. As different regions in the universe are causally disconnected, the Higgs field may end up on a different spot on the vacuum manifold (on the rim) in each such a region, resulting in a domain like structure. Cosmic strings form at the intersection of these domains. [1]

A cosmic strings is a heavy filament-like object, a vortex tube with magnetic field trapped inside. Long strings can self-intersect or with each other, thereby chopping off loops. The Higgs field may be coupled to fermions via a Yukawa interaction. This allows for the possibility of having fermionic currents flowing along the loop. Indeed, Jackiw & Rossi [2] found a fermionic zero-mode solution of the form $\psi = \zeta(r,\theta)e^{-E(t-z)}$. The spinor wave function $\zeta(r,\theta)$ only depends on the coordinates transverse to the string, and is localized near the string core (the fermion is bound to the string). From the frequency part, which only depends on the longitudinal coordinates, it follows that the fermion travels at the speed of light in the $+z$ direction; it is effectively massless. The existence of such a bound state solution can be understood from the

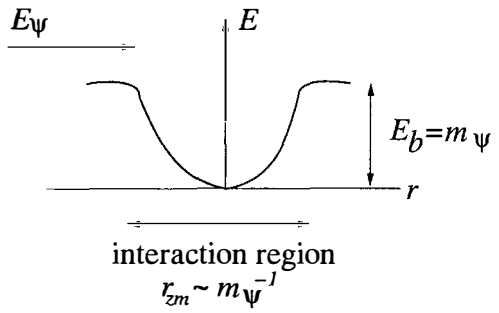

Figure 1: Fermion-string scattering as scattering of a potential well.

fermion mass term. Outside the string the Higgs field is in the true vacuum with $\langle\phi\rangle = \text{const.}$ and the fermion is heavy $m_f = \lambda\langle\phi\rangle \neq 0$, whereas inside the string core the Higgs field is in the false vacuum with $\langle\phi\rangle = 0$ and the fermion is massless. It is therefore energetically favorable for the fermion to be near the string.

The detection of a cosmic string would give us a great deal of information about the underlying theory, information well beyond the reach of terrestrial experiments. The obvious thing to do is look for its gravitational effects: gravitational waves and lensing events produced by a string, or the imprint of strings on the cosmic microwave background. This will be discussed in more detail in the talks of J. Martin and R. Jeannerot. But one could also try to look for observational effects of the fermionic currents; this will be the topic of the remainder of this talk.

3 Vortons

A cosmic string loop will contract under the action of gravity, and it will decay emitting its excess energy in the form of particles and gravitational waves. However, if a large enough fermionic current is flowing along the loop, its angular momentum may halt the contraction resulting in a stable loop configuration.[3] Such a stable loop, called a vorton, will behave like a heavy non-relativistic particle. If produced in just the right amount, it may be the dark matter in the universe. Too many vortons will overclose the universe; this can put strong constraints on the underlying theory.[7] This is especially true for "chiral strings", strings where the current is flowing only in one direction along the string. This is readily understandable. If there are currents flowing in both directions, they can scatter off each other, thereby limiting the maximum current obtainable. For chiral currents such a decay mechanism is absent, enhancing their stability.

The number of zero mode solutions, of fermionic currents, follows from an index theorem.[4] There is one left-moving current for each negatively charged fermion coupling to the Higgs field (with positive charge), and one right-moving current for each positively charged fermion. In anomaly free theories only neutral currents can be chiral. In supersymmetric (SUSY) theories this is not the end of the story. It is important to only count the physical degrees of freedom. Let me explain this using an analogy with the Higgs effect. A theory in which a global symmetry is broken has a massless degree of freedom, the Goldstone boson. If the theory is gauged, i.e., if the symmetry is made local, the Goldstone boson is "eaten" by the gauge field, and disappears from the spectrum. Something similar happens with SUSY cosmic strings. SUSY is broken inside the string. In a global SUSY theory one would conclude that there is a massless goldstino localized on the string (since SUSY is restored outside the string). This would be a zero mode solution.

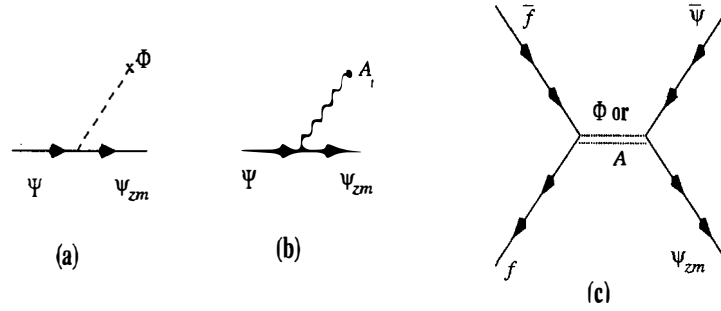

Figure 2: Fermion trapping reactions.

However, if you include gravity in the theory, SUSY becomes a local symmetry. The Goldstino gets eaten by the gaugino, the gauge field of local SUSY, and disappears from the theory.[5] This heuristic argument is confirmed by an explicit calculation.[6] The conclusion is that the number of zero-modes can be different if the theory is coupled to gravity. An explicit example is D-term inflation. There are 2 zero-mode solutions in the global SUSY version of the theory; one of them is nothing but the goldstino of broken SUSY and disappears from the spectrum when gravity is included. Hence, these strings are chiral.

4 Vorton formation

The existence of zero mode solutions is not sufficient to guarantee the formation of vortons. Indeed, these states should, in one way or another, be excited in the early universe.[8] A current may form if fermions are trapped through interactions of the string with the thermal bath. As an explicit example I will consider the case that the reheat temperature is larger than the vacuum fermion mass $T_R > m_\psi$. The fermion is massless on the string and massive outside. One can therefore think of fermion-string scattering as scattering of a potential well with height set by the fermion mass, see Fig. 1. If the temperature is high, and the incoming fermion has an energy much larger than the potential height, the chance of trapping a fermion is negligible; and any fermion trapped will be scattered off. At temperatures much lower than the fermion mass, the fermions in the thermal bath are Boltzmann suppressed, and the number of scatterings is negligible. Hence, fermion trapping and current formation has to take place at temperatures $T \sim m_\psi$. Moreover, a current large enough to stabilize a vorton will only be generated if the trapping rate is larger than the Hubble rate at that time.

Possible interactions to trap fermions are shown in Fig. 2. An incoming fermion can scatter off the string-forming Higgs or gauge field and get trapped, or fermion scattering in the string core can lead to excited zero mode states. The calculation of the cross section in a cosmic string background are analogous to the calculations of scattering off monopoles by Callan and Rubakov.[9,10] They differ from usual scattering amplitudes in that transverse momentum is not conserved, the zero mode wave length is unrelated to its energy ($\lambda \sim 1/k$ does not apply in the transverse plane), and the incoming particles differ from plane wave solutions due to the string background. However, all these effects are minimal at the energies of interest. The first two diagrams in Fig. 2. are forbidden by energy-momentum conservation in the transverse plane. The third diagram gives the dominant contribution. An explicit calculation shows that trapping is only efficient for large Yukawa couplings, and if the fermions ψ are coupled to light particles.[8]

Not only current formation should be considered, but also possible decay. The zero modes are strictly massless — and their decay is forbidden by kinematics — only for an infinitely long

straight string.[11] The dispersion relation for a massless particle is $E = k$. A zero-mode on a string loop has a non-zero centripetal acceleration $\dot{k} \sim k/R$ with R the loop radius, and the dispersion relation picks up an extra term. This gives rise to a momentum dependent "mass" $m^2 \sim k/R$. Decay is no longer forbidden by kinematics. The decay rate $\Gamma \sim \lambda^2 m(m/m_\psi)^2$ (with m the effective mass, and m_ψ as before the fermion vacuum mass) is large for large couplings, and if ψ is coupled to light particles. But these are precisely the conditions favorable for current formation! We conclude that currents that form also decay.

5 Conclusions

In this talk I discussed vorton formation in the early universe. Two ingredients play an important role. Firstly, one should properly count the number of zero modes. This means that in a supersymmetric theory one should not count the goldstino, since it disappears from the spectrum if gravity is included. The stability of vortons is enhanced if the strings are chiral, when there are only currents flowing in one direction along the string. Secondly, one should analyze whether the zero mode solutions are actually excited in a cosmological setting. This is unlikely if the reheat temperature is large. The conditions favorable for current formation are also favorable for their decay, and vortons do not survive. In this case vortons cannot be the dark matter and are not detectable; they also do not constrain the underlying theory.

1. T. W. B. Kibble, JPA **9**, 1387 (1976).
2. R. Jackiw and P. Rossi, NPB **190**, 681 (1981).
3. R. L. Davis and E. P. S. Shellard, NPB **323**, 209 (1989).
4. E. J. Weinberg, PRD **24**, 2669 (1981).
5. R. Jeannerot and M. Postma, JHEP **0412**, 032 (2004).
6. P. Brax, C. . v. de Bruck, A. C. Davis and S. C. Davis, arXiv:hep-th/0604198.
7. R. H. Brandenberger, B. Carter, A. C. Davis and M. Trodden, PRD **54**, 6059 (1996), B. Carter and A. C. Davis, PRD **61**, 123501 (2000).
8. R. Jeannerot and M. Postma, JHEP **0412**, 043 (2004).
9. C. G. . Callan, NPB **212**, 391 (1983), V. A. Rubakov, JETPL **33**, 644 (1981).
10. W. B. Perkins, L. Perivolaropoulos, A. C. Davis, R. H. Brandenberger and A. Matheson, NPB **353**, 237 (1991), R. H. Brandenberger, A. C. Davis and A. M. Matheson, NPB **307**, 909 (1988).
11. S. M. Barr and A. M. Matheson, PLB **198**, 146 (1987).

Numeric simulation of gravitational waves in Randall-Sundrum cosmology

Sanjeev S. Seahra
Institute of Cosmology & Gravitation, University of Portsmouth
Portsmouth, PO1 2EG, UK

Motivated by the problem of the evolution of bulk gravitational waves in Randall-Sundrum cosmology, we have developed a characteristic numerical scheme to solve 1+1 dimensional wave equations in the presence of a moving timelike boundary. This code has been used to predict the spectral tilt of the stochastic gravitational wave background in brane cosmology for a variety of higher-dimensional (i.e. 'bulk') initial conditions. Here, we give a qualitative picture of how gravitational waves behave in the braneworld scenario, and summarize some of our main results.

1 Randall-Sundrum cosmology

It is well known that the Randall-Sundrum (RS) braneworld model [1] is in excellent agreement with general relativity at low energies. This is the principal appeal of the model; it is one of the only examples of a scenario involving a large extra dimension that entails no serious conflicts with general relativity. However, this means that one needs to consider high energy or strong gravity scenarios to properly test the model. One possibility is to examine the high energy epoch of braneworld cosmology, where exact solutions of the 5-dimensional field equations are known. Well-understood braneworld phenomena include a modified cosmic expansion and early times and 'dark radiation' effects, whereby the Weyl curvature of the bulk projected on the brane acts as an additional geometric source in the Friedmann equation.

But if one wants to move beyond the exact description of the background geometry in these cosmological models, there are significant technical difficulties. A cosmological brane is essentially a moving boundary in a static 5-dimensional background — anti-de Sitter space in the RS model (*cf.* Fig. 1) — so perturbations are described by bulk wave equations with boundary conditions enforced on a non-trivial timelike surface. While it is possible to make some analytic progress when the brane is moving 'slowly' [2,3,4], the more interesting case of a fast-moving, high-energy brane remains impervious to such treatment.

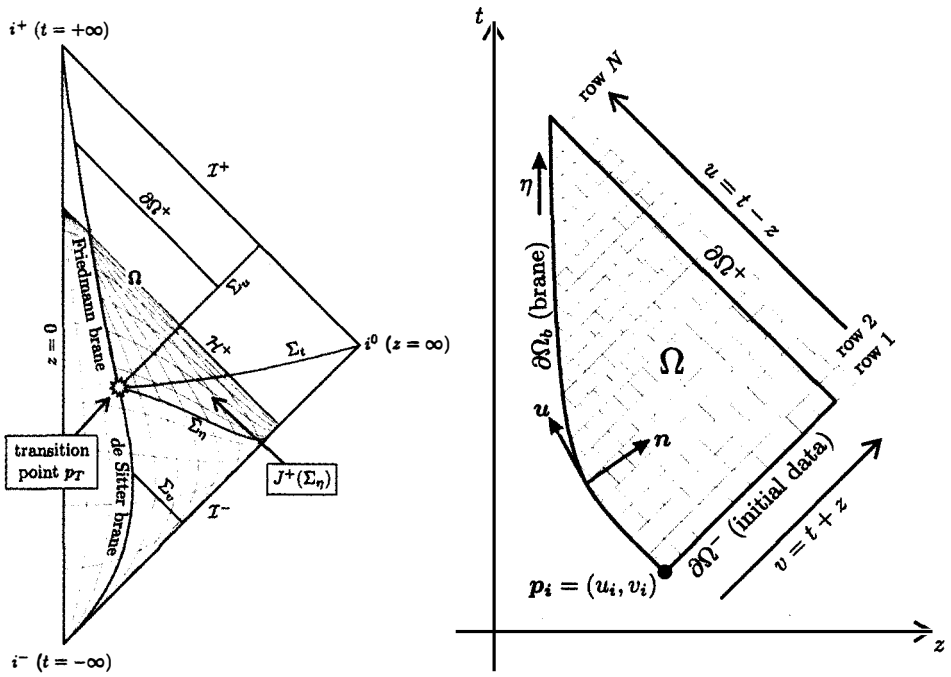

(a) Conformal diagram of RS bulk geometry

(b) The computational domain Ω

Figure 1: Conformal diagram (a) illustrating the causal structure of a braneworld model of the early universe. In this plot, the three 'ordinary' spatial dimensions have been suppressed; hence, the brane is represented by a simple timelike trajectory. An initial purely-de Sitter inflationary phase is followed by a 'Friedmann', or high-energy radiation, phase. Our code assumes that the gravitational wave content of the model is known on the initial null surface Σ_u, and then calculates the field amplitude throughout the spacetime region Ω. The region is shown in a conventional spacetime diagram on the right (b). Superimposed on Ω is a (particularly coarse) example of the computational grid we use to discretize and solve the master wave equation.

The purpose of this work is to present a new numeric algorithm to solve wave equations in the presence of a moving boundary. For the sake of simplicity, we restrict ourselves to a class of wave equations and boundary conditions that correspond to tensor, or gravitational wave (GW), perturbations. This is not the first attempt to deal with these equations numerically: previous efforts include pseudo-spectral[5,6,7] and direct evolution[8,9,10,11,12] methods using various null and non-null coordinate systems in which the brane is stationary. Unfortunately, not all of these algorithms agree with one another. In particular, Hiramatsu et al.[6] predict a flat GW background spectrum at high frequencies, while Ichiki and Nakamura[8] predict a red spectrum. These two groups have very different prescriptions for setting initial conditions in the bulk, and it used to be unclear whether this was the source of tension between the two results. However, with our new code we have been able to definitively state that both initial conditions lead to a flat spectrum, provided that the energy scale of brane inflation is sufficiently high. Furthermore, we have shown have a much wider class of initial conditions can lead to the same result; implying that a flat GW background is a somewhat generic prediction of this class of braneworld models. For a comprehensive account of how these conclusions are obtained, the interested reader should

consult Seahra.[13]

2 Numeric Method

The problem of predicting the propagation of a GW mode with 3-dimensional wavenumber k in this model can be reduced to solving the wave equation

$$\left[\frac{\partial^2}{\partial t^2} - \frac{\partial^2}{\partial z^2} + \epsilon_*(2+\epsilon_*) + \frac{15}{4z^2}\right]\psi(t,z) = 0, \tag{1}$$

on Ω. Here, ϵ_* is a dimensionless parameter that represents the density of brane matter normalized by the brane tension when the mode re-enters the Hubble horizon, ψ is a master variable governing tensor perturbations, and $\ell \lesssim 0.1\,\mathrm{mm}$ is the curvature scale of the bulk. Assuming radiation-domination, the brane's trajectory is given by the Friedmann equation

$$\dot{z}^2 = (H\ell)^2 = \epsilon_* z^4(2+\epsilon_* z^4), \quad \dot{t} = \sqrt{1+\dot{z}^2}, \tag{2}$$

where an overdot indicates a derivative with respect to conformal time. The wavefunction ψ satisfies the following boundary condition on the brane:

$$\left[\mathbf{n}\cdot\nabla\psi + \frac{3}{2}\frac{\sqrt{1+(H\ell)^2}}{z}\psi\right]_b = 0, \tag{3}$$

where $\mathbf{n}$ is the brane normal. To complete the specification of the problem, we need to set initial data on the $\partial\Omega^-$ hypersurface. This surface is located in spacetime by demanding that the perturbation wavelength be s_0 times the horizon size at the epoch when $\partial\Omega^-$ crosses the brane.

To solve for ψ numerically, we take inspiration from well established techniques in black hole perturbation theory. We discretize the computational domain as shown in Fig. 1(b); the evolution of ψ over a given cell is obtained by integrating the wave equation over the 'finite element' and applying the divergence theorem. Because the individual elements are based on the characteristics of the wave equation (1), we obtain a fast, accurate, and stable numeric algorithm.

3 Results

In Fig. 2, we show the result of a typical simulation of the GW amplitude. One can see how the value of the perturbation is frozen on the brane until it re-enters the horizon, as in 4-dimensional theory. After horizon re-entry, some of the GW energy is radiated away into the bulk, and at late times the perturbation on the brane decays as $1/a$ as usual. In Fig. 2(b), we show what the brane signal would be if one ignored the bulk and evolved the GWs as in ordinary general relativity. We see that the '5-dimensional' simulation result shows a suppressed late-time amplitude compared to the reference curve, reflecting the GW energy loss into the bulk that occurs at horizon crossing. Knowledge of the ratio between the simulation and reference amplitudes $\mathcal{R}$ as a function of the observed mode frequency f can be directly translated into a prediction for the spectral energy density Ω_{GW} of the GW background today[13]:

$$\Omega_{\mathrm{GW}} \propto \mathcal{R}^2(f)\begin{cases}54.9, & f \lesssim f_c,\\ 36.4(f/f_c)^{4/3}, & f \gtrsim f_c,\end{cases} \quad f_c \sim 3.3\times10^{-5}\left(\frac{0.1\,\mathrm{mm}}{\ell}\right)^{1/2}\mathrm{Hz}. \tag{4}$$

Our simulations show that as long as $s_0 \gtrsim 100$, $\mathcal{R} \propto (f/f_c)^{-2/3}$ for $f \gtrsim f_c$ and 'reasonable' initial data; i.e., field configurations that do not vary too quickly along Σ_u. On the other hand, we have found $\mathcal{R} \sim 1$ for $f \lesssim f_c$ in all cases. Hence, a flat GW spectrum is recovered for all frequencies.

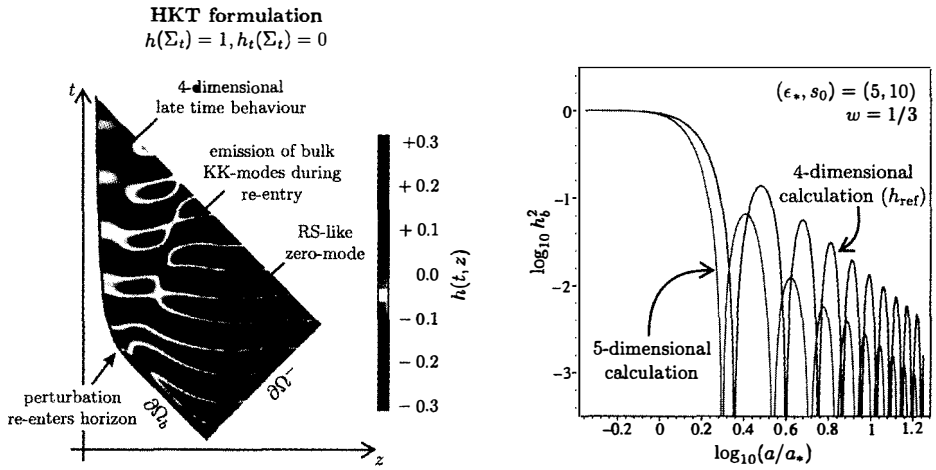

(a) Bulk profile

(b) Brane profile

Figure 2: Results of a typical numeric simulation using the initial conditions favoured by Hiramatsu et al. On the right, we have drawn what the brane GW signal $h_{\rm ref}$ would be if the bulk were neglected; i.e., if one solved the 4-dimensional master equation with a modified expansion rate given by (2).

Acknowledgments

I would like to thank Takashi Hiramatsu, Kazuya Koyama, and Atsushi Taruya for sharing the results of their numerical calculations and useful discussions. I would also like to thank Chris Clarkson, Tsutomu Kobayashi and Roy Maartens for comments. I am supported by PPARC postdoctoral fellowship PP/C001079/1.

References

1. Lisa Randall and Raman Sundrum. *Phys. Rev. Lett.*, 83:4690–4693, 1999. hep-th/9906064.
2. Richard Easther, David Langlois, Roy Maartens, and David Wands. *JCAP*, 0310:014, 2003. hep-th/0308078.
3. Tsutomu Kobayashi and Takahiro Tanaka. *JCAP*, 0410:015, 2004. gr-qc/0408021.
4. Richard A. Battye and Andrew Mennim. *Phys. Rev.*, D70:124008, 2004. hep-th/0408101.
5. Takashi Hiramatsu, Kazuya Koyama, and Atsushi Taruya. *Phys. Lett.*, B578:269–275, 2004. hep-th/0308072.
6. Takashi Hiramatsu, Kazuya Koyama, and Atsushi Taruya. *Phys. Lett.*, B609:133–142, 2005. hep-th/0410247.
7. Takashi Hiramatsu. 2006. hep-th/0601105.
8. K. Ichiki and K. Nakamura. *Phys. Rev.*, D70:064017, 2004. hep-th/0310282.
9. Kiyotomo Ichiki and Kouji Nakamura. 2004. astro-ph/0406606.
10. Tsutomu Kobayashi and Takahiro Tanaka. *Phys. Rev.*, D71:124028, 2005. hep-th/0505065.
11. Tsutomu Kobayashi and Takahiro Tanaka. 2005. hep-th/0511186.

12. Tsutomu Kobayashi. 2006. hep-th/0602168.
13. Sanjeev S. Seahra. 2006. hep-th/0602194.

DARK MATTER FROM ALMOST-COMMUTATIVE GEOMETRY

C.A. STEPHAN
Centre de Physique Théorique, Campus de Luminy
13288 Marseille, France

During the last two decades Alain Connes developed Noncommutative Geometry [2], which allows to unify two of the basic theories of modern physics: General Relativity and the Standard Model of Particle Physics as classical field theories [1]. In the noncommutative framework the Higgs boson, which had previously to be put in by hand, and many of the ad hoc features of the standard model appear in a natural way. The aim of this presentation is to motivate this unification from basic physical principles and to give a flavour of its derivation. A classification of the relevant noncommutative geometries was achieved [3,5,9,4] as well as possible extensions [11,13] which arise from it. These extensions of the standard model contain novel fermions which provide viable candidates for the dark matter problem [12,13]. A short overview on the cosmological implications of these fermions will be presented.

1 Noncommutative Geometry

The aim: To unify general relativity (GR) and the standard model of particle physics (SM) on the same geometrical level. This means to describe gravity and the electro-weak and strong forces as gravitational forces of a unified space-time.

First observation, the structure of GR: gravity emerges as a pseudo-force associated to the space-time symmetries, i.e. the diffeomorphisms of the manifold M. If one tries to put the SM into the same scheme, one cannot find an underlying geometric structure, which is equivalent to space time.

Second observation: one can find an equivalent description of space-time: Trade the differential geometric description of the manifold M with metric g for the algebraic description of a spectral triple $(C^\infty(M), \not{\partial}, \mathcal{H})$. A spectral triple consists of the following entities:

- An algebra $\mathcal{A}$ $(= C^\infty(M))$, the equivalent of the topological space M
- A Dirac operator D $(= \not{\partial})$, the equivalent of the metric g on M
- A Hilbert space $\mathcal{H}$, on which the algebra is faithfully represented and on which the Dirac operator acts. It contains the fermions, i.e. in the space-time case, its the Hilbert space of Dirac 4-spinors.
- A set of axioms [2], to ensure a consistent description of the geometry

This allows to describe GR in terms of spectral triples. Space-time is replaced by the algebra of C^∞-functions over the manifold and the Dirac operator plays a double role: it is the algebraic equivalent of the metric and it gives the dynamics of the Fermions.

The Einstein-Hilbert action is replaced by the spectral action [1], which is the simplest invariant action, given by the number of eigenvalues of the Dirac operator up to a cut-off. A most important point is that the geometrical notions of the spectral triple remain valid, even if the algebra is *noncommutative*. The simplest way of achieving noncommutativity is done by multiplying the function algebra $C^\infty(M)$ with a sum of matrix algebras

$$\mathcal{A}_f = M_1(\mathbb{K}) \oplus M_2(\mathbb{K}) \oplus \dots \tag{1}$$

with $\mathbb{K} = \mathbb{R}$, $\mathbb{C}$ or $\mathbb{H}$. These algebras, or *internal spaces* have exactly the $U(N)$- or $SU(N)$-type Lie groups as their symmetries. The choice

$$\mathcal{A}_f = \mathbb{C} \oplus \mathbb{H} \oplus M_3(\mathbb{C}) \tag{2}$$

allows to construct the SM. The combination of space-time and internal space can be considered as a *discrete Kaluza-Klein space*. Here the Dirac operator plays again a multiple role:

1. It is the algebraic equivalent of the metric for the external and the internal space
2. It gives the dynamics and the mass matrix of the Fermions
3. It contains the Higgs and the gauge Bosons

The internal Hilbert space $\mathcal{H}_f$ is given by the Fermion multiplets of the SM.

Now the spectral triple approach, combined with the spectral action [1] allows to unify GR and the SM as classical field theories:

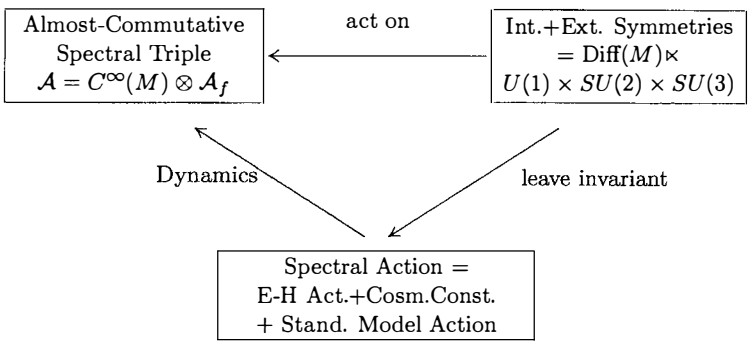

The almost-commutative SM automatically produces:

- The combined GR and SM action
- A cosmological constant
- The Higgs boson with the correct quartic Higgs potential

2 Classifying Almost-Commutative Geometries

A classification of almost-commutative geometries was done [3,5,9,4] with respect to the number of summands in the internal algebra (1) and a "shopping list" for the physical properties of the models. The physical models emerging from the spectral action were required to have a non-degenerate fermionic mass spectrum, to be free of harmful anomalies, to have unbroken colour groups and to possess no uncharged massless Fermions.

The classification for up to four summands in the internal algebra (1) gives for

1 summand: No physical models

2 summands: No physical models

3 summands: The first generation of the standard model

4 summands: The same as for 3 summands + an "electro-strong" model

3 One Step Beyond: The AC-Model

Rule of thumb: Enlarging the internal space, i.e adding summands to the internal algebra, will require new particles. They correspond to the enlarged Dirac operator which gives the necessary internal metric. One almost-commutative extension of the SM is known [11]. It has as its internal algebra

$$\mathcal{A}_f = \mathbb{C} \oplus \mathbb{H} \oplus M_3(\mathbb{C}) \oplus \mathbb{C} \oplus \mathbb{C} \oplus \mathbb{C}$$

which is the SM algebra (2) plus three times the complex numbers. It predicts two new particles, A and C with the following properties:

- Opposite (vectorlike) electro-magnetic charge
- Opposite Z boson charge
- Sterile to $W^{\pm}$ and strong interactions
- Sterile to the Higgs boson
- Their masses have their origin in the internal geometry and not in the Higgs mechanism

These particles A and C may play the role of dark matter [12] if their electro-magnetic charge is $\pm 2e$, e being the charge of the electron. We take A to be of double negative charge and C of double positive charge. They appear bound in atom-like (AC)-systems and if their masses are sufficiently high $m_{AC} \geq 100$ GeV to escape experimental constraints from particle colliders. Their mass is usually measured in units of 100 GeV called S_2. These bound (AC)-atoms are neutral, have a sufficiently small cross section

$$\sigma_{(AC)} \sim 6 \cdot 10^{-28} \cdot S_2^{-2} \text{ cm}^2.$$

and can thus be considered as WIMPs. Properties (problems or advantages?) of the AC-model:

- A^{--} binds in the early universe with ${}^4He^{++}$ nuclei into (AHe)-systems (OLe-Helium) which should pollute the matter today. They can be considered as SIMPs and may trigger nuclear reactions due to the lacking of a Coulomb barrier.
- C^{++} binds into anomalous Helium (Cee). It is the most problematic byproduct due to severe experimental constraints on anomalous helium in terrestrial matter.
- The (AHe)-systems can "catalyse" the binding into (AC) dark matter.
- The mass of the AC-particles is bounded by $S_2 \sim 10^5$ since heavier AC-particles would over-close the Universe

There are two possible mechanisms to solve the problem of OLe-Helium and anomalous Helium and to escape the experimental constraints:

1. The gas shield of the heliopause is opaque to anomalous Helium and thus decreases the incoming flux significantly [12]. This is sufficient to meet the severe experimental bounds in terrestrial matter. OLe-Helium seems to have quasi-elastic interaction and should thus be difficult to detect directly. But recombination with anomalous Helium into (AC)-atoms may be detectable due in large volume detectors (like Super Kamiokande).

2. Almost-commutative geometry allows a Coulomb like interaction between the AC-particles which is not shared by the standard model particles [13]. The AC-particles are again oppositely charged with respect to this "invisible light". In this way their binding is enhanced and the abundances of anomalous Helium and OLe-Helium can be reduced significantly.

4 Outlook

→ What are the influences of the AC-particles on SM parameters such as $(g-2)$ for electrons & muons?

→ Is OLe-Helium detectable?

→ A classification of almost-commutative geometries with more than 4 summands in the matrix algebra is in work. Is the AC-model unique?

Acknowledgments

The author wishes to thank Thomas Schücker, Jan-Hendrik Jureit, Bruno Iochum and Maxim Khlopov. This work is funded by the Alexander von Humboldt-Stiftung.

References

1. A.H. Chamseddine and A. Connes, *Commun. Math. Phys.* **186**, 731 (1997).
2. A. Connes, *Noncommutative Geometry* 1*Academic Press*1994.
3. B. Iochum, T. Schücker and C.A. Stephan, *J: Math. Phys.* **45**, 5003 (2004).
4. J.-H. Jureit, T. Schücker and C.A. Stephan, *J. Math. Phys.* **46**, 72303 (2005).
5. J.-H. Jureit and C.A. Stephan, *J. Math. Phys.* **46**, 43512 (2005).
6. J.-H. Jureit and C.A. Stephan, *hep-the/0503085.*
7. T.Krajewski, *J. Geom. Phys.* **28**, 1 (1998).
8. M. Paschke and A. Sitarz, *J. Math. Phys.* **39**, 6191 (1998).
9. T. Schücker, *hep-th/0501181.*
10. T. Schücker, *Lect. Notes Phys.* **659**, 285 (2005).
11. C.A. Stephan, *hep-th/0509213.*
12. D. Fargion, M. Khlopov and C.A. Stephan, *astro-ph/0511789.*
13. M. Khlopov and C.A. Stephan, *astro-ph/0603187.*

NON-GAUSSIANITY AND CONSTRAINTS FOR THE VARIANCE OF PERTURBATIONS IN THE CURVATON MODEL

JUSSI VALIVIITA*, MISAO SASAKI‡ and DAVID WANDS*
Institute of Cosmology and Gravitation, University of Portsmouth, Portsmouth PO1 2EG, UK
‡ *Yukawa Institute for Theoretical Physics, Kyoto University, Kyoto 606-8503, Japan*

Recently, the primordial non-gaussianity in the curvaton model has been predicted assuming sudden decay of the curvaton. We extend the calculation to non-instantaneous decay by employing δN formalism. The difference between the sudden decay approximation and our numerical result is larger than 1% *only if* the non-linearity parameter is small, $-1.16 < f_{\rm NL} < 60$. Thus it is safe to use the sudden decay approximation when deriving constraints for the curvaton model from WMAP3 ($f_{\rm NL} < 114$), but with the Planck forecast $|f_{\rm NL}| < 5$ one should employ the fully numerical result. Often, the curvaton perturbations $\delta\sigma$ have been assumed to be small compared to the background value of the curvaton field σ_0. Consequently, the variance $\Delta^2 = \langle\delta\sigma^2\rangle/\sigma_0^2$ has been assumed to be negligible. However, the measurements of CMB or large scale structure perturbation amplitude do not constrain the variance if the main contribution to it comes from the ultraviolet (UV) scales, i.e., from smaller than observable scales. We discuss how, even in this case, observational constraints on non-gaussianity set an upper bound to the small scale variance, $\Delta^2_{UV} < 90$.

1 Introduction

Most inflationary models give rise to nearly Gaussian primordial curvature perturbations. Typically, prediction for the non-linearity factor $f_{\rm NL}$ in *single-field* models is of the order of ϵ — the slow roll parameter which must be $\lesssim 10^{-1}$ to guarantee the near scale-invariance of the primordial perturbations. In principle, measurement of $f_{\rm NL}$ would give valuable information on the inflaton potential, but unfortunately such a tiny non-gaussianity will remain unobservable. The current upper bound from the WMAP three-year data [1] is $|f_{\rm NL}| < 114$ while Planck is expected to bring this down to $|f_{\rm NL}| \lesssim 5$, which is still orders of magnitude larger than the typical inflationary prediction.

Nevertheless, there are classes of *multi-field* models that can lead to an observable non-gaussianity. One well-motivated example is the curvaton model.[2] In addition to the inflaton ϕ there would be another light weakly coupled scalar field (e.g., MSSM flat direction), curvaton σ, which would be completely subdominant during inflation so that the inflaton would drive the expansion of the universe. The potential could be [3] $V = \frac{1}{2}M^2\phi^2 + \frac{1}{2}m^2\sigma^2$. At horizon exit both fields acquire some classical perturbations that freeze in. However, the observed cosmic microwave (CMB) and large-scale structure (LSS) perturbations can result from the curvaton instead of the inflaton, if the inflaton perturbations are much smaller than 10^{-5}. To simplify the analysis, in this talk, we assume that the curvature perturbation from inflaton is completely negligible $\zeta_\phi \approx 0$, and the curvature perturbation from curvaton ζ_σ is such that it leads to the observed amplitude of perturbations.

After the end of inflation the inflaton decays into ultra-relativistic particles ("radiation") the curvaton energy density still being subdominant. At this stage the curvaton carries *pure entropy (isocurvature) perturbation* instead of the usual adiabatic perturbation. Namely, the entropy perturbation between radiation and curvaton is $\mathcal{S}_{r\sigma} = 3(\zeta_r - \zeta_\sigma) \approx -3\zeta_\sigma$. Since the observations have ruled out pure isocurvature primordial perturbation[4,5], a mechanism — curvaton decay into "radiation" — that converts the isocurvature perturbation to the adiabatic one is needed at some stage of the evolution before the big bang nucleosynthesis.

As the Hubble rate H decreases with time, eventually $m^2 \gtrsim H^2$, and curvaton starts to oscillate about the minimum of its potential. Then it behaves like pressureless dust ("matter", $\rho_\sigma \propto a^{-3}$) so that its relative energy density starts to grow with respect to radiation

($\rho_r \propto a^{-4}$). Finally, curvaton decays into ultra-relativistic particles leading to the standard radiation dominated adiabatic primordial perturbations.[a] However, this mechanism may create from the initially Gaussian curvaton field perturbations strongly non-gaussian primordial curvature perturbations. The more subdominant the curvaton is during its decay the more non-gaussianity results in. Since the time of the decay depends on the model parameters (such as the curvaton mass m and decay rate Γ_σ), the observational upper bounds on non-gaussianity provide a powerful method to constrain these parameters.

In the simplest case the (possible) non-gaussianity results from the second order correction to the linear result

$$\zeta = \zeta_1 + \frac{3}{5} f_{\rm NL} \zeta_1^2 \,. \tag{1}$$

Here ζ_1 is proportional to the Gaussian field perturbation at horizon exit, so it is Gaussian, and ζ_1^2 is χ^2 distributed. In this talk we briefly derive $f_{\rm NL}$ in the sudden decay approximation using a slightly different and more general approach than in [6,7] and then, for the first time, present the results in the case of non-instantaneous decay of curvaton. For the full derivation and discussion of our results, see [8]. Since, in the early universe, all today's observable scales are super-Hubble, we take advantage of the *separate universe* assumption throughout the calculations.

2 Sudden decay approximation

In the absence of interactions, fluids with a barotropic equation of state, such as radiation ($P_r = \rho_r/3$) or the non-relativistic curvaton ($P_\sigma = 0$), have a *conserved* curvature perturbation [11]

$$\zeta_i(t,\vec{x}) = \delta N(t,\vec{x}) + \frac{1}{3}\int_{\bar{\rho}_i(t)}^{\rho_i(t,\vec{x})} \frac{d\rho_i'}{\rho_i' + P_i(\rho_i')} \,, \tag{2}$$

where $\delta N = N(t,\vec{x}) - \bar{N}(t)$ with $N(t,\vec{x})$ being the perturbed (i.e. local) number of e-folds of expansion until time t and $\bar{N}(t)$ being the average expansion. At the first order this fully non-linear definition reduces to the usual definition: $\zeta_{i1} = -\psi_1 - H\frac{\delta_1\rho_i}{\dot{\rho}_i}$ with $\psi_1 = -\delta_1 N$.

Applying (2) for the curvaton during its oscillation but before the decay, we have

$$\zeta_\sigma(t,\vec{x}) = \frac{1}{3}\ln\left[\frac{\rho_\sigma(t_{\rm in},\vec{x})}{\bar{\rho}_\sigma(t_{\rm in})}\right]_{\delta N=0} \,, \tag{3}$$

where $\rho_\sigma(t_{\rm in},\vec{x}) = \frac{1}{2}m^2\sigma_{\rm in}^2(\vec{x})$ is evaluated on spatially flat ($\delta N = 0$) hypersurface. The time of the beginning of the curvaton oscillation, $t_{\rm in}$, is defined in terms of the local Hubble rate as $H(t_{\rm in},\vec{x}) = m$. Since $H^2 = (8\pi G/3)\rho_{\rm tot}$, the constant time $t = t_{\rm in}$ surface is a uniform-total density hypersurface.

In general, $\sigma_{\rm in}$ depends non-linearly on the field value at horizon exit σ_*. Thus we write[7] $\sigma_{\rm in} = g(\sigma_*) = g(\bar{\sigma}_*) + g'\delta\sigma_* + \frac{1}{2}g''(\delta\sigma_*)^2 + \ldots$, where $' = \partial/\partial\sigma_*$. (For exactly quadratic potential g'' and higher derivatives vanish, but even a slight deviation from quadratic potential can change the resulting $f_{\rm NL}$ considerably [12] via g''.) Substituting this into (3) and expanding up to second order we obtain $\zeta_\sigma = \zeta_{\sigma 1} + \frac{1}{2}\zeta_{\sigma 2} + \ldots$ with $\zeta_{\sigma 1} = \frac{2}{3}\frac{g'}{g}\delta\sigma_*$ and $\zeta_{\sigma 2} = -\frac{3}{2}\left(1 - gg''/g'^2\right)\zeta_{\sigma 1}^2$, where $\delta\sigma_*$ is well described by a Gaussian random field as we assume the inflaton and curvaton to be uncoupled (or only weakly coupled).

Assume now that the curvaton decays instantaneously at time $t_{\rm dec}$ (before it has become completely dominant) on a uniform-total density hypersurface corresponding to $H = \Gamma_\sigma$, i.e., when

[a] Hadn't we assumed negligible inflaton curvature perturbation, $\zeta_\varphi \approx 0$, some "residual" isocurvature would have resulted if the curvaton was sub-dominant during its decay. This would have lead to an interesting mixture of correlated adiabatic and isocurvature perturbations which was studied in [9]. Following the guidelines of [9] our calculation should be straightforward to generalise. It should be noted that *observations do not rule out* a correlated isocurvature component if it is less than 20% of the total primordial perturbation amplitude [10]

the local Hubble rate equals the decay rate for the curvaton (assumed constant). Hence

$$\rho_r(t_{\rm dec},\vec{x}) + \rho_\sigma(t_{\rm dec},\vec{x}) = \bar{\rho}(t_{\rm dec})\,, \tag{4}$$

where we use a bar to denote the homogeneous, unperturbed quantity. Note that from Eq. (2) we have $\zeta = \delta N$ on the decay surface, and we can interpret ζ as the perturbed expansion, or "δN". Assuming all the curvaton decay products are relativistic ($P = \rho/3$), we have that ζ is conserved after the curvaton decay. The local curvaton and radiation densities on this decay surface may be inhomogeneous. Indeed we have from Eq. (2) $\zeta_r = \zeta + \frac{1}{4}\ln(\rho_r/\bar{\rho}_r)$ and $\zeta_\sigma = \zeta + \frac{1}{3}\ln(\rho_\sigma/\bar{\rho}_\sigma)$ or. equivalently, $\rho_r = \bar{\rho}_r e^{4(\zeta_r-\zeta)}$ and $\rho_\sigma = \bar{\rho}_\sigma e^{3(\zeta_\sigma-\zeta)}$. Requiring that the total density is uniform on the decay surface, Eq. (4), then gives the simple relation $(1-\Omega_{\sigma,\rm dec})e^{4(\zeta_r-\zeta)} + \Omega_{\sigma,\rm dec}e^{3(\zeta_\sigma-\zeta)} = 1$, where $\Omega_{\sigma,\rm dec} = \bar{\rho}_\sigma/(\bar{\rho}_r+\bar{\rho}_\sigma)|_{\rm dec}$ is the dimensionless density parameter for the curvaton at the decay time. This equation can be rewritten in the form

$$e^{3\zeta_\sigma} = \tfrac{3+r}{4r}e^{3\zeta} + \tfrac{3r-3}{4r}e^{-\zeta}\,, \tag{5}$$

where $r = \frac{3\Omega_{\sigma,\rm dec}}{4-\Omega_{\sigma,\rm dec}}$. Recalling Eq. (3) the LHS of Eq. (5) is $\rho_\sigma(t_{\rm in},\vec{x})/\bar{\rho}_\sigma(t_{\rm in}) = g^2[\sigma_*(\vec{x})]/g^2[\bar{\sigma}_*]$.

As Eq. (5) is a fourth degree equation for e^ζ, the primordial curvature perturbation ζ as a function of Gaussian σ_* can be solved *exactly*. Remarkably, Eq. (5) was derived using fully non-linear definitions. Hence we have found an exact fully non-linear solution for ζ (as opposite to second order calculations in the literature). Expanding this solution in $\delta\sigma_*$ up to second order we then find $f_{\rm NL}$, up to third order the so called $\tau_{\rm NL}$, etc. Since the exact solution is quite long, it turns out to be easier to directly expand RHS of Eq. (5) up to any wanted order, and then equate it to the LHS, i.e., to $g^2[\sigma_*(\vec{x})]/g^2[\bar{\sigma}_*]$ order by order.

Up to second order the solution is $\zeta_1 = r\zeta_{\sigma 1} = r\frac{2}{3}\frac{g'}{g}\delta\sigma_*$ and $\zeta_2 = \left[\frac{3}{2r}\left(1+gg''/g'^2\right) - 2 - r\right]\zeta_1^2$. These give the non-linearity parameter (1) in the sudden-decay approximation [6,7]

$$f_{\rm NL} = \tfrac{5}{4r}\left(1+\tfrac{gg''}{g'^2}\right) - \tfrac{5}{3} - \tfrac{5r}{6}\,. \tag{6}$$

3 Non-instantaneous decay

After the curvaton has decayed the universe is dominated by "radiation", with equation of state $P = \rho/3$, and hence the curvature perturbation is non-linearly conserved on large scales. Although the sudden decay approximation gives a good intuitive derivation of both the linear curvature perturbation and the non-linearity parameter arising from second-order effects, it is only approximate since it assumes the curvaton is not interacting with the radiation, and hence ζ_σ remains constant on large scales, right up until curvaton decays. In practice the curvaton energy density is continually decaying once the curvaton begins oscillating until finally (when $\Gamma > H$) its density becomes negligible, and during this process ζ_σ does evolve, until it reaches equilibrium with $\zeta = \zeta_\sigma$ [13]. Another problem with results derived from the sudden-decay approximation is that the final amplitude of the primordial curvature perturbation, and its non-linearity, are given in terms of the density of the curvaton at the decay time which is not simply related to the initial curvaton density, especially as the decay time itself is somewhat ambiguous.

In the non-instantaneous case we can still define the first order transfer efficiency "r" of the initial curvaton perturbation to the output radiation perturbation, but now it must be calculated numerically from the definition $r = \zeta_{1r,\rm out}/\zeta_{1\sigma,\rm in}$. It turns out to be a function solely of the parameter [13] $p_{\rm in} \equiv [\Omega_\sigma(\frac{H}{\Gamma_\sigma})^{1/2}]_{\rm in} = \frac{\sigma_{\rm in}^2}{3M_{\rm Pl}^2}(\frac{m}{\Gamma_\sigma})^{1/2}$, where $M_{\rm Pl}^2 \equiv 1/(8\pi G)$.

We start the numerical integration of the background Friedmann eqn together with radiation and curvaton continuity eqns (with $\pm\Gamma_\sigma\rho_\sigma$ as a source term) from uniform-density surface at $t_{\rm in}$ and end it when curvaton has completely decayed at some suitable uniform-density hypersurface $H(t_{\rm end},\vec{x}) = H_{\rm end}$. Then the fully non-linear primordial curvature perturbation will be $\zeta = \zeta_{r,\rm out} = \delta N(t_{\rm end},\vec{x})$. Repeating the calculation with hundreds of different initial values $\sigma_{\rm in}$ we

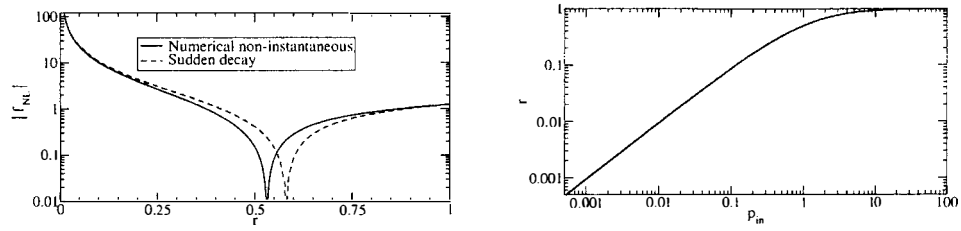

Figure 1: (a) The non-linearity factor $f_{\rm NL}$ as a function of curvature perturbation transfer efficiency $r = \zeta_{r,\rm out}/\zeta_{\sigma,\rm in}$. The analytical approximative, i.e., sudden decay result (*red dashed line*) crosses zero at $r = 0.58$ and is negative for $r > 0.58$. The exact numerical result (*black solid line*) crosses zero at $r = 0.53$. (b) r vs $p_{\rm in}$.

find a function $N(\sigma_{\rm in})$. From this we then calculate the first and second order quantities by employing $\delta N = N'\delta\sigma_* + \frac{1}{2}N''(\delta\sigma_*)^2 + \ldots \equiv \zeta_1 + \frac{1}{2}\zeta_2 + \ldots$, and finally [7] $f_{\rm NL} = \frac{5}{6}N''/(N')^2$. From Fig. 1a we see that if $f_{\rm NL} > 60$ ($r < 0.02$) or $f_{\rm NL} < -1.16$ ($r > 0.95$), the sudden decay result differs from the non-instantaneous decay result less than 1%.[b] In the both cases as $r \to 1$, we have $f_{\rm NL} \to -\frac{5}{4}$. As $r \to 0$, the sudden decay result is $f_{\rm NL} \to \frac{5}{4}\frac{1}{r}(1 + gg''/g'^2) - 1.67$, whereas the non-instantaneous decay gives $f_{\rm NL} \to \frac{5}{4}\frac{1}{r}(1 + gg''/g'^2) - 2.27$. We can write the full result in a form $f_{\rm NL} = \frac{5}{4}\frac{1}{r}(1 + gg''/g'^2) + \frac{5}{4}h(r)/r^2$, where the function $h(r)$ is defined by $r' = [2r + h(r)]g'/g$, and determined numerically in the non-instantaneous case. For the sudden decay we have from (6) $h(r) = -\frac{4}{3}r^2 - \frac{2}{3}r^3$.

Finally, we consider the possibility of a large small-scale variance $\Delta^2 \equiv \langle(\frac{\delta\sigma_{\rm in}}{\dot\sigma_{\rm in}})^2\rangle$. Let us name the observable CMB scales as infrared (IR) and smaller scales as ultraviolet (UV) so that $\lambda_{IR} \gg \lambda_{UV} \gg H_{\rm in}^{-1}$. As the observations require $\langle\zeta_1^2\rangle_{IR} \lesssim 10^{-9}$, they set constraint for $\frac{4}{9}r^2\Delta^2_{IR}$. However, observations do not directly constrain Δ^2_{UV}. Allowing large Δ^2_{UV} we find $f_{\rm NL} = \frac{5}{4}(1+\Delta^2_{UV})\frac{1}{r}(1+gg''/g'^2)+\frac{5}{4}h(r)/r^2$, where $h(r)$ remains same as without large variance. Thus, large homogeneous small-scale variance modifies the first term of $f_{\rm NL}$ only. Recalling that $r \leq 1$, and $-54 < f_{\rm NL} < 114$ (from WMAP3[1]), we find an upper bound $1+\Delta^2_{UV} < \frac{4}{5}\times 114 = 91$.

References

1. D. N. Spergel *et al.*, arXiv:astro-ph/0603449.
2. D. H. Lyth and D. Wands, Phys. Lett. B **524**, 5 (2002).
3. N. Bartolo and A. R. Liddle, Phys. Rev. D **65**, 121301 (2002).
4. K. Enqvist, H. Kurki-Suonio and J. Valiviita, Phys. Rev. D **62**, 103003 (2000).
5. K. Enqvist, H. Kurki-Suonio and J. Valiviita, Phys. Rev. D **65**, 043002 (2002).
6. N. Bartolo, S. Matarrese and A. Riotto, Phys. Rev. Lett. **93**, 231301 (2004).
7. D. H. Lyth and Y. Rodriguez, Phys. Rev. Lett. **95**, 121302 (2005).
8. M. Sasaki, J. Valiviita and D. Wands, in preparation.
9. F. Ferrer, S. Rasanen and J. Valiviita, JCAP **0410**, 010 (2004).
10. H. Kurki-Suonio, V. Muhonen and J. Valiviita, Phys. Rev. D **71**, 063005 (2005).
11. D. H. Lyth, K. A. Malik and M. Sasaki, JCAP **0505**, 004 (2005).
12. K. Enqvist and S. Nurmi, JCAP **0510**, 013 (2005).
13. S. Gupta, K. A. Malik and D. Wands, Phys. Rev. D **69**, 063513 (2004).
14. K. A. Malik and D. H. Lyth, arXiv:astro-ph/0604387.

[b] After this talk the non-instantaneous decay calculation was done in [14] employing *second order perturbation equations* instead of δN formalism which we use. The results agree after taking into account that the authors of [14] compare $f_{\rm NL}$s resulting from the fixed $p_{\rm in}$ while we prefer to compare $f_{\rm NL}$ when the sudden decay and non-instantaneous decay produce same r, or, in other words, *the same observable first order curvature perturbation*. To achieve this, we need to start from different $p_{\rm in}$ for sudden decay than for non-instantaneous decay. The non-trivial mapping between $p_{\rm in}$ and r is demonstrated in Fig. 1b for the non-instantaneous decay.

Long distance modifications of gravity in four dimensions.

I. NAVARRO* and K. VAN ACOLEYEN†
*DAMTP, University of Cambridge, CB3 0WA Cambridge, UK
† IPPP, University of Durham, DH1 3LR Durham, UK

We discuss some general characteristics of modifications of the 4D Einstein-Hilbert action that become important for low space-time curvatures. In particular we focus on the chameleon-like behaviour of the massive gravitational degrees of freedom. Generically there is at least an extra scalar that is light on cosmic scales, but for certain models it becomes heavy close to any mass source.

1 The models

In this talk we will look at some aspects of modifications of the four dimensional Einstein-Hilbert action that are of the following general form:

$$S = \int d^4x\sqrt{-g}\frac{1}{16\pi G_N}\left[R + F(R,P,Q)\right] , \tag{1}$$

with $P \equiv R_{\mu\nu}R^{\mu\nu}$ and $Q \equiv R_{\mu\nu\lambda\rho}R^{\mu\nu\lambda\rho}$. We want to modify gravity at long distances or low curvatures, so we introduce some *crossover scale* μ where the modification kicks in, such that we have conventional general relativity (GR) for large curvatures and something different for low curvatures:

$$R \gg F(R,P,Q) \text{ for } R^2,P,Q \gg \mu^4 \quad \text{and} \quad R \ll F(R,P,Q) \text{ for } R^2,P,Q \ll \mu^4 . \tag{2}$$

Models of this kind have been proposed as a way to generate late time acceleration without a cosmological constant[1]. For this to work the crossover scale has to be of the order of today's Hubble constant: $\mu \sim H_0$. In the Friedmann equation obtained for these theories, the modification then only becomes important at the present stage of the expansion of the Universe. Obviously the detailed predictions will depend on the specific model at hand. So far the only model that has been put to test is the $n = 1$ case of:

$$F(R,P,Q) = -\frac{\mu^{2+4n}}{(aR^2 + bP + cQ)^n} , \tag{3}$$

and it was found that it can fit the SN data[2] for a certain range of parameters a, b, c (but see[3] for stability constraints).

2 The excitations

To understand the physics of the models (1) a good starting point is to examine their excitations. In the case of GR, the two only degrees of freedom are contained in the massless spin 2 graviton.

For a massless spin 2 particle the weak field limit is unique and this mediates the gravitational force in a very specific way. For the models (1), one will have six more degrees of freedom in addition to the massless spin 2 graviton[4]. On vacuum, one of them is a massive scalar and the other five are contained in a massive spin 2 ghost, whose negative kinetic energy would arguably lead to the decay of a homogeneous background into a complete inhomogeneous state full of negative and positive energy excitations. To check the validity of these type of models one could try to calculate the decay time of the vacuum and check if the result is compatible with observations, but it is probably safer not to have ghosts at all.

Fortunately one can show that the massive spin 2 ghost disappears altogether for modifications of the form $F(R, Q-4P)$ [5,6] , and we will assume this form from now on. The modification is then characterized by one extra scalar degree of freedom in addition to the massless spin 2 graviton of GR. Remember that by the conditions (2) we can neglect the corrections due to the modification for large curvatures. This will translate itself to a large mass of the extra scalar on backgrounds that have a large curvature. Indeed, since the interaction range of an excitation is typically of the order of the inverse mass (we use units such that $c = \hbar = 1$), the scalar will effectively decouple on those backgrounds. For the models (3) for instance, the running of the mass m_s with the background curvature $\mathcal{R}$ is given by an expression like [5]:

$$m_s^2 \sim \mathcal{R}\left(\frac{\mathcal{R}}{\mu^2}\right)^{2n+1} , \tag{4}$$

where $\mathcal{R}$ stands for a certain combination of components of the background Riemann tensor. Also the effective Newton's constant, describing the coupling of the gravitational excitations to matter, will run with the background curvature:

$$G_N^{eff} \sim \frac{G_N}{1+(\frac{\mu^2}{\mathcal{R}})^{2n+1}} , \tag{5}$$

and again we see that we recover GR for large curvatures ($G_N^{eff} \to G_N$).

This background dependence of the mass of the scalar and of the effective Newton's constant is a manifestation of the violation of the strong equivalence principle for this type of theories: the properties of the local gravitational excitations depend intrinsically on the background, in that sense they behave like a gravitational chameleon[7]. In general, one can have a complete breakdown of the local Lorentz symmetry for the short distance excitations. To assess the stability of a certain background under short distance fluctuations, one will have to look at the propagation of the degrees of freedom *on that background.* On general FRW backgrounds for instance, the propagation of the spin 2 graviton can be sub- or superluminal and its kinetic energy can be positive or negative[3].

3 The Schwarzschild solution

Gravity, like electromagnetism, has infinite range. This means that GR influences a huge variety of phenomena on a vast range of distance scales. So if you fiddle with it to get some interesting modification for the expansion of the Universe, you should check the effect on all the other gravitational phenomena. Now, if we think about the modification in terms of extra degrees of freedom there seems to be a problem. On one hand, if we want a modification at cosmic scales, we need the mass of these extra degrees of freedom to be at most of the order of today's Hubble constant, giving them an effectively infinite interaction range. But on the other hand we know that GR has been tested in our Solar System to very high accuracy which seems to exclude any extra light degrees of freedom. The way out of this problem is to have some mechanism that can decouple the extra degrees of freedom in the Solar System. As explained in the previous

section, for the type of models (1) the mass of the extra scalar grows for large curvatures which suggests that such a mechanism could take place. It is instructive to see how this happens and what the modification will be for a spherically symmetric solution corresponding to a central mass source M on a cosmological background, which we will take to be de Sitter for simplicity. (Notice that flat Minkowski space typically won't be solution.) From (4) we see that on the cosmic background the extra scalar is indeed very light: $m_s \sim H_0 (\sim \mu)$. And at first order in the weak field expansion the Schwarzschild solution reads[5] (for distances $r \ll H_0^{-1}$):

$$ds^2 \simeq -\left(1 - \frac{2G_N^{eff}M}{r} - \frac{2G_N^{eff}M}{3r}\right)dt^2 + \left(1 + \frac{2G_N^{eff}M}{r} - \frac{2G_N^{eff}M}{3r}\right)dr^2 + r^2 d\Omega_2^2 , \quad (6)$$

where we have written separately the contributions from the spin 2 graviton and the scalar. If this was the solution in the Solar system, the theory would be clearly ruled out. Indeed, the contribution from the scalar in (6) would make it impossible to fit both the orbits of the planets and the observed light bending with the same value for Newton's constant. However, the weak field expansion breaks down at a huge distance $r_V = (G_N M/H_0^3)^{1/4}$. For the Sun this distance is of the order of 10 kpc[a]. For shorter distances, inside the Solar system for instance, one can not trust the perturbative solution (6) anymore. This is in stark contrast with GR, where the weak field expansion can be trusted throughout the whole Solar System.

In fact we could have guessed the perturbative expansion to break down when approaching the mass source, simply because we know that we should recover something very close to the GR solution for short distances. This happens because the curvature of the GR Schwarzschild solution ($Q = 48(G_N M)^2/r^6$) blows up close to the mass source, thereby killing the modification[b]. We can then estimate the distance r_c where the modification becomes important by looking at the extra scalar. This scalar will produce an order one modification for distances r, *smaller* than its inverse mass. But we know that the mass depends on the background curvature (Eq. 4). For the GR Schwarzschild solution this gives a mass that runs with the distance as:

$$m_s(r) \sim \mu \left(\frac{G_N M}{\mu^2 r^3}\right)^{n+1} . \quad (7)$$

So we can expect the scalar to really modify things, only for distances for which:

$$r < \frac{1}{m_s(r)} \quad \Rightarrow \quad r > r_c \equiv \left(\frac{(G_N M)^{n+1}}{\mu^{2n+1}}\right)^{\frac{1}{3n+2}} . \quad (8)$$

For the Sun, r_c is at least of the order of 10 pc (for $n \geq 1$), so the background dependence of the scalar mass indeed provides a mechanism that decouples the scalar in the Solar System. We recover therefore GR, up to small corrections. We have calculated these corrections in an expansion on the GR solution[8]. They are typically smaller for larger values of n in (3) and their effects are too small for detection.

So the situation for a static mass source on a cosmic background can be summarized as follows. At ultra large distances we get the perturbative solution (6) corresponding to an extra massless scalar with, in addition, a rescaled Newton's constant G_N^{eff}. For distances smaller than r_V this perturbative picture breaks down and we enter a non-perturbative regime. So far we can not say that much about this regime, since the expansions that we have used break down. But then, at distances smaller than $r_c (< r_V)$, the scalar decouples and we can expand on GR, finding a solution that is very close to the GR one and where the corrections can be quantified.

[a] A more realistic set up for the Sun would be to treat it as a probe on the background of the Milky Way, one then finds $r_V \sim$10 pc.

[b] We are assuming a modification that contains the Kretschmann scalar Q. This observation does not apply to $F(R)$ modifications.

Let us now put the centre of a galaxy as the mass source. One could impose as a condition in these theories that they produce no modification in the dynamics of the galaxy. This will be the case for large values of n in (3), that give $r_c \sim 1$Mpc. A more ambitious alternative is to look for models that give a modification that could simulate the effects of dark matter at the galactic level. First of all, one can take a model for which $G_N^{eff} > G_N$. Measuring rotation curves at ultra large distances, one would then infer the mass of the galaxy to be larger than what it actually is. In that sense the non-perturbative region indeed seems to have the characteristics of a dark matter halo. However, from the success of MOND[9], we know that the distance (r_c) where the would-be dark matter halo begins should correspond to a universal acceleration $a_0 \sim H_0$. This is precisely the case for logarithmic actions[10]. But due to lack of space we will have to refer to the proceedings of another talk[11], given by one of us at a different session of this year's Rencontres de Moriond, for a report on the interesting phenomenology of this class of models.

4 Conclusions

Models of the type (1) clearly have potential as a possible alternative for ΛCDM. Obviously, for them to become a real contender there are still a lot of questions that need to be answered. What is for instance the effect of the chameleon-like behaviour of the gravitational excitations on the CMB? Another concern, derived from the non-perturbative behaviour of these models, is that it is not yet clear how to estimate the effects of quantum corrections for this type of actions. This would be necessary, for instance, to have an idea of the amount of fine tuning required in these effective actions. Still, we believe that it is worthwhile to explore the bottom-up approach of building a generally covariant classical action to model long distance modifications of gravity; the advantage being that one can make clear contact with experiment at many levels.

Acknowledgments

We would like to thank the organizers of the Rencontres de Moriond for inviting us to give a talk. K.V.A. is supported by a postdoctoral grant of the Fund for Scientific Research Flanders (Belgium). He would also like to thank the participants of the cosmology session for stimulating discussions and interactions of a more practical nature after an unpleasant encounter with one of the slopes.

References

1. S. Capozziello, S. Carloni and A. Troisi, arXiv:astro-ph/0303041; S. M. Carroll, V. Duvvuri, M. Trodden and M. S. Turner, Phys. Rev. D **70** (2004) 043528 [arXiv:astro-ph/0306438]; S. M. Carroll, A. De Felice, V. Duvvuri, D. A. Easson, M. Trodden and M. S. Turner, Phys. Rev. D **71** (2005) 063513 [arXiv:astro-ph/0410031].
2. O. Mena, J. Santiago and J. Weller, arXiv:astro-ph/0510453.
3. A. De Felice, M. Hindmarsh and M. Trodden, arXiv:astro-ph/0604154.
4. A. Hindawi, B. A. Ovrut and D. Waldram, Phys. Rev. D **53** (1996) 5597.
5. I. Navarro and K. Van Acoleyen, arXiv:gr-qc/0511045.
6. D. Comelli, Phys. Rev. D **72** (2005) 064018 [arXiv:gr-qc/0505088].
7. J. Khoury and A. Weltman, Phys. Rev. Lett. **93** (2004) 171104 [arXiv:astro-ph/0309300].
8. I. Navarro and K. Van Acoleyen, Phys. Lett. B **622** (2005) 1 [arXiv:gr-qc/0506096].
9. R. H. Sanders and S. S. McGaugh, Ann. Rev. Astron. Astrophys. **40** (2002) 263.
10. I. Navarro and K. Van Acoleyen, arXiv:gr-qc/0512109.
11. I. Navarro and K. Van Acoleyen, arXiv:astro-ph/0605322.

Inflation with large gravitational waves.

A. Vikman
ASC, Physics Department LMU, Theresienstr. 37, Munich, Germany

It is well known that in manifestly Lorentz invariant theories with nontrivial kinetic terms, perturbations around some classical backgrounds can travel faster than light. These exotic "supersonic" models may have interesting consequences for cosmology and astrophysics. In particular, one can show [1] that in such theories the contribution of the gravitational waves to the CMB fluctuations can be significantly larger than that in standard inflationary models. This increase of the tensor-to-scalar perturbation ratio leads to a larger B-component of the CMB polarization, thus making the prospects for future detection much more promising. Interestingly, the spectral index of scalar perturbations and mass of the scalar field considered in the model are practically indistinguishable from the standard case. Whereas the energy scale of inflation and hence the reheating temperature can be much higher compared to a simple chaotic inflation.

1 Introduction

One of the main consequences of inflation is the generation of primordial cosmological perturbations [2] and the production of long wavelength gravitational waves (tensor perturbations) [3]. The predicted slightly red-tilted spectrum of the scalar perturbations is at present in excellent agreement with the measurements of the CMB fluctuations [4]. The observation of primordial gravitational waves together with the detection of a small deviation of the spectrum from flat would give us further strong confirmation of inflationary paradigm. The detection of primordial gravitational waves is not easy, but they can be seen indirectly in the B-mode of the CMB polarization (see, for example, [5]). In standard slow-roll inflationary scenarios [6] the amplitude of the tensor perturbations can, in principle, be large enough to be observed. However, it is only on the border of detectability in future experiments.

There are a lot of inflationary scenarios where the tensor component produced during inflation is much less then that in the chaotic inflation. In particular, in models such as new inflation [7] and hybrid inflation [8], tensor perturbations are typically small [5]. Moreover, in the curvaton scenario [9] and k-inflation [10], they can be suppressed completely.

A natural question is whether the gravitational waves can be significantly enhanced compared to standard scanarious. Recently it was argued that the contribution of tensor perturbations to the CMB anisotropy can be much greater than expected [11,12]. However, it was found in [13] that in the models considered in [11,12] one cannot avoid the production of too large scalar perturbations and therefore they are in contradiction with observations.

In the paper [1] we introduced a class of inflationary models where the B-mode of polarization can exceed that predicted by simple chaotic inflation. These models resemble both k-inflation [10] and chaotic inflation [6]. Inflation occurs due to the potential term in the Lagrangian, and the kinetic term has a nontrivial structure responsible for the large sound speed of perturbations. In this talk I will review the model from [1].

2 Basic equations and main idea

The generic action describing a scalar field interacting with the gravitational field is

$$S = S_g + S_\varphi = \int d^4x\sqrt{-g}\left[-\frac{R}{16\pi} + p(\phi, X)\right], \tag{1}$$

where R is the Ricci scalar and $p(\phi, X)$ is a function of the scalar field ϕ and its first derivatives $X = \frac{1}{2}\nabla_\mu\phi\nabla^\mu\phi$. We use Planck units, where $G = \hbar = c = 1$. In the case of the usual scalar field the X–dependence of p is trivial, namely, $p = X - V(\phi)$, while k-inflation and k-essence [10,14,5] are based on the non-trivial dependence of p on X. For $X > 0$, variation of the action (1) with respect to the metric gives the energy momentum tensor for the scalar field in the form of an "hydrodynamical fluid":

$$T^\mu_{\ \nu} = (\varepsilon + p)u^\mu u_\nu - p\delta^\mu_\nu. \tag{2}$$

Here the Lagrangian $p(\phi, X)$ plays the role of pressure, the "four-velocity" is $u_\mu = \nabla_\mu\phi/\sqrt{2X}$. and the energy density is given by $\varepsilon = 2Xp_{,X} - p$ where $p_{,X} = \partial p/\partial X$. Let us consider a spatially flat Friedmann universe with small perturbations:

$$ds^2 = (1 + 2\Phi)\,dt^2 - a^2(t)\,[(1 - 2\Phi)\,\delta_{ik} + h_{ik}]\,dx^i dx^k, \tag{3}$$

where Φ is the gravitational potential characterizing scalar metric perturbations and h_{ik} is a traceless, transverse perturbations describing the gravitational waves. The minimal set of equations for the evolution of the scale factor $a(t)$ and the scalar field $\phi(t)$ is given by

$$H^2 \equiv \left(\frac{\dot{a}}{a}\right)^2 = \frac{8\pi}{3}\varepsilon \quad \text{and} \quad \ddot{\phi} + 3c_S^2 H\dot{\phi} + \frac{\varepsilon_{,\phi}}{\varepsilon_{,X}} = 0, \tag{4}$$

where the dot denotes the derivative with respect to time t and the "speed of sound" is

$$c_S^2 \equiv \frac{p_{,X}}{\varepsilon_{,X}} = \left[1 + 2X\frac{p_{;XX}}{p_{,X}}\right]^{-1}. \tag{5}$$

One can show that c_S is in fact the speed of propagation of the cosmological perturbations [15,5]. The stability condition with respect to the high frequency cosmological perturbations requires $c_S^2 > 0$. For simplicity let us consider theories with Lagrangians of the form $p = K(X) - V(\phi)$. From the equations of motion (4) it is clear that, if the slow-roll conditions

$$XK_{,X} \ll V, \quad \text{and} \quad K \ll V, \qquad \left|\ddot{\phi}\right| \ll \frac{V_{,\phi}}{\varepsilon_{,X}} \tag{6}$$

are satisfied for at least 75 e-folds then we have a successful slow-roll inflation due to the potential V. In contrast to ordinary slow-roll inflation one can arrange here practically any speed of sound

c_S^2 by taking an appropriate kinetic term $K(X)$ [1]. The crucial point is that the amplitude of the final scalar perturbations (during the postinflationary, radiation-dominated epoch) and the ratio of tensor to scalar amplitudes on supercurvature scales are given by (see, [5]):

$$\delta_\Phi^2 \simeq \frac{64}{81}\left(\frac{\varepsilon}{c_S\left(1+p/\varepsilon\right)}\right)_{c_S k \simeq Ha}, \qquad \frac{\delta_h^2}{\delta_\Phi^2} \simeq 27\left(c_S\left(1+\frac{p}{\varepsilon}\right)\right)_{k\simeq Ha}. \tag{7}$$

Here it is worthwhile reminding that all physical quantities on the right hand side of Eqs. (7) have to be calculated during inflation at the moment when perturbations with wave number k cross corresponding Horizon: $c_S k \simeq Ha$ for δ_Φ and $k \simeq Ha$ for δ_h respectively. The amplitude of the scalar perturbations δ_Φ is a free parameter of the theory which is taken to fit the observations. Therefore, it follows from (7) that the tensor-to-scalar ratio can be arbitrarily enhanced in such models.

3 "Simple" model

As a concrete example let us consider a simple model with Lagrangian

$$p(\phi, X) = \alpha^2\left[\sqrt{1+\frac{2X}{\alpha^2}}-1\right]-\frac{1}{2}m^2\phi^2, \tag{8}$$

where constant α is a free parameter. For $2X \ll \alpha^2$ one recovers the Lagrangian for the usual free scalar field. The function p is a monotonically growing concave function of X, therefore the system is ghost-free. The effective speed of sound, $c_S^2 = 1 + 2X/\alpha^2$, is larger than the speed of light, approaching it as $X \to 0$. In the slow-roll regime and for p given in (8), equations (4) reduce to

$$H \simeq \sqrt{\frac{4\pi}{3}}m\phi, \qquad 3p_{,X}H\dot{\phi}+m^2\phi \simeq 0. \tag{9}$$

For $12\pi\alpha^2 > m^2$ there exists a slow-roll solution:

$$\dot{\phi} \simeq -\frac{mc_\star}{\sqrt{12\pi}}, \quad \text{where} \quad c_\star = \left(1-\frac{m^2}{12\pi\alpha^2}\right)^{-1/2}, \tag{10}$$

is the sound speed during inflation. The sound speed is constant and can be arbitrarily large, if we take $12\pi\alpha^2 \to m^2$. The pressure and energy density during the slow-roll regime are given by

$$p \simeq m^2\left(\frac{1}{12\pi}\frac{c_\star^2}{1+c_\star}-\frac{\phi^2}{2}\right), \quad \varepsilon \simeq m^2\left(\frac{1}{12\pi}\frac{c_\star}{1+c_\star}+\frac{\phi^2}{2}\right), \tag{11}$$

respectively. And for the scale factor we have

$$a(\phi) \simeq a_f \exp\left(\frac{2\pi}{c_\star}\left(\phi_f^2-\phi^2\right)\right), \tag{12}$$

where we have introduced subscript f for the quantities at the end of inflation. The inflation is over when $(\varepsilon+p)/\varepsilon \simeq c_\star/\left(6\pi\phi^2\right)$ becomes of order unity, that is, at $\phi \sim \phi_f = \sqrt{c_\star/6\pi}$. After that the field ϕ begins to oscillate and decays. Given a number of e-folds before the end of inflation N, we find that at this time $2\pi\phi^2/c_\star \simeq N$, and, hence, $(\varepsilon+p)/\varepsilon \simeq 1/3N$ does not depend on $c_\star$. Thus, for a given scale, which crosses the Hubble scale N e-folds before the end of inflation, the tensor-to-scalar ratio is $\delta_h^2/\delta_\Phi^2 \simeq 27c_\star\left(1+p/\varepsilon\right) \simeq 9c_\star/N$. It is clear that by choosing α close to the critical value $m/\sqrt{12\pi}$ we can have a very large $c_\star$ and consequently enhance this ratio almost arbitrarily. Finally one can estimate the mas which is needed in order to reproduce the observed $\delta_\Phi \sim 10^{-5}$. Combining estimations made above we obtain $m \simeq 3\sqrt{3\pi}\delta_\Phi/4N$ or for $N \sim 60$, $m \sim 3\cdot 10^{-7}$ similarly to the usual chaotic inflation. The spectral index of scalar perturbations reads [5] : $n_s - 1 \simeq -3\left(1+p/\varepsilon\right) - H^{-1}d\left(\ln\left(1+p/\varepsilon\right)\right)/dt \simeq -2/N$ this is exactly the same tilt as for the usual chaotic inflation.

4 Conclusions

We have shown above that in theories where the Lagrangian is a nontrivial, nonlinear function of the kinetic term, the scale of inflation can be pushed to a very high energies without coming into conflict with observations. As a result, the amount of produced gravitational waves can be much larger than is usually expected. If such a situation were realized in nature then the prospects for the future detection of the B-mode of CMB polarization are greatly improved. Of course, the theories where this happens are very unusual. For example, the Cauchy problem is well-posed not for all initial data [16,17]. Moreover, the horizons lose their universality [18,19]. Therefore, future observations of the CMB fluctuations are extremely important since they will not only restrict the number of possible candidates for the inflaton but also shed light on the problem of the "superluminal" propagation.

Acknowledgments

I am grateful to Viatcheslav Mukhanov and Eugeny Babichev for very useful discussions and fruitful collaboration.

References

1. V. F. Mukhanov, A. Vikman, JCAP 0602 (2006) 004, [astro-ph/0512066]
2. V.F. Mukhanov and G.V. Chibisov, JETP Lett. **33**, 532 (1981).
3. A. A. Starobinsky, JETP Lett. **30** (1979) 682
4. H. V. Peiris *et al.*, Astrophys. J. Suppl. **148**, 213 (2003); C. J. MacTavish *et al*, arXiv:astro-ph/0507503.
5. V. Mukhanov, *"Physical Foundations of Cosmology"* (2005) Cambridge Univ.Press.
6. A. D. Linde, Phys. Lett. B **129**, 177 (1983).
7. A. D. Linde, Phys. Lett. B **108**, 389 (1982); A. Albrecht and P. J. Steinhardt, Phys. Rev. Lett. **48**, 1220 (1982).
8. A. D. Linde, Phys. Rev. D **49**, 748 (1994).
9. A. D. Linde and V. Mukhanov, Phys. Rev. D **56**, 535 (1997); D. H. Lyth and D. Wands, Phys. Lett. B **524**, 5 (2002); D. H. Lyth, C. Ungarelli and D. Wands, Phys. Rev. D **67**, 023503 (2003); D. H. Lyth and D. Wands, Phys. Rev. D **68**, 103516 (2003); K. Dimopoulos, G. Lazarides, D. Lyth and R. Ruiz de Austri, Phys. Rev. D **68**, 123515 (2003); B. A. Bassett, S. Tsujikawa and D. Wands, arXiv:astro-ph/0507632; A. Linde and V. Mukhanov, arXiv:astro-ph/0511736.
10. C. Armendáriz-Picón, T. Damour, V. Mukhanov, Phys.Lett. B **458**, 209 (1999).
11. N. Bartolo, E. W. Kolb and A. Riotto, arXiv:astro-ph/0507573.
12. M. S. Sloth, hep-ph/0507315.
13. A. Linde, V. Mukhanov and M. Sasaki, arXiv:astro-ph/0509015.
14. C. Armendáriz-Picón, V. Mukhanov, P. J. Steinhardt, Phys. Rev. Lett. **85**, 4438 (2000); C. Armendáriz-Picón, V. Mukhanov, P. J. Steinhardt, Phys. Rev. D **63**, 103510 (2001).
15. J. Garriga, V.F. Mukhanov, Phys.Lett. B **458**, 219 (1999).
16. A. D. Rendall, Class. Quant. Grav. 23 (2006) 1557-1570, [gr-qc/0511158].
17. A. Adams, N. Arkani-Hamed, S. Dubovsky, A. Nicolis, R.Rattazzi, [hep-th/0602178].
18. E. Babichev, V. Mukhanov, A. Vikman, [hep-th/0604075].
19. S.L. Dubovsky, S.M. Sibiryakov, [hep-th/0603158].

Constraining Inverse Curvature Gravity with Supernovae

J. Weller[1], O. Mena[2] and J. Santiago[2]
[1] *Department of Physics and Astronomy, University College London, Gower Street, London WC1E 6BT, UK.*
[2] *Fermi National Accelerator Laboratory, Batavia, IL 60510-0500, USA.*

We show how modifications of gravity, which involve inverse curvature terms, can fit the observed magnitude - redshift relation of distant type Ia Supernovae. In order to achieve this we have to solve the modified Friedmann equations and we discuss different regimes of the solution, dependent on the free parameters, which lead to accelerated expansion.

1 Introduction

Evidence for an accelerated expansion of the Universe has been mounting in recent years [1,2,3,5,6,7,8,4]. While the precision of the data is continually improving, explanations for the cause of accelerated expansion are still in its infancy and at best ad hoc. In principle there are four possible ways to explain the observations: the strong energy condition is violated, i.e. the late Universe; is dominated by a fluid with $\rho + 3p \leq 0$, with ρ the energy density in the fluid and p its pressure; gravity is modified on large scales and this modification leads to accelerated expansion; the Universe as a whole is not homogeneous and we are happening to be in a bubble, which is expanding in an accelerated fashion; or the data might be wrong. In this talk we concentrate on the second possibility. In a similar fashion as models of Quintessence [9,10,11,12] are motivated by inflationary models, the modification of gravity we discuss here, has been first discussed by Starobinsky for early de Sitter Universes [13]. If we look at the action for gravity

$$S_{E-H} = \frac{1}{16\pi G} \int d^4x \sqrt{-g} \, (R + \mathcal{L}_m) \ ,$$

where g is the determinant of the metric, R the Ricci curvature scalar and $\mathcal{L}_m$ the matter Lagrangian. The curvature term can be generalized to $R + mR^n$. Starobinsky noticed that for $n > 0$ this can lead to de Sitter solutions in the early Universe. In order to obtain acceleration in the late Universe at large scales, where the Universe is approximately flat the only requirement is $n < 0$. This has been investigated in [14]. The surprising finding was that an additional $1/R$ term in the Einstein-Hilbert action would allow for accelerated expansion solutions in the late Universe, which are attractor solutions. In other words they do not require extremely fine tuning of the initial conditions in order to explain the observations. However, it was soon noticed that these models are in serious trouble with solar system tests [15].

2 General Inverse Curvature Models

However, the form of the gravitational action suggested by Starobinsky [13] is not completely general. In general one can try to add any quadratic combination of the curvature scalar, Ricci and Riemann tensor to the action. In order to obtain accelerated expansion the general allowed form of the action is

$$S = \frac{1}{16\pi G} \int d^4x \sqrt{-g} \left(R + \frac{\mu^{4+n}}{(aR^2 + bP + cQ)^n} + \mathcal{L}_m \right) \ , \qquad (1)$$

with $P \equiv R_{\mu\nu} R^{\mu\nu}$ the square of the Ricci tensor, $Q \equiv R_{\mu\nu\rho\sigma} R^{\mu\nu\rho\sigma}$ the square of Riemann tensor and G Newton's constant. Models with this action have an unstable de Sitter solution and later

time power law acceleration [16]. However, if one introduces explicit dependence on the Riemann tensor into the action the equations of motion become fourth order and there might be ghost-like excitation due to the presence of a massive spin-2 gravitons with negative energy eigenstates. However it was shown in [17] that in case P and Q appear in the combination $4P - Q$, which interestingly is also realized in Gauss-Bonnet gravity, the massive spin-2 excitations vanish. Furthermore it was shown that for the models, which lead to accelerated expansion today all solar system tests are passed [18]. This is due to the fact that in order to obtain accelerated expansion μ has to be chosen roughly of the order of the observed Hubble constant H_0, ie. $\mu \approx 10^{-33}$ eV. After the presentation of this talk a paper was submitted [19], which showed that besides the problem with ghost-like excitations, these models are also threatened by tachionic propagation modes. However there are parameter combination of a, b and c, where non such modes are present!

3 Solving the Modified Friedmann Equation

In order to obtain a theoretical prediction we have to solve the modified Friedman equation for the $n = 1$ model [20]. For a compact notation we define the following quantities: $\alpha \equiv \frac{12a+4b+4c}{12a+3b+2c}$, $\hat{\mu} \equiv \frac{\mu}{|12a+3b+2c|^{1/6}}$, $\sigma \equiv \text{sign}\,(12a + 3b + 2c)$. We will solve the dynamical system in the variables $u \equiv \ln(H/\hat{\mu})$, with $H = \dot{a}/a$ the Hubble parameter. As time variable we choose e-foldings $N \equiv \ln a$. We then obtain for the modified Friedman equation

$$u''\mathcal{P}_1(u') + \mathcal{P}_2(u') + 18\sigma(\mathcal{P}_3(u'))^3 e^{6u}(e^{2(\bar{u}-u)} - 1) = 0, \tag{2}$$

where a prime denotes the derivative with respect to N and we have defined the following polynomials, $\mathcal{P}_1(y) = 6\alpha^2y^2 + 24\alpha y + 32 - 8\alpha$, $\mathcal{P}_2(y) = 15\alpha^2y^4 + 2\alpha(50 - 3\alpha)y^3 + 4(40 + 11\alpha)y^2 + 24(8 - \alpha)y + 32$, $\mathcal{P}_3(y) = \alpha y^2 + 4y + 4$. The source is $\bar{u} \equiv \ln\left[\bar{\omega}_r \exp(-4N) + \bar{\omega}_m \exp(-3N)\right]/2$, where we have defined the appropriately normalized values of the energy densities *today* as $\frac{8\pi G}{3}\frac{\rho_{r,m\,0}}{\hat{\mu}^2} \equiv \bar{\omega}_{r,m}$, with $\rho^0_{\mathrm{r,m}}$ the present densities in matter and radiation and we have exploited the fact that the energy-momentum tensor is still covariantly conserved. This means that the source in Eqn. (2) corresponds to a matter component with no dark energy. In theory one would solve the Friedmann equation in (2) for arbitrary initial conditions. However since the 2nd order differential equation is stiff and possibly ill-conditioned, this seems impossible to achieve. We therefore took the following approach: We assumed that in order to obtain cosmologies, which are not ruled out by observations, the Universe has to have phases, where it is radiation and matter dominated. Starting from these initial conditions allows one to construct *stable* approximate solution, which exhibit small corrections to the scaling of H compared to a matter or radiation dominated Universe. However, at late times there are significant deviations from a matter dominated Universe. We found that our approximate solution is valid to within 0.1% for $z > 7$. We hence employ the approximate solution for large redshift and then use this solution as an initial condition for the exact numerical solution starting at $z = 7$. This is numerically feasible and stable [20]. However we also have to make sure that this method of solving the equations is valid for all possible parameter choices of $\bar{\omega}_m$, α and σ. In order to classify the different regions, we define the following special values of α: $\alpha_1 \equiv 8/9$, $\alpha_2 \equiv 4(11 - \sqrt{13})/27 \approx 1.095$ and $\alpha_3 \equiv 20(2 - \sqrt{3})/3 \approx 1.786$. For $\alpha < \alpha_1$ both signs of σ result in an acceptable (non-singular) dynamical evolution, but nevertheless in a bad fit for Supernovae data. For $\alpha_1 < \alpha < \alpha_2$ only $\sigma = -1$ leads to an acceptable expansion history, since for $\sigma = +1$ a singular point is violently approached in the past. For $\alpha_2 < \alpha$ the singular point is approached for $\sigma = -1$, hence $\sigma = +1$ is the only physically valid solution. In this latter case, when $\alpha_2 < \alpha < \alpha_3$, the system goes to a stable attractor that is decelerated, thus giving a bad fit to SNe data, for $\alpha < 32/21$ and gets accelerated for larger α. For $\alpha_3 < \alpha$ there is no longer a stable attractor and the system smoothly goes to a singularity in the future. That singularity occurs earlier as α increases so that there is

a limiting function $\alpha_4(\bar{\omega}_m)$, at which the singularity is reached today. It is important to stress that this singularity is approached in a very smooth fashion, allowing for a phenomenologically viable behaviour of the system, as opposed to the evolution when the *wrong* value of σ is chosen, where the singularity is hit almost instantaneously. Finally, for values of $\alpha > 24.9$, there are stable attractors again but these are never accelerated and the resulting fit to SNe data is not acceptable. To summarize, there are two regions that give a dynamical evolution of the system compatible with SNe data, the *low* region with $\alpha_1 < \alpha < \alpha_2$, for which $\sigma = -1$, and the *high* region where $\alpha_2 < \alpha < \alpha_4$, for which $\sigma = +1$.

4 Comparison to Supernovae Data

In order to compare to the observed magnitude-redshift relation we have to work out the luminosity distance in a flat Universe $d_L(z) = c(1+z)\int_0^z \frac{dz'}{H(z')}$. In order to fit the theory to the observed magnitude - redshift relation there is an additional ambiguity of choice of the intrinsic magnitude $\mathcal{M}$ of the Supernovae. This leads in standard gravity to the inability to obtain constraints on H_0 just from SNe. For the modified gravity model this results in the inability to constrain $\hat{\mu}$. Taking into account the results from the dynamical analysis we can hence simultaneously fit for α and $\bar{\omega}_m$ with the Supernovae data. For the analysis presented here we choose a recent compilation of Supernovae samples by [3]. In Fig. 1 we show the results

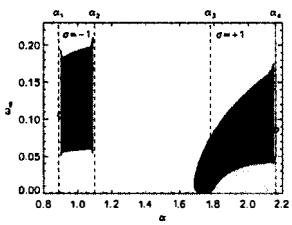

Figure 1: 1 and 2-σ joint likelihoods on $\bar{\omega}_m$ and α. In the *low* region $\sigma = -1$ whereas in the *high* region $\sigma = +1$. The shaded area on the right determines the region $\alpha > \alpha_4$ that is excluded because of a singularity being hit in the past. The diamonds denote the maximum likelihood points.

of this analysis. The best fit value in the low region is $\alpha = 0.9$ and $\bar{\omega}_m = 0.105$ and in the high region $\alpha = 2.15$ and $\bar{\omega}_m = 0.085$. In order obtain constraints on the physical matter density ω_m and $\hat{\mu}$ we have to use additional data, which measures the expansion rate today. This can be achieved either with direct measurements of the Hubble rate, like with the Hubble Key Project [21] with $H_0 = 72 \pm 8\,\mathrm{km/sec/Mpc}$ or with estimates of the age of the Universe via the age of globular clusters [22] with a mean $t_0 = 13.4\,\mathrm{Gyr}$ with t_0 larger than $11.2\,\mathrm{Gyr}$ at the 95% confidence level. In Fig. 2 we show the results for including a prior on H_0. In this case we obtain $\omega_m = 0.14 \pm 0.03$ in the low region and $\omega_m = 0.14 \pm 0.04$ in the high region. An additional constraint we applied is the measurement of the angular diameter distance to the last scattering of cosmic microwave photons. This was given by the WMAP team first year data release to be $d_A(z = 1100) = 14.0 \pm 0.3\,\mathrm{Gpc}$. Note that this number has hardly changed with the third year release of the WMAP data [6]. In oder to compare the modified gravity models with the constraints from WMAP one can calculate $d_A(z) = d_L(z)/(1+z)^2$. However, we want to caution the reader here. In order to use CMB data to constrain modified gravity models one has really to perform a full perturbation analysis for the modified models. Otherwise one can not be sure that the results presented in the dotted lines of Fig. 2 are valid. It might be that the modifications to gravity we propose here are not stable and the whole linear perturbation regime breaks down. This might be a drastic view, but all we want to emphasize is that one

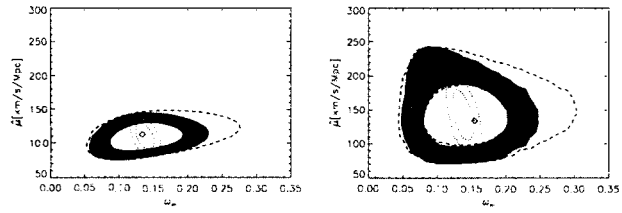

Figure 2: Joint $1-$ and $2-\sigma$ contours, in ω_m-$\hat{\mu}$. The large dashed contours are with a prior on H_0 only, filled contours with an additional prior on t_0 and the dotted innermost contours with an additional prior from the angular diameter distance to the CMB last scattering surface as measured by WMAP first year release.

can not be sure before doing such a calculation. Nevertheless the presented constraint can act as a guideline as what is to be expected from CMB constraints if "everything goes well" in a perturbation analysis.

5 Conclusion

We have presented an analysis, which shows that an inverse curvature gravity model can explain Supernovae observations of the expansion rate to a satisfactory level. While these models might have many problems regarding their consistent theoretical formulation, one should nevertheless be open minded, that not just an additional component in the Einstein equations, i.e. dark energy, can explain accelerated expansion of the Universe.

References

1. A. G. Riess *et al.*, Astron. J. **116** (1998) 1009.
2. S. Perlmutter *et al.*, Astrophys. J. **517** (1999) 565.
3. A. G. Riess *et al.*,Astrophys. J. **607** (2004) 665.
4. P. Astier *et al.*, Astron.Astrophys. 447 (2006) 31-48.
5. D. N. Spergel *et al.*, ApJS **148** (2003) 175.
6. D. N. Spergel *et al.*, astro-ph/0603449.
7. M. Tegmark *et al.*, Phys.Rev. **D69** (2004) 103501.
8. S. W. Allen *et al.*, MNRAS **353** (2004) 457; D. Rapetti *et al.*, MNRAS **360** (2005) 555.
9. Wetterich C., 1988, Nucl. Phys., **B302**, 668.
10. Peebles P., Ratra B., 1988, ApJ, **325**, L17.
11. Ferreira P., Joyce M., 1998, Phys. Rev. D, **D 58**, 023503.
12. Caldwell R., Dave R., Steinhardt P., 1998, Phys. Rev. Lett., **80**, 1582.
13. Starobinsky, A. A., Phys. Lett. B,**91**, 99 (1980).
14. S. M. Carroll, V. Duvvuri, M. Trodden and M. S. Turner, Phys. Rev. D **70** (2004) 043528.
15. T. Chiba, Phys. Lett. B **575** (2003) 1; M. E. Soussa and R. P. Woodard, Gen. Rel. Grav. **36** (2004) 855.
16. S. M. Carroll *et al.*, Phys. Rev. D **71** (2005) 063513.
17. I. Navarro, K. Van Acoleyen, JCAP **0603** (2006) 008.
18. I. Navarro, K. Van Acoleyen, Phys.Lett. **B622** (2005) 1.
19. A. De Felice, M. Hindmarsh, M. Trodden, astro-ph/0604154.
20. O. Mena, J. Santiago, J. Weller, Phys.Rev.Lett. 96 (2006) 041103.
21. W. L. Freedman *et al.*, Astrophys. J. **553** (2001) 47.
22. L. M. Krauss and B. Chaboyer, Science, 299 (2003) 65.

IV – THE FUTURE

BLIND MD-MC COMPONENT SEPARATION FOR POLARIZED OBSERVATIONS OF THE CMB WITH THE EM ALGORITHM

J. AUMONT
Laboratoire de Physique Subatomique et de Cosmologie
53, avenue des Martyrs, Grenoble, France

We present the POLEMICA [1] (Polarized Expectation-Maximization Independent Component Analysis) algorithm which is an extension to polarization of the SMICA [2] temperature component separation method. This algorithm allows us to estimate blindly in harmonic space multiple physical components from multi-detectors polarized sky maps. Assuming a linear noisy mixture of components we are able to reconstruct jointly the electromagnetic spectra of the components for each mode T, E and B, as well as the temperature and polarization spatial power spectra, TT, EE, BB, TE, TB and EB for each of the physical components and for the noise on each of the detectors. This has been tested using full sky simulations of the Planck satellite polarized channels for a 14-months nominal mission assuming a simple linear sky model including CMB, and optionally Galactic synchrotron and dust emissions.

1 Introduction

Mapping the Cosmic Microwave Background (CMB) polarization is one of the major challenges of future missions in observational cosmology. CMB polarization is linear and therefore can be described by the first three Stokes parameters I, Q and U which are generally combined to produce three fields (modes), T, E and B. The polarization of the CMB photons carries extra physical informations that are not accessible by the study of the temperature anisotropies. Therefore its measurement helps breaking down the degeneracies on cosmological parameters as encounter with temperature anisotropies measurements only. Furthermore, the study of the CMB polarization is also a fundamental tool to estimate the energy scale of inflation.

However, CMB polarization is several orders of magnitude weaker than the temperature signal and therefore, its detection needs an efficient separation between the CMB and the astrophysical foregrounds which are expected to be significantly polarized.

A direct subtraction of these foreground contributions on the CMB data will require an accurate knowledge of their spatial distributions and of their electromagnetic spectra. But these latter are not yet well characterized in polarization.

To try to overcome the above limitations, a great amount of work has been dedicated to design and implement algorithms for component separation which can discriminate between CMB and foregrounds. We present here the POLEMICA (Polarized Expectation-Maximization Independent Component Analysis) algorithm which is an extension of the Spectral Matching Independent Component Analysis (SMICA) [2] which has been developed to consider both a full blind analysis for which no prior is assumed and a semi-blind analysis incorporating previous physical knowledge on the astrophysical components. This extension allows to estimate jointly

the temperature and polarization parameters from a set of multi-frequencies I, Q and U sky maps.

2 Model of the microwave and sub-mm sky

To perform the separation between CMB and the astrophysical foregrounds, the diversity of the electromagnetic spectra and of the spatial spectra of the different components is generally used. Observations from a multi-band instrument, for the Stokes parameters I, Q and U, can be modeled as a linear combination of multiple physical components leading to what is called a Multi-Detectors Multi-Components (MD-MC) modeling.

Assuming an experiment with n_ν detector-bands at frequencies ν_i and n_c physical components in the data, working in the spherical harmonics space, we can model the observed sky for $X = \{T, E, B\}$, for each frequency band and for each $\{\ell, m\}$

$$y_{\ell m}^{\nu,X} = \sum_{c=1}^{n_c} A_c^{\nu,X} s_{\ell m}^{c,X} + n_{\ell m}^{\nu,X} \tag{1}$$

where $y_{\ell m}^{\nu,X}$ is a vector of size $(3 \cdot n_\nu \cdot n_\ell \cdot n_m)$ containing the observed data, $s_{\ell m}^{c,X}$ is a $(3 \cdot n_c \cdot n_\ell \cdot n_m)$ vector describing each component template and $n_{\ell m}^{\nu,X}$ is a vector of the same size than $y_{\ell m}^{\nu,X}$ accounting for the noise. $A_c^{\nu,X}$ is the *mixing matrix* containing the electromagnetic behaviour of each component and is of size $(3 \cdot n_\nu) \times (3 \cdot n_c)$

The aim of the component separation algorithm presented in here is to extract $A_c^{\nu,X}$, $s_{\ell m}^{c,X}$ and $n_{\ell m}^{\nu,X}$ from the $y_{\ell m}^{\nu,X}$ sky observations.

3 A MD-MC component separation method for polarization

To reduce the number of unknown parameters in the model described by equation (1), it is interesting to rewrite this equation in terms of the temperature and polarization auto and cross power spectra and to bin them over ℓ ranges.

$$R_y(b) = A R_s(b) A^T + R_n(b) \tag{2}$$

where $R_y(b)$ and $R_n(b)$ are $(n_\nu \cdot 3) \times (n_\nu \cdot 3)$ matrices and $R_s(b)$ is a $(n_c \cdot 3) \times (n_c \cdot 3)$ matrix. We assume that the physical components in the data are statistically independent and uncorrelated and that the noise is uncorrelated between channels.

To estimate the above parameters from the data we have extended to the case of polarized data the spectral matching algorithm developed in SMICA [2] for temperature only. The key issue of this method is to estimate these parameters, or some of them (for a semi-blind analysis), by finding the best match between the model density matrix, $R_y(b)$, computed for the set of estimated parameters and the data density matrix $\tilde{R}_y(b)$ obtained from the multi-channel data. The likelihood function is a reasonnable measure of this mismatch. We have extended this method to jointly deal with the temperature and polarization power spectra and also to estimate the TE, TB and EB cross power spectra [1].

The maximization of the likelihood function is achieved via the Expectation-Maximization algorithm (EM) [3]. This algorithm will process iteratively from an initial value of the parameters following a sequence of parameter updates called 'EM steps'. By construction each EM step improves the spectral fit by maximizing the likelihood. For a more detailed review of the spectral matching EM algorithm used here, see [2].

4 Simulated microwave and sub-mm sky as seen by Planck

Following the MD-MC model discussed above and given an observational setup, we construct, using the HEALPix pixelization scheme[5] and in CMB temperature units, fake I, Q and U maps of the sky at each of the instrumental frequency bands. For these maps we consider three main physical components in the sky emission: CMB, thermal dust and synchrotron. Instrumental noise is modeled as white noise.

The CMB component map is randomly generated from the polarized CMB angular power spectra for a set of given cosmological parameters. In the following we have used $H_0 = 71$ km $\cdot$ s^{-1} $\cdot$ Mpc^{-1}, $\Omega_b = 0.044$, $\Omega_m = 0.27$, $\Omega_\Lambda = 0.73$ and $\tau = 0.17$ that are the values of the cosmological concordance model according to the WMAP 1 year results[7].

For the diffuse Galactic synchrotron emission we use the template maps in temperature and in polarization provided by[4]. Here we have chosen to use a constant spectral index equal to the mean of the spectral index map, $\alpha = -2.77$, so that the simple linear model of the data holds.

In the case of the thermal dust we dispose of few observational data of the polarized diffuse emission and to date no template for this is available. Thus, we have considered a power-law model, renormalized to mimic at large angular scales the TE cross power spectrum measured by Archeops at 353 GHz[6]. I, Q and U full-sky maps are generated randomly from these power spectra. We extrapolate them to each of the frequency of interest by assuming a grey body with an emissivity of 2.

Noise maps for each channel are generated from white noise realizations normalized to the nominal level of instrumental noise for that channel.

We have performed sets of simulations of the expected Planck satellite data to intensively test the algorithm presented above. We present here results from 300 realizations considering full-sky maps at the LFI and HFI polarized channels, 30, 40 and 70 GHz for LFI and 100, 143, 217 and 353 GHz for HFI for a nominal 14-month survey. We have simulated maps at $n_{\rm side} = 512$ which permits the reconstruction of the angular power spectra up to $\ell \simeq 1500$. The reconstructed spectra will be averaged over bins of size 20 in ℓ.

5 Results

We have applied the PolEMICA component separation algorithm to the simulations presented above. From them, we have computed the data density matrix R_y and applied the algorithm. We simultaneously estimate the R_s, R_n and A matrices, with no priors, for temperature and polarization. To ensure the reliability of the results we have performed 10000 EM iterations and checked, for each simulation, the convergence of the EM algorithm.

We present in figure 1 the reconstructed CMB power spectra. We can see that for the TT, TE, TB and EB spectra, we are able to reconstruct the C_ℓ over the full range of ℓ values that are accessible at this pixelization resolution ($\ell_{\rm max} \sim 1500$). The EE spectrum is recovered accurately up to $\ell \simeq 1200$. For smaller angular scales, a bias appears. This bias is a pixelization problem that would occur at a larger ℓ if the resolution was higher. The BB spectrum is reconstructed up to $\ell \simeq 70$. For larger ℓ, the reconstructed spectrum is residual noise arising from the fact that the convergence of the EM algorithm is slow and therefore we have not properly converged. This bias appears in our separation when the signal over noise ratio is below 10^{-2} and does not affect the reconstruction of the other parameters. Even if we were able to avoid this effect, the recovered BB spectrum would be compatible with zero for $\ell > 70$ thanks to the size of the error bars.

The power spectra from our input synchrotron and dust emissions are recovered with efficiency up to $\ell \simeq 1500$ for TT, EE, BB, TE, TB and EB [1]. Power spectra of the noise in

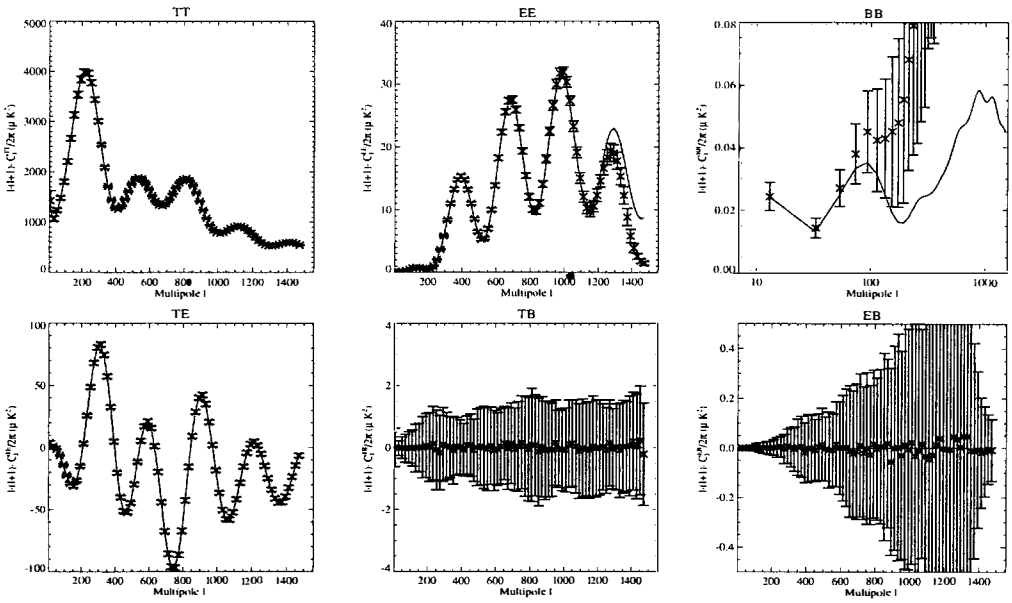

Figure 1: Reconstruction of the CMB power spectra for C_ℓ^{TT}, C_ℓ^{EE}, C_ℓ^{BB}, C_ℓ^{TE}, C_ℓ^{TB} and C_ℓ^{EB} at 100 GHz in μK^2_{CMB} performed on Planck full sky maps simulations. Crosses represent the reconstructed spectra, solid lines the input model. Error bars are the dispersion over $\sim$ 300 simulations.

temperature and in polarization are also fully reconstructed [1].

The mixing matrix A elements corresponding to CMB and dust emission are recovered efficiently, for temperature and polarization. For the synchrotron emission, mixing matrix elements corresponding to polarization are well recovered and those corresponding to temperature are biased at intermediate frequency values [1]. This bias is due tu a slight mixing up between synchrotron and CMB in temperature. It does not happen in polarization where the synchrotron dominates the CMB. This bias can be avoided by the adjunction of priors in the separation, like for example assuming an equal electromagnetic spectrum in temperature and polarization for each component [1]

To evaluate the impact of foregrounds in the determination of the CMB temperature and polarization power spectra we have compared the results of the presented analysis to those on simulations that contain only CMB and noise. In the presence of foregrounds, the error bars on the reconstruction of the CMB power spectra are increased by at least a factor of two both in temperature and in polarization [1]. Therefore, although the foreground contribution in the data can be removed, it significantly reduces the precision to which the CMB polarization signal can be extracted from the data.

1. Aumont J. & Macías-Pérez J.-F., 2006, submitted to MNRAS, astro-ph/0603044
2. Delabrouille J., Cardoso J.-F. & Patanchon G., 2003, MNRAS, 346, 1089
3. Dempster A., Laird N. & Rubin D, 1977, J. of the Roy. Stat. Soc. B, 39, 1
4. Giardino G., Banday A. J., Górski K. M., Bennet K., Jonas J. L. & Tauber J., 2002, A&A, 387, 82
5. Górski K. M., Hivon E. & Wandelt B. D., 1999, astro-ph/9812350
6. Ponthieu N. et al., 2005, A&A, 444, 327
7. Spergel D. N. et al., 2003, ApJS, 148, 175

SZ Surveys are Coming: What should we do?

J.G. Bartlett
APC, 11 pl. Marcelin Berthelot, 75231 Paris Cedex 05, FRANCE (UMR 7164 - CNRS, Université Paris 7, CEA, Observatoire de Paris)

Galaxy clusters furnish extremely rich information on the contents and structure of our universe. The potential of galaxy cluster studies to constrain dark energy, for example, motivates a number of ambitious cluster surveys. Among these, surveys based on the Sunyaev-Zel'dovich (SZ) effect are particularly powerful for their ability to cleanly select clusters out to redshifts $z > 1$. Now poised to begin surveying substantial areas of sky, dedicated interferometers, bolometer cameras and the Planck satellite will soon produce large cluster catalogs that will provide a precise measure of the cosmic expansion rate over a range of redshifts and precipitate a new understanding of structure and galaxy formation. I review the science potential of these surveys and examine some issues of SZ cluster catalog construction.

1 Introduction

Detailed observations of the cosmic microwave background anisotropies [1], distant SNIa [2] and of the galaxy distribution [3] have driven the tremendous advance in recent years leading to the development of a standard cosmological model. Ongoing research aims to test the model's coherence and to answer outstanding fundamental questions: What is the nature of dark matter and of the mysterious dark energy accelerating the present expansion of the universe? What is the physics of the early universe, in particular of the inflation epoch? How can we use detailed cosmological observations to probe fundamental physics, such as the neutrino sector? And how do galaxies form and evolve in the cosmic web of large-scale structure. These exciting questions inspire large observational programs centered on the CMB, SNIa searches and wide-field multiband surveys.

Galaxy clusters offer a unique avenue of attack on several of these key questions:

1. Their abundance and evolution with redshift are highly sensitive to the statistics and growth rate of the density perturbations, which in turn depends on the cosmological parameters;

2. They are ideal tracers of the largest scale structures. With a mean separation of ~ 50 Mpc, they efficiently sample structures of wavelength ~ 100 Mpc and larger, such as the baryon acoustic peaks in the matter power spectrum (see Figure 1) [4];

3. They provide a well-defined, quasi-closed environment for galaxy formation studies. In the cluster environment we directly observe the stellar, diffuse gas and dark matter components of the cosmic fluid;

4. Combined X-ray and millimeter cluster observations (the Sunyaev-Zel'dovich effect; see below) permit distance measurements and hence the construction of a Hubble diagram with

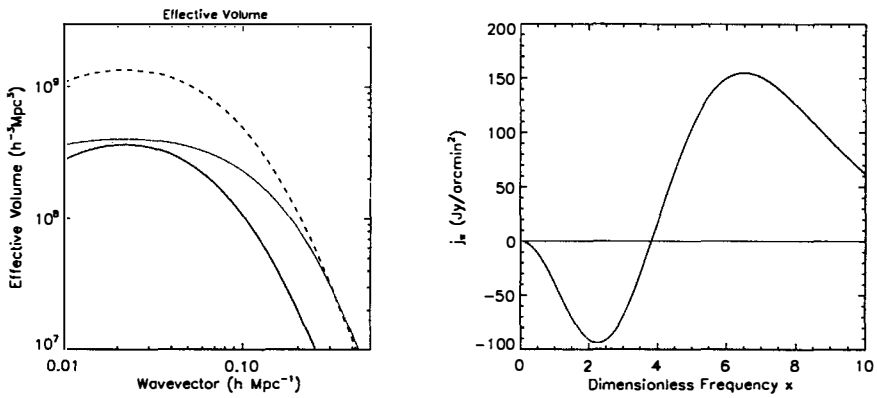

Figure 1: *Left:* The effective volume as a function of wavenumber for the SDSS LRG sample (middle, red solid curve) and for two mass-limited cluster samples, one at $M > 10^{14} M_\odot$ (upper, blue dashed line) and one at $M > 2 \times 10^{14} M_\odot$ (lower, blue solid line). In all cases the survey area is $\Omega_{\rm survey} = 4000$ deg^2, corresponding to the actual survey area of the SDSS LRG sample that detected the baryon acoustic peak and to the proposed South Pole Telescope SZ survey, which targets these cluster mass limits. *Right:* The thermal SZ spectrum j_ν as a function of dimensionless frequency $x = h\nu/kT_{\rm cmb}$ ($T_{\rm cmb} = 2.725$ K). The zero crossing is at 217 GHz.

which to measure the matter density and dark energy abundance and equation–of–state (like SNIa distance measurements).

2 Cluster Surveys

Tapping the cosmological potential of galaxy clusters requires large, homogeneous cluster catalogs extending to redshifts greater than unity. The strongest constraints on dark energy, for example, will come from observed cluster evolution in the transition between matter and dark energy domination around $z = 1$ and beyond. Note that today there are only of order 10 clusters with spectroscopically confirmed redshifts $z > 1$ [5]. The need for deeper and larger catalogs motivates a number of substantial observational efforts in different wavebands.

We may search for clusters in a variety of ways:

1. As overdensities in the galaxy population. This may either be done in redshift space, or in color space using multiband imaging which can provide estimated photometric redshifts over large areas of sky;

2. By their gravitational lensing of background galaxy images. With a large imaging survey, we could search for clusters both via their lensing signal and in color space (as above);

3. By the X–ray emission from their intracluster medium (ICM), which at keV temperatures emits copiously in X-rays. Cluster surveys and observations in the X–ray band with satellites like ROSAT, Chandra and XMM have significantly advanced our understanding of clusters and their evolution, and have played an important role in establishing the standard cosmological model [6].

4. By the Sunyaev–Zel'dovich (SZ) effect, a distortion of the CMB frequency spectrum caused by a transfer of energy from the hot ICM electrons to CMB photons via Compton scattering.

Each of these techniques has its own advantages and disadvantages. To appreciate them we should situate clusters in the standard theoretical framework that describes them as single, massive dark matter halos containing hot gas and galaxies with their subhalos. Dominated by dark matter and its gravitational evolution, clusters are fundamentally described by their halo mass and redshift. When building a cluster catalog, therefore, one should quantify its properties in terms of these basic parameters in order for proper comparison to theory. Specifically, we must accurately calculate the survey selection function and determine the observable–mass relation. Doing the latter is often referred to as calibrating the observable–mass relation, or for short, survey calibration.

Large area redshift surveys are prohibitively expensive. Less expensive, imaging surveys rely on a consistent relation between the parent cluster halo and its member galaxy population; in particular, the relation between cluster mass and redshift, and galaxy colors and luminosity. Therein lies a potentially large uncertainty due to our limited understanding of galaxy formation and evolution (which these cluster surveys are designed to help us improve!).

Lensing–based cluster surveys are appealing because they select clusters on their projected mass density. They will, however, suffer from the projection of mass along the line–of–sight, and their detection efficiency depends on the redshift distribution of the lensed galaxies. The latter is relatively easily controlled with photometric redshift information, while the impact of projection effects on survey selection functions and mass recovery requires further study[7].

The properties of the hot ICM are closely linked to those of the cluster gravitational potential, implying that X–ray surveys select clusters based on their dark matter halos, similarly to lensing surveys. In addition, X–ray surveys do not suffer from projection effects, because cluster X–ray emission varies as the square of the gas density. For this same reason, however, the cluster X–ray emission is dominated by the core regions and hence physics that is difficult to model. Furthermore, X–ray surveys require large, expensive satellite missions. Not designed as survey instruments, Chandra and XMM–Newton will provide only relatively limited area surveys[8].

Our focus here is on the fourth method based on the SZ effect, which possesses a number of advantageous properties for cluster surveying, as I detail below. As for X–ray observations, the SZ effect selects clusters based on their ICM properties and potential well; and like lensing surveys, SZ surveys tend to suffer from projection effects, since the SZ signal is proportional to the projected gas mass density. A number of planned SZ surveys have heightened anticipation as they prepare to observe large areas of sky over the next few years. These include ground–based instruments starting operations this year, as well as the Planck satellite scheduled for launch in 2008 and which will cover the entire sky.

3 The Sunyaev-Zel'dovich Effect

The SZ signal arises from the energy transfer via Compton scattering from hot electrons in the ICM to CMB photons traversing the cluster[9]. Conserving photon number, the scattering diffuses photons from low to high energies and creates a unique frequency–dependent spectral distortion that is negative at low frequencies and positive at high frequencies. We quantify the distortion by the change in observed sky brightness towards the cluster relative to the unperturbed CMB seen from surrounding blank sky:

$$\Delta i_\nu = y j_\nu \tag{1}$$

where the Compton–y parameter specifies the amplitude of the distortion as an integral of the ICM pressure along the line–of-sight:

$$y \equiv \int d\tau \, \frac{kT}{mc^2} = \int dl \, \frac{kT}{mc^2} n_e \sigma_T \tag{2}$$

with T being the electron (ICM) temperature, m the electron mass, n_e the electron number density and σ_T the Thomson scattering cross section (we're in the non-relativistic limit of Compton scattering). The function j_ν gives the frequency dependence of the spectral distortion and is universal to all clusters at all redshifts (See Figure 1). It is negative below 217 GHz, where the effect is a brightness decrement relative to the mean sky brightness (the CMB), and positive above, where the effect produces an excess brightness.

We refer to the total *SZ flux* as

$$S_\nu = Y j_\nu \tag{3}$$

where the integrated Compton parameter is

$$Y = \int d\Omega\, y \propto \frac{M_{\rm gas} T}{D^2_{\rm ang}(z)} \tag{4}$$

4 SZ Cluster Surveys

The SZ signal has a number of virtues when considered as a means of cluster surveying. Firstly, the surface brightness Δi_ν is independent of distance and depends only on intrinsic cluster properties; this is also manifest by the fact that Y varies with the *angular diameter* distance, as opposed to the luminosity distance. Secondly, the spectral signature is unique, unlike any other astrophysical source, and it is universal to all clusters.

Thirdly, the total SZ flux S_ν is directly proportional to the total thermal energy of the ICM, a quantity fixed by energetics during cluster formation and independent of the final spatial and temperature structure of the gas. For this reason, we expect the SZ signal to tightly correlate to cluster virial mass, as indeed borne out in numerical simulations; for example, Motl et al. [10] simulated examined different simulations, including a variety of cooling and feedback mechanisms, and find only a $\sim 5\%$ scatter in Y at a given mass.

These characteristics of the SZ signal lead to one to expect that a SZ survey will select clusters based on their mass, and that the limiting mass will be nearly constant with redshift. This is a valuable property for studying any evolutionary trends, for we can compare similar mass objects at different epochs.

5 SZ Catalog Construction

In anticipation of the upcoming surveys, we have undertaken an extensive simulation effort to study survey selection functions and observational uncertainties, and I will report here two key results from this work to date. Details can be found in Melin *et al.* [11] and Bartlett & Melin [12].

We have developed a cluster detection algorithm based on a filter matched to both the spectral (j_ν) and spatial (isothermal β-model) signature of the cluster SZ signal [13]. The filter is designed to rapidly and optimally extract clusters of all sizes from the astrophysical foregrounds. Rapidity is essential because we want to simulate a given survey many times in order to accurately quantify selection effects and observational uncertainties.

Applying the detection routine to Monte Carlo simulations of the AMI, ACT, Planck and SPT surveys, we calculated the survey sensitivities, counts and completeness values shown in Figure 2. In this Figure, σ_Y is the total noise through the matched filter generated by both instrumental noise and primary CMB anisotropy (for the standard WMAP cosmology), and θ_c refers to the core radius of our simulated SZ profiles truncated at 10 core radii. The curves correspond to the different surveys as labeled. A cluster observed by SPT, for example, with angular core radius θ_c and $Y = \sigma_Y(\theta_c)$, i.e., on the solid, red line, would have a $S/N = 1$.

We see from this Figure that the surveys are not simply limited in flux; cluster selection depends on both flux and angular size. This is particularly true for the high resolution ground-based surveys, while the lower resolution of Planck yields a nearly flux-limited catalog. In this

Name	Frequencies [GHz]	Res. *fwhm* [arcmin]	Start date	Inst. noise [μK/beam]	Surf. dens. (5σ) [deg^{-2}]	Survey Area [deg^2]
Interferometers						
AMI	15	1–2	2006	8	16	10
AMiBA	95	~ 2	2006			
SZA	30 (+90)	~ 1	2006			
Bolometers						
ACT	145	1.7	2006	1.7	40	200
	225	1.1		4.8		
	265	0.93		7.8		
APEX	150	0.8	2006			
	217	0.8				
SPT	150	1	2007	10	11	
	220	0.7		60		4000
	275	0.6		100		
Planck	143	7.1	2008	6	0.35	
	217	5		13		40000
	353	5		40		

Table 1: Characteristics of some of the large SZ surveying instruments. We give the instrumental noise, counts detected at $S/N > 5$ with our matched filter and survey area for the 4 experiments that we have simulated in detail, namely AMI, ACT, SPT & Planck (see text). A list of web pages for these and other experiments is given in the reference section. Adapted from Melin et al. (2006) [11]. **Note added:** The new WMAP3 results were published at the time of writing. The lower value of σ_8 favored by the new release can lower the predicted cluster counts by up to a factor ~ 2. We are evaluating the changes for each experiment in detail.

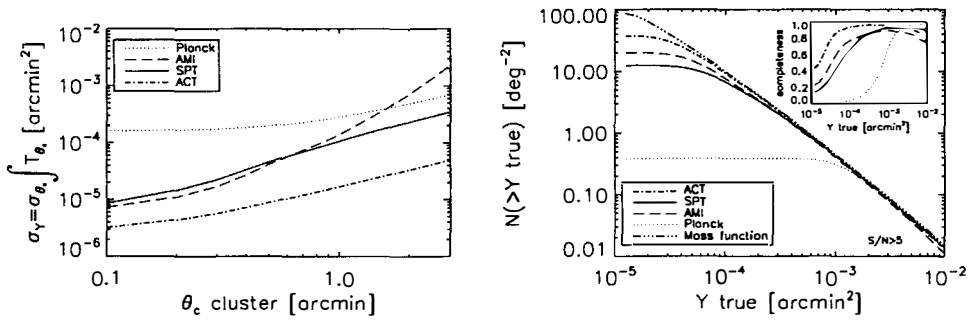

Figure 2: The *left-hand panel* plots the matched filter noise σ_Y as a function of filter scale θ_c (core radius of a cluster matched to the filter) for different surveys, as labeled. The filter noise is generated by primary CMB anisotropy and instrumental noise. Clusters lying above the curve of a particular experiment have $S/N > 1$. Integrated source counts at $S/N > 5$ for each survey are shown in the *right-hand panel*, along with the simulation input counts (curve labeled "mass function"). We give the catalog completeness percentage (ratio of the experimental curve to the input mass function counts) in the inset. The important point is that the surveys are not flux limited, and are significantly incomplete even at 5 times their point source sensitivities (5 times the y-intercept of the left-hand curves). Adapted from Melin et al. (2006). **Note added:** The new WMAP3 results were published at the time of writing. The lower value of σ_8 favored by the new release can lower the predicted cluster counts by up to a factor ~ 2. We are evaluating the changes for each experiment in detail.

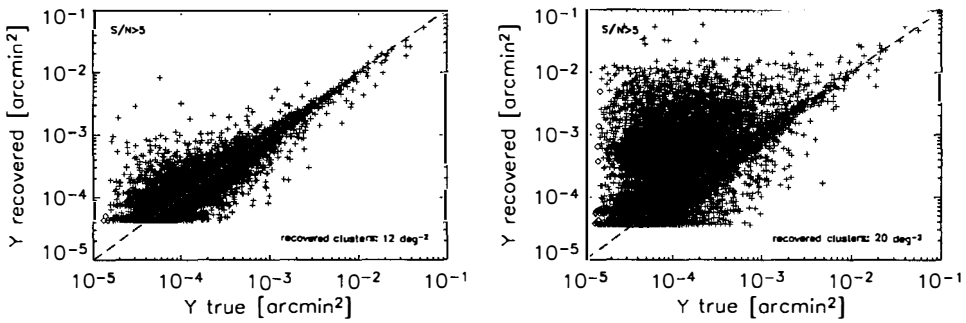

Figure 3: Photometric recovery in terms of integrated Compton Y parameter for SPT (left) and AMI (right). Compton Y values (in arcmin^2) recovered by the matched filter are plotted against the input Y values taken from the simulation catalog. Each point represents a single cluster detected at $S/N > 5$. The red dashed curve gives the equality line. For SPT the characteristic scatter at fixed $Y_{\rm true}$ is $\sim 40\%$. Confusion with primary CMB anisotropy seriously compromises photometric recovery of the single frequency survey (chosen here as AMI). Adapted from Melin et al. (2006).

Figure we only show the effects of instrumental noise and CMB anisotropies. In Bartlett & Melin [12] we examine the additional effects caused by extragalactic point sources.

In the right–hand panel I show the integrated counts of clusters detected at $S/N > 5$. These are objects to be found in the left–hand panel above the corresponding curves, each displaced upward by a factor of 5. The counts roll away from the input counts (labeled *mass function*) at the faint end as the catalogs become incomplete. In the inset, we see the completeness defined as the ratio of detected to input clusters (ratio of one of the experimental curves to the mass function curve). It is important to note that all of the surveys are significantly incomplete even at 5 times their point–source sensitivities, which are given by 5 times the y–intercept of the curves shown in the left–hand panel. This just illustrates again that the surveys are not simply flux limited.

I now turn to another important, but often neglected issue – photometric recovery. In Figure 3 I plot recovered Y versus input Y for clusters detected at $S/N > 5$ in SPT (left–hand panel) and AMI (right–hand panel); the Planck case is similar to SPT. We see that when applied to SPT our algorithm gives an unbiased estimate of the true SZ flux, but with $\sim 40\%$ scatter (at fixed $Y_{\rm true}$), which is much larger than the intrinsic scatter predicted by numerical simulations [10]. The photometry of the single frequency AMI survey, on the other hand, is very seriously compromised; the distribution at fixed $Y_{\rm true}$ is in fact bimodal. We have traced this effect to confusion with primary CMB anisotropy that is unavoidable with single frequency observations. The conclusion is that such single frequency surveys must follow–up their clusters at a second frequency in order to eliminate the confusion.

6 Conclusions

Future galaxy cluster surveys will provide a wealth of information on dark energy, dark matter and structure and galaxy formation. Among these surveys, those based on the SZ signal will profit from its intrinsic ability to find clusters at high redshift and its expected tight correlation to halo mass. Over the next 5 years, these surveys will provide large, well–defined (in terms of mass) catalogs containing hundreds to thousands of clusters at redshifts beyond unity or, in

other words, multiplying by 10–100 the number of known clusters at these redshifts[a]. This will give us a new view of galaxy formation in dense environments and a measure of the expansion rate at this crucial epoch marking the transition between matter and dark energy domination.

Many of the surveys will begin this year (2006), and a number of important surveying issues require further study. These include accurate evaluation of survey selection functions and observational errors. I have shown two results from our studies based on a matched filter detection algorithm and simulations of different surveys. We find that high resolution ground–based surveys select clusters not simply on flux, but on a combination of flux and angular size, and that this must be properly accounted for when modeling cluster counts. We also find that observational scatter on measured cluster flux Y (e.g., $\sim 40\%$ in the case of SPT) largely exceeds the intrinsic scatter predicted by numerical simulations [10]. Furthermore, confusion with primary CMB anisotropy severely compromises photometry in single frequency observations; follow–up at a second frequency (or in X–rays) will therefore be necessary for these surveys.

Acknowledgments

I wish to thank the organizers of the *Rencontres de Moriond* for a pleasant meeting, and P. Richards for a very instructive discussion on bolometer surveying sensitivity. I also thank my collaborators J.–B. Melin and J. Delabrouille.

References

1. E.g., C.L. Bennett *et al*, *Astrophys. J. Supp.* **148**, 1 (2003); D.N. Spergel *et al*, astro–ph/0603449 (2006).
2. R.A. Knop *et al*, *Astrophys. J.* **598**, 102 (2003); A.G. Riess *et al*, *Astrophys. J.* **607**, 665 (2004); P. Astier *et al*, *Astron. & Astrophys.* **447**, 31 (2006).
3. M. Tegmark *et al*, *Astrophys. J.* **606**, 702 (2004); S. Cole *et al*, *Mon. Not. Roy. Astron. Soc.* **362**, 505 (2005); U. Seljak, A. Slosar & P. McDonald, astro–ph/0604335.
4. D.J. Eisenstein *et al*, *Astrophys. J.* **633**, 560 (2005); S. Cole *et al*, *Mon. Not. Roy. Astron. Soc.* **362**, 505 (2005).
5. P. Eisenhardt *et al*, Ringberg Workshop (2005); G. Hasinger *et al*, *Astron. & Astrophys.* **340**, L27 (1998); C.R. Mullis *et al*, *Astrophys. J.* **623**, L85 (2005); S.A. Stanford *et al*, *Astron. J.* **114**, 2232 (1997); S.A. Stanford *et al*, *Astron. J.* **123**, 619 (2002); S.A. Stanford *et al*, astro–ph/0510655; P. Rosati *et al*, *Astron. J.* **118**, 76 (1999); P. Rosati *et al*,AJ **127**, 230 (2004)
6. P. Rosati, S. Borgani & C. Norman, *Ann. Rev. Astron. Astrophys.* **40**, 539 (2002)
7. J.Y Tang & Z.H. Fan, *Astrophys. J.* **635**, 60 (2005)
8. A.K Romer *et al*, *Astrophys. J.* **547**, 594 (2001); P.J. Green *et al.*, *Astrophys. J. Supp.* **150**, 43 (2004)
9. R.A. Sunyaev& Ya. B. Zel'dovich, *Comm. Astrophys. Space Phys.* **2**, 66 (1970); R.A. Sunyaev& Ya. B. Zel'dovich, *Comm. Astrophys. Space Phys.* **4**, 173 (1972); M. Birkenshaw, *Phys. Rep.* **310**, 97 (1999); J.E. Carlstrom, G.P. Holder & E.D. Reese, *Ann. Rev. Astron. Astrophys.* **40**, 643 (2002)
10. P.M. Motl *et al*, *Astrophys. J.* **623**, L63 (2005)
11. J.–B. Melin, J.G. Bartlett & J. Delabrouille, Å **429**, 417 (2005); J.–B. Melin, J.G. Bartlett & J. Delabrouille, astro–ph/0602424
12. J.G. Bartlett & J.–B. Melin, Å **447**, 405 (2006)

[a]The new WMAP3 results were published at the time of writing. The lower value of σ_8 favored by the new release can lower the predicted cluster counts by up to a factor ~ 2. We are evaluating the changes for each experiment in detail.

13. D. Herranz *et al*, APJ **580**, 610 (2002); D. Herranz *et al*, *Mon. Not. Roy. Astron. Soc.* **336**, 1057 (2002)
Web pages of various SZ experiments:
    - ACBAR `http://cosmology.berkeley.edu/group/swlh/acbar/`
    - ACT `http://www.hep.upenn.edu/~angelica/act/act.html`
    - AMI `http://www.mrao.cam.ac.uk/telescopes/ami/index.html`
    - AMiBA `http://www.asiaa.sinica.edu.tw/amiba`
    - APEX `http://bolo.berkeley.edu/apexsz`
    - SPT `http://astro.uchicago.edu/spt/`
    - SZA `http://astro.uchicago.edu/sze`
    - Olimpo `http://oberon.roma1.infn.it/`
    - Planck `http://astro.estec.esa.nl/Planck/`

NASA's Roadmap for Cosmological Research

Steven V. W. Beckwith
Space Telescope Science Institute & Johns Hopkins University
3700 San Martin Drive
Baltimore, MD, USA 21204
svwb@stsci.edu

NASA space missions have compiled an impressive record of answering fundamental questions in cosmology. NASA's ambitious roadmap for future missions includes a strong component of cosmological research into the properties of the Big Bang, the creation of the elements, the event horizons of giant black holes, understanding early inflation through the polarization of the cosmic background radiation, and an observatory for gravitational waves. The roadmap has a sound basis in our present day understanding of the universe with a good plan to develop new technology needed to address the outstanding questions. There is great uncertainty about the amount of time it will take to execute this plan given competing priorities within NASA particularly for the human spaceflight program and the modest projected budget growth to support these competing priorities.

1 Organization of NASA's Space Science Goals (science.hq.nasa.gov)

NASA's space science missions are the responsibility of its Science Missions Directorate of which the Astrophysics Division handles cosmology. The Directorate organizes its research by positing four fundamental questions about the universe and designing missions to address one or more of these questions in its Level 1 science goals. These questions are subdivided into two lines:

- Beyond Einstein
    1. How did the Universe begin?
    2. Does time have a beginning and an end?
    3. Where did we come from?

- Pathways to Life

    1. Are we alone?

These questions are sufficiently broad to allow almost any research relevant to cosmology under at least one of them. They have the virtue of appealing to a wide, non-specialist public as a reason for supporting space science. Many of NASA's missions address more than one of these questions.

This organization is a shift from the previous generation's "Great Observatories" program. The Great Observatories gave us the Hubble Space Telescope (ultraviolet to near infrared), the Compton Observatory (γ-rays), the Chandra X-ray Observatory (soft x-rays), and the Spitzer Observatory (near to far infrared) that have proven to be a great boon to cosmological research. The Great Observatories recognized that astronomy is an empirical science often depending on serendipity for its most important insights and therefore provided us with general tools to expand our ability to view the cosmos at different wavelengths.

The focus on key questions still allows room for observatories, as we shall see, but recognizes that a great deal of the exploration phase of astronomy has already taken place and emphasizes facilities that address specific questions arising from this early exploration. There is likely to be an ongoing debate about the relative emphasis on exploration vs. targeted missions that will play out as adjustments to the priorities of the current roadmap.[1]

2 Currently planned missions

Figure 1 shows a timeline of planned missions for the Beyond Einstein and Pathways to Life programs as of March 2005. The acronyms for the major missions are: Laser Interferometer Space Antenna (3-element gravitational wave observatory), Constellation-X (4 element x-ray observatory emphasizing spectroscopy), Joint Dark Energy Mission (optical/infrared study of supernovae or other objects to determine the expansion history of the universe), James Webb Space Telescope (near to far-infrared space telescope), Herschel (far-infrared/sub-millimeter observatory), and Stratospheric Observatory For Infrared Astronomy (3-m telescope in a Boeing 747 to supersede the Kuiper Airborne Observatory.) These missions are broadly defined and in some cases close to completion (SOFIA). The missions, IP, BHFP, Big Bang Observer, Black Hole Imager, and Pathways to Life Observatory, are placeholders for undefined missions aimed at future ways to further address the four main questions posed in the previous section.

The missions under development of immediate interest to the cosmology community are Hubble (Servicing Mission 4), JWST, WISE, Con-X, LISA, GLAST, and JDEM. It is likely that there will be competed missions in the Explorer line addressing cosmology, similar to the way COBE and WMAP have profoundly influenced our understanding of the current concordance model of the Big Bang. These competed missions remain undefined. Although Hubble is currently operating, planned upgrades to the instrumentation during servicing mean that NASA still treats Hubble as a development project, and the new instruments will address cosmological issues.

The following sections briefly describe some of the science goals of these missions and their potential importance for cosmology. Almost all the important references to these missions are available on the internet and are kept current with frequent updates. In lieu of the usual references to the literature, this article will provide website addresses that give more in-depth information about the evolving status of the different missions.

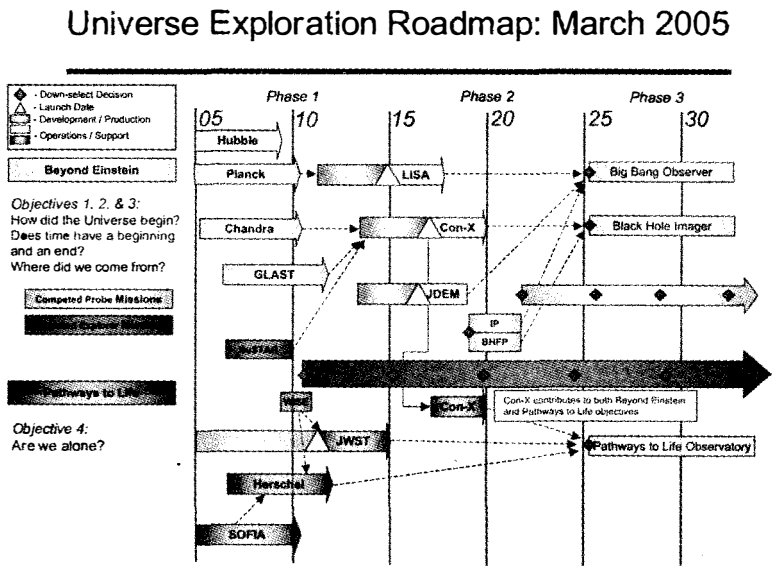

Figure 1: NASA's planned suite of missions and their launch dates from p. 28 of the NASA Roadmap.[1] The triangles indicate planned launch dates as of March 2005 for the missions such as LISA, Con-X, and JWST. Most of these dates will be delayed if NASA's budget for fiscal year 2007 is approved as requested (cf Section 3.)

2.1 Hubble Space Telescope (hubblesite.org)

Hubble's next servicing mission includes the installation of two new instruments, Wide Field Camera 3 (WFC3) and the Cosmic Origins Spectrograph (COS.) In addition, NASA is working to repair the Space Telescope Imaging Spectrograph (STIS) that lost both power modules two years ago, and there is some hope that it can restore STIS to it full capabilities.

Hubble has already had a strong impact on cosmology through the measurement of H_0, the first images of galaxies at lookback times of approximately 13 billion years, and measurement of the time history of the expansion rate between 4 and 6 Gyr after the Big Bang to constrain the dark energy. Two of these themes—formation of early galaxies and the early expansion history of the universe—will be enhanced by the addition of WFC3.

Hubble's observations of young galaxies rely on detecting the neutral-hydrogen absorption edge from the intergalactic medium (Lyman-Break technique) in deep multicolor images. The most distant samples studied to date emit radiation only at wavelengths longer than about 800 nm and are typically seen only in a single filter, F850LP, making it impossible to use color information to study their properties. These "i-dropout" galaxies are at redshifts greater than 5.7 corresponding to an epoch less than one billion years after the Big Bang. WFC3 will have sufficient sensitivity and survey speed at wavelengths between 1 and 1.7 μm to discern the colors of these distant galaxies and to search for objects at redshifts as large as 10. Hubble will be unique for this research until JWST is operating, making it an essential tool to understand the

formation of the first stars and galaxies.

WFC3 also has the capability of finding and measuring SN Ia out to redshifts of order 2. Using the supernovae as standard candles will allow Hubble to measure the historical Hubble flow from 3 Gyr after the Big Bang until the present with far more precision than possible today. Hubble will also be unique for this research and will provide us with the only constraints on variations of the equation of state of dark energy in this early epoch until superseded by JDEM.

COS is designed to study the baryonic component of the intergalactic medium from absorption lines in distant quasars at ultraviolet wavelengths. COS will improve Hubble's sensitivity for these spectra by more than an order of magnitude compared to the present, allowing it to map the distribution of local intergalactic baryons—and by inference the distribution of cosmic dark matter on much finer angular scales than presently possible. Hubble's ability to observe at ultraviolet wavelengths coupled with its large aperture make it unique for these studies for the foreseeable future. There are no plans for future ultraviolet telescopes in NASA's current roadmap.

2.2 James Webb Space Telescope (www.jwst.nasa.gov)

JWST is designed to study the formation of the first stars and galaxies following the period of darkness (the "dark ages") after the Big Bang. It is a 6.5 m aperture infrared telescope to be operated at the second Lagrangian point of the Earth-Sun system. Passively cooled to 40° K and optimized between 3 and 28 μm (with some sensitivity into the visible band), it will be sensitive enough to detect normal galaxies at redshifts as large as 20, corresponding to 200 Myr after the Big Bang.

The primary cosmological questions addressed by JWST are:

- What are the first galaxies?
- When did re-ionization of the universe occur?
- What sources caused re-ionization?
- Where and when did the Hubble Sequence form?
- How did the heavy elements form?
- Can we test hierarchical formation and global scaling relations?
- What roles to Ultra-Luminous Infrared Galaxies (ULIRG) and Active Galactic Nuclei (AGN) play?

The observational plan calls for a deep near-infrared survey to a sensitivity of 1.4 nJy to discover the distant populations and follow-up spectroscopic and mid-infrared observations to assess their properties. It will be possible to detect Balmer lines in the spectra of distant galaxies to a level of $2 \times 10^{-19}\,\mathrm{erg\,cm^{-2}\,s^{-1}}$. It should be possible to distinguish the epoch of re-ionization by detecting patchy Lyman-forest absorption and a Gunn-Peterson trough in very distant objects, delineating the redshifts at which the universe was in different ionization states.

Wide-area imaging surveys will harvest thousands of galaxy spectra ($\lambda/\Delta\lambda \sim 1000$) in the redshift range $1 < z < 6$, providing a comparison of galaxy properties in time and over large angular scales as hierarchical clustering developed the structure we see today. Targeted observations of ULIRGs and AGN will be used to understand the relative contribution of these bright but rare objects to global structure development, ionization, and the energy budget of the early universe.

JWST, like Hubble, will be an observatory. We can anticipate many of the most important discoveries to be serendipitous. It will be such a powerful observatory that it is likely to have

a much larger impact on our understanding of the early universe and cosmology than what is outlined in this baseline science plan.

2.3 *Widefield Infrared Survey Explorer* (www.astro.ucla.edu/ wright/WISE)

WISE is a 40 cm telescope that will survey the entire sky at four wavelengths: 3.3, 4.7, 12. and 24 μm. In many respects, it will be a shorter wavelength version of the IRAS survey. It is planned as a 7 month mission launched in 2009 in a 500 km Sun-synchronous orbit.

From the standpoint of cosmology, the main goal of WISE is to detect the most luminous galaxies in the sky. It will be able to see an L_* galaxy at a redshift of 1 and a ULIRG at a redshift of 3. We anticipate the most luminous galaxies will be too rare to be seen in smaller field surveys such as those carried out with Hubble and JWST, and they will be too faint to be seen with ground-based telescopes at infrared wavelengths.

2.4 *Constellation-X* (constellation.gsfc.nasa.gov)

The successor to Chandra, Con-X, is an array of four telescopes at Earth-Sun L2 orbit (like JWST) designed for high resolution spectroscopy of x-rays with up to 100 times the throughput (sensitivity) of current missions and the ability to take spectra of sources discovered in deep imaging surveys by Chandra, for example. Its targets include the strong gravitational effects of black holes, their effect on galaxy formation, study of clusters of galaxies through x-ray emission from hot gas, and studies of the cosmic feedback of galactic winds, stellar coronas, and supernovae on the intergalactic medium.

Con-X will study giant black holes in ways that may impact our understanding of gravitation and thus cosmological expansion. Like JWST, it will be an observatory, albeit one concentrating on spectra rather than imaging—it will not be survey the sky. Assessing the impact of black holes on the formation of galaxy structure and their contribution to the total energy budget will be a major contribution of Con-X to our understanding of the early universe.

Clusters of galaxies are useful tracers of the location of dark matter. They also provide independent probes of the evolution of dark energy through the Sunyaev-Zeldovich effect. S-Z studies using Con-X observations of distant clusters is an independent way to constrain the strength of dark energy at different epochs and therefore provides an important check on any conclusions reached using SN Ia.

The S-Z effect can be used to measure absolute distances to clusters. Combined with redshifts for the clusters, it is a potentially powerful method to assess cosmological parameters. Furthermore, the mass fraction of cluster gas might be used as a standard candle similar to the way supernovae are used to get a separate handle on the distance to the clusters to measure these parameters. The evolution of cluster parameters and the cluster mass function can then be studied as functions of redshift.

These cluster measurements constrain the cosmological parameters, Ω_Λ and Ω_m, differently from either the cosmic microwave background or the supernovae. In the Ω_Λ, Ω_m plane, the cluster constraints are an important addition to the CMB and SN Ia, making Con-X an integral part of our determination of cosmological constants.

Con-X will be sensitive to very hot gas in the intergalactic medium and to the missing baryonic matter in the cosmic web. Although Hubble's COS instrument will also look for this missing matter, it is not known what the typical temperatures might be. If it resides primarily in very hot gas, Con-X will be the most important means for detecting it and assessing its impact on the intergalactic medium.

2.5 *LISA* (lisa.nasa.gov)

LISA is designed to detect gravitational waves in the low-frequency range 10^{-4}—10^{-1} Hz. It consists of three identical satellites arranged in a precessing triangle about ~ 1 AU in size in a 1 AU Sun-centered orbit trailing the Earth. Small displacements of inertial masses within the satellites by gravitational waves are sensed by laser interferometers operating between all pair combinations of the array.

The kind of objects expected to be seen in this range are Galactic binaries and the coalescence of massive black holes at cosmological distances. The latter are of most interest for cosmology.

If a coalescence event can be observed for a period of several months, LISA will process far enough to allow a determination of the position of the source. Because of the way that gravitational waves propagate across space time, it is possible in principle to derive the absolute distance to the source from the observations themselves. Combining this knowledge separately with the redshift to the source gives an independent measure of the cosmological parameters.

It is not clear if LISA will be important for cosmology, but it does provide a precursor to the Big Bang Observer (see Fig. 1), a conceptual mission with enough sensitivity to measure gravitational waves from the early epochs of the Big Bang. It is also uncertain if NASA can develop the technology for such a mission within its current budget.

2.6 *GLAST* (glast.gsfc.nasa.gov)

The Gamma-ray Large Array Survey Telescope is designed as a 5 year mission with about 15 times more sensitivity than EGRET over tens times greater energy range, from 20 to 300 GeV. GLAST is scheduled for launch in 2007. It will investigate a number of high-energy phenomena, including black holes and AGN, supernova remnants, gamma-ray bursts, and the origin of cosmic rays.

For cosmology, GLAST has three high level goals. It will search for supersymmetric dark matter annihilations that if found will help point the way toward a grand unified theory of physics. It will look for violations of Lorentz invariance, and it will search for exotic relics of the Big Bang, if any. By targeting extremely high energy radiation, GLAST can study particles at energies above those reached by ground-based particle accelerators. Candidates for weakly interacting cold dark matter include a broad range of supersymmetric particles that have spectral signatures of line emission in the 10's to 100's of GeV range. GLAST can also search for photons from primordial black holes.

2.7 *JDEM* (snap.lbl.gov & destiny.asu.edu)

The Joint Dark Energy Mission is specifically designed to measure the effects of dark energy on cosmological expansion. There are currently two mission concepts, the Supernova Acceleration Probe (SNAP) led by Lawrence Berkeley Laboratory and Destiny from Arizona State University. Both missions use supernovae as standard candles and have as their goal the measurement of thousands of supernovae to provide distances (from the observed brightness) and redshifts to objects in the cosmic flow between redshifts of order 0.5 to 1.7. Both missions also plan to map the distribution of dark matter by measuring the weak gravitational lensing of background galaxies in response to its mass.

SNAP is a 2 m diameter wide field (0.34 degree FOV) optical/near-infrared telescope that will scan the sky to discover supernovae and follow up with an on-board spectrometer. Measurements from space allow high-quality photometry of supernovae at redshifts beyond 1.5. With a wide field, it should be possible to discover several supernovae in a few hours of scanning the sky.

Destiny provides the same information using a different approach. It employs a 1.8 m near-infrared telescope with an objective prism (a grism) to search for supernovae for which it gives

simultaneous photometry—by compressing the spectra—and spectra to measure redshifts from the dispersed light. Like SNAP, it exploits the extraordinarily low background light of space to achieve high sensitivity even in dispersed light through the grism, a technique routinely used on the Hubble Space Telescope.

The discovery that supernovae can be used as standard candles to measure the acceleration of the universe[2,3] has stimulated the drive to make thousands of such measurements to reduce the uncertainties in the cosmological parameters. If there are no systematic uncertainties discovered in the analysis of these very large samples, JDEM could provide an accurate enough measure of the acceleration to test whether it is consistent with a cosmological constant within a few percent.

3 Changes to NASA's Roadmap in 2006

In January 2004, President George W. Bush announced a new vision for NASA's space exploration program. This vision stressed a renewed emphasis on human spaceflight by sending humans back to the moon and eventually to Mars. To achieve this vision, NASA will have to develop a new human-rated spacecraft known generically as the Crew Exploration Vehicle (CEV.) It will also need to retire the Space Shuttle but not before completing construction of a scaled back International Space Station.

The cost of repairing the shuttle for its return to routine operations has proven to be more expensive than NASA first anticipated. This cost has must be born by the rest of NASA's budget. There is also a political imperative to minimize any gap between the end of shuttle operations—currently planned for 2010—and the first launch of the CEV, originally planned for 2014, at least partly because of China's vigorous pursuit of its own human spaceflight program. An accelerated CEV development puts further pressure on NASA's budget that further limits NASA's ability to fund new science spacecraft.

As a result, the President's budget for fiscal year 2007 is insufficient to maintain the space science budget at levels planned in 2005. The roadmap is changing, although the final results will not be known until the US Congress votes a formal budget later this year and NASA submits a new program plan.

Most of the major missions are still in the plan, but most have been delayed compared to their original time lines. Some of the more unfortunate changes include the cancellation of SOFIA, cancellation of NuSTAR, and delays in funding for LISA, Con-X, and JDEM. On the positive side, the budget provides funds for a Hubble servicing mission in early 2008 that would extend its life until 2013 or beyond, full funds for a 2013 launch for JWST, and funding to keep WISE on schedule. There have been protests about the cancellation of SOFIA and NuSTAR. NASA's Space Science Directorate promised to reconsider these decisions,[4] but without new money or a willingness to slow down the development of the CEV the restoration of the cancelled missions will probably come at the expense of the other space science programs.

There is currently a general pessimism about the state of NASA's budget in the science community owing to projections of an overall decrease in real (inflaction-adjusted) funding for science in the five-year projection. Major missions have been cancelled or delayed. NASA has slowed the development of technologies needed to build the next generation of missions in its science roadmap.

There are, however, reasons to be optimistic about NASA's science program over the long run. NASA's annual budget for space science is approximately $4 billion. It represents a substantial fraction of support for astrophysics in the United States, and it provides a tremendous benefit to science despite cyclical fluctuations in the absolute level. The opportunities for space science research have never been richer. Technology now allows us to measure the properties of the first stars and galaxies born after the Big Bang, test the concept of a cosmological

constant with some precision, study the event horizons of black holes, search for emission lines from supersymmetric particles making up dark matter, and detect gravitational waves resulting from the coalescence of giant black holes in the early universe. Astrophysics is experiencing a renaissance unlike any in recorded history, and we can expect that after a lean period during which NASA shepherds the human spaceflight program through its needed transition, space science will emerge once again as NASA's most productive program, one that will guarantee public support far into the future.

Acknowledgments

I am grateful to Bruce Margon and David Leckrone for providing me with materials for this talk and to my colleagues at the Space Telescope Science Institute and NASA for many stimulating conversations that taught me about the new opportunities in space science.

References

1. *Universe Exploration: From the Big Bang to Life*, May 20, 2005. http://www.hq.nasa.gov/office/apio/pdf/universe/universe_roadmap.pdf
2. Riess, Adam G.; Filippenko, Alexei V.; Challis, Peter; Clocchiatti, Alejandro; Diercks, Alan; Garnavich, Peter M.; Gilliland, Ron L.; Hogan, Craig J.; Jha, Saurabh; Kirshner, Robert P.; and 10 coauthors, *Astron. J.* **116**, 1009 (1998).
3. Perlmutter, S.; Aldering, G.; Goldhaber, G.; Knop, R. A.; Nugent, P.; Castro, P. G.; Deustua, S.; Fabbro, S.; Goobar, A.; Groom, D. E.; and 23 coauthors, *Astrophy. J.* **517**, 565 (1999).
4. *Science* **311**, 1359 (2006).

The OSER project

Moniez, M.
Laboratoire de l'Accélérateur Linéaire, IN2P3-CNRS, *Université de Paris-Sud, B.P. 34, 91898 Orsay Cedex, France. E-mail: moniez@lal.in2p3.fr*

The OSER project (Optical Scintillation by Extraterrestrial Refractors) is proposed to search for scintillation of extragalactic sources through the galactic – disk or halo – transparent H_2 clouds, the last unknown baryonic structures. This project should allow one to detect column density stochastic variations in cool Galactic molecular clouds of order of $\sim 3 \times 10^{-5}\,g/cm^2$ per $\sim 10\,000$ km transverse distance.

1 The transparent baryonic matter and its possible signature

Considering the results of baryonic compact massive objects searches [1], cool molecular hydrogen (H_2) clouds should now be seriously considered as a possible major component of the Galactic baryonic hidden matter. It has been suggested that a hierarchical structure of cold H_2 could fill the Galactic thick disk [9] or halo [2], providing a solution for the Galactic hidden matter problem. This gas should form transparent "clumpuscules" of 10 AU size, with a column density of $10^{24-25}\,cm^{-2}$, and a surface filling factor smaller than 1%. Refraction through such an inhomogeneous transparent H_2 cloud (hereafter called screen) distorts the wave-front of incident electromagnetic waves (Fig. 1, see [7] for details). The phase delay induced by a screen at distance z_0 can be described by a function $\Phi(x_1, y_1)$ in the plane transverse to the observer-source line. The amplitude in the observer's plane after propagation is described by the Huygens-Fresnel diffraction theory. For a *point-like* source, the intensity in the observer's plane is affected by interferences which, in the case of stochastic inhomogeneities, takes on the speckle aspect. In the case of an accidental local inhomogeneity, the interfringe is characterized by the Fresnel radius $R_F = \sqrt{\lambda z_0 / 2\pi}$, of order of 1000 km to 7000 km at $\lambda = 1000$ nm, for a screen distance z_0 between 160 pc (distance of the Bok globule B68) to 10 kpc (typical distance of a halo-clumpuscule). The fluctuations of $\Phi(x_1, y_1)$ needed to produce strong interferences turn out to be the same order of magnitude as the average gradient that characterizes the hypothetic galactic H_2 structures. This numerical coincidence encourages us to develop a specific interference search program. As for radio-astronomy [8], the stochastic variations of $\Phi(x_1, y_1)$ are characterized by the diffusion radius R_{diff}, defined as the transverse separation for which the root mean square of the phase difference is 1 radian. Two different scintillation modes are expected when the screen crosses the line of sight of a point-like source:

- A short time scale mode (minutes) called diffractive mode is induced by the streaming of interference patterns at the $min(R_{diff}, R_F)$ spatial scale. Due to severe spatial coherence limitations, the modulation of light in this mode will be measurable only on the smallest stars. In contrast, temporal coherence with the standard UBVRIJH filters is sufficiently high to enable the formation of contrasted interferences in the configurations considered here.

Screen Distance				160pc-dark cloud	1kpc-thick disc	10kpc-halo
R_F to × by $\sqrt{\lambda/(1000\,\mathrm{nm})}$				890 km	2200 km	7000 km
Transverse speed V_T (typical)				30 km/s	40 km/s	200 km/s
t_{diff} to × by $\frac{R_{diff}}{R_F}\sqrt{\frac{\lambda}{1000\mathrm{nm}}}$				30 s	56 s	35 s
SOURCE				DIFFRACTIVE MODULATION INDEX m_{diff}		
Location	Type	r_S	M_I	(to multiply by $\sqrt{\lambda/1000\,\mathrm{nm}} \times R_{diff}/R_F$)		
spiral	B5V	$3.9r_\odot$	13.5	2%		
arm	A5V	$1.7r_\odot$	16.3	4%	1%	
8kpc	K0V	$0.85r_\odot$	19.4	7%	3%	
LMC	B8V	$3.r_\odot$	18.3	(14%)	6%	1.5%
55kpc	A5V	$1.7r_\odot$	20.4	(25%)	10%	3%

Table 1: *Configurations leading to strong diffractive scintillation assuming $R_{diff} \leq R_F$. Here $\lambda = 1000\,\mathrm{nm}$.*

- A long time scale mode (hours or more) called refractive mode is induced by the local focusing/defocusing configurations in the long scale structure of the screen. The modulation of light in this mode is essentially insensitive to the size of the source-star.

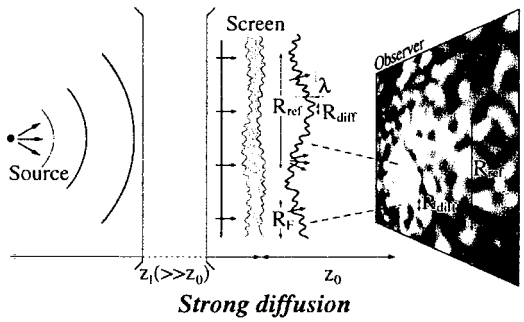

Figure 1: *The two scintillation modes: In the case of a point-like source, if $R_{diff} < R_F$, the distorted wavefront produces scintillations at scales $\sim R_{diff}/V_T$ (diffractive mode) and R_{ref}/V_T (refractive mode).*

2 Detectable features

A pattern with interferences of inter-fringe of $\sim min(R_F, R_{diff})$ sweeps across the Earth when the line of sight of a sufficiently small astrophysical source crosses an inhomogeneous transparent Galactic structure (Table 1). This pattern moves at the relative transverse velocity V_T of the screen, assuming that the scintillation is mainly due to screen motion rather than pattern instability (frozen screen hypothesis), as it is usually the case in radioastronomy observations[6]. For the Galactic H_2 clouds we are interested in, we expect intensity variations at time scale $t_{diff} < R_F/V_T \sim 1\ minute$, with a modulation index m_{diff} that can reach $\sim 20\%$ at $\lambda = 500nm$, critically depending on the source apparent size for the diffractive mode. As R_F scales with $\sqrt{\lambda}$ and R_{diff} also depends on λ, this induces a significant difference in the time scale t_{diff} between the red side of the optical spectrum and the blue side. This property might be used to sign the diffraction scintillation mode. A long time scale intensity modulation with characteristic time $t_{ref} = R_{ref}/V_T$ is superimposed on this diffractive mode. The contrast for this refractive mode is also a few percent, insensitive to the bandwidth and much less affected by the source-size.

3 Feasibility studies: simulation

We have simulated the phase delay function $\Phi(x_1, y_1)$ of a fractal cloud, described by the Kolmogorov turbulence law (Fig. 2 up-left). Then we calculated the diffracted amplitude from

a *point* source on Earth (Fig. 2 up-right). The illumination on Earth due to an *extended* incoherent source of radius r_s is obtained by integrating the *intensities* due to each elementary source. This is equivalent to integrate the intensity image of a point source within the projected

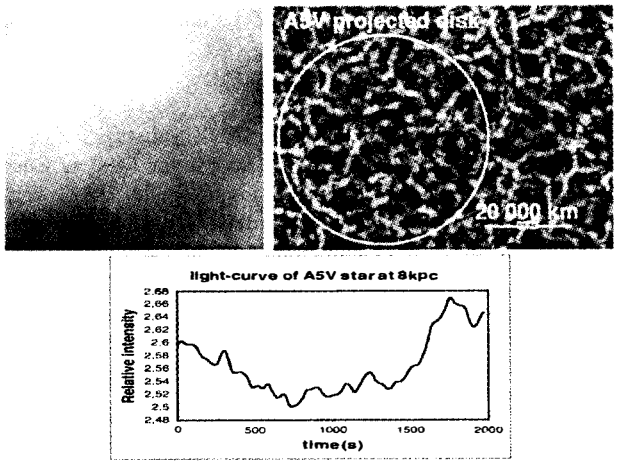

Figure 2: *Phase delay $\Phi(x_1, y_1)$ induced by a turbulent cloud (up-left); Illumination map on Earth from a point source (up-right)- the cloud is assumed to be at 160 pc. Illumination variations from an A5V star at 8kpc (down).*

source stellar-disk of radius $r_s \times z_0/z_1$ where z_1 is the distance from the cloud to the source. The expected light-curve from a A5V star located at 8kpc, as seen through a cloud located at 160pc, with $R_{diff} = 1000km$ and transverse speed $V_T = 30km/s$, is given in Fig. 2 down. Using this simulation, we have been able to estimate the modulation index as a function of the crucial parameter R_{diff}.

4 Toward an experimental setup for searching hidden matter

Table 1 shows that the search for diffractive scintillation induced by a remote Galactic molecular cloud needs the capability to sample every ~ 10 s (or faster) the luminosity of LMC stars with $M_V > 20$ (A5V type), with a precision of $\sim 1\%$. This performance can be achieved using a telescope diameter larger than two meters, with a high quantum efficiency detector allowing a negligible dead-time between exposures (like frame-transfer CCDs). Multi-wavelength detection capability is highly desirable to exploit the dependence of the diffractive scintillation pattern with the wavelength. The probability for a star to be subject to such scintillation is estimated to be $10^{-7}\alpha < \tau_{scint} < \alpha \times 1\%$ [7], where α is the fraction of halo made of gaseous objects. Then, the average exposure needed to observe one fluctuation of ~ 5 minute duration is $< 10^6/\alpha$ star $\times$ hr. At isophot $M_V = 23\ mag/arcsec^2$ of LMC or SMC, about 10^5 stars per square degree with $20 < M_V < 21$ —i.e. small enough— can be monitored [4,5]. It follows that a wide field detector is necessary to monitor enough small stars.

Foreground effects, background to the signal Conveniently, atmospheric *intensity* scintillation is negligible through a large telescope ($m_{scint} \ll 1\%$ for a > 1 m diameter telescope [3]). Any other atmospheric effect such as absorption variations at the minute scale (due to fast cirruses for example) should be easy to recognize as long as nearby stars are monitored together. Asterosismology, granularity of the stellar surface, spots or eruptions produce variations of very

different amplitudes and time scales. A rare type of recurrent variable stars exhibit emission variations at the minute scale, but they are easy to identify from spectrum. Scintillation will also be easily distinguishable from absorption variations due to the dust distribution in the cloud; indeed, the relative column density fluctuations within a domain of R_{diff} size is only a few 10^{-7} for the clumpuscules, and 10^{-3} for the Bok globules; it is smaller by orders of magnitudes than the fluctuation of dust column density needed to produce measurable absorption variations.

5 Preliminary studies with the NTT

To test the concept, we searched for gas induced scintillation of stars located behind or on the edge of Bok globules with the ESO-NTT. In june 2005 we got 5400 exposures of $T_{exp} = 7s$, taken with the infra-red SOFI detector in J and K towards B68, cb131 and Bhr71. SOFI is the only detector operating with a short readout time (5.5s), and IR allows star monitoring through the dusty Bok clouds. For a future search for transparent hidden matter, visible light —corresponding to the maximum stellar emission— would be more optimal. From reddening studies, we confirmed column densities of $\sim 10^{22}$ atoms/cm^2. The average phase delay induced by the medium is $500 - 1000 \times 2\pi$ at $\lambda = 1000nm$. According to our studies, a few percent scintillation signal is expected if relative column density fluctuations of $\sim 10^{-3}$ occur within less than a few thousand kilometers (corresponding to $R_{diff} < 2000km$). Due to poor atmospheric conditions, only 948 measurements had a seeing smaller than $1.5''$ towards B68. We produced the light curves of 2873 stars using the EROS software. After selection and identification of known artifacts (hot pixels, dead zones, bright egrets...), we found only 4 stars with significant variability, all of four interestingly located near the Bok globule limit. Their status should be clarified with better quality data expected in june 2006. Nevertheless we can already conclude that the signal we are searching for should not be overwhelmed by background. We also got confirmation from these data that a good seeing is mandatory for a significant sensitivity.

6 Conclusions and perspectives

The opportunity to search for scintillation results from the subtle coincidence between the arm-lever of interference patterns due to hypothetic diffusive objects in the Milky-Way and the size of the extra-galactic stars. The hardware and software techniques required for such searches are available just now, and a light project could be operational within a year or two. Alternatives under study are the use of the data from the LSST project and from the GAIA mission. If a scintillation signal is found, one will have to consider an ambitious project involving synchronized telescopes, a few thousand kilometers apart. Such a project would allow to temporally and spatially sample an interference pattern, unambiguously providing the diffusion length scale R_{diff}, the speed and the dynamics of the scattering medium.

1. Afonso, C., *et al.* (EROS coll.), A&A **400**, 951 (2003).
2. De Paolis, F. *et al.*, PRL **74**, 14 (1995)
3. Dravins, D. *et al.*, Pub. of the Ast. Soc. of the Pacific **109** (I, II) (1997), **110** (III) (1998).
4. Elson, R.A.W., Gilmore, G.F., & Santiago, B.X. 1997, `astro-ph/9705149`.
5. Hardy, Pub. of the Astron. Soc. of the Pacific **90**, 132 (1978)
6. Lyne, A.G. & F. Graham-Smith, *Pulsar Astronomy*, Cambridge University Press (1998)
7. Moniez, M., A&A **412**, 105 (2003).
8. Narayan, R. Phil. Trans. R. Soc. Lond. A **341**, 151 (1992)
9. Pfenniger, D. & Combes, F., A&A **285**, 94 (1994).

Studying Cosmic Acceleration with Galaxy Cluster Surveys

Joseph J. Mohr
Department of Astronomy, Department of Physics and NCSA,
University of Illinois, 1002 W. Green St,
Urbana, IL 61802, USA

Large scale X–ray, mm-wave and optical cluster surveys hold great promise for understanding the origin of the cosmic acceleration. With their sensitivity to the growth rate of cosmic structure and the distance–redshift relation, growth of structure tests such as galaxy cluster surveys and weak lensing cosmic shear offer the possibility of differentiating between dark energy models and models of modified gravity. Moreover, the rich set of observables in a galaxy cluster survey, including the cluster redshift distribution within luminosity slices, the cluster spatial clustering, and weak lensing mass estimates, makes it possible to internally check the self–consistency of cosmological constraints. Recent studies highlight the importance of scatter in the mass–observable relations and of weak lensing mass constraints in robustly calibrating these relations and their evolution. Forecasts for upcoming Sunyaev-Zel'dovich effect surveys like the South Pole Telescope provide an exciting glimpse of the power of this technique. Current cluster survey experiments will pave the way for all sky surveys like the proposed X-ray Dark Energy Cluster Survey, that would deliver 10^5 detections and detailed imaging spectroscopy of thousands of systems.

1 Cluster Surveys Complement Other Probes of Cosmic Acceleration

Several independent lines of observational evidence indicate that the expansion of the universe has entered an accelerating phase [1,2,3,4]. A key objective in cosmology and high-energy physics today is to understand the underlying cause of this comic acceleration. It can be explained by a ubiquitous dark energy component that dominates the current energy density of the universe; it can also be explained by a flaw in our understanding of gravity on the largest scales. Several promising astrophysical methods for studying the cosmic acceleration have been developed, and each draws upon distance measurements extending over cosmological scales and/or studies of the growth rate of cosmic structures.

The galaxy cluster survey is one of the four key methods for studying cosmic acceleration. The other three are SNe Ia distances, weak lensing cosmic shear, and power spectrum standard rods (often referred to as baryon acoustic oscillations). These techniques all employ the sensitivity of the distance-redshift relation and the growth rate of cosmic structures to the expansion history of the universe $H(z)$. The root of both of these sensitivities lies in the direct connections between the expansion history $H(z)$ and the contents of the universe, which is described by the Friedman equation(assuming zero curvature: $H(z) = \sqrt{(8\pi G/3)\rho(z)}$ where $\rho(z)$ describes the redshift evolution of the mean matter and energy density of the universe).

The distance d to a redshift z in a geometrically flat expanding universe is

$$d(z) \propto \int_0^z dz' \frac{c}{H(z')}$$

where c is the speed of light. Thus, distance measurements over a range of redshifts can be used to precisely describe the way the dark energy density changes with redshift. Constant energy density would signal a cosmological constant; ruling out that possibility would be a fundamental breakthrough. Of course, it is also possible the observed acceleration of the universe implies a deep flaw in our model of gravity on cosmic scales. Precisely constraining the expansion history of the universe using multiple techniques is a promising way to address these two possibilities.

One typically casts the study of the cosmic acceleration in terms of a measurement of the equation of state parameter w of the dark energy. The energy density of a component described by equation of state parameter w varies as

$$\rho_E(z) = \rho_E(z=0)(1+z)^{3(1+w)}$$

In fact, these measurements deliver a more general and fundamental property of the universe: the way the universal expansion has changed over cosmic time.

Models where the equation of state parameter varies with redshift are qualitatively similar. A generic problem with distance measurements is that the resulting constraints exhibit very strong parameter degeneracies. For constant w models, for example, the distance change corresponding to a shift in w can be exactly offset by an associated shift in Ω_M. Thus, in general, distance measurement techniques have to be combined with precise measurements of the matter density parameter Ω_M to obtain useful constraints on the nature of the dark energy [5,6].

The growth rate of structures in the universe is also sensitive to the expansion history of the universe, but, in addition, the growth rate is affected by the clustered matter density ρ_M. The differential equation for the linear evolution of density perturbations with overdensity δ in an expanding universe is

$$\frac{\partial^2\delta}{\partial t^2} + 2H(t)\frac{\partial\delta}{\partial t} = 4\pi G\rho_M\delta$$

where $H(t=t_o)$ is the present epoch Hubble parameter [7,8]. Because of the sensitivity of the growth rate to both the expansion history and the clustered matter density ρ_M, structure formation based studies that measure the growth rate to constrain the nature of dark energy do not suffer from parameter degeneracies to the same degree as simple distance measurement techniques. Structure formation based techniques include studies of the clustering of matter through measurements of the cosmic shear (the variations in the weak lensing shear distortions due to the projected matter distribution from location to location on the sky) [9,10], galaxy clustering techniques [11,12,13], and galaxy cluster surveys [14,15,16]. The cluster survey technique is especially powerful, because the change in the number density of clusters as a function of redshift is exponentially sensitive to the growth rate of structure [17,18,19]. Thus, even in the face of long term weak lensing experiments like LSST, we must proceed with large scale galaxy cluster surveys, because they provide another highly sensitive probe of the expansion history of the universe. In addition, galaxy cluster surveys offer high sensitivity to any possible non-Gaussianity in the distribution of density fluctuations like that predicted by recent theories like Ghost Inflation [20]. Naturally, using cluster surveys to characterize any non-Gaussianity would weaken the constraints on the expansion history $H(z)$.

The bottom line is that a large scale cluster survey provides a wealth of information about structure formation over the past 10 Gyr, and this in turn provides profound leverage on a variety of cosmological questions [21,16]. The cluster survey technique for studying dark energy has been improved significantly since its introduction through the efforts of many scientists [22,23,24,25,26,27,28,29,30,31,32,33]. A cluster survey carried out over large solid angle also constrains cosmology through the spatial clustering of the galaxy clusters [34,30,31]. The correlated positions of galaxy clusters (encoded in the cluster power spectrum) reflect the underlying correlations in the dark matter; these correlations contain a wealth of cosmological information, much like the information contained in the CMB anisotropy power spectrum. We plan to use the cluster

redshift distribution and the cluster power spectrum as powerful cosmological probes to study the cosmic acceleration.

Each of the key techniques for studying dark energy is subject to different systematics, and so studying the cosmic expansion history with multiple, independent techniques is a promising way of testing the accuracy of the measurements. The current state of the art in observational constraints on w requires combining multiple experiments to obtain a single interesting constraint (i.e. WMAP, SNe distances, galaxy power spectra) [4,35,36]. One should keep in mind that these combined analyses require consistency among the datasets, but the constraints from each individual experiment are currently so weak that it is challenging to make meaningful tests of this assumption. With the cluster surveys described below, we will move into a regime where a single experiment can provide interesting constraints by itself (as strong as or stronger than the best current combined constraints). With several precise measurements it will be possible to carry out meaningful tests of consistency among the independent experiments before combining them to obtain the highest possible precision. With proper control of systematics, any disagreement among the experiments indicates a breakdown in the theoretical context of the analysis– perhaps pointing to a flaw in our understanding of gravity! Thus, there is a huge payoff in accurately characterizing systematic uncertainties, and modern dark energy experiments are designed to meet this goal.

2 Cluster Surveys Present: The South Pole Telescope (SPT) Survey

Cluster surveys have been the focus of intense interest over the years. Currently, there are many serendipitous X-ray surveys underway using Chandra and XMM–*Newton*. In addition, large scale multiband optical surveys are underway using the SDSS data[37] and deeper, special purpose imaging[38]. A new generation of Sunyaev-Zel'dovich effect (SZE) interferometric instruments is now being turned to the task of SZE cluster finding, and two multiband, high angular resolution, 10^3 element bolometric mapping experiments have been designed to produce the arcminute scale angular resolution and low noise CMB maps required for cluster finding. These two experiments are the South Pole Telescope (SPT) and the Atacama Cosmology Telescope (ACT). Another arcminute resolution mapping experiment currently underway is the single frequency Atacama Pathfinder Expertiment (APEX). Below I will describe the SPT survey in some detail.

Beginning this fall the 10 meter South Pole Telescope (SPT; http://spt.uchicago.edu; PI Carlstrom)[39] will be deployed, beginning a three year program to survey the southern extragalactic sky in four frequencies (95 GHz, 150 GHz, 220 GHz and 274 GHz). A large ground screen will restrict SPT observations to sky south of -30° declination, leaving a roughly 4000 deg^2 region of low galactic dust emission. With a 10^3 element bolometer array, the SPT can rapidly survey large regions with arcminute angular resolution to target depths of between 10 and 30 μK per arcmin^2, depending on the band. Mock observations by T. Crawford (U Chicago) using hydrodynamical simulations and including primary CMB and extrapolations of the radio galaxy populations to the SPT frequencies indicate that the 5σ detection threshold in an SPT Sunyaev-Zel'dovich Effect (SZE) survey corresponds to clusters with virial masses of approximately 2.5×10^{14} $M_\odot$. With the WMAP3 [40] cosmology this corresponds to a sample of approximately 6500 galaxy clusters ($\sigma_8 = 0.75$). The 3σ sample is considerably larger, but it is potentially more difficult to interpret [41,42].

2.1 Staged Optical Followup

Multiband optical data are needed over the SPT region to determine cluster photometric redshifts, provide weak lensing mass constraints and enable multiwavelength galaxy cluster finding. For the SPT we have developed a staged optical followup program, which has already begun

with the Blanco Cosmology Survey (BCS '05-'07; http://cosmology.uiuc.edu/BCS; PI Mohr). The BCS is a 100 deg^2 *griz* imaging survey of sufficient depth to deliver photometric redshifts for L_* galaxies out to $z = 1$; it is being carried out on the Blanco 4m at CTIO, using 45 nights granted through the NOAO Survey program. The second stage involves a collaboration with the Kilo-degree Imaging Survey (KIDS '07+; http://www.strw.leidenuniv.nl/ kuijken/KIDS/), which will image at least 400 deg^2 of the SPT region using the ESO VST survey telescope. These first two stages provide imaging data for a sample of approximately 800 SPT clusters, which we will use to test our model of the SPT cluster selection (through comparisons of optical and mm-wave cluster lists) and to constrain the mm-wave cluster mass–observable relations with weak lensing. What we learn in these first two stages should enable us to take advantage of much larger samples in the subsequent stages. The third stage involves the Parallel Imager for Southern Cosmology Observations (PISCO '07-'09; PI Stubbs), which is a 5 arcmin field of view imager on Magellan that will simultaneously obtain *griz* images. Armed with SPT cluster lists, we estimate that we can obtain redshifts for approximately 100 clusters per night, making it possible to followup 3000 SPT clusters in a 30 night program. Full followup with deep, uniform photometry over the entire SPT region awaits the Dark Energy Survey (DES '09-'14; http://www.darkenergysurvey.org; Dir. Peoples). This final stage involves building a new 3 deg^2 camera (PI Flaugher) for the CTIO Blanco 4m and creating a data management system (PI Mohr) at NCSA to process 500 nights of survey data into science ready images and catalogs.

2.2 Forecasts and Challenges

Most forecasts for SPT constraints on the dark energy equation of state parameter have been around the 5% level (1σ). Early forecasts adopted essentially no priors from other experiments but used only the redshift distribution of the clusters [16,22]. More recent calculations included information from the cluster power spectrum and the luminosity function or mass function within redshift bins, but included our lack of knowledge of the mass-observable relations (so-called self-calibration)[29,27,30]. Over the past year new calculations have focused on the importance of determining the scatter about the mass–observable relations, something that can also be self-calibrated [31,32].

The most recent calculations (courtesy W. Hu, U Chicago) include (1) variation of the the dark energy equation of state, (2) our lack of knowledge of the scatter in the mass-observable relation, (3) the factor of four reduction in clusters with the latest WMAP constraints on the power spectrum normalization, (4) crude weak lensing mass constraints and (5) Planck priors from polarization and temperature anisotropy. Within this context the forecast 1σ fully marginalized constraints on $w_p(w_a)$ are 0.04(0.84).

The biggest uncertainty facing SPT cluster cosmology is the poorly constrained cluster radio galaxy population at high frequencies. In general, radio galaxy spectra extend to higher frequency and then break[43]. However, the behavior of the population above 100 GHz and at SPT fluxes of a few mJy are not well known. A study of the local 1.4 GHz radio galaxy population in about 600 X–ray selected clusters provides a strong constraint on their radial distribution within clusters (very centrally concentrated) and their luminosity function. Extrapolations to 150 GHz using a simple spectral model suggested by others for studies of the density of phase calibrators for ALMA suggest that cluster radio galaxies could significantly affect up to 10% of SPT clusters [44]. We are attacking this problem through studies of the spectra of local cluster radio galaxies and the redshift evolution of the cluster radio galaxy population. Ultimately, the SPT cluster selection model must be compared to cluster selection at other wavelengths where radio galaxies are not a problem. We plan to do this in the optical and X–ray; indeed, with our collaborators we are following up all the XMM–*Newton* fields within the SPT region to provide an X–ray selected comparison sample for tests of the SPT cluster selection. Our goal is

to push our understanding of the cluster selection to the level that it does not make a significant contribution to the forthcoming SPT cosmological constraints.

3 Cluster Surveys Future: The Dark Energy Cluster Survey (DECS)

With all the excitement about the current generation of cluster survey experiments it can be easy to lose sight of even more powerful future experiments. A survey of the entire extragalactic sky to the depths required to detect significant numbers of clusters out to redshift z$\sim$1 and beyond would enable new tests of the underlying cause for the cosmic acceleration. Mining the cosmological information from such a survey would require exquisite control of systematics in cluster mass estimation and cluster selection. At present the best understood and cleanest cluster selection technique is the X–ray, where the primary concern is the separation of cluster extended sources from AGN emission; with adequate angular resolution this challenge can be overcome. Moreover, all sky X–ray surveys are quite natural with available mirror and detector configurations in space, while 90GHz to 270Ghz SZE surveys with adequate angular resolution require exceptionally dry sites and 10 meter scale telescopes. Any large scale X–ray or SZE survey requires a multiband optical survey to obtain cluster photometric redshifts and constrain cluster masses using shear. Optical cluster surveys in themselves show great promise, but they may ultimately be limited in their cosmological utility by two factors: (1) the very large scatter ($\sim$75% 1σ) in the relationship between halo mass and the galaxy observables[38,45], and (2) the difficulty of reliably creating self–consistent, simulated universes that include galaxy formation, which can then be used to characterize the optical cluster selection. Weak lensing cluster finding has been shown to produce highly incomplete and contaminated cluster samples, and so proponents are now refocusing away from clusters and back on the very rich weak lensing cosmic shear experiments[46,9].

A recent proposal to study a large scale X–ray survey mission and to futher quantify and address the key systematic concerns is led by Mark Bautz (MIT). This mission, the Dark Energy Cluster Survey (DECS), would survey the entire extragalactic sky with novel X-ray optics that deliver XMM-like angular resolution over a wide field of view. Chandra-like CCD detectors would cover the focal plane, making for a very high etendue observatory, which could deliver samples of 10^5 X-ray cluster detections and detailed followup imaging of thousands of those systems. There is another pending mission called e-ROSITA (led by Guenther Hasinger; MPE, Garching) that employs different mirror and detector technology but would also lead to samples of 10^5 clusters. Missions of this sort during the next decade are especially interesting, because the required large scale optical imaging for cluster photometric redshifts and weak lensing mass constraints will have be acquired by the planned PAN-STARRs, DES and LSST large scale imaging experiments.

Forecasts for this "ultimate" cluster survey experiment were estimated by S. Wang and Z. Haiman (Columbia U) and include several novel elements to address systematic effects. The basic approach follows that described in the first section of this paper and recently endorsed by the Dark Energy Task Force report on dark energy experiments. Planck CMB temperature and polarization anisotropy are assumed as priors, and cosmological constraints on the dark energy density, dark energy equation of state parameter w_p and its variation with redshift w_a are examined within the context of varying curvature, matter density, baryon density, initial power spectrum index, power spectrum normalization, and Hubble parameter. The relationship between cluster observables (X–ray luminosity and emission weighted mean temperature) is modeled as a power law relation (i.e. slope changes with cluster mass) that evolves with redshift. A curvature parameter for these power law relations is introduced, and the scatter about these relations is modeled as log-normal. In addition, uncertainties in cluster survey selection and contamination are modeled by introducing a free scaling parameter into each redshift and mass

bin. Constraints on this system with 8 free cosmological parameters, 33 parameters to describe the evolution of the normalization, scatter and slope of the mass-observable relation, and an additional 45 selection scaling parameters come from (1) the redshift and flux distribution of the cluster sample, (2) the weak lensing cluster mass constraints (assumed to be 30% accurate at 1σ level), and (3) the clustering of the galaxy clusters.

Forecast 1σ constraints on the equation of state parameters are quite exciting, even in the face of the large amount of parametrized "freedom" introduced in our model. In particular, constraints on the equation of state parameter evolution are a factor of three better than for the case of SPT described above. Moreover, we use the 45 selection scaling parameters to examine how well we need to understand the cluster selection in each flux and redshift bin to be able to harvest the statistical information in the survey. Specifically, we introduce priors on these selection parameters, and these act essentially as a noise floor within each flux and redshift bin. For example, a 10% floor in selection that is added in quadrature with the statistical uncertainty in that bin makes samples exceeding $\sim$100 clusters in that bin of little utility. We examine forecasts with 10%, 1% and 0.1% selection floors. Our calculations indicate that to fully use the 10^5 clusters delivered by the DECS survey one must use simulations and mock observations to understand the incompleteness and contamination at about the 1% level. For X-ray surveys the primary selection concern is that combinations of X-ray point sources might masquerade as extended sources. In previous serendipitous ROSAT surveys with significantly worse image quality[47], contamination levels at the $\sim$1% level were achieved (confirmed through later high angular resolution Chandra imaging of these clusters). Therefore, we are optimistic that with the superior angular resolution of DECS and a program of mock observations to fully characterize the selection, it should be possible for us to achieve 1% control of selection systematics. The smaller sample of thousands of clusters observed for longer periods of time can be used to carry out an essentially independent cluster survey experiment that employs cluster X-ray emission weighted temperatures rather than fluxes. Built in cross-checks like these and robustness to uncertainties in the mass-observable relations make this future mission quite exciting. More details of this calculation will be reported elsewhere in a DECS paper.

4 Summary

There continues to be significant development of the large scale cluster survey technique for precise studies of cosmology and structure formation. This technique combines the growth of structure and the distance–redshift relation tests to enable powerful new probes of the nature of the cosmic acceleration. In combination, distance–redshift relation and growth of structure tests can in principle be used to differentiate simple dark energy models from modifications of gravity; in practice, differentiating these two possibilities will require exquisite control of systematics in multiple, independent tests.

Serendipitous X-ray surveys and dedicated, large scale optical and SZE surveys are now underway, and results should be available in the next year. The first multi-wavelength, arcminute resolution SZE imaging experiments SPT and ACT will become operational this winter. These current experiments will provide exciting cosmology and lay the groundwork for even larger scale future experiments. In addition, continuing advances in direct simulation of structure formation are providing the tools required to improve our understanding of systematics in cluster selection and the cluster mass–observable relations; these tools will enable even more powerful future cluster survey based studies of cosmology and structure formation. One such mission is DECS, a full sky X–ray cluster survey mission that will deliver a sample of 10^5 clusters with deep imaging spectroscopy of thousands.

Acknowledgments

Special thanks to Mark Bautz, John Carlstrom, Zoltan Haiman, Subha Majumdar, Sheng Wang and the South Pole Telescope and Dark Energy Cluster Survey teams for their important contributions to this review. This work is supported in part by a NASA Long Term Space Astrophysics program (NAG5-11415) and the NSF Office of Polar Programs (OPP-0130612) .

1. Perlmutter, S. et al., ApJ **517**, 565 (1999).
2. Schmidt, B. et al., ApJ **507**, 46 (1998).
3. Bahcall, N.A., Ostriker, J.P., Perlmutter, S. & Steinhardt, P.J., Science **284**, 1481 (1999).
4. Spergel, D.N., et al., ApJS **148**, 175 (.)
5. Perlmutter, S. & Schmidt, B., astro-ph/0303428 , (2003).
6. Reiss, A. et al., ApJ **607**, 665 (2004).
7. Peebles, P.J.E., *Principles of Physical Cosmology*, Princeton University Press: Princeton, 1994.
8. Peacock, J.A., *Cosmological Physics*, Cambridge University Press: Cambridge, 1999.
9. Kaiser, N., ApJ **388**, 272 (1992).
10. Hu, W. & Jain, B., *Phys. Rev.* D **70**, 043009 (2004).
11. Feldman, H.A., Kaiser, N., & Peacock, J.A., ApJ **426**, 23 (1994).
12. Matsubara, T. & Szalay, A., ApJ **556**, L57 (2001).
13. Hu, W. & Haiman, Z., *Phys. Rev.* D **68**, 063004 (.)
14. Perrenod, S.C., & Henry, J.P., ApJ **247**, L1 (1981).
15. Bahcall, N.A., Fan, **X.** & Cen, R., ApJ **485**, L53 (1997).
16. Haiman, Z., Mohr, J.J. & Holder, G.P. ApJ **553**, 545 (2001).
17. Press, W.H. & Schechter, P., ApJ **187**, 425 (1974).
18. Sheth, R.K. & Tormen, G., MNRAS **308**, 119 (1999).
19. Jenkins, A., Frenk, C.S., White, S.D.M., Colberg, J.M., Cole, S., Evrard, A.E., Couchman, H.M.P. & Yoshida, N., MNRAS **321**, 372 (2001).
20. Arkani-Hamed, N., Creminelli, P., Mukohyama, S. & Zaldariaga, M., JCAP **001**, 1 (2004).
21. Wang, L. & Steinhardt, P.J., ApJ **508**, 483 (1998).
22. Holder, G., Z. Haiman, and J.J. Mohr, ApJ **560**, L111 (2001).
23. Levine, E.S., Schulz, A.E. & White, M., ApJ **577**, 569 (2002).
24. Benson, A.J., Reichart, C. & Kamionkowski, M., MNRAS **331**, 71 (2002).
25. Weller, J., Battye, R.A. & Kneissl, R., *Phys. Rev. Lett.* **88**, 231301 (2002).
26. Weller, J., & Battye, R.A., New Astronomy Reviews **47**, 775 (2003).
27. Hu, W. *Phys. Rev.* D **67**, 081304 (2003).
28. Hu, W. & Kravtsov, A.V., ApJ **584**, 702 (2003).
29. Majumdar, S. and J.J. Mohr, ApJ **585**, 603 (2003).
30. Majumdar, S. and J.J. Mohr, ApJ **613**, 41 (2004).
31. Lima, M. and W. Hu, *Phys. Rev.* D **70**, 043504 (2004).
32. Lima, M. and W. Hu, *Phys. Rev.* D **72**, 043006 (2005).
33. Wang, S., Khoury, J., Haiman, Z. & May, M., *Phys. Rev.* D **70**, 13008 (2004).
34. Cooray, A., Hu, W., Huterer, D. & Joffre, M., ApJ **557**, L7 (2001).
35. Tegmark, M., *Phys. Rev.* D **69**, 103501 (2004).
36. Seljak, U. et al., *Phys. Rev.* D **71**, 103515 (2004).
37. Bahcall, N.A. et al, ApJS **148**, 243 (2003).
38. Gladders, M.D., Yee, H.K.C, Majumdar, S., Barrientos, L.F., Hoekstra, H., Hall, P.B. and Infante, L., ApJ **in press**, (2006).
39. Ruhl, J., P. A. R. Ade, J. E. Carlstrom, H.-M. Cho, T. Crawford, M. Dobbs, C. H. Greer, N. w. Halverson, W. L. Holzapfel, T. M. Lanting, A. T. Lee, E. M. Leitch, J. Leong, W. Lu, M. Lueker, J. Mehl, S. S. Meyer, J. J. Mohr, S. Padin, T. Plagge, C. Pryke,

M. C. Runyan, D. Schwan, M. K. Sharp, H. Spieler, Z. Staniszewski, and A. A. Stark, Proceedings of the SPIE **5498**, 11 (2004).
40. Spergel, D. N., R. Bean, O. Dore', M. R. Nolta, C. L. Bennett, G. Hinshaw, N. Jarosik, E. Komatsu, L. Page, H. V. Peiris, L. Verde, C. Barnes, M. Halpern, R. S. Hill, A. Kogut, M. Limon, S. S. Meyer, N. Odegard, G. S. Tucker, J. L. Weiland, E. Wollack, and E. L. Wright, ApJ **in press**, (2006).
41. Melin, J.-B., J. G. Bartlett, and J. Delabrouille, AA **429**, 417 (2005).
42. Melin, J.-B., J. G. Bartlett, and J. Delabrouille, AA **in press**, (2006).
43. Bolton, R.C., G. Cotter, G. Pooley, J.M. Riley, E.M. Waldram, C.J. Chandler, B.S. Mason, T.J. Pearson and A.C.S Readhead, MNRAS **354**, 485 (2004).
44. Lin, Y.-T. and J. J. Mohr, ApJ **submitted**, (2006).
45. Barkhouse, W. et al., ApJ **in press**, (2006).
46. Hennawi, J.F. & Spergel, D.N., ApJ **624**, 59 (2005).
47. Vikhlinin, A., McNamara, B.R., Forman, W., Jones, C., Quintana, H. & Hornstrup, A., ApJ **502**, 558 (1998).

A long duration balloon borne mm and sub-mm telescope for multi-frequency survey of galaxy clusters and CMB

F. Nati, L. Nati, L. Conversi, S. Masi, M. Calvo, P. de Bernardis, M. De Petris, G. De Troia, A. Iacoangeli, L. Lamagna, C. Marini Bettolo, A. Melchiorri, F. Melchiorri, F. Piacentini, G. Polenta,
Dipartimento di Fisica, Universita' La Sapienza, P.le A. Moro 2, 00185 Roma, Italy

P. Ade, P. Hargrave, P. Mauskopf, A. Orlando, G. Pisano, G. Savini, C. Tucker
Department of Physics and Astronomy, University of Cardiff, The Parade, Cardiff, UK

A. Boscaleri
IFAC-CNR, Via Panciatichi 64, Firenze, Italy

S. Peterzen
ISTARS and Agenzia Spaziale Italiana, Rome, Italy

S. Colafrancesco
INAF, Osservatorio di Monte Porzio, Rome, Italy

Y. Rephaeli
Tel Aviv University, Israel

G. Romeo, L. Salvaterra
Istituto Nazionale di Geofisica, Rome, Italy

A. Delbart, J.B. Juin, C. Magneville, J.P. Pansart, D. Yvon
DAPNIA/SPP CEA-Saclay, Gif sur Yvette, France

The main objective of the OLIMPO project, a large stratospheric telescope, is the measurement of the Sunyaev-Zeldovich effect in many clusters of galaxies during a long-duration balloon flight. We describe the OLIMPO experiment, and outline the scientific rationale of balloon-borne measurements of the effect.

1 OLIMPO Science

The high Galactic latitude sky at infrared and millimetric frequencies has three main sources of diffuse emission: the Cosmic Microwave Background (CMB) primary anisotropy, the Sunyaev-Zeldovich effect in clusters of galaxies, and the Far Infrared Background (FIRB) from early galaxies. The "cosmological window" extends roughly from 90 to 600 GHz. At lower frequencies interstellar emission of spinning dust grains, free-free and synchrotron emission from the interstellar medium dominate over the cosmological background, while at higher frequencies the clumpy foreground from "cirrus clouds" of interstellar dust dominates the sky brightness even at high Galactic latitudes. The only way to separate these different emissions - in order to allow cosmological parameter extraction - is to use multi-band experiments. OLIMPO will carry out

a survey in four frequency bands centered at 140, 220, 410 and 540 GHz. In this section we give a brief description of the different observables relevant for these surveys.

1.1 CMB Primary Anisotropy

CMB primary anisotropy can be detected in the lower frequency bands of OLIMPO. Taking advantage of its high angular resolution (a few arcmin, depending on the frequency), and concentrating on a limited area of the sky, OLIMPO will be able to measure the angular power spectrum of the CMB up to multipoles $\ell \lesssim 3000$, significantly higher than BOOMERanG, WMAP and Planck.

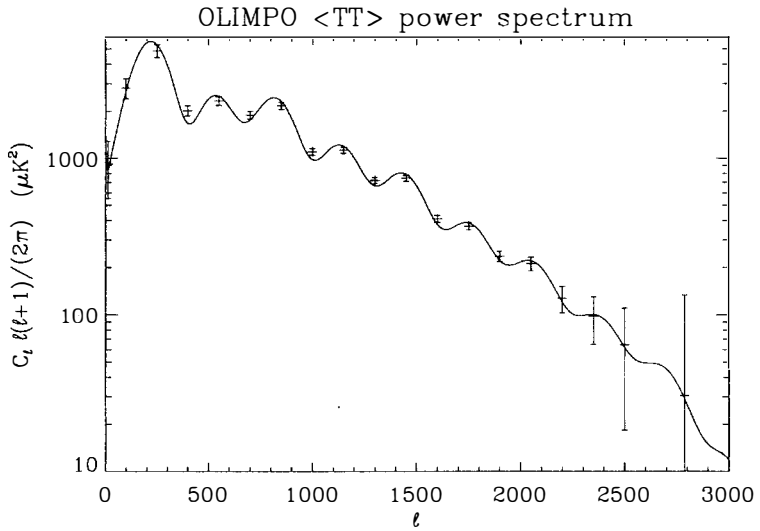

Figure 1: Angular power spectrum of CMB anisotropy expected from OLIMPO observations. For the simulations we assumed 4 days of integration over $f_{sky} = 0.3\%$ of the sky; 37 detectors with $NET = 200\mu K/\sqrt{Hz}$, and a resolution of 5′ FWHM.

OLIMPO measurements will be complementary and affected by very different systematics than those of the low-frequency (30 - 90 GHz) ground-based interferometers (see e.g. CBI, [3]), allowing a necessary cross-check for potential foregrounds. Also, the high multipoles tail of the power spectrum of the sky includes contributions from populations of discrete sources, such as distant clusters, early galaxies and AGNs. Only multi-band observations can discriminate between the contributions from these sources. The bands of OLIMPO listed above have been selected for optimal component separation by means of extensive simulations of the mm/sub-mm sky (see fig. 2).

1.2 S-Z Effect in Cluster of Galaxies

Clusters of Galaxies represent a late development in the bottom-up scenario for the formation of structures. The intra-cluster (IC) gas is bright in the X-ray band, due to thermal bremmstrahlung, and in the mm/sub-mm band due to Compton scattering of the CMB - the Sunyaev-Zeldovich (S-Z) effect. The effect is a systematic shift of photons from the R-J to the Wien side of the Planck spectrum [10,?,?], amounting to a decrement below 217 GHz, and an increment

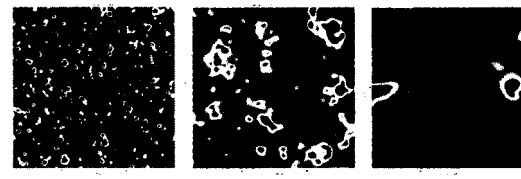

(a) Components maps at 143GHz

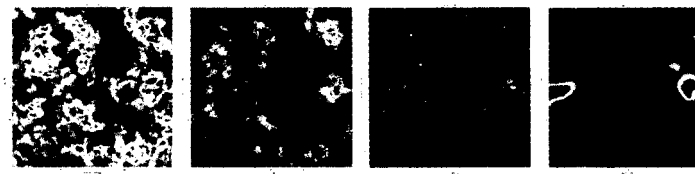

(b) Total maps for the four OLIMPO bands

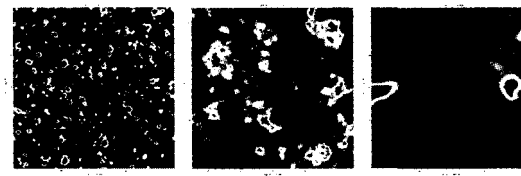

(c) Extracted maps at 143GHz

Figure 2: Simulations of expected signals: CMB anisotropies, SZ effect due to intracluster medium and IR background. OLIMPO is capable to disentangle the various components thanks to its characteristics: high resolution, high frequency channel that covers full SZ spectra, many low noise receivers

above this crossover frequency. Moreover, the S-Z effect is redshift independent, thus it can be measured in high redshift clusters much more optimally than in the complementary optical and X-ray surveys. This advantage obviously provides a unique tool to investigate the early evolution of structures. The OLIMPO bands are chosen to optimally sample the S-Z effect in clusters (see fig. 3) and distinguish it from CMB primary anisotropies and competing foregrounds. Moreover, the simultaneous observation of an increment at 410 and 540 GHz, in addition to measurements near the crossover frequency will allow us to measure the relativistic corrections (see e.g. [13,14,15]) and possibly also the gas temperature. even in the absence of X-ray data (fig. 3). We have carried out extensive simulations of the OLIMPO observations of clusters in the presence of Galactic Dust, CMB anisotropy, and instrumental noise. We plan to map about 40 known clusters during each of the planned OLIMPO flights. Reasonable integration time for each target can thus easily be several hours, spread on a sky patch of about 1 square degree centered on the cluster. Assuming a detector noise similar to the one achieved with BOOMERanG (i.e. 150 $\mu K/\sqrt{Hz}$ for each detector at 140 GHz), and using the nominal configuration of the four arrays, simulations show that the cluster parameters y, T_e and the CMB (ΔT) and dust ($\Delta\tau$) anisotropy can all be recovered with $\lesssim 10\%$ accuracy. In particular, if $y \sim 5 \times 10^{-5}$ and

$T_e \sim 10keV$, we get $\sigma_y \sim 10^{-6}$ and $\sigma_{T_e} \sim 2keV$ (see [16]). We will combine these measurements with X-ray measurements to build a "Hubble diagram" for the determination of H_o. We also expect to detect previously unknown clusters in the deep CMB anisotropy survey by OLIMPO. Such deep S-Z surveys will yield independent estimates of Ω_Λ and of Ω_m through the evaluation of clusters counts, and the shape of the power spectrum (see e.g. [17]).

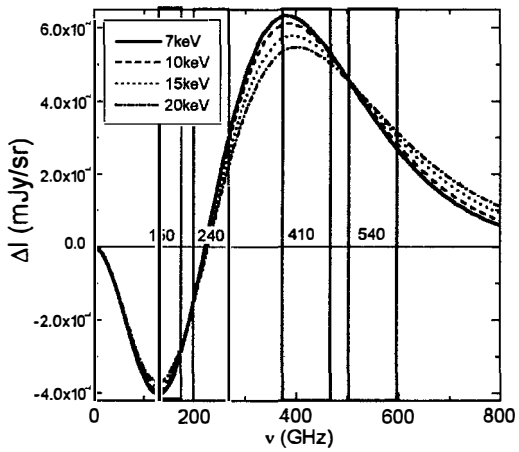

Figure 3: Spectrum of the Sunyaev-Zeldovich effect in a rich cluster of galaxies, for different temperatures of IC electrons (7 to 20 keV). The spectrum is compared to the OLIMPO bands at 150, 240, 410 and 540 GHz. Notice that the relativistic correction for high temperatures has opposite effects in the two high frequency bands of OLIMPO, thus breaking a degeneracy in the determination of the cluster temperature.

1.3 FIR Background

Many indications favor the bottom-up scenario for structure formation in the Universe. Small structures formed first, and larger structures merged later. Star forming regions in early galaxies produce intense thermal radiation from heated dust, which is now visible in the sub-mm band as the Extragalactic Far Infrared Background (FIRB) detected by COBE-FIRAS [4]. Resolving the FIR background and studying the unresolved component will allow us to investigate the cosmic "middle ages" at z = 1-10, when light shone again in the Universe after the "dark ages" following recombination. The steep spectrum of dust in the far infrared produces a large K-correction at redshift of 3-10, which is mostt optimally probed by sub-mm observations [5]. Cosmic star formation history can thus be investigated in a way completely orthogonal to the visible and NIR deep surveys. OLIMPO will be sensitive to the anisotropy of the FIRB, in an observational niche still to be explored (see [6,7]).

2 OLIMPO: the payload

OLIMPO is implementing a number of advanced technical solutions.

The main frame (fig. 4)is made out of aluminum alloys, and has been optimized to withstand 10g shocks (vertical) and 5g shocks (horizontal, any azimuth) at parachute opening.

The inner frame, with the attached telescope and the cryostat housing the detector system, can be tilted to set the observing elevation from 0^o to 60^o. The low elevations achievable allow

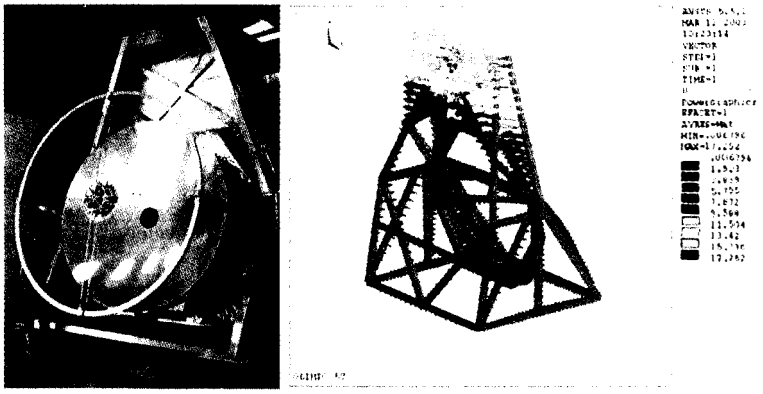

Figure 4: Left: The OLIMPO payload in a recent picture (all shields removed). Right: Structure deformations for a 5g horizontal load, as computed by finite elements modelling.

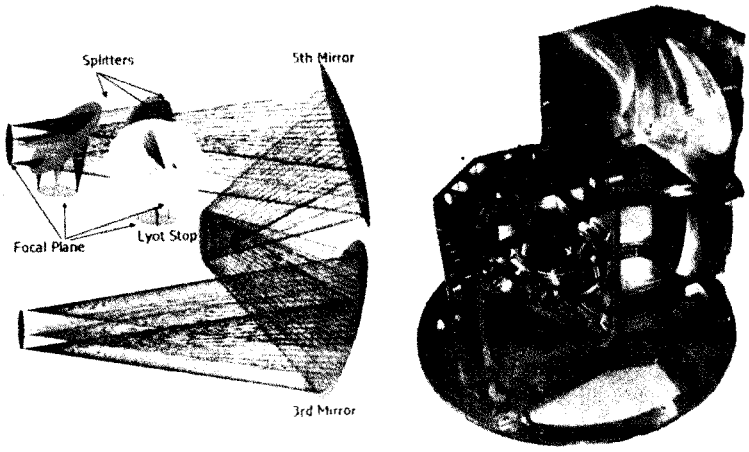

Figure 5: Left: Ray Tracing of the cryogenic section of the optics. From top to bottom are shown the vacuum window of the cryostat, the tertiary mirror, the Lyot Stop, the fifth mirror and the two dichroics splitting the beam on the four detector arrays. Right: its realization.

accurate ground-based calibrations of the system and the observation of planets for calibration during polar flights.

The telescope, developed in Rome, is an on-axis Cassegrain configuration with a 2.6m aluminum primary [18]. The secondary mirror is suspended by means of thin stainless steel blades to minimize the background from local structures and to avoid beam vignetting.

Sky scans are performed by slowly scanning the primary mirror in the cross-elevation direction. The modulator design is similar to the ones in [19,20], but allows a substantial reduction of the scan-synchronous offset by moving the primary mirror instead of the sub-reflector. Up to 3^o wide, 1^o/s cross-elevation scans are possible with this system. The full payload can also perform azimuthal scans, to cover wider regions. The telescope has been assembled; focusing and beam characterization at 90GHz and 140GHz are underway.

The detector system is made of four bolometer arrays, which are being developed in Cardiff together with the dichroics that allow multiband operation. These detectors are an evolution of the highly successful devices used in the BOOMERanG and Planck-HFI instruments [21]. In order to achieve low dispersion in the characteristics of the detectors, a fully photo-lithographic process producing TES (transition edge superconductor) sensors on silicon nitride islands on a Si wafer has been developed. In this way the entire bolometric arrays are being fabricated with a fully automated process. Filters and antennas can be integrated on the detectors wafer by means of micro-strip technology. The four arrays at 140, 220, 410 and 540 GHz will be composed of 19, 37, 37, 37 detectors, respectively. Each array will fill the optically correct area of the focal plane (about 0.25^o in diameter projected on the sky).

The cryogenic reimaging optics is being developed in Rome. It is mounted in the experiment section of the cryostat, at 2K, while the bolometers are cooled at 0.3K. Extensive baffling and a cold Lyot stop reduce significantly straylight and sidelobes. Optics have been optimized to allow diffraction-limited operation even with significant tilt of the primary mirror during sky scans.

The bolometer arrays and the reimaging optics will be arranged into a modified version of the long duration cryostat developed for BOOMERanG [22,23]. The main difference here is the use of fiberglass cylinders to replace the kevlar cords suspending the LN and LHe tanks. Fiberglass cylinders provide higher stiffness to the system, which is a primary requisite to keep the detector arrays centered on the optical axis within diffraction limits during operation at different elevations.

Radiation is refocused into the cryogenic optics through a side of the cryostat, to allow operation of the system with the telescope axis horizontal or at low elevation, during ground based calibrations and during in-flight calibrations on planets. The side window is made of Propozote foam, a material with extremely high (> 99%) transmittance at the operating frequencies, thus ensuring minimum excess background on the detectors, while preserving excellent mechanical strength and vacuum tightness.

The other payload systems (on-board data conversion and acquisition, Attitude Control System, Telemetry, Thermal Shields and Housekeeping) are similar to those of the BOOMERanG experiment [24,25]. The Attitude Control System is derived from that of BOOMERanG and completed with day and night-time attitude sensors: laser gyroscopes, sun sensors, and star camera. The first flight will be from Svalbard to Greenland.

Acknowledgments

This work is supported in Italy by the Agenzia Spaziale Italiana and by MIUR.

1. White M., Ap.J. **555**, 2001 (88)
2. Bond J.R., et al., MNRAS **291**, 1997 (L33)
3. Readhead A.C.S. et al., Ap.J. **609**, 2004 (498)

4. Puget J.L. et al., Astron. Astrophys. **308**, 1996 (L5)
5. Hughes D.H. et al., MNRAS **871**, 2002 (335)
6. Hauser M.G. & Dweck E., Ann. Rev. Astron. Astrophys. **39**, 2001 (249)
7. Magliocchetti M., et al., MNRAS **325**, 2001 (1553)
8. Giommi P. & Colafrancesco S., Astron. Astrophys. **414**. 2004 (7)
9. Mason B.S. et al., Ap.J. **591**, 2003 (540)
10. Sunyaev R. & Zeldovich Y., Astrophysics and Space Science **7**, 1970 (3)
11. Birkinshaw M., Phys. Rept **310**, 1999 (97)
12. Rephaeli Y., Ann. Rev. Astron. Astrophys. **33**, 1995 (541)
13. Shimon M., Rephaeli Y., New Astron. **9**, 2004 (69)
14. Hansen S., Pastor S., Semikoz D.V., Ap.J. **573**, 2002 (L69)
15. Colafrancesco S., Marchegiani P., Palladino E., Astron. Astrophys. **397**, 2003 (27)
16. Conversi L. et al., in preparation (2004)
17. Carlstrom J.E., Holder G.P., Reese E.D., Ann. Rev. Astron. Astrophys. **40**, 2002 (643)
18. De Petris M., Liberati F., Gervasi M., Appl. Optics **28**, 1989 (1785D)
19. de Bernardis P., et al., Infrared Phys. **29**, 1989 (1005)
20. Mainella G., et al., Appl. Opt. **35**, 1996 (2246)
21. Mauskopf P., et al., Appl. Opt. **36**, 1997 (765)
22. Masi S., et al., Cryogenics **39**, 1999 (217)
23. Masi S., et al., Cryogenics **38**, 1998 (319)
24. Piacentini F., et al., Ap.J.Suppl. **138**, 2002 (315)
25. Crill B., et al., Ap.J.Suppl. **148**, 2003 (527)

The impact of instrumental systematics on CMB polarimetry experiments

D. T. O'Dea
Astrophysics Group, Cavendish Laboratory,
J. J. Thomson Avenue, Cambridge, CB3 0HE, U.K.

The effects of instrumental systematic errors on the potential of CMB polarization experiments targeted to detect primordial B-modes is investigated. The errors are parameterized in a general manner, and their transformation under instrument rotation is discussed. The correspondence to known errors introduced via the receiver and the optics is found, with a half-wave-plate receiver considered as an example. This receiver is found to have the significant property of not coupling the total intensity into polarization, provided the optics are perfect. A fast method for finding appropriate limits for such errors is presented, which includes the propagation of systematic errors through to biases in cosmological parameters. This method incorporates an arbitrary scan strategy, specified by a list of instrument orientations for each pixel. Example results are given in the context of next-generation experiments such as Clover.

1 Introduction

There is currently a great deal of interest and activity in the field of CMB polarimetry as recent advances in technology are beginning to open up the possibility of accessing the expected wealth of cosmological information encoded in the polarization of the CMB. In particular, a detection of primordial B-modes is seen as a promising method for measuring the tensor-to-scalar ratio, r, which would help constrain the current plethora of inflationary scenarios. However, B-mode anisotropies are known to be at least two orders of magnitude smaller than the temperature anisotropies, and so their detection presents a great experimental challenge, and requires, amongst other things, exquisite control of instrumental systematic errors.

2 Modelling instrumental systematic errors

2.1 Müller matrices and receiver errors

For systems that simply alter the state of polarization of the incoming radiation, we can describe the effects on the Stokes parameters via a Müller matrix, $\mathbf{M}$. The observed Stokes vector, $\boldsymbol{s}_{\rm obs}$ is related to the Stokes vector of the incoming radiation, $\boldsymbol{s} = (T, Q, U)^T$, by $\boldsymbol{s}_{\rm obs} = \mathbf{M}\boldsymbol{s}$. Working in the flat-sky limit, we adopt Cartesian co-ordinates with the z-axis outward along the line of sight, and x- and y-axes pointing north-south and west-east respectively. Therefore, to comply with IAU standards, the Stokes parameters are defined using the x and negative y directions. It is useful to work with the complex Stokes vector, $p = (T, P, P^*)^T$, where $P = Q + iU$, as these spin states have a particularly simple transformation under basis rotation. Rotating the x-axis through an angle ψ towards the negative y-axis, we find $P \mapsto Pe^{-2i\psi}$; that is the P field has a spin of -2. We adopt the conventions that the Müller matrices are defined in the instrument basis,

and the Stokes parameters are always expressed in the sky basis. When these two bases coincide the instrument is in its fiducial orientation. Under a rotation of the instrument by ψ, the observed Stokes vector becomes $\boldsymbol{p}_{\rm obs}(\boldsymbol{x};\psi) = \boldsymbol{\Lambda}^{\dagger}(\psi)\mathbf{M}\boldsymbol{\Lambda}(\psi)\boldsymbol{p}(\boldsymbol{x})$, where $\boldsymbol{\Lambda}(\psi) \equiv {\rm diag}(1, e^{-2i\psi}, e^{2i\psi})$. We will make use of the parameterization for the differences between observed and actual Stokes parameters defined by Hu *et al.*[1],

$$\delta(Q \pm iU) = (a \pm 2i\omega)(Q \pm iU) + (f_1 \pm if_2)(Q \mp iU) + (\gamma_1 \pm i\gamma_2)T. \tag{1}$$

Of particular interest are γ_1 and γ_2 as they measure the level of total intensity leakage to polarization, and, as the total intensity signal is expected to be several orders of magnitude greater than the one we wish to detect, the tolerance limits on these parameters will be very strict.

The propagation of radiation through a receiver can be described by a Jones matrix, **J**. Importantly, any systematic errors in a component of the receiver can generally be parameterized in its Jones matrix. There are many different receiver architectures, and here we will consider one with particular relevance to CMB polarimetry, the rotating half-wave-plate receiver, in which the incoming radiation passes through a half-wave-plate rotating at a constant rate, ν, before being split into orthogonal components by an OMT. In the ideal case, the final Jones matrix is

$$\mathbf{J}_{\rm tot} = \mathbf{J}_{\rm omt}\mathbf{J}_{\rm rot}^{\rm T}\mathbf{J}_{\rm hwp}\mathbf{J}_{\rm rot} = \begin{pmatrix} \cos 2\nu t & \sin 2\nu t \\ \sin 2\nu t & -\cos 2\nu t \end{pmatrix}. \tag{2}$$

After propagating through the receiver, the two components pass into detectors which measure their power. The Stokes parameters can then be recovered, for the Q and U parameters by integrating the detector difference multiplied by $\cos 4\nu t$ and $\sin 4\nu t$ respectively over time. We can now introduce systematic errors, parameterized in the Jones matrices such that

$$\mathbf{J}_{\rm omt} = \begin{pmatrix} 1+g_1 & \epsilon_1 e^{i\theta_1} \\ \epsilon_2 e^{i\theta_2} & (1+g_2)e^{i\alpha} \end{pmatrix}, \qquad \mathbf{J}_{\rm hwp} = \begin{pmatrix} 1+h_1 & \zeta_1 e^{i\chi_1} \\ \zeta_2 e^{i\chi_2} & -(1+h_2)e^{i\beta} \end{pmatrix}. \tag{3}$$

We also introduce a phase shift error of $\delta\phi$ into the rotation. Following these errors through, and expanding to first order in each parameter, we find perturbations to the observed Stokes parameters that can be expressed as

$$a = g_1 + g_2 + h_1 + h_2, \qquad 2\omega = \epsilon_1\cos\theta_1 - \epsilon_2\cos\theta_2 - 4\delta\phi - \zeta_1\cos\chi_1 - \zeta_2\cos\chi_2 \tag{4}$$

with $f_1 = f_2 = \gamma_1 = \gamma_2 = 0$. Significantly, this suggests that, assuming the rest of the instrument is perfect, a rotating-half-wave plate will not cause total intensity to leak into polarization.

2.2 Müller fields and optical errors

The propagation of the Stokes vector through the optics is described by matrix-valued fields, $\mathbf{M}(\boldsymbol{x})$, which couple the Stokes vector fields on the sky to the observed vector for a particular pointing. That is, with the instrument at an angle ψ, the observed Stokes vector is

$$\boldsymbol{p}_{\rm obs}(\boldsymbol{x};\psi) = \int {\rm d}^2\boldsymbol{x}'\, \boldsymbol{\Lambda}^{\dagger}(\psi)\mathbf{M}(\mathbf{R}_{\psi}^{-1}\boldsymbol{x}')\boldsymbol{\Lambda}(\psi)\boldsymbol{p}(\boldsymbol{x}+\boldsymbol{x}'), \tag{5}$$

where **R** is the rotation matrix. The relevant matrix fields are related to the far-field radiation patterns of the instrument, $\boldsymbol{E}_A$ and $\boldsymbol{E}_B$ as

$$\begin{aligned}
M_{QT} &= \tfrac{1}{2}(|\boldsymbol{E}_A|^2 - |\boldsymbol{E}_B|^2) \\
M_{QQ} &= \tfrac{1}{2}(|E_{A\,\rm co}|^2 - |E_{A\,\rm cross}|^2 + |E_{B\,\rm co}|^2 - |E_{B\,\rm cross}|^2) \\
M_{QU} &= \tfrac{1}{2}(E_{A\rm co}E^*_{A\,\rm cross} + E_{B\,\rm co}E^*_{B\rm cross}) + {\rm c.c.} \\
M_{UT} &= \tfrac{1}{2}(-E_{A\,\rm co}E^*_{B\,\rm cross} + E_{A\,\rm cross}E^*_{B\,\rm co}) + {\rm c.c.} \\
M_{UQ} &= \tfrac{1}{2}(-E_{A\,\rm co}E^*_{B\rm cross} - E_{A\,\rm cross}E^*_{B\,\rm co}) + {\rm c.c.} \\
M_{UU} &= \tfrac{1}{2}(E_{A\,\rm co}E^*_{B\,\rm co} - E_{A\,\rm cross}E^*_{B\,\rm cross}) + {\rm c.c.}
\end{aligned} \tag{6}$$

where, for example, M_{QT} is the matrix element that couples T into Q. We have defined the co-polar components along the x- and negative y-axes respectively, and adopt the Ludwig-III standard for cross-polar directions.

We can introduce systematic errors parameterized in the beam fields. We consider pointing errors $\boldsymbol{b}_A$ and $\boldsymbol{b}_B$ and ellipticities e_A and e_B aligned with the instrument axes. For brevity we neglect cross-polar errors, but they can be included straightforwardly. Hence, we have

$$E_{A\,\mathrm{co}} = \frac{1}{\sqrt{2\pi\sigma^2(1-e_A^2)}} e^{-\frac{1}{4\sigma^2}\left(\frac{(x-b_{A,x})^2}{(1+e_A)^2}+\frac{(y-b_{A,y})^2}{(1-e_A)^2}\right)}, \quad (7)$$

with a similar form for $E_{B\,\mathrm{co}}$, with $A \mapsto B$. We reparameterize the errors as $\boldsymbol{p} = \frac{1}{2\sigma}(\boldsymbol{b}_A + \boldsymbol{b}_B)$, $\boldsymbol{b}_d = \frac{1}{2\sigma}(\boldsymbol{b}_A - \boldsymbol{b}_B)$, $e_s = \frac{1}{2}(e_A + e_B)$ and $q = \frac{1}{2}(e_A - e_B)$. Expanding equation (5) to first order in these parameters, and integrating by parts we find (see Hu *et al.* [1]),

$$\delta(Q\pm iU)(\sigma) = \sigma\boldsymbol{p}\cdot\nabla(Q\pm iU)(\sigma)+\sigma\boldsymbol{b}_d\cdot\nabla T(\sigma)+\sigma^2 e_s(\partial_x^2-\partial_y^2)(Q\pm iU)(\sigma)+\sigma^2 q(\partial_x^2-\partial_y^2)T(\sigma) \quad (8)$$

with the instrument in its fiducial orientation and where $T(\sigma)$ is the beam-smoothed T field etc.

For general errors, it is useful to introduce a decomposition of the Müller fields into components that transform irreducibly under rotation. That is,

$$\mathbf{M}(\boldsymbol{x}) = \frac{1}{2\pi\sigma^2}\sum_{mn}\mathbf{M}_{mn}\sigma^{m+n}(\partial_x + i\partial_y)^m(\partial_x - i\partial_y)^n \exp[-\boldsymbol{x}^2/2\sigma^2]. \quad (9)$$

Using this decomposition, equation (5) becomes

$$\boldsymbol{p}_{\mathrm{obs}}(\boldsymbol{x};\psi) = \sum_{mn} e^{i(m-n)\psi}\boldsymbol{\Lambda}^\dagger(\psi)\mathbf{M}_{mn}\boldsymbol{\Lambda}(\psi)(-\sigma)^{m+n}(\partial_x + i\partial_y)^m(\partial_x - i\partial_y)^n\boldsymbol{p}(\boldsymbol{x};\sigma). \quad (10)$$

All errors considered above can be expressed in this general manner.

The perturbations in equations (1) and (8) are relevant for a raster scan, in which each sky pixel is visited in the fiducial orientation. Importantly, the different spin properties of the contamination fields means that some of the errors can be controlled through beam rotation, for example, for an 'ideal' scan, in which each pixel is visited in every orientation, the γ, f, $\boldsymbol{b}_d$, p and e_s terms disappear from these equations. Only those fields with the correct spin remain.

3 Power spectra and cosmological constant biases

In order to assess fully the impact of a systematic error, it is necessary to follow its effect through to the fundamental science products of the experiment. Here, initially this is the B-mode power spectrum. To calculate the power spectrum, we take the simple approach of Fourier transforming the Stokes parameter fields and averaging the power in each mode in annuli in Fourier space. For example an e_s error with a raster scan leads to a bias in the power spectrum of $e_s^2(\sigma^4 l^4 - \sigma^2 l^2)\mathcal{C}_b^B$, and a γ_1 error a bias of $\frac{1}{2}\gamma_1^2\mathcal{C}_b^T$. These biases are scan dependent: for an ideal scan the e_s bias is $e_s^2(\sigma^4 l^4/2 - \sigma^2 l^2)\mathcal{C}_b^B$ and the γ_1 bias disappears. (The e_s results require map perturbation terms proportional to e_s^2.) We can also consider an arbitrary scan strategy, which is useful for two reasons. Firstly, to assess the extent to which we can control errors with beam rotation with a realistic scan (the ideal scan is unrealizable from the ground). Secondly, for a realistic scan, each pixel is treated differently and this can lead to a mixing of the E- and B-modes in a manner that isn't seen for either the raster or ideal scans. Due to the nature of the mixing, it may be difficult to remove the effects even for calibrated errors. For a γ_1 error, averaging over the visits to a pixel during a scan (labeled by j), the observed spin states are

$$(Q \pm iU)_{\mathrm{obs}}(\mathbf{x}) - (Q \pm iU)(\mathbf{x}) = \frac{\sum_j e^{\pm 2i\psi_j}}{\sum_j}\gamma_1 T(\mathbf{x}) = \gamma_1 R_{\pm 2}(\mathbf{x})T(\mathbf{x}) \quad (11)$$

Table 1: Tolerance limits for a raster scan.

Parameter	a	ω	$\gamma_{1,2}$	$f_{1,2}$	q	$\lvert\boldsymbol{b}_d\rvert$
Limit	5×10^{-3}	4×10^{-3}	1×10^{-4}	1×10^{-2}	1×10^{-2}	2×10^{-3}

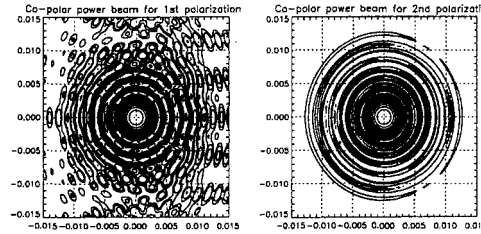

Figure 1: Power distribution of simulated co-polar beams. (Simulations by Grimes, Yassin and Johnson 2006).

where we have introduce the scan dependent function, $R(\boldsymbol{x})$. This leads to

$$C^B_{\rm obs} = C^B + \frac{\gamma_1^2}{32\pi^2 f_{\rm sky}} \int {\rm d}\phi_l \int {\rm d}^2\boldsymbol{l}' |(R_2(\boldsymbol{l}-\boldsymbol{l}')e^{2i\phi_l} + R_{-2}(\boldsymbol{l}-\boldsymbol{l}')e^{-2i\phi_l}|^2 C^T(l') \qquad (12)$$

By starting with equation (10) we can derive an equivalent result for the irreducible decomposition. This is useful as it removes the need to undertake Monte-Carlo simulations to investigate the effects of systematic errors with an arbitrary scan and so provides a much faster method.

Having described the biases in the power spectrum, we can use a simple maximum likelihood method to find the expected bias in r, the ultimate target of CMB polarimetry. Assuming Gaussian errors, σ_b, in the power spectrum estimates, with b labelling the bands we have

$$\Delta r_{\rm sys} = \frac{\sum_b \partial_r C_b^B (C^B_{\rm obs} - C^B)_b/\sigma_b^2}{\sum_b (\partial_r C_b^B)^2/\sigma_b^2} \qquad (13)$$

We are now armed to find tolerance limits on the defined errors. Here, we set tolerances such that the bias introduced in r is less than 10% of the expected random error in r, under conditions appropriate for next-generation ground-based experiments. For a raster scan we find the limits shown in Table 1. For a semi-realistic scan, based on constant elevation scans of a low foreground patch from Dome C, we find that the contamination in r increases ten fold for an e_s error over the raster scan result (which is similar to the ideal scan result) as a result of E- and B-mode mixing, and decreases by almost a factor of two from the $\boldsymbol{b}_d$ error shown in Table 1 due to beam rotation.

We can also calculate the biases in the power spectra and r caused by real (or simulated) beam patterns, which can help uncover unexpected errors, or to investigate errors that are hard to parameterize. For example, the beams shown in Figure 1 are co-polar power beams with contours down to the -63dB level simulated using GRASP 9 for a realistic optical setup. By forming the Müller fields as given in equation (6) we can find the power spectrum bias by averaging the power in the fields in annuli in Fourier space. For a raster scan, this reveals a contamination to the power spectrum at $l < 70$ that leads to a bias in r of around 15% of the random error. This is due to the small (less than -50dB) differences in the two beams away from the beam centres, that cause total intensity leakage into Q, as M_{QT} is proportional to the beam difference. This leakage can be controlled with beam rotation.

References

1. W. Hu, M. M. Hedman and M. Zaldarriaga, *Phys. Rev.* D **67**, 043004 (2003)

Inflationary model selection and the Planck satellite

Cédric Pahud, Andrew R. Liddle, Pia Mukherjee, David Parkinson
Astronomy Centre, University of Sussex, Brighton BN1 9QH, United Kingdom

This article gives a brief overview of results given in Ref. [1]. We use Bayesian model selection techniques to explore the ability of the Planck satellite to constrain inflationary parameters, here focussing on its ability to distinguish a power-law spectrum from a Harrison-Zeldovich spectrum.

1 The Planck Satellite

Figure 1: Satellite to be launched by ESA in 2008. [Image courtesy ESA/Planck collaboration]

2 Model Selection

One of the key goals in cosmology is to determine the necessary number of cosmological parameters to describe the Standard Model. As such, the aim is to differentiate between cosmological models with different numbers of parameters. To solve this problem, we use a statistical approach known as **Bayesian model selection**.

We are interested in forecasting the ability of the Planck satellite to determine the nature of the primordial perturbation spectrum. For this purpose, we compare the two following models:

M_1) a flat, Harrison-Zel'dovich model with a cosmological constant,
M_2) the same as M_1, except allowing the scalar spectral index to vary in the range of 0.8-1.2.

3 The Evidence

The Bayesian model selection technique consists of evaluating the evidence $E(M)$ for each model M, given by

$$E(M) \equiv P(D|M) = \int d\theta P(D|\theta, M) P(\theta|M). \quad (1)$$

It corresponds to the integration of the likelihood $P(D|\theta, M)$ over the set of parameters θ of a model M, considering the data D, and the prior $P(\theta|M)$ is normalized to unity. We use a **nested sampling** algorithm (Skilling [2], Mukherjee et al. [3]) to find the points to compute the evidence and simulate the data D using the best-fit WMAP models [4]. The evidence characterizes how well a model M can fit the data D. To compare our two models, we consider the Bayes factor, defined as $B_{12} \equiv E(M_1)/E(M_2)$, and we use the Jeffreys' scale [5] to determine the significance of any difference in evidence between the two models.

Jeffreys' Scale (Let's suppose that M_1 has the higher evidence)

$\ln B_{12} < 1$	=>	not worth more than a bare mention
$1 < \ln B_{12} < 2.5$	=>	substantial
$2.5 < \ln B_{12} < 5$	=>	strong to very strong
$5 < \ln B_{12}$	=>	decisive

4 Main Point of Interest

Using parameter values consistent with WMAP, Planck-quality data was simulated for different values of the scalar spectral index n_S. We aim to forecast Planck's ability to distinguish between the Harrison-Zel'dovich model and a model where n_S varies and is to be fit from the data. Thus, we calculate the Bayes factor for different simulated data, corresponding to different possible values of n_S, which the Planck satellite is expected to measure at the precision of ± 0.005 [6]. In the future, the Planck measurement of the scalar spectral index will make it possible, considering the Jeffreys' scale, to discriminate between the two models.

5 Results

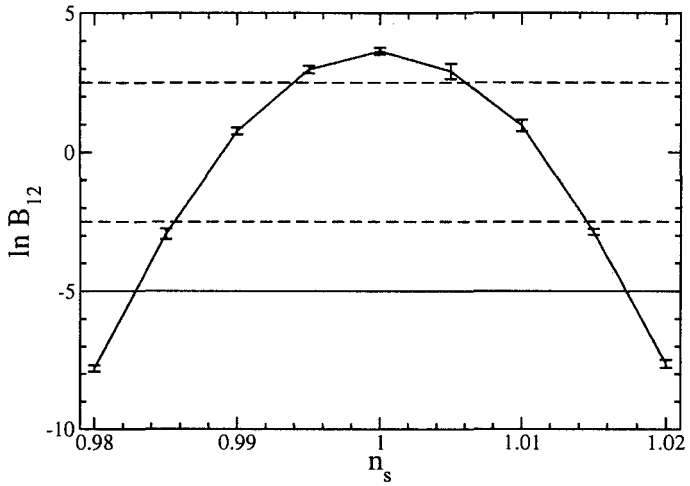

Figure 2: The horizontal lines indicate where the comparison becomes 'strong' (dashed) and 'decisive' (solid) on the Jeffreys' scale. The calculations were done using CosmoNest, available at www.cosmonest.org.

We see that if the true value lies in the range $0.989 < n_S < 1.011$, Bayesian model selection will favour the Harrison-Zel'dovich model, and within the narrower range $0.994 < n_S < 1.006$ it will give strong support to that model, though Planck on its own is not powerful enough to be able to decisively favour Harrison-Zel'dovich over n_S-varying model even if Harrison-Zel'dovich is the true case. Only once $n_S < 0.986$ or $n_S > 1.014$ can Planck offer strong evidence against Harrison-Zel'dovich, rapidly becoming decisive as the fiducial value moves away from unity beyond 0.983 or 1.017.

References

1. C. Pahud, A.R. Liddle, P. Mukherjee and D. Parkinson, astro-ph/0605004, accepted by *Phys. Rev.* D.
2. J. Skilling, in *Bayesian Inference and Maximum Entropy Methods in Science and Engineering*, ed. R. Fischer et al., Amer. Inst. Phys., conf. proc., 735, 395 (2004), (available at http://www.inference.phy.cam.ac.uk/bayesys/).
3. P. Mukherjee, D. Parkinson and A.R. Liddle, 2006, astro-ph/0508461.
4. D. N. Spergel et al. (WMAP Collaboration), astro-ph/0603449.
5. H. Jeffreys, *Theory of probability*, 3rd ed, Oxford University Press (1961).
6. Planck HFI blue book.

THE HUBBLE SPHERE HYDROGEN SURVEY

Jeffrey B. Peterson[a] and Kevin Bandura[b]
Department of Physics, Carnegie Mellon University
5000 Forbes Ave, Pittsburgh, PA 15213, USA

Ue Li Pen[c]
Canadian Institute for Theoretical Astrophysics, University of Toronto
60 St. George StreetToronto, Ontario, M5S 3H8, Canada

An all sky redshift survey, using hydrogen 21 cm emission to locate galaxies, can be used to track the wavelength of baryon acoustic oscillations imprints from $z \sim 1.5$ to $z = 0$. This will allow precise determination of the evolution of dark energy. A telescope made of fixed parabolic cylindrical reflectors offers substantial benefit for such a redshift survey. Fixed cylinders can be built for low cost, and long cylinders also allow low cost fast fourier transform techniques to be used to define thousands of simultaneous beams. A survey made with fixed reflectors naturally covers all of the sky available from it's site with good uniformity, minimizing sample variance in the measurement of the acoustic peak wavelength. Such a survey will produce about a billion redshifts, nearly a thousand times the number available today. The survey will provide a three dimensional mapping of the bulk of the Hubble Sphere.

1 Introduction

If the universe today is accelerating as it expands, some anti-gravity agent, some Dark Energy, must be acting on Hubble-radius scales. On galactic scales, however, ordinary attractive gravity dominates, otherwise galaxies and galaxy clusters would never have assembled. The strength of the dark energy force must be a different function of distance than the force of ordinary gravity.

In the past physical scales were compressed, and average matter densities were higher, so attractive gravity dominated, even on hubble-radius scales. This means the universal expansion has likely made a recent transition from deceleration to acceleration. We should be able to witness this shift by measuring the expansion rate history $H(z)$ from redshift zero to ~ 1.5.

A wide variety of programs have been proposed to measure the expansion history, and some of the most promising techniques involve the measurement of baryon acoustic oscillations[1]. Before the recombination epoch, at redshift 1100, the ionized cosmic material supported acoustic oscillations. Loss of ionization at that epoch decoupled the baryonic material from the CMB photons, terminating these oscillations and establishing in the CMB the acoustic peak patterns[2] [3] shown in detail by the WMAP satellite[4]. The baryon density field was also imprinted with acoustic oscillation structure and these $\sim$ $100Mpc$ acoustic peaks have survived to today[3]. Both the 2df[5] and Sloan Digital Sky Survey[6] teams report two sigma detection of acoustic peak

[a] jbp@cmu.edu
[b] ace@cmu.edu
[c] pen@cita.utoronto.ca

features in the power spectrum of the low redshift galaxy density field. Since the wavelength of the acoustic oscillation spectral peak was imprinted at a particular comoving wavelength throughout the universe, it can be used as a standard ruler[7]. Measuring the angular and redshift-space wavelengths of the acoustic peaks over a wide range of redshifts allows measurement of the history of the expansion rate $H(z)$[8].

Because the acoustic peak wavelength is so long, the peak can be detected in the power spectrum and measured well, even with a low-completeness survey[9]. The density field is sampled only where galaxies are detected, so there will be a shot noise contribution to the wavelength uncertainty[10]. There will also be an unavoidable cosmic variance uncertainty, and these two contributions are equal at about 1000 galaxies per square degree ($z = 1.5$, $\Delta z = 0.2$). Assuming a Schecter mass function, this corresponds to a survey detection threshold at about M^{*}[11], so only the brightest one percent of the luminosity function need be detected to reach the cosmic variance limit.

The use of redshift surveys to constrain the expansion history has been studied by several authors[1,8,10,12,13]. An all sky survey with sufficient sensitivity to detect M* galaxies at redshift 1.5 is estimated to have about 5 % sensitivity to the equation of state of dark energy $w = p/\rho$, and 10 % sensitivity to variation of w across the redshift range zero to one[1,10,12,13]. The purpose of this paper is not to review these estimates, but rather to introduce a survey program that, using off the shelf technology, at modest cost, can accomplish this important measurement.

The survey telescope discussed here uses the 21 cm hyperfine emission of hydrogen, both for detection of galaxies and for measurement of their redshift. This allows the techniques and advantages of GHz-frequency radio astronomy to be applied. Recent advances in digital signal processing technology and in mobile telephone technology, combined with proven techniques of reflector engineering make the construction of this telescope much simpler than a few years ago.

If galaxies did not evolve, and if a concordance model with $w = -1$ applies, the received 21 cm flux from a galaxy at redshift 1.5 would be about $2\mu Jy$ (see the appendix). But galaxies do evolve, and at $z = 1.5$ we are looking back to about half the current age of the universe. In spiral galaxies gas is turned into stars over time. At the current epoch the gas mass to stellar mass ratio is about 0.1. The gas supply is heavily depleted. The star formation rate at $z = 1.5$ is about ten times the rate today, indicating a higher gas mass fraction, but there is currently no good direct measurement of the neutral gas content at high redshift. We need a number to begin our design work, and assume a factor three more neutral gas at redshift 1.5.

2 Survey Telescope

To detect the 21 cm flux from high redshift galaxies, across the entire sky, in less than a year of observation, requires a collecting area of several hundred thousand square kilometers. Such a telescope would be about a factor ten larger than any in existence today. Fortunately, the goal of the program is an all sky survey, so inexpensive fixed cylindrical reflectors can be used. The parameters of the telescope and survey are listed in Table 1, and the design is described below.

2.1 Suspended Mesh Cylindrical Reflectors.

A flexible cable tied to a support at each end, held up against gravity by its own tension, will take on a catenary shape, $\cosh \alpha x$. This shape is very close to the parabolic shape that is needed to precisely focus radiation. The scheme discussed here uses two parallel horizontal rails as supports for square-cell welded wire mesh. Draping the mesh from rail to rail, with the mesh grid aligned to the rails, allows individual wires of the mesh to each follow parallel catenary curves. The mesh will naturally form a cylindrical, nearly-parabolic reflector. Backside stay cables can then be added to increase the tension in the mesh so it is stable under varying wind

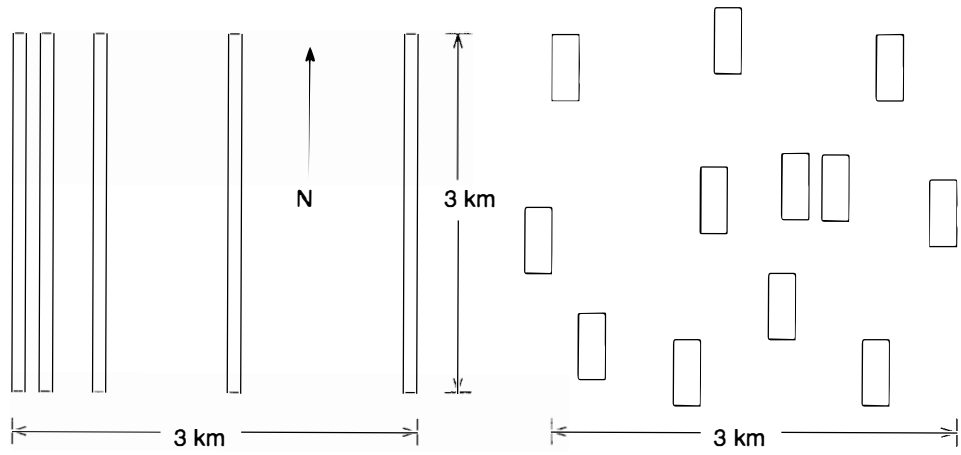

Figure 1: **Possible Telescope Layouts** Left: Five long cylindrical reflectors are oriented north-south. For each cylinder a fan of thousands of simultaneous half-arc-minute (N-S) by one degree (E-W) beams is formed along the meridian. For each beam in the fan, interferometry in the east-west direction is used to achieve half-arcminute resolution. There is some wasted reflector area at the ends of the cylinders, and this layout minimizes that waste. Right: The same collecting area is distributed among 12 cylinders. This layout offers lower sidelobe response and better image quality.

Table 1: **Approximate Telescope and Survey Parameters.** Presented are rough parameters, which will be refined using results of tests of prototype components, and results of simulated observations.

Redshift Range	0 - 1.5
Frequency Range	1500 - 500 MHz
Effective Area	400,000 m^2
System Temperature	75 K
Simultaneous Beams	>1000
Instantaneous Bandwidth	200 MHz
Redshift Resolution	$3x10^{-5}$
Angular Resolution	0.5 arcminute
Frequency Resolution	25 Khz
Sky Coverage	2 π steradians
One Sigma Flux Sensitivity in one hour on target	8 μ Jy

loading. These stays can be adjusted to correct the shape to the desired parabolic cylinder.

Orienting the support rails in the North South direction allows the parabolic cylinder to focus in the East-West direction while not focusing in the North-South direction. The line-focus of the cylinder can then be outfitted with a full-length set of small feed antennas that collect the radiation from the sky. These feeds are spaced at even intervals about one half wavelength apart. Diffraction defines the E-W angular width λ/w. In the North-South direction the reflector does not focus and the pattern is approximately that of a dipole. So, each feed sees a stripe along the Meridian, the only difference from one to the next being the North-South displacement. If we assemble a signal that consists of the sum, with no phase difference, of all feed signals for a length l, we get a beam at the zenith with the N-S angular width $\sim \lambda/l$. Using the same set of feed signals, a second beam at another North-South elevation angle can be simultaneously observed by taking a second sum, this time with a uniform phase shift from one feed to the next. In fact, a complete fan of narrow beams, spanning the entire meridian can be simultaneously created by taking a full set of sums, or alternatively, one can fourier transform the set of feed signals versus North-South displacement. The fast fourier transform calculation has asymptotic order $n \log n$ rather than order n^2 for the summing solution, so for a long, evenly spaced set of feeds the FFT technique offers substantially lower computational cost.

2.2 Large Reflector History.

Cylindrical reflectors became popular in radio astronomy beginning in the 1950s, because they offer large collecting area at low cost. However, a cylindrical reflector needs an array of quiet amplifiers to service its line feed. In the 1980s, cryogenically cooled low noise amplifiers were developed for use in satellite downlink receivers. Using such amplifiers, reflectors curved in both dimensions (dishes) gained the advantage over cylinders. A dish needs only one quiet amplifier, and the quiet amplifiers were expensive. Now, low noise HEMT amplifiers, which operate at room temperature, are available for a few dollars each, and cylindrical layouts are again economical. At the same time, computing speeds have advanced to the point that inexpensive PC computers can carry out FTT operations real-time, with bandwidths of hundreds of Megahertz. It is now reasonable to use a cylindrical reflector to observe over 1000 simultaneous beams.

Mesh reflectors are common on radio telescopes for the GHz frequency range. Mesh with spacing 1 cm, when used at wavelengths longer than 20 cm, acts as a high efficiency reflector, one which allows wind to pass through. Also, infrared and optical sunlight are not significantly focused by the mesh, preventing solar-radiation damage to the feed system. GMRT[15], Ooty[16],

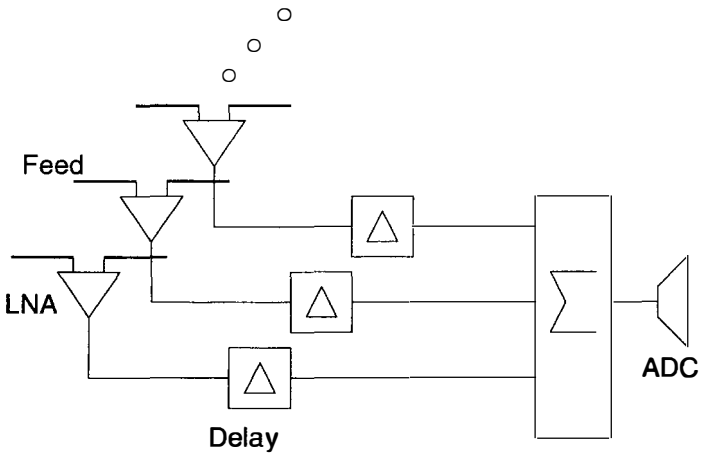

Figure 2: **Signal summing** By summing the signals from several feeds, each digitized signal can service the optimal area of cylinder, with a cylinder width of tens, rather than 100 meters.

Illinois[17], and Mologlo[18] all use mesh reflectors.

The Arecibo telescope uses multiple cables to support the zenith-pointed spherical dish[14]. The feed system moves to track objects. Objects can be tracked for a few hours, but must pass close to the zenith to be observed at all. North-South cylinders allow the entire sky to be observed, with no moving parts, however any particular object is available for only a short time each day.

2.3 Survey Speed.

The flux sensitivity of a radio telescope is $\Delta S \sim 2kT_{sys}/A\sqrt{2\Delta t \Delta \nu}$, where k is Boltzmann's constant, T_{sys} is the noise temperature of the system, A is the effective area of the telescope, t is the observing time, and $\Delta\nu$ is the frequency width of the line being observed. The survey will cover solid angle Ω_{survey}, repeating this coverage each day. However, at any instant the telescope sees only a strip along the meridian of solid angle Ω_{tel}. The survey speed, the reciprocal of the time needed to reach the required flux limit is $SP \sim [\frac{\Delta S}{2kT_{sys}}]^2[\frac{\Delta\nu}{\Omega_{survey}}]A^2\Omega_{tel}$. The factors in brackets are not easily adjustable, these values are set by the desired result and the amplifier noise temperature. The last two factors can be chosen for engineering or financial reasons. The telescope soild angle Ω_{tel}, also known as the instantaneous field of view, is proportional to the number of signals being processed simultaneously.

Cost optimization is straightforward for fixed cylinder telescopes, since the cylinder width can be adjusted. Survey speed is maximized when twice as much is spent on collecting area (steel) as is spent on signal processing (silicon). Assuming cost coefficients \$20 per square meter of collecting area and \$500 per signal processor channel, each processed signal needs 50 square meters of collecting area. If we digitize and process the signal from every feed, with feeds spaced 30 cm, the cylinder width would be 166 m. If it is found that maintaining the required surface

precision (< 1 cm) across such a large span entails substantial additional cost, there is another alternative. One can use a stage of analog summing, shown schematically in Figure 2, before digitization. The width of the cylinder can then be reduced by increasing the number of feed signals summed before digitizing. Such a system is used on narrow cylinders like Ooty and Molonglo. Note that the cost to process a signal will come down substantially over the next few years, eventually eliminating the need for analog summing.

2.4 No Galaxy Detection Threshold

Rather than use a galaxy catalog, we will calculate sky-structure power spectra directly from the measured 21 cm flux. The use of a catalog, restricting the data set to high significance detections, throws away useful signal. Because neutral hydrogen is concentrated in galaxy-size clumps, it makes sense to pass the signal stream through filters that emphasize the spatial and spectral pattern of a galaxy, but the galaxies need not be cataloged. Our no-threshold approach is roughly equivalent to including in a catalog all galaxies with signal to noise greater than one, rather than the usual practice of including only 3 or 5 sigma detections. While we will not use a catalog to detect the acoustic peaks, we will still produce a catalog for use in other analyses.

3 Conclusions

Fixed cylindrical reflector technology can be used to build a low cost radio telescope capable of measuring redshifts of galaxies across the sky out to redshift 1.5. The use of FFT beam forming, which is a natural choice when using cylindrical reflectors, further reduces cost. Data from this survey can be used to detect and measure baryon acoustic oscillations, sharply constraining dark energy models.

Acknowledgments

This work was supported in the US by grant AST 0507665 from the NSF, and in Canada by funds from NSERC.

Appendix: Sensitivity Calculations

The emissivity of hydrogen is

$$\epsilon_\nu = \frac{1}{4\pi} h\nu_{12} A_{12} \frac{N_2}{N_H} N_H \phi(\nu) \tag{1}$$

where the transition frequency $\nu_{12} = 1420$ MHz, the Einstein coefficient $A_{12} = 2.85 \times 10^{-15}\mathrm{s}^{-1}$, N_H is the total number of hydrogen atoms in the galaxy, N_2 is the number of hydrogen atoms in the excited state, and $\phi(\nu)$ is the line profile, which we treat as a delta function.

Since $h\nu_{12}/k = 0.06K$, even the CMB temperature is much higher than the transition energy, and the system is in the high temperature regime. The upper state is a triplet and the lower a singlet, so $N_2/N_H \approx 3/4$.

The monochromatic luminosity is

$$L_\nu = \int_\Omega \epsilon_\nu d\Omega = \frac{3}{4} h\nu A_{12} \frac{M_{HI}}{m_H} \phi(\nu) \tag{2}$$

where M_{HI} is the mass of neutral hydrogen, and m_H is tha mass of the hydrogen atom. The monochromatic flux density is related to the monochromatic luminosity by

$$S_\nu = L_{\nu(1+z)} \frac{1}{4\pi(1+z)^3 D_A^2(z)} \tag{3}$$

Assuming a flat universe, the angular diameter distance

$$D_A(z) = \frac{c}{1+z}\int_0^z \frac{dz}{H(z)} \tag{4}$$

and

$$H(z) = H_o\sqrt{\Omega_m\,(1+z)^3 + \Omega_\Lambda e^{\left[3\int_0^z \frac{1+w(z)}{1+z}dz\right]}} \tag{5}$$

Integrating both sides of equation 3 gives

$$\int S_\nu d\nu = \frac{3}{4}hA_{12}\frac{M_{HI}}{m_H}\frac{1}{4\pi(1+z)^3 D_A^2(z)}\int \nu\phi(\nu)d\nu \tag{6}$$

and the received flux in the 21 cm line is

$$S_{obs}\Delta\nu = \frac{3}{4}h\nu_{12}A_{12}\frac{M_{HI}}{m_H}\frac{1}{4\pi(1+z)^4 D_A^2(z)} \tag{7}$$

Using the low-redshift luminosity function of Zwann etal [11], $M_{HI} = M_* = 1.23 \times 10^{40} kg$. Placing this galaxy at redshift 1.5, and adopting $\Delta\nu = 0.568$MHz, $\Omega_m = 0.3$, $\Omega_\Lambda = 0.7$ and $w = -1$ the observed flux would be 2.09μJy .

The flux limit of a radio astronomy observation is

$$S_{lim} = \frac{2kT_{sys}}{A_{eff}\sqrt{2\Delta\nu t}} \tag{8}$$

where t is the integration time, $T_{sys} = 75K$ is the system temperature and $A_{eff} = 400,000 m^2$ is the effective area.

Using these values, and assuming that galaxies were three times more luminous at redshift 1.5 than they are today, the required on-target integration time for signal to noise ratio one is about 6000 seconds. If the telescope sees a strip along the meridian of width 0.2 degree, it would take $\approx$ 130 days to detect all M_* galaxies on the sky at redshift 1.5.

References

1. F.B. Abdalla and S. Rawlings, *MNRAS* **360**, 27 (2005).
2. P.J.E. Peebles, and J. T. Yu, *Astrophys. J.* **162**, 815 (1970).
3. D.J. Eisenstein and W. Hu, *Astrophys. J.* **496**, 605 (1998).
4. D.N. Spergel *et al*, *Astrophys. J. Supp.* **148**, 175 (2003).
5. S. Cole *et al*, *MNRAS* **362**, 505 (2005).
6. D.J. Eisenstein *et al*, *Astrophys. J.* **633**, 560 (2005).
7. D.J. Eisenstein, W. Hu and M. Tegmark, *Astrophys. J.* **504**, L57 (1998)
8. H. Seo and D.J. Eisenstein, *Astrophys. J.* **598**, 720 (2003).
9. M. Tegmark *et al*, *Astrophys. J.* **499**, 555 (1998).
10. K. Glazebrook and C. Blake, *Astrophys. J.* **631**, 1 (2005).
11. Zwaan *et al*, *Astronom. J.* **125**, 2858 (2003).
12. C. Blake and K. Glazebrook, *Astrophys. J.* **594**, 665 (2003).
13. H. Seo and D.J. Eisenstein, *Astrophys. J.* **633**, 575 (2005).
14. P.S. Kildal, L.A. Baker, and T. Hagfors, *Proc. IEEE* **82**, 714 (1994)
15. G. Swarup *et al*, *Current Sci.* **60**, 2 (1991)
16. G. Swarup *et al*, *Nat. Phys. Sci.* **230**, 185 (1971).
17. G.W. Swenson Jr., *IEEE Ant. and Prop. Soc. Newsletter* **28**, 13 (1986)
18. B.Y. Mills, *Proc. Astron. Soc. Aust.* **4**, 156 (1981).

Spectal Matching Independent Component Analysis, a method of blind component separation for observations of the Cosmic Microwave Backgound polarization.

J. F. Taylor, M. A. J. Ashdown, M. P. Hobson
Cavendish Laboratory, JJ Thomson Avenue, Cambridge CB3 0HE.

The process of component separation is expected to be especially problematic for measurements of the polarisation of the CMB, as knowledge of the polarised foregrounds is limited. Spectral Matching Independent Component Analysis (SMICA) [1] is a (semi)-blind method that requires little or no a priori knowledge of the properties of the foregrounds. It has already proved useful for temperature only observations and has recently been extended to polarisation observations [2]. We demonstrate the method's performance on simulated observations with varying degrees of realism, necessitating the handling of instrument beams and the effects of incomplete sky coverage.

1 Approach

We model a multi-channel n_ν observation of the microwave emission as a noisy linear mixture of n_c Gaussian random fields. The observations are most naturally described in the spherical harmonic basis.

$$\boldsymbol{d}^X_{lm} = \mathbf{B}_l \mathbf{A}^X \boldsymbol{s}^X_{lm} + \boldsymbol{n}^Z_{lm}$$

where X is T, E or B, $\boldsymbol{d}$ and $\boldsymbol{s}$ are n_ν and n_c dimensional vectors respectively. $\mathbf{B}$ describes the instrument beam.

SMICA consists of maximizing the likelihood of the data given the parameters of the model. The model implies covariance matrices of the form

$$\mathbf{D}^{XY}_l = \mathbf{B}_l \mathbf{A}^{XY} \mathbf{S}^{XY}_l \mathbf{A}^{XY} \mathbf{B}^t_l + \mathbf{N}^{XY}_l$$

and as we assume that the noise between channels and the signal from different components are uncorrelated, we obtain diagonal noise- and block diagonal signal-, covariance matrices. If we construct a complimentary set of auto and cross power spectra from observations, $\tilde{\mathbf{D}}^{XY}_l$, then the logarithm of the likelihood takes the form,

$$\mathcal{L} = -\frac{1}{2} \sum_l (2l+1) \left(\mathrm{trace}\left(\tilde{\mathbf{D}}^{XY}_l \mathbf{D}^{XY\,-1}_l \right) + \log\det\left(\mathbf{D}^{XY}_l \right) \right)$$

We maximise the likelihood using a combination of EM [3] and a conjugate gradient technique [4]. We are able to select the number of components that best represent the data by use of the Bayesian evidence, e.g. [5]. The evidence takes into consideration the balance between achieving a good fit to the data and the desirability of a simpler model with fewer parameters. This is particularly useful for the detection of unforseen contaminants to the data.

2 Results

We demonstrate the method on simulated observations which include *Planck* beams and white noise with *Planck* nominal RMS values. The tests are performed at $Nside = 128$. The foregrounds considered are emission from dust and galactic synchrotron.

2.1 Test one

Foregrounds are random Gaussian fields with power spectra extracted from the templates of the Planck reference sky model and an isotropic mixing matrix, Fig. 1. All the components

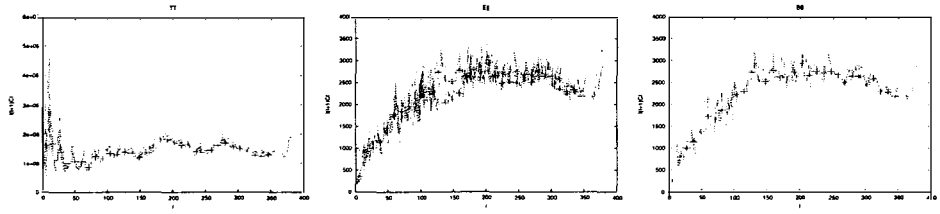

Figure 1: Recovered dust TT, EE and BB power spectrum from test one. Solid lines are the input power spectra, points are parameters recovered by SMICA.

are recovered well and the evidence correctly identifies a three component model as being most appropriate.

2.2 Test two

Foregrounds are based on the *Planck* reference sky with but with fixed emission laws across the sky. The components are recovered well despite the necessity of introducing a galactic cut. The evidence correctly identifies the appropriate number of components to fit. Applying SMICA on the incomplete sky results in mixing between the a_{lm}s and between polarizations. An attempt is made to correct some of the mode-to-mode coupling by using SMICA as a way to compute pseudo-C_ls [6] but this is far from a complete solution.

2.3 Test three

Foregrounds are based on the *Planck* reference sky including varying spectral indices, Fig. 2. The foregrounds now violate our simple model of the observation, Eq. 1 which requires that the components have the same emission law across the sky. A galactic cut is required to remove the areas of highest foreground contanimation. We do not recover the foregrounds well but the

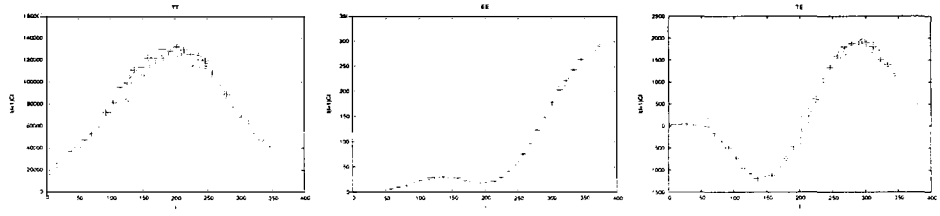

Figure 2: CMB TT, EE and TE power spectrum from test three.Solid lines are the input power spectra, points are parameters recovered by SMICA.

CMB power spectrum is still determined with increased error bars. The evidence now prefers a

model with more components than input.

3 Conclusions

SMICA is an effective method for the extraction of the CMB power spectrum even when the foregrounds deviate from our simple model. Model selection by the Bayesian evidence gives us a useful tool for component detection and discovery.

Acknowledgements

We thank J.-F. Cardoso and G. Patanchon for many useful discussions. The Healpix package was used extensively throughout this work. We acknowledge the use of version 1.1 of the Planck reference sky model, prepared by the members of Working Group 2 and available at www.planck.fr/heading79 .

1. Delabrouille J., Cardoso J.-F. & Patanchon G., MNRAS **386**, 1089 (2003)
2. Aumont J. & Macias-Peres J.F., astro-ph/0603044 , (2006)
3. Dempster A., Laird N. & Rubin D., J. of the Roy. Stat. Soc. B **39**, 1 (1977)
4. Mackay D., http://www.inference.phy.cam.ac.uk/mackay/c/macopt.html
5. Hobson M.P., Bridle S.L. & Lahav O., MNRAS **335**, 377 (2002)
6. Efstathiou G., astro-ph/0601107 , (2006)
7. Bouchet F.R., Prunet S. & Sethi Shiv K., MNRAS **302**, 663 (1999)

V – COSMOLOGY WITH HIGH ENERGY PARTICLES AND DIRECT DARK MATTER SEARCHES

STATUS OF THE DARK MATTER SEARCH PROJECT "ULTIMA"

Yu. M. Bunkov, E. Collin, J. Elbs, H. Godfrin and C. Winkelmann
CRTBT-CNRS, 25 av. des Martyrs, 38042, Grenoble, France

The new project "Ultra Low Temperature Instruments for Measurements in Astrophysics" (ULTIMA) is based on a new target material for bolometric particle detection: superfluid ^{3}He-B at ultra-low temperatures, of the order of 100 μK. At these temperatures the quantum excitations in ^{3}He are nearly frozen and the heat capacity exponentially vanishes. The advantages of a ^{3}He based detector are the direct channels of temperature and ionization measurements, 30% concentration of unpaired neutrons, as well as the virtually absolute ^{3}He purity and giant neutron cross section.

1 Introduction

Superfluid ^{3}He-B at ultra-low temperatures was suggested by G. R. Pickett in 1988 [1] as an appealing target material for bolometric particle detection. The first application of superfluid ^{3}He as a detector was published in 1995 under the title "Potential dark matter detector..." [2]. From that time we considered superfluid ^{3}He as one of the most promising materials for the search for non-baryonic Dark Matter. The main arguments in favor of ^{3}He are first of all its working temperature of about 100 μK, at which thermal fluctuations are extremely small. As a result an extremely high sensitivity of the superfluid ^{3}He bolometer can be achieved [3,4]. It is important also that ^{3}He has a non-zero nuclear magnetic moment (allowing therefore to explore the Spin-Dependent interaction channel) with a high density of non-paired neutrons (33%).

^{3}He is a quantum fluid obeying Fermi statistics, and it remains liquid down to the the absolute zero of temperature. At about 1 mK (depending on the pressure), liquid ^{3}He displays a second order phase transition to its superfluid A- and B-phases. The superfluid A phase has an anisotropic gap structure and an order parameter mixing magnetic and flow properties, while the B phase is characterized by an isotropic gap $\Delta = 1.76\ k_B T_c$ well described at 0 pressure by the weak coupling BCS theory [5]. Experimental temperatures as low as 100 μK are achieved by adiabatic nuclear demagnetization of a copper stage, which then cools down the liquid ^{3}He [6]. At these temperatures far below the transition temperature T_c, the superfluid is in its isotropic B-phase and the density of thermal excitations (quasiparticles) n decreases exponentially with temperature

$$n = \int g(E)dE = \frac{N_A}{V}\sqrt{2\pi\frac{\Delta}{k_B T}}\ \exp(-\Delta/k_B T), \tag{1}$$

where $g(E)$ is the density of states, N_A is Avogadro's number and V the molar volume of the fluid. This density is so low that the liquid can be represented as a renormalized quantum vacuum carrying a dilute quasiparticle gas. In the range of 100 to 200 μK, the heat capacity of

the superfluid is dominated by the ballistic quasiparticle gas and reduces to

$$C = C_0 \left(\frac{T_c}{T}\right)^{3/2} \exp(-\Delta/k_B T), \tag{2}$$

with $C_0 \approx 2.1$ mJ $K^{-1}cm^{-3}$.

A direct and rather rapid method of thermometry of the superfluid is achieved by measuring the density of thermal excitations (quasiparticles) using Vibrating Wire Resonators (VWRs) [7]. A VWR is a fine superconducting wire bent into semi-circular shape and oscillating perpendicularly to its plane. The excitation and the read-out of the VWR are respectively an a.c. current and voltage.

2 Achievements

For the bolometric particle detection we use copper cells of typical dimensions of about 5 mm, filled with superfluid ^{3}He which is in weak thermal contact with the outer bath through a small orifice [2,3]. The interaction of a particle with the ^{3}He in the cell releases energy which results in an increase of temperature, and thus n. The time constants of internal equilibrium of the quasiparticle gas are small (< 1 ms), while the time constant for thermal relaxation of quasiparticles through the orifice after a heating event is tuned to be $\tau_{cell} \approx 5$ s. The heat leak through the container walls can be neglected because of the huge thermal resistance (Kapitza resistance) of the solid-liquid interfaces at very low temperatures. Each bolometric cell contains at least one VWR-thermometer which allows to follow the rapid variations of the temperature.

Neutrons were the first particles studied in superfluid ^{3}He for their large energy release after the capture reaction [2]. Of particular interest was the study of the rapid and inhomogeneous phase transition of a small region around the neutron impact, because of the possibility of topological defects creation in the superfluid in analogy with the Kibble mechanism in cosmology [3,4]. The neutrons, emitted by a moderated AmBe source, produce large signals in the bolometer. A deficit of about 120 keV with respect to the expected 764 keV is observed; part of this deficit is accounted for by ultra-violet (UV) scintillation of the ^{3}He, the rest is interpreted in terms of energy trapped in the form of metastable topological defects of the superfluid (e. g. quantized vortices).

Cosmic muons are expected to deposit about 16 keV/mm in liquid ^{3}He at 0 bar. Muons represent thus bolometric events about an order of magnitude below neutrons. A muon test of the detector and its comparison to a numerical simulation by Geant4 in the frame of the MACHe3 collaboration yielded good agreement, the 20-25 % difference between the experimental and the calculated detection spectra being due to ultra-violet scintillation [8].

Final evidence for the muonic nature of the observed energy peak at about 50~60 keV at ground level was brought by the recent experiment with a 3-cell prototype. The simultaneous detection in 3 adjacent cells allowed to discriminate with large efficiency the muons, who are, depending on their trajectory, generally detected coincidently in two or more cells. This setup therefore allowed to demonstrate the large muon rejection efficiency of a future underground multicell detector. Since the energy range of a neutralino scattering is expected to be in the keV range, the proof that a 1 keV detection resolution and threshold could be attained had to be brought using a known particle source. A low activity ^{57}Co source was therefore implemented directly in one cell. Such a source emits γ-rays mainly at about 120 keV, which have a weak Compton scattering cross-section with the ^{3}He, but also low energy electrons (from internal conversion and the Auger effect) which thermalize completely in the liquid of the cell. Such low energy electron events are expected mainly at about 7 and 14 keV, and only in one cell [8,9]. Measurements on the 3-cell prototype indeed allowed to identify such bolometric events, again an order of magnitude below typical muons. The low energy detection spectrum from the cell

with source and its comparison to another cell (without source) allows to clearly identify these events as produced by the ^{57}Co source.

Bolometric calibration of the detector cells is achieved by an extra VWR present in the cell that can produce a short mechanical pulse at its resonant frequency and thus deposit a well-controlled amount of energy (heat) to the liquid through mechanical friction [4]. The results of the calibration are compared to measured heat depositions by the nuclear neutron capture reactions as well as muon impacts and low energy electron irradiation. A deficit of about 15 % is found in the case of neutrons, in good agreement with previous measurements at 0 bar [3]. In the case of high energy muons, as well as electrons in the 10 keV range, a deficit of about 25 % is found which can be entirely attributed to UV scintillation emission. It is not surprising to find the scintillation rates resulting from these two types of irradiation to be of the same order since the much larger incident energy of cosmic muons is compensated by their larger mass.

3 Recent development

Recently quartz forks have been tested as ^{3}He thermometers [10]. To be applied to our experimental cell, the quartz oscillators signal to noise ratio should be improved by about one order of magnitude. We are working now on the design of quartz forks adapted for bolometric conditions. Another new development is the use of Silicon structures as vibrating sensors [11]. We are also developing these devices for bolometric applications.

Parallel methods of discrimination of ionizing events are in study. The fraction of energy released by a particle going into the ionization of ^{3}He can provide a fine criterium of discrimination. Ion dynamics in ^{3}He have been studied for a long time already, for positive ions as well as for negative ^{3}He ions. Ions create a ball of solid ^{3}He with a mass of about 100 atoms due to the van der Waals interaction. The main problem is the small velocity of ions in an applied electric field, which can move without friction only with a velocity below a critical one, which is of the order of 10 cm/s. Consequently, the time constant of the ionization channel in ^{3}He is of the order of seconds. However there is a possibility to create an ion amplification for thermal signal. At a high electric field the accelerated ions deposit more thermal energy to the ^{3}He liquid, than is deposited by the scattering of particles. An amplification by a factor of 10 is possible for our experimental conditions.

Last year we have studied carefully the heat capacity of superflid ^{3}He at different pressures, magnetic fields and temperatures. Some unexpected phenomena have been found and will be published in condensed matter journals.

Finally, we are working on the design of a new nuclear demagnetization cryostat for underground environment. In which particular underground laboratory this experiment will be conducted is still open.

4 Axial interaction with ^{3}He

In the non-relativistic limit, which is appropriate for WIMPs in our Galaxy, the variety of possible forms of WIMP-nucleus interactions is reduced to two cases, namely, to a spin-spin interaction and to a scalar one. The fundamental constants of the WIMP interaction with nucleon constituents, specified by each concrete particle model, determine the effective coupling of WIMPs to nucleons, which, in turn, define constants of the WIMP-nucleus interaction (for a more detailed review see [12]). The essential difference between spin-spin and scalar interactions is in the following. In the scalar case, the WIMP-nucleus interaction amplitude (A_{XA}) is given by the WIMP-nucleon ($A_{Xp,n}$) one, multiplied by the number of respective nucleons, while in the spin-spin case A_{XA} is proportional to the nucleon spin averaged over the nucleus state $S_{p,n}$, which for heavy non-zero spin nuclei is, as a rule, even smaller than that for a single nucleon

($S_p = S_n = 1/2$). It leads to a loss of advantage in using heavy target-nuclei in the exploration of WIMPs with spin dependent interaction. The ^{3}He nucleus having a non-zero magnetic moment and a huge density of non-paired neutrons (33%), a ^{3}He detector will be mainly sensitive to the axial interaction [13,14], making this device complementary to existing ones, mainly sensitive to the scalar interaction. The axial interaction is largely dominant in most of the SUSY region associated with a substantial elastic cross-section.

5 Conclusion

While the use of ^{3}He imposes challenging technological - namely cryogenical - constraints, this material has nevertheless extremely appealing features for Dark Matter detection. Since the original proposal of the use of ^{3}He for particle detection, the detection threshold and sensitivity have been improved by 2 orders of magnitude, reaching nowadays 1 keV, which covers already most of the expected energy range for a neutralino impact. The use of a ^{57}Co source producing a well known γ-ray and low energy electron spectrum directly in one bolometric cell allowed to illustrate both our understanding of the detector at keV level and the high transparency of the target material to γ-rays. In addition, the simultaneous detection in 3 adjacent cells demonstrated the future rejection efficiency versus ionizing events of a large multicell detector.

On the basis of the last several years of investigations on superfluid ^{3}He, the new direct Dark Matter search project "Ultra Low Temperature Instruments for Measurements in Astrophysics" (ULTIMA) has started in December 2005 at the CRTBT-CNRS, Grenoble. We are thankful to the French National Research Funding Agency ANR for financial support of the new project.

References

1. G. R. Pickett, in *"Proc. of the Second European worshop on neutrinos and dark matter detectors"*, 377, ed. by L. Gonzales-Mestres and D. Perret-Gallix (Frontiers, 1988).
2. D. I. Bradley *et al*, *Phys. Rev. Lett.* **75,** 1887 (1995).
3. C. Bäuerle *et al*, *Nature* **382**, 332 (1996).
4. C. Bäuerle *et al*, *Phys. Rev.* B **57**, 14381 (1998).
5. A. J. Leggett, *Rev. Mod. Phys.* **47**, 331 (1975).
6. D. I. Bradley *et al*, *J. Low Temp. Phys.* **57,** 359 (1984).
7. C. B. Winkelmann *et al*, *J. Low Temp. Phys.* **135**, 3 (2004).
8. C. B. Winkelmann *et al*, in *"Exploring the Universe"*, 71, ed. Giraud-Heraud and Thanh Van (The Gioi pbl, 2004).
9. E. Moulin, *et al*, *Nucl. Instrum. Methods* **A** 548, 411 (2005).
10. R. Blaauwgeers, *et al*, *J. Low Temp. Phys.*, accepted.
11. S. Triqueneaux *et al*, *Physica B*, **284**, 2141 (2000).
12. A. Kurilov and M. Kamionkowski, *Phys. Rev.* D **69**, 063503 (2004).
13. V.A. Bednyakov, F. Šimkovic, *Phys. Rev.* D **72**, 035015 (2005).
14. K. Belotsky *et al*, to be published.

INDIRECT DARK MATTER SEARCH WITH AMS-02

S. DI FALCO
on behalf of the AMS Collaboration
INFN & Università di Pisa, Largo B. Pontecorvo 3,
56100 Pisa, Italy

The Alpha Magnetic Spectrometer (AMS), to be installed on the International Space Station, will provide data on cosmic radiations in the energy range from 0.5 GeV to 3 TeV. The main physics goals are the anti-matter and the dark matter searches. Observations and cosmology indicate that the Universe may include a large amount of unknown Dark Matter. It should be composed of non baryonic Weakly Interacting Massive Particles (WIMP). In R-parity conserving models a good WIMP candidate is the lightest SUSY particle. AMS offers a unique opportunity to study simultaneously SUSY dark matter in three decay channels resulting from the neutralino annihilation: e^+, antiproton and gamma. Either in the SUSY frame and in alternative scenarios (like extra-dimensions) the expected flux sensitivities as a function of energy in 3 year exposure for the e^+/e^- ratio, gamma and antiproton yields are presented.

1 The search for dark matter

The evidence for dark matter existence has become more and more robust in the recent years: several independent indications were provided by rotation curves and mass to light ratios of galaxies, by X rays emissions from clusters and by gravitational lensing. The very recent results from the WMAP collaboration [1] confirm that baryon matter density ($\Omega_b = 0.0223^{+0.0007}_{-0.0009}$) is largely insufficient to saturate the total matter density ($\Omega_m = 0.127^{+0.007}_{-0.013}$).

The known non baryonic dark matter candidates, such as massive neutrinos or massive black holes, don't reach the required dark matter density. Other, still undiscovered, possible candidates are the axions and the weakly interacting particles (WIMPs). These latest include as most favourites the *neutralino*, the lightest supersymmetric particle (LSP) [2], and the lightest Kaluza-Klein particle (LKP) of certain extra-dimensions models [3].

The search for WIMPs can be performed either *directly* or *indirectly*. Direct obervations look for the nuclear recoils in the elastic scattering on nuclei [4]. Indirect searches look for anomalies in the expected spectra of primary cosmic rays due to the annihilation of dark matter candidates.

Hints for anomalies in the positron and photon spectra around 10 GeV have been observed by the HEAT [5] and EGRET [6] collaborations, respectively.

The AMS02 experiment can confirm or disprove these hints by measuring simultaneously the spectra of positrons, photons and antiprotons. Together with the search for dark matter, the main goals of the experiment will be the search for antimatter and a precise measurement of cosmic ray fluxes in the energy range between 0.5 GeV and 3 TeV, including nuclei up to Z=26 and gamma rays.

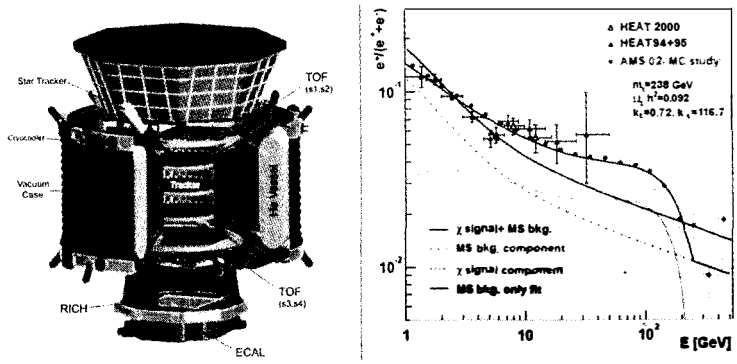

Figure 1: a) The AMS-02 experiment layout. b) Example of the statistical accuracy on positron fraction measurement in 3 years in case of neutralino annihilation (m_χ=238 GeV, boost factor =166).

2 The AMS experiment

The Alpha Magnetic Spectrometer (AMS) [a] is a cosmic ray detector which will operate on the International Space Station (ISS) for at least three years. AMS will be ready for launch in 2008.

The experimental layout (fig.1a) consists of a *Transition Radiation Detector (TRD)* [8], a *Time of Flight (TOF)* [9], a *Silicon tracker (TRACKER)* [10], a *Ring Imaging Cherenkov (RICH)* [11], an *Electromagnetic Calorimeter (ECAL)* [12], an *Anti-Coincidence Counter (ACC)* and a Star Tracker. A large superconducting magnet, the first operating on Space, will provide a bending power of $BL^2 = 0.85\ Tm^2$.

3 Dark Matter signal in e^+ spectrum

The measurement of positron spectrum requires all the AMS subdetectors: a rejection factor of $10^2 \div 10^3$ on protons is obtained by TRD for proton energies up to 300 GeV [b]; the time measurements by TOF and the track curvature by TRACKER permit the charge sign determination, so rejecting electrons up to 2 TeV; the Z measurement by TOF, TRACKER and RICH make the He background negligible; the velocity (β) measurement by RICH allows the rejection of protons up to 10 GeV; the energy deposit profile inside ECAL ensures a lepton/proton rejection factor of $\sim 10^3$; finally, the matching between TRACKER momentum and ECAL energy furtherly suppresses the hadronic component.

Combining all these informations together a global rejection factor of 10^5 for p and 10^4 for e^- is achieved. The mean acceptance for positrons in the energy range form 3 to 300 GeV is 0.045 m^2sr, with a proton contamination of $\sim 4\%$ [14].

Fig. 1b shows an example of *positron fraction* [c] measured by AMS if the excess on the HEAT data were due to the annihilation of 238 GeV neutralinos: a signal boost factor [d] of $\sim$ 100 has been used to fit the HEAT data [15]. Significantly lower boost factors are required if the anomaly is due to LKPs with masses of few hundreds GeV [16].

[a] A precursor flight (AMS-01) succesfully flew for 10 days in June 1998 on the Space Shuttle Discovery [7].
[b] No transition radiation is expected for relativistic factors $\gamma < 10^3$.
[c] This ratio is preferred to the simple spectrum since less dependent on cosmic ray propagation.
[d] These boost factors can be explained assuming a clumpy dark matter halo.

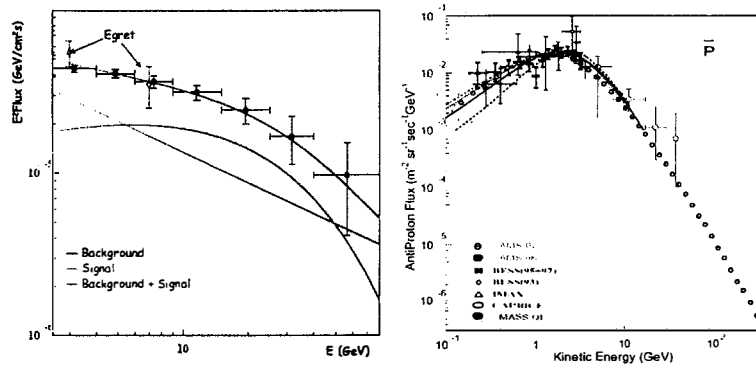

Figure 2: a) Statistical accuracy in photon spectrum with 1 year data taking supposing a 208 GeV neutralino annihilation. b) Expected precision on the antiproton spectrum measurement by AMS in 3 years.

4 Dark Matter signal in γ spectrum

In AMS photons are detected using two complementary techniques: *photon conversions* in e^+e^- pairs that can be detected by the TRACKER and *direct photon* measurements in ECAL.

The conversion mode ensures an excellent photon angle resolution (0.02^o at 100 GeV), a good energy resolution (3% up to 20 GeV, 6% at 100 GeV), a good acceptance (0.06 $sr\ m^2$ at 100 GeV) and a large field of view ($\sim 43^o$). The background is mainly due to δ rays and can be strongly reduced (rejection factor $\sim 10^5$) vetoing with the TRD and cutting on the pair invariant mass.

The measurement with ECAL has an angular resolution of 1^o at 100 GeV, an excellent energy resolution (3% at 100 GeV), a large acceptance at high energies ($\sim 0.1\ sr\ m^2$ above 100 GeV) but a reduced field of view of $\sim 23^o$. The main background is due to π^0s produced by proton interactions in the material surrounding ECAL. A rejection factor of $\sim 5 \cdot 10^6$ on protons is obtained analyzing the cascade profile in ECAL and vetoing on charged particles[17].

In 3 years the exposure to the galactic center [e] will amount to 40 days for the conversion mode and to 15 days for the direct photon mode; the integrated acceptance will be practically the same for the two methods: $\sim 1.5 \cdot 10^5\ m^2 s$.

In the case of a photon spectrum anomaly due a 208 GeV neutralino annihilation fitting the EGRET data, the statistical evidence obtainable by AMS in 1 year of direct photon detection is shown in fig. 2a[18].

In absence of any anomaly in the spectrum a large part of SUSY and Kaluza-Klein model parameter space could be excluded, in particular in the case of a cuspy halo profile[19].

5 Dark Matter signal in $\bar{p}$ spectrum

In AMS the antiprotons will be detected as negative single charged tracks reconstructed by TRD and TRACKER. The acceptance for this signal is $\sim 0.16\ sr\ m^2$ between 1 and 16 GeV and $\sim 0.033\ sr\ m^2$ between 16 and 300 GeV [20]. Misreconstructed proton interactions and unrecognized electrons are the main background sources: the rejection factors are better than 10^6 against protons and $10^3 \div 10^4$ against electrons.

[e] This quantity is not important for positrons or antiprotons since they suffer large energy losses and scatterings so that they lose memory of their initial direction.

Fig. 2b shows the expected profile after 3 years together with the existing measurements of the antiproton flux: the dot dimensions correspond to the statistical error. The low energy part of the spectrum is consistent with the secondary production by interaction of primary cosmic radiation with the interstellar medium. The most interesting region is the one between 10 and 300 GeV where, supposing that large boost factors ($\sim 10^3$) enhance the process, a dark matter annihilation could be revealed [21].

6 Conclusions

In three years of data taking the AMS experiment will be able to measure with unprecedented accuracy the rates and spectra of positrons, photons amd antiprotons in the GeV-TeV range, looking for an excess of events consistent with a dark matter annihilation signal. Several models for dark matter candidates will be constrained by the new AMS data.

The simultaneous measurements of other fundamental quantities, such as the proton and electron spectra and the B/C ratio, will help to refine the astrophysical predictions enhancing the compelling evidence for a dark matter signal.

References

1. D.N. Spergel *et al.*, Submitted to Astrophys.J., *astro-ph/0603449*.
2. See for example: G. Jungman *et al.*, Phys.Rept. 267:195-373,1996.
3. See for example: G. Servant, T.M.P. Tait, Nucl.Phys. B650:391-419,2003.
4. B. Serfass, these proceedings.
5. M.A. DuVernois *et al.*, Astrophys.J.559:296-303,2001.
6. S. D. Hunter *et al.*, Astrophys.J.481:205-240,1997.
7. M. Aguilar *et al.*, Phys. Rep. 366/6: 331-404,2002.
8. T.Siedenburg *et al.*, Nucl. Phys. B (Proc. Suppl.) 150:30-33,2006.
9. G. Levi *et al.*, Nucl.Instrum.Meth.A530:419-425,2004.
10. M. Bourquin *et al.*, Nucl.Instrum.Meth.A541:110-116,2005.
11. B.Baret *et al.*, Nucl.Instrum.Meth.A525:126-131,2004.
12. F. Cadoux *et al.*, Nucl.Phys.Proc.Suppl.113:159-165,2002.
13. I. V. Moskalenko and A. W. Strong, Astrophys.J. 493:694-707,1998.
14. P. Maestro, Ph.D. Thesis, University of Siena, Italy,2003.
15. E. A. Baltz *et al.*, Phys. Rev. D65:063511,2002.
16. J. Pochon, Ph.D. Thesis, University of Lion 1, France,2005.
17. F. Pilo, Ph.D. Thesis, University of Siena, Italy,2004.
18. L. Girard, Ph.D. Thesis, University of Savoie, France,2004.
19. A. Jacholkowska *et al.*, astro-ph/0508349.
20. V. Choutko, Nucl.Phys.Proc.Suppl.113:170-176,2002.
21. L. Bergstrom *et al.*, astro-ph/9906034.

Cosmic ray physics in calculations of cosmological structure formation

T.A. Enßlin[1], M. Jubelgas[1], C. Pfrommer[1,2], V. Springel[1]
1) Max-Planck Institut für Astrophysik
2) Canadian Institute for Theoretical Astrophysics

Non-equilibrium processes like shock waves and turbulence can generate and energise magnetic fields and cosmic rays (CRs) in the interstellar medium of galaxies and in the intragalactic gas. Cosmic rays in particular play a decisive role within our own Galaxy. To study the impact of CRs on galaxy formation and evolution, we develop an approximative framework for treating dynamical and radiative effects of CRs in cosmological simulations. Our guiding principle is to try to find a balance between capturing as many physical properties of CR populations as possible while at the same time requiring as little extra computational resources as possible. The processes considered include compression and rarefaction, CR injection via shocks in supernova remnants, injection in structure formation shock waves, in-situ re-acceleration of CRs, CR spatial diffusion, CR energy losses due to Coulomb interactions, ionisation losses, Bremsstrahlung losses, and, finally, hadronic interactions with the background gas. We present an implementation of the formalism in the Lagrangian simulation code GADGET-2. Using a number of test problems, we show that our scheme is numerically robust and efficient, allowing us to carry out cosmological structure formation simulations that account for cosmic ray physics. In simulations of isolated galaxies, we find that cosmic rays can significantly affect the star formation efficiencies of small galaxies, an effect that becomes progressively stronger towards low mass scales. In cosmological simulations of the formation of dwarf galaxies at high redshift, we find that both the mass-to-light ratio and the faint-end of the luminosity function are strongly affected, as required to reconcile the faint-end slope of the observed galaxy luminosity function with the halo mass function of the LCDM cosmology.

1 Motivation

The interstellar medium (ISM) of galaxies has an energy budget composed both of thermal and non-thermal components. The non-thermal components which are magnetic fields and cosmic rays (CRs) are known to contribute a significant part of the energy and pressure to the ISM. Magnetic fields couple the otherwise dynamically independent ingredients like the ISM plasma, and the CR gas into a single, however complex fluid.

CRs behave quite differently compared to the thermal gas. Their equation of state is softer, they are able to propagate over macroscopic distances, and their energy loss time-scales are typically larger than the thermal ones. Furthermore, roughly half of the particle's energy losses are due to Coulomb and ionisation interactions and thereby heat the thermal gas. Therefore, CR populations are an important galactic reservoir for energy from supernova explosions, and thereby help to maintain dynamical feedback of star formation for periods longer than thermal gas physics alone would permit. In a galactic context, an important CR loss mechanism is escape from the galaxy by diffusion and (evt. CR driven) galactic winds. The spectral distribution of CRs is much broader than that of thermal populations (see Fig. 1), which has to be taken into account in estimating their dynamical properties.

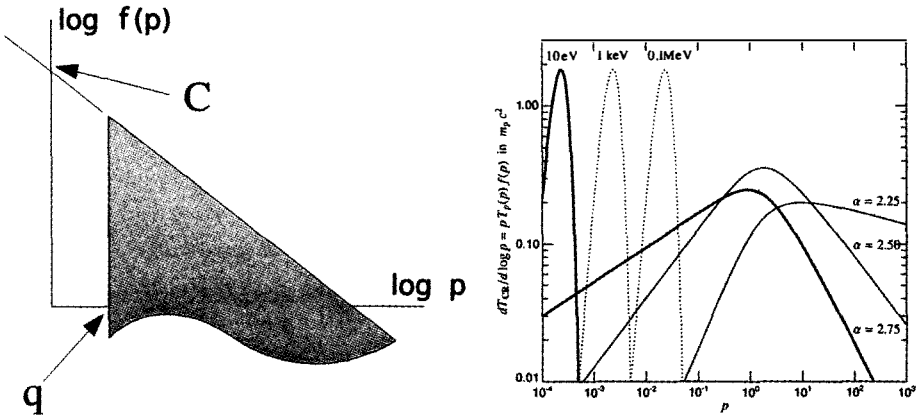

Figure 1: Left: power-law momentum spectrum and its basic variables C and q; Right: kinetic energy per logarithmic momentum interval of thermal and CR energy spectra for various temperatures and spectral indices α but with the same pressure. The dynamical important part of CR spectral distributions in momentum space easily encompasses a few orders of magnitude, whereas thermal distributions appear nearly mono-energetic on logarithmic scales. The thick lines correspond to a possible situation in the ISM.

Numerical simulations and semi-analytical models of galaxy and large-scale structure formation neglected the effects of CRs and magnetic fields so far, despite their dynamical importance. An accurate description of CRs should follow the evolution of the spectral energy distribution of CRs as a function of time and space, and keep track of their dynamical, non-linear coupling with the hydrodynamics. In order to allow the inclusion of CRs and their effects into numerical simulations and semi-analytic descriptions of galaxy formation, we present a simplified description of the CR dynamics and physics. We seek a compromise between two opposite requirements, namely: (i) to capture as many physical properties and peculiarities of CR populations as possible, and (ii) to require as little extra computational resources as possible. In our model, the emphasis is given to the dynamical impact of CRs on hydrodynamics, and not on an accurate spectral representation of the CRs. The guiding principles are energy, pressure, and particle number conservations, as well as adiabatic invariants. Non-adiabatic processes will be mapped onto modifications of these principles.

The CR description and implementation into the GADGET-2 code (Springel 2005) presented in this article was introduced in three papers: Enßlin, Pfrommer, Springel, Jubelgas (2006) introduced the basic description and the dynamical equations for the simplified CR gas. Jubelgas, Springel, Enßlin, Pfrommer (2006) present the implementation details, the code tests and first application. Pfrommer, Springel, Enßlin, Jubelgas (2006) build a smoothed-particle hydrodynamics shock wave tracer, needed for the CR injection. Here, we concentrate on the first two papers. Pfrommer et al. (2006) is presented in a parallel article.

2 Formalism for simplifying cosmic ray physics

We introduce the dimensionless proton momentum $p = P_\mathrm{p}/m_\mathrm{p}\,c$ and write the CR spectra as

$$f(p) = \frac{dN}{dp\,dV} = C\,p^{-\alpha}\,\theta(p-q)\,. \tag{1}$$

The normalisation C and the spectral cutoff q (see Fig. 1) can be easily followed through adiabatic changes if one introduces adiabatic invariant variables C_O and q_0 defined for some

reference gas density ρ_0:

$$q(\rho) = \left(\frac{\rho}{\rho_0}\right)^{\frac{1}{3}} q_0, \quad C(\rho) = \left(\frac{\rho}{\rho_0}\right)^{\frac{\alpha+2}{3}} C_0\,. \tag{2}$$

The CR number density $n_{\rm CR} = \frac{C q^{1-\alpha}}{\alpha-1}$, pressure $P_{\rm CR} = \frac{C m_{\rm p} c^2}{6} \mathcal{B}_{\frac{1}{1+q^2}}\left(\frac{\alpha-2}{2}, \frac{3-\alpha}{2}\right)$, and other variables can easily be expressed in terms of C and q.

Non-adiabatic processes are described by their effects on spectral normalisation C and cutoff q (or C_0 and q_0) following energy and particle number conservation. We implemented the following CR processes into the GADGET-2 smooth particle hydrodynamics code: a) CR pressure on hydrodynamics, b) CR injection by supernova (sub-grid), c) CR injection in shock waves , d) CR spatial diffusion, e) Coulomb & ionisation losses, and f) hadronic interactions. Mathematical details can be found in Enßlin et al. (2006) and a description of the implementaion and its tests can be found in Jublegas et al. (2006).

3 CR modified galaxy formation

We have performed simulations of forming galaxies of different masses, with and without CR physics. Fig. 2 presents the result of our simulation runs. The morphology and star formation rate of small mass galaxies is strongly affected by the presence of CRs, whereas massive galaxies appear to be relatively unmodified. The suppression of star formation by CRs in small galaxies is an attractive explanation of the observed low faint end of the luminosity function of galaxies. This suppression, and also the oscilations in the star formation rate are a result of an inverted effective equation of state of a CR gas energised by supernovae (see Jubelgas et al. (2006) for details).

4 Conclusions

We have argued that cosmic rays are an active agent of galaxies and the large scale structure. In order to permit studies of cosmic rays we developed and presented new self-consistent CR simulations in cosmological setting using the GADGET-2 code. These include adiabatic and non-adiabatic cosmic ray processes. We find that star formation is strongly CR-suppressed in small galaxies. This is a result of the inverted effective equation of state of CRs in the ISM (less energy at higher pressure) and leads to a suppression of the faint end of the galaxy luminosity function and thereby help to reconcile observations with computational models of galaxy formation. A number of future studies enclosing CR in cosmological structure formation are underway.

References

1. Springel V. *MNRAS* **364**, 1105 (2005).
2. T.A. Enßlin, C. Pfrommer, V. Springel and M. Jubelgas *astro-ph/***0603484**, (2006).
3. M. Jubelgas, V. Springel, T.A. Enßlin and C. Pfrommer *astro-ph/***0603485**, (2006).
4. C. Pfrommer, V. Springel, T.A. Enßlin and M. Jubelgas *MNRAS* **367**, 113 (2006).

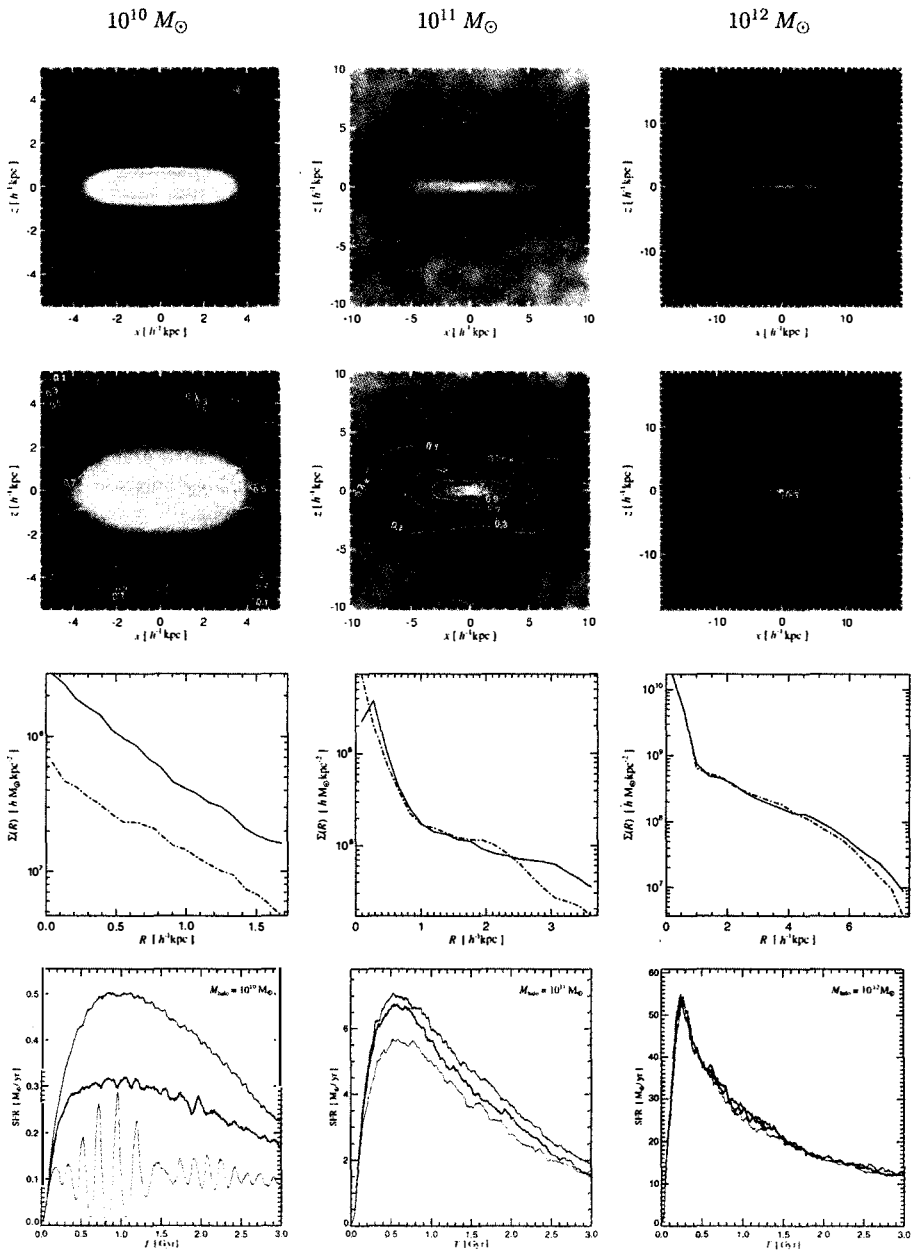

Figure 2: Simulation of isolated galaxies with different masses (different columns). The top row shows the gas distribution of galaxies without CRs. The second row shows the same with CRs included. The contour lines indicate the relative level of CR pressure support. Massive galaxies are mostly unaffected by CRs, whereas small galaxies exhibit a puffed-up gas distribution, and a strongly reduced stellar surface brightness profiles (third row). Finally, the star formation histories of galaxies for different levels of CR injection efficiencies are shown in the last row.

We need lab experiments to look for axion-like particles

Joerg Jaeckel[1], Eduard Masso[2], Javier Redondo[2], Andreas Ringwald [1], Fuminobu Takahashi [1]

[1] *Deutsches Elektronen Synchrotron, Notkestrasse 85, 22607 Hamburg, Germany*

[2] *Grup de Física Teòrica and Institut de Física d'Altes Energies Universitat Autònoma de Barcelona 08193 Bellaterra, Barcelona, Spain*

The PVLAS signal has renewed the interest in light bosons coupled to the electromagnetic field. However, astrophysical bounds coming from the lifetime of the sun and the CAST experiment are seemingly in conflict with this result. We discuss effective models that allow to supress production of axion-like particles in the sun and thereby relax the bounds by some orders of magnitude. This stresses the importance of laboratory searches.

1 Introduction

Recently the PVLAS collaboration has reported a rotation of the polarization plane of an originally linearly polarized laser beam propagating through a magnetic field [1]. This signal could be explained by the existence of a light neutral spin zero boson with a coupling to two photons, e.g. a pseudoscalar ϕ,

$$\mathcal{L}_\phi = \frac{1}{2}(\partial_\mu \phi)^2 - \frac{1}{2} m_\phi^2 \phi^2 - g \phi \tilde{F}^{\mu\nu} F_{\mu\nu}, \tag{1}$$

with

$$m_\phi^{\rm PVLAS} = (1 - 1.5) \times {\rm meV}, \quad g_\phi^{\rm PVLAS} = (1.7 - 5) \times 10^{-6} {\rm GeV}^{-1}. \tag{2}$$

The favorite candidate for such a light and neutral particle is the axion, the pseudo-Goldstone boson of the Peccei-Quinn symmetry that was proposed to explain the so called strong CP problem[2,3,4]. However, the PVLAS measurements are not compatible with the expectations for a standard axion, for which one has a relation that essentially determines $m_\phi g_\phi^{-1}$ in terms of QCD quantities. All natural axion models are located in the green vertically shaded strip in Fig. 1. As we can see from the same figure, the PVLAS result is far outside this region. Hence, it is probably not an axion. We will call it an axion like particle (ALP) due to its similar properties.

The troubling point of the particle interpretation of the PVLAS data is that the action (1) with parameters (2) already is in conflict with observations. Astrophysical considerations based on the production of ϕ's from photons via the coupling $g\phi F\tilde{F}$ in Eq. (1) actually give the strong bounds depicted in Fig. 1. We will briefly review these bounds in Sect. 2.

The motivation for our work[a] is the question: Can we resolve the conflict between the astrophysical bounds and the particle interpretation of PVLAS[b] and how can this be tested? We attack the first part of this question in Sect. 3. In our final Sect. 4 we argue that Laboratory

[a] This note is based on a talk given at the by J. Jaeckel at the "Rencontres des Moriond: Contents and structures of the universe" in La Thuile, Italy in March 2006. For more details see [5].

[b] For other attempts in this direction see [6,7].

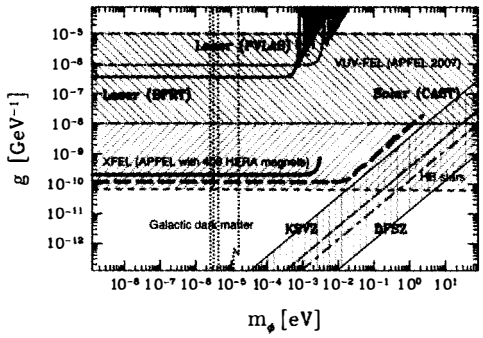

Figure 1: Various bounds on the coupling g and mass m_ϕ of a (light) boson coupled to two photons (areas above single lines are excluded). The green vertically shaded strip gives the range of all reasonable axion models. The two lines within its boundaries give a typical KSVZ and DFSZ model. The green and red diagonally shaded areas give the additional area allowed when we suppress the production of ALP's in the sun (the green smaller one is a little bit more conservative).

experiment are the prime tool to give a conclusive answer if the particle interpretation of PVLAS is invalid or if astrophysical bounds are evaded and PVLAS has detected signals of new exciting physics.

2 Astrophysical bounds revisited

The basic problem of the particle interpretation of the PVLAS data is that it is in conflict with astrophysical bounds. For a better understanding of the problem let us briefly review these bounds.

2.1 Energy loss of stars

The simplest bound comes from the energy loss argument. If any weakly interacting particle is produced in a star and escapes, it takes a certain amount of energy with it, thus contributing to the stellar luminosity. The amount of energy in exotic particles can contribute to shorten the duration of the different phases of stellar evolution, which can be observed (for a review see [8]).

Here, we focus on the sun, for which we have a solid standard solar model from which we can accurately calculate emission of ALPs.

The lifetime of the sun is known to be around 10 billion years from radiological studies of radioactive isotopes in the solar system (see [9]). Solar models reproduce this quantity (among others, like today's solar luminosity, solar radius). From this one concludes that the exotic contribution to the luminosity cannot exceed the standard solar luminosity in photons. For our purposes this means

$$L_{\rm ALP} < L_\odot = 3.8 \times 10^{26}\, W \approx 1.6\ 10^{30}\, {\rm eV}^2. \tag{3}$$

We compute the ALP emission in the standard solar model BP2000 [10] using Eq. (1) and no further assumptions. We obtain a slightly bigger value than that of [11], where the calculation was done using an older solar model.

$$L_{\rm ALP} = 0.063\, g_{10}^2\ L_\odot, \tag{4}$$

where $g_{10} = g\ 10^{10}\,{\rm GeV}$. Together with Eq. (3) this gives a bound on the coupling. A somewhat strengthened bound including data from so called horizontal brach (HB) stars is shown in Fig. 1.

Another bound comes from the CAST experiment[12]. The CAST experiment tries to detect the axion flux (4) by reconverting the axions in the strong magnetic field generated by an LHC test magnet. The rate of photons in the detector is

$$\text{rate} \sim g^2 L_{\rm ALP} \sim g^4. \tag{5}$$

So far no significant photon flux has been measured. The resulting bound is depicted in Fig. 1.

$R_0/R_\odot$	$\rho_0/(\mathrm{g\,cm^{-3}})$	T_0/eV	$S(R_0)$
0	150	1200	1
0.79	0.1	120	10^{-4}
0.97	0.003	12	10^{-20}

Table 1: Several values for suppression factors.

3 Evading astrophysical bounds

Our strategy to evade the astrophysical bounds is rather simplistic. In the center of the sun where most ALPs are produced the environment is different from the environment of the PVLAS experiment. If the parameters m_ϕ and M_ϕ depend on the environment

$$m_\phi \to m_\phi(\text{environment}), \quad M_\phi \to M_\phi(\text{environment}), \tag{6}$$

in a suitable way the production of the ϕ particles inside the sun is strongly suppressed. In particular, we consider the following:

1. The density ρ inside the sun is quite high.
2. Inside the sun the temperature T is high.
3. The average momentum transfer $\langle q \rangle$ in the Primakoff processes generating the ALP's is high.

We will not try to construct micro physical explanations but rather write down simple effective models and fix their parameters in order to be consistent with PVLAS as well as the astrophysical bounds.

For simplicity we allow in this note only a variation of the coupling g. Suppression via a high mass term in the sun environment is more difficult since it involves a strong coupling to generate the high mass (for more details see [5]). In addition, we will restrict the dependence to a single parameter $\alpha = \rho$, T, etc.. We are mainly interested in giving conservative bounds for g and the suppression scales involved, so instead of guessing possible dependencies $g = g(\alpha)$ we make the calculations with the most optimistic suppression, a step function, i.e. if $\alpha > \alpha_{\mathrm{crit}}$, $g = 0$, and the generation of ALP's in this region is completely suppressed.

The macroscopic quantities ρ, T depend more or less only on the radius. Therefore, we get the following simple picture. In the center of the sun (where naively most ALP's would be produced) the suppression is switched off while in the remaining shell we have no suppression at all. Using this we only need to calculate the production in the outer shell and compare it with the production within the whole volume happening in a scenario without suppression[c],

$$S(R_0) = \text{suppression factor} = \frac{\text{production}(R > R_0)}{\text{production(full sun)}}. \tag{7}$$

We treat the emission of ALP's as a small perturbation of the solar model and therefore can compute the emission of these particles from the unperturbed solar model. We have chosen the BP2000 of Bahcall et al [10]. The suppression factor S for some radii is given in Tab. 3.

Similar reasoning can be applied to $\langle q \rangle$. However, writing down a model it is preferable to use directly the microscopic quantity q. In this situation one has to perform the thermal average

[c]For CAST actually one has to take into account that the CAST detector measures a number and not an energy flux and is only sensitive in a certain energy range. This gives a slightly modified suppression factor $\tilde{S}$ (see [5]).

over the scattering processes (see [5]). For the suppression factors in the range $10^{-4} - 10^{-20}$ the resulting critical q lie in the meV – eV range.

Using Eqs. (4) and (5) we find that a suppression

$$S_{\rm loss} = g_{\rm supp}^2/g_{\rm loss}^2, \quad S_{\rm CAST} = g_{\rm supp}^4/g_{\rm CAST}^4, \tag{8}$$

is needed to achieve a less restrictive bound $g_{\rm supp}$.

The necessary critical values for the temperature, density and momentum transfer for certain suppression factors can be read off from Tab. 3. It is rather obvious that none of these values is very extreme. However, one has to compare to the values in PVLAS. These are even smaller.

$$\rho_{\rm PVLAS} < 2 \times 10^{-5} {\rm g\,cm^{-3}}, \quad T < 300\,{\rm K} \approx 0.025\,{\rm eV}, \quad q \sim 10^{-6}\,{\rm eV}. \tag{9}$$

Hence, we have room for some *exotic* possibilities. Even a suppression factor of 10^{-20} is marginally possible, allowing for the PVLAS result. This gives the red (large) shaded region in Fig. 1. For a somewhat more conservative suppression factor we find the green (smaller) shaded region in Fig. 1.

4 Conclusions: We need lab experiments!

Naively, the particle interpretation of the PVLAS data is in conflict with astrophysical bounds. If we allow for an interaction between photons and axion like particles (ALP's) that depends on other physical quantities (density, temperature and momentum are candidates), the production of ALP's can be suppressed and the astrophysical bounds can be evaded. However, the typical scales appearing in these models are rather low (typically eV and smaller) and the physics must be exotic in this sense. Nevertheless, one cannot rule out these exotic possibilities from the start and PVLAS is a good motivation to look more closely. Since astrophysical bounds can be evaded, a true test can only come from laboratory experiments where we have control of the environmental parameters. A conclusive answer about the particle interpretation of PVLAS can come in particular from so called light shining through walls experiments, where the photon not only disappears but is regenerated. It is exciting that experiments of this type with enough sensitivity to test PVLAS could be built in the next one or two years. An example of such an experiment is APFEL (axion production by a free electron laser) which has been proposed at DESY (see also Fig. 1) and is sensitive enough to test PVLAS[13].

J. Jaeckel would like to thank the organizers for the wonderful conference.

References

1. E. Zavattini *et al.* [PVLAS Collaboration], Phys. Rev. Lett. **96** (2006) 110406 .
2. R. D. Peccei and H. R. Quinn, Phys. Rev. Lett. **38** (1977) 1440.
3. S. Weinberg, Phys. Rev. Lett. **40** (1978) 223.
4. F. Wilczek, Phys. Rev. Lett. **40** (1978) 279.
5. J. Jaeckel, E. Masso, J. Redondo, A. Ringwald, F. Takahashi in preparation.
6. E. Masso and J. Redondo, JCAP **0509** (2005) 015 .
7. P. Jain and S. Mandal, astro-ph/0512155.
8. G. G. Raffelt, "Stars as laboratories for fundamental physics: The astrophysics of neutrinos, axions, and other weakly interacting particles". University of Chicago press (1997).
9. J. N. Bahcall and M. H. Pinsonneault, Rev. Mod. Phys. **67** (1995) 781 .
10. J. N. Bahcall, M. H. Pinsonneault and S. Basu, Astrophys. J. **555** (2001) 990 .
11. K. van Bibber, P. M. McIntyre, D. E. Morris and G. G. Raffelt, Phys. Rev. D **39** (1989) 2089.
12. K. Zioutas *et al.* [CAST Collaboration], Phys. Rev. Lett. **94** (2005) 121301 .
13. R. Rabadan, A. Ringwald and K. Sigurdson, Phys. Rev. Lett. **96** (2006) 110407 .

STATUS AND OUTLOOK OF THE EDELWEISS WIMP SEARCH

M. LUCA
FOR THE EDELWEISS COLLABORATION
Institut de Physique Nucléaire de Lyon, Université Claude Bernard Lyon 1
4 rue Enrico Fermi, 69622 Villeurbanne Cedex, France
E-mail : luca@ipnl.in2p3.fr

EDELWEISS is a direct dark matter search using cryogenic germanium heat–ionisation detectors, located in the Modane underground laboratory beneath the Alps. We summarize the final results of EDELWEISS I, which deployed up to almost one kg of detectors in its final stage. EDELWEISS II recently started commissioning runs. With an increased detection mass and better shielding, this stage aims to gain two orders of magnitude in sensitivity and to serve as a testbed for a larger, ton–scale experiment.

1 Introduction

Understanding the nature of dark matter in the universe is a major challenge for modern cosmology and astrophysics. One of the well–motivated candidates is the particle generically named WIMP (Weakly Interacting Massive Particle), such as the lightest supersymmetric particle. The main constraints when attempting to detect WIMPs are low event rate (less than a few events per kg of detector and per year) and small recoil energies (a few keV).

EDELWEISS (Expérience pour Détecter les WIMPs en Site Souterrain) is a direct dark matter detection experiment using the elastic scattering of WIMPs off target nuclei. EDELWEISS is situated in the Modane Underground Laboratory, in the Fréjus highway tunnel between France and Italy. An overburden of 1700 m of rock, equivalent to 4800 m of water, reduces the muon flux down to 4.5 $\mu/m^2/day$, that is about 10^6 times less than at the surface.

2 EDELWEISS I final results

EDELWEISS uses cryogenic germanium detectors, in a dilution fridge working at about 17 mK. Each detector has a NTD–Ge thermistor that measures the heat signal and two Al electrodes for the ionisation. [1] This technique of measuring two signals simultaneously allows an event by event discrimination between electronic (induced by photons or electrons) and nuclear (induced by neutrons or WIMPs) recoils (Fig. 1). [2]

EDELWEISS I used 320 g Ge detectors during several campaigns. Between 2002 and 2003, three 320 g detectors have been operated simultaneously in a cryostat shielded by 10 cm of Cu, 15 cm of Pb, 7 cm of internal roman Pb and 30 cm of paraffin. After a total fiducial exposure of 62 kg·day with an effective threshold of 15 keV, 59 events have been observed in the nuclear–recoil band. [3] As shown in Fig. 3, most of the events are at low energy, between 10 and 30 keV. The simulated spectra of WIMPs having a scattering cross section on nucleons of 10^{-5} pb and

masses of 20, 40, 100 and 500 GeV/c^2 show that the events in the nuclear recoil band can not be explained by a single WIMP mass, a part of the spectrum has to be attributed to a non–WIMP background.

The two main sources of background that can mimic WIMP events are the mis–collected ionisation events and the neutrons. A two detector coincident event with both hits in the nuclear recoil band has been observed. The most likely source of this event is a neutron scattering. Monte–Carlo simulations predicted about two neutron single events for a total exposure of 62 kg·day. Nevertheless, the exclusion limit in Fig. 2 is derived without any background subtraction. It confirms, after a longer fiducial exposure, the previously published EDELWEISS I limits [4].

EDELWEISS I, once the most sensitive direct dark matter search, became limited mainly because of the radioactive background (neutrons and surface events) and detection mass (the cryostat could not host more than three 320 g detectors). Therefore, the experiment has been stopped in March 2004, and is now replaced by EDELWEISS II.

3 EDELWEISS II

The second stage of the experiment is EDELWEISS II. By diminishing the radioactive background and increasing the detection mass, it should gain a factor of 100 in sensitivity compared to EDELWEISS I. Among the numerous improvements in EDELWEISS II, the main ones are: a new, larger, low consumption cryostat, a larger detection mass, improved detectors, new shieldings and an active muon veto, a class 100 clean room, new electronics and acquisition system.

In order to host up to 120 detectors, the new cryostat is larger (50 l) and has an innovative reversed geometry. Three pulse tubes replace liquid nitrogen cooling and a cold vapor reliquefier reduces helium consumption. The compact and hexagonal arrangement of the detectors should increase the neutron coincidence rate.

3.1 Radioactive background

The main limiting factor for EDELWEISS I was the radioactive background.

In a Ge detector, the ionisation signal coming from particles that interact very close to the surface can be mis–collected, hence the resulting events appearing in the nuclear recoil band. One way of dealing with this problem is by depositing a 60 nm Ge or Si amorphous layer on the crystal surface which diminishes the number of surface events [8]. All detectors used for EDELWEISS I 2002–2003 runs had such layers. Concentric electrodes provide a radial sensitivity allowing to select events occuring in the central part of the detector [9] where the electric field is more homogeneous and the detector better shielded from its environement.

A promising R&D project on surface events uses the sensitivity of NbSi thin film thermometers to athermal phonons [10]. As surface events have a higher athermal component, they can be identified and excluded during analysis. A 200 g detector with NbSi thin films on each end has already been tested in the EDELWEISS I cryostat with good results [10] and is part of the EDELWEISS II setup for the first commissioning runs.

High energy neutrons are hard to moderate and can penetrate the shielding. When interacting with the detector, neutrons can mimic WIMP events, therefore they are an important issue for EDELWEISS II. Some of the ways of dealing with this problem in EDELWEISS II are a better shielding, a muon veto and the increase in the number of neutron coincident events.

3.2 SciCryo

Another R&D project, *SciCryo*[a], studies the possibility of using heat–scintillation bolometers for dark matter detection. For now, *SciCryo* has focused on light targets, complementary to Ge detectors and interesting for both neutron detection and spin–dependent interactions. So far, the most promising light target is Al_2O_3. Several nominally pure sapphire crystals have been tested in Lyon at room temperature and all of them have been seen to scintillate. Some of the crystals have also shown very encouraging low temperature light yields in tests performed at the IAS and the MPP. As a result of these tests, a 50 g IAS sapphire heat–scintillation detector has been included in the first EDELWEISS II commissioning runs to check its compatibility with the setup.

3.3 EDELWEISS II near future

Since January 2006, commissioning runs are taking place in order to check the level of microphonics and to test the new electronics and acquisition system. For now, eight detectors have been mounted in the cryostat: 4 Ge/NTD EDELWEISS I detectors, 2 new 320 g Ge/NTD detectors and 2 R&D detectors (a 200 g Ge/NbSi and a 50 g sapphire heat–scintillation detector). The goals for this year are to increase the number of bolometers to 28 and to define the next stage that may include up to 120 detectors.

4 Conclusion

EDELWEISS I, once the most sensitive direct dark matter search has been stopped in 2004. An important result of EDELWEISS I was the identification of the two main sources of background, surface events and neutrons. EDELWEISS II should gain a factor of 100 in sensitivity thanks to improved detectors, shielding, cleanliness and a higher detection mass. The main R&D projects concern the NTD and NbSi Ge detectors as well as the cryogenic heat–scintillation detectors. Preliminary results are expected in 2006.

Acknowledgments

This work has been partially funded by the EEC Network program under the contract HPRN–CT–2002–00322, the ILIAS integrating activity contract RII3-CT-2003-506222 and by Agence Nationale de la Recherche grant JC05_41907.

References

1. A. Benoit *et al.*, *Phys. Rev. B* **479**, 8 (2000).
2. P. Di Stefano *et al.*, Astropart. Phys. **14**, 329 (2001).
3. V. Sanglard *et al.*, *Phys. Rev. D* **71**, 122002 (2005).
4. A. Benoit *et al.*, *Phys. Rev. B* **545**, 43 (2002).
5. G. Angloher *et al.*, Astropart. Phys. **23**, 325 (2005).
6. D. Abrahams *et al.*, *Phys. Rev. D* **66**, 122003 (2002).
7. R. Bernabei *et al.*, *Phys. Rev. B* **480**, 23 (2000).
8. T. Shutt *et al.*, *Nucl. Instrum. Methods A* **444**, 340 (2000).
9. O. Martineau *et al.*, *Nucl. Instrum. Methods A* **530**, 426 (2004).
10. S. Marnieros *et al.*, *Nucl. Instrum. Methods A* **520**, 185 (2004).

[a] Institut de Physique Nucléaire de Lyon (IPNL), Institut d'Astrophysique Spatiale Orsay (IAS), Max Planck Physik Munich (MPP), Laboratoire de Physico–Chimie des Materiaux Luminescents Lyon (LPCML)

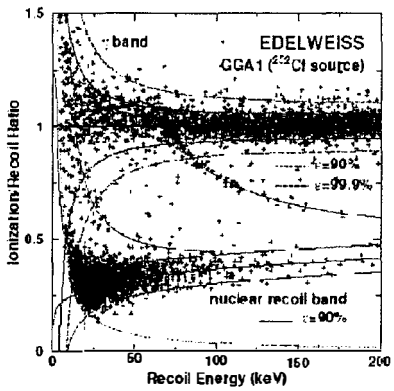

Figure 1: Ratio between the ionisation and the recoil energy versus the recoil energy. The separation between the electronic and the nuclear recoil band is excellent down to an energy of about 15 keV.

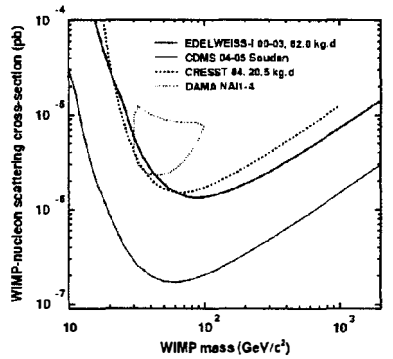

Figure 2: Spin independent exclusion limits on WIMPs, obtained with standard astrophysical assumptions within a 90% C.L.. Solid dark curve is the EDELWEISS I final limit, dashed curve is the CRESST limit from $CaWO_4$ [5], solid light curve is the CDMS limit from the Soudan mine [6] and closed contour is the allowed region at 3σ C.L. from DAMA NaI1-4 annual modulation data [7].

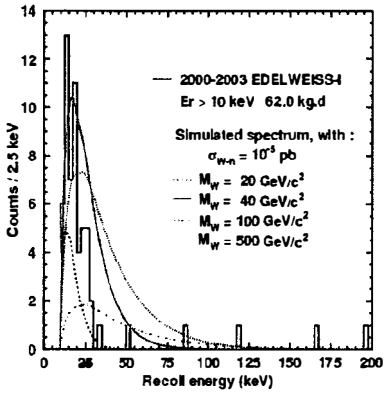

Figure 3: Energy spectrum of the EDELWEISS I experimental data compared to simulated spectra for different WIMP masses in the range of interest.

Galactic hidden compact objects: the EROS results

M. Moniez
Laboratoire de l'Accélérateur Linéaire, IN2P3 CNRS, Université Paris-Sud, 91405 Orsay Cedex, France

We present the results of the EROS2 search for the hidden galactic matter of the halo through the gravitational microlensing of stars in the Magellanic clouds. Microlensing was also searched for and found in the Milky-Way plane, where foreground faint stars are expected to lens background stars. A total of 67 million of stars were monitored over a period of about 7 years. Hundreds of microlensing candidates have been found in the galactic plane, but only one was found towards the bright –well measured– subsample of the Magellanic stars. This result implies that massive compact halo objects (machos) in the mass range $10^{-7} M_\odot < M < 5 M_\odot$ are ruled out as a major component of the Milky Way Halo.

1 Introduction

From 1990 to 2003, EROS team has performed a large program of microlensing survey towards the Magellanic Clouds (LMC and SMC), the Galactic center (CG) and the Galactic spiral arms (GSA), as far as 55° longitude away from the galactic center. Gravitational microlensing [11] occurs if a massive compact object passes close enough to the line of sight of a star, temporarily magnifying its light. In the approximation of a single point-like object moving with a relative constant speed in front of a single point-like source, the visible result is an achromatic and symmetric variation of the apparent source luminosity as a function of time. The "lensing time scale" t_E, given by the ratio between the Einstein radius of the deflector and its transverse speed V_T, is the only measurable parameter bringing useful information on the lens configuration:

$$t_E(days) = 78 \times \left[\frac{V_T}{100 km/s}\right]^{-1} \times \left[\frac{M}{M_\odot}\right]^{\frac{1}{2}} \times \left[\frac{L}{10\ Kpc}\right]^{\frac{1}{2}} \times \frac{[x(1-x)]^{\frac{1}{2}}}{0.5},$$

where L is the distance to the source, xL is the distance to the deflector and M its mass. The optical depth τ towards a target is defined as the average probability for the line of sight of a target star to intercept the Einstein ring of a deflector (magnification > 1.34).

2 Observations and data reduction

EROS2 uses a $\sim$ 1 deg^2 CCD mosaique mounted on the MARLY 1 meter diameter telescope installed at the La Silla ESO observatory (see [6] and references therein). We monitored 98 deg^2 in the Magellanic Clouds, 60 deg^2 in the CG, and 29 deg^2 in the GSA. Images were taken simultaneously in two wide passbands. To a precision of $\sim$ 0.1 mag, the Eros magnitudes satisfy

$$R_{\rm eros} = I_{\rm C} \quad B_{\rm eros} = V_{\rm J} - 0.4(V_{\rm J} - I_{\rm C}).$$

Each field has been measured at least a few hundred times in each passband.

The production of light curves proceeded in three steps : template images construction, star catalog production from the templates, and photometry of individual images to obtain the light curves. Our catalogues contain about 29.2×10^6 objects from the LMC, 4.2×10^6 from the SMC, $20. \times 10^7$ from the CG and 13.3×10^7 from the GSA. After alignement with the catalogue, photometry is performed on each image with software specifically designed for crowded fields, PEIDA (Photométrie et Étude d'Images Destinées à l'Astrophysique) [4].

3 Using the brightest stars to escape the blending problems

Using sophisticated simulations, we found that the optical depth underestimate due to the microlensing magnification underestimate induced by source confusion (blending) is compensated by extra events due to faint stars within the seeing disk of resolved objects. Nevertheless, considering the size of the effects, we decided to consider only the subsample of the brightest stars, that do much less suffer from blending complications, to obtain reliable microlensing optical depth estimates towards the Magellanic clouds and the Galactic center. We then concentrated on the clump red-giant stars towards the CG, and on the stars with $R_{eros} < 18.2$ to 19.7 (depending on the field density) towards the LMC. Another advantage to use these brightest stars is that they also benefit from the best photometric resolution. The philosophy is somewhat different towards the Galactic spiral arms, because of, contrary to the other targets, the distance of the sources is widely distributed and poorly known. We therefore decided to keep all the stars for the optical depth estimates, and to define the concept of "catalogue optical depth", that is relative to our specific catalogue of monitored stars. The interpretation of this optical depth requires a carefull modelisation of the galaxy plane as it results from an average of optical depth on a continuum of source distances. The final sample of light-curves on which we have searched for microlensing then contains respectively 6.05×10^6 and 0.9×10^6 bright stars towards LMC and SMC, 5.6×10^7 clump-giant stars towards the CG and 13.3×10^7 stars towards the GSA.

4 The search for lensed stars

Before the analysis is started, we remove from the light curves measurements taken in far from normal conditions. The general philosophy for the event selection is common to all the targets. The details vary with the monitored population, through the magnitudes, the typical exposure durations, the sampling and the seasonal observation conditions. Here we will only give the general outline of the selection. Details on the analysis of CG and LMC can be found in [9] and [12].

We first searched for bumps in the light curves, that we characterized by their probability to be due to accidental occurence on a stable star light curve. We select the light curves that have a significant positive fluctuation in both colours with a sufficient time overlap. To reject most of the periodic or irregular variable stars, we remove the light curves that have significant other bumps (*positive or negative*). After this filtering, the remaining light curves can be fitted for the microlensing hypothesis, and the final selection is based on variables using the fitted parameters. We apply criteria devised so as to select microlensing events, keeping in mind that such analysis should also detect events with second order effects such as parallax, binary lens... Specific rejection criteria against background supernovae have also been applied towards the Magellanic clouds. We estimate our detection efficiency using the technique of the superposition of simulated events on experimental light curves from an unbiased sub-sample of our catalogues.

5 Candidate sample

We found 120 events towards the sample of clump-giants of the CG [9], 26 events towards the GSA, and only one event [1] (see Fig. 1) towards the bright stellar population of SMC/LMC.

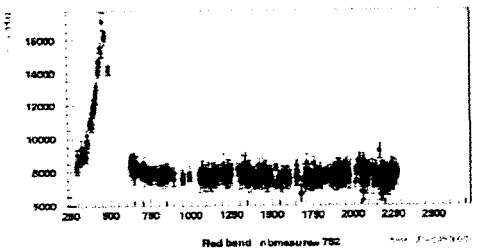

Figure 1: *Light-curve of the SMC microlensing event in the EROS red-passband.*

With respect to previous EROS publications [3,10], the number of events towards LMC/SMC has changed. Amongst the reasons are the fact that we now concentrate on the bright stars, and the fact that candidates died because they exhibited another significant bump years after their selection.

6 Discussion. Limits on the abundance of machos

We find that the optical depths towards the CG and the 4 targets in the GSA are in good agreement with the predictions from the galactic models [9,7] (Fig. 2).

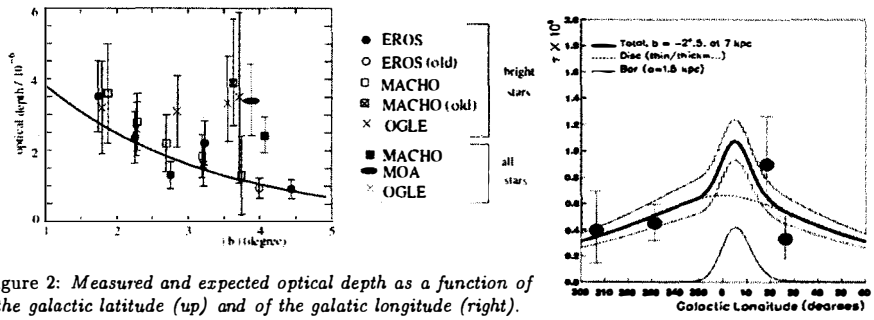

Figure 2: *Measured and expected optical depth as a function of the galactic latitude (up) and of the galatic longitude (right).*

In contrast, we have found only one event towards the Magellanic clouds, whereas ~ 50 events would have been expected if the halo were entirely populated by objects of mass $0.2M_{\odot} < M < 0.8M_{\odot}$. We then deduce an upper limit on the contribution of the compact objects to the so-called standard spherical halo (see Fig. 3). This limit can also be expressed in optical depth. In the $t_{\rm E}$ range favored by the MACHO collaboration, we find $\tau_{\rm lmc} < 0.3 \times 10^{-7}$ *at* 95% CL, in clear conflict with the value of the MACHO collaboration, $\tau_{\rm lmc} = 1.2^{+0.4}_{-0.3} \times 10^{-7}$, based on the observation of 17 events [2]. For the SMC, the one observed event corresponds to an optical depth of 1.7×10^{-7}. Taking into account only Poisson statistics on one event, this gives $.085 \times 10^{-7} < \tau_{\rm smc} < 8.7 \times 10^{-7}$ *at* 95% CL. This is consistent with the expectations of lensing by objects in the SMC itself [8], $\tau_{\rm smc-smc} \sim 0.4 \times 10^{-7}$. The value of $t_{\rm E} = 120$ *days* is also consistent with expectations for self-lensing as $\langle t_{\rm E} \rangle \sim 100$ *days* for a mean lens mass of $0.35M_{\odot}$. We also note that the self-lensing interpretation is favored from the absence of an indication of parallax in the light curve [5].

There are considerable differences between the EROS and MACHO data sets that may explain the conflict. Generally speaking, MACHO uses faint stars in dense fields (1.2×10^7 stars over 14 deg^2) while EROS2 uses bright stars in sparse fields (0.7×10^7 stars over 90 deg^2). As a consequence of the use of faint stars, only two of the 17 MACHO candidates are sufficiently bright to be compared to our bright sample (and the corresponding events occured before EROS

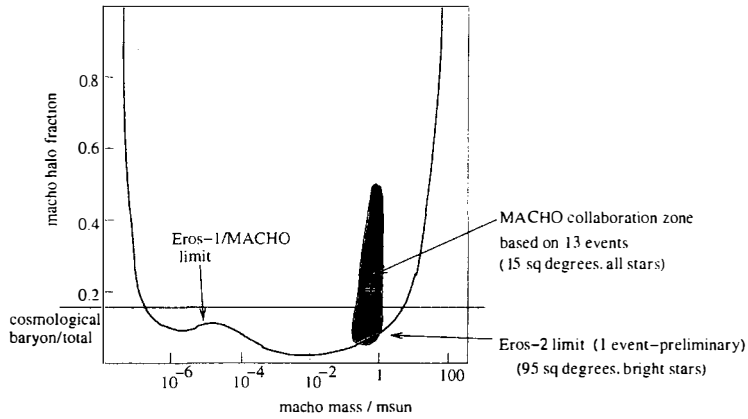

Figure 3: The solid line shows the EROS upper limit on the contribution of compact objects to a standard spherical Galactic halo, as a function of their mass, based on zero observed LMC events and assuming that the one observed SMC event is not due to halo lensing.

data taking). The use of dense fields by the MACHO group also suggests that the higher MACHO optical depth may be due, in part, to self lensing in the inner parts of the LMC. The contamination of irregular variable objects faking microlensing in low photometric resolution events should also be stronger in the faint sample of stars used by MACHO. As already mentionned, another problem with the use of faint source stars is the large blending effects that must be understood. The experience with the use of faint stars in the Galactic Bulge suggest that the uncertainty induced by the blending effects in such a sample may be underestimated.

7 Conclusions

The EROS and MACHO programs were primarily motivated by the search for halo brown dwarfs of $M \sim 0.07 M_{\odot}$. EROS has demonstrated its sensitivity to microlensing events, finding microlensing rates compatible with the predictions of the galactic models in the Galactic plane. The lack of events towards the Magellanic clouds clearly indicates that the Galactic hidden matter is not made of compact objects in the mass range $10^{-7} M_{\odot} < M < 5 M_{\odot}$. Whatever the source of the disagreement between EROS and MACHO on this subject, we can hope that new data from the OGLE3 , MOA and SUPER-MACHO collaborations will settle the matter.

1. Afonso, C., et al., ApJ **400**, 951 (2003)
2. Alcock, C., et al. (MACHO coll.) ApJ **541**, 734 (2000)
3. Ansari, R., et al. (EROS-1 coll.), A&A **314**, 94 (1996)
4. Ansari, R. (EROS-2 coll.), Vistas in Astronomy **40**, 519 (1996)
5. Assef, R.J., et al, astro-ph/0604147, 2006, submitted to ApJ.
6. Bauer, F. et al., Proc. of the "Optical Detectors for Astronomy" workshop, ESO, 1997
7. Derue F., et al. (EROS-2 coll.), A&A **373**, 126 (2001)
8. Graff, D. & Gardiner, L.T., MNRAS **307**, 577 (1999)
9. Hamadache, C., et al., astro-ph/0601510, accepted for publication in A&A
10. Lasserre, T. et al., A&A **355**, L39 (2000)
11. Paczyński, B., ApJ **304**, 1 (1986)
12. Tisserand, P. 2004, Thesis Université de Paris VI, *http://tel.ccsd.cnrs.fr/*

SLAC-PUB-11863

Search for Gamma-rays from Lightest Kaluza-Klein Particle Dark Matter with GLAST

E.Nuss[a], J.Cohen-Tanugi[b] and A.Lionetto[c]
on behalf of GLAST LAT Dark Matter and New Physics Working Group

[a] *LPTA Montpellier II University*
[b] *Stanford Linear Accelerator Center, Stanford, California*
[c] *Physics Department & INFN Roma Tor Vergata*

The Gamma-Ray Large Area Space Telescope (GLAST), scheduled to be launched in 2007, is the next generation satellite for high-energy gamma-ray astronomy. The Large Area Telescope (LAT), GLAST main instrument, has a wide field of view (> 2 sr), a large effective area and a 20 MeV - 300 GeV energy range. It provides excellent high-energy gamma-ray observations for Dark-Matter searches. Here we study the possibility to detect gamma-rays coming from Lightest Kaluza-Klein Particle (LKP) annihilations in the context of the minimal Universal Extra Dimensions (UED) models. We perform the analysis for different LKP masses and for a Galactic Center (GC) Navarro, Frenk and White (NFW) halo model modified by a boost factor parameter. Finally we give an estimate of the background to obtain the expected total gamma-ray flux and the corresponding expected GLAST sensitivity.

1 Introduction

The nature of the Cold Dark Matter (CDM) is probably one of the most outstanding open questions in present day Cosmology. It has been a subject of special interest to high-energy physicists, astrophysicists and cosmologists for many years. According to a wealth of observations and arguments, such as excessive peculiar velocities of galaxies within clusters of galaxies or gravitational arcs, it can make up a significant fraction of the mass of the universe. On the galactic scale, dark matter halos are required to explain the observed rotation curves in spiral galaxies or the velocity dispersion in elliptical galaxies. Virtually all proposed candidates require physics beyond the standard model of particle physics and could be detected through stable products of their annihilations: energetic neutrinos, antiprotons, positrons, gamma-rays etc. Supersymmetric extensions of the standard model of particle physics provide a natural candidate for CDM in the form of a stable uncharged Majorana fermion (Neutralino). However, Kaluza-Klein (KK) Dark Matter in the framework of Universal Extra Dimensions (UED) has been proposed [1] as an interesting alternative scenario and received much attention in recent years.

Hereafter, we briefly report on the potential of the GLAST high-energy gamma-ray telescope to detect KK Dark Matter indirectly through their annihilation in the halo of the galaxy.

2 The Gamma-ray Large Area Space Telescope (GLAST) mission

GLAST is an international satellite-based observatory that will study the gamma-ray Universe [a]. Its main instrument, the Large Area Telescope (LAT), is a modular 4x4-tower pair-conversion telescope instrumented with a plastic anticoincidence shield which vetoes charged cosmic rays, a tracker of silicon strip planes with foils of tungsten converter followed by a segmented CsI electromagnetic calorimeter. A photon traversing the tracker will have some probability of converting into the tungsten foils, thus forming an electron-positron pair, subsequently tracked

[a] For more details, see the GLAST website at: http://glast.gsfc.nasa.gov/

by the silicon strip detectors. The reconstructed trajectories of this pair, together with their energy deposition in the calorimeter, allows to reconstruct the direction and energy of the incident gamma-ray photon. The main characteristics of the full LAT detector, i.e. the effective area, point spread function and energy dispersion, have been obtained from detailed Monte Carlo studies and parameterized by a series of functions: the Instrument Response Function (IRF) [b]. The LAT takes much of its basic design concept from its predecessor EGRET but the energy range (20 MeV-300 GeV and above), field-of-view (greater than 2 steradians) and angular resolution will provide the LAT with a factor ~30 better sensitivity. This improvement should allow the LAT to detect several thousands of new high-energy sources and shed light on many issues left open by EGRET.

A detailed description of GLAST science prospects and an introduction to the experiment can be found in [2]. The LAT is now completed, and represents the largest silicon strip detector ever built. It will undergo environmental testing soon, and then will be handed to the spacecraft vendor for integration.

GLAST is scheduled for launch in September 2007.

3 Kaluza-Klein Dark Matter with GLAST in minimal universal extra dimensions models

Models with extra spatial dimensions predict a tower of Kaluza-Klein (KK) particles for every field that propagates in the higher dimensional bulk. In universal extra dimensions models (UED), all standard model fields propagate and it is natural to attempt to identify one of these KK particles with dark matter.

Here, we will consider the simplest, five-dimensional model with one compactified UED on an S^1/Z_2 orbifold of radius R. As the extra dimensions are compactified on orbifolds, a discrete symmetry, called KK parity, is preserved and ensures the stability of the lightest KK particle (LKP). Then, as the LKP is neutral with respect to the SM gauge groups with a mass (which is inversely proportional to the compactification radius R) at the weak scale, an excellent dark matter candidate naturally emerges in a stable WIMP with relic density naturally in the right range [1]. In supersymmetric theories superpartners differ in spin by 1/2, while in scenarios with extra dimensions, the excited KK states have the same spin as their ground state standard model partners. A one-loop calculation shows that the LKP is likely to be associated with the first KK excitation of the photon, more precisely the first excited KK state of the hypercharge gauge boson B. The $B^{(1)}$ relic density depends on the mass spectrum and the coannihilation channels. It was shown [1] that the limit from the Wilkinson Microwave Anisotropy Probe (WMAP) of $\Omega_{CDM}h^2 = 0.12 \pm 0.02$ corresponds to $500\ GeV \lesssim m_{B^{(1)}} \lesssim 1000\ GeV$ where h is the Hubble constant. The lower bound on the $B^{(1)}$ mass in UED models excludes any possibility of gamma-ray line signal from UED models with GLAST ($E_\gamma \lesssim 300$ GeV) and we will therefore concentrate on continuum spectra.

Unlike the supersymmetric case, charged lepton production is not helicity suppressed and then, the suppression factor associated to Majorana fermion dark matter does not apply. At tree level, the branching ratios for $B^{(1)}$ pairs annihilation are [1] quark pairs (35%), charged lepton pairs (59%), neutrinos (4%), charged (1%) and neutral (0.5%) gauge bosons, and Higgs bosons (0.5%).

We will consider the primary gamma-rays from cascading decays of $q\bar{q}$ final states and, as proposed in [3], we will also consider secondary gamma-rays from radiative photon emission of high-energy charged leptons and the semi-hadronic decays of τ leptons. For primary gamma-rays, we will use the approximation of Fornengo et al [4], who have used the PYTHIA Monte Carlo

[b] http://www-glast.slac.stanford.edu/software/IS/glast_lat_performance.html

code to parametrize $dN_\gamma^{q,\tau}/dE$ for quarks and τ leptons with a center of mass energy of 1 TeV. Using DarkSusy [5] simulations, we checked that the approximations was still valid for the energy range we have considered ($m_{B^{(1)}} = 500, 800$ and $1000\ GeV$). We neglect the few percent going into W, Z, and Higgs final states. For secondary gamma-rays from charged leptons, we will use de analytic computation given in Bergström et al [3].

Following [6], the differential gamma-ray flux from dark matter particle annihilation in the GC can be written as

$$\Phi_\gamma = \frac{1}{4\pi} \frac{\langle N_\gamma \sigma v \rangle}{2m^2_{B^{(1)}}} \int_{\Delta\Omega} \int_{\text{line of sight}} \rho^2(l)\ dl(\psi)\ d\Omega$$

where the integral runs along the line of sight, in a direction making an angle ψ respect to the direction of the GC and $\Delta\Omega$, the angular acceptance of the detector. $m_{B^{(1)}}$ is the mass of the LKP and N_γ is the total number of photons per annihilation above a given energy threshold E_{th}. The annihilation cross section $\langle \sigma v \rangle$ can be computed in the non relativistic expansion limit ($\langle \sigma v \rangle \simeq a + bv^2$) from [1]. Here we are only concerned with the annihilation into fermions f which, is given by $< \beta \sigma_{B^{(1)}B^{(1)} \to f\bar{f}} >_{v \to 0} = 0.518 \times (1\ TeV/m_{B^{(1)}})^2\ pb$. In order to separate the factors depending on the profile from those depending only on particle physics, we introduce the quantity $J(\psi)$, as defined in [6] and $\overline{J}(\Delta\Omega)$, the average of $J(\psi)$ over a spherical region of solid angle $\Delta\Omega$, centered on $\psi = 0$. We can then express the differential flux from a solid angle $\Delta\Omega$ as

$$\frac{d\Phi_\gamma}{dE_\gamma} = 1.4\ 10^{-8}\ \frac{dN_\gamma}{dE} \left(\frac{1\ TeV}{m_{B(1)}} \right)^4 \bar{J}(\Delta\Omega) \times \Delta\Omega\ \ m^{-2}\ s^{-1}$$

The details of the dark matter distribution in the Galactic halo remains rather uncertain. Numerical N-body simulations favor cuspy halos, with radial density distributions ranging from r^{-1} to $r^{-1.5}$ in the inner regions [7,8]. Bearing these uncertainties in mind, we will assume a moderately cuspy (r^{-1}) Navarro, Frenk and White (NFW) profile with a boost factor b. The boost factor parameter allows for deviation from a pure NFW profile (for which $b = 1$). It can be as high as 1000 in case of adiabatic compression effects [9].

The total number of photons per $B^{(1)}B^{(1)}$ annihilation is given by $dN_\gamma/dE = \sum_i B_i dN\gamma^i/dE$ where the sum is over all processes that contribute to primary and secondary gamma-rays with B_i the corresponding branching ratio.

In the left panel of Fig.1 we show (for comparison with Bergström et al [3]) the differential spectra we computed for a 800 GeV LKP with a boost factor $b \simeq 200$ in considering a region of 10^{-5} sr around the GC. We also show the various contributions to the differential flux as discussed above. In the right panel, we plotted the (normalized) differential spectra obtained for a 500, 800 and 1000 GeV LKP as compared with a E^{-2} spectra and a typical mSUGRA neutralino of 500 GeV. We clearly see that in the energy range we have considered for GLAST (5 GeV-300 GeV) the differential flux of the KK particle is close to a E^{-2} spectrum which is typical from standard astrophysical source : the connection with ground based Cherenkov arrays will be needed to disentangle both KK signal from standard astrophysical one. We can also see that the KK spectral shape is weakly dependent on the $B^{(1)}$ mass and we will only consider the 500 GeV LKP spectra in our simulations.

4 Simulations and preliminary LAT sensitivity to Kaluza-Klein Dark Matter

Using the differential spectra obtained for a 500 GeV LKP as described in the previous section, we performed a full detector simulation including the latest IRF, orbit dependent effects, dead time and South Atlantic Anomaly for one year operation. Using a modeling of the astrophysical sources, we simulated a 30 degree radius FOV centered at the GC with a NFW dark matter profile and $m_{B^{(1)}} \simeq 500$ GeV. We also simulated the diffuse background based on GALPROP

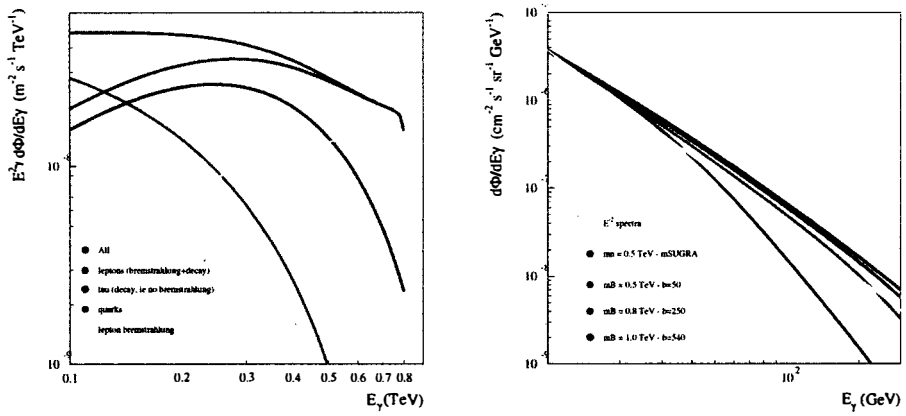

Figure 1: Various contributions to the differential spectra (left) for a 800 GeV LKP and 500,800 and 1000 GeV spectra (right) as compared with E^{-2} and typical mSUGRA neutralino of 500 GeV differential spectra.

code (point source substracted). For $E_{th} = 5$ GeV and $\Delta\Omega = 0.84\ sr$, the total integrated flux leads to the 5 σ sensitivity flux $\Phi_\gamma(\Delta\Omega, E_\gamma \geq E_{th}) = 4\ 10^{-4}\ m^{-2}\ s^{-1}$. For comparison, a NFW profile with a 500 GeV LKP leads to $\Phi_\gamma(\Delta\Omega, E_\gamma \geq E_{th}) = 2\ 10^{-5}\ m^{-2}\ s^{-1}$ which shows that a moderate boost factor of $b \simeq 20$ is needed to reach the 5 σ sensitivity.

5 Conclusions

In this paper we computed a preliminary GLAST-LAT sensitivity to indirect gamma-ray signature of KK dark matter, based on the best simulations currently available to the LAT collaboration. Despite its dependancy on a still unprecisely known background, our estimate shows that the GLAST telescope, should be capable of searching for Kaluza-Klein dark matter in the energy range $E_\gamma \geq 5$ GeV with moderate boost factors. However, due to the $\sim E^{-2}$ spectral shape of the KK spectra in the energy range we considered, joint observations with ground based Cherenkov arrays (continuum and gamma-ray lines) will be needed to disentangle KK signal from the signal of a standard astrophysical source.

References

1. G. Servant, T. M.P. Tait, *Nucl. Phys.* B **650**, 391 (2003).
2. P.F. Michelson, "The Gamma-ray Large Area Space Telescope Mission: Science Opportunities" in *AIP Conf. Proc. 587: Gamma 2001 : Gamma-Ray Astrophysics*, 2001, pp.713-+.
3. L. Bergstrom *et al*, *Phys. Rev. Lett.* **94**, 131301 (2005).
4. N. Fornengo, L. Pieri, S. Scopel, *Phys. Rev.* D **70**, 103529 (2004)
5. P. Gondolo *et al*, *JCAP* 0407 008 (2004)
6. L. Bergstrom *et al*, *Astropart.Phys.* **9**, 137 (1998).
7. J.F. Navaro, C.S. Frenk & S.D.M. White, *ApJ* **462**, 563 (1996).
8. B. Moore et al, *MNRAS* **310**, 1147 (1999).
9. F. Prada et al, *astro-ph/0401512.*

PROBING DARK ENERGY WITH CONSTELLATION-X

D. A. RAPETTI[1], S. W. ALLEN[1], CON-X FACILITY TEAM
[1]*Kavli Institute for Particle Astrophysics and Cosmology, Stanford University, 382 Via Pueblo Mall, Stanford 94305-4060, USA.*

Constellation-X will carry out two powerful and independent sets of tests of dark energy based on X-ray observations of galaxy clusters: The first group of tests will measure the absolute distances to clusters, primarily using measurements of the X-ray gas mass fraction in the largest, dynamically relaxed clusters, but with additional constraining power provided by follow-up observations of the Sunyaev-Zel'dovich (SZ) effect. As with supernovae studies, such data determine the transformation between redshift and true distance, $d(z)$, allowing cosmic acceleration to be measured directly. The second, independent group of tests will use the spectroscopic capabilities of Con-X to determine scaling relations between X-ray observables and mass. Together with theoretical models for the mass function and X-ray and SZ cluster surveys, these data will help to constrain the growth of structure, which is also a strong function of cosmological parameters.

1 Introduction

The late-time accelerated expansion of the Universe is now a well measured fact[15,2,17]. However, the underlying cause of this cosmic acceleration remains completely unknown. Assuming general relativity, a new energy component of the Universe, so-called dark energy, is required. In order to pin down its nature, several future experiments have been projected.

Con-X [a] data will constrain dark energy with comparable accuracy and in a beautifully complementary manner to the best other techniques available circa 2018. For example, with a modest $\sim 10-15\%$ (10-15Ms) investment of the available observing time over the first 5 years of the Con-X mission, we will be able to measure the X-ray gas mass fraction (or predict the Compton y-parameter) to 5% or 3.5% accuracy for 500 or 250 clusters, respectively, with a median redshift $z \sim 1$. When combined with CMB data, the predicted dark energy constraints from Con-X X-ray gas mass fraction data are comparable to those projected by e.g. future supernovae, weak lensing and baryon oscillations experiments. Only by combining such independent and complementary methods can a precise understanding of the nature of dark energy be achieved.

2 Gas mass fraction, $f_{\rm gas}$, in X-ray galaxy clusters

The matter content of rich clusters of galaxies is expected to provide an almost fair sample of the matter content of the Universe, $\Omega_{\rm m}$[20,21,6]. The ratio of baryonic to total mass in these clusters should closely match the ratio of the cosmological parameters $\Omega_{\rm b}/\Omega_{\rm m}$ (where $\Omega_{\rm b}$ is the mean baryonic matter density of the Universe in units of the critical density). Measurements of the

[a] http://constellation.gsfc.nasa.gov/

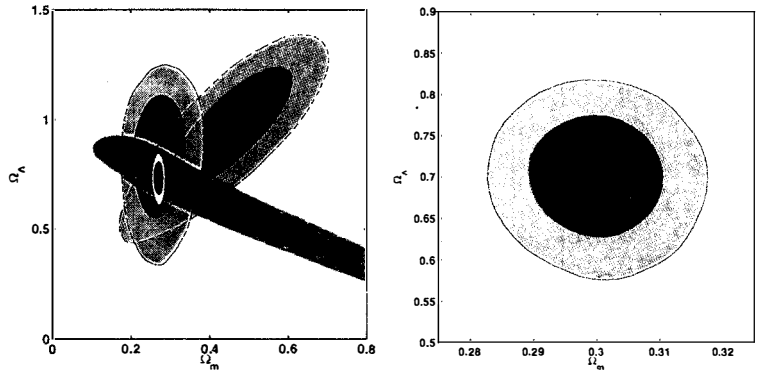

Figure 1: (left panel) The joint 1 and 2 σ contours on Ω_m and Ω_Λ from the current Chandra $f_{gas}(z)$ data (red; Allen et. al 2006, in preparation). Also shown are the constraints from SNIa (green; Riess et al. 2004) and CMB studies (blue; WMAP+CBI+ACBAR). The same contours from the analysis of the simulated Con-X f_{gas} data set of Fig. 2 are shown in orange. These constraints are also shown alone in the right panel of this figure.

X-ray emitting gas mass fraction as a function of redshift can also be used to measure cosmic acceleration directly.

Measuring $f_{gas}(z)$, the ratio of X-ray gas mass to total mass within a radius corresponding to a fixed overdensity of 2500 times the critical density using current Chandra X-ray Observatory data of the largest, dynamically relaxed clusters in the Universe [1,2,3] [b], provide us with one of our most accurate measurements of Ω_m and a $> 99.99\%$ significant detection of the effects of dark energy (cosmic acceleration) on distances to the clusters at the observed redshifts.

The observed f_{gas} values for a chosen reference cosmology are fitted with a model that accounts for the expected apparent variation in $f_{gas}(z)$ as the true, underlying cosmology is varied

$$f_{gas}^{\Lambda CDM}(z) = \frac{b\,\Omega_b}{\left(1+0.19\sqrt{h}\right)\Omega_m}\left[\frac{d_A^{\Lambda CDM}(z)}{d_A^{de}(z)}\right]^{1.5}, \qquad (1)$$

where $d_A^{de}(z)$ and $d_A^{\Lambda CDM}(z)$ are the angular diameter distances ($d_A = d_L/(1+z)^2$) to the clusters for a given dark energy (de) model and the reference standard ΛCDM cosmology, respectively. $H_0 = 100\,h\,\mathrm{km\,sec^{-1}\,Mpc^{-1}}$ is the present Hubble parameter and b is the 'bias' factor by which the baryon fraction is depleted with respect to the universal mean (a small amount of gas is expelled by shocks when the cluster forms). As discussed by Allen *et al* (2004), a Gaussian prior on $b = 0.824 \pm 0.089$ is appropriate for clusters of the masses studied here.

Current constraints from 41 hot ($kT > 5keV$), X-ray luminous ($L_X > 10^{45} h_{70}^{-2} ergs^{-1}$), dynamically relaxed clusters spanning the redshift range $0.06 < z < 1.07$ are shown in Figure 1 (red contours). Rapetti *et al* (2005, 2006 in preparation) show the complementary nature of the f_{gas}, type Ia supernovae and CMB experiments and its crucial degeneracy breaking power.

3 Dark energy constraints from Con-X

Our f_{gas} projected from Con-X constraints assume a modest 10-12Ms investment of Con-X observing time (approximately 10 per cent of the available observing time over the first 5 years

[b] http://www.stanford.edu/group/xoc/

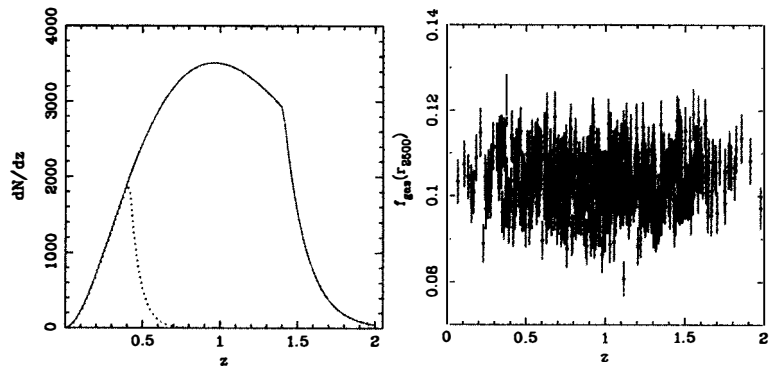

Figure 2: (left panel) The predicted number density of clusters with bolometric X-ray luminosities $L_X > 2 \times 10^{45} h_{70}^{-2} erg/s$ for a cluster survey flux limit of $5 \times 10^{-14} erg/cm^2/s$ in the $0.1 - 2.4\,keV$ band (red, solid curve). The blue, dotted curve shows the results for the same luminosity limit but a flux limit of $10^{-12} erg/cm^2/s$, appropriate for the ROSAT All-Sky Survey [4]. These predictions are consistent with the observed number density of clusters of similar L_X at lower redshifts in the BCS [5] and MACS [4] samples. (right panel) The predicted $f_{gas}(z)$ values for the proposed Con-X survey of 500 clusters with individual f_{gas} uncertainties of 5%. A systematic scatter of 4% due to cluster-cluster variations in the bias parameter b is included.

of the mission). Using an existing Xray-SZ cluster sample and having identified the 200 -500 most dynamically relaxed systems from short Con-X snapshot observations (budget 2Ms), we will re-observe those clusters for a further 10Ms total. This implies a typical exposure time of 20ks for a 500 cluster sample leading to individual statistical error bars in f_{gas} of 5% (our analyses include a conservative 4% systematic scatter predicted from cluster to cluster). Figure 2 shows our predicted f_{gas} sample. We analyse this simulated Con-X f_{gas} data set either alone, imposing 2% priors on $\Omega_b h^2$ and h (Fig. 1, orange contours) or combined with a simulated CMB data set as shown in Figure 3. We use 2% priors on b in both cases. For the evolving dark energy case of Fig. 3 we obtain comparable results to those projected by supernovae [8] and baryon oscillations experiments [9].

The combination of X-ray and Sunyaev-Zel'dovich (SZ) data provides a second, independent method by which to measure absolute distances to clusters. The observed SZ flux can be expressed in terms of the Compton y-parameter. This same Compton y-parameter can be predicted from the X-ray data ($y_{mod} \propto \int n_e T dl$), with the predicted value depending on the assumed cosmology. For the correct cosmology, the observed and predicted y-parameters should agree [11,12,16]. The right panel of Figure 3 shows the projected constraints for a standard ΛCDM cosmology using the 500 cluster sample.

Clusters of galaxies are sensitive probes of the rate at which cosmic structure evolves. Their number density at a fixed mass threshold is exponentially sensitive to the amplitude of linear matter density perturbations. The cluster mass function observed at different redshifts constrains the perturbation growth parameter, $G(z)$, which is the second (together with $d(z)$), crucial dark energy observable. Statistically, detailed studies of a sample of 1000 clusters can constrain the growth factor to better than 0.5%, leading to constraints on w_0 to $\pm 0.06 - 0.08$ [10,19,7]. The primary contribution of Con-X to this work will be the precise calibration of cluster mass measurements.

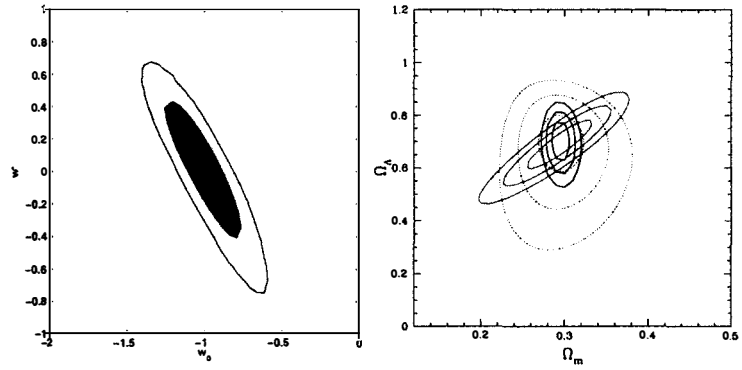

Figure 3: (left panel) Results from the analysis of simulated Con-X $f_{\rm gas}$+CMB data. The CMB data are WMAP TT data appropriate for 8 years of that mission [18]. The 68.3 and 95.4 per cent uncertainties in the (w_0, w') plane for the $w(a) = w_0 + 2w'(1-a)$ model are shown. No priors on $\Omega_{\rm b}h^2$, h or $\Omega_{\rm k}$ are assumed in the analysis. (right panel) The projected 1, 2 and 3 σ constraints for the Con-X X-ray+SZ experiment for the 500 cluster sample of Fig. 2 with 5% statistical errors in the predicted Compton y-values. The blue curve shows the result from the $f_{\rm gas}$ experiment, as in Fig. 1 (orange). The dotted red curve shows the results assuming a combined overall 2% systematic uncertainty in the normalization of the X-ray and SZ y-values and the solid red curve when the systematic uncertainty in this and h (combined) is reduced to 0.1%.

4 Conclusions

In terms of direct distance measurements the X-ray method provides similar accuracy to SNIa studies and has several advantages: (*i*) the physics of galaxy clusters can be well modelled with simulations; (*ii*) clusters can be revisited to improve the signal-to-noise for individual targets; (*iii*) the technique includes complementary constraints on $\Omega_{\rm m}$ from both the normalization and shape of the $f_{\rm gas}$ curve; (*iv*) the combination of $f_{\rm gas}$+CMB data breaks additional, key cosmological parameter degeneracies [13,14]; (*v*) The systematic scatter in the $f_{\rm gas}(z)$ is small (undetected and < 10% in current Chandra data); (*vi*) direct checks on the assumptions in the $f_{\rm gas}$ method, like the form of $b(z)$, are possible using the X-ray+SZ data. The $f_{\rm gas}$ and X-ray+SZ experiments also complement 'cluster counting' experiments excellently in that they (*i*) do not require complete samples but can simply 'cherry pick' the best clusters to work with, (*ii*) do not rely on crude calibration relations to link observables to mass, (*iii*) do not need to model the complex effects of cluster mergers on the observables.

Acknowledgments

This work was supported in part by the U.S. Department of Energy under contract number DE-AC02-76SF00515. SWA acknowledges support from the NASA through Chandra Award Number DD5-6031X issued by the Chandra X-ray Observatory Center.

References

1. S. W. Allen, R. W. Schimdt, A. C. Fabian, *Mon. Not. R. Astron. Soc.* **334**, L11 (2002)
2. S. W. Allen, R. W. Schmidt, H. Ebeling, A. C. Fabian, L. van Speybroeck, *Mon. Not. R. Astron. Soc.* **353**, 457 (2004)
3. S. W. Allen *et al*, 2006, in preparation
4. H. Ebeling, A. C. Edge, J. P. Henry *Astrophys. J.* **553**, 668 (2001)

5. H. Ebeling, A. C. Edge, H. Bohringer, S. W. Allen *et al Mon. Not. R. Astron. Soc.* **301**, 881 (1998)
6. V. R. Eke, J. F. Navarro, C. S. Frenk, *Astrophys. J.* **503**, 569 (1998)
7. Z. Haiman *et al*, 2005, astro-ph/0507013
8. E. Linder (for the SNAP collaboration), 2004, astro-ph/0406186
9. E. Linder, 2005, astro-ph/0507308
10. S. Majumdar, J. J. Mohr, *Astrophys. J.* **613**, 41 (2004)
11. S. M. Molnar, M. Birkinshaw, R. F. Mushotzky, *Astrophys. J.* **570**, 1 (2002)
12. S. M. Molnar, Z. Haiman, M. Birkinshaw M., R. F. Mushotzky, *Astrophys. J.* **601**, 22 (2004)
13. D. Rapetti, S. W. Allen, J. Weller, *Mon. Not. R. Astron. Soc.* **360**, 555 (2005)
14. D. Rapetti *et al*, 2006, in preparation
15. A. G. Riess *et al*, *Astrophys. J.* **607**, 665 (2004)
16. R. Schmidt, S. W. Allen, A. Fabian, *Astrophys. J.* **352**, 1413 (2004)
17. D. N. Spergel *et al*, 2006, astro-ph/0603449
18. A. Upadhye, M. Ishak, P. J. Steinhardt, *Phys. Rev.* D **72**, 063501 (2005)
19. A. Vikhlinin *et al*, 2005, White Paper to DETF
20. S. White, C. S. Frenk, *Astrophys. J.* **379**, 52 (1991)
21. S. White, G. Efstathiou, C. Frenk, *Mon. Not. R. Astron. Soc.* **262**, 1023 (1993)

VI – COMMON SESSION WITH QCD

PHYSICS AT THE INTERNATIONAL LINEAR COLLIDER

J. LIST
DESY, Notkestr. 85,
22607 Hamburg, Germany

The International Linear Collider (ILC) is the next large project in accelerator based particle physics. It is complementary to the LHC in many aspects. Measurements from both machines together will finally shed light onto the known deficiencies of the Standard Model of particle physics and allow to unveil a possible underlying more fundamental theory. Here, the possibilities of the ILC will be discussed with special emphasis on the Higgs sector and on topics with a strong connection to cosmological questions like extra dimensions or dark matter candidates.

1 Introduction

The Standard Model of particle physics (SM) provides a unified and precise description of all known subatomic phenomena. It is consistent at the quantum loop level and it covers distances down to 10^{-18} m and times from today until 10^{-10} s after the Big Bang. Despite its success, the SM has some deficiencies which indicate that it is only the effective low energy limit of a more fundamental theory. These deficiencies comprise the absence of experimental evidence for the Higgs particle, its number of free parameters and their values, fine–tuning and stability problems above energies of about 1 TeV, and, last but not least, its ignorance of gravity. Furthermore, the SM contains no particle which could account for the cold dark matter observed in the universe.

There are good reasons to expect phenomena beyond the SM at the TeV scale, i.e. in the reach of the immediate generation of new accelerators. Any new physics which solves the hierarchy problem between the electroweak and the Planck scale needs to be close to the former. Experimental hints arise from the fits to electroweak precision data, which require either a Higgs boson mass below 250 GeV or something else which causes similar loop corrections. Furthermore, most cold dark matter scenarios based on the hypothesis of a weakly interacting massive particle favour masses of about 100 GeV.

If there are new particles "around the corner", the LHC is likely to discover them. The ultimate goal, however, is not only to discover new particles, but to measure their properties and interaction with high precision in order to pin down the underlying theory and to determine its parameters. In the unlikely case that the LHC will not find any new particles, the task of the ILC would be to measure the SM parameters with even higher precision than before in order to find out what is wrong with todays fits that point to a light Higgs and new physics at the TeV scale. In any case, an electron position collider will provide an invaluable tool complementary to the LHC.

2 The Accelerator

Due to the synchrotron radiation, whose power increases with the energy to the forth power, storage rings become impractical for electrons or positrons at energies significantly higher than those achieved at LEP. Thus, two linear accelerators, whose beams collide in the center, are the only way to realise electron positron collisions at center of mass energies of 500 GeV - 1 TeV. There is a worldwide consensus to build such a linear collider with the following parameters: The center of mass energy should be tunable between 200 and 500 GeV and upgradable to up to 1 TeV. The integrated luminosity for the first 4 years should be 500 fb^{-1} and the beams should be polarised to 80% for the electrons and up to 60% for the positrons. There should be two interaction regions and the experiments should run concurrently with the LHC.

In the 1990ies, several linear collider projects were developped; the first one to publish a technical design report including a full costing was the TESLA project in 2001. In the following years there was a competition between designs based on warm or superconducting technology. In 2004, an international agreement was achieved to use the superconducting technology, because of its high energy efficiency, the less stringent alignment tolerances, its use for the planned X-FEL at DESY and because its functionality has been demonstrated at the TESLA Test Facility at DESY. Since 2005, the Global Design Effort, lead by Barry Barish from Caltech, is coordinating the further design of the ILC. Its first achievement was a new common definition of the baseline parameters of the accelerator. The next steps will be the costing of the current design by the end of 2006 and a full engineering until 2008.

For a high luminosity machine as the ILC, also the experiments have to fulfill high demands on precision. Thus, in parallel to the design of the accelerator, the development of the different detector components and the optimisation of their combination is pursued with high intensity.

3 Higgs Physics

The last unobserved ingredient of the Standard Model of particle physics is the Higgs boson. It gives mass to the originally massless weak gauge bosons and to all quarks and charged leptons, and it is essential to keep the theory finite. The most characteristic property of this fundamental scalar field is that its couplings have to be proportional to the mass of the particles it interacts with – if the interaction with the Higgs field is indeed responsible for the mass generation.

If the SM Higgs boson exists, it will be discovered at the LHC once the data from about one year of running time have been analysed. The LHC experiments will also be able to measure quite precisely its mass and the ratios of couplings.

The ILC on the other hand would be a factory for Higgs bosons, with as many Higgs events expected per day as the LHC experiments collect per year. The high production rate and the clean environment of an electron positron collider will allow to determine very precisely the complete profile of the Higgs boson and thus to establish the Higgs mechanism experimentally and to prove that this new particle *really* is the SM Higgs boson. If it turns out that it is not, it might be one of several Higgs bosons appearing in alternative models, e.g. in Supersymmetry. Then it is even more important to analyse the profile of all accesible Higgs bosons in order to determine the type and the parameters of the underlying theory.

At the ILC, the SM Higgs boson will be produced by two processes Higgsstrahlung and WW fusion, whose Feynman diagrams and cross sections are shown in figure 1. The Higgsstrahlungs process, which dominates for center of mass energies up to about 300 GeV above the Higgs mass, provides the possibility of a decay mode independent mass measurement via the recoil mass against the Z^0 boson produced together with the Higgs, which even works for decays to invisible particles. In addition, the mass measurement has been studied in many decay channels of the Higgs boson. With the detectors planned for the ILC, precisions below 0.1% are achievable

over the mass range favoured by the SM. The WW fusion process is a unique tool for determining the total width of the Higgs boson even for low higgs masses, i.e. $m_H < 200$ GeV, by measuring the total WW fusion cross section and the branching ration BR($H \to WW^*$). At high masses, the Higgs is so broad that its width can be determined directly from its lineshape. The total width then gives access to all couplings via measuring the branching fractions. Figure 2 shows the expected precision for the different Higgs branching ratios. Especially disentangling decays to $b\bar{b}$, $c\bar{c}$ and gg is challenging and requires an excelent vertex detector.

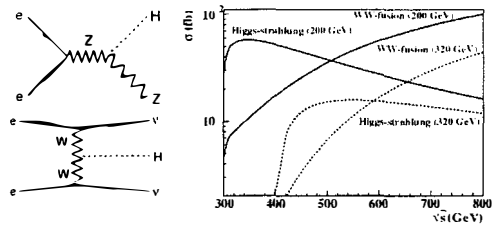

Figure 1: Left: Feynman diagrams for Higgsstrahlung (top) and WW fusion (bottom) Right: cross sections of the two processes as function of the center of mass energy for Higgs masses of 200 and 320 GeV.

The only coupling not accessible in decays is the top Higgs Yukawa coupling g_t due to the high mass of the top quark. At the ILC alone, one would need to collect 1000 fb^{-1} at 800 GeV to produce enough $e^+e^- \to t\bar{t}H$ events to reach a precision of 5% to 10% for g_t. A more elegant way to extract g_{ttH} would be to combine the rate measement of $q\bar{q}/gg \to t\bar{t}H$ (with the Higgs decaying further to $b\bar{b}$ or W^+W^-) from the LHC, which is proportional to $g_t^2 g_{b/W}^2$ with the absolute measurements of g_b and g_W from the ILC. The mass of the top quark is one of the most important SM parameters in order to check the overall consistency of the Higgs mechanism. With a scan of the production threshold, the top mass can be measured at the ILC to 50-100 MeV and its width to 3-5%.

The ultimate proof of the Higgs mechanism is the measurement of the Higgs self coupling λ, which allows to map the Higgs potential and check the relation between λ, the Higgs mass and its vacuum expectation value: $\lambda = m_H^2/2v^2$. This needs Higgsstrahlungs events, where the Higgs itself radiates off a second Higgs boson, which leads to 6-fermion final states, including 6-jet final states. These require an excellent jet energy resolution, much superior to for example the LEP detectors.

Once all Higgs parameters are measured, a global fit to all Higgs properties will answer the question if it really is the SM Higgs boson - or for example a supersymmetric one - even if no other new particle should be observed at the LHC. Even if other particles will have been already discovered, a careful analysis of the Higgs sector is essential to unveil the model beneath the new phenomena and to determine its parameters. Figure 2 shows the SM and some MSSM expectations in the g_t-g_W plane and the precisions achievable a the LHC and the ILC.

If Supersymmetry (SUSY) is realised in nature, there will be at least five physical Higgs bosons: two CP-even bosons h and H, similar to the SM one, a neutral, CP-odd boson A, and two charged Higgs bosons $H^\pm$. In contrast to the SM case, the Higgs masses are not free parameters, but depend in on other SUSY and SM paramcters. The lightest CP-even Higgs h, for example, must have a mass of less than about 135 GeV. Despite its large center of mass energy, there are regions in the SUSY parameter space where the LHC can see only one of the Higgs bosons, depending on the parameters of the Higgs sector, for example in maximal mixing scenario at intermediate values of $\tan\beta$. In these cases, the additional precision information from the ILC will be especially important.

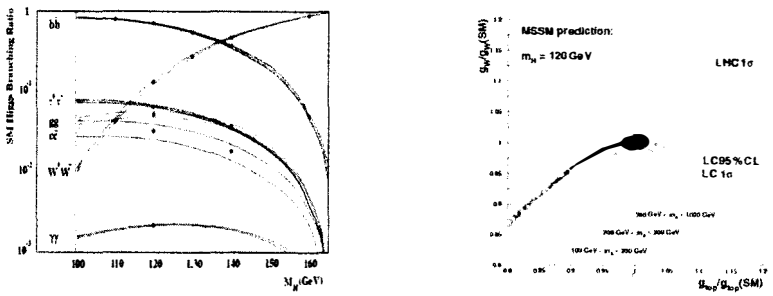

Figure 2: Left: Expected precision of the Higgs branching ratio measurements at the ILC as a function of the Higgs mass [1]. Right: SM and MSSM predictions for g_{ttH} vs g_{WWH} and expected precision of the corresponding LHC and ILC measurements [1].

At the ILC, associated hA and HA production allows very precise measurements of the SUSY Higgs bosons. As an example, figure 3 shows the reconstructed mass sum and difference for $HA \to 4b$ for masses of $m_H = 250$ GeV and $m_A = 300$ GeV at a center of mass energy of 800 GeV. The determination of the spin and the CP quantum numbers of the Higgs bosons via their threshold behaviour, their production angles or even via decays into τ pairs will then allow to disentangle the various Higgs bosons.

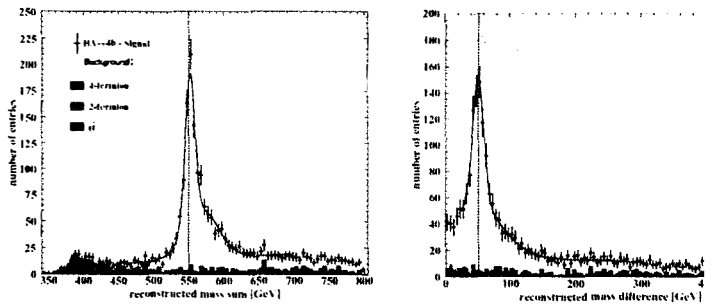

Figure 3: Reconstructed mass sum and difference for $HA \to 4b$ for masses of $m_H = 250$ GeV and $m_A = 300$ GeV at a center of mass energy of 800 GeV [1].

If there is no light Higgs boson found at the LHC, then the serious questions is: "what makes todays precision observables behave as if there were a light Higgs in the loops?" In this case, it is especially important to use the ILC's precision to probe virtual effects. For those, the sensitivity of the ILC reaches far beyond its center of mass energy into the multi–TeV range, in many cases substantially beyond even the LHC reach.

4 Dark Matter & Extra Dimensions

The notion of additional space-time dimensions appears in many theories beyond the Standard Model of particle physics. Especially models in which only gravity can propagate in the extra dimensions, while all other particles and interactions are confined in the usual four dimensional world, are very attractive because they could explain why gravity appears to be so much weaker than the other interactions. Inother words, it provides a solution to the problem of the large hierarchy between the electroweak and the Planck scale. If such a model is realised in nature,

then some of the gravitons produced at the ILC via $e^+e^- \to \gamma G$ will escape into the extra dimension, producing events with a photon and missing energy and momentum w.r.t. to the initial beam particles. The energy dependence of the cross section for this process is closely correlated to the number of extra dimensions δ. The main background for such processes is SM neutrino production with an additional hard initial state photon, which can be suppressed by one order of magnitude by chosing the right beam polarisations, allowing thus to determine the number of extra dimensions as shown in figure 4.

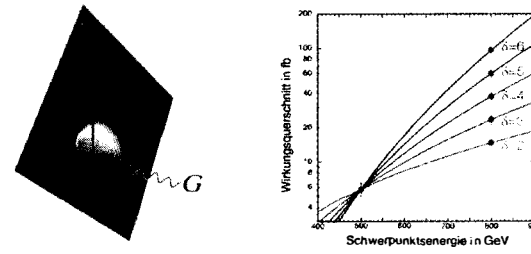

Figure 4: Left: Production mechanism for $e^+e^- \to \gamma G$, the graviton escapes into extra dimensions. Right: The cross section of this process as a function of the center of mass energy for different numbers of extra dimensions. The points with error bars indicate the precision of the ILC measurements [1].

Another intriguing topic for the ILC is the understanding of the dark matter which makes up 23% of our universe according to recent cosmological observations[2]. The Standard Model of particle physics does not contain a suitable candidate to explain this large amount. One type of candidates which is predicted in many models beyond the SM are weakly interacting massive particles (WIMPs). In Supersymmetry (SUSY) for example, the lightest supersymmetric particle (LSP) can be such a WIMP candidate, provided it is electrically neutral, not coloured and stable, i.e. if R–parity is conserved. In many SUSY scenarios the lightest neutralino plays this role, which would be discovered at the LHC. The observation and even the mass measurement alone however do not answer the question whether the LSP accounts for the dark matter in the universe. This can only be clarified when all relevant parameters of the model are determined, so that the cross section for all reactions of the WIMPs with themselves and/or other particles and thus the relic density can be calculated. This is illustrated in figure 5, which shows the calculated relic density as a function of the mass of the lightest neutralino in the so called LCC1 scenario. The yellow band shows the current knowledge of the relic density from the WMAP experiment, which is expected to be improved significantly by the Planck satellite in the future (green band). The scattered points result from a scan over the free parameters of this scenario, which can for the same LSP mass yield a large variation in the relic density. The light blue and dark blue boxes indicate the precision of the measurements at the LHC and ILC, respectively. It is evident that only the precision of the ILC can match in an appropriate way the precision of the cosmological observations.

Another unique opportunity for dark matter searches at the ILC opens up independently from specific models. By only assuming that WIMPs annihilate into SM particles, one can use the observed relic density and crossing symmetries to calculate an expected rate for WIMP pair production via $e + e^- \to \chi\chi$. The predicted rates[3] show that such events could be observed at the ILC by the detection of an additional hard initial state radiation photon, however further more detailed studies are needed.

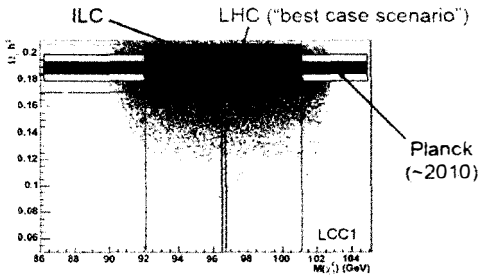

Figure 5: Dark matter relic density vs WIMP mass in the LCC1 SUSY scenario. Possible paramter choices are indicated as black dots, which are compared to the sensitivity of present and future measurements from satelite and accelerator based experiments[4].

5 Conclusions

New physics phenomena related to the electroweak symmetry breaking are likely to appear at the TeV scale and new particles will then be observed at the LHC. However, only high precision measurements can unveil the underlying theories at higher scales, as for example the question if the strong, electronmagnetic and weak couplings unify indeed near the GUT scale. Maybe the extrapolation of couplings and masses will be the only experimental clue to GUT scale physics.

The physics case for a (sub-)TeV electron positron collider running in parallel with the LHC is compelling. The ILC will be ideally suited to map out the profile of the Higgs boson – or what ever takes its role - and provide a telescopic view to physics at highest energy scales. Furthermore, the ILC will make significant contributions to the understandig of cosmological questions like the nature of dark matter. The detector for such a precision machine is a challenge. Conceptual detector design choices need to be made in a few years time and must be prepared now in parallel to the ongoing R&D for the single detector components.

Acknowledgments

I thank my colleagues Felix Sefkow and Klaus Desch for their valuable input to this talk.

References

1. R. D. Heuer, D. Miller, F. Richard, P. Zerwas (Editors), "TESLA Technical Design Report, Part III," http://tesla.desy.de/new_pages/TDR_CD/start.html.
2. D. N. Spergel *et al.*, arXiv:astro-ph/0603449.
3. A. Birkedal, K. Matchev and M. Perelstein, Phys. Rev. D **70** (2004) 077701.
4. J. Feng, "ILC Cosmology," arXiv:hep-ph/0509309.

Alexey Anisimov
EPFL
EPFL/SB/ITP/LPPC
BSP 720
1015 Lausanne
Switzerland
alexey.anisimov@epfl.ch

Reza Ansari
Université Paris-Sud
LAL Bâtiment 200
BP 34
91898 Orsay
France
ansari@lal.in2p3.fr

Stephen Appleby
Jodrell Bank Observatory
Macclesfield
Cheshire
SK11 9DL Macclesfield
UK
sappleby@jb.man.ac.uk

Irina Arefeva
Steklov Mathematical Institute
RAS
Gubkin St. 8
119991 Moscow
Russia
arefeva@mi.ras.ru

Yago Ascasibar
Astrophysikalisches Institut

An der Sterwarte 16
14482 Potsdam
Germany
yago@aip.de

Pierre Astier
LPNHE - Université de Paris
Tour 33 (RdCh)
4 place Jussieu
75005 Paris
France
pierre.astier@in2p3.fr

Tom Auld
Cavendish Laboratory
Dept of Physics
JJ Thomson Avenue
CB3 0HE Cambridge
UK
tauld@mrao.cam.ac.uk

Jonathan Aumont
LPSC

5 avenue des Martyrs
38026 Grenoble
France
aumont@lpsc.in2p3.fr

Myron Bander
University of California Irvine
Dept of Physics & Astronomy
Newport Beach Irvine
92697-4575 Irvine
USA
mbander@uci.edu

James Bartlett
APC

11 place Marcellin Berthelot
75005 Paris
France
bartlett@apc.univ-paris7.fr

Richard Battye
University of Manchester
Jodrell Bank Observatory
Lower Withington
SK11 9DL Macclesfield
UK
Richard.Battye@Manchester.ac.uk

Steven Beckwith
Space Telescope Science Institute

3700 San Martin Drive
21204 Baltimore
USA
svwb@stsci.edu

Maria Beltran
Universidad Autonoma de Madrid
Dept of Physics
Cantoblanco
28049 Madrid
Spain
maria.beltran@uam.es

Joël Berge
CEA Saclay
Dept Astrophysique
Orme des Merisiers - Bât 709
91191 Gif-sur-Yvette cédex
France
joel.berge@cea.fr

Lars Bergstrom
Stockholm University
Dept of Physics
AlbaNova University Centre
SE-10691 Stockholm
Sweden
lbe@physto.se

François Bouchet
IAP

98 bis bld Arago
75014 Paris
France
bouchet@iap.fr

Mariam Bouhmadi Lopez
University of Portsmouth
Institute of Cosmology & Gravitation
Mercantile House, Hampshire Terrace
mariam.bouhmadi@port.ac.uk

Michael Bridges
University of Cambridge
Cavendish Laboratory
JJ Thomson Avenue
CB3 0HE Cambridge
UK
mb435@cam.ac.uk

Martin Bucher
Université Paris-Sud
LPT
Bât 210
91045 Orsay
France
bucher@th.u-psud.fr

Yuriy Bunkov
CRTBT-CNRS

25 avenue des Martyrs
38042 Grenoble
France
yuriy.bunkov@grenoble.cnrs.fr

Clifford Burgess
McMaster University
Dept of Physics
1280 Main Street West
L8S 4M1 Hamilton, Ontario
Canada
cburgess@perimeterinstitute.ca

David Burke
Kavli Institute Particle Astroph.
Linear Accelerator Center
PO Box 20450, Kipac MS-29
94309 Stanford CA
USA
daveb@slac.stanford.edu

Carla Carvalho
IST
Dipartimento Fisica
Av. Rovisco Pais
1049-001 Lisbon
Portugal
ccarvalho@ist.edu

Luca Conversi
Universita la Sapienza
Dipartimento Fisica
Piazzale Aldo Moro 5
00161 Roma
Italy
luca.conversi@roma1.in n.it

Paolo De Bernardis
INFN La Sapienza
Dipartimento Fisica
Piazzale Aldo Moro 2
00185 Roma
Italy
paolo.debernardis@roma1.infn.it

Simone De Gregori
Universita la Sapienza
Dipartimento Fisica
Piazzale Aldo Moro 2
00185 Roma
Italy
simone.degregori@roma1.infn.it

Axel De La Macorra
University of Mexico
UNAM
Apdo. Postal 20-364
04100 Mexico City
Mexico
macorra@fisica.unam.mx

Jacques Delabrouille
APC

11 place Marcellin Berthelot
75231 Paris cédex 5
France
delabrouille@apc.univ-paris7.fr

Stefano Di Falco
INFN

Largo B. Pontecorvo 3
56100 Pisa
Italy
stefano.difalco@pi.infn.it

Jose M. Diego Rodriguez
IFCA
Dept of Cosmology
Avda Los Castros s/n
39005 Santander
Spain
jdiego@ifca.unican.es

Sandro Dodorico
ESO
Dept of Physics
K. Schwarzschildstrasse 2
85748 Garching
Germany
sdodoric@eso.org

Vyacheslav Dokuchaev
Laboratory del Gran Sasso
Institute for Nuclear Physics
60th Anniversary of October
Prospect 7a
117312 Moscow
dokuchaev@lngs.in n.it

Michael Doran
Heidelberg Universitaet
Institute fuer Theoretische Physik
Philisophenweg 16
69120 Heidelberg
Germany
M.Doran@gmx.de

Alan Duffy
University of Manchester
Jodrell Bank Observatory
Lower Withington
SK11 9DL Macclesfield
UK
ad@jb.man.ac.uk

Jacques Dumarchez
LPNHE - Université de Paris
Tour 33 (RdCh)
4 place Jussieu
75252 Paris cédex 5
France
jacques.dumarchez@cern.ch

Anne Ealet
CPPM
Case 902
163 avenue de Luminy
13288 Marseille cedex 09
France
ealet@cppm.in2p3. r

Khadija El Bouche ry
University of KwaZulu-Natal
School of Physics - Science Block
P6
Private Bag X01
3209 Pietermaritzburg
khadija@ukzn.ac.za

Céline Eminian
University of Sussex
Dept of Physics & Astronomy
Pevensey II
BN1 9QH Brighton
UK
C.Eminian@sussex.ac.uk

Torsten Ensslin
Max Planck Institute
Dept Astrophysik
Karl Schwarzschildstr. 2
85741 Garching
Germany
ensslin@mpa-garching.mpg.de

Pirin Erdogdu
University of Nottingham
School of Physics & Astronomy
University Park
NG7 2RD Nottingham
UK
Pirin.Erdogdu@nottingham.ac.uk

Orrin Fackler

USA

Enrique Fernandez
University A. Barcelona / IFAE
Campus UAB, Edif. Cn
08193 Bellaterra
Spain

enrique.fernandez@ifae.es

Dominique Fouchez
Centre de Physique des Particules
163 avenue de Lumigny
Case 902
13288 Marseille
France
fouchez@cppm.in2p3.fr

Ken Ganga
APC

11 place Marcellin Berthelot
75005 Paris
France
ganga@apc.univ-paris7. r

Bjorn Garbrecht
University of Manchester
School of physics & astronomy
Oxford Road
M13 9PL Manchester
UK
bjorn@hep.man.ac.uk

Yannick Giraud-Héraud
APC
Collège de France
11 place Marcellin Berthelot
75231 Paris
France
ygh@apc.univ-paris7.fr

Richard Holman
Carnegie Mellon University
Dept of Physics
5000 Forbes Avenue
15213 Pittsburg
USA
rh4a@andrew.cmu.edu

Tanya Larchenkova
Lebedev Physics Institute
Astro Space Centre
Leninsky Prospect 53
119991 Moscow
Russia
tanya@lukash.asc.rssi.ru

Ariel Goobar
Stockholm University
Dept of Physics
AlbaNova University Centre
10691 Stockholm
Sweden
ariel@physto.se

Natasha Hurley-Walker
Cavendish Laboratory
Dept of Physcis
JJ Thomson Avenue
CB3 0HA Cambridge
UK
nh313@cam.ac.uk

Anthony Lasenby
University of Cambridge
Cavendish Laboratory
Madingley Road
CB3 0HE Cambridge
UK
a.n.lasenby@mrao.cam.ac.uk

Keith Grainge
Cavendish Laboratory
Dept Astrophysics
Madingley Road
CB3 0HE Cambridge
UK
kjbg1@mrao.cam.ac.uk

Joerg Jaeckel
DESY
Dept of Physics
Notkestrasse 85
22603 Hamburg
Germany
jjaeckel@mail.desy.de

Bruno Leibundgut
ESO

Karl Schwarzschildstr. 2
85748 Garching
Germany
bleibundgut@eso.org

Claude Grillo
University of Milan
Dept of Physics
Via Celoria 16
20133 Milan
Italy
cgrillo@eso.org

Rachel Jeannerot
University of Leiden
Insitute Lorenz for Theoretical Physics
Niels Bohrweg 2
2333 CA Leiden
jeannerot@lorentz.leidenuniv.nl

Anthony Lewis
Cambridge University
Institute of Astronomy
Madingley Road
CB3 0HA Cambridge
UK
antony@cosmologist.info

Julien Guy
LPNHE - Université de Paris
Tour 33 (RdCh)
4 place Jussieu
75252 Paris cédex 5
France
guy@lpnhep.in2p3.fr

Bradley Johnson
University of Oxford
Dept of Astrophysics
Denys Wilkinson Building - Keble Road
OX13RH Oxford
bjohnson@astro.ox.ac.uk

Jon Loveday
University of Sussex
Astronomy Centre
Falmer
BN1 9QH Brighton
UK
J.Loveday@sussex.ac.uk

Lisa Hall
University of Sheffield
Dept of Applied Mathematics
Hicks Building - Hounsfield Road
S3 7RH Sheffield
UK
lisa.hall@sheffield.ac.uk

Sonia Karkar
LAPP
9 chemin de Bellevue
BP 110
74941 Annecy cédex
France
karkar@lapp.in2p3.fr

Melisa Luca
Institut de Physique Nucléaire MANOIR
4 rue Enrico Fermi
69100 Villeurbanne
France
luca@ipnl.in2p3.fr

Troels Haugbolle
Dark Cosmology Centre
Dept of Astrophysics
Juliane Maries Vej 30
2100 Copenhagen
Denmark
troels_h@astro.ku.dk

Georges Kohnen
Université Mons-Hainaut
Dept Physique Particules Elémentaires
20 place du Parc
7000 Mons
kohnen@umh.ac.be

Vladimir Lukash
Lebedev Physics Institute

Profsoyuznaya 84/32
117997 Moscow
Russia
lukash@asc.rssi.ru

Reece Heineke
University of Cambridge
Cavendish Laboratory
JJ Thomson Avenue
CB3 0HE Cambridge
UK
rh316@mrao.cam.ac.uk

Martin Landriau
University of Texas
Dept of Astronomy
1 University Station C1400
78712-0259 Austin, TX
USA
landriau@astro.as.utexas.edu

Vincent Lusset
CEA Saclay
DAPNIA/SPP
Bât 141
91191 Gif-sur-Yvette cédex
France
vincent.lusset@cea.fr

Alexander Lutovinov
Space Research Institute
Dept of Astrophysics
Profsoyuznaya 84/32
117997 Moscow
Russia
aal@hea.iki.rssi.ru

Christophe Magneville
CEA/DSM/DAPNIA/SPP
CEN Saclay
91191 Gif-sur-Yvette cédex
France

cmv@hep.saclay.cea.fr

Irit Maor
Case Western Reserve University
Dept of Physics
10900 Euclid Avenue
44106 Cleveland OH
USA
irit.maor@case.edu

Valerio Marra
Padua University
Dept of Physics
Via Marzolo 8
35131 Padova
Italy
valerio.marra@pd.infn.it

Carlos Martins
Faculta de Ciencias
Universidad do Porto
Rua do Campo Alegre 687
4169-007 Porto
Portugal
cmartins@fc.u.pt

Richard Massey
California Institute of Technology
Mail code 105-24
1200 E. California Blvd
91125 Pasadena CA
USA
RJM@ASTRO.CALTECH.EDU

Jason McEwen
University of Cambridge
Cavendish Laboratory
JJ Thomson Avenue
CB3 0HE Cambridge
UK
mcewen@mrao.cam.ac.uk

Elena Mikheeva
Lebedev Physics Institute

Profsoyuznaya 84/32
117997 Moscow
Russia
helen@asc.rssi.ru

Joe Mohr
University of Illinois
Dept of Astronomy
1002 West Green Street
61802 Urbana, IL
USA
jmohr@uiuc.edu

Palle Moller
ESO
Dept of Astronomy
K. Schwarzschildstrasse 2
85748 Garching
Germany
pmoller@eso.org

Marc Moniez
Université Paris-Sud
LAL Bâtiment 200
BP 34
91898 Orsay
France
moniez@lal.in2p3.fr

Adam Moss
Jodrell Bank Observatory
Lower Withington
SK11 9DL Macclesfield
UK

am@jb.man.ac.uk

Simon Muya Kasanda
University of KwaZulu-Natal
School of Mathematical Sciences
Desmond College Campus -
Howard College UKZN
4041 Durban
muyakasanda@nu.ac.za

Lavinia Nati
Universita la Sapienza
Dipartimento Fisica
Piazzale Aldo Moro 2
00185 Roma
Italy
lavinia.nati@roma1.infn.it

Federico Nati
Universita la Sapienza
Dipartimento Fisica
Piazzale Aldo Moro 2
00185 Roma
Italy
federico.nati@roma1.infn.it

Ishwaree Neupane
University of Canterbury
Dept of Physics & Astronomy
Private Bag 4800
8004 Christchurch
New Zealand
ishwaree.neupane@canterbury.ac.nz

Lap Nguyen Gia
Vietnam Academy of Science &
Technology
International Cooperation
Department
18 Hoang Quoc Viet Rd., Cau Giay
nglap@netnam.vn

Luan Nguyen Khoa

France

Eric Nuss
Université Montpellier II
LPTA - UMR 5207-CNRS-UM2
Place Eugène Bataillon CC070
34095 Montpellier
France
eric.nuss@lpta.in2p3.fr

Daniel O'Dea
Cambridge University
Cavendish Laboratory
Madingley Road
CB3 0HA Cambridge
UK
dto22@cam.ac.uk

Angiola Orlando
Cardiff University
Physics & Astronomy Dept
5 The Parade
CF24 3YB Cardiff
UK
angiola.orlando@astro.cf.ac.uk

Lyman Page
Princeton University
Jadwin Hall
Washington Rd
08544 Princeton
USA
page@princeton.edu

Cédric Pahud
University of Sussex
Dept of Physics & Astronomy
Pevensey II
BN1 9QH Brighton
UK
C.C.Pahud@sussex.ac.uk

Chloe Papineau
Université Paris-Sud
LPT Bât 210
91405 Orsay
France

chloe.papineau@th.u-psud.fr

Guillaume Patanchon
University of British Columbia
Henrings Building
6224 Agricultural Road
V6T 1Z1 Vancouver
Canada
patanch@phas.ubc.ca

David Rapetti
SLAC
KIPAC
382 Via Pueblo Mall
94305-4060 Stanford CA
USA
drapetti@slac.stanford.edu

Matts Roos
University of Helsinki
Dept of Physical Sciences
POB 64
FIN-00014 Helsinki
Finland
matts.roos@helsinki.fi

Stéphane Paulin-Henriksson
NAF OACt
Osservatorio Astrofisico
Via Santa Sofia 78
95123 Catania
Italy
paulin@in2p3.fr

Alexandre Refregier
CEA Saclay
Dept Astrophysique
Bâtiment 709
91191 Gif-sur-Yvette cédex
France
refregier@cea.fr

Graziano Rossi
University of Pennsylvania
Dept of Physics & Astronomy
209 South 33rd Street
19104 Philadelphia, PA
USA
graziano@astro.upenn.edu

Jeffrey Peterson
Carnegie Mellon University
Dept of Physics
5000 Forbes Avenue
15217 Pittsburg, PA
USA
jbp@cmu.edu

Nicolas Regnault
LPNHE - Université de Paris
Tour 33 (RdCh)
4 place Jussieu
75252 Paris cédex 5
France
nicolas.regnault@lpnhep.in2p3.fr

Martin Sahlen
University of Sussex
Dept of Physics & Astronomy
BN1 9QH Brighton
UK

m.sahlen@sussex.ac.uk

Christoph Pfrommer
University of Toronto
Dept of Theoretical Physics
60 St George Street
M5S 3H8 Toronto, Ontario
Canada
pfrommer@cita.utoronto.ca

Mathieu Remazeilles
Université Paris-Sud
LPT - Bât 210
91405 Orsay
France

Mathieu.Remazeilles@th.u-psud.fr

Havard Sandvik
Max Planck Institute
Dept of Astrophysics
85741 Garching
Germany

sandvik@mpa-garching.mpg.de

Sandrine Pires
CEA Saclay /Sap
Orme des Merisiers
91191 Gif-sur-Yvette cédex
France

sandrine.pires@cea.fr

James Rich
CEA Saclay
DAPNIA/SPP
91191 Gif-sur-Yvette cédex
France

rich@hep.saclay.cea.fr

Anna Scaife
University of Cambridge
Cavendish Laboratory
Madingley Road
CB4 0HA Cambridge
UK
as595@cam.ac.uk

Marieke Postma
NIKHEF

Kruislaan 409
1098 SJ Amsterdam
The Netherlands
mpostma@nikhef.nl

Paul L. Richards
University of California
Dept of Physics
94720-7300 Berkeley, CA
USA

richards@physics.berkeley.edu

Christoph Schmid
ETH Federal Institut of Techno
Dept Theoretical Physics
ETH Hoenggerberg
8093 Zurich
Switzerland
chschmid@itp.phys.ethz.ch

Claudia Quercellini
Astronomical Observatory of Rome
Via di Frascati 33
Mone Porzio Catone
00040 Roma
claudia@mporzio.astro.it

Rogers Ritter
University of Virginia
Dept of Physics
382 McCormick Road
22911 Charlottesville
USA
rcr8r@virginia.edu

Sanjeev Seahra
University of Portsmouth
Institute of Cosmology & Gravitation
Mercantile House, Hampshire Terrace
sanjeev.seahra@port.ac.uk

Nutan Rajguru
Cardiff University

5 The Parade
CF24 3YB Cardiff
UK
nutan.rajguru@astro.cf.ac.uk

Simon Robbins
Bergische Universitaet

Gaussstr. 20
42199 Wuppertal
Germany
robbins@physik.uni-wuppertal.de

Bruno Serfass
University of Berkeley
Dept of Physics
Leconte Hall 366 - 7300
94720 Berkeley, CA
USA
serfass@cosmology.berkeley.edu

Paolo Serra
University la Sapienza
Dept Cosmology
Piazzale Aldo Moro 5
00185 Roma
Italy
paolo.serra@roma1.infn.it

Huitzu Tu
University of Aarhus
IFA
Ny Munkegade Bld 1520
8000 Aarhus
Denmark
huitzu@phys.au.dk

Joseph Zuntz
mperial College
Dept of Astrophysics
Prince Consort Road
SW7 2AZ London
UK
jaz@imperial.ac.uk

Joe Silk
University of Oxford
Dept of Physics
Denys Wilkinson Building - Keble Road
OX13RH Oxford
silk@astro.ox.ac.uk

Jussi Valiviita
University of Portsmouth
nstitute of Cosmology & Gravitation
Mercantile House, Hampshire Terrace
jussi.valiviita@port.ac.uk

Jonathan Zwart
University of Cambridge
Cavendish Astrophysics
JJ Thomson Avenue
CB3 0HA Cambridge
UK
jtlz2@mrao.cam.ac.uk

Krzysztof Sliwa
Tufts University
Science and Technology Center
4 Colby Street
02155 Medford
USA
krzysztof.sliwa@tufts.edu

Karel Van Acoleyen
IPPP - University of Durham
Dept of Physics
South Road
DH1 3LE Durham
UK
karel.van-acoleyen@durham.ac.uk

Philippe Spindel
Université Mons-Hainaut
Mécanique & Gravitation
20 place du Parc
7000 Mons
Belgium
philippe.spindel@umh.ac.be

Marcella Veneziani
Collège de France
Dept of Astrophysics
11 place Marcellin Berthelot
75005 Paris
France
marcella.veneziani@apc.univ-paris7.

Jack Steinberger
CERN

1211 Geneva
Switzerland

Jack.Steinberger@cern.ch

Matteo Viel
University of Cambridge
nstitute of Astronomy
Madingley Road
CB3 0HA Cambridge
UK
viel@ast.cam.ac.uk

Christoph Stephan
Centre de Physique Thérique
Campus de Lumigny
Case 907
13288 Marseille
France
christoph.stephan@cpt.univ-mrs.fr

Alexander Vikman
Ludwig Maximilians Universitaet
Dept of Cosmology
Theresienstr. 37
80333 Muenchen
Germany
vikman@theorie.physik.uni-muenche

Jeremy Taylor
University of Cambridge
Cavendish Laboratory
JJ Thomson Avenue
CB3 0HE Cambridge
UK
j.taylor@mrao.cam.ac.uk

Jochen Weller
University College London
Dept of Physics & Astronomy
Gower Street
WC1E 6BT London
UK
jochen.weller@ucl.ac.uk

Jean Tran Thanh Van
Université Paris-Sud
LPT
Bât 210
91405 Orsay
France
moriond@wanadoo.fr

Simon White
Max Planck Institute
Dept fuer Astrophysik
Karl Schwarzschildstr. 2
85740 Garching
Germany
swhite@mpa-garching.mpg.de